Transactions of the ASME, Journal of Engineering for Gas Turbines and Power (ISSN 0742-4795) is published quarterly (Jan., April, July, Oct.) for $175.00 per year by The American Society of Mechanical Engineers, 345 East 47th Street, New York, NY 10017. Second class postage paid at New York, NY and additional mailing offices. POSTMASTER: Send address changes to Transactions of the ASME, Journal of Engineering for Gas Turbines and Power, c/o THE AMERICAN SOCIETY OF MECHANICAL ENGINEERS, 22 Law Drive, Box 2300, Fairfield, NJ 07007-2300.

CHANGES OF ADDRESS must be received at Society headquarters seven weeks before they are to be effective. Please send old label and new address.

PRICES: To members, $40.00, annually: to nonmembers, $175.00. Add $30.00 for postage to countries outside the United States and Canada.

STATEMENT from By-Laws. The Society shall not be responsible for statements or opinions advanced in papers or ... printed in its publications (B7.1, par. 3).

INDEXED by Applied Mechanics Reviews and Engineering Information, Inc. Canadian Goods & Services Tax Registration #126148048

Journal of Engineering for Gas Turbines and Power

Published Quarterly by The American Society of Mechanical Engineers

VOLUME 117 • NUMBER 4 • OCTOBER 1995

TECHNICAL PAPERS

(Contents continued on page 694)

(Contents continued)

Journal of Engineering for Gas Turbines and Power

Biographies

This issue of the JOURNAL OF ENGINEERING FOR GAS TURBINES AND POWER contains two noteworthy papers. "Combined Power Plants—Past, Present, and Future," by Dr. John Horlock, was presented as the Calvin Rice Award Lecture at ASME Cogen Turbo Power '94, held in Portland, Oregon, October 25–27, 1994. "The Role of Fuel Preparation in Low-Emission Combustion (ASME Paper No. 95-GT-465)," by Professor Arthur H. Lefebvre, was presented as the IGTI Scholar Award Lecture at ASME Turbo Expo '95, the 40th Gas Turbine and Aeroengine Conference, Houston, Texas, June 5–8, 1995. Biographies of these two authors are presented below.

The Rice Lecture was founded in 1934 to honor Calvin W. Rice, who served as secretary of the ASME from 1906 to 1934. The award is intended to increase understanding among engineers worldwide, an activity for which Mr. Rice was well known. The 1994 recipient, Dr. John Horlock, is an international authority on power cycles and on gas turbine engine components, including compressors and turbines. He is well known for his numerous and useful technical books, papers, and lectures on these subjects. He is very active as an author, lecturer, and consultant. Dr. Horlock is also a renowned educator. Earlier in his career, he served on the faculties at M.I.T. and Penn State in the United States, and Liverpool and Cambridge in the United Kingdom. At Cambridge University, he established the Whittle Laboratory as its first director. In 1974, he accepted the post of Vice Chancellor at the University of Salford and in 1981, he began his decade-long leadership of the U.K.'s Open University.

The title of "International Gas Turbine Institute Scholar" is awarded to a person with a significant depth of knowledge in some aspect of gas turbine technology. The 1995 Scholar, Professor Arthur H. Lefebvre, is internationally known for his work on gas turbine combustion and has recently retired from the position of Reilly Professor of Combustion Engineering at Purdue University. Previously, he was head of the School of Mechanical Engineering at Purdue, and at the Cranfield Institute of Technology in the United Kingdom. Professor Lefebvre spent 10 years working in industry with Rolls-Royce. The author of three books and many technical papers on different aspects of gas turbine combustion, Professor Lefebvre holds several patents on the subject. He was the honored recipient of the ASME Gas Turbine Award in 1982 and the prestigious R. Tom Sawyer Award in 1984.

Dr. John Horlock

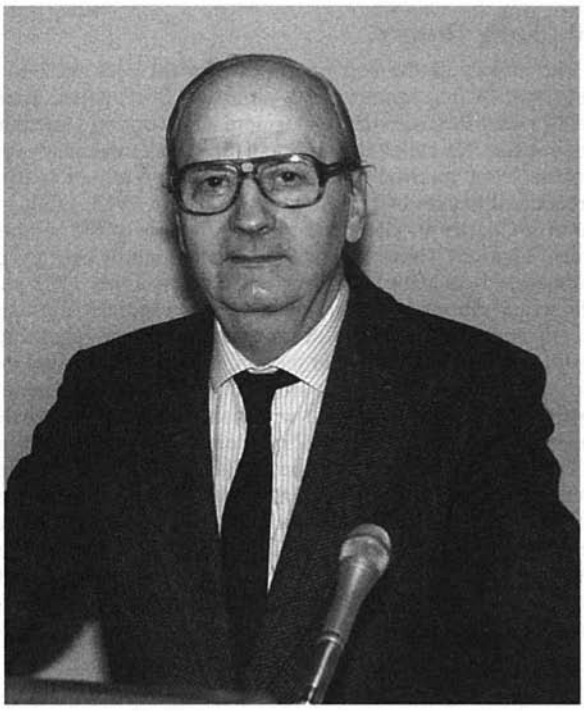

Professor Arthur H. Lefebvre

The 1994 Calvin Winsor Rice Lecture

Combined Power Plants—Past, Present, and Future

J. H. Horlock
Whittle Laboratory,
Cambridge, United Kingdom

The early history of combined power plants is described, together with the birth of the CCGT plant (the combined "cycle" gas turbine). Sustained CCGT development in the 1970s and 1980s, based on sound thermodynamic considerations, is outlined. Finally more recent developments and future prospects for the combined gas turbine/steam turbine combined plant are discussed.

1.0 Introduction

The Calvin Winsor Rice lecture was founded in 1934 to honor the man who had served as Secretary of the American Society of Mechanical Engineers for 28 years. Rice was born into a Massachusetts family, which over the generations produced a number of engineers. He graduated from MIT in 1890, and after work as a consulting electrical engineer, was appointed Secretary of ASME in 1906. The Council of the Society was attracted to Rice because of his experience in the important new field of electric power generation—"an engineer of high standing in practical engineering work"—and his major contributions to the ASME are well illustrated in the centennial history of the Society. This lecture was established to further the objective for which Calvin W. Rice was well known, increased understanding among engineers of various countries.

There can be few better illustrations of a major international engineering activity than the development of the combined power plant. Although it has not been a collaborative effort, it has involved parallel development in many countries, calling on expertise from other engineering fields, such as the aircraft engine industry.

2.0 Early History

The history of the combined power plant goes back to the early part of this century. In a seminal ASME paper, Emmet (1925) described substantial development work on a mercury–steam plant. He called the system "the Emmet mercury–vapor process" but referred back to an earlier presentation to the American Institute of Electrical Engineers in 1913, linking the name of Charles Bradley to the basic principle of the combined cycle. Figure 1 shows a combined temperature–entropy diagram, based on ideal vapor cycles, taken from his 1925 paper (the steam entropy has been scaled). Emmet initially considered superheating of the lower steam cycle and ideal regenerative heating within that cycle, but the figure shows his second more conventional proposal, with similar pressure and temperature levels, a Rankine steam cycle with no feed heating, and consequently a slightly lower overall efficiency (yet still 54 percent).

The early development of the gas/steam turbine plant came somewhat later and was described by Seippel and Bereuter (1960). They showed seven possible combinations of gas turbine and steam turbine plant, two of which are illustrated here. The first (Fig. 2) has developed as the major form of CCGT plant, although not now with supplementary heating of the gas turbine exhaust. The second (Fig. 3) shows the original concept of the pressurized boiler in which the gas turbine compressor charges the steam boiler (the Velox system developed by Brown Boveri in the 1930s). Other proposals by Seippel and Bereuter were not developed, but a useful more modern classification has been given by Wunsch (1978) and is shown in Fig. 4.

By the 1970s the so-called "recuperative" plant [a higher level gas turbine, exhausting to a heat recovery steam generator (HRSG), which supplies steam to the lower (steam turbine) cycle, with no supplementary heating of the exhaust] had become well established, primarily by General Electric and Westinghouse in the United States and by Brown Boveri in Europe. Wood (1971) was able to give a list of some 40 such plants (mostly small, in the range 15–20 MW) installed in the United States, mainly with unfired exhausts and with single pressure steam cycles. But one of the biggest, a combined heat and power plant for Dow Chemical in Texas, produced 63 MW (43 MW from the gas turbines and 20 MW from the steam turbines) was an exception in that it used supplementary firing of the gas turbine exhaust to provide steam at 1200 psia, 950°F, exhausting to process at 185 psia; Wood quotes its nominal efficiency as 41 percent. In Europe the original Brown Boveri Korneuberg A plant in Austria was the biggest in service about that time (75 MW at nearly 33 percent overall efficiency) and this was also an example of a plant with supplementary firing of the HRSG.

The fully fired system, primarily replacing a conventional steam boiler with a main boiler in which the gas turbine exhaust was "supplementary fired," was less well advanced at this time, but major development followed in the mid-70s, for peak and base load operation.

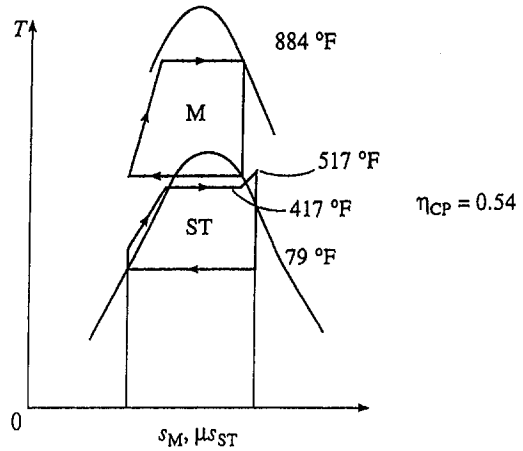

Fig. 1 Emmet's combined mercury (*M*) and steam (*ST*) cycle

Contributed by the International Gas Turbine Institute and presented at ASME Cogen Turbo Power '94, Portland, Oregon, October 25–27, 1994. Manuscript received by the International Gas Turbine Institute November 1994. Associate Technical Editor: H. L. Julien.

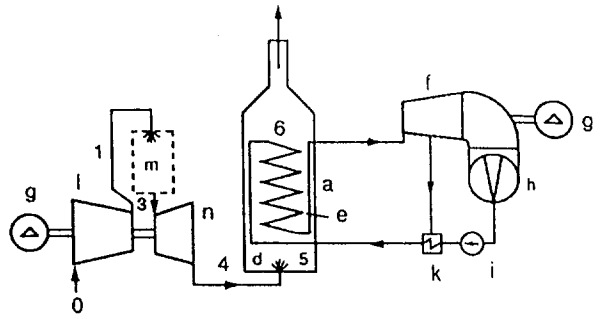

Fig. 2 Seippel/Bereuter combined cycle

Key:
(a) boiler
(c) air heater
(d) combustion chamber with burner
(e) steam part of boiler
(f) steam turbine
(g) generator
(h) condenser
(i) feed water pump
(k) feed water heater and de-aerator
(l) compressor
(m) combustion and swirl chamber
(n) gas turbine
1, 2, 3 . . . state points in higher cycle

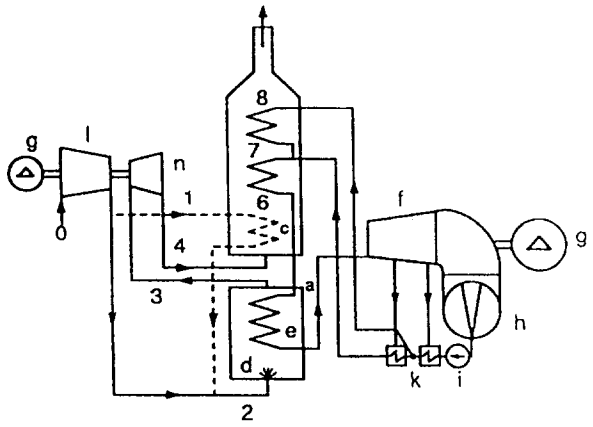

Fig. 3 Seippel/Bereuter Velox type combined cycle

Here we shall concentrate mainly on the recuperative system (unfired HRSG—the left-hand side of Fig. 4) and its variations. This is essentially the combined "cycle" gas turbine or CCGT (although the gas turbine is almost invariably an open plant rather than of closed-cycle form).

3.0 Some Elementary Thermodynamics

Before describing recent major CCGT developments, we consider the elementary thermodynamics of the combined power plant without supplementary heating [more detailed analyses are given in Horlock (1992)]. Figure 5 shows diagrammatically a higher cycle (H) receiving heat Q_B, doing work W_H at a thermal efficiency of η_H ($\eta_H = W_H/Q_B$), and rejecting heat Q_{HR} ($Q_{HR} = Q_B\{1 - \eta_H\}$) to a lower cycle ($L$), which has a work output of W_L at a thermal efficiency of η_L. However, between the cycles there is a heat loss Q_{UN} to the surroundings, so that the heat received by the lower cycle is

$$\begin{aligned} Q_L &= Q_{HR} - Q_{UN} \\ &= Q_B[1 - \eta_H] - Q_{UN} \\ &= Q_B[1 - \eta_H] - \nu_{UN}Q_B \end{aligned} \tag{1}$$

where ν_{UN} is the ratio of the unused heat Q_{UN} to the heat supplied Q_B.

The efficiency of the combined plant is therefore

$$\begin{aligned} \eta_{CP} &= \frac{W_H + W_L}{Q_B} \\ &= \eta_H \frac{Q_B + \eta_L[Q_B[1 - \eta_H] - \nu_{UN}Q_B]}{Q_B} \\ &= \eta_H + \eta_L - \eta_H\eta_L - \nu_{UN}\eta_L \end{aligned} \tag{2}$$

[A form of Eq. (2) was given in an ASME paper on the Field combined cycle (Horlock, 1957) but it is now understood by the author that a similar form had been derived earlier by Meyer of Westinghouse, and no doubt Emmet and his colleagues at

Nomenclature

c_p = specific heat at constant pressure
$c[i, N]$ = defined in text
CAP = annual capital cost
C_0 = initial capital cost
CV = calorific value
F = fuel energy
H = utilization, h/year
i = interest, discount rate
k, K = const
M = annual fuel costs
n = referring to nth year
N = total years
P = price
q, Q = heat
OM = annual operational and maintenance cost
r = pressure ratio
R = miscellaneous charge rates (on capital)
S = fuel price per unit mass
t = tax rate
T = temperature
Y = unit cost
w, W = work
α = fraction (of capital)
β = capital charge rate
γ = ratio of specific heats
$\epsilon = r^{(\gamma-1)/\gamma}$
ζ = fuel price per unit of energy
η = efficiency
θ = temperature ratio
ν = ratio of heat quantities

Subscripts

B = supplied (heat), boiler
C = compressor
CP = combined plant
CPE = for pressure ratio at maximum efficiency
CR = credit rate
d = debt
DT = referring to Daudet and Trimble
e = equity
E = electricity
EX = turbine exit
H = higher cycle
HE = for pressure ratio at maximum efficiency
HR = rejected (heat)
HW = for pressure ratio at maximum specific work
L = lower cycle
max = maximum
min = minimum
O = overall (efficiency)
P = pinch point
T = turbine
UN = unused (heat)
W = referring to Williams

Superscripts

$'$ = nondimensional
$\cdot$ = rate

Note: Specific quantities are denoted by lower case.

GE were well aware of the relationship between the two cycle efficiencies].

This expression for the thermal efficiency of the combined cycle plant may also be written in terms of a "boiler efficiency" (η_B) of the heat exchange process between the two cycles (the heat recovery steam generator, or HRSG, for the gas turbine/steam turbine plant). We may define η_B as

$$\eta_B = \frac{Q_L}{Q_{HR}} = \frac{Q_{HR} - Q_{UN}}{Q_{HR}} = 1 - \frac{[Q_{UN}/Q_B]}{[Q_{HR}/Q_B]}$$

$$= 1 - \frac{\nu_{UN}}{[1 - \eta_H]} \tag{3}$$

Equation (1) may then be written as

$$\eta_{CP} = \eta_H + (\eta_L Q_L)/Q_B$$

$$= \eta_H + \eta_L \eta_B (Q_{HR}/Q_B)$$

$$= \eta_H + \eta_B \eta_L - \eta_B \eta_L \eta_H \tag{4a}$$

$$= \eta_H + (\eta_O)_L - \eta_H (\eta_O)_L \tag{4b}$$

where $(\eta_O)_L = \eta_B \eta_L$ is the overall efficiency of the lower plant, including the HRSG.

We may illustrate this elementary thermodynamic analysis for a practical operating station, the Brown Boveri 125 MW combined gas turbine/steam turbine plant, Korneuberg B (Czermak and Wunsch, 1982). The gas turbine develops some 81 MW and the steam turbine about 49 MW. The efficiency of the gas turbine, with a "heat supplied" of some 276 MW (based on the lower calorific value of the fuel), is about 0.29.

The temperature of the gas turbine exhaust is 491°C, and this gas raises steam in the HRSG for a two pressure level steam turbine cycle. It leaves the HRSG at the low temperature of 96°C, which is permissible for the natural gas fuel with low sulfur content, and the energy loss in the exhaust is therefore restricted to about 34 MW. The ratio

$$\nu_{UN} = \frac{\text{Heat unused}}{\text{Heat supplied}} \approx \frac{34}{276} = 0.12,$$

and the HRSG boiler efficiency is

$$\eta_B = 1 - \frac{0.12}{[1 - 0.29]} = 1 - \frac{0.12}{0.71} = 0.83.$$

The steam plant thermal efficiency is approximately 0.32 and the overall lower plant efficiency is therefore

$$(\eta_O)_L = 0.32 \times 0.83$$

$$= 0.27,$$

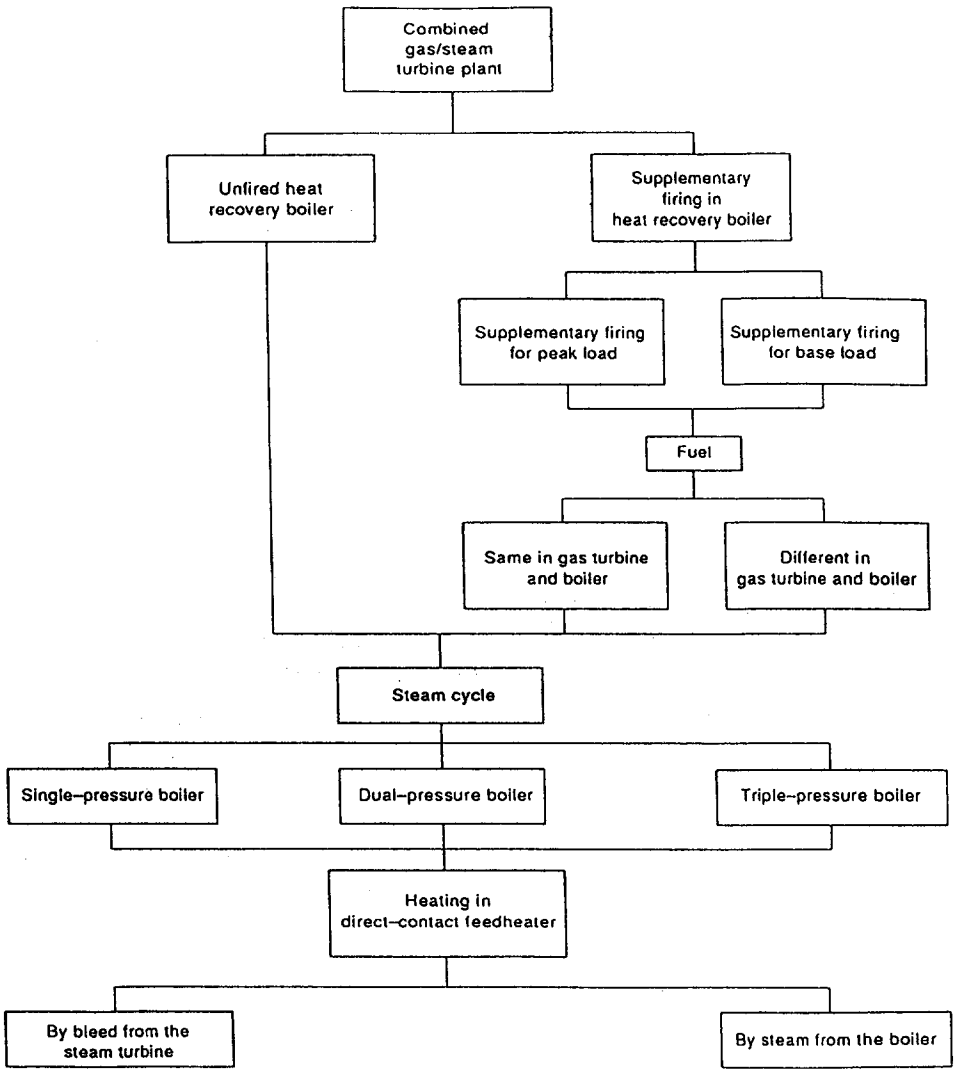

Fig. 4 Wunsch's classification of CCGT plants

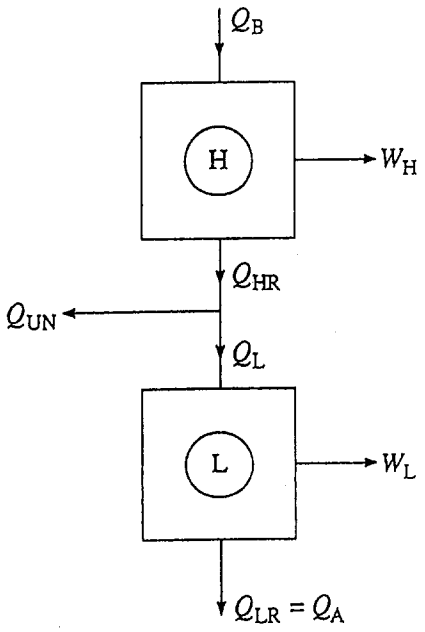

Fig. 5 Simple combined cycle

so the combined plant efficiency is

$$\eta_{CP} = \eta_H + \eta_L - \eta_H\eta_L - \nu_{UN}\eta_L$$
$$= 0.29 + 0.32 - 0.29 \times 0.32 - 0.12 \times 0.32$$
$$= 0.61 - 0.093 - 0.038$$
$$= 0.48,$$

or

$$\eta_{CP} = \eta_H + (\eta_O)_L - \eta_H(\eta_O)_L$$
$$= 0.29 + 0.27 - 0.29 \times 0.27$$
$$= 0.48$$

This discussion may be used to illustrate the important thermodynamic features of the combined power plant, and consequently the way it has been developed. Referring back to the mercury steam plant, it had two major thermodynamic advantages:

(*i*) most of the heat supplied was near the maximum temperature T_{max} (mainly to the mercury boiler);
(*ii*) most of the heat rejected was near to the lowest (ambient) temperature T_{min}.

The overall efficiency of this form of combined power plant should therefore approach Carnot efficiency (for the particular maximum/minimum temperature ratio). There was little heat loss between the mercury and steam cycles and little additional irreversibility (low loss of exergy) because of temperature difference between the two fluid streams in the condenser/boiler. It was a very attractive plant thermodynamically; the great Swiss engineer Stodola was enthusiastic about the Emmet cycle in his book on steam and gas turbines (1924).

These mercury/steam plants were magnificent engineering achievements [for example the Schiller plant in New Hampshire (Hackett, 1951)]. But they proved to be uneconomical in comparison with conventional steam plants, which were gaining in efficiency as steam pressures and temperature were increased.

The developing gas turbine/steam turbine CCGT plant was more feasible practically. It shared with the mercury/steam plant the feature of low-temperature heat rejection, but its "heat" supply was not all near the maximum temperature. There were also irreversibilities in the heat exchange in the HRSG (due to large temperature differences between the two fluid streams), and there was energy loss in gases discharged from the exhaust stack.

4.0 More Recent Developments

We next discuss the "recuperative" combined "cycle" gas turbine [CCGT] plant in more detail, noting the emphasis placed on necessary developments, highlighted by the earlier discussion of the basic thermodynamics:

(*i*) raising the mean temperature of heat supply;
(*ii*) minimizing the irreversibility within the heat recovery steam generator;
(*iii*) keeping the heat loss between the two plants as low as possible.

These main themes of development have been apparent since the 1970s, and we consider them separately here.

4.1 Increasing the Mean Temperature of Heat Supply in the Gas Turbine. Increasing the mean supply temperature can be achieved in three ways: by raising the top temperature (at entry to the gas turbine); less effectively, by supplementary heating after the full turbine expansion; by reheating within the turbine expansion. The first has been the dominant feature, partly through the use of aircraft engine technology in the cooling of the gas turbine blading. The second was a feature of early development, but as the turbine entry temperature has been raised, so the benefits of supplementary heating of the turbine exhaust have lessened [see Davidson and Keeley (1990)] and it has not been used widely in recent plant designs. The third has been advocated strongly by Rice (1980), and it has recently been put into practice (in the ABB GT24/26 plant).

Figure 6[1] shows how overall (net) efficiency of the basic recuperative CCGT plant has improved with increasing maximum temperature, over the past 20–25 years; also shown is the parallel increase in specific work of the higher (gas turbine) plant, which it has been argued [e.g., Timmermans (1978)] is the important feature in increasing overall plant efficiency. Figure 7, from Davidson and Keeley, shows how the optimum efficiency of a CCGT plant occurs quite close to the pressure ratio for maximum specific work in the higher (gas turbine) plant. There is ample evidence that designers have indeed sought maximum overall efficiency by optimizing at a relatively small pressure ratio (10–14), rather than the larger values required for maximum higher (gas turbine) efficiency. A plot of pressure ratios used in various plants is shown in Fig. 8, together with the values obtained from "air standard" cycle analysis (for a constant ratio of gas specific heats, $\gamma = 1.4$) to give maximum efficiency and maximum specific work respectively in the higher (gas turbine) plant. The design pressure ratios used are much lower than those that would have given maximum efficiency in the (higher) gas turbine plant (r_{HE}) and closer to those which would give maximum specific work (r_{HW}).

The reason for this choice of low pressure ratio is illustrated by an approximate analysis [Horlock (1995a), which extends a graphic method of calculating gas turbine performance developed by Hawthorne and Davis (1956)]. If the higher plant is assumed to operate on an air standard cycle (i.e., the working fluid is a perfect gas with a constant ratio of specific heats, γ), then the compressor work, the turbine work, the net work output, and the heat supplied may be written as

[1] Net [LHV] efficiencies and maximum temperatures obtained from brochures and journals, for ISO standard conditions. The maximum temperatures quoted are usually first rotor inlet temperatures (i.e., burner outlet temperatures reduced by cooling of the first stator row).

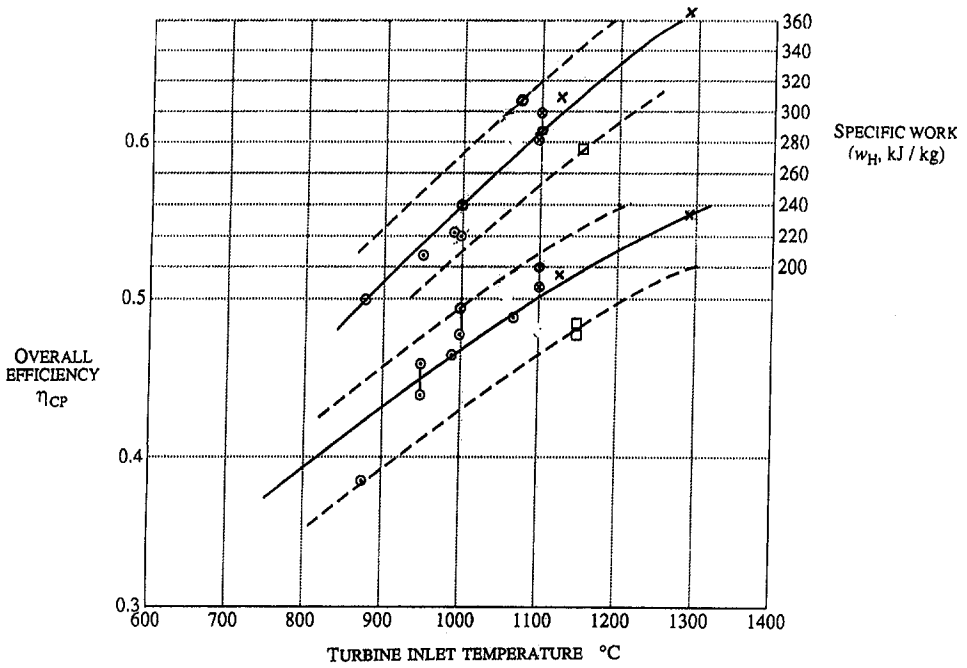

Fig. 6 Recent plants: overall net efficiency and specific work (various symbols indicate different manufacturers)

$$w'_C = (\epsilon - 1)/\eta_C(\theta - 1) \tag{5}$$

$$w'_T = \eta_T\theta(\epsilon - 1)/\epsilon(\theta - 1) \tag{6}$$

$$w'_H = w'_T - w'_C \tag{7}$$

$$q'_H = (1 - w'_C) \tag{8}$$

respectively, where the primes indicate that all are have been made nondimensional by dividing by the product of the gas flow rate and $c_p(T_{max} - T_{min})$. These quantities are plotted against $\epsilon = r^{(\gamma-1)/\gamma}$ in Fig. 9, constant values being assumed for $\theta = (T_{max}/T_{min}) = 5.0$, and compressor and turbine efficiencies ($\eta_C = 0.9$, $\eta_T = 0.889$, $\eta_C\eta_T = 0.8$).

Timmermans (1978) suggested that the steam turbine work output (per unit gas flow in the higher plant) is given approximately by

$$w_L = Kc_p(T_{EX} - T_P) \tag{9}$$

where T_{EX} is the temperature at gas turbine exit, T_P is the temperature in the HRSG at the lower pinch point, and K is a constant. The (nondimensional) steam turbine work may then be written

$$w'_L = K(T_{EX} - T_P)/(T_{max} - T_{min}) \tag{10}$$

and the total (nondimensional) work output from the combined plant becomes

$$w'_{CP} = (1 - K)w'_H + Kq'_H - k \tag{11}$$

where $k = K[(T_P/T_{min}) - 1]/(\theta - 1)$ is a small quantity and

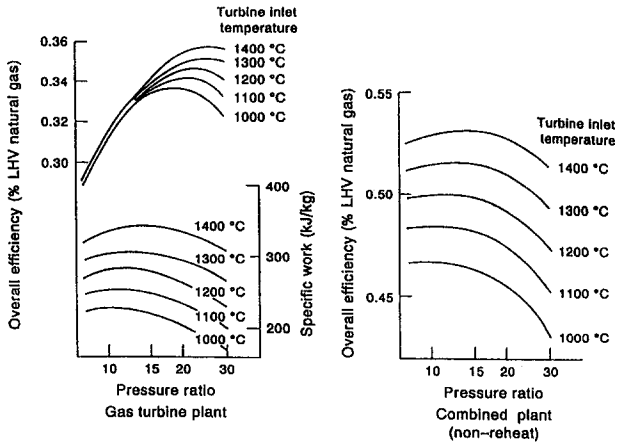

Fig. 7 Efficiency of gas turbine and combined plants

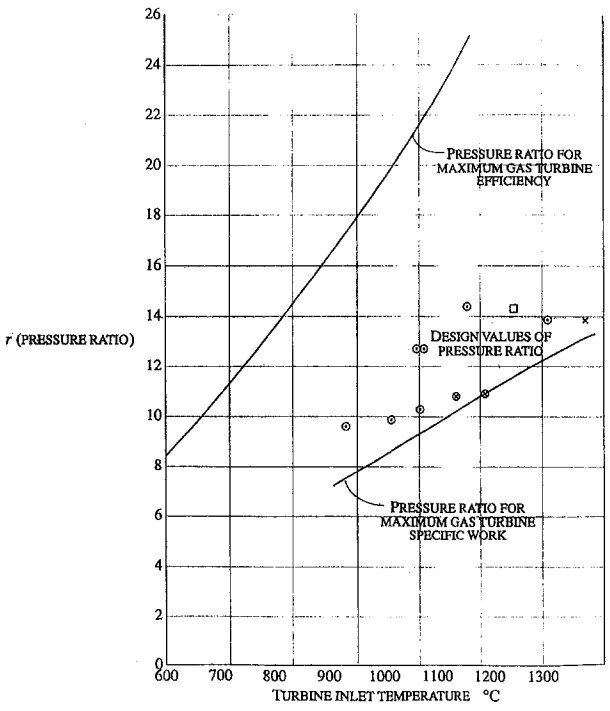

Fig. 8 Combined plants: pressure ratios (various symbols indicate different manufacturers)

may for an approximate analysis be taken as constant ($k = 0.06$ has been assumed in Fig. 9).

As for the gas turbine cycle, the pressure ratio for maximum efficiency in the combined plant (r_{CPE}) may be obtained by drawing a tangent to the work output curve from a point on the ϵ axis, where $\epsilon = 1 + \eta_C(\theta - 1)$, i.e., $\epsilon = 4.6$ in the example. It is seen that because the curve for w'_{CP} lies above that for w'_H, the optimum pressure ratio for the combined plant ($r_{CPE} \approx 18$) is less than that for the gas turbine alone ($r_{HE} \approx 30$) although it is still greater than the pressure ratio, which gives maximum specific work in the higher plant ($r_{HW} \approx 11$). However, the efficiency η_{CP} varies little with ϵ about the optimum point, and design pressure ratios may be set close to r_{HW} with little penalty on overall efficiency.[2]

The latest ABB GT24/26 CCGT represents a departure from this practice of designing for relatively small pressure ratio in the higher plant. It employs reheat between the HP and LP turbine, which together expand through a much larger pressure ratio (30:1). There are two thermodynamic features of this type of design. Firstly the staged expansion through the larger pressure ratio means that the temperature leaving the LP turbine is not increased substantially in comparison with nonreheated plants (about 600°C cf 530°–500°C); and second that the pressure ratio for maximum η_{CP} becomes closer to that for maximum efficiency in the higher plant alone. An extension of the approximate analysis outlined above suggests that the pressure ratio for both the combined and higher level plants should now be about 48, for unchanged values of maximum to minimum temperature ratio and turbine and compressor efficiencies, and assuming reheat to the maximum temperature. However, the efficiency curves are very flat and there is little penalty on efficiency in choosing lower design pressure ratios.

4.2 Minimizing the Irreversibility in the HRSG. Minimizing the irreversibility in the HRSG has also been a dominant feature in the development of CCGT plants, through double pressure and even triple pressure steam raising. [It is of interest to the thermodynamicist that the basic expressions for combined plant efficiency (Eqs. (2) and (4)) are still valid even when there are such exergy losses due to temperature differences within the HRSG, although the efficiency of the lower plant appearing in the equations is now smaller]. It is, however, somewhat surprising that the degree of sophistication associated with triple pressure steam raising has been worthwhile, because thermodynamic calculations illustrate that the gains in overall efficiency are not very large. For example, the initial work of Manfrida and Manucci (1986) suggested that the gain in overall efficiency in going to double pressure steam raising from a single pressure steam plant was not substantial, although their subsequent calculations indicated a somewhat greater benefit. Tomlinson et al. (1993) suggest that while a gain of nearly 4 percent comes from changing from single to dual pressure steam raising, the further gain by moving from dual pressure to triple pressure yields only about 1 percent.

The Kalina cycle, in which a mixture of ammonia and water is used in the lower cycle, offers worthwhile reduction in the irreversibility in the heat transfer from the higher plant [see discussion in Horlock (1992)].

4.3 Reduction of the Heat Loss Between the Two Plants. Relatively high "boiler" efficiency in the HRSG has been achieved by the use of natural gas, the low sulfur content of which has allowed low stack temperatures to be employed, while still avoiding corrosion of the water tubes. The loss term $[\nu_{UN}\eta_L]$ in Eq. (2) for overall plant efficiency is thus kept small, and the need for extensive feed heating in the steam cycle has also been obviated. (We may note the thermodynamic reservation expressed by Wood in the early fifties about the probable loss of low temperature feed heaters and air preheaters for the boiler in the use of supplementary fired gas turbines for the conversion of conventional steam power plants, a concern subsequently withdrawn.)

In the recuperative plant it is the product of steam cycle thermal efficiency and HRSG "boiler efficiency" that is important—lower steam thermal efficiency can be accepted if boiler efficiency can be increased by reduction of stack loss. An excellent discussion of this balance between exhaust stack temperature, HRSG boiler efficiency, and feed heating is given in Kehlhofer's book (1991).

5.0 Economics

A simplified way of assessing the economics of a power plant is to calculate the unit price of electricity produced by the plant [e.g., in pence or cents per kilowatt hour), the method adopted by Williams (1982), Daudet and Trimble (1980), and Wunsch (1985)].

The annual cost of electricity generation [P_E] is given by

$$P_E = CAP + M + OM \tag{13}$$

where CAP is the annual cost of capital (interest and debt repayment), M is the annual cost of the fuel supplied, and OM is the annual cost of operation and maintenance.

The levelized unit cost for the plant is then given by

$$Y_E = \frac{P_E}{\dot{W}H} = \frac{\beta C_0}{\dot{W}H} + \frac{M}{\dot{W}H} + \frac{OM}{\dot{W}H} \tag{14}$$

where C_0 is the capital cost of the plant, $\beta(i, N)$ is the capital charge factor, related to a discount rate (i) on capital and the life of plant (N years), $\dot{W}$ is the rating of the plant (kW), and H is the utilization factor (hours per annum).

The annual cost of fuel (M) may be written as the product of the cost of fuel (ζ, cost per unit of energy), the rate of supply of energy ($\dot{F}$), and the utilization factor (H). Then the unit generation cost is

$$Y_E = \frac{\beta C_0}{\dot{W}H} + \frac{\zeta \dot{F} H}{\dot{W}H} + \frac{OM}{\dot{W}H} = \frac{\beta C_0}{\dot{W}H} + \frac{\zeta}{\eta_{CP}} + \frac{OM}{\dot{W}H}, \tag{15}$$

where η_{CP} is the overall efficiency of the plant. [The unit price of fuel may be written as the price per unit mass S divided by the calorific value (CV) so that $\zeta = S/(CV)$.] With appropriate choice of units, Y_E is usually expressed in p/kWh [or cents/kWh].

We may note that Williams adopts a weighted interest or discount rate,

$$i = \alpha_e i_e + \alpha_d(1 - t)i_d \tag{16}$$

where α_e and α_d are the fractions of equity and debt, i_e and i_d

[2] It may also be noted that by differentiating Eq. (4*b*) with respect to r (or ϵ) and setting

$$\frac{\partial \eta_{CP}}{\partial \epsilon} = 0,$$

it follows that

$$\frac{\partial \eta_H}{\partial \epsilon} = -\frac{(1 - \eta_H)}{[1 - (\eta_O)_L]} \frac{\partial (\eta_O)_L}{\partial \epsilon} \tag{12a}$$

and

$$\frac{\partial \eta_H}{\partial \epsilon} \approx -\frac{\partial (\eta_O)_L}{\partial \epsilon} \tag{12b}$$

since η_H and $(\eta_O)_L$ are little different in most cases. Hence the maximum combined cycle efficiency [η_{CP}] occurs when the efficiency of the higher cycle is increasing with r at about the same rate as that of the lower cycle is decreasing. Clearly this will be at a pressure ratio less than that at which the higher cycle reaches peak efficiency, and when the lower cycle efficiency is decreasing because of the dropping gas turbine exit temperature.

This approach was suggested to the author by Cumpsty and Young (1994) and is well illustrated by Briesch et al. (1995), who show separate plots of η_H, $(\eta_O)_L$, and η_{CP} against pressure ratio, for given T_{max} and T_{min}.

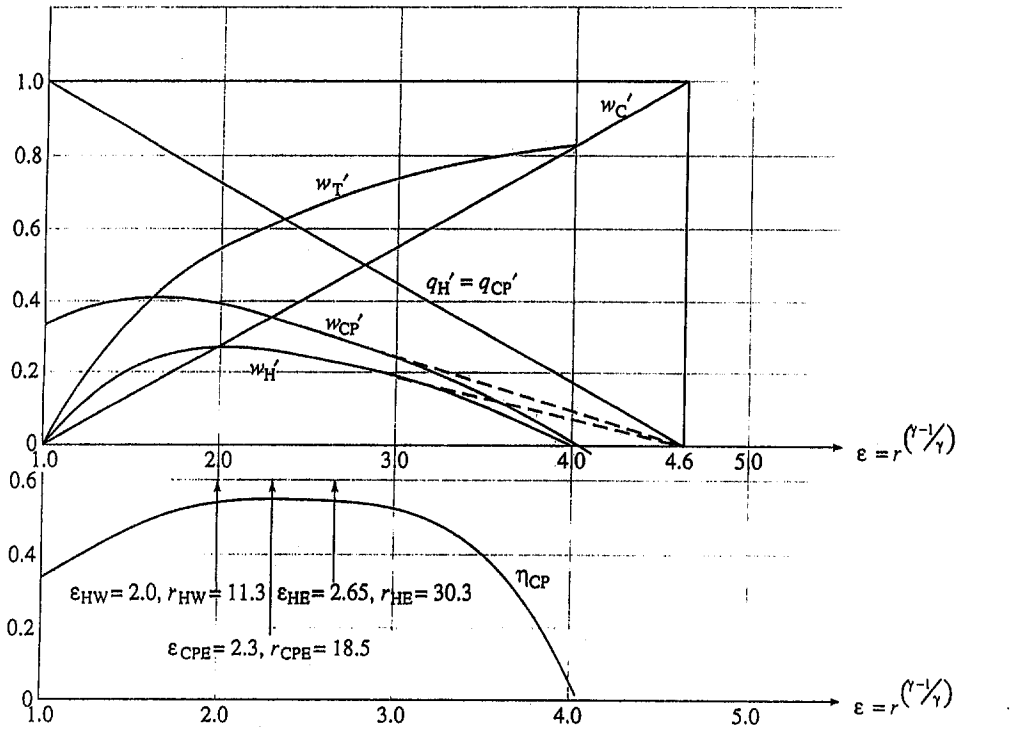

Fig. 9 Optimum pressure ratio: recuperative plant

are the corresponding interest rates, and t is the tax rate. His value of β is then

$$\beta_W = \frac{1}{(1-t)}\left[c(i,N) - \frac{t}{N} - \frac{t_{CR}c(i,N)}{(1+i)}\right] + R, \quad (17)$$

where t_{CR} is an investment tax credit rate, R is the rate of charge on capital for miscellaneous items, and

$$\frac{1}{c(i,N)} = \sum_{n=1}^{N} \frac{1}{(1+i)^n} \quad (18)$$

An alternative expression, taking separate account of discounting for debt and equity, based on the work of Daudet and Trimble (1980) and Uhl and Hawkins (1971) is given by Horlock (1995b) as

$$\beta_{DT} = \frac{1}{(1-t)}\left[\alpha_d(c_d - ti_d) + c_e\alpha_e - \frac{t}{N} - c_e t_{CR}\right] + R, \quad (19)$$

where c_d and c_e are values based now on i_d and i_e rather than i. However, this gives little difference from the Williams expression in the numerical assessment of unit costs for most practical cases.

It is of interest to compare approximate levelized costs for a typical CCGT plant and a nuclear plant—a matter of major significance in the review of the nuclear industry in the United Kingdom at the present time.

The capital cost term for the CCGT plant is relatively low (say £450/kW) and the fuel cost relatively high, so that Y_E is dominated by the second term in Eq. (15). Thus with (OM) taken as, say, 0.4 p/kWh

$$Y_E \approx 0.8 + 1.4 + 0.4 = 2.6 \text{ p/kWh},$$

for an 85 percent utilization of a 54 percent efficient plant over 20 years, with C_0/W = £450/kW and a discount rate of 11 percent, and with ζ = 0.75 p/kWh.

For the next pressurized water reactor nuclear plant proposed in the United Kingdom (Sizewell C), capital costs are high (£3.5b for a 2600 MW plant, or approximately £1400/kW), whereas the fuel cost term is low (say 0.4 p/kWh). Then with a higher OM at 0.6 p/kWh, the unit cost is given by

$$Y_E \approx 1.9 + 0.4 + 0.6 = 2.9 \text{ p/kWh},$$

for an 85 percent utilization for 40 years, and a discount rate of 10 percent.

Thus the strength of the case for the CCGT plant is related to keeping the capital cost term low (high utilization and benefiting from speed of construction), but also depends on obtaining high efficiency η_{CP} (and of course on security of a continuing fuel supply at noninflating fuel prices). Its advantages could be lost if the basic simplicity of the CCGT plant were sacrificed in the search for higher efficiency, and the capital cost substantially increased as a result. This is illustrated simply by differentiating Eq. (15) with respect to efficiency η_{CP}, so that

$$\frac{\partial Y_E}{\partial \eta_{CP}} = \frac{\beta}{\dot{W}H}\frac{\partial C_0}{\partial \eta_{CP}} - \frac{\zeta}{\eta_{CP}^2} \quad (20)$$

For unit cost to fall with increasing efficiency ($(\partial Y_E/\partial \eta_{CP}) < 0$) it follows that

$$\frac{\partial (C_0/\dot{W})}{\partial \eta_{CP}} \le \frac{\zeta H}{\beta \eta_{CP}^2} \quad (21)$$

In other words there is a limiting rate of increase of capital cost for efficiency gain if unit cost is not to increase. The numbers used in the example of CCGT prices given above suggest that for a 1 percent gain in efficiency, capital cost should not increase by more than about £20/kW. This is the basis of the earlier comment in this paper—the author's surprise that increase in the complexity of the HRSG (to minimize internal irreversibility) has been worthwhile, in view of the undoubted increases in capital cost.

6.0 Future Developments

The efficiencies of the latest CCGT plants are already incredibly high. The latest ABB GT24/26 plant has a claimed overall efficiency of 58 percent (gross) compared with a Carnot efficiency of about 81 percent based on the quoted (ISO equivalent) turbine entry temperature of 1235°C and a heat rejection temperature of 15°C. There cannot be much to come in terms of overall efficiency.

However, innovative cycles of higher efficiency are being considered. For example, Bannister et al. (1994) of Westinghouse have proposed a novel intercooled cycle with cooling of the gas turbine by steam, which then enters the steam turbine at low pressure. An overall efficiency greater than 60 percent is anticipated if higher gas turbine entry temperatures become possible in this way.

Other innovative proposals include the cascaded humid air turbine (CHAT), and the intercooled thermochemical recuperative cycle (Bannister et al., 1994), in which the gas turbine only produces power, burning reformed recuperative fuel (CO and H).

Steam injection in the mainstream flow of the gas turbine (STIG, a form of CCGT in which the Rankine cycle is effectively "hidden" within the Joule cycle) is a proven technology as Tuzson has pointed out in an excellent review (1992). However, Larson and Williams suggested in an earlier thermodynamic and economic study (1987) that even for the more complex ISTIG (intercooled steam injection gas turbine) the overall efficiency might be surpassed by the next generation of advanced "conventional" CCGT plants, and that prediction has proved accurate. Tuzson's conclusion, that the best application for STIG may well be in cogeneration[3] plants when surplus steam from process becomes available for injection, appears to be valid, as does his philosophy of modifying existing gas turbines for STIG rather than developing special plants.

As in due course gas prices rise, there will still be incentive to reach for higher CCGT efficiency, to prevent unit generation costs rising, and an overall efficiency of 60 percent may be achievable (Kehlhofer, 1994). But such increased efficiency will probably require increased capital cost and that in turn will threaten unit generation costs, as indicated earlier.

One can perhaps identify two lines of recuperative CCGT development. The first is based on pushing the gas turbine to its limits, using aircraft engine technology to obtain even higher turbine inlet temperatures (as in the Collaborative Advanced Gas Turbine program), marketing those gas turbines mainly in their own right as efficient prime movers and adding the lower steam cycle for extra efficiency as occasion may require. The second line involves thinking about the complete CCGT plant as an integrated design from the beginning, but possibly for a more limited market.

However, a new factor has recently entered into power plant design: the environmental disbenefit of the exhaust gases produced, especially in relation to global warming. For CCGT plants low sulfur natural gas has produced negligibly low SO_2, and major combustion development has also reduced NO_X. Further, the CO_2 produced per unit energy output (in kg/kWh) is much lower than that from conventional coal-fired steam power plants (Fig. 10). But the future status of coal-fired CCGT plants is now much affected by these environmental issues (and international limitations on CO_2 production in particular).

There are many variants of coal-fired plants under discussion, and some under development. An excellent review by Todd (1993) compares the option of pressurized fluidized bed combustion (PFBC) to that of the integrated gasification combined cycle (IGCC), favoring the latter, which is ahead in development. Todd argues that the combined cycle plant is now so

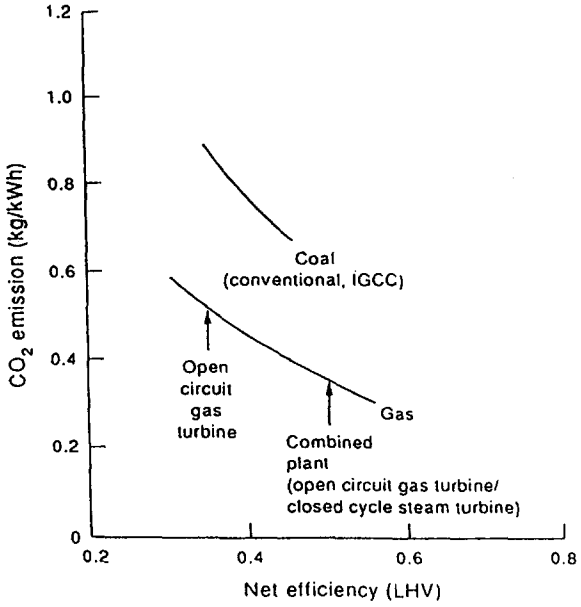

Fig. 10 Carbon dioxide emissions

efficient that an IGCC can absorb the fuel processing losses and still deliver an efficiency (LHV) of some 43 percent.

The increased cost of the gasification part of the IGCC plant obviously has an adverse effect on the economics. Oxidation can either be by air (giving low heating values and hence large plant size) or by oxygen (giving higher heating values, about one third of natural gas, and lower plant size). But capital cost comparison between the two forms of oxidation is difficult.

However, while the use of coal in an IGCC plant has been demonstrated at Cool Water, and is now in hand at bigger plants at Buggenhum and Puertollano, the CO_2/kWh produced is not reduced very much in comparison with conventional coal-fired plants. The engineering achievement of the Cool Water plant was convincing, even if the economic case is less so, but the CO_2 problem remains.

The chemical engineering processes involved in separating out the CO_2 may be feasible, but will lead to yet further capital costs. For example, Hendriks et al. (1991) refer first to a chemical absorption process based on the reaction of monoethanolamine (MEA) with CO_2, which could lead to removal of 90 percent of the CO_2 from the exhaust gases. It is suggested by the authors that this process would reduce overall efficiency from over 40 percent to below 30 percent and put up the cost of generation by about 65 percent. But Hendriks and his colleagues favor a second approach, that of removing CO_2 from the syngas before the gas turbine (in a "shift reaction" between CO and steam, producing the CO_2 early for separation and liberating hydrogen for subsequent combustion). They suggest that this may drop overall efficiency of an IGCC plant from some 44 to 38 percent, and lead to an increased generation cost of less than 30 percent.

With either method there remains the problem of CO_2 disposal (Hendriks et al. suggest the use of depleted underground reservoirs, formerly holding natural gas). One is bound to concur with the view of the UK Energy Technology Support Unit (ETSU), which identified CO_2 removal as "an unpromising technology".

7.0 Conclusions

The existing development of combined cycle gas turbines has placed this type of plant at the forefront of power generation. The new plants are the product not only of high class practical engineering development but also good basic thermodynamics.

[3] Cogeneration is usually referred to in Europe as CHP [combined *heat* and power [see Horlock (1987)].

If an academic engineer may add a thermodynamic comment, it is most satisfying to see the increasing use of exergy in the analysis of combined plant performance. The "exergoeconomic" work of Tsatsaronis and his colleagues (1984) will also become increasingly widely recognized as a useful approach. The development of exergy as a new and useful thermodynamic tool has truly been an international one, with major contributions coming from engineers on both sides of the Atlantic.

Indeed the history of combined power plants is an international story, and this would have given electrical power engineer Calvin Winsor Rice much satisfaction.

Acknowledgments

The author is grateful to various engineers from industrial companies [particularly K. Bray (European Gas Turbines), M. W. Sharpe (Siemens), R. Kehlhofer and D. Mukherjee (ABB)] for their assistance in the preparation of this lecture and paper.

References

Bannister, R. L., Cheruvu, N. S., Little, D. A., and McGuiggan, G., 1994, "Turbines for the Turn of the Century," *Mechanical Engineering,* Vol. 116, June, pp. 455–463.

Briesch, M. S., Bannister, R. L., Diakunchak, I. S., and Huber, D. J., 1995, "A Combined Cycle Designed to Achieve Greater Than 60 Percent Efficiency," ASME JOURNAL OF ENGINEERING FOR GAS TURBINES AND POWER, Vol. 117, this issue, pp. 733–740.

Cumpsty, N. A., and Young, J. B., 1994, private communication.

Czermak, H., and Wunsch, A., 1982, "The 125 MW Combined Cycle Plant Korneuburg B; Design Features, Plant Performance and Operating Experience," ASME Paper No. 82-GT-323.

Daudet, H. C., and Trimble, S. W., 1980, "Evaluation Method for Closed Cycle Gas Turbines in Cogeneration Applications," ASME Paper No. 80-GT-176.

Davidson, B. J., and Keeley, K. R., 1991, "The Thermodynamics of Practical Combined Cycles," *Proc. I. Mech. E. Conference on Combined Cycle Gas Turbines,* pp. 28–50.

Emmet, W. L. R., 1925, "The Emmet Mercury-Vapour Process," *Trans. ASME,* Vol. 46, pp. 253–285.

EPRI, 1988, "Cool Water Coal Gasification Project 5th Annual Progress Report," AP-5931.

Hackett, H. N., 1951, "Mercury-Steam Power Plants," *Mechanical Engineering,* July, pp. 559–564.

Hawthorne, W. R., and Davis, G. de V., 1956, "Calculating Gas Turbine Performance," *Engineering,* Vol. 181, p. 461.

Hendriks, C. A., Blok, K., and Turtenburg, W. C., 1991, "Technology and Cost of Recovering and Storing Carbon Dioxide From an Integrated-Gasifier Combined-Cycle Plant," *Energy,* Vol. 16, No. 11/12, pp. 1277–1293.

Horlock, J. H., 1957, "The Thermodynamic Efficiency of the Field Cycle," ASME Paper No. 57-A-44.

Horlock, J. H., 1987, *Co-generation: Combined Heat and Power,* Pergamon Press, Oxford, United Kingdom.

Horlock, J. H., 1992, *Combined Power Plants,* Pergamon Press, Oxford, United Kingdom.

Horlock, J. H., 1995a, "The Optimum Pressure Ratio for a CCGT Plant" *Proc. IMechE,* in press.

Horlock, J. H., 1995b, "Electricity Pricing—A Discussion of Discounting Methods" *Energy,* Vol. 20, No. 4, pp. 273–278.

Kehlfofer, R., 1991, *Combined Cycle Gas and Steam Turbine Power Plants,* Fairmont Press, Lilburn, GA.

Kehlhofer, R., 1994, private communication.

Larson, E. D., and Williams, R. H., 1987, "Steam Injection Gas Turbines," ASME JOURNAL OF ENGINEERING FOR GAS TURBINES AND POWER, Vol. 106, pp. 731–736.

Manfrida, G., and Mannucci, M., 1986, "Exergy Analysis of Possible Solutions for Combined Gas-Steam Cycles," *Proc. 21st Intersociety Energy Conversion Engineering Conference,* pp. 123–128.

Manfrida, G., Bosio, A., and Bidini, G., 1988, "Second Law Analysis of Combined Gas-Steam Power Plants," *Proc. 23rd Intersociety Energy Conversion Conference,* pp. 391–397.

Rice, I. G., 1980, "The Combined Reheat Gas Turbine/Steam Turbine Cycle," ASME JOURNAL OF ENGINEERING FOR POWER, Vol. 102, Part 1, pp. 35–41; Part 2, pp. 42–49.

Seippel, C., and Bereuter, R., 1960, "The Theory of Combined Steam and Gas Turbine Installations," *Brown Boveri Review,* Vol. 47, pp. 83–799.

Stodola, A., 1924, *Dampf und Gas Turbinen,* Springer, Berlin.

Timmermans, A. R. J., 1978, "Combined Cycles and Their Possibilities," Von Karman Institute for Fluid Dynamics, Lecture Series 6, Vol. 1.

Todd, D. M., 1993, "Clean Coal Technologies for Gas Turbines," GE Power Generation GER-3650C.

Tomlinson, L. O., Chase, D. L., Davidson, T. L., and Smith, R. W., 1993, "GE Combined Cycle Product Line and Performance," GE Power Generation, GER-3574D.

Tsatsaronis, G., and Winfold, M., 1984, "Thermoeconomic Analysis of Power Plants," EPRI AP3651.

Tuzson, J., 1992, "Status of Steam Injection Gas Turbines," ASME JOURNAL OF ENGINEERING FOR GAS TURBINES AND POWER, Vol. 114, pp. 682–687.

Uhl, U. W., and Hawkins, A. W., 1971, "Technical Economics for Engineers," AIChE Continuing Education Series No. 5, 44.

Williams, R. H., 1982, "Industrial Cogeneration," *Ann. Review Energy,* Vol. 3, pp. 313–356.

Wood, B., 1971, "Combined Cycles—A General Review of Achievements," *Modern Steam Practice,* Proc. I. Mech. E., Apr., pp. 75–86.

Wunsch, A., 1978, "Combined Gas/Steam Turbine Power Plants—The Present State of Progress and Future Developments," *Brown Boveri Review,* Vol. 65, No. 10, pp. 646–655.

Wunsch, A., 1985, "Highest Efficiencies Possible by Converting Gas Turbine Plants Into Combined Cycle Plants," *Brown Boveri Review,* Vol. 10, pp. 455–463.

The Role of Fuel Preparation in Low-Emission Combustion

A. H. Lefebvre
Reilly Professor Emeritus of Combustion Engineering,
Thermal Science and Propulsion Center,
Purdue University,
West Lafayette, IN 47907

The attainment of very low pollutant emissions, in particular oxides of nitrogen (NO_x), from gas turbines is not only of considerable environmental concern but has also become an area of increasing competitiveness between the different engine manufacturers. For stationary engines, the attainment of ultralow NO_x has become the foremost marketing issue. This paper is devoted primarily to current and emerging technologies in the development of ultralow emissions combustors for application to aircraft and stationary engines. Short descriptions of the basic design features of conventional gas turbine combustors and the methods of fuel injection now in widespread use are followed by a review of fuel spray characteristics and recent developments in the measurement and modeling of these characteristics. The main gas-turbine-generated pollutants and their mechanisms of formation are described, along with related environmental risks and various issues concerning emissions regulations and recently enacted legislation for limiting the pollutant levels emitted by both aircraft and stationary engines. The impacts of these emissions regulations on combustor and engine design are discussed first in relation to conventional combustors and then in the context of variable-geometry and staged combustors. Both these concepts are founded on emissions reduction by control of flame temperature. Basic approaches to the design of "dry" low-NO_x and ultralow-NO_x combustors are reviewed. At the present time lean, premix, prevaporize combustion appears to be the only technology available for achieving ultralow NO_x emissions from practical combustors. This concept is discussed in some detail, along with its inherent problems of autoignition, flashback, and acoustic resonance. Attention is also given to alternative methods of achieving ultralow NO_x emissions, notably the rich-burn, quick-quench, lean-burn, and catalytic combustors. These concepts are now being actively developed, despite the formidable problems they present in terms of mixing and durability. The final section reviews the various correlations now being used to predict the exhaust gas concentrations of the main gaseous pollutant emissions from gas turbine engines. Comprehensive numerical methods have not yet completely displaced these semi-empirical correlations but are nevertheless providing useful insight into the interactions of swirling and recirculating flows with fuel sprays, as well as guidance to the combustion engineer during the design and development stages. Throughout the paper emphasis is placed on the important and sometimes pivotal role played by the fuel preparation process in the reduction of pollutant emissions from gas turbines.

Introduction

The gas turbine is often described as the prime mover of the twentieth century. The tremendous advantages offered by the aircraft gas turbine in terms of range, speed, fuel economy, and passenger comfort have assured its preeminent position as the power plant for aircraft. Also, it continues to find increasingly wide applications as a power source in a wide variety of industrial and transport applications. In particular, the gas turbine is widely used for both mechanical drive and electrical power generation within the oil and gas industry. Its advantages in terms of high thermal efficiency and potential for low pollutant emissions in the combined cycle mode will ensure that most new utility power generation plants will also utilize the gas turbine as the prime mover.

When faced with new and challenging problems, the combustion engineer has traditionally looked to the fuel injector to provide a solution. This is not merely a pious hope, because in the past more than one problem that appeared at first sight to constitute a fundamental barrier to further progress in combustion performance was solved either by modifications to existing fuel injector designs or by the introduction of new and sometimes revolutionary atomizer concepts. So today, when faced with continuous and growing pressure to minimize pollutant emissions from gas turbines, the combustion engineer regards the fuel preparation process as one that must necessarily play a key role in achieving this objective.

This paper is a review of recent and current research activities in low-emissions gas turbine combustors. It describes research and development work that is directly related to fuel injector and combustor design and performance, as opposed to the more fundamental aspects of atomization, fuel–air mixing, and combustion. The subject matter is divided into seven main sections:

- An introduction to the main components of a conventional gas turbine combustor and their principal functions, along with brief descriptions of the types of fuel injectors now in widespread use.
- The properties of fuel sprays and recent developments in the measurement and modeling of spray characteristics.
- A general overview of emissions concerns, their mechanisms of formation, and the methods employed to alleviate pollutant emissions in conventional combustors.
- The use of variable geometry and staged combustion for emissions reduction by control of flame temperature.

Contributed by the International Gas Turbine Institute and presented at the 40th International Gas Turbine and Aeroengine Congress and Exhibition, Houston, Texas, June 5–8, 1995. Manuscript received by the International Gas Turbine Institute April 12, 1995. Paper No. 95-GT-465. Associate Technical Editor: C. J. Russo.

- Basic approaches to the design of "dry" low NO_x and ultralow NO_x combustors, with emphasis on the need to feed the combustion zone with completely homogeneous fuel–air mixtures, with the attendant problems of autoignition and flashback.
- Alternative methods for achieving ultralow NO_x emissions, notably rich-burn, quick-quench, lean-burn, and catalytic combustors, both of which combine high potential for very low levels of nitric oxides with formidable mixing and mechanical design problems.
- Correlation and modeling of nitric oxides and carbon monoxide emissions.

Throughout the paper emphasis is placed on the important and sometimes pivotal role played by the fuel preparation process in all efforts to reduce pollutant emissions from gas turbines. Today the pollutant emission of primary concern is oxides of nitrogen (NO_x), and it is of interest to recall that combustors designed specifically for low NO_x first appeared on the scene in the 1970s, but remained "on the shelf" for another decade due to a greater interest during that time in reducing the other important emissions of carbon monoxide (CO), unburned hydrocarbons (UHC), and smoke.

An attempt is made to address both aircraft and stationary gas turbines because neither one is more or less important than the other in regard to their contribution to atmospheric pollution. However, there are two compelling reasons why aircraft engines should receive the most attention. One is that aircraft engines employ liquid fuels, which must first be atomized and vaporized before they can burn. These additional processes increase the degree of difficulty in achieving low emissions by almost an order of magnitude. The second reason is that natural gas—the favored fuel for stationary gas turbines—has a peak flame temperature around 140°C less than that of the distillate fuels employed in aircraft engines. As the formation of NO_x is exponentially dependent on temperature, this lower flame temperature reduces NO_x levels by a factor of around two. For these reasons the emissions goals set for stationary engines tend to be much more severe than for aero-engines.

Conventional Combustors

There are two basic types of gas turbine combustor: tubular, or can, and annular. A tubular chamber is composed of a cylindrical liner mounted concentrically inside a cylindrical casing. Most of the early jet engines featured tubular chambers, usually in numbers varying from seven to sixteen per engine. For aircraft applications, the tubular system is now regarded as too long and too heavy and the annular system is now the automatic choice for all new engines. However, tubular chambers do have significant advantages in terms of easy accessibility and maintenance, and they are still preferred for large stationary engines in the 80-plus megawatt range, such as the General Electric MS7001 engine, which has ten separate cans.

The annular combustor comprises an annular liner mounted concentrically inside an annular casing. In many ways it represents an ideal form of chamber, since its "clean" aerodynamic layout results in a compact unit of lower pressure loss than other combustor designs. All modern aero-engines employ annular combustors, which means that modern aero-derived industrial engines, such as the General Electric LM6000 and the Rolls Royce RB211, all have annular combustors.

The volume contained within the liner of a conventional combustor may be divided conveniently into three main zones: primary, intermediate, and dilution. The function of the primary zone is to anchor the flame and to provide sufficient time, temperature, and turbulence to achieve essentially complete combustion of the fuel. The hot combustion products issuing from the primary zone flow into the intermediate zone, which provides a region in which combustion can proceed to completion

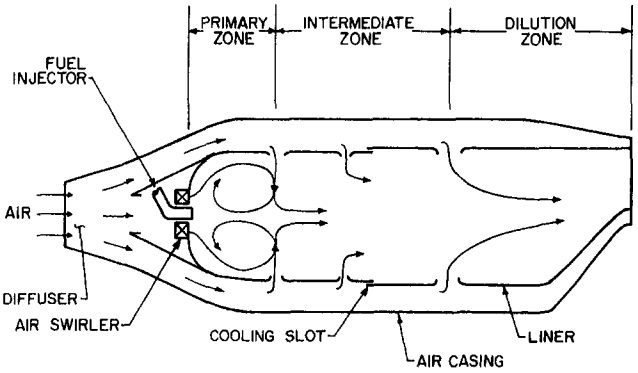

Fig. 1 Main components of a conventional gas turbine combustor

upstream of the dilution zone. The role of the dilution zone is to admit the air remaining after the combustion and wall-cooling requirements have been met, and to provide an outlet gas stream with a mean temperature and a temperature distribution that are acceptable to the turbine.

The locations of the three main zones described above in relation to the various combustor components and the air admission holes, are shown in Fig. 1.

Liquid Fuel Injection. The liquid fuels employed in aircraft engines must first be atomized before being injected into the combustion zone. Fortunately, atomization is easy to accomplish; for most liquids, all that is needed is a high relative velocity between the liquid to be atomized and the surrounding air or gas. Pressure atomizers accomplish this by discharging the liquid at high velocity into a relatively slow-moving stream of air. An alternative approach is to expose a slow-moving liquid to a high-velocity airstream. The latter method is generally known as airblast atomization. Pressure atomizers are usually of the "dual-orifice" type, as shown in Fig. 2. As its name suggests, this atomizer incorporates two orifices, arranged concentrically. The inner primary orifice is small, while the outer secondary orifice is of larger area. At low fuel flows, only the primary operates and atomization quality is good because injection pressures are fairly high. With increasing fuel flow, the injection pressure rises and would soon become excessive but, at a predetermined pressure, a valve opens and fuel is then conveyed to the secondary orifice. This arrangement gives satisfactory atomization over a wide range of fuel flows without calling for excessive fuel delivery pressures. The principal advantage of dual-orifice nozzles is good mechanical reliability. Their drawbacks include potential plugging of the small passages and orifices by contaminants in the fuel and an inate tendency toward high concentrations of exhaust smoke at high combustion pressures.

The most widely used type of airblast atomizer is illustrated in Fig. 3. In this design the bulk fuel is first spread into a thin continuous sheet, a process called "prefilming," and then exposed to high-velocity, swirling air streams on both sides of the sheet. Prefilming airblast atomizers are capable of producing fine atomization and a virtually smoke-free exhaust at high combustion pressures. The main drawbacks of airblast atomizers are poor lean blowout performance and poor atomization during engine startup when air velocities are low. These problems can be readily overcome by incorporating a pilot or primary nozzle. At low fuel flows, all of the fuel is supplied through the pilot nozzle, and a well-atomized spray is obtained, giving efficient combustion at start-up and idling. At higher power settings, fuel is supplied to both the airblast and pilot nozzles. The relative amounts are such that at the highest fuel flow conditions most of the fuel is supplied to the airblast atomizer. By this means, the performance requirements of wide burning range and low exhaust are both realized.

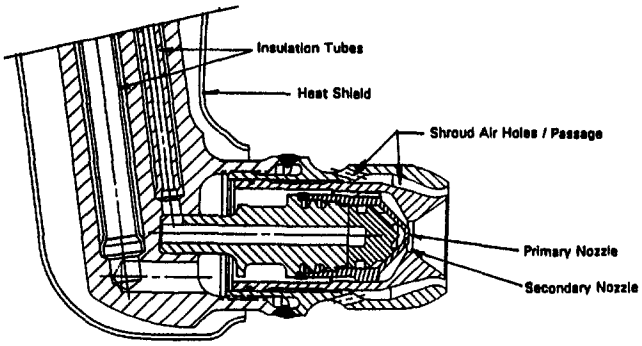

Fig. 2 Dual-orifice, pressure-swirl atomizer (courtesy of the Parker Hannifin Corporation)

Gas Injection. For almost all stationary gas turbines the fuel employed is natural gas. Some engines are fitted with dual-fuel nozzles, which allow both liquid and gaseous fuels to be used, but usually the liquid fuel is for backup purposes only. The methods used to inject gaseous fuels tend to be simple as there are no requirements for atomization and fuel evaporation. They include injecting the gas through plain orifices, slots, swirlers, and venturi nozzles.

The main problem with gas injection is that of achieving the optimal level of mixing between air, fuel, and combustion products in the combustion zone. Too high a mixing rate produces narrow burning limits. On the other hand, if the rate of mixing is too low, the system may be prone to low-frequency, combustion-induced pressure oscillations. On engines designed to operate on both gaseous and liquid fuels, it is important that the gas flow pattern be matched to that of the liquid fuel; otherwise some variation in the temperature distribution of the combustor outlet gases would occur during changeover from one fuel to the other.

Fuel Spray Characteristics

The spray properties of most relevance to the formation of pollutant emissions are mean drop size, drop size distribution, cone angle, and patternation. Other properties of special importance for the successful modeling of spray characteristics include droplet and gas velocities, droplet trajectories, and mass flux distributions.

Mean Drop Size. Various definitions of mean drop size are available, of which the most widely used is the Sauter mean diameter (SMD), which represents the volume/surface ratio of the liquid in the spray. Unfortunately, the physical processes involved in atomization are not yet sufficiently well understood for mean diameters to be expressed in terms of equations de-

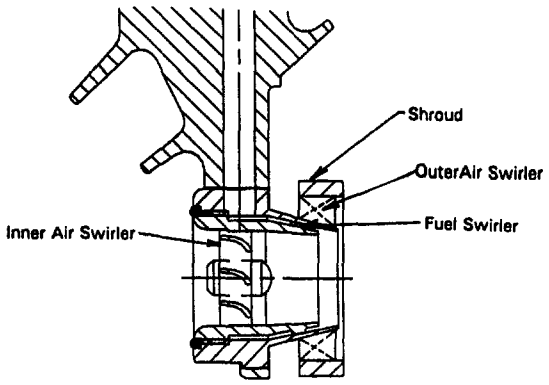

Fig. 3 Prefilming airblast atomizer (courtesy of the Parker Hannifin Corporation)

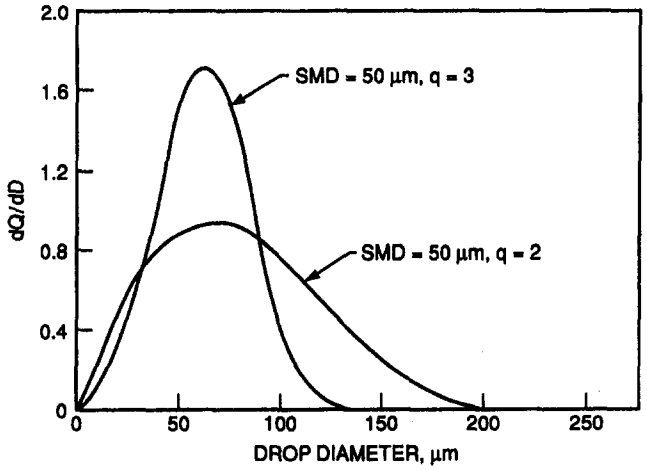

Fig. 4 Influence of drop size distribution parameter on frequency distribution curve

rived from basic principles. In consequence, the majority of investigations into the drop sizes produced in atomization have resulted in empirical equations for mean drop size. Lefebvre (1989) has reviewed the available equations for the mean drop sizes produced by the types of atomizers employed in gas turbine combustion. They show that mean drop sizes are largely dependent on atomizer size, design features, and operating conditions, and also on the physical properties of the liquids employed and the density of the surrounding gaseous medium.

Most of the equations for mean drop size published before around 1970 should be regarded as suspect due to deficiencies in the methods available for drop size measurements. Even expressions based on accurate experimental data should only be used within the ranges of air properties, liquid properties, and atomizer operating conditions employed in their derivation. Extrapolation to other conditions is fraught with risk because changes in any of these variables could produce a change in the mode of atomization, which could have a significant effect on the manner and extent to which variations in the relevant flow parameters affect the drop size distribution in the spray.

Drop Size Distribution. Owing to the random and chaotic nature of the atomization process, the threads and ligaments formed by the various mechanisms of jet and sheet disintegration vary widely in diameter, and their subsequent breakup yields a correspondingly wide range of drop sizes. Most practical atomizers produce droplets in the size range from a few microns up to several hundred microns.

As no complete theory has yet been developed to describe the hydrodynamic and aerodynamic processes involved when jet and sheet disintegration occurs under normal atomizing conditions, a number of functions have been proposed, based on either probability or purely empirical considerations, that allow the mathematical representation of measured drop size distributions. The simplest expression for drop size distribution is that of Rosin and Rammler (1933). It may be expressed in the form

$$1 - Q = \exp - (D/X)^q \qquad (1)$$

where Q is the fraction of the total volume contained in drops of diameter less than D, and X and q are constants. Thus, the Rosin–Rammler relationship describes the drop size distribution in terms of the two parameters X and q. The exponent q provides a measure of the spread of drop sizes. The higher the value of q, the more uniform is the spray.

Figure 4 shows frequency distribution plots for two sprays, both having the same SMD of 50 μm, but in one case the distribution parameter q has a value of 2 and in the other case a value of 3. This figure clearly demonstrates that knowledge

of SMD alone is not sufficient to determine the spray evaporation time. One spray contains no drops larger than 130 μm whereas the other contains drops up to 200 μm in diameter. This represents a difference in total spray evaporation time of more than two to one. Differences of this magnitude must necessarily have a pronounced effect on the formation rates of all the main pollutants.

Cone Angle. A major difficulty in the definition and measurement of cone angle is that the spray cone has curved boundaries, owing to the effects of air interaction with the spray. To overcome this problem, the cone angle is often given as the initial angle as measured close to the nozzle where the spray contour is still in the form of a perfect cone. Rizk and Lefebvre (1987) used their own results and those of other workers to derive the following expression in which the cone angle, as measured close to the nozzle, is expressed as the product of two dimensionless groups:

$$2\theta = 6K^{-0.15}(\Delta P_L d_o^2 \rho_L / \mu_L^2)^{0.11} \qquad (2)$$

where K is the dimensionless geometric group $A_p/D_s d_o$. A_p is the inlet port area, D_s is the swirl chamber diameter, d_o is the diameter of the discharge orifice, ΔP_L is the liquid injection pressure, and ρ_L and μ_L are the liquid density and absolute viscosity, respectively.

This equation shows that spray cone angles widen with increase in fuel injection pressure, corresponding to an increase in fuel flow rate. This effect has been confirmed in a number of experimental studies; for example, Chen et al. (1992). Equation (2) also suggests that ambient air or gas pressure has no effect on cone angle, but this is only true in the region near the nozzle. As the droplets move away from the nozzle they are subjected to radial air currents generated by their own kinetic energy, as described by De Corso and Kemeny (1957). These air currents become stronger with increase in ambient air pressure, with the result that although the cone angle as measured close to the nozzle does not change appreciably as the pressure is increased, the spray width further downstream contracts markedly. This decrease in spray cone angle with increase in ambient pressure is one of the main reasons why combustors featuring pressure-swirl atomizers generate more soot and smoke as the combustion pressure is increased.

Airblast atomizers are much less susceptible to variations in fuel and ambient air pressure than pressure-swirl atomizers. The liquid sheet or jet exposed to the atomizing air has little momentum and the droplets formed in atomization are entirely dependent on the kinetic energy of the atomizing air to transport them away from the nozzle. This means that droplet trajectories are dictated by the air movements created by air swirlers and other aerodynamic devices, which form an integral part of the nozzle configuration. Thus, airblast atomizers are characterized by a lack of sensitivity of spray geometry characteristics to the physical properties of both the liquid and the surrounding gaseous medium.

From tests carried out on prefilming airblast atomizers, Ortman and Lefebvre (1985) found that increasing the air pressure differential across the nozzle caused the spray angle to contract slightly. Custer and Rizk (1988) observed a similar effect. For one prefilming atomizer, operating at an air/fuel ratio of 5, they found that a large increase in air pressure differential from 1 to 4 percent caused the spray angle to be reduced from 100 to 80 deg.

Circumferential Fuel Distribution. Drop sizes are, of course, of great importance in low-emission combustion because of their strong influence on fuel evaporation rates and droplet lifetimes. Of equal importance, however, is the symmetry of the spatial distribution of fuel within the spray. Failure to achieve a symmetric mass flux distribution can result in local regions of mixture inhomogeneity in the combustion zone, a situation that is highly detrimental to low-emissions combustion. The term adopted by the gas turbine industry for the purpose of defining spray distribution is "spray patternation" and the instruments used to measure liquid flux distributions in sprays are commonly referred to as "spray patternators."

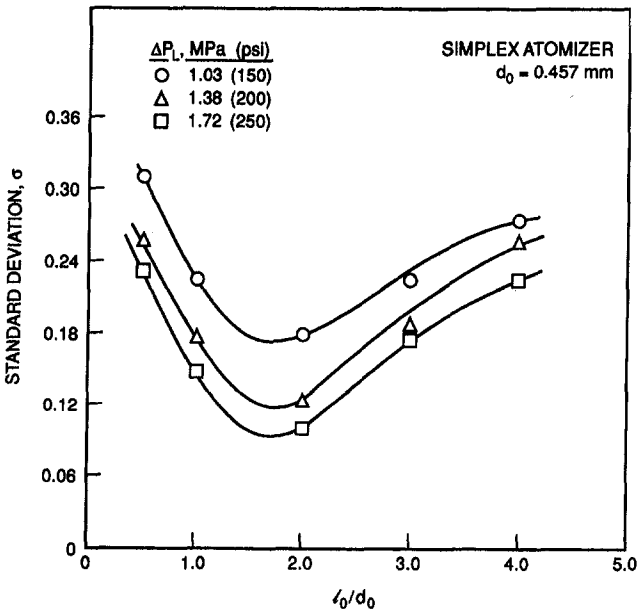

Fig. 5 Influence of discharge orifice length/diameter ratio on circumferential fuel distribution

The simplest form of patternator comprises a cluster of collection tubes, which are located under the test nozzle. The nozzle sprays downward into the tubes and the duration of each test is the time required for one of the sampling tubes to become nearly full. After the level of fuel in each tube is measured and recorded, the values are averaged to get a mean height. The levels of the tubes are normalized against the mean, and the standard deviation of the normalized values is calculated. The normalized standard deviation provides a quantitative indication of the symmetry of the distribution of fuel within the spray. More sophisticated spray patternators have been devised that are capable of high-resolution measurements of the mass flux distributions produced by gas turbine fuel injectors (McVey et al., 1987, 1989). These methods are not necessarily more accurate than the simple patternators described above, but they do allow a large amount of data to be collected in a relatively short time.

Circumferential patternation is sensitive to the dimensional relationships characteristic of a particular nozzle design. For example, for pressure-swirl atomizers, patternation has been correlated with the degree of eccentricity between the swirl chamber and the final discharge orifice (Tate, 1960). Nozzle quality is also important, and spray patternation may be impaired by poor surface finish, orifice imperfections, plugged or contaminated flow passages, eccentric alignment of key nozzle components, and other conditions. For airblast atomizers, lack of symmetry in the various air passages and swirlers can also have an adverse effect on spray patternation, as discussed below.

Chen et al. (1993) used several different pressure-swirl nozzles to examine the effects of variations in liquid properties, operating conditions, and atomizer design features, on spray patternation. Of special interest are the results obtained on the effects of varying the length/diameter ratio of the final discharge orifice, l_o/d_o, as illustrated in Fig. 5. In this figure the circumferential maldistribution is expressed in terms of a standard deviation, σ. If the circumferential distribution of liquid within the spray were completely uniform, the value of σ would be zero. Figure 5 shows that σ declines, i.e., patternation im-

proves, with increase in liquid injection pressure, presumably because high injection pressures promote more turbulence and better mixing in the swirl chamber. It also shows that the circumferential distribution is most uniform for a value of l_o/d_o of 2. This optimum value of 2 was found to apply at all operating conditions to all of the liquids tested, some of which varied in viscosity by a factor of twelve. This result is of considerable practical interest because for many years the trend in pressure-swirl atomizer design has been toward lower values of l_o/d_o in order to reduce internal losses and thereby improve atomization. Most current atomizer designs have values of l_o/d_o of 0.5 or less. Figure 5 clearly demonstrates that reducing l_o/d_o can appreciably worsen the spray patternation.

Spray Diagnostics. In recent years considerable advances have been made in the development of laser diagnostic techniques for measuring the properties of sprays. The methods used in spray analysis have been reviewed by Chigier (1983), Chigier and Stewart (1984), and Durst et al. (1981). Laser-Doppler velocimetry and phase-Doppler anemometry, interfaced with signal processing and high-speed data acquisition systems, are now being used routinely in simultaneous measurements of drop size, drop velocity, and local drop drag coefficients (Bauckhage, 1988; Delarosa et al., 1993; Dittmann et al., 1992; Naqwi et al., 1991). High-speed pulsed microphotography, cinematography, and holography are also used to study drop size distributions and spray structure (Santangello and Sojka, 1994). Much of the tedium normally involved in detailed studies of drop size distributions in various regions of the spray can now be alleviated using automatic image analysis, in which droplet images are enlarged, counted, and sorted by electronic scanning devices and analyzed by microprocessors.

Many efforts are now underway to gain a better understanding of the basic phenomena occurring within complex practical systems currently in service on advanced turbojet engines. Wang et al. (1992a, b, 1994, 1995) and McDonell et al. (1994a, b) used a two-component phase-Doppler interferometry system to make detailed measurements in the flows downstream of a SNECMA/GE CFM-56 airblast atomizer. In addition to time-averaged properties, transient phenomena were also examined. These studies have provided great insight into the general structure of the gas phase as well as details regarding the complex behavior of drops. Of special interest from a practical viewpoint is that actual engine hardware was used to examine the sensitivity of the spray structure to scaling and hardware variations. One study was devoted to an examination of the effects of nozzle defects on spray characteristics. Figure 6 presents a schematic diagram of the CFM-56 atomizer and swirl cup used in this investigation. It features a pair of concentric air inlets, which generate two separate swirling airflows in opposite directions. The swirl cup acts as a "hybrid" injector, with drops produced from a combination of airblast and pressure atomization. This figure illustrates what can happen to the swirl cup assembly during the engine operating cycle. The design calls for concentric alignment at altitude cruise conditions. However, due to "throttle pushes" over the years, the assembly can become eccentric by up to around 3 mm (0.125 in.), as indicated in Fig. 6. This occurs because the secondary swirler is attached to the combustor liner, whereas the burner feed arm is mounted directly onto the combustor casing. Since the two components are pinned at two different locations to the casing, the thermal expansion of the casing causes misalignment.

Results showing the effect of misalignment on the flow field downstream of the atomizer are presented in Fig. 7. In this figure the two circles on each cartoon represent the primary and secondary swirlers. The vector quantities represent the gas velocities in the $r-Z$ plane, while the contours are the turbulent kinetic energies based on the measured rms velocity components. The highest velocity variations occur in the shear layer between the recirculating flow and the surrounding flow moving

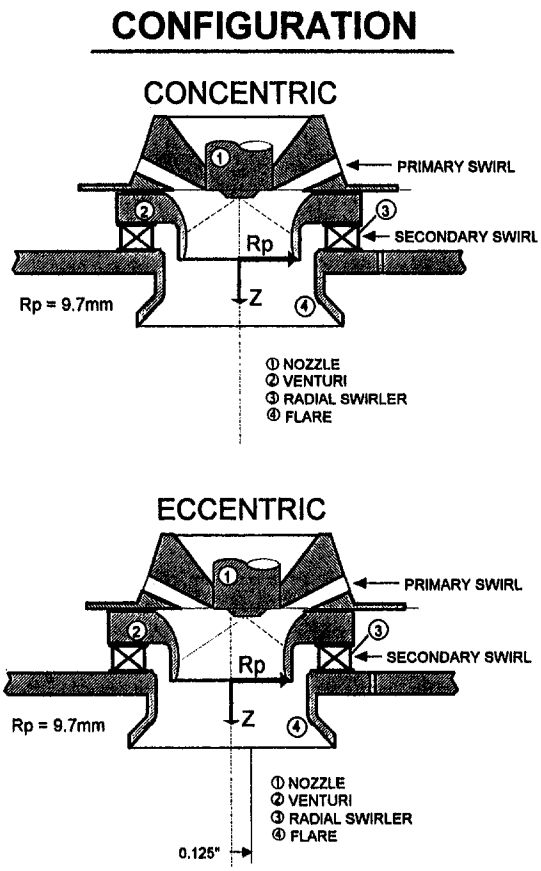

Fig. 6 Concentric and eccentric airblast atomizers

downstream. The slight flow asymmetries observed with concentric alignment of the swirlers is attributed to normal hardware tolerance. The measurements obtained with the eccentric swirler assembly exhibit asymmetries in both mean velocities and turbulence.

Hebrard et al. (1991, 1993) also used two-component phase-Doppler interferometry to characterize the two-phase flow field generated by an engine airblast atomizer. Their measurements included mean axial and transverse velocities for each phase as well as volume flux and drop size distributions. They used surface plots to illustrate the local variation of Sauter mean diameter for cross sections of the spray at several different distances downstream from the atomizer. Close to the nozzle, they observed a dome-shaped distribution of drop sizes. Air flowing through the inner and outer swirlers of the airblast atomizer produced a nearly uniform drop size distribution, but recirculating air jets caused some secondary atomization. Some large drops were observed in the core, generated by the inner swirling air. Farther downstream the drop size distribution broadened and indentations appeared on the spray boundary, caused by the presence of air jets emanating from the holes located near the edge of the atomizer cup.

Wynne and Jasuja (1991) and Jasuja and Lefebvre (1994) used various nonintrusive techniques, including phase-Doppler interferometry, high-intensity spark photography, high-speed cinephotography, and video imaging to capture the dynamic and unsteady spray characteristics produced in prefilming airblast atomization. All of the injectors used in this program were typical of modern gas turbine practice and differed from each other only in regard to various design features, such as swirler flow area and vane angle. A special feature of this work is that it covers a very wide range of ambient air pressures. The results obtained are generally consistent with the findings reported above in showing that the sprays produced by actual engine

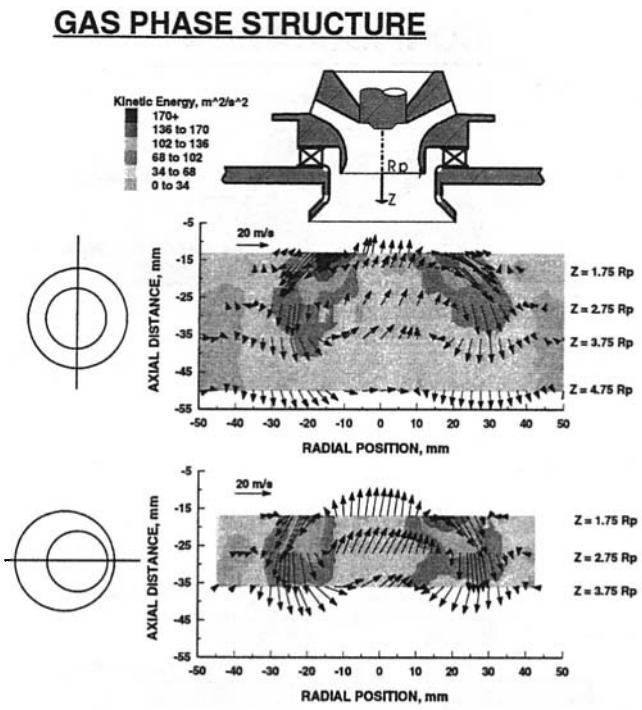

Fig. 7 Influence of atomizer misalignment on flow field

nozzles exhibit appreciable nonuniformities in regard to droplet trajectories and mass flux distributions.

A number of laboratories throughout the world are now using advanced laser diagnostics to characterize the sprays produced in airblast atomization. Much of this work is confined to dilute and simple sprays operating in easily probed laboratory conditions at normal atmospheric pressure. The special merit of the researches summarized above is their focus on full-scale engine nozzles, operating in some cases over wide ranges of ambient air pressure. The information they are providing on the complex, near-field bulk liquid behavior and droplet physical processes is making a significant contribution to fuel injector modeling capabilities and the development of low-emissions combustors.

Modeling of Spray Characteristics. The development of new diagnostic techniques as discussed above has encouraged the formulation of empirical and analytical models to describe the fuel injection process. Rizk and his co-workers (see, for example, Rizk et al., 1987; Custer and Rizk, 1988; and Rizk and Mongia, 1992a, b) have been especially active in this field. One overall model, which combines three submodels, addresses various processes of fuel and air preparation for atomization and formation of the final spray. The first submodel describes the velocity profiles of the air passing through and exiting from the nozzle passages. The second submodel deals with the fuel prefilming process and the conversion of the thin fuel sheet into droplets. Finally, the third model represents the turbulent dispersion effects on the spray.

The results of this model highlight the need to define both the air flowfield and the film breakup process with good accuracy. The model also indicates how improvements in atomization quality can be achieved by careful design of the prefilmer and internal passages of the atomizer. A thinner fuel film, which, for any given fuel flow rate, is governed by local air velocity and nozzle geometry, results in shorter ligaments that disintegrate into drops closer to the nozzle in regions of relatively high air velocity. This enhances the secondary atomization process and reduces the final drop sizes in the spray.

Sultanian and Mongia (1986) used the $k-\epsilon$ turbulence model in conjunction with a boundary-fitted curvilinear orthogonal grid to compute the internal flow characteristics of an injector. Their calculations were compared with LDV measurements on four nozzle configurations with variations in size, swirl strength, and swirl direction. For most mean velocity components, the agreement between measurements and calculations was good. These workers concluded that the modeling results indicate that calculations can be used for design and analysis.

Hebrard et al. (1993) have reported on the development of a similar $k-\epsilon$ code, which shows good correlations between predictions and measurements of drop trajectories from an airblast atomizer. Data were taken using a high-speed video camera. A Weber number relationship was derived for predicting whether a droplet will bounce or film when hitting a wall, and it was also noted that fuel droplets are capable of burning either singly, in groups, or en masse.

The examples given above are intended to illustrate current efforts in fuel injector modeling. These models, in conjunction with the detailed knowledge on spray characteristics that new advances in laser diagnostics are making available at an ever-increasing rate, are providing better insight on the critical role of the fuel injection process on low-emissions combustor performance.

Fuel Nozzle Coking

No discussion on spray characteristics would be complete without reference to the deleterious effects on atomization and spray symmetry caused by the partial or complete blockage by carbon deposition of one or more of the flow passages within the fuel nozzle. This problem is one of growing importance and has special implications for the development of many types of low-emission combustors for which a uniform distribution of fuel within the spray is a basic requirement. It is especially serious for advanced turbojet engines due to the growing use of the fuel as a heat sink for cooling the airframe, avionics, and engine lubricating oil. The problem is further exacerbated by the fact that the fuel feed arm is immersed in the compressor efflux air. This high-temperature, high-pressure, high-velocity airflow causes convective heating, which further raises the temperature of the fuel before it flows into the fuel injector. The combined effect of all these various inputs is that by the time the fuel is sprayed into the combustion zone, its temperature is appreciably higher than when it left the fuel tank.

From a combustion viewpoint this elevation in fuel temperature is not altogether undesirable because it reduces fuel viscosity and thereby promotes finer atomization. Unfortunately, high fuel temperatures stimulate oxidation reactions, which lead to the formation of gums and other insoluble materials (including carbon), which tend to deposit on the walls of the passages and metering orifices within the nozzle. These deposits can distort the fuel spray and create appreciable nonuniformities in spray patternation.

The problems created by the deposition of carbonaceous materials, generally referred to as "coke," within the fuel nozzle are of special importance for small gas turbines. As the engine size is reduced, the dimensions of various engine components must also decrease. This is particularly disadvantageous for the fuel injector because it embodies small internal flow passages, which are especially prone to plugging and blockage. In small gas turbines, the swirl-inducing and fuel metering passages can have linear dimensions as small as 200 μm (McCaldon et al., 1993). Fuel passages are often convoluted, thus creating local regions in which the flow velocity is low and thermal degradation and coking can occur. The pressure-swirl atomizer, having very small hole and passage sizes, is especially prone to coke formation. Coke agglomerates, formed either upstream of the nozzle tip or within the nozzle itself, can break off and be carried in to the metering passages.

Airblast atomizers are inherently less susceptible than pressure-swirl atomizers to the problems of fuel coking because

they employ much larger fuel passages in the nozzle tip. However, the inability of airblast atomizers always to meet the requirements of cold day starting has prevented pure airblast systems from completely displacing pressure-swirl atomizers from engine designs.

The effects of partially or totally blocked fuel metering passages on the fuel–air distributions produced by an airblast atomizer have been examined by McCaldon et al. (1993). They found that as more and more fuel metering holes become obstructed with increasing operating time, more fuel is forced through the remaining nozzles. Consequently, engine damage may be caused by those injectors, which, if tested individually, still flow within tolerances. Although the report of McCaldon et al. contains no data on NO_x, it is clear that the fuel flux variations found must also give rise to substantial increases in NO_x emissions at high power conditions and increased emissions of CO and UHC at low power conditions.

The studies carried out by Nickolaus and Lefebvre (1987) and McCaldon et al. (1993), among others, have demonstrated that coke formation within fuel nozzles can have a serious adverse effect on spray pattern. Although it has long been recognized that "cleaner" fuels of low aromatics content can greatly reduce the potential for fuel coking, this has never been regarded as a practical option due to the requirements of fuel flexibility for the military and lower-cost, heavier distillate fuels for civilian and commercial applications.

The discussion above on the effects of fuel thermal degradation on fuel injector performance has tended to focus on the deleterious effects caused by the elevation in temperature experienced by the fuel upstream of the nozzle tip. Another important effect on fuel coking is the fuel-wetted wall temperature within the nozzle. An increase in wall temperature greatly accelerates the rate of coke deposition. The flow of heat into the nozzle tip by air flows introduced to prevent soot accumulation, and by intense radiation from the combustion gases, cause fuel-wetted wall temperatures to be appreciably higher than the temperature of the adjacent fuel. This temperature gradient near the wall not only enhances deposition rates by raising the fuel temperature but also has a separate additional effect due to the higher wall temperature.

In recent years the U.S. Naval Air Propulsion Center has sponsored an innovative high-temperature fuel nozzle program with the objective of designing and evaluating fuel nozzles capable of operating satisfactorily despite extreme fuel and air inlet temperatures. As part of this program, Stickles et al. (1993) evaluated 27 different nozzle designs, all of which were based on the production GE F404 fuel nozzle. The design approach was to use improved thermal protection and fuel passage geometry in combination with fuel passage surface treatment to minimize coking. Heat transfer analysis highlighted several important design features for reducing wetted-wall temperatures.

1 Reduce fuel flow passage area to increase fuel velocity
   * Increases heat transfer coefficients
   * Reduces wetted-wall temperature
   * Reduces fuel residence time
2 Add air gaps
   * Metals with air gaps are more effective than solid ceramics
3 Substitute ceramics for metal parts
   * Ceramics are very effective in combination with air gaps
4 Avoid bends and steps in the fuel flow path
   * They create stagnant fuel regions that have low transfer coefficients and thus high wetted-wall temperatures

Sample tube coking test results showed the importance of surface finish on the fuel coking rate. Reducing the surface roughness from 3.1 μm to 0.25 μm reduced the deposition rate by 26 percent. In summary, Stickles et al. found that reduced passage flow area, reduced surface roughness, additional insulating air gaps, and replacement of metallic tip components with ceramics minimized the wetted-wall temperature. Vacuum gaps, reduced emissivity coatings, and thermal barrier coatings did not offer significant wall-temperature reductions.

Thermal modeling studies carried out by Myers et al. (1992) suggested that the two major sources of heat absorption into the fuel nozzle were the air swirl vanes and any surface exposed to the flame. At an altitude cruise condition, for example, the predicted heat flux entering the nozzle face from flame radiation is more than 20 times that absorbed by conduction and convection through the burner feed arm. The frontal area exposed to the flame is thus a key element in nozzle thermal loading.

Myers et al. concluded that substantial reductions in wetted-wall temperatures can be realized at extreme fuel and air inlet temperatures by using simple air gaps as thermal barriers. Detailed thermal analysis and simple thermal barriers, rather than exotic cooling schemes, can produce dramatic improvements in thermal protection.

The problem of fuel coking and its strong adverse effects on spray uniformity and pollutant emissions is one of growing concern due to the anticipated gradual deteriorations in fuel quality and the continuing trends toward higher temperature engines.

Table 1 Principal pollutants emitted by gas turbines

POLLUTANT	EFFECT
Carbon monoxide (CO)	Toxic
Unburned hydrocarbons (UHC)	Contributes to urban smog
Particulate matter (C)	Visible. Possible link to asthma and other respiratory diseases
Oxides of nitrogen (NO_X)	Toxic, precursor of chemical smog, depletion of ozone in stratosphere
Oxides of sulfur (SO_X)	Toxic, corrosive
Carbon dioxide (CO_2)	Contributes to greenhouse effect

Emissions Concerns

The exhaust from an aircraft gas turbine is composed of carbon monoxide (CO), carbon dioxide (CO_2), water vapor (H_2O), unburned hydrocarbons (UHC), particulate matter (mainly carbon), oxides of nitrogen, and excess atmospheric oxygen and nitrogen. Carbon dioxide and water vapor have not always been regarded as pollutants because they are the natural consequence of complete combustion of a hydrocarbon fuel. However, they both contribute to global warming and can only be reduced by burning less fuel. With industrial gas turbines burning residual fuels, an additional pollutant of concern is oxides of sulfur, mainly SO_2 and SO_3. They are toxic and corrosive and lead to the formation of sulfuric acid in the atmosphere. Since virtually all the sulfur in the fuel is oxidized to SO_x, the only viable limitation strategy is to remove sulfur from the fuel prior to combustion.

The principal pollutants are listed in Table 1. Carbon monoxide reduces the capacity of the blood to absorb oxygen and, in high concentrations, can cause asphyxiation and even death.

Unburned hydrocarbons are not only toxic, but they also combine with oxides of nitrogen to form photochemical smog. Particulate matter, often called soot or smoke, is generally not considered toxic at the levels emitted, but recent studies by Seaton et al. (1995) indicate a strong association between asthma and other respiratory diseases and atmospheric pollution by concentrations of small particles in the microgram range. Oxides of nitrogen (NO + NO_2), of which the predominant compound at high emission levels is NO, not only contribute to the production of photochemical smog at ground level but also cause damage to plant life and add to the problem of acid rain. Relative to other sources, aircraft engines are only minor contributors to the overall NO_x burden. For example, in the United States NO_x emissions from aircraft engines account for only about 0.5 percent of the total emissions nationwide from all sources (Bahr, 1991). On a global basis, NO_x emissions from aircraft engines constitute less than 3 percent of all man-made NO_x emissions. However, of special concern is that these emissions are released at altitude and lead to the formation of ozone in the troposphere. This is the region in which stationary gas turbines and subsonic aircraft operate. Measurements taken over a long period of time at altitudes from one to three kilometers indicate that the level of ozone over Western Europe is now approaching 50 ppb (parts per billion). Prolonged exposure to ozone concentrations around 100 ppb is associated with respiratory illnesses, impaired vision, headaches, and allergies. Ground level ozone is especially important in regions where the topographical features prevent the local weather system from removing the ozone formed in combustion and where strong sunshine can promote the photochemical reactions that lead to smog. Los Angeles is the classic example of such a region. It is hardly surprising therefore that the drive toward very stringent emissions legislation on NO_x first emanated from this city.

Similar studies indicate that NO_x emissions emitted at higher altitudes can contribute to the depletion of the stratospheric ozone layer. Unfortunately, supersonic aircraft are required to operate at such high altitudes. Ozone depletion results in an increase in ground level ultraviolet radiation, which leads to an increase in the incidence of skin cancer.

For industrial gas turbines the problems posed by exhaust gas emissions are no less challenging than for aero-engines. World energy demand is forecast to grow over the next 30 years at around 1.4 percent per annum. This demand will be met predominantly by the combustion of fossil fuels (Singh, 1994). Thus the manufacturers and users of gas turbines for utility power generation now find themselves at the forefront in regard to responsibility for emissions issues.

Emissions Regulations

The International Civil Aviation Organization (ICAO) has promulgated regulations for civil subsonic turbojet/turbofan engines with rated thrust levels above 26.7 kN (6,000 pounds) for a defined landing-takeoff cycle (LTO) which is based on an operational cycle around airports. This LTO cycle is intended to be representative of operations performed by an aircraft as it descends from an altitude of 914 m (3000 ft) on its approach path to the time it subsequently attains the same altitude after takeoff.

Table 2 ICAO gaseous emissions standards

Emission, g/kN	Subsonic turbojet/ turbofan engines*	Supersonic turbojet/ turbofan engines
o HC	19.6	$140(0.92)^{\pi_{oo}}$
o CO	118.0	$4550(\pi_{oo})^{-1.03}$
o NOx	$40+2\pi_{oo}$	$36+2.42\pi_{oo}$

*Newly manufactured engines with rated takeoff thrust greater than 26.7 kN.

π_{oo} = engine pressure ratio at takeoff

Table 3 Typical aircraft emissions

TYPICAL DISTRIBUTION OF TOTAL EMISSION MASS QUANTITIES GENERATED DURING A FLIGHT OF AN AIRCRAFT EQUIPPED WITH MODERN ENGINES			
	o Aircraft: Twin-engine transport o Range: 500 nautical miles		
Category	Percent of total emission mass		
	During ICAO landing-takeoff cycle	During climbout/ cruise/descent	Overall
Smoke	- - -	0.1	0.1
HC	0.6	1.0	1.6
CO	5.4	7.0	12.4
NOx	7.8	78.1	85.9
Total	13.8 (56.5% NOx)	86.2 (90.6% NOx)	100.0

The standards for CO, UHC, and NO_x emissions are presented in Table 2, in which π_{oo} is the engine pressure ratio at takeoff. They are expressed in terms of a parameter that consists of the total mass in grams of any given gaseous pollutant emitted during the LTO cycle per kilonewton of rated thrust at sea level.

We have

$$\text{Emission} = \text{Emission Index (EI)} \quad \left[\frac{\text{g/kN}}{}\right] \quad \left[\frac{\text{g/kg fuel}}{}\right] \times \text{Engine SFC} \left[\frac{\text{kg fuel/h kN}}{}\right] \times \text{Time in Mode} \left[\text{h}\right] \tag{3}$$

This equation demonstrates that improving (i.e., reducing) the specific fuel consumption results directly in a reduction of the pollution levels. Because the CO and UHC levels of modern engines have been greatly reduced at all low power conditions, and only NO_x is emitted in appreciable amounts at altitude cruise, in practice the emissions generated by aircraft engines consist primarily of NO_x. A typical example of the emissions mass distribution associated with the flight of a modern subsonic aircraft has been provided by Bahr (1992) and is shown in Table 3. This table represents a flight of 900 km (500 nautical miles) and shows that NO_x emissions predominate both in the vicinity of the airport and during altitude cruise. For a longer flight, NO_x emissions would account for an even larger fraction of the total emissions mass.

The ICAO standard for smoke measurement is expressed in terms of a Smoke Number (SN), which is related to the engine takeoff thrust (F_{00}) by the expression

$$SN = 83.6(F_{00})^{-0.274} \tag{4}$$

This expression is shown graphically in Fig. 8. The intention of this standard is to eliminate any visible smoke from the engine exhaust. As smoke visibility depends on both the smoke

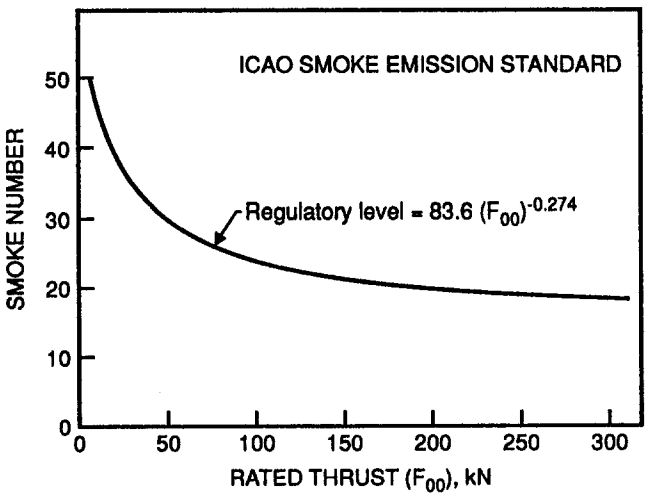

Fig. 8 ICAO smoke emissions standards

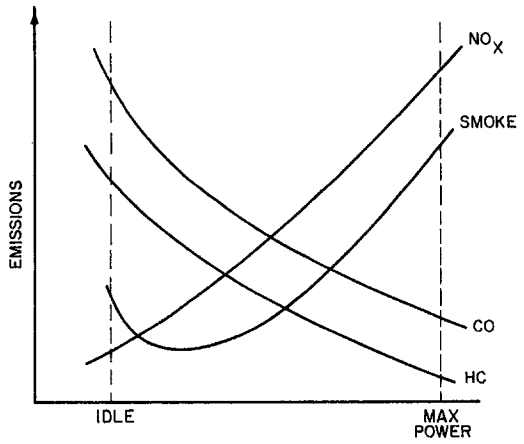

Fig. 10 Emissions characteristics of gas turbine engines

concentration, as indicated by the value of SN, and on the viewing path length, the allowable SN of a high thrust engine is lower than for a low thrust engine because of its larger exhaust diameter.

As far as subsonic aircraft engines are concerned, the situation in regard to compliance with ICAO regulations is generally satisfactory, due mainly to the engine manufacturers' efforts during the past 20 years in improving combustor design and in reducing engine specific fuel consumption. However, in view of the continuing pressure to reduce NO_x emissions from all sources, efforts by ICAO to formulate more rigorous NO_x standards are in progress and a 20 percent increase in the stringency of the current ICAO standard has been enacted and will come into effect at the end of 1995. In Sweden a tax is now imposed on NO_x and UHC emissions generated during domestic flights, while limits on the total yearly emissions quantities at some airports are being considered in both Sweden and Switzerland (Bahr, 1995). These steps could constitute important precedents. For future supersonic aircraft engines, very stringent goals have been established. The future of second-generation supersonic aircraft depends crucially on compliance with these goals, which can only be met by the use of yet-to-be-developed ultralow NO_x combustor designs.

The discussion so far has focused mainly on aircraft engines, but the same general considerations apply with equal force to the use of gas turbines in other applications. Regulations governing emissions from gas turbines at ground level tend to be highly complex because the legislation varies from one country to another and is supplemented by local or site-specific regulations and ordinances governing the size and usage of the plant under consideration and the type of fuel to be used. Figure 9, due to

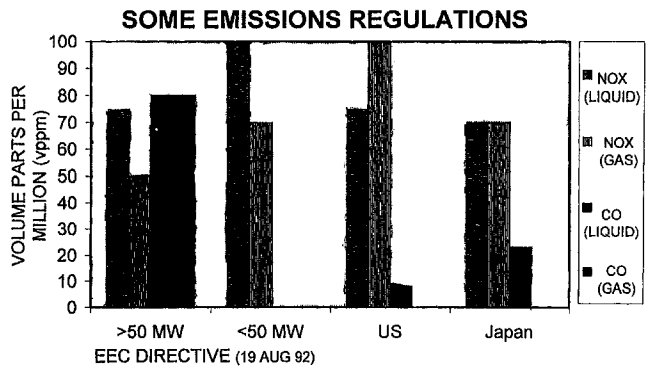

Fig. 9 Some emissions regulations for industrial engines

Singh (1994), summarizes the EEC Directive of August 19, 1992, concerning CO and NO_x emissions for gaseous and liquid fuels for gas turbines over and under 50 MW. These levels are then compared with some legislation from the U.S. and Japan.

Most of the drive toward more stringent regulations for stationary gas turbines has been directed at oxides of nitrogen. Changes in legislation are now calling for NO_x requirements as low as 25 ppm and even 9 ppm. In some locations the installation of a new gas turbine power generating facility calls for NO_x emissions levels below 5 ppm. Moreover, there is often a requirement to use the "Best Available Control Technology" (BACT) or the "Lowest Available Emission Rate" (LAER). This has led to concerns such as those expressed by Angello and Lowe (1989), that if a new technology is developed that significantly improves the ability to reduce NO_x emissions, it effectively sets the emission standard that all subsequent plants must meet. Thus, as new technologies are developed to meet the ever-increasingly restrictive emission limits, they become the standard by which the next round of emission regulations is guided.

Combustors designed specifically for low-NO_x emissions are often described as "low-NO_x" or "ultralow-NO_x". Broadly speaking, the term "low-NO_x" relates to emissions in the range from 25 to 50 ppm (corrected to 15 percent O_2), whereas "ultralow NO_x" generally denotes emissions below 25 ppm. With advances in low emissions technology, the description "ultralow-NO_x" is becoming increasingly reserved for emission levels below 10 ppm.

Mechanisms of Pollutant Formation

The concentration levels of pollutants in gas turbine exhausts can be related directly to the temperature, time, and concentration histories of the combustion process. These vary from one combustor to another and, for any given combustor, with changes in operating conditions. The nature of pollutant formation is such that the concentrations of carbon monoxide and unburned hydrocarbons are highest at low-power conditions and diminish with increase in power. In contrast, oxides of nitrogen and smoke are fairly insignificant at low power settings and attain maximum values at the highest power condition. These characteristic trends are sketched in Fig. 10.

Carbon Monoxide. In combustion zones designed to operate fuel-rich, large amounts of CO are formed owing to the lack of sufficient oxygen to complete the reaction to CO_2. If, however, the combustion zone mixture strength is stoichiometric or moderately fuel-lean, significant amounts of CO will be present owing to the dissociation of CO_2. In principle, it should be possible to reduce this CO to a very low level by the staged

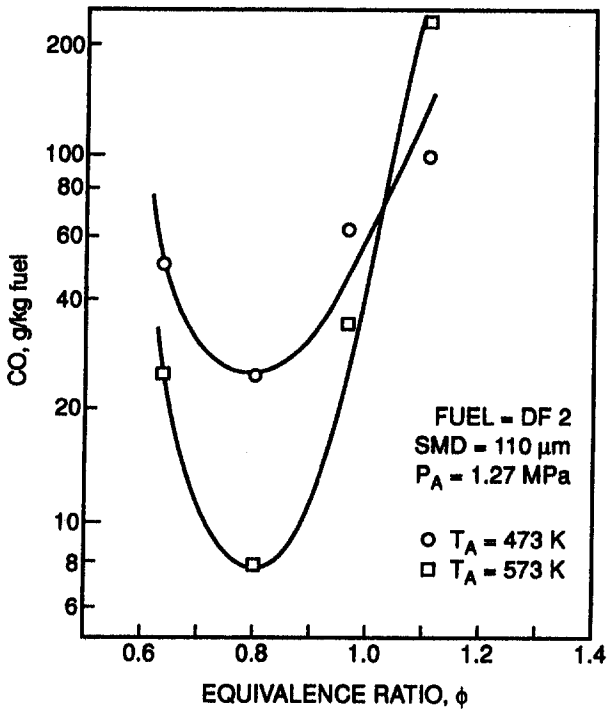

Fig. 11 Influence of inlet air temperature on CO emissions

admission of additional air downstream of the primary zone to achieve a gradual reduction in burned gas temperature. In practice, CO emissions are found to be much higher than predicted from equilibrium calculations and to be highest at low-power conditions, where burning rates and peak temperatures are relatively low.

The main factors influencing burning rates, and hence also CO emissions, are engine and combustor inlet temperatures, combustion pressure, and primary-zone equivalence ratio. (Note that equivalence ratio is the actual fuel/air ratio divided by the stoichiometric value of fuel/air ratio.) All these aspects have been investigated by many workers, including Bahr (1982, 1987, 1991, 1992), Bayle Labouré (1991), Correa (1991), Desaulty (1991), Koff (1993), Mosier and Pierce (1980), and Sturgess et al. (1993). In their studies on pollutant emissions from continuous flow combustors, Rink and Lefebvre (1989a) used a continuous flow tubular combustor, 150 mm in diameter, in conjunction with an array of 36 equally spaced "microscopic" airblast atomizers, to achieve a uniform distribution of fuel in the mixture entering the combustion zone. This method of fuel injection had another useful advantage in that it allowed the mean drop size in the fuel spray to be varied in a controlled manner while maintaining all other flow conditions constant. All measurements of pollutant emissions were carried out at a distance of 170 mm from the fuel injectors.

Influence of Equivalence Ratio. Some of the results obtained by Rink and Lefebvre are presented in Fig. 11, which shows the variation of CO emissions with equivalence ratio for two values of inlet air temperature, namely 473 and 573 K. Both curves exhibit the same general characteristics. They show that CO emissions diminish with increase in equivalence ratio, reaching a minimum value at an equivalence ratio, ϕ, of around 0.8. Beyond this point any further increase in equivalence ratio causes CO emissions to rise. These trends are typical of those observed for other types of combustion systems. The high levels of CO at low equivalence ratios are due to the slow rates of oxidation associated with low combustion temperatures. Increase in equivalence ratio raises the flame temperature, which accelerates the rate of oxidation so that CO emissions decline. However, at temperatures higher than around 1800 K the production of CO by chemical dissociation of CO_2 starts to become significant. Thus, at high equivalence ratios CO levels are high because they attain equilibrium values. Only in the fairly narrow range of equivalence ratios from around 0.7 to 0.9 can low levels of CO be achieved.

Measurements of CO emissions from more practical combustion chambers are fully consistent with these results. For example, Sturgess et al. (1993) used a JT9D-70A combustor supplied with aviation fuel to examine the effects of combustor operating conditions and airflow distribution on the emissions of CO, UHC, NO_x, and smoke. The results obtained for CO at engine idle conditions are shown in Fig. 12. Although this figure demonstrates minimum CO at an equivalence ratio around 1.0 as opposed to the value of 0.8 obtained by Rink and Lefebvre, this difference is not considered significant because the amount of air participating in primary combustion is notoriously difficult to estimate accurately.

Influence of Inlet Air Temperature. The effect of an increase in inlet air temperature is to reduce CO, as illustrated in Fig. 11. This it does by raising the flame temperature, which accelerates the conversion of CO into CO_2. At equivalence ratios of stoichiometric and above, this higher flame temperature promotes the formation of CO by dissociation so that, at the highest equivalence ratios, the CO concentrations are highest for the higher inlet air temperature. These trends are clearly illustrated in Fig. 11.

Influence of Pressure. Figure 13 demonstrates the beneficial effect of an increase in combustion pressure in reducing CO emissions. At low equivalence ratios, increase in pressure diminishes CO by accelerating the rate of conversion of CO into CO_2. At high equivalence ratios, increase in combustion pressure reduces CO emissions, albeit to a lesser extent, by suppressing chemical dissociation.

Influence of Ambient Air Temperature. Hung and Agan (1985) have examined the influence of ambient air temperature on the CO emissions from a 7 MW industrial engine supplied with natural gas fuel. A strong air temperature effect on measured CO was observed. CO emissions for an air temperature

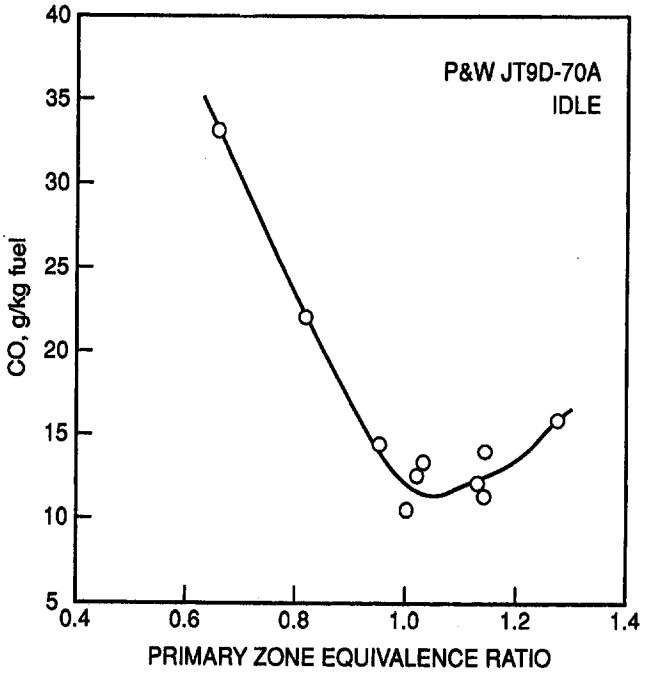

Fig. 12 Influence of primary zone equivalence ratio on CO emissions

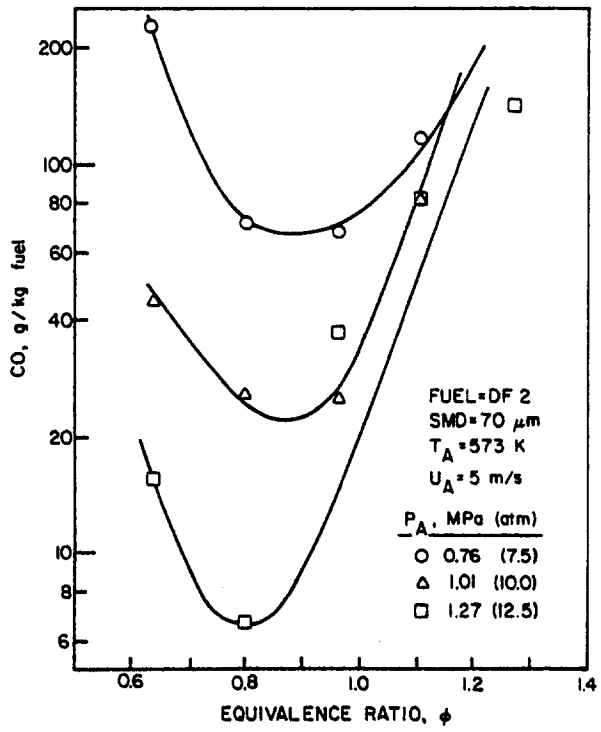

Fig. 13 Influence of combustion pressure on CO emissions

of 287 K were around three times higher than the corresponding values at 298 K. A correlation of these data carried out by Hung (1993) yielded the following expression for calculating the effect of ambient air temperature on CO. It is considered valid for values of temperature up to 303 K.

$$CO_T/CO_{288} = 1 - 0.0634(T - 288) \qquad (5)$$

where CO_T = emissions of CO in ppm at 15 percent O_2 at ambient temperature, T, and CO_{288} = emissions of CO in ppm at 15 percent O_2 at 288 K. This equation should be used with caution because it is likely to be very engine specific. Nevertheless, it describes quantitatively what many other workers have observed, namely the high sensitivity of CO emissions to inlet air temperature. This small but important point needs to be borne in mind constantly when making comparative combustor tests for CO emissions at different times.

A further important factor influencing CO emissions is the amount of liner wall-cooling air employed in the primary combustion zone. CO and UHC formed in primary combustion can migrate toward the liner walls and become entrained in the wall-cooling air. The temperature of this air is so low that all chemical reactions are effectively "chilled." Thus the film-cooling air emanating from the primary zone normally contains high concentrations of CO and UHC. Unless these species are subsequently entrained into the hot central core with sufficient time to react to completion, they will appear in the exhaust gas. Thus, reduction in film-cooling air by more efficient cooling (or even ceramic liners) in the primary zone is effective in reducing CO.

Unburned Hydrocarbons. These include fuel that emerges from the combustor in the form of drops or vapor, as well as the products of the thermal degradation of the parent fuel into species of lower molecular weight. They are normally associated with poor atomization, inadequate burning rates, the chilling effects of film-cooling air, or any combination of these. The reaction kinetics of UHC formation are more complex than for CO formation, but generally it is found that those factors that influence CO emissions also influence UHC emissions and in much the same manner. Thus, in common with CO, UHC emissions are reduced by increases in inlet air temperature and combustor pressure, and by any change in equivalence ratio toward the optimum value of around 0.8.

Smoke. Exhaust smoke is caused by the production of finely divided soot particles in fuel-rich regions of the flame. With pressure-swirl atomizers, the main soot-forming region lies inside the fuel spray, at the center of the combustor, as illustrated in Fig. 14. This is the region in which the recirculating burned products move upstream toward the fuel spray, and in which local pockets of fuel vapor are enveloped in oxygen-deficient gases at high temperature. In these fuel-rich regions, soot may be produced in considerable quantities. Most of the soot produced in the primary zone is consumed in the high-temperature regions downstream. Thus, from a smoke viewpoint, a combustor may be considered to comprise two separate zones—the primary zone, which governs the rate of soot formation, and the intermediate zone (and, on modern high-temperature engines, the dilution zone also), which determines the rate of soot consumption. The soot concentration actually observed in the exhaust gas is an indication of the dominance of one zone over the other.

Influence of Pressure. Problems of soot and smoke are always most severe at high pressures. There are several reasons for this; some derive from chemical effects, while others stem from physical factors that affect spray characteristics and hence the distribution of mixture strength in the soot-forming regions of the flame. For premixed kerosine/air flames it is found that no soot is formed at pressures below 0.6 MPa and equivalence ratios below 1.3.

One adverse effect of an increase in pressure is to extend the limits of flammability, so that soot is produced in regions that, at lower pressures, would be too rich to burn (see Fig. 15). Increased pressure also accelerates chemical reaction rates, so that combustion is initiated earlier and a larger proportion of the fuel is burned in the fuel-rich regions adjacent to the spray. With pressure atomizers, reduced spray penetration is one of the main causes of smoke at high pressures. Thus whereas at low pressures the fuel is distributed across the entire combustion zone, at high pressures it tends to concentrate in the soot-forming region just downstream of the nozzle. Still another adverse effect of an increase in pressure is to reduce the cone angle of the spray. This encourages soot formation, partly by increasing the mean fuel drop size, but mainly by raising the mixture strength in the soot-forming zone.

The total effect of all these factors is that smoke emission increases steeply with pressure, as shown in Fig. 16. Airblast atomizers are spared these problems because the fuel drops they produce are always airborne. The distribution of fuel through the combustion zone is dictated solely by the liner airflow pattern, which is not susceptible to changes in pressure.

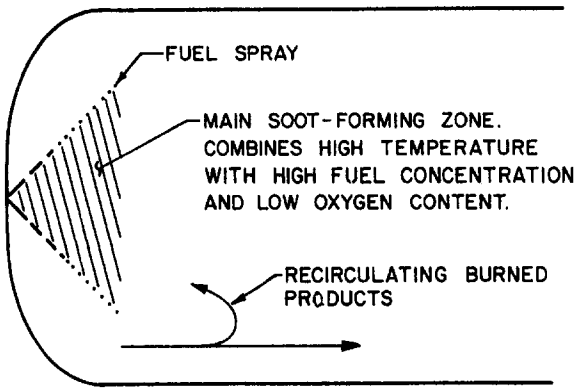

Fig. 14 Soot-forming zone for conventional combustors

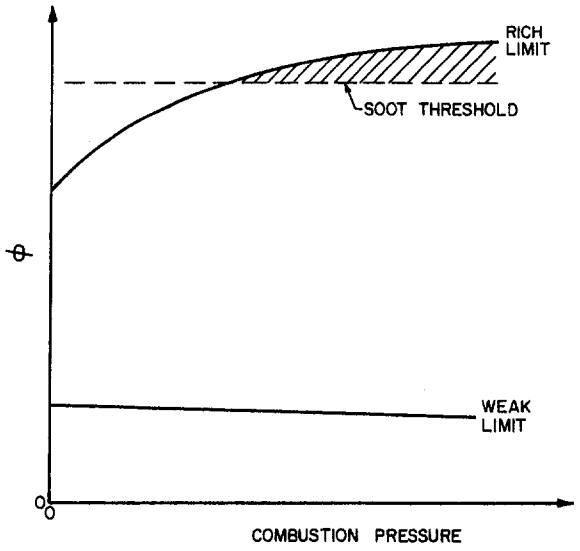

Fig. 15 Influence of pressure on flammability limits

Influence of Fuel Type. Fuel properties can influence smoke production in two ways: first by inducing the formation of local fuel-rich regions, and second, by exerting variable resistance to carbon formation. The former is controlled by physical properties, such as viscosity and volatility, which affect the mean drop size, penetration, and rate of evaporation of the fuel spray, whereas the latter relate to molecular structure. It is well established that smoking tendency increases with a reduction in hydrogen content and, in fact, hydrogen content is commonly used in correlating rig and engine test data on various soot-related parameters such as smoke emissions, flame radiation, and liner wall temperature. However, Chin and Lefebvre (1993) have shown that a better index of sooting tendency is the ASTM smoke point, which is obtained experimentally by burning the test fuel in a wick lamp and slowly increasing the height of the flame until it begins to smoke. The height of the flame in millimeters is the smoke point; the higher this is, the lower is the tendency of the fuel to soot formation.

The correlations shown in Figs. 17 and 18 were obtained from measurements of smoke number carried out on Pratt and Whitney TF33 and F100 combustors, respectively. The generally high quality of the data fit obtained with these and several other aircraft combustors led Chin and Lefebvre to conclude that smoke point is superior to hydrogen content as a correlating parameter for soot-related combustion phenomena.

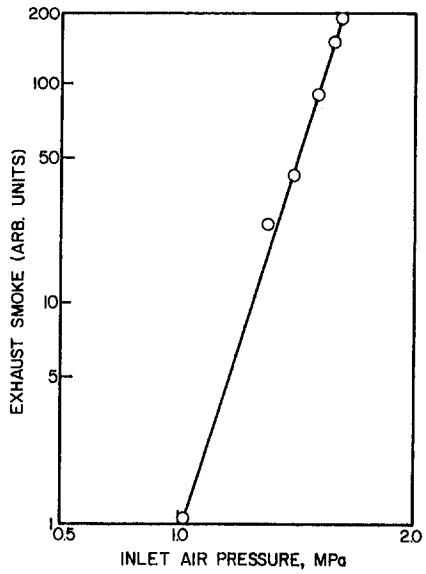

Fig. 16 Data illustrating the effect of pressure on exhaust smoke

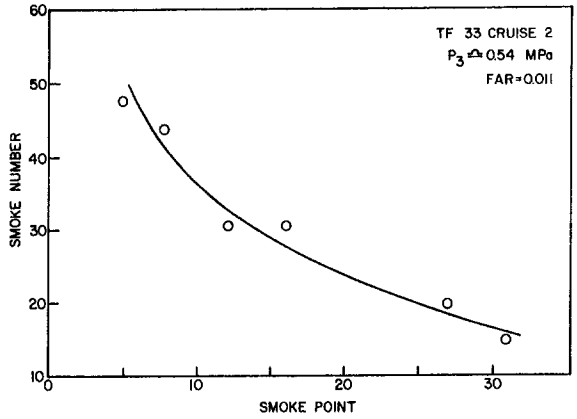

Fig. 17 Correlation of smoke number with smoke point for a TF 33 combustor

Oxides of Nitrogen. Some of the nitric oxide (NO) formed in combustion can subsequently oxidize to NO_2. For this reason it is customary to lump NO and NO_2 together and express results in terms of oxides of nitrogen (NO_x), rather than NO. At high emission levels the predominant compound is nitric oxide, which is produced mainly by the oxidation of atmospheric nitrogen in high-temperature regions of the flame. The process is endothermic and it proceeds at a significant rate only at temperatures above around 1850 K. It can be produced by four different mechanisms, as discussed below.

1 Thermal NO. This is produced by oxidation of atmospheric nitrogen in the postflame gases. Most of the proposed reaction schemes for thermal NO utilize the extended Zeldovich mechanism:

$$N_2 + O = NO + N$$

$$N + O_2 = NO + O$$

$$N + OH = NO + H$$

NO formation is found to peak on the fuel-lean side of stoichiometric. This is a consequence of the competition between fuel and nitrogen for the available oxygen. Although the combustion temperature is higher slightly on the rich side of stoichiometric, the available oxygen is then consumed preferentially by the fuel. For even richer mixtures, a further reduction of NO may

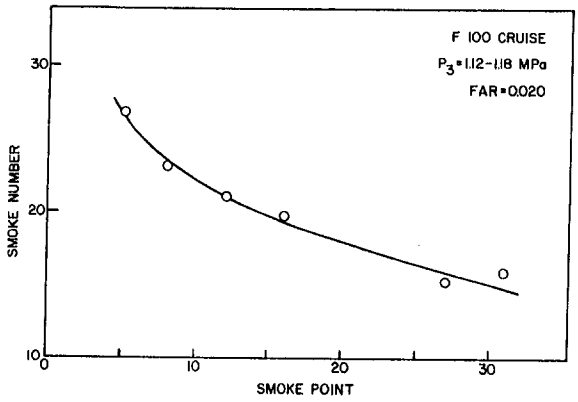

Fig. 18 Correlation of smoke number with smoke point for an F 100 combustor

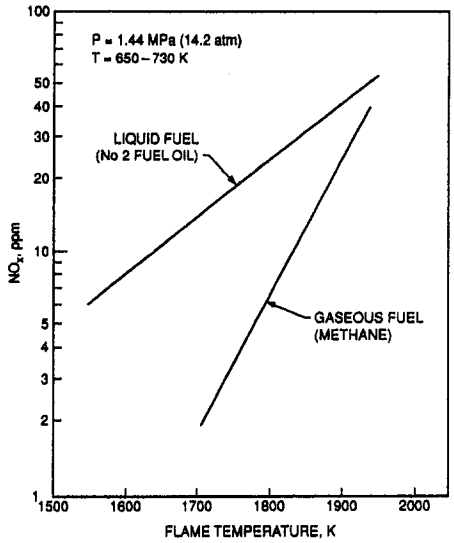

Fig. 19 Dependence of NO_x on flame temperature for liquid and gaseous fuels

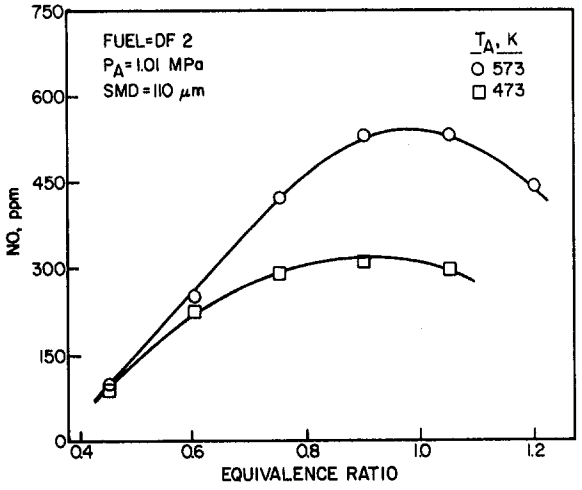

Fig. 20 Influence of inlet air temperature on nitric oxide emissions

occur if sufficient hydrocarbon radicals and adequate residence time are available.

Figure 19 illustrates the exponential dependence of NO_x on flame temperature for both gaseous and liquid fuels. It is based on experimental data (not shown in the figure) obtained by Snyder et al. (1994) in their studies on the combustion performance achieved when using a tangential entry lean-premixed fuel nozzle. Data similar to those shown in Fig. 19 have been obtained by many different workers using many different types of combustion systems. Of special interest in this figure is that the well-known difference in NO_x emissions between liquid and gaseous fuels diminishes with increase in flame temperature, becoming negligibly small at the highest levels of temperature. With liquid fuels there is always the potential for near-stoichiometric combustion temperatures, and consequently high NO_x formation, in the region surrounding the fuel drops, even though the average equivalence ratio throughout the combustion zone is appreciably less than stoichiometric. With increase in equivalence ratio, the ambient flame temperature becomes closer to the stoichiometric value, so that local conditions around the fuel drops have less influence on the overall combustion process and the NO_x emissions begin to approximate those produced by gaseous fuels.

As NO emissions are very dependent on flame temperature, an increase in inlet air temperature would be expected to produce a significant increase in NO, and this is confirmed by the results shown in Fig. 20 from Rink and Lefebvre (1989b). This figure contains data for a mean fuel drop size (SMD) of 110 μm, but similar results were obtained when the SMD was reduced to 30 μm.

Combustor residence time can also influence NO_x emissions, as shown in Fig. 21, which contains results obtained by Anderson (1975) when using a premix-prevaporize combustor burning gaseous propane fuel. It shows that NO_x emissions increase with increase in residence time, except for very lean mixtures (ϕ = 0.4), for which the rate of formation is so low that it becomes fairly insensitive to time. Similar results showing the insensitivity of NO_x formation to residence time in lean premixed combustion have been obtained by Leonard and Stegmaier (1994) and Rizk and Mongia (1993a). These findings have important practical implications to the design of lean premixed combustors.

The key points regarding thermal NO may be summarized as follows:

1 Thermal NO formation is controlled largely by flame temperature.
2 Little NO is formed at temperatures below around 1850 K.
3 For conditions typical of those encountered in conventional gas turbine combustors (high temperatures for less than a few milliseconds), NO increases linearly with time but does not attain its equilibrium value.
4 For very lean premixed combustors ($\phi < 0.5$), NO formation is largely independent of residence time.

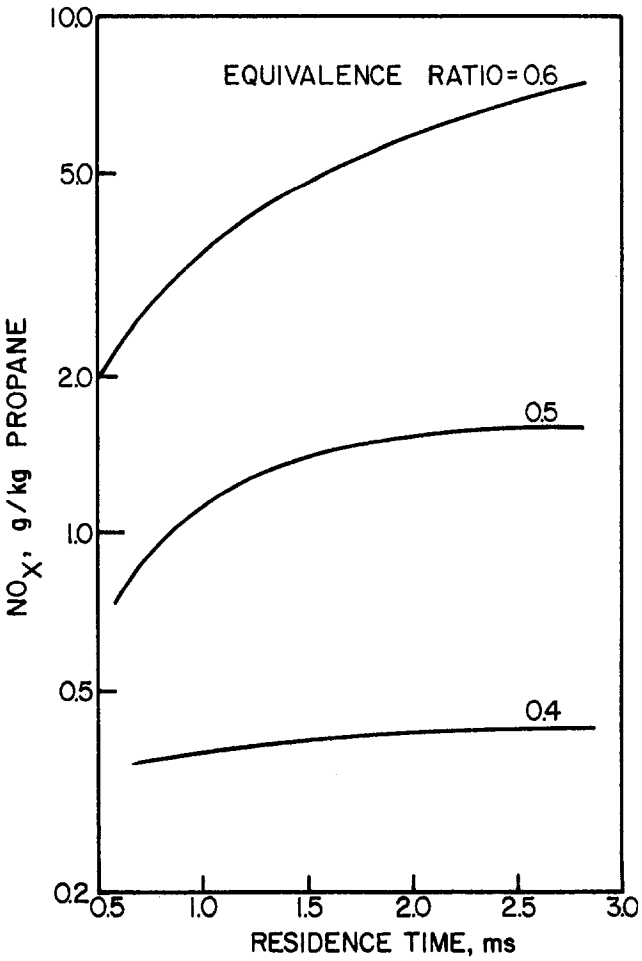

Fig. 21 Effect of residence time on NO_x in a premixed fuel–air system

2 Nitrous Oxide Mechanism. According to Nicol et al. (1992) this mechanism is initiated by the reaction

$$N_2 + O = N_2O$$

and the N_2O (nitrous oxide) formed is then oxidized to NO mainly by the reaction

$$N_2O + O = NO + NO$$

but also by the reactions

$$N_2O + H = NO + NH$$

$$N_2O + CO = NO + NCO$$

3 Prompt NO. Under certain conditions, NO is found very early in the flame region—a fact that is in conflict with the idea of a kinetically controlled process. According to Nicol et al. the initiating reaction is

$$N_2 + CH = HCN + N$$

The balance of the prompt NO_x mechanism involves the oxidation of the HCN molecules and N atoms. Under lean-premixed conditions, the HCN oxidizes to NO mainly by a sequence of reactions involving HCN → CN → NCO → NO. The N atom reacts mainly by the second Zeldovich reaction.

Of special interest and importance is the influence of pressure on prompt NO formation because this could be the main contributor to the NO emissions produced in lean premixed combustion (Correa, 1991). There are, however, few data available on this effect. Fennimore's (1971) pioneering study of prompt NO in ethylene–air flames over a range of pressures from 1 to 3 atm concluded that prompt NO $\propto P^{0.5}$. Later work by Heberling (1976) over a much wider range of pressures from 1 to 18 atm showed that prompt NO was independent of pressure. Altemark and Knauber (1987) also concluded that NO_x is independent of pressure for equivalence ratios below 0.6. The practical implications of these findings are discussed below.

4 Fuel NO. If fuels contain organically bonded nitrogen, then some of this nitrogen will eventually form the so-called "fuel NO." The percentage of nitrogen undergoing this change increases only slowly with increasing flame temperature. Light distillate fuels contain small amounts of organic nitrogen, less than 0.06 percent, but the heavy distillates may contain as much as 1.8 percent. Thus, depending on the degree of nitrogen conversion, the fuel NO can represent a considerable proportion of the total NO (Merryman and Levy, 1975).

Nicol et al. (1992) have examined analytically the relative contributions of the various mechanisms discussed above to the total NO_x emissions produced by a lean-premixed combustor burning methane fuel, for which, of course, the fuel NO is zero. The results of their study showed that at relatively high temperatures of around 1900 K, and equivalence ratios of around 0.8, the contributions are about 60 percent thermal, 10 percent nitrous oxide, and 30 percent prompt. With reductions in temperature and equivalence ratio, the contributions made by nitrous oxide and prompt NO increase significantly until, at a temperature of 1500 K and an equivalence ratio of around 0.6, the relative contributions to the total NO_x emissions become 5 percent thermal, 30 percent nitrous oxide, and 65 percent prompt. These results clearly have great importance to the design of ultralow NO_x lean-premixed combustors.

Influence of Pressure. The influence of pressure on NO_x formation is of special importance due to the continual trend toward engines of higher pressure ratio to meet the need for lower fuel consumption. Combustor testing at high pressures is extremely expensive and it would therefore be highly convenient to carry out combustor development at lower levels of pressure and then extrapolate the results obtained to high levels of pressure where NO_x emissions attain their highest values.

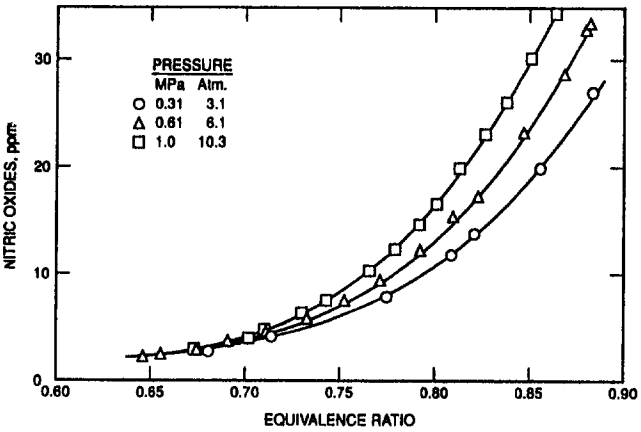

Fig. 22 Data illustrating the effect of pressure on NO_x formation

Such extrapolation could be carried out with confidence if the relationship between NO_x and pressure were accurately known. Unfortunately, the experimental data obtained on different combustor types are conflicting in this regard. They vary from no effect of pressure on NO_x to quite significant increases in NO_x with increase in pressure.

For conventional combustors it is generally found that $NO_x \propto P^n$, where n has values ranging from around 0.5 to around 0.8. Laboratory burners can also exhibit a strong effect of pressure on NO_x. For example, the results of Maughan et al. (1994) from a well-mixed combustor supplied with natural gas fuel showed that raising the combustor outlet temperature from 1227 to 1310 K caused n to increase from 0.38 to 0.51. Maughan et al. regard this result as evidence that the lowest NO_x levels result from the nitrous oxide and prompt mechanisms which dominate at low temperatures and which are independent of pressure, whereas the higher NO_x levels associated with higher combustion temperatures are due primarily to thermal NO_x which exhibits a square root dependence on pressure.

These results and conclusions are fully consistent with those obtained by Correa and co-workers (Leonard and Corea, 1990; Correa, 1991). These workers studied turbulent premixed methane–air flames using an uncooled perforated plate burner operating at pressures from 1 to 10 atm, inlet air temperatures from 300 to 615 K, and equivalence ratios from 0.5 to 0.9. Their modeling featured a stirred reactor for flame stabilization followed by a plug flow reactor and a kinetic scheme which included thermal and prompt NO. The results confirmed that the low temperatures of lean flames preclude significant formation of NO by the thermal mechanism. At temperatures below 1800 K the prompt mechanism appears to be dominant. The implication of these results to the effect of pressure on NO_2 formation is well illustrated in Fig. 22, which contains some of the experimental data of Correa et al. and which highlights their conclusions in regard to the influence of flame temperature on the pressure dependence of NO_x formation. In this and in other figures contained in this paper, the values of NO and NO_x quoted have been corrected to the values that would have been obtained if the combustion air had contained 15 percent oxygen. The following expression is used to make this correction:

$$(NO_x)15\%O_2 = (NO_x) \times 5.9/(20.9 - O_{2meas.}) \quad (6)$$

where NO_x concentrations are expressed in ppm by volume on a dry basis and O_2 content is expressed as a percentage by volume on a dry basis.

The purpose of this parameter is partly to remove ambiguity when comparing different sets of experimental data, but mainly to indicate that combustors burning less fuel are expected to produce less NO_x. Figure 22 shows that NO_x is independent of pressure in the leanest premixed flames. Increase in flame

temperature, corresponding to an increase in equivalence ratio, causes the pressure exponent to increase until, in the near-stoichiometric region, it attains the value of 0.5, corresponding to NO formation by the thermal mechanism.

Additional evidence to support the argument that NO_x formation in well-mixed, low-temperature flames is largely independent of pressure has been provided by Leonard and Stegmaier (1994) and Steele et al. (1995). Their experiments covered ranges of pressure from 1 to 30 atm and 1 to 7.1 atm, respectively. Leonard and Stegmaier found little or no effect of pressure, while the results obtained by Steele et al. using a lean, premixed, high-intensity combustor showed a neutral or even slightly negative effect of pressure on NO_x. Comparatively little is known about the pressure dependence of NO_x formation in fuel-rich flames. Rizk and Mongia (1991b) performed a three-dimensional analysis to examine the influences of pressure and residence time on NO_x formation in the rich zone of a rich/quench/lean (RQL) combustor. Their predictions indicate that the value of the pressure exponent n varies with rich-zone equivalence ratio according to the relationship:

$$n = 116.5 \exp - (\phi/0.222) \quad (7)$$

For a typical rich zone equivalence ratio of 1.4 this equation gives a value for n of 0.68.

Pollutant Reduction in Conventional Combustors

Although it might reasonably be argued that conventional combustors are no longer of any real technical interest, they do nevertheless constitute the big majority of combustors now in service. Furthermore, most of our knowledge of the key factors governing pollutant formation in continuous flow combustion systems, which is now being applied to the design and development of ultralow-NO_x combustors, was acquired from experience gained on what are now called "conventional" combustors.

The main factors controlling emissions from conventional combustors may be considered in terms of:

1 The primary-zone temperature and equivalence ratio.
2 The degree of homogeneity of the primary-zone combustion process.
3 Residence time in the primary zone.
4 Liner-wall quenching characteristics.

With liquid fuels, spray properties are also of prime importance.

In considering practical design methods for pollutant reduction, attention is focused first on individual pollutant species. It will become clear, however, that with conventional combustors a great deal of compromise is involved in design, not only between one species and another, but also among the many other performance requirements, such as lean blowout limits, pattern factor, and size.

Carbon Monoxide and Unburned Hydrocarbons. The presence of these species in the exhaust gases is a manifestation of incomplete combustion. Thus all approaches to CO and UHC reduction are based on a common philosophy, which is to raise the level of combustion efficiency. An effective method of achieving this is by redistributing the airflow to bring the primary-zone equivalence ratio closer to the optimum value of around 0.8. A higher equivalence ratio (up to around 1.0) would increase burning rates even further, but it would not necessarily yield lower emissions of CO and UHC due to the dearth of oxygen, which these species need in order to convert to CO_2 and H_2O. An equivalence ratio slightly less than stoichiometric is usually regarded as optimal for minimum CO and UHC.

Good fuel–air mixing in the primary zone is essential for low CO and UHC. When operating at the optimal equivalence ratio of around 0.8, poor mixing could produce localized regions in which the mixture strength is either too fuel-lean to provide adequate burning rates or so fuel-rich that there is insufficient O_2 to convert all the CO produced into CO_2.

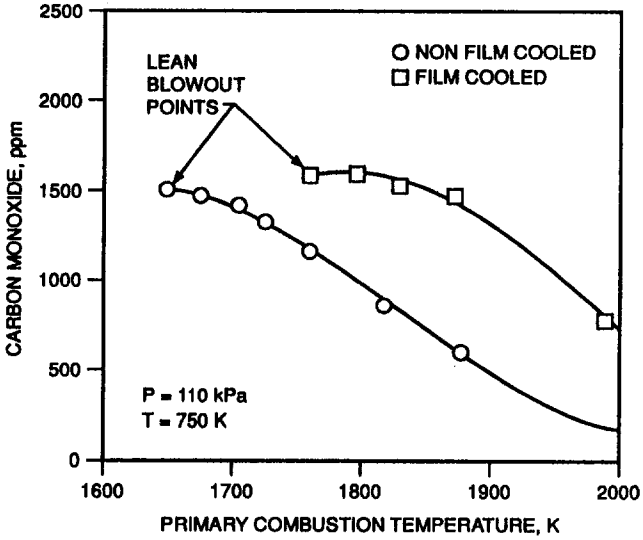

Fig. 23 Effect of eliminating hot-side film cooling on CO

As mentioned earlier, an effective means of reducing CO and UHC is by using less liner wall-cooling air, especially in the primary zone. Figure 23 shows the effect of replacing a conventional film-cooled wall with a non-film-cooled wall in the primary zone of a Rolls-Royce Industrial RB211 low-emissions combustor when operating at atmospheric pressure. CO is significantly reduced (at 1850 K from 1500 ppm to 700 ppm) while the lean blowout temperature is lowered by 110 K (Willis et al., 1993).

The development of new materials and methods of liner wall construction, which allow the liner to operate at higher metal temperatures, along with the development of new methods of wall cooling, which require much less cooling air, such as effusion and transpiration cooling, make a very direct and significant contribution to the reduction of CO and UHC emissions.

Another method of reducing these emissions is by improved fuel atomization. Figure 24 shows that improvements in atomization quality, which enhance evaporation rates, yield appreciable reductions in CO, except at low equivalence ratios where the influence of fuel drop size is less pronounced. This is because the increase in evaporation rates arising from reductions in mean drop size offer little advantage at low equivalence ratios where burning rates tend to be limited more by chemical reaction rates than by evaporation rates. Figure 25 shows that, in common with CO, UHC emissions are greatly reduced by reductions in Sauter mean diameter (SMD). (Note the log scale in this figure.)

The main effect of mean drop size on emissions stems from its strong influence on the volume required for fuel evaporation. At low power operation, where CO and UHC emissions attain their highest concentrations, a significant proportion of the total combustion volume V_c is occupied in fuel evaporation. Consequently, less volume is available for chemical reaction. Under these conditions, any factor that influences evaporation rates, such as fuel volatility and mean drop size, will have a direct effect on the volume available for chemical reaction ($V_c - V_e$) and, therefore, on the emissions of CO and UHC.

Smoke. The main factors governing smoke emissions are combustor inlet air temperature, pressure, and fuel spray characteristics. The influence of inlet air temperature is complex because an increase in this parameter serves to accelerate both the soot-forming and the soot-burnout processes; the net result is usually a reduction in smoke. Smoke problems are most severe

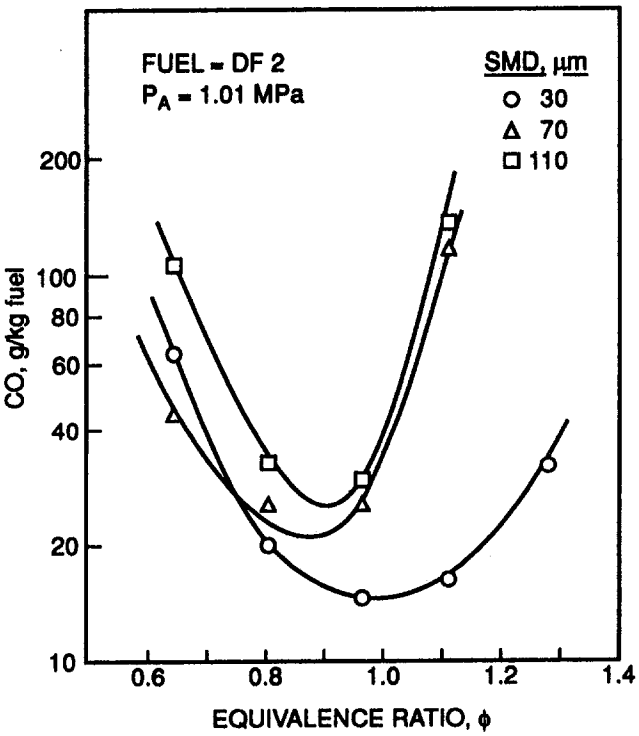

Fig. 24 Influence of mean drop size on CO emissions

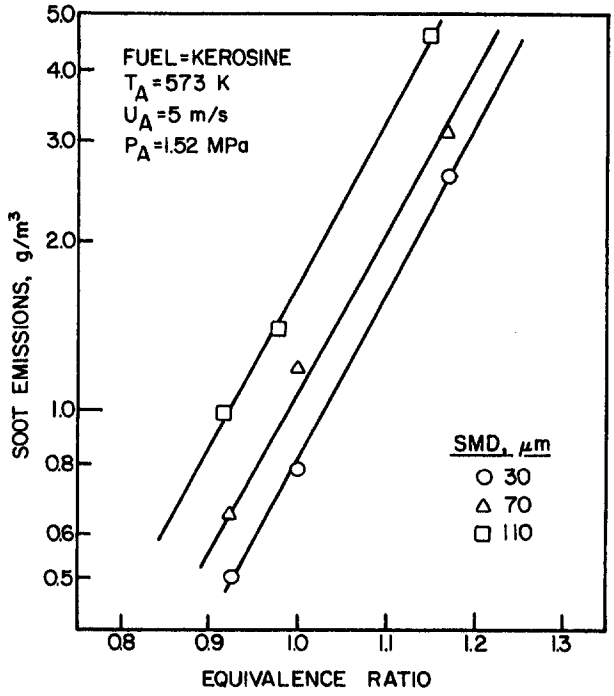

Fig. 26 Influence of mean drop size on smoke emissions

at high pressures. There are several reasons for this, most of which derive from chemical effects. With liquid fuels there are additional physical factors, which affect spray characteristics and hence also the distribution of mixture strength in the soot-forming regions of the flame.

One important consideration is that burning limits widen with pressure. Thus, at high pressures soot is produced in regions which, at lower pressures, would be too rich to burn. Increase in pressure also accelerates chemical reaction rates, so that combustion is initiated earlier and a larger proportion of the fuel is burned in the fuel-rich regions adjacent to the spray.

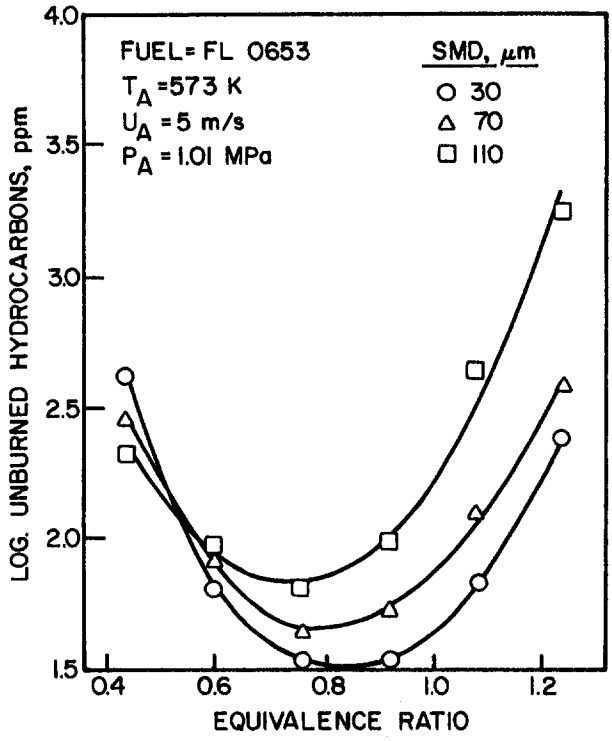

Fig. 25 Influence of mean drop size on UHC emissions

In practice the elimination of exhaust smoke is basically a matter of preventing the occurrence of fuel-rich pockets in the flame. Injecting more air into the primary zone is always beneficial, especially if accompanied by more thorough mixing. Unfortunately, this approach is somewhat limited in scope, owing to the adverse effect of an increase in primary-zone air on ignition and stability limits and on CO and UHC emissions at idle.

The influence of mean drop size on smoke emissions derives from the manner in which each individual droplet evaporates. Conventional gas turbine fuels are generally multicomponent mixtures of various petroleum compounds, each of which has different physical and chemical properties. As evaporation proceeds, the composition of a multicomponent fuel drop changes by a process of simple batch distillation. The more volatile constituents of the fuel drop vaporize first and the concentration of the higher-boiling fractions in the remaining liquid phase increases.

During the droplet evaporation process the droplet receives heat from the surrounding combustion gases. If the droplet is small in diameter it is usually fully evaporated before any significant temperature rise can occur. However, with droplets of large diameter, the heat flowing radially inward during droplet evaporation has sufficient time to raise the droplet temperature, thereby promoting the formation of carbon and soot in the "heavy ends" located at the center of the droplet.

The influence of fuel drop size on exhaust smoke has been investigated by Rink and Lefebvre (1989a, b) using the tubular combustor described above, supplied with a kerosine fuel. Their results for a combustion pressure of 1.27 MPa (12.5 atm) are shown in Fig. 26. This figure shows that particulates are diminished by reductions in mean drop size. For example, at the highest equivalence ratios, reducing the mean drop size from 110 to 30 μm effectively halves the particulate concentration. The importance of atomization quality to soot formation and smoke stems from the fact that, as the fuel spray approaches the flame front, heat transmitted from the flame starts to evapo-

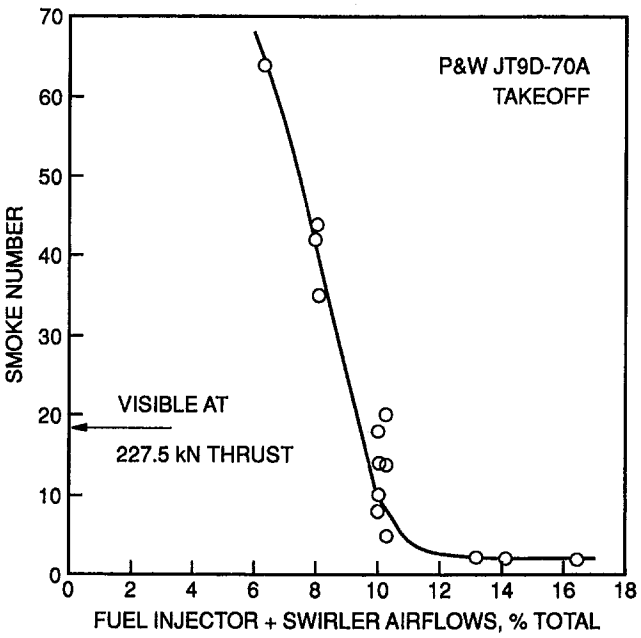

Fig. 27 Control of exhaust smoke through fuel injector and swirler airflows

rate the drops. The smallest droplets in the spray have time to evaporate completely ahead of the flame front, and the resulting fuel vapors then mix with the combustion air and burn in the manner of a premixed flame. The largest drops in the spray do not have time to evaporate fully and mix completely with air. Instead, they burn in the mode of fuel-rich diffusion flames. Clearly, any increase in mean drop size will increase the proportion of large drops in the spray. This, in turn, will raise the proportion of fuel burned in diffusion-type combustion, as opposed to premixed combustion.

It is important to bear in mind that soot formation is nearly always the result of local fuel-rich combustion. In general, exhaust smoke decreases with mean drop size, but if improved atomization leads to a reduction in spray penetration, as occurs with all types of pressure atomizers, the smoke output may actually increase. In fact, reduced spray penetration is one of the main causes of smoke on high-pressure-ratio engines fitted with dual-orifice atomizers.

Another adverse effect of an increase in pressure is to reduce the cone angle of the fuel spray. This encourages soot formation, partly by increasing the mean drop size, but mainly by raising the mixture strength in the soot-forming zone.

The design of the fuel injector and, in particular, the degree of premixing of fuel and air prior to combustion, have a very large influence on whether or not a given combustor will produce significant amounts of smoke. The relatively low smoke emissions from the vaporizer systems employed on some Rolls-Royce engines is not due to prevaporization of the fuel but rather to the premixing of fuel and air which occurs within the vaporizer tubes.

Alleviating soot formation and smoke by fuel–air mixing is only fully effective if sufficient air is used. This is well illustrated in Fig. 27 from Sturgess et al. (1993), which shows how smoke was drastically reduced in a P&W JT9D-70 combustor when operating at takeoff conditions by the addition of more air through the fuel injector and air swirler. The injection of air through these components is particularly effective in reducing smoke because it all flows into the primary combustion zone, which is usually deficient in oxygen and therefore has a high tendency toward soot formation.

The advantage of airblast atomizers over dual-orifice pressure atomizers in regard to smoke emissions is well established. The reason for this is not just better atomization, although this is very significant at high combustion pressures where smoke levels attain their highest values, but because the airblast atomization process virtually guarantees good mixing of air and fuel drops prior to combustion. The marked reduction in exhaust smoke that can be achieved with airblast atomizers is illustrated in Fig. 28, in which smoke levels are plotted against overall combustor air/fuel ratio for a dual-orifice nozzle and a prefilming airblast atomizer at the same operating conditions. The airblast and dual-orifice atomizers exhibit opposite trends in regard to the variation in smoke output with air/fuel ratio. This is because the superior atomization and mixing performance of the airblast atomizer ensures that burning is virtually complete within the primary zone. Thus, any increase in overall air/fuel ratio leads automatically to improved aeration of the combustion process and hence to a decrease in smoke. In contrast, a decrease in fuel flow through the pressure atomizer reduces the atomization quality and raises the fuel concentration in the soot-forming region just downstream of the nozzle.

From an emissions viewpoint, another important advantage of the airblast atomizer is that atomization quality is high over the entire operating range from idle to full power. With a dual-orifice injector, owing to the interaction of the pilot and main sprays, there is always a range of fuel flows, starting at the point where the main fuel is first admitted, over which atomization quality is poor. Since atomization quality has a direct bearing on CO and HC emissions, it follows that the use of dual-orifice atomizers must inevitably aggravate the emissions problem over a significant range of engine operation. With the piloted-airblast injector, there is no physical interference between the pilot and main sprays and, because no fuel is introduced into the airblast section until the air velocity through it has attained its normal operating level, atomization quality is high throughout the entire range of engine operation.

Oxides of Nitrogen. In any attempt to reduce NO_x, the prime goal must be to lower the reaction temperature. The second objective should be to eliminate hot spots from the reaction zone, as there is little point in achieving a satisfactorily low average temperature if the reaction zone contains local regions of high temperature in which the rate of NO_x formation remains high. Finally, the time available for the formation of NO_x should be kept to a minimum.

Practical approaches to low NO_x in conventional combustors include the addition of more air into the primary combustion zone to lower the flame temperature, increase in liner pressure drop to promote better mixing and thereby eliminate hot spots from the combustion zone, and reduction in combustor residence time. Unfortunately, reductions in flame temperature and residence time lead to increased output of both CO and UHC. In fact, as a generalization, it can be stated that any change in operating conditions or combustor configuration that reduces

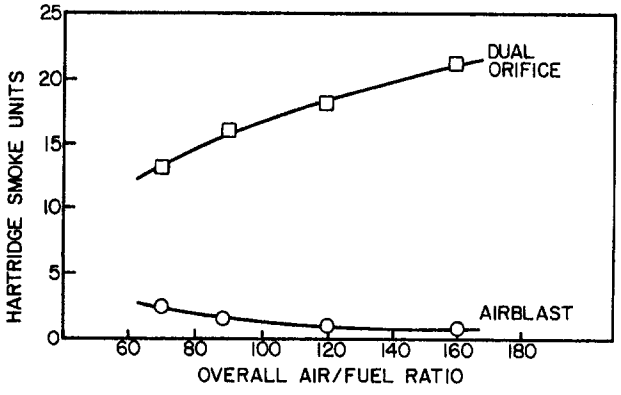

Fig. 28 Influence of fuel injector type on exhaust smoke

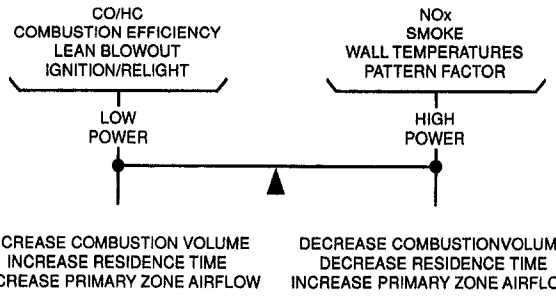

Fig. 29 Illustration of tradeoffs between various aspects of combustion performance

NO_x tends also to exacerbate the problems of CO and UHC, and vice versa.

Design modifications for reducing pollutant emissions generally have an adverse effect on other performance parameters such as ignition and altitude relight, lean blowout, and outlet temperature distribution (pattern factor), as illustrated in Fig. 29 from Bayle-Laboure (1991). Thus, in the design of conventional gas turbine combustors, the end result must inevitably be a compromise of some kind in regard to both emissions and other aspects of combustion performance.

The manner and extent to which oxides of nitrogen are influenced by the sizes of the fuel droplets in the spray is very dependent on equivalence ratio. This aspect was addressed in the experimental studies carried out by Rink and Lefebvre (1989a, b) using the continuous flow combustor referred to above in which the mean drop size could be varied and controlled independently of other operating variables. The data presented in Fig. 30 show that NO emissions increase with increase in mean drop size, especially at low equivalence ratios. At first sight this may seem surprising, because at high pressures evaporation rates are so fast that even for the larger drops the time required for their evaporation is small in comparison with the total residence time of the combustion zone. However, an increase in SMD means that a larger proportion of the total number of fuel drops in the spray are capable of supporting "envelope" flames. These envelope flames, which surround the larger drops, burn in a diffusion mode at near-stoichiometric fuel/air ratios, giving rise to many local regions of high temperature in which NO_x is formed in appreciable quantities. Reduction in mean drop size impedes the formation of envelope flames, so that a larger proportion of the total combustion process occurs in what is essentially a premixed mode, thereby generating less NO_x. Even if no envelope flames are present, with increasing drop size a larger proportion of the fuel burns in the fuel-rich regions created in the wakes of the moving drops. Although in theory combustion can take place at any equivalence ratio within the flammability limits, it tends to occur preferentially at the stoichiometric value, i.e., at the maximum temperature, thereby producing high levels of NO_x. This hypothesis serves to explain why NO_x emissions increase with SMD for lean mixtures. However, as the overall equivalence ratio increases toward unity the local fuel/air ratio adjacent to the fuel drops approaches the premixed value. According to this hypothesis, mean drop size should have no influence on NO_x emissions for stoichiometric mixtures, and this is generally confirmed by the results shown in Fig. 30. This figure is important because it demonstrates that even at low equivalence ratios where the average combustion temperature is so low that only negligible amounts of NO should, in theory, be formed, the presence of fuel drops in the combustion zone must necessarily give rise to conditions in which combustion can and does proceed at near-stoichiometric equivalence ratios regardless of the average equivalence ratio in the combustion zone. This, of course, is the rationale for the various types of lean, premix, prevaporize combustors whose success relies largely on the elimination of all fuel drops from the combustion zone.

Water Injection. As NO_x formation is exponentially dependent on temperature, an obvious way of reducing NO_x emissions is by lowering the temperature of the combustion zone. Additional air is effective, but can only be used sparingly because it raises the primary zone velocity, which has an adverse effect on both ignition and stability performance. An alternative approach is to introduce a heat sink, such as water or steam, into the combustion zone. This is clearly unsuitable for aeroengines but is a practical proposition for large stationary engines, especially if large amounts of water or steam are available. In some cases the water or steam is injected directly into the flame, either through a number of separate nozzles located at the head end of the combustor or through holes that are integrated into the fuel nozzle (Hilt and Waslo, 1984). Alternatively, the water injection may take place upstream of the combustor liner, usually into the air stream, which subsequently flows into the combustion zone through the main air swirler. This method ensures good atomization, because the smaller droplets are carried by the air flow through the swirler into the combustion zone, while the larger drops impinge on the swirler vanes where they form a thin liquid film, which is airblast atomized as it flows over the downstream edge of the vane (McKnight, 1978).

When steam is used to reduce NO_x emissions, it may also be injected directly into the combustion zone or into air, which subsequently flows into the combustion zone. In some installations the steam is injected into the compressor discharge air. This method is simple but inherently wasteful, because only about 40 percent of the steam actually flows into the combustion zone. This may be only a minor consideration if excess steam is available (Hilt and Waslo, 1984).

The effectiveness of water and steam for reducing NO_x has been demonstrated by many workers. According to Hung (1974) the relationship between NO_x reduction and water/fuel mass ratio, X, can be expressed as

$$\text{wet } NO_x/\text{dry } NO_x = \exp - (0.2X^2 + 1.41X) \qquad (8)$$

This relationship was found to apply to both liquid and gaseous fuels. It shows, for example, that equal mass flow rates of water and fuel (for which $X = 1$) yield an 80 percent reduction in NO_x. Very similar results were obtained for both gaseous and liquid fuels by Claeys et al. (1993) on the General Electric MS7001F gas turbine.

Equation (8) should not be regarded as having universal application. For example, Wilkes (1980) has shown that water injection is much less effective with fuels containing fuel-bound nitrogen. The main effect of water addition is to reduce thermal

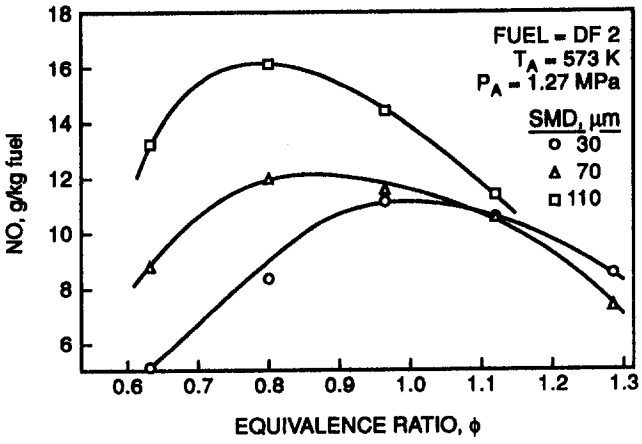

Fig. 30 Influence of mean drop size on NO emissions

NO_x although it does also slightly reduce prompt NO. This implies that water injection is most effective when combustion takes place at high pressures and temperatures where thermal NO_x production is high, and is less effective at low pressures and temperatures where a larger proportion of the total NO_x is formed via the prompt mechanism. The key point is that water and/or steam injection always reduces NO_x, but the extent of the reduction depends on combustor operating conditions and fuel type.

As steam is a less effective diluent than water, the reductions in NO_x achieved with steam injection tends to be less dramatic than when water is used. For example, Hilt and Waslo (1984) have reported NO_x reductions of around 60 percent for a steam/fuel mass ratio of unity on two GE industrial engines burning natural gas.

Although both water and steam injection are very effective in reducing NO_x emissions, and have been used on stationary engines that operate at near-constant load conditions since the early 1970s, they do have a number of drawbacks. White et al. (1982) have reported an increase in capital cost of 10 to 15 U.S. dollars per kW and an increase in fuel consumption of 2 to 3 percent. This additional fuel is needed to heat the water to combustion temperature, although power output is enhanced due to the additional mass flow through the turbine. The water must be of high purity to prevent deposits and corrosion in the hot sections downstream of the combustor. The treatment of this water is expensive and requires a separate plant based on reverse osmosis and de-ionization. Users' experience with water injection has shown a significant increase in inspection and hardware maintenance. There are, therefore, practical limits to the amount of water or steam that can be injected into the combustor. The deterioration in combustion performance arising from water-steam injection is manifested as increases in the levels of CO and UHC emissions and by increases in combustor pressure oscillations. These oscillations can become amplified by coupling with the combustion process, and cause deterioration of combustor hardware.

The drawbacks associated with water and steam injection have encouraged the development of the so-called "dry low NO_x" combustors, i.e., combustors that can meet the emission goals without having to resort to diluent injection.

Selective Catalytic Reduction (SCR). This is a method for converting NO_x in a gas turbine exhaust stream into molecular nitrogen and water vapor by injecting ammonia into the stream in the presence of a catalyst. Exhaust gases first pass through an oxidation catalyst and are then mixed with ammonia before entering the SCR catalyst. The oxidation catalyst removes the CO and UHC emissions by oxidizing them to CO_2 and H_2O. To reduce NO_x emissions, ammonia is injected in a manner designed to achieve intimate mixing with the exhaust stream. After mixing, the exhaust gases pass over a base metal catalyst which results in the selective reduction of NO_x to form N_2 and H_2O. The principal reactions are

$$6NO + 4NH_3 \rightarrow 5N_2 + 6H_2O$$

$$6NO_2 + 8NH_3 \rightarrow 7N_2 + 12H_2O$$

SCR requires that the temperature of the exhaust stream be within a fairly narrow range from 560 to 670 K, and so is restricted to systems in which the exhaust gas flows into a heat recovery device, usually a steam generator (Davis and Washam, 1989). A major problem with this method is the requirement for a control system that feeds the requisite amount of ammonia, and the need for a continuous monitoring system that can give the feedback to the ammonia supply mechanism under differing load conditions. Another problem is the size and weight of the equipment. According to Davis and Washam, for an 83 MW MS7000 gas turbine an SCR designed to remove 90 percent of the NO_x from the exhaust stream has a volume of 175 m^3 and weighs 111 tons. Despite these drawbacks, the method is quite widely used.

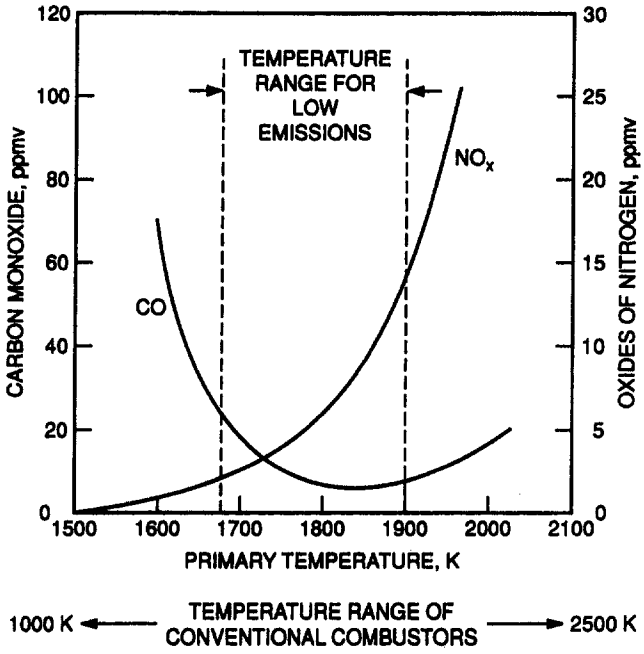

Fig. 31 Influence of primary-zone temperature on CO and NO_x emissions

Exhaust Gas Recirculation. It has been known for many years that recirculation of cooled exhaust products into the inlet of a gas turbine combustor would reduce the emissions of NO_x. The practical feasibility of this method of NO_x reduction has been investigated by Wilkes and Gerhold (1980) who found that significant reductions (50 percent) could be achieved with recirculation rates of 20 percent or less at baseload conditions. The major thermal effect stems from the reduced concentration of oxygen in the inlet air, but there is also a secondary effect due to the higher heat capacity of this air with increased H_2O and CO_2 content.

The main advantage of the method is that little or no combustor development is required and standard production combustors can be used. Its main drawback lies in the need for an intercooler between the exhaust and inlet. This virtually rules it out for simple gas turbines, but application to combined cycle plants offers more promise due to the substantially lower exhaust gas temperatures. Another drawback is that only very clean fuels can be used to avoid problems of fouling and contamination.

Pollutant Reduction by Control of Flame Temperature

From the foregoing discussion it is abundantly clear that the main parameter governing pollutant emissions is the temperature of the combustion zone. With conventional combustors this can range from 1000 K at low power operation to 2500 K at high power operation, as indicated in Fig. 31. This figure also shows that too much CO is formed at temperatures below around 1670 K while excessive amounts of NO_x are produced at temperatures higher than around 1900 K. Only in the fairly narrow band of temperatures between 1670 and 1900 K are the levels of CO and NO_x below 25 and 15 ppm, respectively. The underlying principle of the various approaches toward low-emission combustors described below is that of maintaining the combustion zone (or zones) within a fairly narrow band of temperatures over the entire power range of the engine.

Variable Geometry. The notion of variable-geometry combustors is by no means new. Long before the problems of pollutant emissions were recognized, many different schemes for incorporating variable geometry into gas turbine combustors were considered, usually as a means for improving the altitude relight performance of aircraft engines. These schemes seldom came to fruition because designers, while appreciating the advantages to be gained, were reluctant to accept the mechanical complexities involved. However, the opportunities it offers for emissions reduction has resulted in a revival of interest in the use of variable geometry, especially for nonaeronautical applications.

Many practical forms of variable-geometry combustors have been designed. A fully variable system is one in which large quantities of air are admitted at the upstream end of the combustion liner at max power conditions to lower the primary-zone temperature and provide adequate film-cooling air. As engine power is reduced, an increasing proportion of this air is diverted to the dilution zone to maintain the primary-zone temperature within the low-emissions "window" shown in Fig. 31. Practical ways of achieving this variation in airflow distribution include the use of variable-area swirlers to control the amount of air flowing into the combustion zone; see, for example, Bayle-Labouré (1991) and Micklow et al. (1993), variable air openings into the dilution zone (Roberts et al., 1982; Sasaki et al., 1991), or a combination of these.

The drawbacks to all forms of variable geometry systems include complex control and feedback mechanisms, which tend to increase cost and weight and reduce reliability. Problems of achieving the desired temperature pattern in the combustor efflux gases could also be encountered, especially if the liner pressure drop is allowed to vary too much. The incentive for surmounting these practical problems is that variable geometry has the potential for reducing simultaneously all the main pollutant species without sacrificing other aspects of combustion performance. It also has several other advantages, for example, as the combustion temperature is always maintained above a certain minimum value of around 1670 K, chemical reaction rates are always relatively high. This enables the combustion zone to be made smaller, with consequent advantages in terms of reductions in combustor size and weight. For aircraft applications, variable geometry also has the potential for wide stability limits and improved altitude relight performance.

To be fully effective, variable geometry combustors should ideally be used in conjunction with premix-prevaporize fuel injection systems. Only in this way is it possible to avoid the local high-temperature, high-NO_x-forming regions, created by the presence of fuel droplets in the combustion zone.

Although variable geometry has been used in some large industrial engines, there have been few successful applications of this technique in small-to-medium size gas turbines due to size and cost limitations and also because of concerns regarding operational reliability (Aoyama and Mandai, 1984).

Staged Combustion. Variable-geometry combustors strive to maintain the combustion temperature within fairly narrow limits by switching air from one zone to another depending on the engine power setting. With staged combustors the air flow distribution does not change; instead the fuel flow is switched from one zone to another in order to maintain a fairly constant combustion temperature. One simple method of fuel staging is by "selective fuel injection" as described by Bahr (1987). With this technique, which is sometimes called "circumferential staging," fuel is supplied only to selected combinations of fuel injectors at lightoff, relight, and engine idle conditions, as illustrated in Fig. 32. Only at power settings above idle is the full complement of fuel injectors employed. The objective of this modulation technique is to raise the equivalence ratio and hence also the temperature of the localized combustion zones at low power operation. This approach, which is now in common use, not only reduces CO and UHC emissions but also has the added advantage of extending the lean blowout limit to lower equivalence ratios.

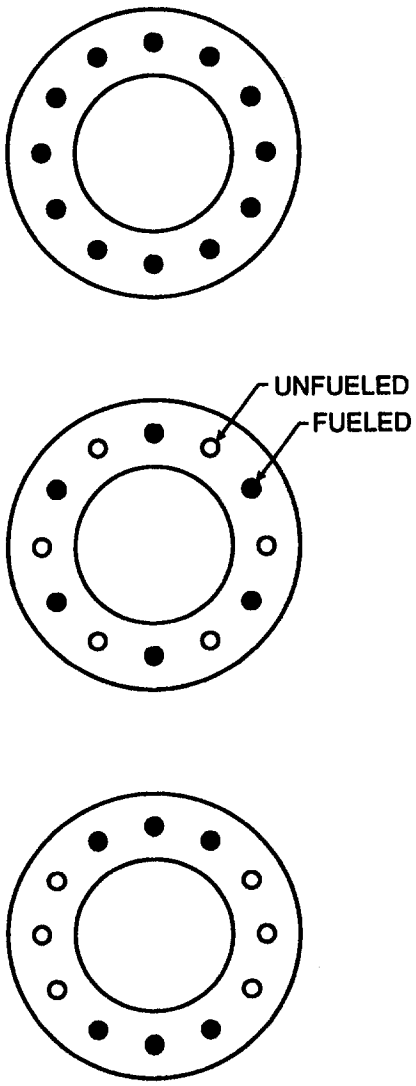

Fig. 32 Illustration of the use of selective fuel injection

A major drawback of circumferential staging is that "chilling" of chemical reactions occurs at the edges of the individual combustion zones. This chilling lowers the combustion efficiency and increases the formation of CO and UHC. Furthermore, the circumferentially nonuniform exit temperature distribution results in loss of turbine efficiency. These limitations have led to the development of "staged" combustors in which no attempt is made to achieve all the performance objectives in a single combustion zone. Instead, two or more zones are employed, each of which is designed specifically to optimize certain aspects of combustion performance.

The principle of staged combustion is illustrated in Fig. 33. Increase in overall combustor fuel/air ratio causes the combustion zone temperature to rise. As this temperature approaches a value above which NO_x levels starts to become excessive, fuel is diverted to a separate combustion zone. This approach allows the combustor to operate over the entire power range while keeping the combustion zone temperatures within the low-emissions "window." A typical staged combustor has a lightly loaded primary zone, which, at low power settings, operates at an equivalence ratio of around 0.8 to achieve high combustion efficiency, low CO and UHC, and also provide the

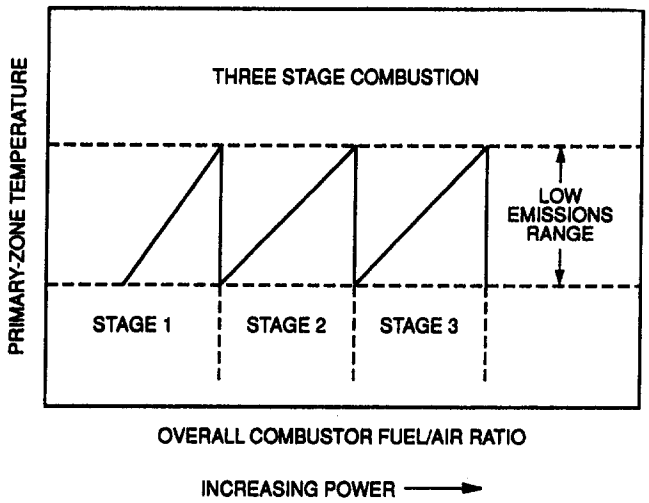

Fig. 33 Principle of staged combustion

desired temperature rise. At high power settings, it acts as a pilot source of heat for the main combustion zone downstream which is supplied with a fully premixed fuel-air mixture. For full-load operation, both zones are supplied with fuel and the equivalence ratio in both zones is kept low, around 0.6, to minimize the emissions of nitric oxide and smoke.

An important choice for the designer is whether the staged combustion should take place in "series" or in "parallel." The latter approach, often called "radial staging," features the use of a dual-annular combustor, as illustrated in Fig. 34. One of these combustors—usually the outer combustor—is designed to operate lightly loaded and provides all the temperature rise needed at startup, altitude relight, and engine idle conditions. At idle the equivalence ratio of the combustion zone is selected to minimize the emissions of CO and UHC. The other annular combustor is designed specifically to optimize the combustion process at high power settings. It features a small, highly loaded combustion zone of short residence time and low equivalence ratio to minimize the formation of NO_x and smoke.

The main advantage of radial staging is that it allows all the combustion performance goals to be achieved, including low emissions, within roughly the same overall length as a conventional combustor. Another advantage of the dual-annular concept employed in radial staging is that it provides a satisfactory liner length/height ratio in both annuli within a short overall length. This short-length feature is attractive from the standpoints of low engine weight and reduced rotor dynamics problems (Bahr, 1987).

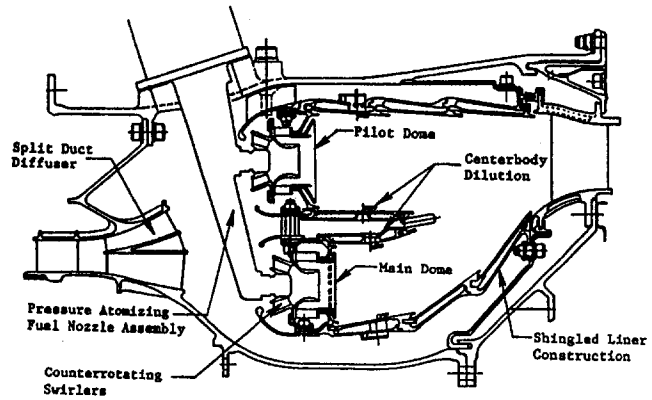

Fig. 34 General Electric dual-annular combustor

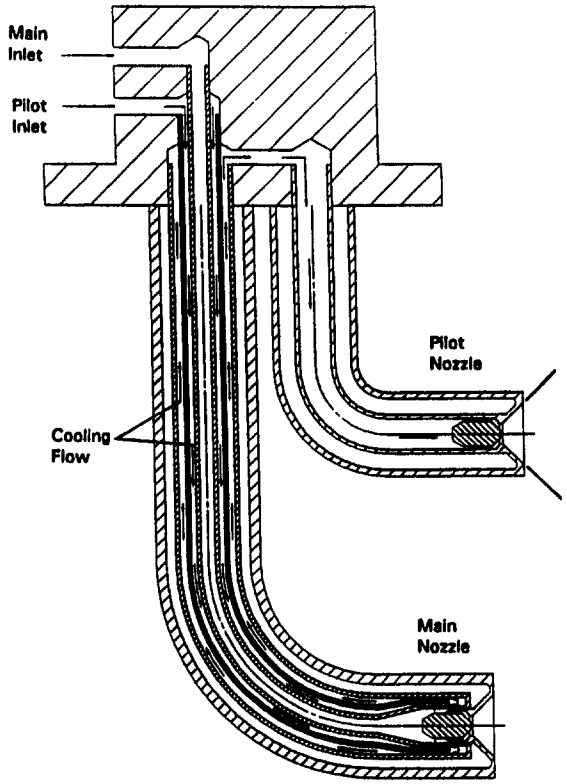

Fig. 35 Fuel nozzle for G.E. dual-annular combustor (courtesy of the Parker Hannifin Corporation)

If the combustor domes of the inner and outer stages are arranged to be radially in-line, this allows the fuel injector tips for both stages to be mounted on a common feed arm, as shown in Fig. 34. An important advantage of this arrangement is that the main stage fuel injectors are cooled by the continuously flowing pilot fuel, as illustrated in Fig. 35. This prevents coking of the main stage nozzles when they are unfueled but still exposed to the hot engine environment.

There are a number of drawbacks to radial staging. One basic drawback is that all zones are supplied with air at the compressor outlet temperature, which means that all zones have the same relatively poor lean blowout limit. It is also clear that pollutant reduction is achieved at the expense of increased design complexity and a marked increase in the number of fuel injectors. The larger liner wall surface area demands additional cooling air, which has an adverse effect on pattern factor. Furthermore, the peaks of the radial temperature profile could shift in radial position as a result of fuel staging, with potential adverse effects on the hot sections downstream of the combustor. Another basic problem with radial staging is that of achieving the desired performance goals at intermediate power settings where both zones are operating well away from their optimum design points.

The radially staged combustor shown in Fig. 34 was designed by the General Electric company. It achieved around 35 percent reductions in CO and UHC, and 45 percent reduction in NO_x in comparison with the corresponding single-annular combustor. The U.S. Federal Aviation Administration (FAA) and the French Direction Generale de l'Aviation (DGAC) have jointly certified the CFM56-5B engine with the dual-annular combustor, thereby paving the way for the first flight and certification on Airbus Industrie A320 and A321 aircraft in 1995.

With "series" or "axial" fuel staging, a portion of the fuel is injected into a fairly conventional primary combustion zone. Additional fuel, usually premixed with air, is injected downstream into a "secondary" or "main" combustion zone, which

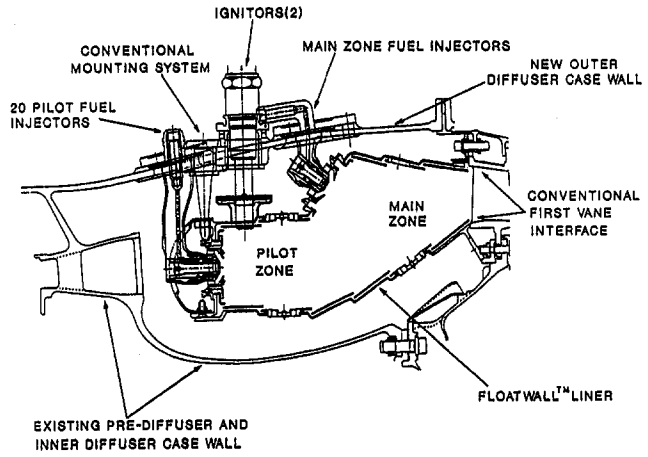

Fig. 36 Pratt and Whitney axially staged combustor

operates at low equivalence ratios to minimize the formation of NO_x and smoke. The primary combustion zone is used on engine startup and generates the temperature rise needed to raise the rotational speed up to engine idle conditions. At higher power settings, fuel is supplied to the secondary combustion zone and, as the engine power rises towards its maximum value, the function of the primary zone becomes increasingly one of providing the heat needed to initiate rapid combustion of the fuel supplied to the second stage.

Axial staging does have certain advantages over radial staging. Since the main stage is downstream of the pilot stage, ignition of the main stage directly from the pilot is both rapid and reliable. Also, the hot gas flow from the pilot into the main combustion zone ensures high combustion efficiency from the main stage, even at low equivalence ratios. According to Segalman et al. (1993), the radial temperature profile at the combustor exit can be developed to a satisfactory level using conventional dilution hole trimming and, once developed, does not change significantly as a result of fuel staging.

The main drawback to axial staging is that the in-line arrangement of stages tends to create additional length, which makes the problem of retrofit difficult for some engines. In comparison with conventional combustors, the liner surface area that needs to be cooled is higher. The fuel injectors for the two combustion stages require separate feed arms, which involve two separate penetrations of the combustor casing. Furthermore, the pilot fuel cannot be used to cool the main stage fuel as can be done quite conveniently with radial staging.

Figure 36 shows a cross-sectional view of an axially staged combustor developed by the Pratt and Whitney company (Koff, 1993). For clarity, the main stage fuel injectors are shown rotated half an injector pitch to be in line with the pilot stage injectors. The engine centerline is at the bottom of the figure. This combustor has the benefits of the axially in-line stage arrangement without any length penalty and is designed to fit into the existing P&W B2500-AS engine.

The pilot combustion zone is designed specifically to provide wide stability limits and high combustion efficiency (low CO and UHC). With increase in engine power above idle, fuel is admitted to the main combustion zone where combustion is initiated and sustained by the hot gas emanating from the pilot zone. The relative amounts of fuel supplied to the pilot and main zones is such that no thrust lag is created when fuel is first introduced into the main zone. In combination, the pilot and main zones maintain a low equivalence ratio, which ensures low NO_x emissions at higher power settings.

Of special interest in Fig. 36 is the inboard location of the pilot combustion zone. This greatly reduces the susceptibility to flame blowout in heavy rain since the compressor centrifuges the water to the outer portion of the air flow path. Another advantage of having the main zone outside of the pilot is that the radial temperature profile at the combustor outlet peaks toward the outer radius of the turbine flowpath, a situation that is conducive to long turbine blade life.

In the longer term it is possible that staging of the air flow by variable geometry in conjunction with fuel staging may become more of a design option.

Dry Low NO_x Combustors

The term "dry" is used to indicate that the combustor in question is capable of achieving low pollutant emissions, in particular low NO_x, without having to resort to the injection of water or steam. Solar Turbines Inc. in San Diego has been among the pioneers in the development of dry low-emissions combustors for industrial gas turbines, and the results of their efforts have appeared in a number of publications, for example, White et al. (1982), Roberts et al. (1982), Smith et al. (1986, 1991), Smith and Cowell (1989), and Etheridge (1994).

Most of the low-NO_x combustors developed by Solar fall into the lean premix family of combustors. Figure 37 shows a cross-sectional view of a fuel injector designed for combustors supplied with natural gas. An 18-vane radial flow swirler is used to impart a high degree of rotation to the combustor primary air, which serves both to promote fuel–air mixing and to induce a recirculatory flow in the primary zone. The fuel injector/air swirler assembly permits three different modes of fuel injection, as indicated in Fig. 37. Best mixing is achieved by injecting the gaseous fuel through 18 spokes, each spoke being located between a pair of swirl vanes. As each spoke contains six holes of 0.89 mm diameter, the total number of injection points is 108. Combustion tests have been carried out with the fuel injector assembly attached to a cylindrical combustion liner, 200 mm in diameter and 450 mm long. According to Smith et al. (1986), these tests showed that the concept is capable of achieving NO_x emissions below 10 ppm when burning natural gas, with simultaneous low values of CO and UHC emissions.

The manner in which the fuel-injection system described above was adapted for liquid fuels by Smith and Cowell (1989) is shown in Fig. 38. The fuel injector/air swirler assembly was designed to permit three different modes of liquid fuel injection. The mode designated as "inner filming" in Fig. 38 involves filming of the fuel on the cylindrical swirler centerbody. Fuel is delivered to the outer surface of the centerbody through eight holes located around the centerbody circumference. This fuel is intended to form a film, which is carried downstream to the

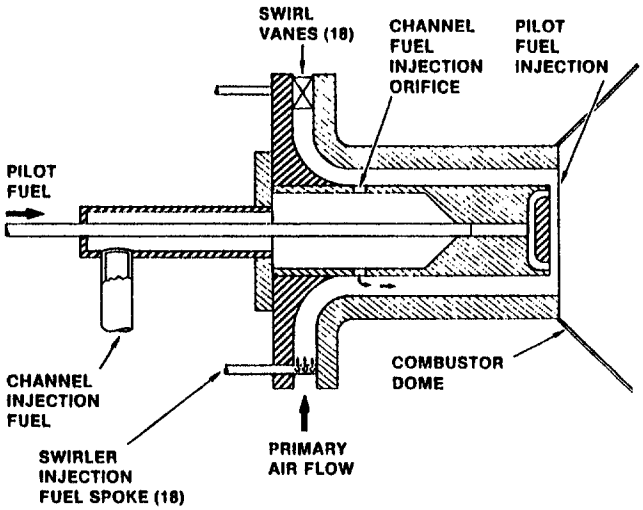

Fig. 37 Solar low-NO_x fuel injector for natural gas

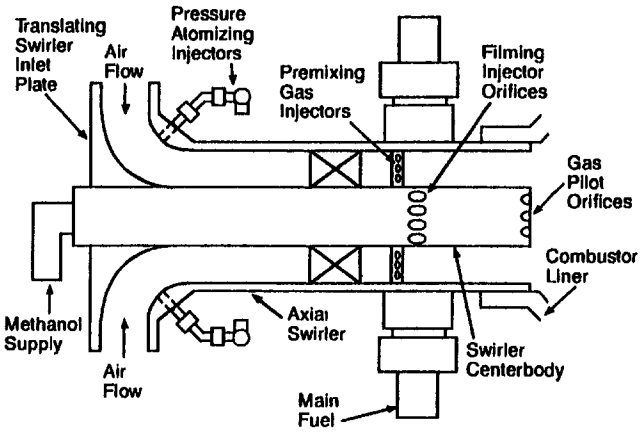

Fig. 38 Solar low-NO_x fuel injector for liquid fuels

primary combustion zone by the swirling primary air flow. The fuel vaporizes and mixes with air as the film progresses along the centerbody. The inner air assist/airblast air exits through an annular gap just inside the centerbody lip. Its function is to break up any remaining fuel film as it flows off the centerbody and into the primary zone.

The outer filming mode involves film formation on the outer cylindrical surface of the air swirler channel. Fuel is delivered to the filming surface in a manner identical to that used for inner filming. Provision is also made for air blasting the outer fuel film at the exit of the swirler channel. Flow visualization tests showed that a pressure drop of at least 3 percent is needed to achieve satisfactory filming of the fuel. At lower pressure drops, the liquid film is not sustained over the length of the injector, but tends to form rivulets that swirl to the bottom of the injector and travel as a thick stream to the end of the injector.

Evaluation of the combustor performance demonstrated that the lowest NO_x emissions were obtained with either total inner fueling or combined inner and outer filming. The combustor yielded around 12 ppm NO_x at 6 atm and 20 ppm at 9 atm. CO was always below 50 ppm. In common with most well-mixed systems, low concentrations of both CO and NO_x were attainable only over a fairly narrow range of operating conditions.

Potential improvements for this fuel prefilming combustor include increasing the number of fuel injection holes used to deliver fuel to the filming surface to aid in the formation of a more uniform film, and lengthening the injector centerbody to allow a longer time for fuel evaporation and mixing.

To produce a dry low-emissions combustor for an industrial version of the Rolls Royce RB 211 engine, the annular aero-combustor has been replaced by nine radially positioned reverse flow combustors, as shown in Figs. 39 and 40 (Willis et al., 1993). This arrangement results in an 80 percent increase in combustion volume. The primary zone is fed by two radial air swirlers. Each swirl passageway has a number of gaseous fuel injection points. Contrarotating swirlers were selected to minimize the length of the recirculation zone and maximize mixing of fuel and air. The outlet of the primary zone is restricted to accelerate the flow and thereby limit the recirculation zone length and prevent the secondary efflux from becoming entrained into the primary zone. The secondary mixing duct is wrapped around the primary combustor but is separated from it by another annular duct, which provides the wall-cooling air. Gaseous fuel is injected into the secondary duct from 36 equispaced axial spray bars, each containing six injection holes. This fuel bar arrangement was determined by trajectory calculations and an air velocity profile predicted by a CFD code. Fuel sampling and combustion tests showed that the resulting fuel–air mixture is uniform to within 4 percent. This mixture is discharged into the secondary zone at an angle that was selected

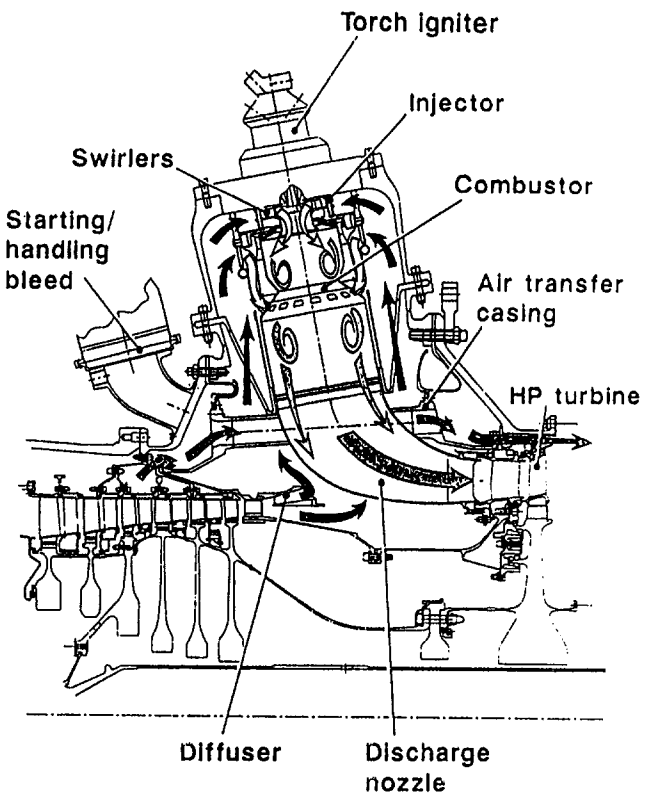

Fig. 39 Rolls-Royce Industrial RB 211 DLE 04 module

to achieve the required level of mixing between the primary efflux and the secondary fuel–air mixture. Combustion testing carried out over a range of pressures from 1 to 20 atm has demonstrated the ability of this axially staged combustor to achieve simultaneously low NO_x and low CO over wide ranges of power and ambient temperature without resorting to either variable geometry or air bleeds. It was also demonstrated that a uniform fuel distribution prior to combustion is essential for achieving low emissions, especially at high pressures. Based on the test data obtained so far, at full baseload conditions the predicted engine emissions are 17.4 ppm NO_x, 5 ppm CO, and zero UHC.

An interesting feature of this combustor is that the level of NO_x emitted when the primary only is burning is reduced by a half when the secondary is ignited, and only when the temperature of the secondary zone approaches that of the primary does the total NO_x exceed the primary-only value.

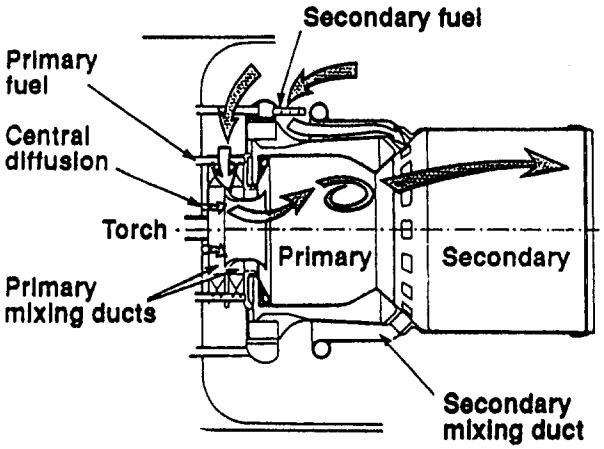

Fig. 40 Rolls-Royce dry low-emissions premix, lean-burn combustor

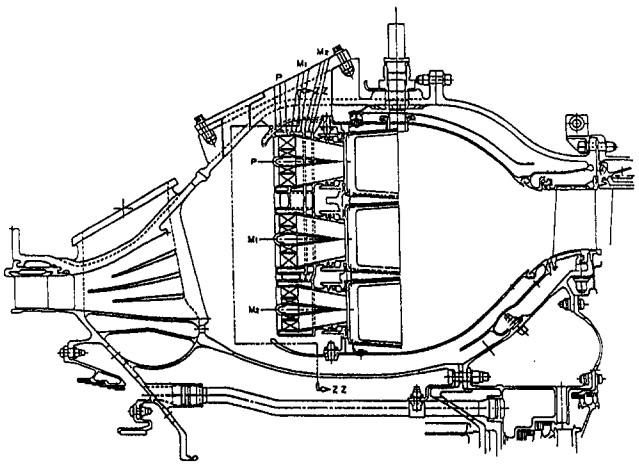

Fig. 41 General Electric LM6000 dry low-NO_x combustor

Figure 41 gives a cross-sectional view of General Electric's new LM6000 dry low-emissions combustor, as described by Leonard and Stegmaier (1994). This premix combustor requires about twice the volume of the conventional annular combustor it replaces in order to reduce the emissions of CO and UHC. Part of the air used in combustion, which at maximum power is around 80 percent of the total combustor airflow, flows into the combustion zone through three annular rings of premixers, as shown in Fig. 41. The two outer rings each have 30 fuel–air premixers while the inner ring has 15. This arrangement of premixers facilitates fuel staging at part-load operation. The total of 75 fuel nozzles is formed by having 15 stems with 3 premixers on each stem, as shown in Fig. 42. Each stem incorporates three separate fuel circuits for independently fueling the three premixers.

A short annular liner was selected to minimize the amount of air needed for wall cooling. Only backside cooling is used, so a thermal barrier coating is applied to both the liner and in the dome area to keep the metal temperatures within acceptable limits. The use of a multipass diffuser also permits further reduction in overall combustor length. Of special interest and importance to the attainment of low emissions is the design of the premixers. Figure 43 shows cross-sectional views of three different mixer designs that were subjected to combustion testing. The Double Annular Counter Rotating Swirler (DACRS) was conceived to satisfy the restraints of autoignition, flashback and size. Its exit velocity is determined by the need to greatly exceed the turbulent flame speed of gaseous fuel–air mixtures. The duct diameter is reduced at the exit in order to create an accelerating flow and thereby prevent flashback. The conical centerbody located along the centerline of the premixer can be used to supply liquid fuel to an atomizer at its tip, and gas passages for diffusion burning at low power conditions (Joshi et al., 1994).

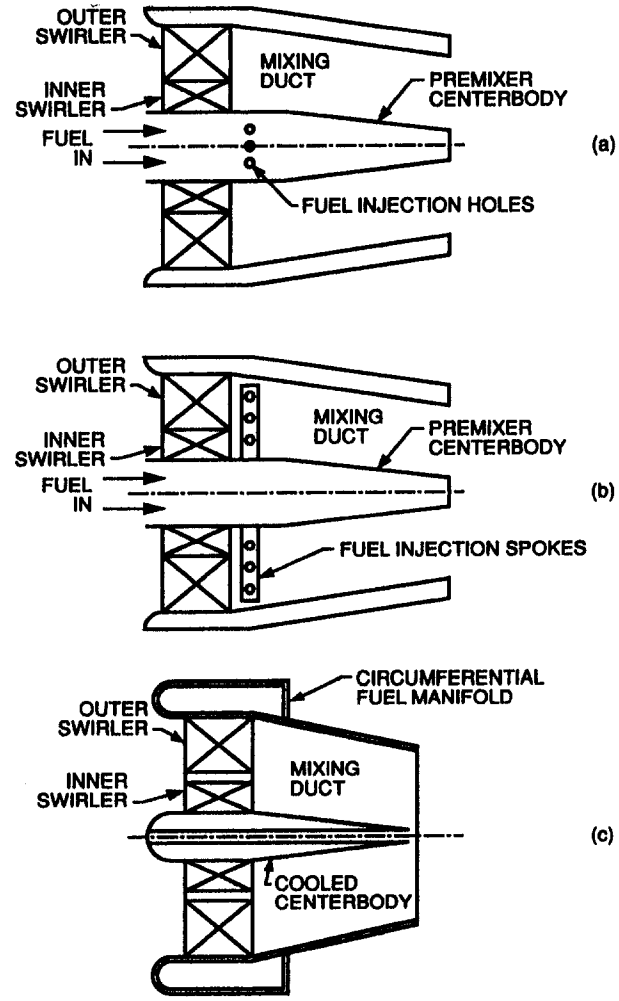

Fig. 43 Cross-sectional views of three mixer designs

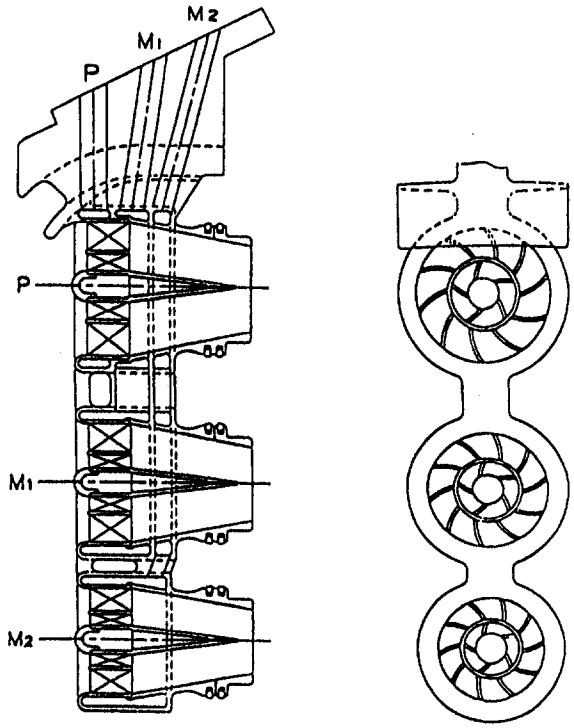

Fig. 42 Fuel nozzle assembly for LM6000 dry low-NO_x combustor

The design objective with this type of mixing device is to produce a completely homogeneous mixture of fuel and air at the premixer exit. As the total area of the fuel injection holes is fixed by the flow rate and the available fuel injection pressure, the design procedure is essentially one of finding the best compromise between the desire for a large number of fuel injection points and the equally important requirement of large injection holes to allow the fuel jets to penetrate across the air stream.

In the premixer design designated as DACRS I in Fig. 43(a), the fuel is injected into the air stream radially outward from holes in the centerbody just downstream of the swirl vanes. This configuration gave low NO_x at some test conditions but not at others. This was attributed to unsatisfactory fuel jet pene-

tration, so a modification was made by adding eight radial spokes in the location of the holes in the centerbody, as shown in Fig. 43(*b*). Each spoke has three holes to inject gaseous fuel perpendicular to the flowing air stream. Combustion testing of this DACRS II mixer showed that single-digit NO_x emissions are attainable with this concept. A further modification to the premixer designs described above was made by incorporating fuel injection holes into the swirl vanes of the outer swirler, as illustrated in Fig. 43(*c*). In this DACRS III configuration, the fuel is injected through three holes in the trailing edge of each outer swirl vane and one hole in the outer wall of the mixing duct in between each swirl vane. Fuel is fed to the hollow outer vanes through a manifold on the outside of the premixing duct. The NO_x emissions obtained with the DACRS III mixer were very similar to the DACRS II design.

A big advantage of this type of premixer module is that, once developed, it has broad applications in a wide range of combustor sizes. The basic module remains the same regardless of combustor size; only the number varies. According to Joshi et al., the DACRS II and DACRS III mixers could be applied to a range of GE engines, including the LM1600, LM2500, and LM6000, since single-digit NO_x emissions have been attained with both these mixers at test conditions encompassing the operating regions of these engines.

The ABB company has developed a Conical Premix Burner module, called the EV-burner, which also appears to have good potential for a wide range of dry low-emissions combustion applications. A cross-sectional view to illustrate the operating principles of the burner is given in Fig. 44 from Sattelmayer et al. (1992). A unique feature of this burner is the flame stabilization in free space near the burner outlet, which utilizes the sudden breakdown of a swirling flow. The swirler consists of two halves of a cone, which are shifted to form two air inlet slots of constant width. The device is claimed to be equally satisfactory for both gaseous and liquid fuels. Gaseous fuels are injected into the combustion air by means of two fuel distribution tubes comprising two rows of small holes, which are located parallel to the inlet parts of the swirler. Fairly complete mixing of fuel and air is obtained shortly after injection. Liquid fuels are injected at the apex of the cone using a pressure or air-assist type of atomizer. Fuel evaporation and mixing of fuel vapor with air is accomplished within the burner and upstream of the recirculation zone. In contrast to most LPP designs, no diffusion or pilot stage is needed to improve the stability of the premix flame. Also, because the combustion zone is displaced from the burner walls, the heat transfer to the burner section is minimized.

In February 1991 an ABB GT11N gas turbine was retrofitted with a new silo combustor of the type shown in Fig. 45. This silo combustor is equipped with 37 EV burners, all of which operate in a pure premix mode. For part-load operation, fuel is supplied to only a fraction of the total number of burners. At

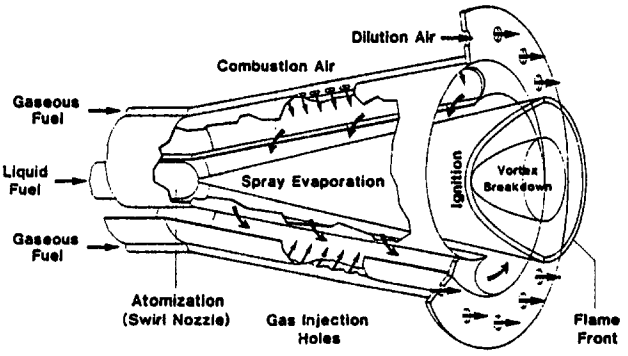

Fig. 44 Operating principle of ABB conical premix burner

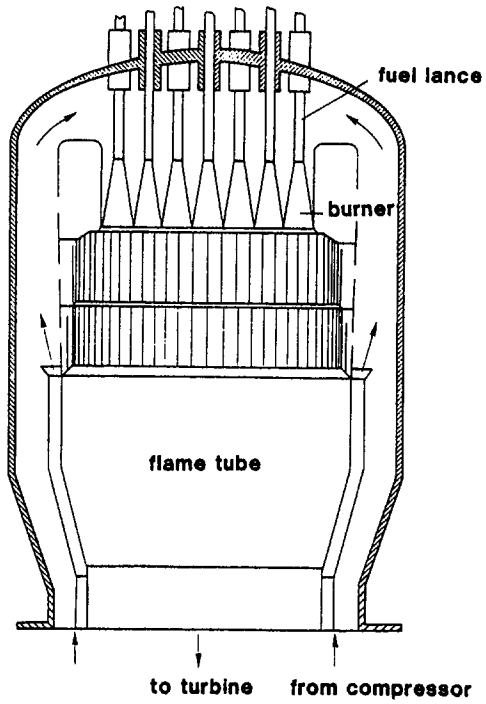

Fig. 45 Silo combustor equipped with conical premix burner

the baseload conditions of 12.5 bar and T_{inlet} = 643 K, NO_x values of 13 ppm were measured (Aigner and Muller, 1993).

The EV-burner technology has also been applied to the design of an annular combustor for the heavy duty ABB GT13E2 gas turbine (Senior et al., 1993). This is a single shaft industrial engine in the large size range (>150 MW). The EV burners have a double offset row arrangement within the annular combustor. As the power setting is reduced, the overall equivalence ratio eventually becomes too low to allow lean premix operation in all burners. The technique used to overcome this problem is to maintain some burners at a stable equivalence ratio while others run leaner but are stabilized by the first burner group. Combustion tests carried out at atmospheric pressure on a scaled-down combustor have shown that the presence of these "cold" burners has no significant effect on combustor pattern factor. These tests also indicated very low values of CO, UHC, and NO_x, in agreement with previous experience of EV burners.

The strict NO_x regulations in Japan have promoted several recent developments in dry low-NO_x combustion. During the past 5 years, Kawasaki Heavy Industries Ltd., a manufacturer of small-to-medium size gas turbines, has been developing a dry low-NO_x combustor burning natural gas for application to a 1.5 MW gas turbine. The tubular combustor employs a combination of lean premixed combustion and fuel staging (multiple fuel injectors). The pilot nozzle is a conventional multi-orifice type, which supplies up to 5 percent of the total fuel. The eight main nozzles are subdivided into four groups, with two in each group. At full load all eight nozzles are flowing. With gradual reduction in load, successive groups of nozzles are shut off, until at idle only the pilot nozzle and one group of main nozzles are supplied with fuel. This combustor has demonstrated a maximum NO_x level of 42 ppm and work is in progress to reduce this to 20 ppm (Kajita et al., 1993).

Nakata et al. (1992) have designed an RQL combustor to burn a coal-gasified fuel having a calorific value of only one tenth that of natural gas. Its main combustible component is carbon monoxide, but it also contains appreciable concentrations of ammonia, which is converted into NO_x during the combustion process. Even so, this combustor achieved an NO_x level

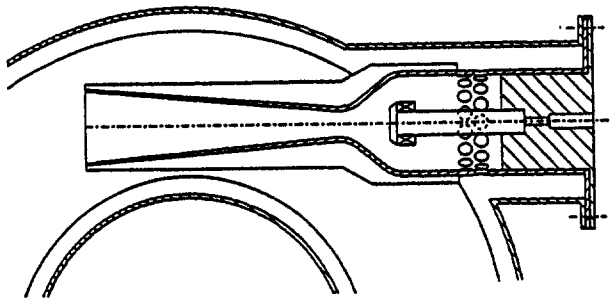

Fig. 46 Schematic cross-section of venturi mixer for the ALEC combustor

of 60 ppm when burning the standard fuel containing 1000 ppm of ammonia.

The Japan Automobile Research Institute is collaborating with the Toyota Central Research and Development Laboratory in the development of a low-emissions combustor for a 100 kW automotive ceramic gas turbine (Kumakura et al., 1994). Studies are being carried out in a premix-prevaporize tube operating both at atmospheric pressure and on the engine at high pressures to provide quantitative data on the influence of fuel drop size and fuel distribution on the degree of vaporization achieved (Ohkubo et al., 1994).

Other dry low-NO_x combustor concepts for small gas turbines include the Annular Low-Emission Combustor (ALEC), which is being developed in several forms by Gasunie Research in the Netherlands (Bahlmann and Visser, 1994). It is basically a lean-premix combustor in which mixing of gaseous fuel and air is accomplished using a venturi premixer, as illustrated in Fig. 46. The venturi extends inwardly (tangentially) into the annular combustion liner and is double-walled and air-cooled. To avoid combustion within the venturi mixers, the diameter of the venturi outlet is such that the average flow velocity at exit is 30 m/s. The diffuser angle of the venturi is set at 5.5 deg. Preliminary tests with a 7 deg angled venturi resulted in flow separation and combustion inside the venturi. The ALEC concept has demonstrated very low NO_x levels (<10 ppm) along with satisfactory CO levels (<50 ppm).

Lean Premix Prevaporize Combustion

As the turbine inlet temperatures of many gas turbines are well below the temperatures needed to produce NO_x in significant quantities, it should, in principle, be possible to achieve low levels of NO_x without any sacrifice of cycle efficiency. In practice, the requirements of flame stability and high heat release rates usually demand flame zones in which the gas temperature is appreciably higher than the turbine inlet temperature. Conventional combustors typically inject fuel directly into the primary combustion zone with little or no premixing with air. Consequently, combustion takes place in local regions at near-stoichiometric temperatures with consequent high rates of NO_x formation.

A common feature of all the dry low-NO_x combustors described above is that positive efforts are made to eliminate these local regions of high temperature by mixing the fuel and air upstream of the combustion zone. The lean, premix, prevaporize (LPP) concept represents the ultimate in this regard. Its underlying principle is to supply the combustion zone with a completely homogeneous mixture of fuel and air, and then to operate the combustion zone at an equivalence ratio which is very close to the lean blowout limit. The smaller the margin between stable combustion and flame blowout, the lower will be the output of NO_x.

A typical LPP combustor can be divided into three main regions. The first region is for fuel injection, fuel vaporization, and fuel–air mixing. Its function is to achieve complete evaporation and complete mixing of fuel and air prior to combustion. By eliminating droplet combustion and supplying the combustion zone with a homogeneous mixture of low equivalence ratio, the combustion process proceeds at a uniformly low temperature and very little NO_x is formed. In the second region the flame is stabilized by the creation of one or more recirculation zones. Combustion is completed in this region and the resulting products then flow into region three, which may comprise a fairly conventional dilution zone.

A useful byproduct of LPP combustion is that it is essentially free from carbon formation, especially when gaseous fuels are used, in which case the description "lean premixed combustor" is more appropriate. The absence of carbon not only eliminates soot emissions but also greatly reduces the amount of heat transferred to the liner walls by radiation, thereby reducing the amount of air needed for liner wall cooling. This is an important consideration because it means that more air is made available for lowering the temperature of the combustion zone and improving the combustor pattern factor.

Another important advantage of LPP systems is that for flames in which the temperature nowhere exceeds 1900 K the amount of NO_x formed does not increase with increase in residence time (Anderson, 1975; Leonard and Stegmaier, 1994). This means that LPP systems can be designed with long residence times to achieve low CO and UHC, while maintaining low NO_x levels. This finding is especially significant for industrial engines, where size is less important than for aero-engines. According to Leonard and Stegmaier, this approach leads to an LPP combustor volume that is approximately twice that of a conventional combustor.

The main drawback to the LPP concept is that the long time required for fuel evaporation and fuel–air premixing upstream of the combustion zone may result in the occurrence of autoignition or flashback at the high inlet air temperatures associated with operation at high power settings. Another drawback is that some form of piloting device may be needed to facilitate ignition and sustain combustion at arduous operating conditions. Also, the airflow rate needed for lean combustion during high-power operation may result in flame blowout at low power conditions. To alleviate this problem, which is endemic to the LPP combustor due to its need to operate close to the lean blowout limit, some form of fuel staging or variable geometry is usually required.

Another problem associated with all well-mixed combustion systems is that of acoustic resonance, which occurs when the combustion process becomes coupled with the acoustics of the combustor. This phenomenon has been encountered many times in the past and is often manifested merely as noise, but in severe cases it creates mechanical vibrations, which may cause damage to engine components. Improvements in fuel–air mixing always encourage the onset of combustion noise. This problem is therefore of great importance to the future development of lean premixed combustors.

In summary, lean premix prevaporize combustion has considerable potential for ultralow-NO_x emissions. Several workers have reported NO_x levels below 10 ppm, even with flame temperatures higher than 2000 K (Poeschl et al., 1994). However, many formidable problems remain, the principal being that of achieving complete evaporation of the fuel and thorough mixing of fuel and air within the autoignition delay time and without risk of acoustic resonance or flashback.

Droplet and Spray Evaporation. The evaporation of drops in a spray involves simultaneous heat and mass transfer processes in which the heat for evaporation is transferred to the drop surface by conduction and convection from the surrounding air or gas, and vapor is transferred by convection and diffusion back into the gas stream. The overall rate of evaporation depends on the pressure, temperature, and transport proper-

ties of the gas; the temperature, volatility, and diameter of the drops in the spray; and the velocity of the drops relative to that of the surrounding gas.

If a single-component fuel drop is suddenly immersed in gas at high temperature, initially almost all of the heat supplied to the drop serves to raise its temperature. As the fuel temperature rises, fuel vapor is formed at the drop surface and part of the heat transferred to the drop is used to furnish the heat of vaporization of the fuel. Eventually, a stage is reached where all of the heat transferred to the drop is used as heat of vaporization and the drop stabilizes at its "wet-bulb" or "steady-state" temperature. Thus the total drop evaporation time can be subdivided into two main components, one for the heat-up period and another for the steady-state phase.

During the steady-state phase, evaporation rates are relatively high, but during the initial heat-up period much of the heat transferred to the drop is absorbed in heating it up, so the amount of heat available for fuel vaporization is correspondingly less. This lower rate of vaporization, when considered in conjunction with the significant proportion of the total drop lifetime occupied by the heat-up period, especially at high pressures, means that overall evaporation rates can be appreciably lower than the experimental values quoted in the literature, most of which were measured during steady-state evaporation at normal atmospheric pressure.

In most continuous flow combustors, the fuel is sprayed into air or gas flowing at high velocity. Where relative motion exists between the droplets and the surrounding gas, the rate of evaporation is enhanced. The effect of convection on evaporation rates can be accommodated by applying a correction factor to the evaporation rate calculated for quiescent conditions. Where heat transfer rates are controlling, the correction factor is

$$1 + 0.22\ \mathrm{Re}_D^{0.5}$$

where Re_D, the drop Reynolds number, is typically around 5.

From a practical viewpoint it would be very convenient if the effect of the heat-up period could be combined with that of forced convection in a manner that would allow an "effective" value of evaporation constant to be assigned to any given fuel at any stipulated conditions of ambient pressure, temperature, velocity, and drop size. To accomplish this, Chin and Lefebvre (1982) defined an effective evaporation constant as

$$\lambda_{\mathrm{eff}} = D^2/t_e \tag{9}$$

where t_e is the total time required to evaporate the fuel drop, including both convective and transient heat-up effects, and D_o is the initial drop diameter.

Calculated values of λ_{eff} for an ambient air pressure of 100 kPa are plotted in Fig. 47. Similar plots for higher levels of pressure may be found in Chin and Lefebvre (1982). Figure 47 shows plots of λ_{eff} versus T_{bn}, the normal boiling point, for various values of UD_o at three levels of ambient temperature, namely, 500, 1200, and 2000 K. While recognizing that no single fuel property can fully describe the evaporation characteristics of any given fuel, the normal boiling point, T_{bn}, has much to commend it for this purpose, because it is directly related to fuel volatility and vapor pressure. It also has the virtue of being quoted in fuel specifications. Figure 47 shows that λ_{eff} increases with increases in ambient temperature, pressure, velocity, and drop size and diminishes with increase in normal boiling temperature.

The concept of an effective value of evaporation constant considerably simplifies calculations of the evaporation characteristics of fuel drops. For example, for any given conditions of pressure, temperature, and relative velocity, the lifetime of a fuel drop of any given size is obtained from Eq. (9) as

$$t_e = D_o^2/\lambda_{\mathrm{eff}} \tag{10}$$

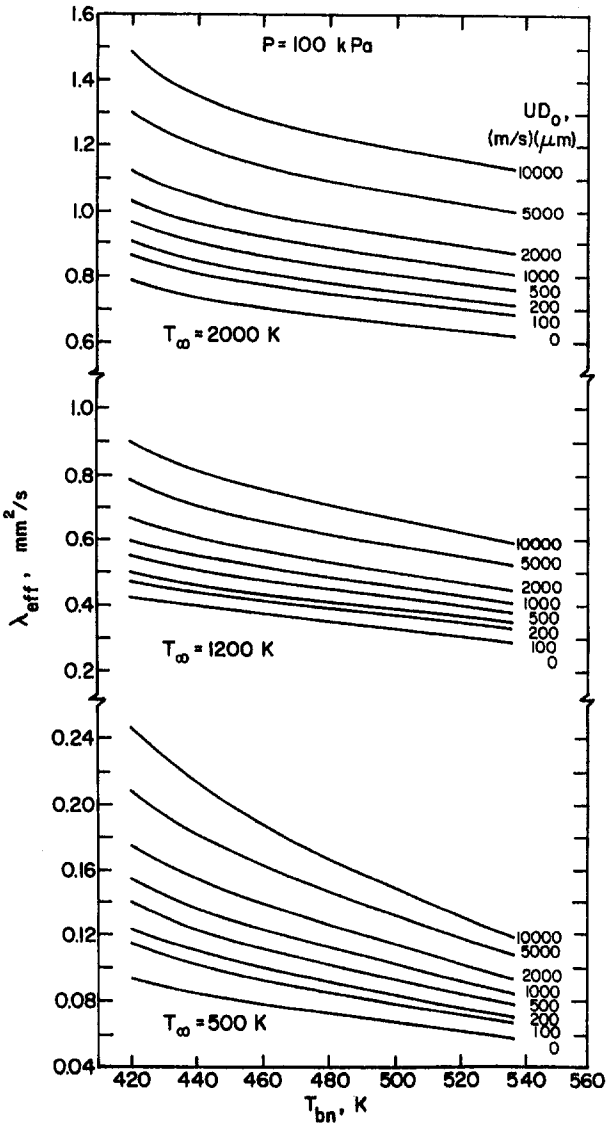

Fig. 47 Variation of effective evaporation constant with normal boiling point for a pressure of 100 kPa

while the average rate of fuel evaporation is readily determined as

$$m_F = (\pi/6)\rho_F \lambda_{\mathrm{eff}} D_o \tag{11}$$

The velocity term U in Fig. 47 is the relative velocity between the drop and the surrounding gas. However, small droplets rapidly attain the same velocity as the surrounding gas, after which they are susceptible only to the fluctuating component of velocity, u'. Thus for gas turbine combustors, where the value of u' is usually high enough to affect evaporation rates, U in Fig. 47 should be replaced with u'.

For sprays, the average rate of fuel evaporation is obtained as

$$m_F = \rho_A \lambda_{\mathrm{eff}} V q / D_o^2 \tag{12}$$

where ρ_A is the air or gas density, V is the spray volume, q is the fuel/air ratio by mass, and D_o is the Sauter mean diameter of the droplets in the spray.

Equation (12) may be used to calculate average rates of fuel spray evaporation, while Eq. (10) gives the length of duct required for complete evaporation if the spray is injected into a ducted air stream. The drop diameter selected for insertion

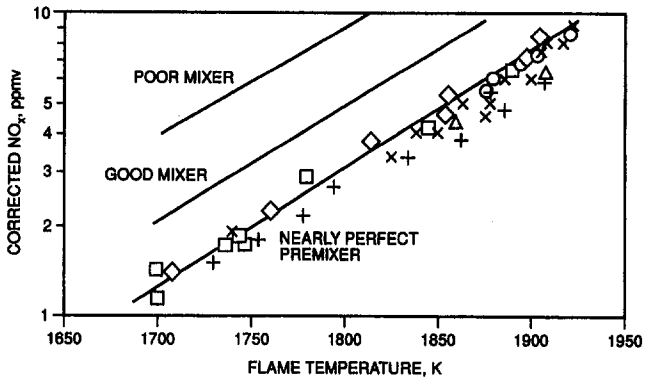

Fig. 48 Effects of nonuniform fuel–air mixing on NO_x formation

into Eq. (10) should, of course, be that of the largest drop in the spray.

In a number of recent publications, Chin (1994, 1995a, b) has developed and extended the λ_{eff} concept to include several phenomena of practical importance, including the secondary breakup of droplets as well as real gases, near-critical temperature, and multicomponent fuel effects. Recent advances in the modeling of droplet vaporization have been reviewed by Peng and Aggarwal (1995). Their review also includes the methodologies currently available for representing droplet motion and vaporization history in two-phase flow computations.

Mixing. The attainment of perfect mixture homogeneity prior to combustion is of paramount importance to the success of most types of low-emissions combustors. The influence of mixture inhomogeneity on NO_x formation has been examined by several workers, both theoretically and experimentally. Appleton and Heywood (1973) employed a burner in which kerosine fuel was injected using an air-assist atomizer, which allowed the degree of fuel–air mixing to be varied by changing the atomizing air pressure. For low equivalence ratios, they found that NO_x emissions decreased by a factor of ten as a result of better fuel–air mixing. In a similar study by Semerjian et al. (1979) it was found that poorer fuel–air mixing resulted in increased NO_x emissions for overall fuel-lean flames. Lyons (1981) used a multipoint fuel injector spraying Jet A fuel to achieve different equivalence ratio profiles across the diameter of the flametube. The results showed that spatial nonuniformity in equivalence ratio resulted in increased NO_x emissions for equivalence ratios below 0.7 and decreased NO_x emissions for near-stoichiometric mixtures.

Flanagan et al. (1992) used a simple mixing tube fitted with a bluff-body flameholder at its exit. By changing the location of the natural gas fuel injector along the length of the tube, the degree of fuel-air mixing in the mixture approaching the stabilizer could be varied. When the system was operating at an equivalence ratio of 0.66, a nearly fivefold increase in NO_x emissions was recorded when going from well-mixed to incompletely mixed conditions.

Fric (1992) used an experimental apparatus very similar to that employed by Flanagan et al. to examine the NO_x emissions produced when burning natural gas fuels at normal atmospheric pressure. He found that temporal fluctuations in equivalence ratio can also raise NO_x emissions, in addition to spatial nonuniformities. For example, temporal fluctuations of 10 percent resulted in a doubling of NO_x emissions.

Leonard and Stegmaier (1994) used a gas-fired GE LM6000 combustor to examine the effects of premixing on NO_x formation. The results obtained are given in Fig. 48, which shows NO_x as a function of average flame temperature for various degrees of premixing. Nonuniformities are the result of fluctuations in time as well as variations in space. Figure 48 gives data for a nearly perfect premixer, a well-designed premixer, and a nonoptimized premixer. It clearly illustrates the tremendous advantage to be gained from thorough mixing of air and fuel. These workers also noted that the amount of NO_x formed in a nonoptimized premixer increased with increasing pressure. They attributed this result to the fact that reactions taking place in the hot spots (>2000 K) of poorly premixed flames are pressure dependent.

The only exception to the general rule that better premixing yields less NO_x are the results obtained by Santavicca et al. (1993). These workers examined the effects of incomplete fuel–air mixing on the lean blowout limits and emissions characteristics of an LPP coaxial mixing tube combustor. A fluorescence technique was used to determine the degree of fuel vaporization and mixing at the combustor inlet. Contrary to what was expected, it was found that an improvement in fuel–air mixing resulted in comparable NO_x emissions for the same conditions of inlet temperature and equivalence ratio. Although the better mixed device demonstrated lower NO_x emissions, this was attributed to its ability to operate at lower equivalence ratios.

The formidable problems involved in trying to attain complete homogeneity in the fuel–air mixture entering the combustion zone have prompted studies into the use of mechanical mixers as a means of achieving the desired degree of fuel–air mixing. Static mixers are well known and widely used in process engineering for mixing of both gases and liquids, but as yet they appear to have evoked little interest for combustion applications. Poeschl et al. (1994) examined the mixing capability of a commercially available static mixer after a series of tests using pressure, airblast, air-assist, and multipoint injectors had failed to provide the right degree of homogeneity. All these injection devices had either failed to mix fuel vapor with the air flowing near the duct wall or had deposited liquid fuel on the wall. Tests with the static mixer yielded excellent homogeneity, with a standard deviation of lower than 5 percent for a 2 percent pressure loss. This high degree of homogeneity in the combustible mixture is very desirable, not only from an emissions standpoint, but also because it greatly reduces the possibility of spontaneous ignition. Fuel-lean mixtures tend to have long autoignition delays, but if imperfections in mixing result in local regions in which the equivalence ratio is higher than the average value, the ignition delay time could be greatly reduced. Thus a high degree of mixture homogeneity is essential, not only for the attainment of low NO_x emissions, but also to alleviate the problems of autoignition and flashback. Flashback is unlikely to occur with static mixers if the velocity through the mixer is kept high (>20 m/s). Also, by flattening the velocity profile, the mixer eliminates the boundary layer along which flashback is most prone to occur.

According to Valk (1994) the static mixer system has good potential for engines of modest compression ratio, but more work is needed to reduce length, residence time, and pressure loss, while maintaining good mixing performance.

Spontaneous Ignition. Spontaneous ignition, or autoignition, is a process whereby a combustible mixture undergoes chemical reaction, leading to the rapid evolution of heat in the absence of any concentrated source of ignition such as a flame or spark. In the LPP combustor and other types of low-emission combustors in which fuel and air are premixed prior to combustion, spontaneous ignition must be avoided at all costs since it could damage combustor components and produce unacceptably high levels of pollutant emissions.

Spontaneous ignition delay may be defined as the time interval between the creation of a combustible mixture, say by injecting fuel into a flowing air stream at high temperature, and the onset of flame. In view of their practical importance, measurements of spontaneous ignition delay time have been conducted for many fuels over wide ranges of ambient conditions and in a variety of test vehicles, including constant-volume

bombs, rapid-compression machines, shock tubes, and continuous-flow devices. The test methods employed and the results obtained are described in reviews by Mullins (1955), Spadaccini and Te Velde (1980) and, more recently, by Goodger and Eissa (1987) and Lundberg (1994).

Ignition delay times are frequently correlated using empirical equations of the form

$$\tau = A \cdot P^{-n} \cdot \exp(B/T) \tag{13}$$

where the values of A and B are determined by experiment. A is a proportionality constant that has dimensions, B is an effective activation energy, P is the pressure, and T is a characteristic temperature, usually the initial temperature of the gas (or vapor) fuel–air mixture.

Wolfer (1938) first proposed this form of equation. His analysis of experimental data showed that

$$\tau = 0.43 P^{-1.19} \exp(4650/T) \tag{14}$$

where τ is the ignition delay time in ms, P is the pressure in atm, and T is the initial mixture temperature in degrees Kelvin.

Despite its longevity, Eq. (14) is still in widespread use. To accommodate the effects of equivalence ratio on ignition delay times, it is sometimes modified to

$$\tau = AP^{-n}\phi^{-m} \exp(B/T) \tag{15}$$

There is little agreement between different workers in regard to the influence of equivalence ratio on ignition delay time. For methane, propane, and aviation kerosine, Lefebvre et al. (1986) reported values for m of 0.19, 0.30, and 0.37, respectively. Mullins (1955) observed no effect of equivalence ratio on ignition delay time, while Ducourneau (1974) and Spadaccini and Te Velde (1980) both found strong effects. The explanation for these differences probably lies in the mode of fuel injection. As discussed above, with liquid fuels there is always the potential for stoichiometric combustion in regions close to the evaporating spray. Thus, the ignition delay times will always tend to correspond to those for stoichiometric mixtures, even though the average equivalence ratio of the mixture may be appreciably below the stoichiometric value. Just how close will depend on the mean drop size of the spray, since this governs the rate of fuel evaporation and hence also the length of time that stoichiometric "streaks" of fuel–air mixture can survive, and on the number of fuel injection points. In this context it is of interest to note that Tacina (1983) obtained much more consistent autoignition data with a single orifice injector than with a 41-hole injector, which ostensibly provided a more uniform fuel–air mixture. Presumably this was because with a single injector the rate of fuel–air mixing was so slow that the bulk of the prereactions leading up to the onset of ignition took place in near-stoichiometric mixtures regardless of the average equivalence ratio. With gaseous fuels, the inconsistencies associated with slow fuel evaporation are no longer present, but the measured ignition delay times are still very dependent on the time required for the fuel and air to combine in combustible proportions. As with liquid fuels, the longer the mixing time the closer will the measured ignition delay times approach the stoichiometric values.

In summary, autoignition data are very apparatus dependent and, in particular, very fuel-injector dependent. Considerable caution should be exercised in comparing and selecting autoignition data and in no circumstances should experimentally derived equations be extrapolated to pressures and temperatures outside the range of experimental verification. This is because differences in reaction routes may occur over different levels of temperature and pressure. Only if the available experimental data or calculated values of ignition delay time exceed the residence time by a factor of at least five can the designer feel confident that spontaneous ignition is unlikely to present problems.

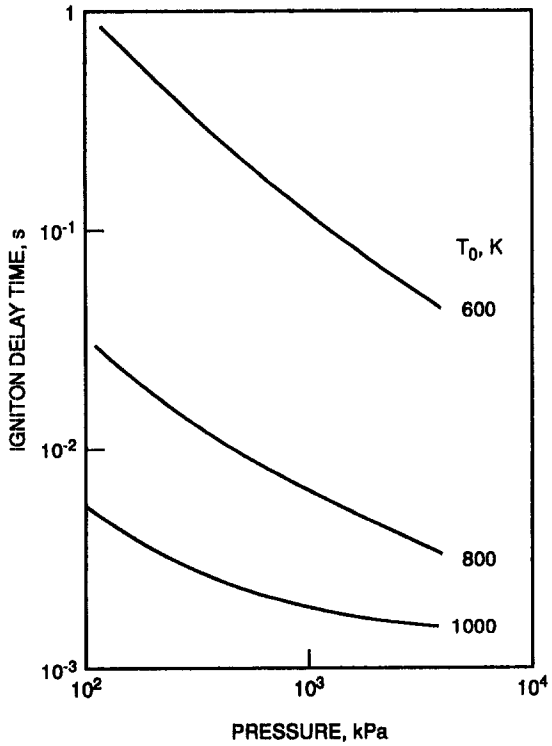

Fig. 49 Variation of ignition delay time with pressure and temperature; SMD = 50 μm, u' = 0.25 m/s

Most analyses and equations for ignition delay time ignore the effects of fuel vaporization, which is reasonable under conditions where the evaporation time is appreciably shorter than the mixing and reaction times. However, it is important to bear in mind that the spontaneous ignition delay time results from both physical and chemical processes. For liquid fuels, the physical delay is the time required to heat and vaporize the fuel drops and to mix the fuel vapor in flammable proportions with the surrounding air. The chemical delay is the time interval between the formation of a flammable mixture and the appearance of flame. Thus, the physical processes dominate in the early stages of spontaneous ignition, while in the later stages the chemical processes become overriding.

Rao and Lefebvre (1981) have proposed a model for spontaneous ignition that takes full account of both chemical and physical effects and has general application to both homogeneous and heterogeneous mixtures, including situations in which both fuel drops and fuel vapor are present at the outset of the preignition process. The spontaneous-ignition delay time t is obtained as the sum of the times required for evaporation and chemical reaction

$$t = (D_o^2/\lambda_{\text{eff}})[1 - (1 - f)^{0.67}] + 4.66 \cdot 10^{-8} \exp(9160/T_m)/\rho_A f \phi \tag{16}$$

where ϕ is the equivalence ratio, T_m is the initial mixture temperature, and f is the fraction of the total fuel that must be converted to vapor to initiate the chemical reaction. As little or no chemical reaction takes place at equivalence ratios much below 0.5, a value of f is recommended for insertion into Eq. (16) such that the product of f and ϕ is 0.5.

Calculated values of t from Eq. (16) are shown plotted against pressure in Fig. 49 for three levels of temperature, namely 600, 800, and 1000 K. Typical values for u' and D_o of 0.25 m/s and 50 μm respectively, were used in calculating λ_{eff}. The results show that the influence of fuel evaporation on t is quite small at the lowest temperature considered (600 K) but becomes increasingly significant with increasing temperature.

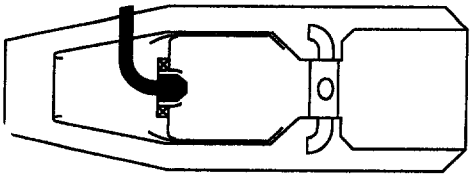

Fig. 50 Schematic diagram of Rich-burn, Quick-quench, Lean-burn (RQL) combustor

This explains the reduced dependence of t on P with increase in temperature, as shown in Fig. 49.

The model proposed by Rao and Lefebvre (1981) shows that fuel evaporation times are negligibly small in comparison with chemical reaction times for well atomized, highly volatile fuels, especially at conditions of low pressure and temperature. However, it also shows that fuel evaporation times become increasingly significant with increase in pressure and temperature, and could be rate-limiting for the autoignition of some of the alternative fuels that are now being considered, many of which have low evaporation rates due to their high viscosity (poor atomization) and low volatility.

Flashback. An intrinsic feature of all premixed-fuel combustion systems is a tendency toward flashback. Flashback occurs when the flame travels upstream from the combustion zone into the premixing sections of the combustor. This upstream propagation of flame takes place whenever the flame speed exceeds the approach flow velocity.

Two main types of flashback have been identified: (1) flashback occurring in the free stream and (2) flashback occurring through the low-velocity flow in the boundary layer along the walls of the premixing section. Either mechanism may involve homogeneous and/or heterogeneous reactions.

The most obvious free-stream mechanism would involve flashback due to a flow reversal in the bulk flow through the combustor. This flow reversal could be a result of compressor surge or combustion instability. Flashback can also occur in the absence of flow reversal if the turbulent flame speed through the gas in the premixing section is greater than the local bulk velocity. Lean combustion tends to reduce flame speeds, but other factors associated with the engine cycle, such as high temperatures, pressures, and turbulence levels, and preignition reactions in the gas due to appreciable residence times at high temperature levels, cause increased flame speed. Therefore, flame speeds may be sufficiently high to necessitate high flow velocities in the premix-prevaporize section.

The boundary-layer mechanism involves flashback through retarded flow in a boundary layer. Important relevant parameters include the wall temperature and temperature distribution, and the boundary-layer structure, turbulence properties, and thickness. For more detailed information on flashback, reference should be made to Plee and Mellor (1978).

Rich-Burn, Quick-Quench, Lean-Burn Combustor

One combustor concept that has been identified as a leading candidate for low NO_x emissions is the Rich-burn/Quick-quench/Lean-burn (RQL) combustor. Originally conceived for industrial engines (Mosier and Pierce, 1980; Pierce et al., 1980), the RQL concept utilizes staged burning, as shown in Fig. 50. Combustion is initiated in a fuel-rich primary zone at equivalence ratios of between 1.2 and 1.6, thereby reducing NO_x formation by lowering both the flame temperature and the available oxygen. Higher equivalence ratios would be even more beneficial from a NO_x standpoint, but could lead to excessive soot formation and smoke. The hydrocarbon reactions proceed rapidly, causing further depletion of oxygen and further inhibiting NO_x formation. This initial fuel-rich combustion also discourages NO_x formation from fuel-bound nitrogen (Martin and Dederick, 1976). For RQL combustion to be fully effective, the fuel must be finely atomized and uniformly distributed throughout the rich combustion zone. Moreover, the primary-zone airflow pattern must be designed to prevent the occurrence of localized flow recirculation zones which can increase residence times and thereby increase NO_x production (Micklow et al., 1993).

As the fuel-rich combustion products flow out of the primary zone, they encounter jets of air that rapidly reduce their temperature to a level at which NO_x formation is negligibly small. Transition from a rich zone to a lean zone must take place rapidly to prevent the formation of near-stoichiometric, high NO_x-forming streaks. The ability to achieve near-instantaneous mixing in this "quick quench" region is the key to the success of the RQL concept.

An important design consideration is the temperature of the lean-burn zone. If this temperature is too high, the production of thermal NO_x becomes excessive. On the other hand, the temperature must be high enough to eliminate any remaining CO, UHC, and soot. Thus, the equivalence ratio for the lean-burn zone must be carefully selected to satisfy all emissions requirements. Typically, lean-burn combustion occurs at equivalence ratios between 0.5 and 0.7 (Talpallikar et al., 1992). After the requirements of combustion and liner wall cooling have been satisfied, any remaining air can be used as dilution air to tailor the exit temperature pattern for maximum turbine durability.

In some designs the atomizing air is arranged to flow over the outside of the liner wall in the rich zone before entering the fuel nozzle. This regenerative backside convective cooling is an important design feature because conventional film cooling in the rich zone would create local near-stoichiometric mixtures that would produce high levels of NO_x.

Most of the work carried out so far on the RQL concept has confirmed its potential for ultralow-NO_x combustion. It also has an important practical asset in that it requires only one stage of fuel injection. However, in order to exploit this potential fully, significant improvements in the quench mixer design are needed. Other inherent problems include high soot formation in the rich primary zone, which gives rise to problems of high flame radiation and exhaust smoke. These problems are exacerbated by long residence times, unstable recirculation patterns, and nonuniform mixing.

Early experimental studies by Novick et al. (1982) suggested that NO_x emissions appear to be controlled only by inlet temperature and rich zone equivalence ratio. Changes in the lean or dilution zone had no observable effect on NO_x. On the other hand, carbon monoxide and smoke emissions were influenced markedly by both rich-zone and lean-zone equivalence ratios, as well as by combustor inlet temperature. A minimum lean-zone equivalence ratio of 0.6 was needed to achieve satisfactory smoke levels. In more recent studies, Rizk and Mongia (1991a, 1993a, b) have applied three-dimensional emissions modeling, using well-established reaction mechanisms to RQL combustion. Their results generally confirm the previous findings of Novick et al. in regard to the importance of rich-zone equivalence ratio to NO_x emissions, but they also stress the contribution to NO_x formation of residence time and combustion pressure.

At the present time the RQL concept is being actively studied by the Pratt and Whitney Company and other laboratories as part of NASA's HSCT (High Speed Civil Transport) program. The aim of this program is to demonstrate the feasibility of attaining NO_x levels of 3 to 8 g/kg fuel (approx. 40 to 100 ppm) at supersonic cruise conditions with kerosine fuel.

Catalytic Combustors

The very strong dependence of NO_x formation on flame temperature means that NO_x emissions are lowest when the combus-

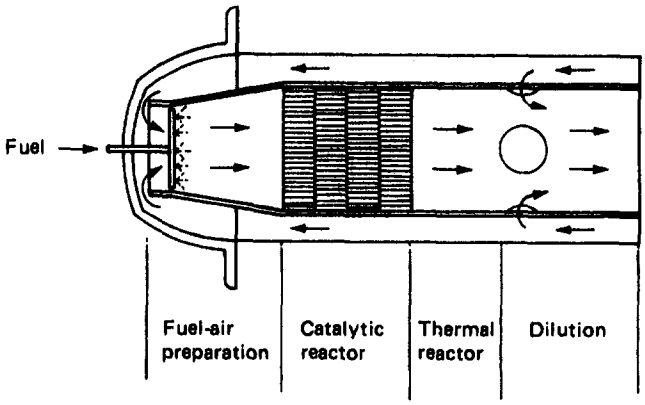

Fig. 51 Schematic representation of catalytic combustor

tor is operating perilously close to the lean blowout limit. One method of extending the lean blowout limit down to lower equivalence ratios is by incorporating a combustion-enhancing catalyst within the combustor. Catalytic combustion is a "flameless" process, which allows fuel oxidation to take place at temperatures well below the normal lean flammability limits of the fuel–air mixture. For this reason, the use of catalysts in gas turbine combustion to replace part of the thermal reaction zone allows stable combustion to occur at peak temperatures that are around 1000 K lower than those of conventional combustors. Combustion at such reduced temperatures can be expected to decrease the production of thermal NO_x dramatically.

A schematic diagram to illustrate the principle of catalytic combustion is shown in Fig. 51. Fuel is injected upstream of the reactor to vaporize and mix with the inlet air. The fuel–air mixture then flows into a catalyst bed, or reactor. This reactor may consist of several sections, each made of a different kind of catalyst. It is desirable to use a catalyst that is active at low temperatures at the inlet, while subsequent sections need to be selected for good oxidation efficiency. Downstream of the catalytic bed, a thermal reaction zone may be provided to permit catalytically initiated reactions to continue. Such reactions can contribute as much as 20 percent of the total temperature rise achieved in the combustor.

One problem with catalytic combustors is a tendency toward autoignition of the fuel upstream of the catalyst. Although the equivalence ratios of interest are well below the lean flammability limit and, in theory, should not be susceptible to autoignition, locally richer mixtures exist near the fuel injector before complete mixing has taken place. Thus, it is essential that mixing be achieved in less than the autoignition delay time. Optimum catalyst performance also requires the inlet fuel–air mixture to be completely uniform in regard to temperature, composition, and velocity profile, since this assures effective use of the entire catalyst area and prevents damage to the substrate due to local high gas temperatures. Thus the primary function of the fuel preparation process is to provide complete and uniform mixing of fuel and air before entry into the catalyst. Rudimentary tests carried out by Anderson et al. (1982) showed that approximately 70 percent fuel vaporization is required for stable catalyst operation when burning liquid fuels. These workers used multiple air-assist atomizers to achieve good atomization and rapid fuel evaporation at turndown ratios in excess of ten to one. This multipoint fuel injection enabled complete fuel vaporization and mixing to occur in a mixing zone with a length/diameter ratio of five.

Cowell and Larkin (1994) have conducted subscale testing on several different designs of catalytic combustors. The most advanced concept is shown schematically in Fig. 52. It is designed to operate at lean conditions to suppress NO_x emissions. CO and UHC emissions are of less concern because they are

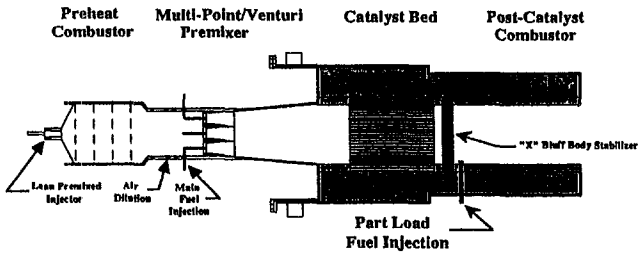

Fig. 52 Subscale catalytic combustor for industrial applications

subsequently oxidized in the catalyst. The preheat burner is a conventional well-mixed combustor, which is used to preheat the premixed fuel–air mixture entering the catalyst. This preheat combustor is not required for inlet air temperatures above 650 K. Main air is introduced immediately downstream of the preheat burner. The multipoint fuel injector is an arrangement of six venturis surrounding a seventh at the center. Gas temperatures entering the catalyst bed are in the range from 644 to 925 K. The catalytic reactor is a multiple-piece bed design using a ceramic honeycomb substrate coated with catalytically active materials. Its function is to initiate reactions of the main fuel–air mixture. Downstream of the catalyst bed is a postcatalyst combustion zone, which is stabilized behind a bluff-body flameholder. This postcatalyst combustor demonstrated efficient CO and UHC burnout. Short duration rig testing at 9 atm pressure indicated NO_x emissions below 5 ppm. The system now being developed at Solar for engine application includes fuel staging and variable geometry.

The advantage of using a postcatalyst combustor to complete the combustion process is that it allows the catalytic bed to operate at temperatures lower than the combustor outlet temperature. This is a significant advantage because it improves the reliability and extends the life of the catalyst bed. Ozawa et al. (1994a, b) used this approach in designing a combined catalytic/premix combustor to operate at a combustor outlet temperature of 1570 K while keeping the catalyst bed temperature down to 1270 K. The system is shown schematically in Fig. 53. It consists of an annular preburner, six catalytic combustor segments, six premixing nozzles, a premixed combustion section downstream of the catalyst, and an air bypass valve. Inlet air is heated to 720 K by the preburner and is distributed to both catalytic segments and premixing nozzles. The premixed, gaseous fuel–air mixture that flows around the catalyst segments is ignited by the hot combustion products emanating from the catalysts, and lean premix combustion then occurs to raise the combustor outlet temperature up to 1570 K. The function of the bypass valve is to add air to the combustor efflux gases at part-load operation.

Measurements of NO_x at atmospheric pressure when burning natural gas were obtained by varying the fuel flow rate and bypass valve opening to maintain the catalyst bed at a constant temperature. NO_x emissions were always below 10 ppm, of

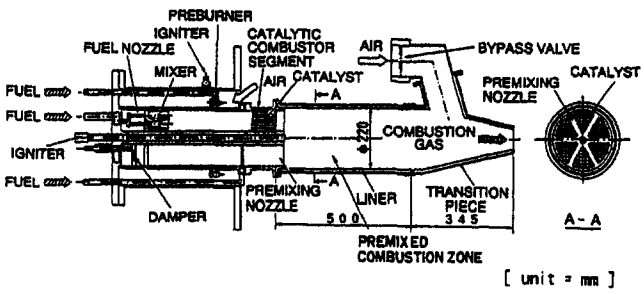

Fig. 53 Catalytic combustor for natural gas

which a significant proportion came from the preburner. The total pressure loss of the combustor was around 3 percent, which is lower than the values normally associated with conventional combustors.

The notion of completing the combustion process in the post-catalyst region to avoid exposure of the catalyst to the high temperatures responsible for deactivation and thermal shock fracture of the supporting substrate has been pursued by other workers, including Dalla Betta et al. (1994). In their combustor, natural gas mixed with air is supplied to the catalyst. Combustion is initiated by the catalyst and is completed by homogeneous reactions downstream. The potential of this approach has been demonstrated in subscale rig tests at pressures up to 14 atm and temperatures above 1500 K. Measured emissions were $NO_x < 1$ ppm, CO < 2 ppm and UHC < 2 ppm, thus demonstrating the capability of achieving ultralow NO_x along with low CO and UHC.

The catalyst employed by these workers required an inlet air temperature of 720 K, which necessitated the use of a preburner. However, it is reported that recent catalyst designs have reduced the required inlet temperature to the point where the catalyst can be operated at the compressor discharge temperature for some machines.

The very low emissions levels achieved by Dalla Betta et al. may be due in part to the high degree of uniformity produced by the fuel–air mixing system used in the test rig, which featured a static mixer located between the fuel injector and the catalyst. Vortmeyer et al. (1994) also integrated static mixers into the premixing/prevaporizing section upstream of the catalyst to minimize imperfections in fuel–air mixing. Their combustor design also featured a thermal reactor downstream of the catalyst to allow it to operate at temperatures well below the maximum flame temperature without the need for tertiary fuel injection into the thermal reactor. This was achieved by employing very short catalyst segments and/or high flow velocities. The test combustor was supplied with three different groups of fuels—paraffins, alcohols, and commercial liquid fuels. The range of operation was limited by the requirements of at least 99.9 percent combustion efficiency at the end of the thermal reactor to minimize the emissions of CO and UHC. Catalyst temperatures never exceeded 1300 K up to a maximum gas temperature at the combustor exit of 1670 K. The overall combustor pressure loss was 6 percent, which is just within the accepted range for conventional combustors. The catalyst of 40 mm length was responsible for almost half of this loss (2.35 percent). The test program was conducted at atmospheric pressure and was characterized by remarkably low NO_x emissions levels. For propane and methanol no measurable NO_x was formed. The combustion of Diesel oil yielded NO_x emissions below 2 ppm.

A main drawback to the application of catalytic combustors in modern gas turbines is the limited life expectancy of catalysts under typical high-temperature conditions. Most combustion rig testing to date has involved relatively short test periods of less than 100 hours. However, lifetimes of around 5000 hours are required for engine applications. It is feared that serious catalyst degradation could occur when operating at high pressures and temperatures for long durations. Another major drawback is that although they are capable of achieving levels of combustion efficiency very close to 100 percent, this occurs only over a fairly narrow range of operating temperatures. The lower temperature bound is set by lean blowout limits; the upper bound is determined by catalyst and substrate material limitations. Depending on the type of catalyst employed, stable combustion can be sustained over a temperature range of only a few hundred degrees Kelvin without serious loss of performance. This corresponds to a range of overall fuel/air ratios of around 1.4 to 1, as opposed to the 5 to 1 readily achieved with conventional combustors. It is essential therefore that catalytic combustion be combined with variable-geometry and/or fuel staging to sustain combustion over the broad range of conditions encountered in modern gas turbines.

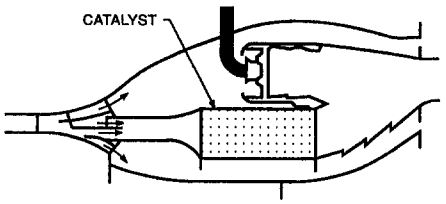

Fig. 54 Combination of catalytic and conventional staged combustor

With variable geometry, as the fuel flow increases with load, proportionally larger amounts of air are diverted through the catalyst to keep its reaction temperature within the allowable limits. The remaining air bypasses the catalyst and dilutes the combustion gases downstream. Fuel staging can be accomplished, for example, by combining a conventional combustor with a catalytic combustor, as illustrated in Fig. 54. The combustion requirements at low load conditions are met using a conventional burner. Then, at full-load conditions, where the overall equivalence ratio is compatible with catalytic combustion, most or all of the required temperature rise is achieved via catalytic combustion. This method of staging requires a careful control of air splits to provide the required catalyst pressure drop. This may necessitate the use of variable geometry in addition to fuel staging to control the air flows to the conventional and catalyst stages.

Most of the work now in progress on catalytic combustion for gas turbines is directed toward stationary applications. For aircraft engines, the concerns expressed above regarding damage to the catalyst when operating for long periods at high pressures and temperatures would appear to put it out of contention at this time, especially as both LPP and RBQ concepts show almost equal promise with less risk.

Correlation and Modeling of NO_x and CO Emissions

Empirical Models. Ever since the gas turbine became recognized in the late 1960s as a significant contributor to atmospheric pollution, efforts have been made to develop simple models for correlating experimental data on exhaust emissions in terms of all the relevant parameters. These include combustor operating conditions, combustor design features, fuel type, and fuel spray characteristics.

Empirical models can play an important role in the design and development of low-emissions combustors. They serve to reduce the complex problems associated with emissions to forms that are more meaningful and tractable to the combustion engineer. They also permit more accurate correlations of emissions for any one specific combustor than can be achieved by the far more comprehensive models discussed below.

In attempting to derive an empirical model for emissions, emphasis is placed on NO_x and CO. For both these species it may be assumed that their exhaust concentrations are dependent on three terms, which are selected to represent the following: (1) mean residence time in the combustion zone, (2) chemical reaction rates, and (3) mixing rates. Expressions for these three parameters can be derived in terms of combustor size, liner pressure loss, airflow proportions, and operating conditions of inlet pressure, temperature, and air mass flow rate. We have

$$\text{Residence time} = L/U \propto PV_c/m_A T \tag{17}$$

$$\text{Reaction rate} \propto P^n \exp aT \tag{18}$$

$$\text{Mixing rate} \propto (\Delta P/P)^x \tag{19}$$

where L = liner length, U = liner flow velocity (average), V_c = combustion volume, P = pressure, T = gas temperature, m_A

= air flow rate, ΔP = liner pressure drop, and a, n, and x are constants to be determined experimentally. By combining these terms we obtain for NO_x,

$$NO_x = f(\text{residence time})(\text{reaction rate})(\text{mixing rate}) \quad (20)$$

From analysis of experimental data for several different combustors (Lefebvre, 1984), values of a, n, and x were established and substituted into Eq. (20) to obtain

$$NO_x = 9 \times 10^{-8} P^{1.25} V_c \exp(0.01 T_{st})/m_A T_{pz} \text{ g/kg fuel} \quad (21)$$

where P is the combustion pressure in kPa and V_c is the combustion volumne in m^3. The effect of variations in overall combustor fuel/air ratio is included via its influence on primary-zone temperature. Fuel type affects both flame temperature and mean drop size. For NO_x, drop size is less important since, at the high pressure conditions where NO_x emissions are most prominent, the fraction of the total combustion volume employed in fuel evaporation is so small that variations in fuel drop size have only a small effect on NO_x emissions. For this reason, most correlating parameters for NO_x ignore the effects of mean drop size.

Equation (21) takes account of the fact that, in the combustion of heterogeneous fuel–air mixtures, it is the stoichiometric flame temperature, T_{st}, that determines the formation of NO_x. However, for the residence time in the combustion zone, which is also significant to NO_x formation, the appropriate temperature term is the average value T_{pz}, as indicated in the denominator of Eq. (21).

Equation (21) is suitable for conventional spray combustors only. For lean premix/prevaporize combustors in which the maximum attainable temperature is T_{pz}, it may still be used, provided that T_{pz} is substituted for T_{st}. The excellent correlation of experimental data on NO_x provided by Eq. (21) for GE J79-17A and F101 combustors is illustrated in Figs. 55 and 56, respectively. Many other semi-empirical models for predicting NO_x emissions have been derived. For a critical review of models developed before 1980, reference should be made to Mellor (1981). Some of the more recent expressions for NO_x emissions include the following:

Odgers and Kretschmer (1985)

$$NO_x = 29 \exp - (21{,}670/T) P^{0.66} \times [1 - \exp - (250t)] \text{ g/kg fuel} \quad (22)$$

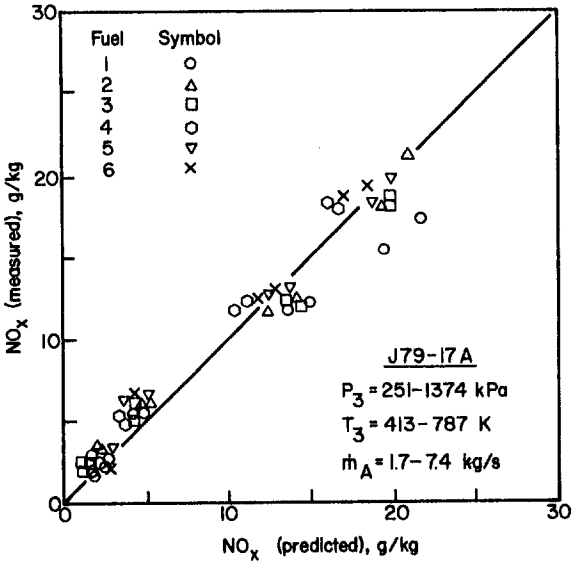

Fig. 55 Comparison of measured and predicted values of NO_x for a GE J79-17A combustor

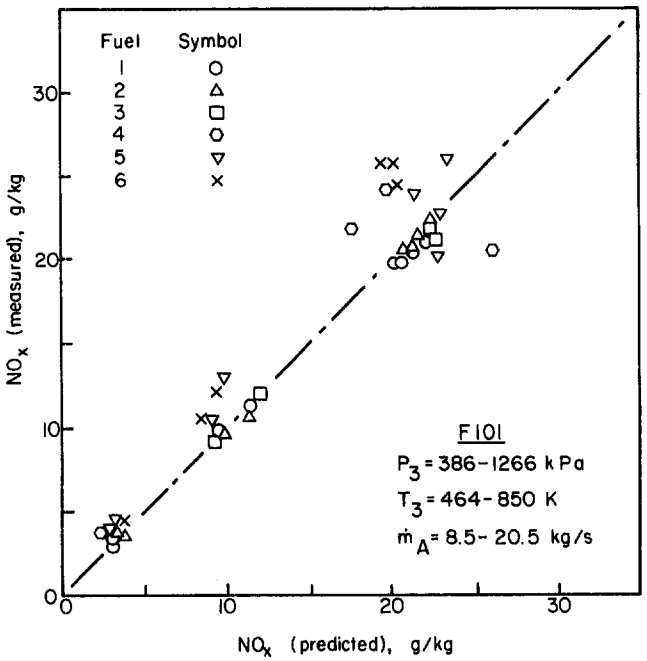

Fig. 56 Comparison of measured and predicted values of NO_x for a GE F101 combustor

where P is the combustion pressure in Pa, T is the combustion temperature in degrees Kelvin, and t is the NO_x formation time in ms. For aircraft combustors, Odgers and Kretschmer quote formation times of 0.8 ms (airblast atomizers) and 1.0 ms (pressure atomizers). For industrial combustors burning liquid fuels, quoted formation times range from 1.5 to 2.0 ms.

Lewis (1991).

$$NO_x = 3.3192 \times 10^{-6} \exp(0.0079776T) P^{0.5} \text{ ppmv} \quad (23)$$

where P is the combustion pressure in atm. This equation is intended to show the amount of NO_x formed in lean, homogeneous combustion. It suggests that NO_x formation depends only on the postcombustion temperature and pressure and is completely independent of the residence time of the gases in the combustor. According to Lewis (1991), "the time involved is not the normal residence time of the combustion products, but rather the relaxation time of the molecules involved, primarily the nitrogen molecule, and thus, is the same in all combustion systems using air." This finding appears to be at variance with published data on the effect of residence time on NO_x formation (see, for example, Rizk and Mongia, 1990; Nicol et al., 1992; Zelina and Ballal, 1994), all of which indicate that NO_x concentrations increase with residence time. However, these workers also noted that the influence of residence time on NO_x formation diminishes with reduction in equivalence ratio, the effect being relatively small for very lean mixtures, as studied by Lewis. Some expressions for NO_x include time directly, as in Eq. (22), but in others it is embodied into the expression via a mass flow rate term, as in Eq. (21). However, even expressions for NO_x that take no account of residence time whatsoever (Eq. (23), for example) can nevertheless provide an excellent prediction of experimental data because the residence time of all aero gas turbine combustors tends to be the same at around a few milliseconds. It is only when expressions derived for industrial gas turbine combustors having much longer residence times are applied to aero combustors, or vice versa, that the lack of a term for residence time becomes important.

Rokke et al. (1993)

$$NO_x = 18.1 P^{1.42} m_A^{0.3} q^{0.72} \text{ ppm} \quad (24)$$

where P is the combustion pressure in atm, m_A is the combustor

air flow in kg/s, and q is the fuel/air ratio. This equation was found to correlate very satisfactorily measurements of NO_x emissions from five different natural gas-fired machines operating in the power range from 1.5 to 34 MW. Although combustion temperature is conspicuous by its absence in Eq. (24), its influence on NO_x emissions is accounted for by the inclusion of a fuel/air ratio term.

Rizk and Mongia (1994)

$$NO_x = 15.10^{14}(t - 0.5t_e)^{0.5} \exp - (71{,}100/T_{st})P^{-0.05}(\Delta P/P)^{-0.5} \text{ g/kg fuel} \quad (25)$$

where t is the primary-zone residence time in seconds, t_e is the fuel evaporation time, and $\Delta P/P$ is the nondimensional liner pressure drop. An interesting feature of this equation is that it includes a term, t_e, to account for the effects of fuel drop size on NO_x emissions. According to Eq. (25), a reduction in mean drop size should increase NO_x emissions by reducing the time required for fuel evaporation. However, if combustion takes place under conditions where evaporation times are negligibly small in comparison with the total combustor residence time, NO_x emissions can actually go down with reduction in mean drop size, as observed by Rink and Lefebvre (1989).

For more information on semi-analytical equations for the estimation of NO_x emissions from gas turbines, reference should be made to Becker and Perkavec (1994) and Nicol et al. (1994).

Comparisons between these different equations for predicting NO_x emissions from conventional combustors is prohibited by the fact that in some cases the units for NO_x are in parts per million and in others grams per kilogram of fuel. These units cannot be interchanged unless the equivalence ratio is also known. However, all of these expressions for NO_x provide an excellent fit to the experimental data employed in their derivation. This is perhaps hardly surprising since the formation of NO_x is largely dominated by one parameter only—the maximum temperature in the combustion zone.

Similar correlations to those presented above for NO_x have been developed for CO. One important difference stems from the fact that the formation of CO in the primary combustion zone takes appreciably longer than the time required to produce NO_x. In consequence, the relevant temperature is not the local peak value adjacent to the evaporating fuel drops, but the average value throughout the primary zone, T_{pz}. Also, because CO emissions are most important at low pressure conditions, where evaporation rates are relatively slow, it is necessary to reduce the combustion volume V_c by the volume occupied in fuel evaporation V_e.

According to Lefebvre (1984) we have

$$CO = 86 \text{ m } T_{pz} \exp - (0.00345T_{pz})/(V_c - V_e)(\Delta P/P)^{0.5}P^{1.5} \text{ g/kg fuel} \quad (26)$$

where V_e, the volume employed in fuel evaporation, is given by

$$V_e = 0.55m_{pz}D_o^2/\rho_{pz}\lambda_{\text{eff}} \quad (27)$$

where m_{pz} is the primary-zone airflow rate, D_o is the Sauter mean diameter of the fuel spray, ρ_{pz} is the density of the primary-zone gas, and λ_{eff} is the effective evaporation constant (Chin and Lefebvre, 1982). In this equation it is of interest to note that V_e is proportional to the square of the initial mean drop size. This highlights the importance of good atomization to the attainment of low CO. The ability of Eq. (26) to predict CO emissions from a P&W F100 and a GE F101 combustor is illustrated in Figs. 57 and 58, respectively.

A similar form of expression to Eq. (26) has been derived by Rizk and Mongia (1994) as

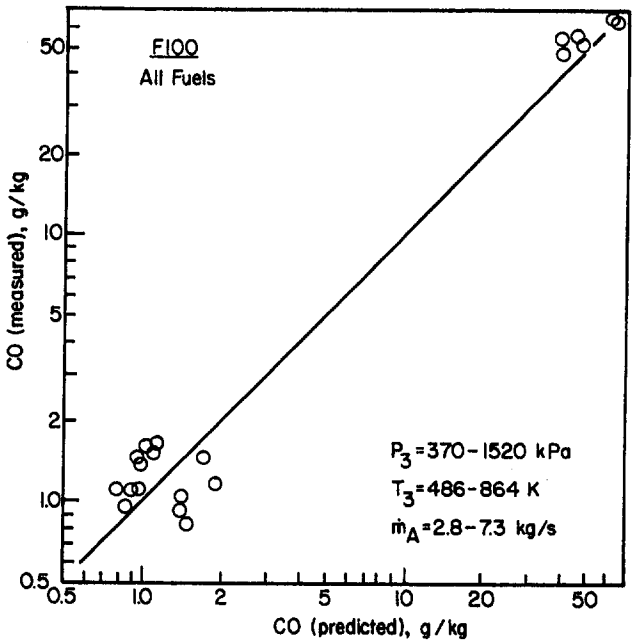

Fig. 57 Comparison of measured and predicted values of CO

$$CO = 0.18 \times 10^9 \exp(7800/T_{pz})/P^2(t - 0.4t_e)(\Delta P/P)^{0.5} \text{ g/kg fuel} \quad (28)$$

where t_e is the fuel evaporation time. This equation exhibits a slightly lower dependence on combustion temperature and a slightly higher dependence on pressure than Eq. (26).

Correlating parameters have also been developed for UHC and smoke. The interested reader is referred to Rizk and Mongia (1994) for the latest work.

Numerical Models. The application of numerical models to the design of gas turbine combustors owes its origin to the pioneering work of several workers, prominent among whom are Jones and Priddin (1978), Mongia (1987), and Serag-Eldin and Spalding (1979).

In recent years, the detailed representation of combustor flow fields made available through numerical methods has been used to provide some insight into the interaction of swirling and recirculating flows with fuel sprays and the effect of this interaction on atomization, dispersion of fuel drops, evaporation, mixing, and turbulent combustion. Mongia and co-workers, in particular, have made extensive use of numerical methods to obtain a better understanding of the formation of various pollutant species within the combustor, while the use of computational combustor dynamics (CCD) to provide guidance to the combustion engineer during the design and development process has become an accepted practice in many gas turbine companies (e.g., Correa and Shyy, 1987; McGuirk and Palma, 1993; Priddin and Coupland, 1986; and Sturgess, 1986).

At the present time much of the computer modeling in gas turbine combustors is accomplished using versions of the TEACH code and the k–e turbulence model. It seems likely that TEACH-based codes and their derivatives, along with the commercially available FLUENT code, will continue to play useful roles for some time to come, with updates to the codes being made in the light of new experimental data. However, it must be stated that the three-dimensional comprehensive models now in vogue are costly in computer time and the results obtained often fall short of expectations. As Rizk and Mongia (1993a) have pointed out, due to the incomplete understanding of the various combustion processes, analytical calculations on practical gas turbine combustors cannot yet be considered quan-

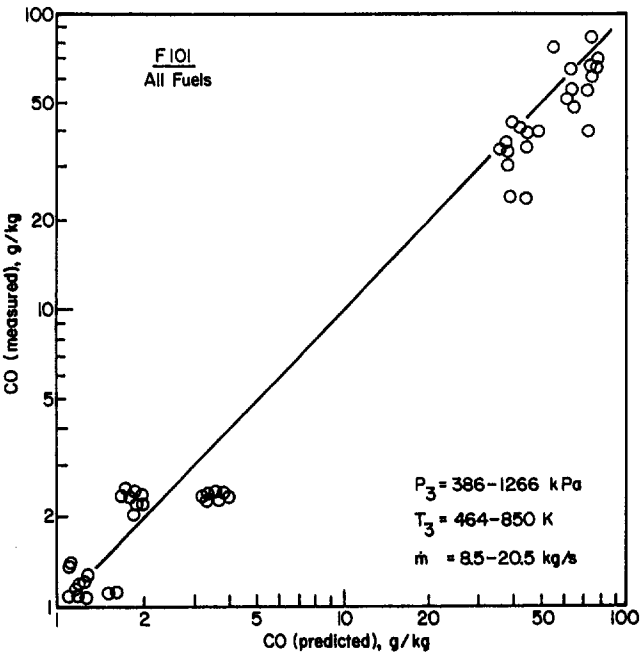

Fig. 58 Comparison of measured and predicted values of CO for a GE F101 combustor

titatively accurate. Significant advances in physical submodels, numerics, and in the simulation of actual hardware are needed to improve the predictive capability of current models (Peters, 1988; Mongia, 1993).

Prompted by the limitations of current CCD models, and encouraged by the long history of success in routine applications of simple correlations to combustor design and development, Rizk and Mongia (1986) proposed a hybrid modeling approach that combines comprehensive modeling with physically realistic and well-established expressions for estimating various important performance parameters such as combustion efficiency, lean blowout limits, pattern factor, liner wall temperatures and gaseous pollutant emissions. This empirical/analytical approach to combustor design has been successfully applied to 22 gas turbine combustors (Mongia, 1993). It represents a logical step forward that could prove of great value to combustion engineers in providing quantitative design guidance until such time as new knowledge on turbulent combustion models, numerics, grid resolution, and boundary conditions become available for improving the accuracy of current CCD models. Examples of the use and application of hybrid models can be found in Rizk and Mongia (1986, 1993b, c, 1994).

Concluding Remarks

It is fortunate that the gas turbine not only offers the highest thermal efficiency as a prime mover for aircraft propulsion and power generation for the foreseeable future, but also has the potential for the lowest possible levels of pollutant emissions. Most of the drive toward more strict control of pollutant emissions from gas turbines is being directed at oxides of nitrogen (NO_x). Low NO_x levels are readily achieved by lowering the peak flame temperature within the combustor. The challenge is to keep flame temperatures down at high-power conditions without incurring unacceptable penalties in combustion performance when operating at low power conditions. For the immediate future, the introduction into service of staged combustion appears to be most promising, despite its attendant penalties for the engine in terms of more complex fuel scheduling and control strategy. In fact, a General Electric dual-annular staged combustor has just received FAA certification on Airbus Industrie A320 and A321 aircraft.

At the present time, lean premixed combustion appears to be the only technology available for achieving sub-10 ppm NO_x emissions in practical combustors. However, such low NO_x levels can only be attained if the fuel and air supplied to the combustion zone are almost perfectly premixed. At high power conditions, where combustor inlet air temperatures can approach 1100 K, most hydrocarbon fuels readily ignite on contact with air. Thus the problems of spontaneous ignition and flashback need to be fully addressed before lean premixed combustion can be applied with confidence to aircraft engines. Another problem associated with well-mixed combustion systems is that of acoustic resonance, which occurs when the combustion process becomes coupled with the acoustics of the combustor. This problem could be of great importance to the future development of lean premixed combustors.

Other main contenders as ultralow-NO_x combustors are the rich-burn, quick-quench, lean burn (RQL) and catalytic combustion concepts. The work carried out so far on various RQL configurations has shown that this concept has considerable promise for very low NO_x emissions. Its future prospects depend largely on whether the rich combustion products emanating from the primary zone can be mixed with the remaining combustion air quickly enough to avoid the creation of high-temperature, NO_x-forming regions. Catalytic combustors allow very low combustion temperatures, which ensure exceptionally low levels of NO_x. Their main drawback is the limited life expectancy of catalysts and substrates under typical high temperature conditions. The use of postcatalyst combustion allows the catalytic bed to operate at lower temperatures with consequent benefits in terms of reliability and longer life. Most of the work now in progress is directed toward catalytic combustors for stationary engines. Considerable advances in high-temperature materials will be needed to raise their reliability to the standard required for aircraft engines.

The continuing pressure to conserve fuel resources can only be met by raising the engine cycle efficiency. This approach yields an important additional bonus in the form of less CO_2 but it also results in higher combustion temperatures and higher levels of NO_x. Thus, the need to burn less fuel and thereby generate less CO_2 is in direct conflict with the equally important need to reduce NO_x. For the forseeable future it seems likely that engine pressure ratios will rise up to a maximum value of around 50, beyond which any further increase will depend on the outcome of current research and development efforts in ultralow NO_x combustion.

We are now entering into an area of increasing competitiveness between different engine manufacturers in regard to low-NO_x combustors. For stationary gas turbines, the attainment of low-NO_x has become the foremost marketing issue, thus offering important opportunities to those engine manufacturers who are willing to commit large resources to pollutants reduction programs.

Fuel reserves are notoriously difficult to predict but, for the next twenty years or thereabouts, kerosine-type fuels should be fairly readily available for aircraft engines, while natural gas will continue to be the favored fuel for baseload operations of stationary engines. With the ultimate depletion of conventional hydrocarbon fuels and natural gas, oils derived from coal, shales, and tar sands will assume increasing importances. Such fuels are known to be of higher viscosity and lower volatility than current light-distillate fuels, thus exacerbating the problems of atomization and fuel prevaporization.

Fuel preparation is of vital importance in the attainment of low pollutant emissions. Future advances in low-emissions combustion technology will demand a detailed knowledge of the properties and structure of the sprays produced in airblast and pressure atomization. The properties of prime interest include drop size distributions, droplet and gas velocities, droplet

trajectories, and droplet mass flux. Such detailed information is essential for the successful modeling of sprays, but the extent to which predictions based on spray models can be utilized in combustor design depends largely upon the degree to which they can be validated or refuted by accurate experimental data. This situation calls for more collaborative efforts between the modeling and experimentation communities.

Although considerable insight has been gained into the internal flow patterns and external spray characteristics of both pressure-swirl and airblast atomizers, considerable work remains to be done. Except for atomization occurring at impractically low velocities, there is still no basic method for predicting the drop size distributions that will result from the disintegration under controlled conditions of a liquid jet or sheet. It has been known for more than thirty years that the geometry, size, shape, and surface finish of the flow passages within an atomizer have a strong influence on the internal flow patterns and the external spray characteristics, but these important effects are not yet sufficiently well understood to form an integral part of the design process. The widespread use of laser diagnostic techniques in spray characterization has created a rapidly growing data base that provides theoreticians and modelers with new opportunities for establishing a scientific basis for a methodical approach to the design of fuel injectors and fuel–air mixing systems.

A drawback to advanced laser diagnostics and comprehensive modeling is that because they are both challenging and intellectually rewarding in their own right it is easy to forget that they are only means to an end. This author is not aware of any significant advance in atomizer or combustor technology that can be attributed to laser diagnostics or comprehensive modeling. All too often these activities are pursued to the detriment of innovation and creativity, which are the two essential ingredients for progress in these areas.

Acknowledgments

Any paper that attempts to review a given topic must necessarily draw heavily on the work of others and this paper is no exception in this regard. If the author's name appears more often than is merited by his contribution to the subject, this is due in large measure to his desire to recognize the valuable contributions made by his various co-authors of many publications in the areas of fuel injection and gas turbine combustion, most of whom were his students either at Cranfield University in the U.K. or at Purdue University in the U.S.A.

I would like to express my gratitude to the IGTI Gas Turbine Scholar Program and to Professor John Denton, the Chairman of the IGTI Scholar Award Review Committee, for his encouragement and support during the preparation of this paper. I would also like to thank my friends and colleagues in the gas turbine combustion community for their confidence in nominating me for this award.

References

Aigner, M., and Muller, G., 1993, "Second Generation Low-Emission Combustors for ABB Gas Turbines: Field Measurements With GT11N-EV," ASME JOURNAL OF ENGINEERING FOR GAS TURBINES AND POWER, Vol. 115, pp. 533–536.

Altemark, D., and Knauber, R., 1987, VDI Berichte No. 645, pp. 299–311.

Anderson, D. N., 1975, "Effects of Equivalence Ratio and Dwell Time on Exhaust Emissions From an Experimental Premixing Prevaporizing Burner," ASME Paper No. 75-GT-69.

Anderson, S. J., Friedman, M. A., Krill, W. V., and Kesselring, J. P., 1982, "Development of a Small-Scale Catalytic Gas Turbine Combustor," ASME JOURNAL OF ENGINEERING FOR GAS TURBINES AND POWER, Vol. 104, pp. 52–57.

Angello, L., and Lowe, P., 1989, "Dry Low NO_x Combustion Development for Electric Utility Gas Turbine Applications; A Status Report," ASME Paper No. 89-GT-254.

Aoyama, K., and Mandai, S., 1984, "Development of a Dry Low NO_x Combustor for a 120 MW Gas Turbine," ASME JOURNAL OF ENGINEERING FOR GAS TURBINES AND POWER, Vol. 106, pp. 795–800.

Appleton, J. P., and Heywood, J. B., 1973, "The Effects of Incomplete Fuel–Air Mixing in a Burner on NO Formation From Nitrogen in the Air and in the Fuel," *Fourteenth Symposium (International) on Combustion,* The Combustion Institute, Pittsburgh, PA, pp. 777–786.

Bahlmann, F. C., and Visser, B. M., 1994, "Development of a Lean-Premixed Two-Stage Annular Combustor for Gas Turbine Engines," ASME Paper No. 94-GT-405.

Bahr, D. W., 1982, "HC and CO Emission Abatement via Selective Fuel Injection," ASME Paper No. 82-GT-178.

Bahr, D. W., 1987, "Technology for the Design of High Temperature Rise Combustors," *AIAA Journal of Propulsion and Power,* Vol. 3, No. 2, pp. 179–186.

Bahr, D. W., 1991, "Aircraft Engines NO_x Emissions—Abatement Progress and Prospects," *Proceedings of Tenth International Symposium on Air-Breathing Engines,* Nottingham, England.

Bahr, D. W., 1992, "Aircraft Turbine Engine NO_x Emission Limits—Status and Trends," ASME Paper No. 92-GT-415.

Bahr, D. W., 1995, Lecture notes for short course on gas turbine combustion; held at the University of California, Irvine, Mar. 13–17.

Bauckhage, K., 1988, "The Phase-Doppler Difference Method. A New Laser-Doppler Technique for Simultaneous Size and Velocity Measurement," *Particles and Particle System Characterization,* Vol. 5, pp. 16–22.

Bayle-Labouré, G., 1991, "Pollutant Emissions From Aircraft Engines: a Situation Under Control," *Revue Scientifique SNECMA,* 2nd ed.,

Becker, T., and Perkavec, M. A., 1994, "The Capability of Different Semianalytical Equations for Estimation of NO_x Emissions of Gas Turbines," ASME Paper No. 94-GT-282.

Chen, S. K., Lefebvre, A. H., and Rollbuhler, J., 1992, "Factors Influencing the Spray Cone Angle of Pressure-Swirl Atomizers," ASME JOURNAL OF ENGINEERING FOR GAS TURBINES AND POWER, Vol. 114, pp. 97–103.

Chen, S. K., Lefebvre, A. H., and Rollbuhler, J., 1993, "Factors Influencing the Circumferential Liquid Distribution From Pressure-Swirl Atomizers," ASME JOURNAL OF ENGINEERING FOR GAS TURBINES AND POWER, Vol. 115, pp. 433–438.

Chigier, N., 1983, "Drop Size and Velocity Instrumentation," *Prog. Energy Combust. Sci.,* Vol. 9, pp. 155–177.

Chigier, N., and Stewart, G., 1984, "Particle Sizing and Spray Analysis," *Optical Engineering,* Vol. 23, No. 5, pp. 554–640.

Chin, J. S., and Lefebvre, A. H., 1982, "Effective Values of Evaporation Constant for Hydrocarbon Fuel Drops," *Proceedings of the 20th Automotive Technology Development Contractor Coordination Meeting,* pp. 325–331.

Chin, J. S., Lefebvre, A. H., and Sun, F. T.-Y., 1992, "Temperature Effects on Fuel Thermal Stability," ASME JOURNAL OF ENGINEERING FOR GAS TURBINES AND POWER, Vol. 114, pp. 353–358.

Chin, J. S., and Lefebvre, A. H., 1993, "Influence of Flow Conditions on Deposits From Heated Hydrocarbon Fuels," ASME JOURNAL OF ENGINEERING FOR GAS TURBINES AND POWER, Vol. 115, pp. 433–438.

Chin, J. S., 1994, "An Engineering Calculation Method for Multi-component Stagnant Droplet Evaporation With Finite Diffusivity," ASME Paper No. 94-GT-440.

Chin, J. S., 1995a, "Advanced Droplet Evaporation Model for Turbine Fuels," AIAA Paper No. 95-0493.

Chin, J. S., 1995b, "An Engineering Calculation Method for Turbine Fuel Droplet Evaporation at Critical Conditions With Finite Liquid Diffusivity," AIAA Paper No. 95-0494.

Claeys, J. P., Elward, K. M., Mick, W. J., and Symonds, R. A., 1993, "Combustion System Performance and Field Test Results of the MS7001F Gas Turbine," ASME JOURNAL OF ENGINEERING FOR GAS TURBINES AND POWER, Vol. 115, pp. 537–546.

Correa, S. M., and Shyy, W., 1987, "Computational Models and Methods for Continuous Gaseous Turbulent Combustion," *Prog. Energy Combust. Sci.,* Vol. 13, pp. 249–292.

Correa, S. M., 1991, "Lean Premixed Combustion for Gas Turbines: Review and Required Research," *Fossil Fuel Combustion,* ASME PD-Vol. 33.

Cowell, L. H., and Larkin, M. P., 1994, "Development of a Catalytic Combustor for Industrial Gas Turbines," ASME Paper No. 94-GT-254.

Custer, J. R., and Rizk, N. K., 1988, "Influence of Design Concept and Liquid Properties on Fuel Injector Performance," *AIAA Journal of Propulsion and Power,* Vol. 4, No. 4, pp. 378–384.

Dalla Betta, R. A., Schlatter, J. C., Nickolas, S. G., Yee, D. K., and Shoji, T., 1994, "New Catalytic Combustor Technology for Very Low Emissions Gas Turbines," ASME Paper No. 94-GT-260.

Davis, L. B., and Washam, R. M., 1989, "Development of a Dry Low NO_x Combustor," ASME Paper No. 89-GT-255.

De Corso, S. M., and Kemeny, G. A., 1957, "Effect of Ambient and Fuel Pressure on Nozzle Spray Angle," Trans. ASME, Vol. 79, pp. 607–615.

Delarosa, A. B., Sankar, S. V., Wang, G., and Bachalo, W. D., 1993, "Particle Diagnostics and Turbulence Measurements in a Confined Isothermal Liquid Spray," ASME JOURNAL OF ENGINEERING FOR GAS TURBINES AND POWER, Vol. 115, pp. 499–506.

Desaulty, M., 1991, "Turbine Engine Combustor Design at SNECMA," *Proceedings of International Symposium on Air-Breathing Engines,* ISABE 91-7064, pp. 80–90.

Dittman, R., Feld, H. J., Samenfink, W., and Wittig, S., 1992, "Multiple Wavelength Extinction Technique for Particle Characterization in Dense Particle Clouds," Nuremburg, Germany, Preprint 2, pp. 507–518.

Ducourneau, F., 1974, "Inflammation Spontanee de Melanges Riches Air-Kerosine," *Entropie,* No. 59.

Durst, F., Melling, A., and Whitelaw, J., 1981, *Principles and Practice of Laser-Doppler Anemometry.*

Etheridge, C. J., 1994, "Mars Solo NO_x Lean Premix Combustion Technology in Production," ASME Paper No. 94-GT-255.

Fennimore, C. P., 1971, "Formation of Nitric Oxide in Premixed Hydrocarbon Flames," *Thirteenth Symposium (International) on Combustion,* The Combustion Institute, Pittsburgh, PA, pp. 373–380.

Flanagan, P., Gretsingir, K., Abbasi, H. A., and Cygan, D., 1992, "Factors Influencing Low Emissions Combustion," ASME PD-Vol. 89, *Fossil Fuels Combustion.*

Fric, T. F., 1992, "Effects of Fuel-Air Unmixedness on NO_x Emissions," AIAA Paper No. 92-3345.

Goodger, E. M., and Eissa, A. F. M., 1987, "Spontaneous Ignition Research; Review of Experimental Data," *Journal of the Institute of Energy,* Vol. 84, pp. 84–89.

Heberling, P. V., 1976, "Prompt NO Measurements at High Pressures," *Sixteenth Symposium (International) on Combustion,* The Combustion Institute, Pittsburgh, PA, pp. 159–168.

Hebrard, P., Trichet, P., and Bardey, X., 1991, "Experimental Investigation of Two-Phase Flow in the Near Field of an Airblast Atomizer," *Fifth International Conference on Liquid Atomization and Spray Systems,* Gaithersberg, MD, pp. 669–678.

Hebrard, P., Laverge, G., Beard, P., Donnadille, P., and Trichet, P., 1993, "Modelisation de las Phase Liquide dans les Chambres de Combustion," AGARD Conference Proceedings 536, pp. 36/1–12.

Hilt, M. B., and Waslo, J., 1984, "Evolution of NO_x Abatement Techniques Through Combustor Design for Heavy-Duty Gas Turbines," ASME JOURNAL OF ENGINEERING FOR GAS TURBINES AND POWER, Vol. 106, pp. 825–832.

Hung, W. S. Y., 1974, "Accurate Method of Predicting the Effect of Humidity or Injected Water on NO_x Emissions From Industrial Gas Turbines," ASME Paper No. 74-WA/GT-6.

Hung, W. S. Y., and Agan, D. D., 1985, "The Control of NO_x and CO Emissions From 7-MW Gas Turbines With Water Injection as Influenced by Ambient Conditions," ASME Paper No. 85-GT-50.

Hung, W. S. Y., 1993, "Carbon Monoxide Emissions From Gas Turbines as Influenced by Ambient Temperature and Turbine Load," ASME JOURNAL OF ENGINEERING FOR GAS TURBINES AND POWER, Vol. 115, No. 3, pp. 588–593.

Jasuja, A. K., and Lefebvre, A. H., 1994, "Influence of Ambient Pressure on Drop Size and Velocity Distributions in Dense Sprays," *Twenty-Fifth Symposium (International) on Combustion,* The Combustion Institute, Pittsburgh, PA, pp. XX–00.

Jones, W. P., and Priddin, C. H., 1978, "Predictions of the Flow Field and Local Gas Comosition in Gas Turbine Combustors," *Proceedings of the 17th International Symposium on Combustion,* The Combustion Institute, Pittsburg, PA, pp. 399–409.

Joshi, N. D., Epstein, M. J., Durlak, S., Marakovits, S., and Sabla, P. E., 1994, "Development of a Fuel–Air Premixer for Aero-Derivative Dry Low Emissions Combustors," ASME Paper No. 94-GT-253.

Kajita, S., Ohga, S., Kitajima, J., Kimura, T., and Sasaki, T., 1993, "Development of a Dry Low NO_x Combustor for 1.5 MW Gas Turbines," ASME Paper No. 93-GT-393.

Koff, B. L., 1993, "Aircraft Gas Turbine Emissions Challenge," ASME Paper No. 93-GT-422.

Kumakura, H., Sasaki, M., Suzuki, D., and Ichikawa, H., 1994, "Development of a Low-Emission Combustor for a 100-kW Automotive Ceramic Gas Turbine," ASME Paper No. 94-GT-33; accepted for publication in *Trans. ASME.*

Lefebvre, A. H., 1984, "Fuel Effects on Gas Turbine Combustion—Liner Temperature, Pattern Factor, and Pollutant Emissions," *AIAA Journal of Aircraft,* Vol. 21, No. 11, pp. 887–898.

Lefebvre, A. H., 1986, "Fuel Effects on Gas Turbine Combustion," *International Journal of Turbo and Jet Engines,* Vol. 3, No. 2, pp. 231–243.

Lefebvre, A. H., Freeman, W., and Cowell, L., 1986, "Spontaneous Ignition Delay Characteristics of Hydrocarbon Fuel/Air Mixtures," NASA Contractor Report 175064.

Lefebvre, A. H., 1989, *Atomization and Sprays,* Hemisphere Publishing Corp., New York.

Leonard, G. L., and Correa, S. M., 1990, "NO_x Formation in Lean Premixed High-Pressure Methane Flames," *Second ASME Fossil Fuel Combustion Symposium,* ASME PD-30, pp. 69–74.

Leonard, G., and Stegmaier, J., 1994, "Development of an Aeroderivative Gas Turbine Dry Low Emissions Combustion System," ASME JOURNAL OF ENGINEERING FOR GAS TURBINES AND POWER, Vol. 116, pp. 542–546.

Lewis, G. D., 1991, "A New Understanding of NO_x Formation," *Proceedings of International Symposium on Air-Breathing Engines,* ISABE 91-7064, pp. 625–629.

Lundberg, K., 1994, Ulstein Turbine Technical Report UTU94003.

Lyons, V. J., 1981, "Fuel-Air Non-Uniformity Effect on Nitric Oxide Emissions," AIAA Paper No. 81-0327.

Martin, F. J., and Dederick, P. K. J., 1976, "NO_x From Fuel Nitrogen in Two-Stage Combustion," *Sixteenth Symposium (International) on Combustion,* The Combustion Institute, Pittsburgh, PA, pp. 191–198.

Maughan, J. R., Luts, A., and Bautista, P. J., 1994, "A Dry Low NO_x Combustor for the MS3002 Regenerative Gas Turbine," ASME Paper No. 94-GT-252.

McCaldon, K., Prociw, L. A., and Sampath, P., 1993, "Design Aspects for Small Aircraft Gas Turbine Fuel Injectors," *Fuels and Combustion Technology for Advanced Aircraft Engines,* AGARD Conference Proceedings 536, pp. 21-1-10.

McDonell, V. G., Lee, S. W., and Samuelson, G. S., 1994a, "Spray Behavior in Reacting and Non-reacting Flow Fields Downstream of an Aero-engine Combustor Dome," *Twenty-Fifth Symposium (International) on Combustion,* The Combustion Institute, Pittsburgh, PA.

McDonell, V. G., Seay, J. E., and Samuelson, G. S., 1994b, "Characterization of the Non-reacting Two-Phase Flow Downstream of an Aero-engine Combustor Dome Operating at Realistic Conditions," ASME Paper No. 94-GT-263.

McGuirk, J. J., and Palma, J. M. L. M., 1993, "The Flow Inside a Model Gas Turbine Combustor: Calculations," ASME JOURNAL OF ENGINEERING FOR GAS TURBINES AND POWER, Vol. 115, pp. 594–602.

McKnight, D., 1978, "Development of a Compact Gas Turbine Combustor to Give Extended Life and Acceptable Exhaust Emissions," ASME JOURNAL OF ENGINEERING FOR POWER, Vol. 100, July.

McVey, J. B., Russell, S., and Kennedy, J. B., 1987, "High-Resolution Patternator for the Characterization of Fuel Sprays," *AIAA Journal of Propulsion and Power,* Vol. 3, No. 3, pp. 202–209.

McVey, J. B., Kennedy, J. B., and Russell, S., 1989, "Application of Advanced Diagnostics to Airblast Injector Flows," ASME JOURNAL OF ENGINEERING FOR GAS TURBINES AND POWER, Vol. 111, No. 1, pp. 53–62.

Mellor, A. M., 1981, "Semi-empirical Correlations for Gas Turbine Emissions, Ignition, and Flame Stabilization," *Prog. Energy Combust. Sci.,* Vol. 6, pp. 347–358.

Merryman, E. L., and Levy, A., 1975, "Nitric Oxide Formation in Flames: The Role of NO_2 and Fuel Nitrogen," *Fifteenth Symposium (International) on Combustion,* The Combustion Institute, Pittsburgh, PA, pp. 1073–1083.

Micklow, G. J., Roychoudhury, S., Nguyen, H., and Cline, M. C., 1993, "Emissions Reduction by Varying the Swirler Airflow Split in Advanced Gas Turbine Combustors," ASME JOURNAL OF ENGINEERING FOR GAS TURBINES AND POWER, Vol. 115, No. 3, pp. 563–569.

Mongia, H. C., 1987, "A Status Report on Gas Turbine Modeling," *Combustion and Fuels in Gas Turbine Engines,* AGARD CPP-422.

Mongia, H. C., 1993, "Application of CFD in Combustor Design Technology," *AGARD Conference Proceedings 536,* pp. 12/1–18.

Mosier, S. A., and Pierce, R. M., 1980, *Advanced Combustion Systems for Stationary Gas Turbine Engines,* Vol. 1, EPA Contract 68-02-2136.

Mullins, B. P., 1955, "Spontaneous Ignition of Liquid Fuels," AGARDograph 4.

Myers, G. D., Armstrong, J. P., White, C. D., Clouser, S., and Harvey, R. J., 1992, "Development of an Innovative High-Temperature Gas Turbine Fuel Nozzle," ASME JOURNAL OF ENGINEERING FOR GAS TURBINES AND POWER, Vol. 114, pp. 401–408.

Nakata, T., Sato, M., Ninomiya, T., Yoshine, T., and Yamada, M., 1992, "Design and Test of a Low-NO_x Advanced Rich-Lean Combustor for LBG Fueled 1300°C-Class Gas Turbine," ASME Paper No. 92-GT-234.

Naqwi, A., Durst, F., and Liu, X. Z., 1991, "Optical Methods for Simultaneous Measurements of Particle Size, Velocity, and Refractive Index," *Applied Optics,* Vol. 30, No. 33, pp. 4949–4959.

Nickolaus, D., and Lefebvre, A. H., 1987, "Fuel Thermal Stability Effects on Spray Characteristics," *AIAA Journal of Propulsion and Power,* Vol. 3, No. 6, pp. 502–507.

Nicol, D. G., Malte, P. C., Lai, J., Marinov, N. N., and Pratt, D. T., 1992, "NO_x Sensitivities for Gas Turbine Engines Operated on Lean-Premixed Combustion and Conventional Diffusion Flames," ASME Paper No. 92-GT-115.

Nicol, D. G., Malte, P. C., and Steele, R. C., 1994, "Simplified Models for NO_x Production Rates in Lean-Premixed Combustion," ASME Paper No. 94-GT-432; accepted for publication in *Trans. ASME.*

Novick, A. S., Troth, D. L., and Yacobucci, H. G., 1982, "Design and Preliminary Results of a Fuel Flexible Industrial Gas Turbine Combustor," ASME JOURNAL OF ENGINEERING FOR GAS TURBINES AND POWER, Vol. 104, pp. 368–376.

Odgers, J., and Kretschmer, D., 1985, "The Prediction of Thermal NO_x in Gas Turbines," ASME Paper No. 85-1GT-126.

Ohkubo, Y., Idota, Y., and Nomura, Y., 1994, "Evaporation Characteristics of Spray in a Lean Premixed-Prevaporization Combustor for a 100 kW Automotive Ceramic Gas Turbine," ASME Paper No. 94-GT-401.

Ortman, J., and Lefebvre, A. H., 1985, "Fuel Distributions from Pressure-Swirl Atomizers," *AIAA Journal of Propulsion and Power,* Vol. 1, No. 1, pp. 11–15.

Ozawa, Y., Fujii, T., Kikumoto, S., Sato, M., Fukuzawa, H., Saiga, M., and Watanabe, S., 1994a, "Development of Low NO_x Catalytic Combustor for Gas Turbine," *Proceedings of International Workshop on Catalytic Combustion,* Tokyo, Japan, Apr. 18–20, pp. 166–169.

Ozawa, Y., Hirano, J., Sato, M., Saiga, M., and Watanabe, S., 1994b, "Test Results of Low NO_x Catalytic Combustors for Gas Turbines," ASME JOURNAL OF ENGINEERING FOR GAS TURBINES AND POWER, Vol. 116, pp. 511–516.

Peng, F., and Aggarwal, S. K., 1995, "A Review of Droplet Dynamics and Vaporization Modeling for Engineering Calculations," ASME JOURNAL OF ENGINEERING FOR GAS TURBINES AND POWER, Vol. 117, July.

Peters, J. E., 1988, "Current Gas Turbine Combustion and Fuels Research and Development," *AIAA Journal of Propulsion and Power,* Vol. 4, No. 3, pp. 193–206.

Pierce, R. M., Smith, C. E., and Hinton, B. S., 1980, "Advanced Combustion Systems for Stationary Gas Turbine Engines," Vol. III, EPA Contract 68-02-2136.

Plee, S. L., and Mellor, A. M., 1978, "Review of Flashback Reported in Prevaporizing Premixing Combustors," *Combustion and Flame,* Vol. 32, pp. 193–203.

Poeschl, G., Ruhkamp, W., and Pfost, H., 1994, "Combustion With Low Pollutant Emissions of Liquid Fuels in Gas Turbines by Premixing and Prevaporization," ASME Paper No. 94-GT-443.

Priddin, C. H., and Coupland, J., 1986, "Impact of Numerical Methods on Gas Turbine Combustor Design and Development," in: *Calculation of Turbulent Reacting Flows,* R. M. C. So, J. H. Whitelaw, and H. C. Mongia, eds., ASME AMD-Vol. 81, pp. 335–348.

Rao, K. V. L., and Lefebvre, A. H., 1981, "Spontaneous Ignition Delay Times of Hydrocarbon Fuel-Air Mixtures," *First International Specialist Combustion Symposium,* Bordeaux, France, pp. 325–330.

Reeves, C. M., and Lefebvre, A. H., 1986, "Fuel Effects on Aircraft Combustor Emissions," ASME Paper No. 86-GT-212.

Rink, K. K., and Lefebvre, A. H., 1989a, "Influence of Fuel Drop Size and Combustor Operating Conditions on Pollutant Emissions," *International Journal of Turbo and Jet Engines,* Vol. 6, No. 2, pp. 113–122.

Rink, K. K., and Lefebvre, A. H., 1989b, "The Influences of Fuel Composition and Spray Characteristics on Nitric Oxide Formation," *Combust. Sci. and Tech.,* Vol. 68, pp. 1–14.

Rizk, N. K., and Mongia, H. C., 1986, "Gas Turbine Combustor Design Methodology," AIAA Paper No. 86-1531.

Rizk, N. K., and Lefebvre, A. H., 1987, "Prediction of Velocity Coefficient and Spray Cone Angle for Simplex Swirl Atomizers," *International Journal of Turbo and Jet Engines,* Vol. 4, pp. 65–73.

Rizk, N. K., Mostafa, A. A., and Mongia, H. C., 1987, "Modeling of Gas Turbine Fuel Nozzles," *Atomization and Spray Technology,* Vol. 3, pp. 241–260.

Rizk, N. K., and Mongia, H. C., 1990, "Three-Dimensional Combustor Performance Validation With High-Density Fuels," *AIAA Journal of Propulsion and Power,* Vol. 6, No. 5, pp. 660–667.

Rizk, N. K., and Mongia, H. C., 1991a, "Low NO_x Rich-Lean Combustion Concept Application," AIAA Paper No. 91-1962.

Rizk, N. K., and Mongia, H. C., 1991b, "A Three-Dimensional Analysis of Gas Turbine Combustors," *AIAA Journal of Propulsion and Power,* Vol. 7, No. 3, pp. 445–451.

Rizk, N. K., and Mongia, H. C., 1991c, "Gas Turbine Combustor Performance Evaluation," AIAA Paper No. 91-0640.

Rizk, N. K., and Mongia, H. C., 1992a, "Semi-analytical Fuel Injector Performance Correlation Approach," *International Journal of Turbo and Jet Engines,* Vol. 9, pp. 205–213.

Rizk, N. K., and Mongia, H. C., 1992b, "Calculation Approach Validation for Airblast Atomizers," ASME JOURNAL OF ENGINEERING FOR GAS TURBINES AND POWER, Vol. 114, pp. 386–393.

Rizk, N. K., and Mongia, H. C., 1993a, "Three-Dimensional NO_x Model for Rich-Lean Combustor," AIAA Paper No. 93-0251.

Rizk, N. K., and Mongia, H. C., 1993b, "Three-Dimensional Emission Modeling for Diffusion Flame, Rich-Lean, and Lean Gas Turbine Combustors," AIAA Paper No. 93-2338.

Rizk, N. K., and Mongia, H. C., 1993c, "Three-Dimensional Gas Turbine Combustor Emissions Modeling," ASME JOURNAL OF ENGINEERING FOR GAS TURBINES AND POWER, Vol. 115, No. 3, pp. 603–611.

Rizk, N. K., and Mongia, H. C., 1993d, "Semianalytical Correlations for NO_x, CO, and UHC Emissions," ASME JOURNAL OF ENGINEERING FOR GAS TURBINES AND POWER, Vol. 115, No. 3, pp. 612–619.

Rizk, N. K., and Mongia, H. C., 1994, "Emissions Predictions of Different Gas Turbine Combustors," AIAA Paper No. 94-0118.

Roberts, P. B., Kubasco, A. J., and Sekas, N. J., 1982, "Development of a Low NO_x Lean Premixed Annular Combustor," ASME JOURNAL OF ENGINEERING FOR POWER, Vol. 104, pp. 28–35.

Rokke, N. A., Hustad, J. E., and Berg, S., 1993, "Pollutant Emissions From Gas Fired Turbine Engines in Offshore Practice—Measurements and Scaling," ASME Paper No. 93-GT-170.

Rosin, P., and Rammler, E., 1933, "The Laws Governing the Fineness of Powdered Coal," *J. Inst. Fuel,* Vol. 7, No. 31, pp. 29–36.

Santangello, P. J., and Sojka, P. E., 1994, "Focused-Image Holography as a Dense Spray Diagnostic," *Applied Optics,* Vol. 93, No. 19, pp. 4132–4136.

Santavicca, D. A., Steinberger, D. L., Gibbons, K. A., Citeno, J. V., and Mills, S., 1993, "The Effect of Incomplete Fuel–Air Mixing on the Lean Limit and Emissions Characteristics of a Lean Prevaporized Premixed (LPP) Combustor," AGARD Conference Proceedings 536, pp. 22/1–12.

Sasaki, M., Kumakura, H., and Suzuki, D., 1991, "Low NO_x Combustor for Automotive Ceramic Gas Turbine—Conceptual Design," ASME Paper No. 91-GT-369.

Sattelmayer, Th., Felchlin, M. P., Haumann, J., Hellat, J., and Styner, D., 1992, "Second Generation Low-Emissions Combustors for ABB Gas Turbines: Burner Development and Tests at Atmospheric Pressure," ASME JOURNAL OF ENGINEERING FOR GAS TURBINES AND POWER, Vol. 114, No. 1, pp. 118–125.

Seaton, A., MacNee, W., Donaldson, K., and Godden, E., 1995, "Particulate Air Pollution and Acute Health Effects," *Lancet,* Vol. 345, pp. 176–178.

Segalman, I., McKinney, R. G., Sturgess, G. J., and Huang, L. M., 1993, "Reduction of NO_x by Fuel-Staging in Gas Turbine Engines—A Commitment to the Future," AGARD Conference Proceedings 536, pp. 29/1–17.

Semerjian, H. G., Ball, I. C., and Vranos, A., 1979, "Pollutant Emissions From Partially Mixed Turbulent Flames," *Seventeenth Symposium (International) on Combustion,* The Combustion Institute, Pittsburgh, PA, pp. 679–687.

Senior, P., Lutum, E., Polifke, W., and Sattelmayer, T., 1993, "Combustion Technology of the ABB GT13E2 Annular Combustor," *20th International Congress on Combustion Engines,* CIMAC, London, Paper No. G22.

Serag-Eldin, M. A., and Spalding, D. B., 1979, "Computation of Three-Dimensional Gas Turbine Combustion Chamber Flows," ASME JOURNAL OF ENGINEERING FOR POWER, Vol. 101, pp. 326–336.

Shaw, R. J., Gilkey, S., and Hines, R., 1994, "Engine Technology Challenges for a 21st Century High Speed Civil Transport," *IGTI Global Gas Turbine News,* Fall 1994, pp. 14–16.

Singh, R., 1994, "An Overview: Gas Turbine Generated Pollutants and the Emerging Technology Solutions," Keynote paper presented at The Gas Turbine Users Association 39th Annual Conference, Caracas, Venezuala, July.

Smith, K. O., Angello, L. C., and Kurzynske, F. R., 1986, "Design and Testing of an Ultra-low NO_x Gas Turbine Combustor," ASME Paper 86-GT-263.

Smith, K. O., and Cowell, L. H., 1989, "Experimental Evaluation of a Liquid-Fueled, Lean-Premixed Gas Turbine Combustor," ASME Paper No. 89-GT-264.

Smith, K. O., Holsapple, A. C., Mak, H. H., and Watkins, L., 1991, "Development of a Natural Gas-Fired, Ultra-Low NO_x Can Combustor for an 800 kW Gas Turbine," ASME Paper No. 91-GT-303.

Snyder, T. S., Rosfjord, T. J., McVey, J. B., and Chiappetta, L. M., 1994, "Comparison of Liquid Fuel/Air Mixing and NO_x Emissions for a Tangential Entry Nozzle," ASME Paper No. 94-GT-283.

Spadaccini, L. J., and Te Velde, J. A., 1980, "Autoignition Characteristics of Aircraft-Type Fuels," NASA Contractor Report 159886.

Steele, R. C., Jarrett, A. C., Malte, P. C., Tonouchi, J. H., and Nicol, D. G., 1995, "Variables Affecting NO_x Formation in Lean-Premixed Combustion," ASME Paper No. 95-GT-107; accepted for publication in *Trans. ASME.*

Stickles, R. W., Dodds, W. J., Koblish, T. R., Sager, J., and Clouser, S., 1993, "Innovative High-Temperature Aircraft Engine Fuel Nozzle Design," ASME JOURNAL OF ENGINEERING FOR GAS TURBINES AND POWER, Vol. 115, pp. 439–446.

Sturgess, G. J., 1986, "Calculations of Aerospace Propulsion Combustors: A View From Industry," *Calculation of Turbulent Reactive Flows,* R. M. C. So, J. H. Whitelaw, and H. C. Mongia, eds., ASME AMD-Vol. 81, pp. 185–231.

Sturgess, G. J., McKinney, R., and Morford, S. A., 1993, "Modification of Combustor Stoichiometry Distribution for Reduced NO_x Emission From Aircraft Engines," ASME JOURNAL OF ENGINEERING FOR GAS TURBINES AND POWER, Vol. 115, pp. 570–580.

Sultanian, B. K., and Mongia, H. C., 1986, "Fuel Nozzle Air Flow Modeling," AIAA Paper No. 86-1667.

Tacina, R. R., 1983, "Autoignition in a Premixing–Prevaporizing Fuel Duct Using Three Different Fuel Injection Systems at Inlet Air Temperatures to 1250K," NASA TM-83938.

Talpallikar, M. V., Smith, C. E., Lai, M. C., and Holdeman, J. D., 1992, "CFD Analysis of Jet Mixing in Low NO_x Flametube Combustors," ASME JOURNAL OF ENGINEERING FOR GAS TURBINES AND POWER, Vol. 114, pp. 416–424.

Tate, R. W., 1960, "Spray Patternation," *Ind. Eng. Chem.,* Vol. 52, No. 10, pp. 49–52.

Valk, M., 1994, Private Communication.

Vortmeyer, N., Valk, M., and Kappler, G., 1994, "A Catalytic Combustor for High-Temperature Gas Turbines," ASME Paper No. 94-GT-211; accepted for publication in *Trans. ASME.*

Wang, H. Y., McDonell, V. G., and Samuelson, G. S., 1992a, "The Two-Phase Flow Downstream of a Production Engine Combustor Swirl Cup," *Twenty-Fourth Symposium (International) on Combustion,* The Combustion Institute, Pittsburgh, PA, pp. 1457–1463.

Wang, H. Y., McDonell, V. G., Sowa, W. A., and Samuelson, G. S., 1992b, "Scaling of the Two-Phase Flow Downstream of a Gas Turbine Combustor Swirl Cup," ASME JOURNAL OF ENGINEERING FOR GAS TURBINES AND POWER, Vol. 115, pp. 453–460.

Wang, H. Y., McDonell, V. G., Sowa, W. A., and Samuelson, G. S., 1994, "Experimental Study of a Model Gas Turbine Combustor Swirl Cup, Part II: Droplet Dynamics," *AIAA Journal of Propulsion and Power.*

Wang, H. Y., McDonell, V. G., and Samuelson, G. S., 1995, "Influence of Hardware Design on the Flow Field Structures and the Patterns of Droplet Dispersion: Part I—Mean Quantities," ASME JOURNAL OF ENGINEERING FOR GAS TURBINES AND POWER, Vol. 117, pp. 282–289.

White, D. J., Batakis, A., Le Cren, R. T., and Yacabucci, H. G., 1982, "Low NO_x Combustion Systems for Burning Heavy Residual Fuels and High Fuel-Bound Nitrogen Fuels," ASME JOURNAL OF ENGINEERING FOR GAS TURBINES AND POWER, Vol. 104, pp. 377–385.

Wilkes, C., 1980, "Residual Fuel Combustion in Industrial Gas Turbines," in: A. H. Lefebvre, ed., *Gas Turbine Combustor Design Problems,* Hemisphere Publications, New York.

Wilkes, C., and Gerhold, B., 1980. "NO_x Reduction From a Gas Turbine Using Exhaust Gas Recirculation," ASME Paper No. 80-JPGC/GT-5.

Willis, J. D., Toon, I. J., Schweiger, T., and Owen, D. A., 1993, "Industrial RB211 Dry Low Emission Combustion System," ASME Paper No. 93-GT-391.

Wolfer, H. H., 1938, "Der Zundverzug im Dieselmotor," *V.D.I. Forschungsh,* Vol. 392, pp. 15–24.

Wynne, A., and Jasuja, A., 1991, "Visualization of Airblast Atomizer Spray Structure Under Varying Air Pressure Conditions," AIAA Paper No. 91-2199.

Zelina, J., and Ballal, D. R., 1994, "Combustion Studies in a Well-Stirred Reactor," AIAA Paper No. 94-0114.

Integration of Magnetic Bearings in the Design of Advanced Gas Turbine Engines

A. F. Storace

D. Sood

General Electric Aircraft Engines,
General Electric Company,
Cincinnati, OH 45215

J. P. Lyons

M. A. Preston

Corporate Research and Development,
General Electric Company,
Schenectady, NY 12301

Active magnetic bearings provide revolutionary advantages for gas turbine engine rotor support. These advantages include tremendously improved vibration and stability characteristics, reduced power loss, improved reliability, fault tolerance, and greatly extended bearing service life. The marriage of these advantages with innovative structural network design and advanced materials utilization will permit major increases in thrust-to-weight performance and structural efficiency for future gas turbine engines. However, obtaining the maximum payoff requires two key ingredients. The first is the use of modern magnetic bearing technologies such as innovative digital control techniques, high-density power electronics, high-density magnetic actuators, fault-tolerant system architecture, and electronic (sensorless) position estimation. This paper describes these technologies and the test hardware currently in place for verifying the performance of advanced magnetic actuators, power electronics, and digital controls. The second key ingredient is to go beyond the simple replacement of rolling element bearings with magnetic bearings by incorporating magnetic bearings as an integral part of the overall engine design. This is analogous to the proper approach to designing with composites, whereby the designer tailors the geometry and load-carrying function of the structural system or component for the composite instead of simply substituting composites in a design originally intended for metal material. This paper describes methodologies for the design integration of magnetic bearings in gas turbine engines.

Introduction

The development of active magnetic bearings (AMB) for advanced gas turbine engines is key to expanding present performance envelopes to achieve the goals of the IHPTET (Integrated High Performance Turbine Engine Technology) initiative; namely, doubling propulsion system capability by the turn of the century. The term active magnetic bearings includes the magnetic bearings (actuators), the controller, and the power electronics. The integration of active magnetic bearing rotor suspension and the high specific stiffness and strength primary load path structures integral to IHPTET propulsion systems provides a significant further opportunity to increase the structural efficiency, performance, reliability, and maintainability of advanced turbine engines. For example, the payoffs obtainable by this marriage of advanced structures/materials technologies with the revolutionary advantages of active magnetic bearings are exemplified by the integration of a ceramic fiber-filament reinforced titanium-based metal matrix composite (MMC) main engine (fan) shaft with the precise bearing force control provided by magnetic bearing suspension. The main engine shaft operates in a very rigorous, complex loading environment. The loads acting on the main engine shaft include rotordynamic transverse loads, transverse, axial, and torsional loads due to compressor rotor/low pressure turbine gas pressure loads and compressor flow distortion loads, maneuver loads, and blade-loss loads. Common practice for these shafts has been to use super alloy materials, such as Inconel 718 or Marage 250. The strengths of these materials are satisfactory except their densities are also high, which results in relatively low specific stiffness (E/ρ) values. The main engine shaft tends to have significant participation in engine system imbalance response, and supercritical operation is sometimes required. In many cases, complex soft mount bearing support systems incorporating dampers are required. The use of active magnetic bearings and MMC shaft material provides a direct approach for achieving superior dynamic characteristics and high load capability. The high specific stiffness of the MMC shaft material and the larger rotor diameters made possible by the elimination of the *DN* number (bearing diameter in mm × shaft rpm) restrictions of conventional rolling element bearings results in a dynamically rigid rotor at the high speeds required for advanced gas turbine engines. The result is that vibrational energy is driven into the magnetic bearings where tuning, damping, and active control strategies can be used to suppress the dynamic response for operating conditions extending into the extreme temperatures and speeds required for future advanced gas turbine engines.

The methodologies for the design integration of active magnetic bearings in the engine structural network to achieve a compact, simplified, and structurally efficient engine system are described in this paper. The elements of the advanced fault-tolerant active magnetic bearing system to be described herein include the magnetic bearings (which function as both high-density electromagnetic actuators and displacement transducers—in essence sensorless air gap estimation), the high-speed digital controller, and the high-density power electronics. The control algorithm for the digital controller has the capability to employ a variety of closed and open-loop (feed-forward) control strategies, dependent on the engine operating speeds, and external and internal engine loads. Also discussed are auxiliary bearings, which are an additional element in the AMB system. They are needed as a backup for the magnetic bearings, and to supplement the magnetic bearings for hard maneuvers and extreme loadings, such as blade-loss loads.

Engine Structural Tailoring for Active Magnetic Bearings

To meet the exceedingly challenging performance goals of the IHPTET initiative, stringent rotor stage clearance control,

Contributed by the International Gas Turbine Institute and presented at the 39th International Gas Turbine and Aeroengine Congress and Exposition, The Hague, The Netherlands, June 13–16, 1994. Manuscript received by the International Gas Turbine Institute February 19, 1994. Paper No. 94-GT-201. Associate Technical Editor: E. M. Greitzer.

engine weight reduction, high cycle temperatures, and higher rotor speeds will be required. The major increases required for the advanced turbine engine concepts in thermal efficiency, thrust/weight for fan engines, and power/weight for turboshaft engines, will be obtained by adapting structural geometry for rotors, frames, cases, blades, and disks to take full advantage of advanced material characteristics such as provided by metal matrix composites (MMC) and ceramic matrix composites (CMC).

Beyond the innovative structural arrangements and utilization of advanced materials, the incorporation of magnetic bearing rotor suspension provides a significant further capability to increase propulsion efficiency. Furthermore, the use of an Integral Starter/Generator (IS/G) mounted directly on the high-pressure shaft provides on-board power for the magnetic bearings and engine starting capability (Richter and Severt, 1992). A magnetic bearing engine with an IS/G forms one of the cornerstones of a "More-Electric" engine. The IS/G precludes the need for a power takeoff (tower) shaft and an external gearbox to drive engine accessories (external generator, starter, pumps, actuators) such as shown in Fig. 1 for present day engines. The magnetic bearing–IS/G combination provides for the virtual elimination of engine self-generated rotor whirling, elimination of the lube system required for rolling element bearings (refer to Fig. 2), elimination of rotor dampers, engine structural simplification, engine weight reduction, potential for unlimited bearing service life, elimination of secondary engine power extraction, reduced vulnerability, and improved reliability and maintainability.

The synergism of magnetic bearings and improved component designs incorporating advanced materials permits the development of turbine engines with fewer bearings while also achieving significant improvement in rotordynamics characteristics and greatly reduced sensitivity of rotor stage clearance closures due to maneuver loads. Consider the main engine or fan shaft. This shaft spans across the core engine and in conventional engines has a large length-to-diameter ratio. In order to avoid critical speed problems and unacceptable maneuver load deflections at the fan and low-pressure turbine for fan engines, redundant mounting is used. Figure 1 shows a large present-day five-bearing military engine, which uses three rolling element bearings (Nos. 1, 2, and 5) to support the main shaft.

Couple support across the No. 1 and No. 2 bearings reacts the large overturning moment generated by the fan during in-flight gyro maneuver conditions and provides the stiffness required to avoid fan nodding modes in the operating speed range. This couple support is needed to control fan tip deflection as very little moment carrying capability is provided by the main shaft aft of the two forward bearings due to its low bending stiffness. This low bending stiffness is caused by the relatively small outer diameter of the main shaft required to meet core rotor bearing *DN* number (approximately 1.5 million) and disk bore diameter limits. The bore diameters of the core rotor disks of present-day engines are minimized to maintain the stresses in the monolithic material disks within allowable limits at the maximum engine speeds. However, when magnetic bearings are used, *DN* numbers approaching or exceeding 3.5 million (based on maintaining magnetic bearing rotor lamination stresses within allowable limits) are achievable. In addition, significantly increased allowable disk stress levels and the attendant larger disk bore diameters can be achieved through the use of circumferential fiber-reinforced composite material, such as titanium-based MMC for the compressor disks, and ceramic matrix composite for the turbine disk.

The need for three-bearing support of the main engine shaft to prevent unacceptable fan pitching under gyro maneuver and dynamic loads is eliminated through the use of magnetic bearings and a high stiffness main shaft. Fabricating the main shaft from Ti 6Al–2Sn–4Zr–2Mo matrix material reinforced with continuous ceramic (silicon carbide) fibers allows the obtainment of high shaft stiffness. Note that the metal matrix composite (MMC) material is not stiffer than superalloy materials presently used in turbine engine shafts. However, it has a lower density, allowing larger main shaft diameters to be used to obtain high stiffness without a weight penalty. The increase in high-pressure rotor bore diameters required to obtain sufficient main shaft stiffness to permit two-bearing support (at each end of the shaft with the two forward-couple bearings replaced by a single bearing) requires core rotor-bearing *DN* numbers in the range of 3.5 million—well within the capability of magnetic bearings. The equivalence between three-bearing support and an increased stiffness main shaft supported by two bearings is shown in Fig. 3. In addition to controlling fan pitching due to gyro maneuver loads and avoiding fan nodding modes in the operating speed range, the high specific stiffness (E/ρ) MMC material reduces the participation of the main shaft midregion in engine system criticals, with the result that main shaft unbalance response sensitivity is further decreased.

Running the reinforcing fibers parallel to the axis of the main shaft results in the greatest improvement of shaft bending stiffness. However, in order to provide the required torsional strength, angle-ply fiber orientations are used. The MMC lamina are wrapped so that the fibers form a helix, which advances along the shaft length. This scheme still provides a significant payoff in increased absolute and specific stiffness in the axial direction. Storace (1989) and Signorelli (1983) discuss the benefits in gas turbine engine structural efficiency and performance achievable through the use of metal matrix composites with continuous fiber reinforcement in component structures. Table 1 shows a stiffness comparison of Ti 6-2-4-2/SiC angle-plied MMC material and selected superalloys at elevated temperature. Note the increased specific stiffness in the axial direction obtainable with angle-plied Ti 6-2-4-2/SiC MMC material.

In addition to a stiff main shaft, the higher DN numbers made possible by magnetic bearings also permit a stiff high pressure or core rotor. This results in dynamically rigid rotors with the result that vibration energy is driven into the magnetic bearings. This permits a number of different control strategies to be effectively used to suppress rotor vibration over the complete operating spectrum. These control strategies will be discussed later in this paper.

It should be noted that auxiliary or back-up bearings are an integral part of the magnetic bearing design. These bearings are designed to operate at approximately half the clearance of the magnetic bearings and thus prevent damage to the magnetic bearings at touchdown. In addition to providing support during shipment, storage, and for all other nonoperational time, the auxiliary bearings share momentary overloads due to shock and blade loss, and provide support following magnetic bearing failure. There are two likely candidates for the auxiliary bearings. The first auxiliary bearing candidate is a hydrostatic gas bearing integrated with the magnetic bearing structure and configured to act in parallel continuously or be activated on demand. This gas bearing would be supplemented by a self-lubricated sleeve bearing for shock and extreme-load conditions as well as at low engine speeds (below idle). The second auxiliary bearing candidate is a dry-lubricated, high-temperature, rolling-element bearing designed to operate for short periods at above 3.0 million *DN* at temperatures above 800°F. To dissipate the heat generated by the dry-lubricated bearing, cooling air will be supplied by engine bleed. Lubrication can be provided by a dry powder delivered to the bearing from an emergency canister activated when a loss of rotor control is sensed by the magnetic bearing controller. The following dry bearing configurations are candidates for auxiliary bearings: a hybrid with rolling elements and tungsten alloy races, a hybrid with rolling elements and intermetallic races, and an all fiber-reinforced-ceramic bearing.

Figure 4 shows a simplified engine structural network made possible by full magnetic bearing integration and incorporation of an integral starter/generator on the high-pressure spool.

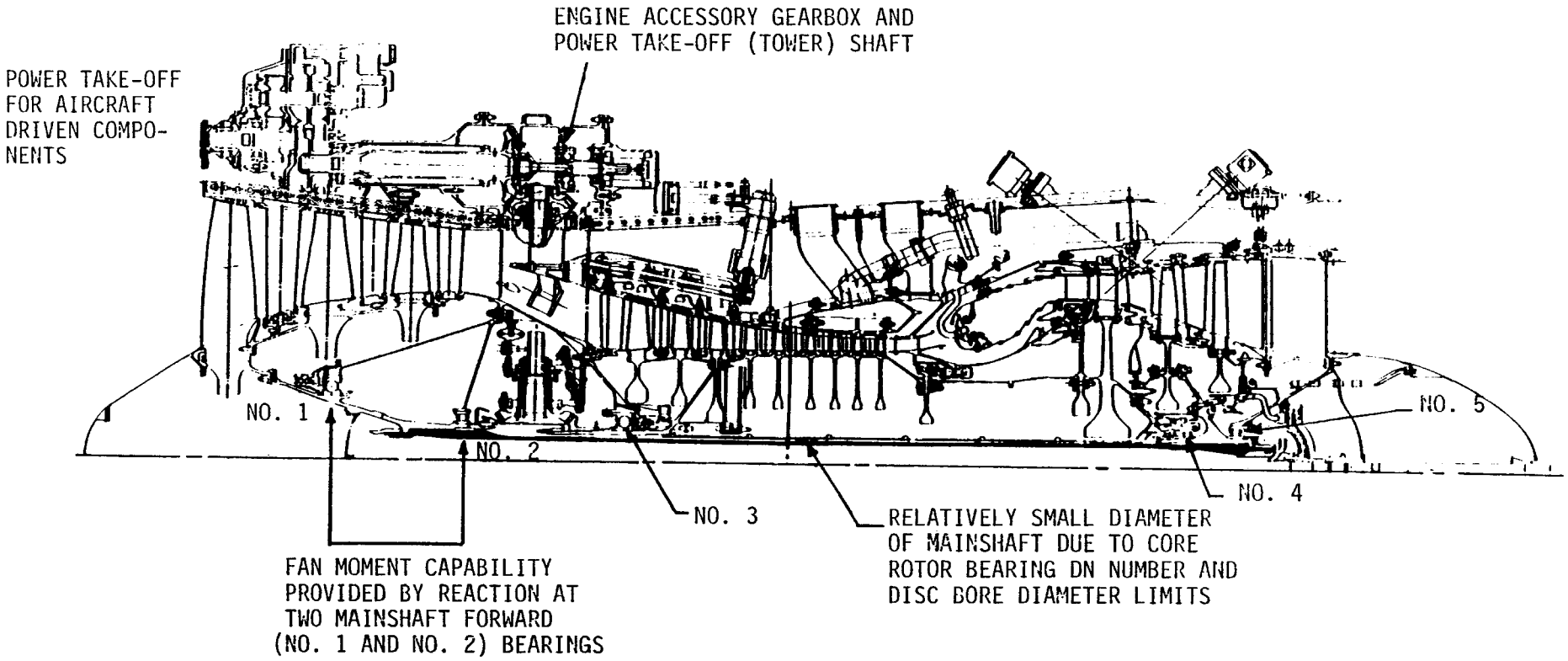

Fig. 1 Present-day five-bearing turbofan engine structural and accessory gear box arrangement

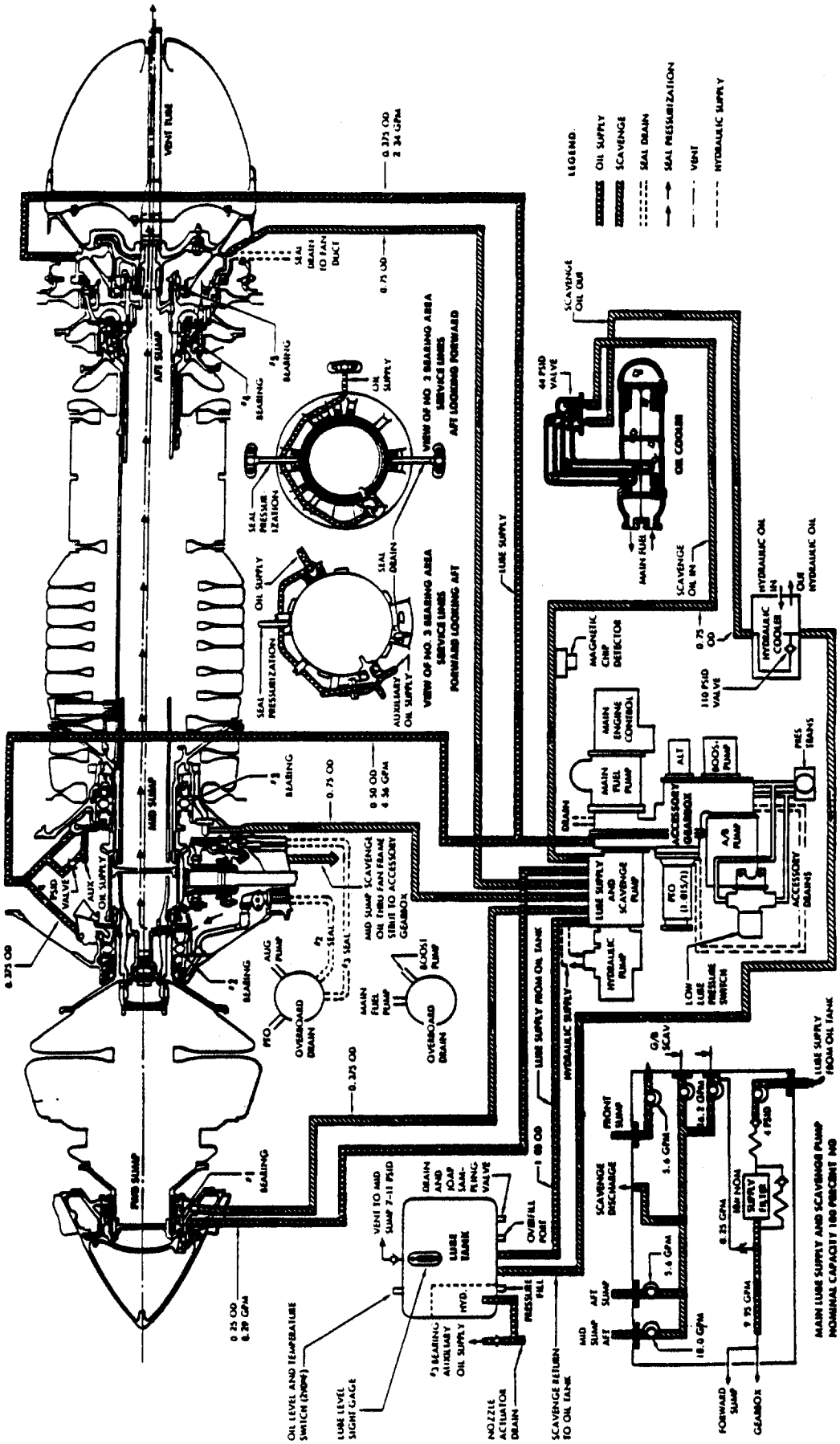

Fig. 2 Present-day engine lubrication system schematic

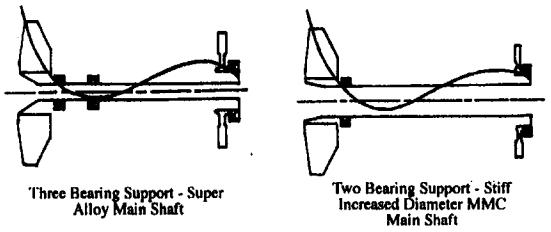

Fig. 3 Main engine gyroscopic loading deflections

These technologies permit a four-bearing configuration, and the elimination of the lube system, power takeoff shaft, and the external gearbox. In addition to significantly improved reliability and maintainability, the weight savings are substantial, amounting to more than 200 lb for a large military engine.

Control Algorithms

A digital controller will be used to implement control algorithms for rotor stabilization and vibration reduction. It will be noted that a digital controller permits the easy change of algorithms. Hence, a wide range of control options is easy to implement for the magnetic bearing suspension control system. The control strategies fall into two categories: closed and open-loop control. The former is incorporated into the feedback loop and can impact stability of the active magnetic bearing system. The latter is a feed-forward method whereby external control forces are superimposed on the feedback control forces to reduce vibration. This method separates the rotor suspension and vibration control problems, and thus permits the feedback control to be designed solely to provide maximum stability. Matsumura et al. (1990) discuss the use of feedback or closed-loop control to reduce synchronous response by the placement of a notch filter at the running speed. However, stability of the magnetic suspension was compromised. Knospe et al. (1991) discuss the use of magnetic bearings to cancel rotor synchronous response through the injection of open-loop feed-forward control forces and reported over 50 db of orbit attenuation.

Two approaches that can be used to implement closed-loop control are adaptive stiffness/damping control, and the tracking notch filter method. The former method reduces vibration by critical speed tuning and vibration energy dissipation. This is accomplished by varying bearing stiffness and damping to eliminate resonances or to heavily suppress response at rotor critical speeds. This method can provide robust performance when the shaft/bearing system is subjected to external disturbances. For the latter closed-loop method, a tracking notch filter is placed in the feedback loop to permit accommodation of synchronous disturbances. This causes the magnetic bearing to have greatly reduced stiffness and damping at the running speed, thus desensitizing the rotor to imbalance because it tends to spin about its inertial axis.

Table 1 Stiffness weight comparison of titanium-based MMC to selected superalloys

	TI 6-2-4-2 SIC Angle Plied MMC	INCO 718	RENE 95	MARAGE 250
Density				
(gm/cm^3)	4.01	8.19	8.22	8.00
(lb/in^3)	0.145	0.296	0.297	0.289
538°C (1000°F) Modulus				
(MPA)	$172*10^3$	$172*10^3$	$186*10^3$	$145*10^3$
(MSI)	25	25	27	21
538°C (1000°F) E/ρ				
(m)	$437*10^4$	$213*10^4$	$231*10^4$	$185*10^4$
(in)	$172*10^6$	$84*10^6$	$91*10^6$	$73*10^6$

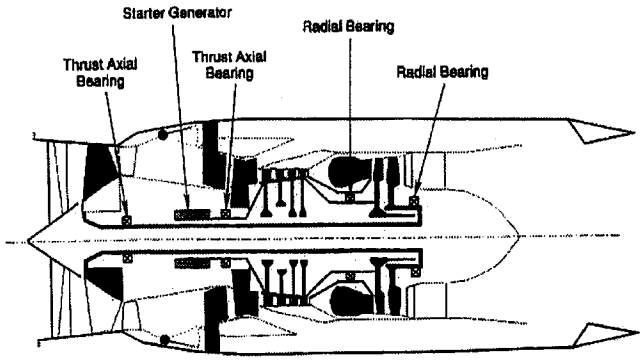

Fig. 4 Advanced four-bearing turbofan engine with magnetic bearings and integral starter/generator

The open-loop control can be implemented as either an active vibration control scheme, or as a bearing synchronous force cancellation scheme for selected frequencies. Typically, for the former approach, vibration displacements are canceled at the magnetic bearing plane or at some other location, such as on the engine casing. This is a disturbance rejection method and is accomplished by the injection of open-loop forces, which can be calculated using influence coefficients. In the latter open-loop approach, the force actuator commands can be adjusted so as to eliminate the synchronous component of these forces. This disturbance accommodation approach can be characterized as an open-loop notch filter, as the bearings exert no active synchronous forces, which results in isolation of the rotor at the running frequency.

Effective control of the magnetic bearing/rotor system will require the implementation of a combination of the control elements discussed above. For example, active vibration control accomplished through the injection of open-loop forces can be used for low-speed operation (rotor startup to idle speed) to cancel rotor synchronous vibration displacements at the magnetic bearing planes. In this scheme, the engine is modeled *on line* through the generation of dynamic influence coefficients, which are used to construct reduced dynamic stiffness matrices

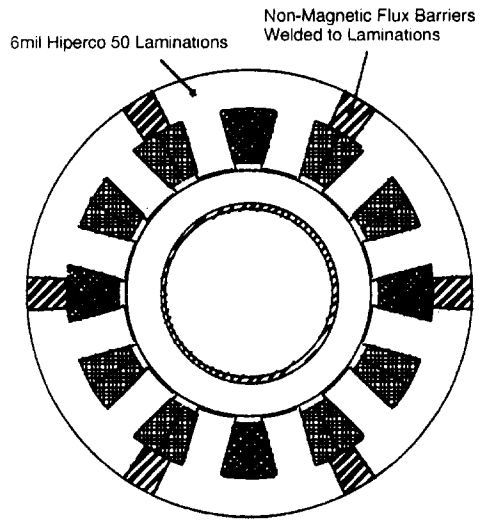

Fig. 5 Fault-tolerant radial magnetic bearing

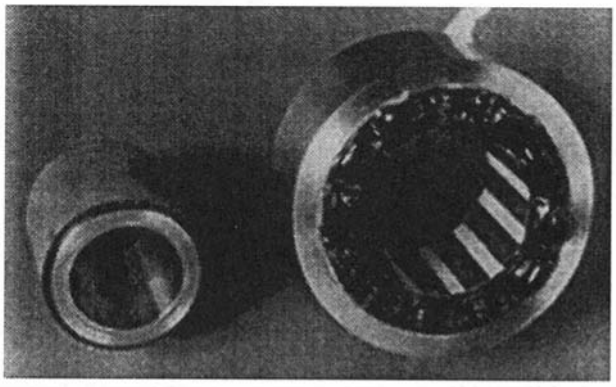

Fig. 6(*a*) Test rig radial magnetic bearing

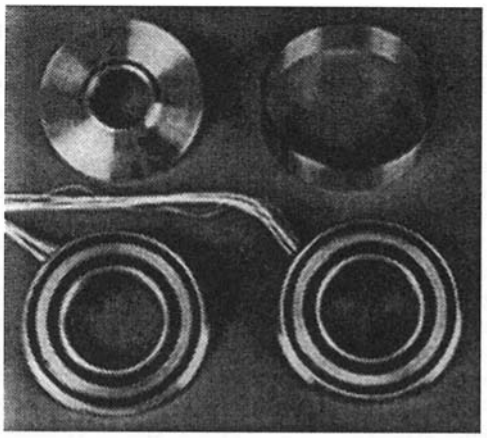

Fig. 6(*b*) Test rig axial magnetic bearing

used in the calculation of vibration canceling forces. One method to obtain the influence coefficients involves processing trial force signals injected at the magnetic bearings and the resulting response signals at discrete rotor speed points during exploratory accels/decels. This method is adaptive in that the amplitudes and phases of the corrective forces are dependent on the engine speed, vibratory characteristics, and imbalance levels, and the influence coefficients are updated to reflect changes in the engine system frequency response characteristics. The influence coefficients and measured response are then used to calculate corrective forces, which are used in an open-loop mode to cancel the synchronous response due to rotor imbalance. Since the synchronous response is highly correlated,

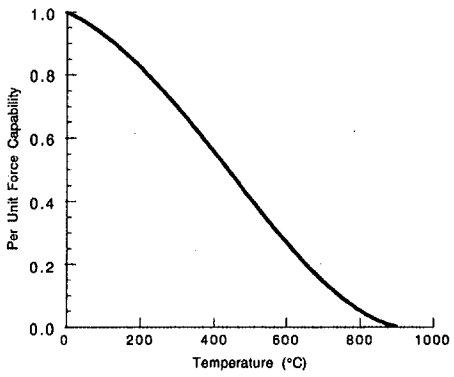

Fig. 7 Effect of temperature on cobalt–iron force-production capability

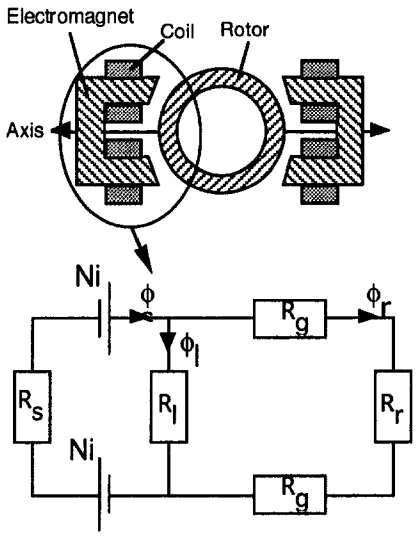

ϕ_S - Stator Flux
$R_s(\phi_S)$ - Stator Reluctance, Saturable
f_l - Leakage Flux
R_l - Leakage Reluctance
R_g - Airgap Reluctance
ϕ_r - Rotor Flux
$R_r(\phi_r)$ - Rotor Reluctance, Saturable
Ni - Ampere-Turns per Coil

Fig. 8 Magnetic model of fault-tolerant bearing

it may be altered without feedback. Thus, the system stability is not affected by the open-loop control. This active vibration control method would not be used for high-speed operation because the injected forces needed to reduce displacement levels at the magnetic bearing sensors can actually increase the transmittal forces at the magnetic bearings in this speed regime.

For operation above idle speed, the closed or open-loop notch filter method can be used to suppress synchronous vibration. This method is not suitable for low-speed operation in the vicinity of the rigid body criticals (resulting from bearing stiffness suppression) because the synchronous imbalance response is basically uncontrolled in this speed regime.

Electromagnetic Actuators

Figure 5 shows a fault-tolerant radial magnetic bearing. The bearing uses 3 radial control axes, which are made up of 12 electromagnetic stator poles organized into 6 force-producing pole pairs with 60 deg radial spacing. Two pole pairs at 180 deg radial separation combine to create a single control axis.

The stator core is segmented with nonmagnetic sections in order to minimize the magnetic coupling between adjacent pole pairs. The magnetic isolation provided by the stator segmentation will allow nonfaulted force-actuation pole pairs to continue functioning in the proximity of faulted magnetic poles. Since any two of the three (or more) control axes are sufficient to maintain rotor suspension, the third control axis in this magnetic structure provides inherent redundancy, and given appropriate control measures, continued bearing operation in the presence of a variety of faults (e.g., faulted magnetic poles, power electronic shorts, phase power loss, etc.) is possible. Greater inherent redundancy/fault tolerance can be readily achieved by adding more than three axes of control. Figures 6(*a*) and 6(*b*) show the fault-tolerant radial and axial magnetic bearings used in a single-spool test rig and described later in this paper.

This magnetic structure for the stator can be constructed using a stack of composite laminations as has been done for electric

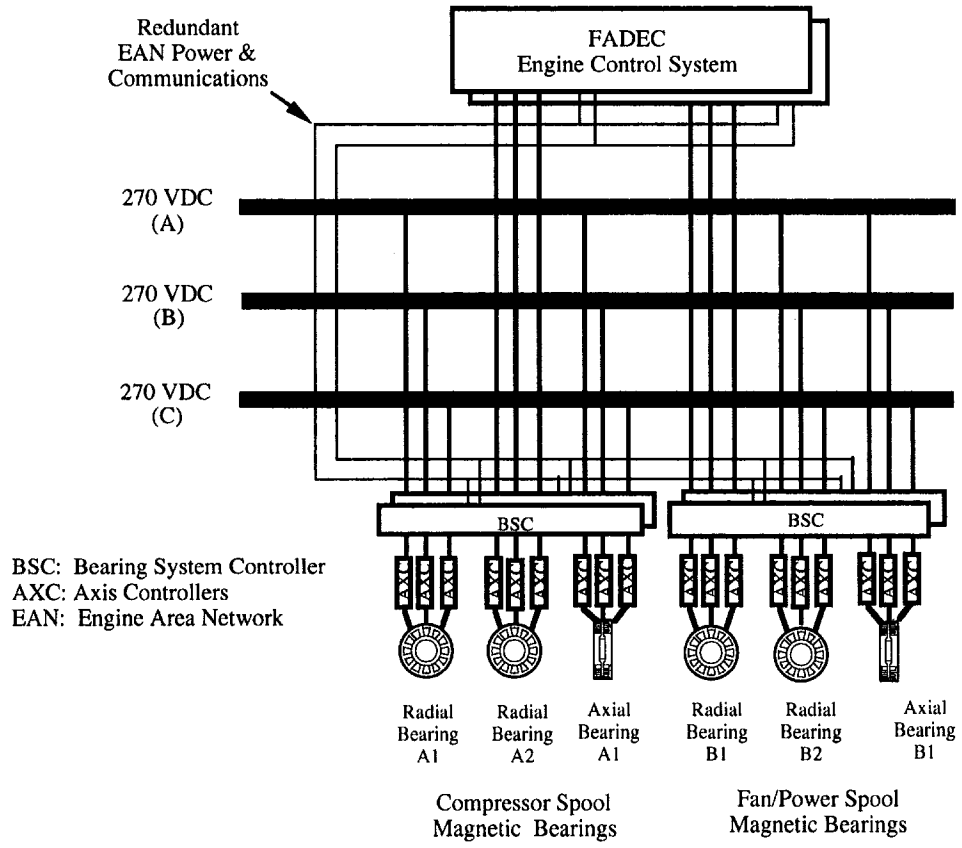

Fig. 9 More electric engine electrical system

machine rotors (Kliman, 1987, 1989) or by bonding solid nonmagnetic segments to a stack of laminations as has also been done for electric machine rotors (Kliman, 1987, 1989). The bearing laminations are made from a cobalt–iron alloy that has superior magnetic, thermal degradation, and mechanical properties, but is slightly more lossy than alternative materials.

A maximum operating temperature is chosen as a compromise between bearing size and cooling requirements. Bleed air would be used to limit the temperatures. Figure 7 shows the effect of temperature on per unit force production capability of cobalt–iron laminations. The magnetic material used for rotors has to withstand the centrifugal force induced stresses at maximum rotor speed and maximum temperature. Cobalt–iron in its normal anneal at 1550°F (840°C) has a 0.2 percent yield of 303 MPa (44 ksi) up to 300°F (150°C). At temperatures of 500°F (260°C) this reduces to less than 276 MPa (40 ksi). A second material option is the 1350°F (740°C) anneal version of the same cobalt–iron. This material has a 0.2 percent yield of better than 552 MPa (80 ksi) at 140°C and remains much stronger at higher temperatures—517 MPa (75 ksi) at 500°F (260°C). The price paid for the higher strength is 5 to 10 percent reduction in maximum force production capability and higher rotor eddy current losses.

The stator windings must withstand temperatures significantly higher than the magnetic material since heat transfer from the windings to the stator is generally poor. A silicon-mica based insulation system, Thermidur, as demonstrated by Siemens, Germany, for 10,000 h life at 400°C (752°F) with occasional excursions to 500°C (932°F) is preferred.

Electronic (Sensorless) Position Estimation

The rotor position sensors used with magnetic bearings are a major cost and reliability handicap. It is possible to use the magnetic bearing actuators themselves as magnetic position sensors, thereby eliminating the need for external position sensors. This can be done using one of two methods, inductance or flux-current, which are based on the magnetic model shown in Fig. 8.

The inductance measurement measures time rate of change of current to estimate inductance, which can be functionally related to rotor–stator airgap. There are two problems with this approach. First the rate of change of current is dependent on airgap velocity as well as rate of change of current and this causes large errors in the airgap estimate for high-speed bearings. Second, when the soft magnetic materials in the bearing begin to saturate, the relationship between inductance and airgap becomes multivalued; that is, there are many possible airgaps associated with a given inductance. The actuator current can be used to reduce this to two choices, but some knowledge of position history is required to choose the correct airgap.

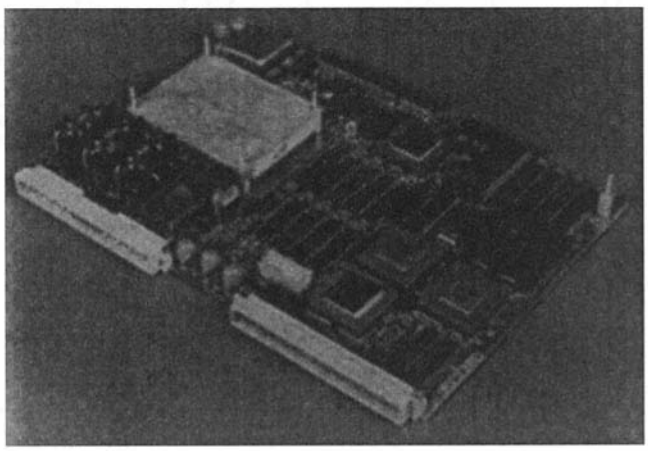

Fig. 10 Single board axis controller

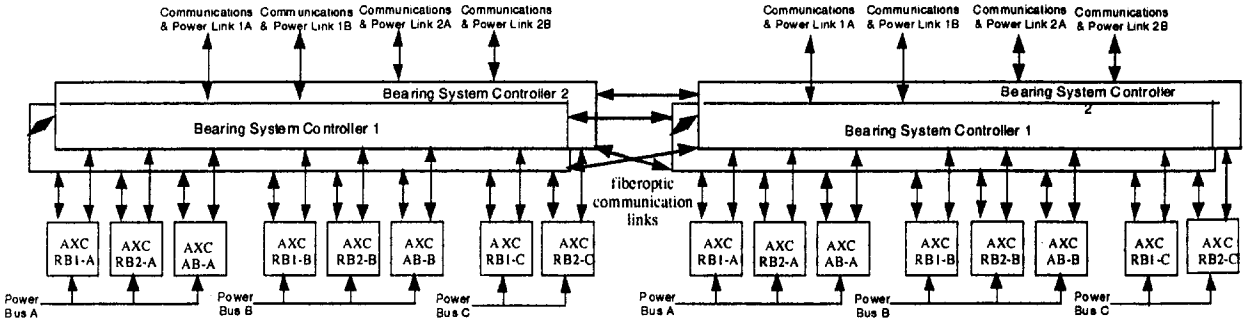

Fig. 11 Twin spool active magnetic bearing control system with duplex supervisor

The flux-current method uses the relationship $\phi_s = \int [(v - ir)/N]dt$ to determine the flux in an excited winding. Then, given the actuator current and a suitable magnetic model of the actuator, a unique rotor–stator airgap can be determined. This method works regardless of airgap velocity or magnetic saturation. The primary difficulty is in maintaining an accurate flux estimate where the excitation waveform is not cyclic and the required integrator cannot be reset periodically. This method

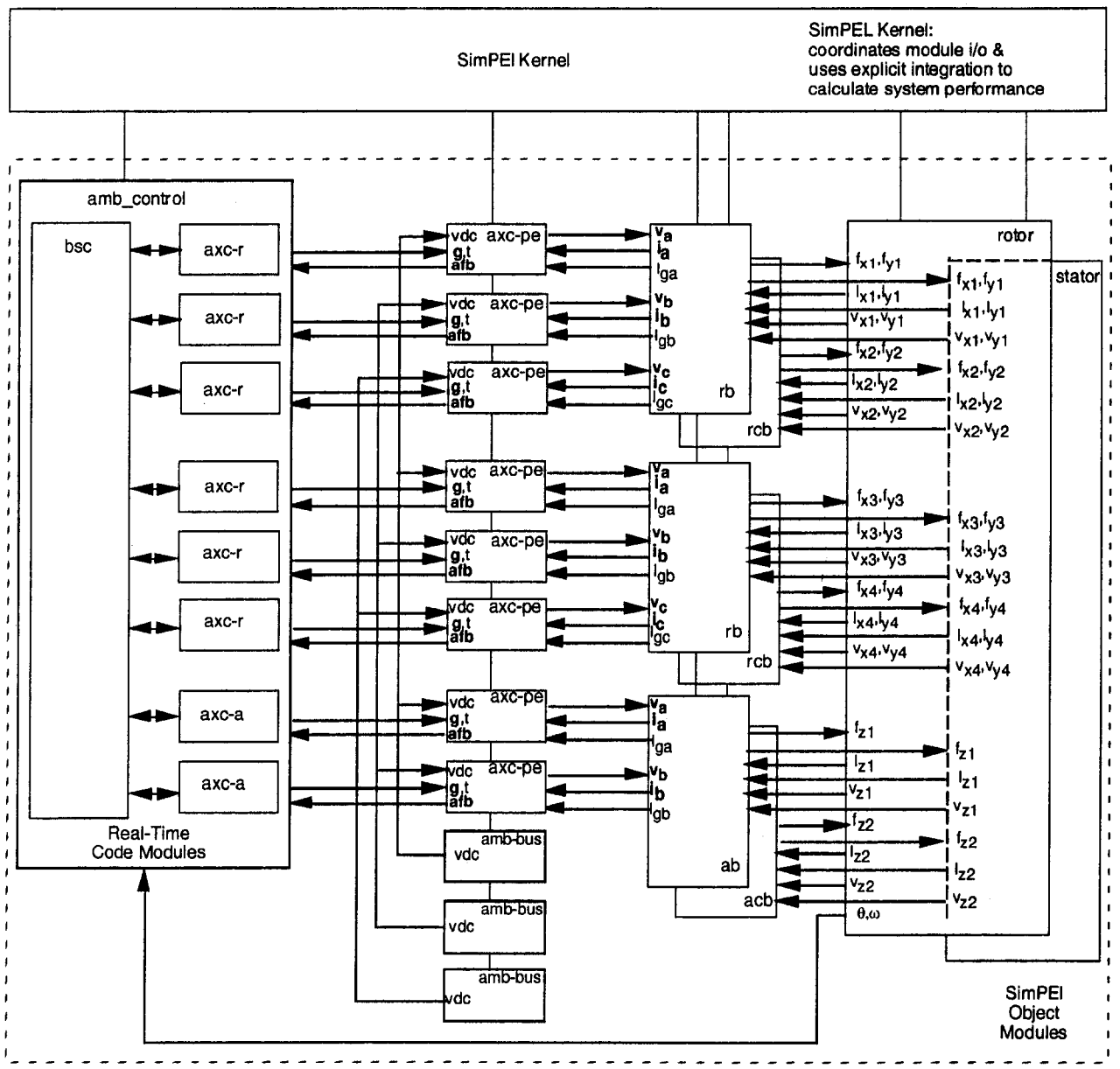

Fig. 12 SimPEI active magnetic bearing system simulation

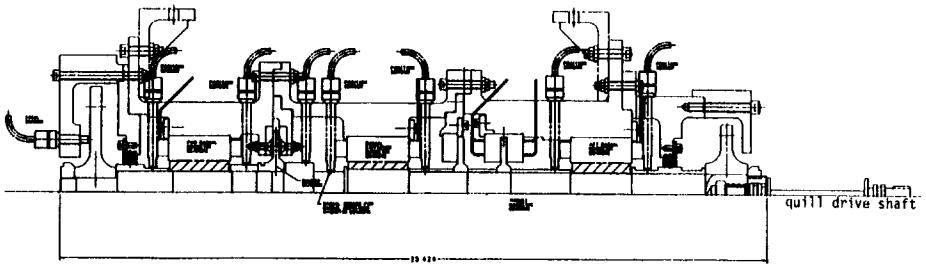

Fig. 13 Single-spool magnetic bearing test rig

has been used successfully with switched reluctance motors (Lyons et al., 1991; Preston and Lyons, 1991).

Fault-Tolerant Engine Electrical System

Figure 9 illustrates a conceptual electric system for an advanced aircraft engine. This is a fault-tolerant system relying on three independent 270 vdc buses for distribution among a variety of loads, including active magnetic bearing (AMB) controls and power electronics.

The three distribution buses would appear to represent a conventional triple modular redundancy with 200 percent overcapacity, but this is not the case. The electric distribution system is designed for 50 percent overcapacity, i.e., each bus designed for 50 percent of the needed system capacity, thereby requiring two of the three buses at any time in order to avoid system failure.

The radial active magnetic bearings are configured with three magnetically independent control axes per bearing placed at 60 deg radial separation. These three control axes cooperate to control the radial rotor position such that control can be maintained with only two of the control axes functioning. Each of the three bearing control axes is powered from a different dc bus; therefore the radial bearings require two active dc distribution buses in order to maintain rotor position control. The total available force vector is angle dependent, but is a minimum of 0.866 times that of a single axis.

The axial active magnetic bearings are configured in a similar fashion with three magnetically independent control axes, each control axis with 50 percent force capability; thus two of the three available control axes are required for rated thrust loading. Each of the axial control axes are also fed from different dc electrical distribution buses.

Magnetic Bearing Controls

The magnetic bearing controls consist of two hierarchical levels: a supervisory level—Bearing System Controller (BSC), and an actuation level—Axis Controller (AXC). The supervisor controllers are configured in a duplex fault tolerant configuration, with one supervisor in active control and the second in an active standby mode. Each bearing system controller is configured to control one engine spool (eight control axes).

The actuation controllers are essentially smart, self-protecting, power amplifiers capable of exciting a single independent AMB axis (two electromagnetic windings, + and −). A radial bearing will thus require three AXCs. Each actuation controller is capable of accepting commands from and delivering feedback information to multiple supervisors, thereby enabling redundancy at the supervisor level. Figure 10 shows a single board AXC capable of 50 A, 500 V.

The duplex supervisory controllers are essentially an extension of the dual-redundant engine controller (FADEC) acting as intelligent high-bandwidth actuators. The supervisor controllers are powered from the FADEC control power and communicate with the FADEC via a multidrop Engine Area Network (EAN). Two redundant EAN communication/control power channels are provided. An actuation controller is powered, along with the power electronic switches it controls, directly from an individual DC electrical distribution bus. Communication between the supervisory and actuation levels is accomplished in a manner to maintain electrical isolation, e.g., fiberoptic communication links.

Figure 11 illustrates the active magnetic bearing controller architecture for a twin spool engine. Each spool has a duplex supervisory bearing system controller, which is responsible for coordinated control of the rotor position, vibration, and imbalance—this coupled control will execute at a 5 kHz task execu-

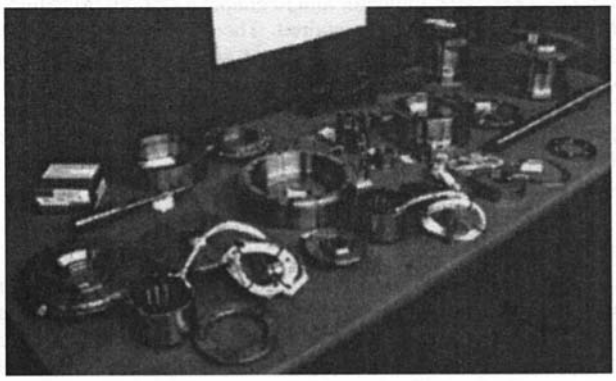

Fig. 14(*a*) Test rig before assembly

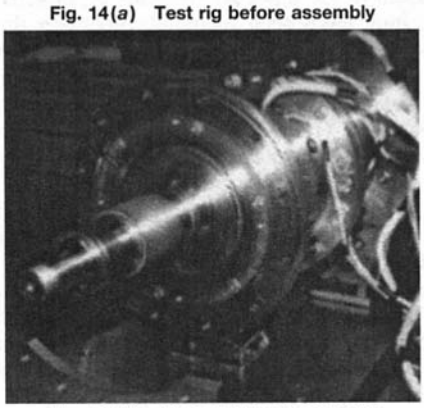

Fig. 14 (*b*) Test rig during assembly

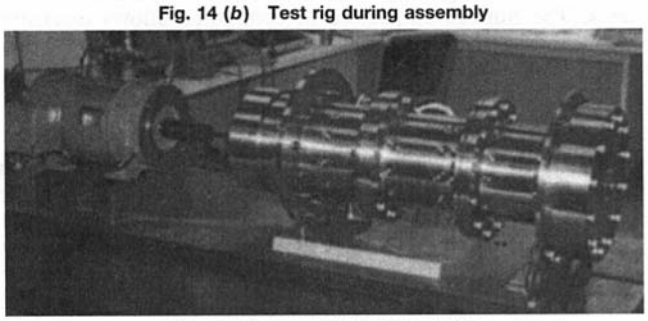

Fig. 14 (*c*) Test rig after assembly

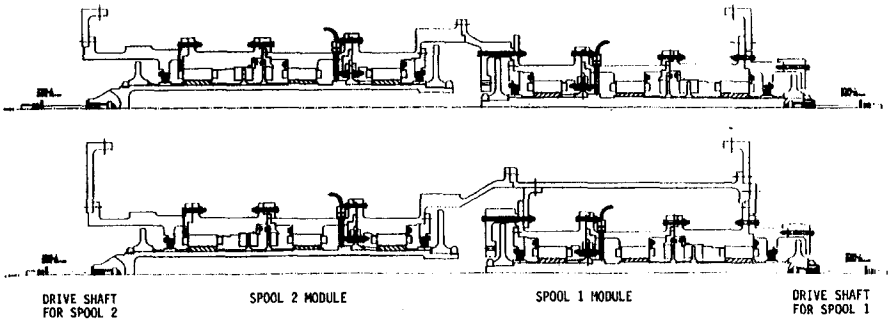

Fig. 15 Twin spool magnetic bearing test rig configurations

tion rate and transmit new force commands to the axis controllers. The axis controllers are responsible for force control and linearization, gap position and velocity inference, fault detection and isolation; the axis controller will execute at a 10 kHz task execution rate, which results in power electronic switching at an equivalent frequency.

Each axis controller is capable of accepting two command streams from each of the duplex bearing system controllers via high-bandwidth half-duplex serial communication channels. The controlling supervisor will transmit a current state information packet, once per control iteration, to the active standby BSC both as a heartbeat indicator and to enable a smooth transition to the backup supervisor if required. The supervisory controllers for each engine spool are capable of communicating once per control iteration with each other, to transmit required dynamic coupling information. The BSC peer-peer communications are high-bandwidth full duplex serial communications link. The BSCs are also required to communicate with the FADEC over slower half-duplex communication links.

AMB System Modeling and Simulation

Figure 12 illustrates a SimPEl simulation of the AMB control system. SimPEl (Simulator for Power Electronics) is an object-oriented dynamic simulator, which uses explicit numerical integration procedures to predict the responses of dynamic systems. Each of the physical elements of an active magnetic bearing system have been included, including the three 270 vdc buses (amb-bus in Fig. 12), axis controller power electronic converters (axc-pe), radial and axial bearing magnetic actuators (rb and ab), rotor dynamics (rotor), axial and radial catcher bearings (rcb and acb), bearing mechanical support structures (stator), and the AMB control system itself (amb_control). The rotor model includes rigid body rotor dynamics, which are currently being extended to include flexible-rotor modeling. The magnetic bearings are modeled using the model shown in Fig. 8.

The SimPEl amb_control module contains the target source codes for the BSC and AXC digital signal processor modules. These source codes enable simulated rotor suspension along with axis availability dependent force and gap transformations to and from orthogonal *yz* control axes and coupled *abc* control axes. The SimPEl simulation as configured allows extensive debugging of the control source codes under simulated conditions, prior to the availability of the target hardware.

Magnetic Bearing Test Rig

The test rig shown in Fig. 13 was developed for validation testing of advanced magnetic bearings and digital controls/power electronics systems. Figures 14(*a*), 14(*b*), and 14(*c*) show the test rig components before, during, and after assembly, respectively. This effort will encompass programs for the use of magnetic bearings for marine and aeroengine main shaft support and applications for stationary power plant turbomachinery and generator rotor support. The conventional proximity sensors depicted in Fig. 13 will be used initially for rotor displacement calibration measurements. Later, the sensorless air gap estimation technique based on utilizing the magnetic bearings as both force actuators and displacement transducers will be used.

The test rig utilizes two radial magnetic bearings located fore and aft, an excitation radial magnetic bearing located at approximately midspan, a thrust magnetic bearing, and a thrust excitation magnetic bearing. The forward direction is to the left. Radial auxiliary bearings are mounted outboard of the radial magnetic bearings. The radial auxiliary bearings are turbine engine class bearings, and the radial clearance between the shaft OD and the bearing inner ring ID is equal to 0.0254 cm (10 mils). This precludes the possibility of damage to the radial magnetic bearings for overloads or rotor drop as the radial clearance of the magnetic bearings is equal to 0.0508 cm (20 mils). An axial auxiliary or bumper bearing is utilized to prevent damage to the thrust magnetic bearing.

Overhung disks, fore and aft, simulate a fan and turbine and provide balance planes for mechanical balancing. An additional balance plane is available at the disk of the thrust excitation magnetic bearing. The rig is driven by a 20 hp electric motor through a quill drive shaft located at the aft end of the rotor.

A generic two-shaft magnetic bearing test rig will be developed for use in dual rotor magnetic bearing engine studies. This will be accomplished by developing a shaft/case module and coupling case to permit expansion of the single shaft rig shown in Fig. 13 into a two-shaft magnetic bearing test rig. The two-shaft rig will provide experience and proven methodologies for use in the design of future twin spool magnetic bearing engines.

Figure 15 shows initial layouts for the two-shaft magnetic bearing test rig. The lower configuration has a tuning spring (shown as an outer case over the right shaft/case module), which may be necessary to achieve dynamic coupling between the two shafts representative of two-spool engine dynamics.

Acknowledgments

The work reported herein dealing with controls, control algorithms, fault tolerance, and AMB system modeling and simulation was carried out using internal GE funding. This technology is being further enhanced under the auspices of an Army program awarded to GE Aircraft Engines by the Aviation Applied Technology Directorate (AATD), U.S. Army Aviation and Troop Command, Fort Eustis, Virginia 23604-5577, under contract No. DAAJ02-92-C-0055. The contributions, suggestions, and encouragement of Bert Smith, the Army Program Manager for Magnetic Bearings, are greatly appreciated.

References

Kliman, G. B., 1987, "Composite Rotor Lamination for Use in Reluctance, Homopolar and Permanent Magnet Machines," U.S. Patent No. 4,916,346.

Kliman, G. B., 1989, "Method of Fabricating Composite Rotor Laminations for Use in Reluctance, Homopolar and Permanent Magnet Machines," U.S. Patent No. 4,918,831.

Knospe, C., Humphris, R., and Sundaram, X. X., 1991, "Flexible Rotor Balancing Using Magnetic Bearings," presented at Recent Advances in Active Control of Sound and Vibration Conference, Virginia Polytechnic Institute and State University, Apr. 15–17.

Lyons, J. P., MacMinn, S. R., and Preston, M. A., 1991, "Flux/Current Methods for SRM Rotor Position Estimation," *Proceedings of the 1991 IEEE Industry Applications Society Annual Meeting,* pp. 482–487.

Matsumura, F., Fujita, M., and Okawa, K., 1990, "Modeling and Control of Magnetic Bearing Systems Achieving a Rotation Around the Axis of Inertia," *2nd International Symposium on Magnetic Bearings,* Tokyo, Japan, July 12–14, pp. 273–280.

Preston, M. A., and Lyons, J. P., 1991, "A Switched Reluctance Motor Model With Mutual Coupling and Multi-phase Excitation," *IEEE Transactions on Magnetics,* Vol. 27, No. 6, pp. 5423–5425.

Richter, E., Anderson, R. E., and Severt, C., 1992, "The Integral Starter/Generator Development Progress," SAE Paper No. 920967.

Signorelli, R. A., 1983, "Metal Matrix Composites for Aircraft Engines," NASA Technical Memorandum 83379.

Storace, A., 1989, "Turbine Engine Structural Efficiency Determination," AIAA Paper No. 89-2571.

A Methodology to Assess Design Uncertainty in Selecting Affordable Gas Turbine Technology

J. L. Younghans

J. E. Johnson

S. J. Csonka

General Electric Aircraft Engines,
General Electric Company,
Cincinnati, OH 45215

A methodology is discussed that allows quantification of uncertainty in the gas turbine design and analysis process. The methodology can be employed to rank order the cost effectiveness of advanced component technologies or alternatively can be used to determine probable performance (sfc and thrust) of engines that have component performance uncertainties. Execution of the methodology requires a desktop computer and commercially available software.

Introduction and Background

Gas turbine designers desire advanced technology features such as higher stage efficiencies, higher aerodynamic stage loadings, increased turbine blade temperatures, and lighter structural materials for next generation engines. However, the desire for improved cycle thermodynamics and weight reduction has to be balanced with what the end use customer can afford.

The need to provide cost-effective propulsion technology is critical in today's environment. Severely declining military budgets in the Western world as well as unprecedented levels of airline losses have created economic constraints on development budgets that are more severe than at any time in recent history. Acquisition cost design requirements for next generation engines are being specified (see Fig. 1) such that the cost per pound of thrust is decreasing.

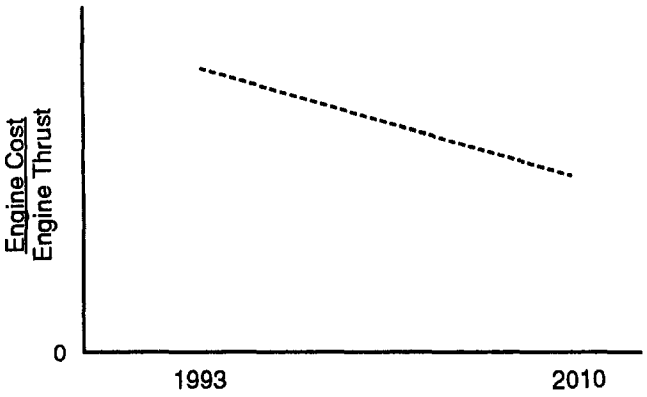

Fig. 1 Requirements for more affordable engines

Next-generation propulsion advances could be less dramatic and more costly than in the past, and will have to be cost effective for the developer as well as the end user. Figure 2 portrays the propulsion system designer's balancing act to introduce only those technologies that are economically viable for the aircraft operator.

A design consideration that typically has not been addressed in propulsion technology advancements is a systematic accounting of risk and uncertainty. Although this probabilistic concept of design was suggested by Timson [1] 25 years ago, no widespread evidence of usage has been noted to date. Failure to account for uncertainty can result in significant shortcomings in performance when the engine is initially tested. Assessment of risk should consider typical performance issues such as specific fuel consumption (sfc) but also account for cost and weight. Addressing uncertainty will require a culture change for most propulsion component designers and technologists, who typically address component performance improvement as a discrete value or level, rather than a distribution of possible performance outcomes.

Effective economic assessments of propulsion technologies for selection of development alternatives must reflect the total technology impact as well as any uncertainty. Total cost accounts for development of the technology, relative cost to manufacture the technology, what cost benefit the technology provides to the user (e.g., less fuel burn, lower weight, smaller size aircraft, etc.), and relative cost to maintain the technology over the life of the engine. Uncertainty accounts for the possibility that the designer will not exactly and uniquely achieve design intent. That is, there is a distribution of possible performance levels associated with a component's improvement, as represented in Fig. 3, rather than a discrete value.

If all relevant component performance improvement opportunities, and the associated economic assessments of this perfor-

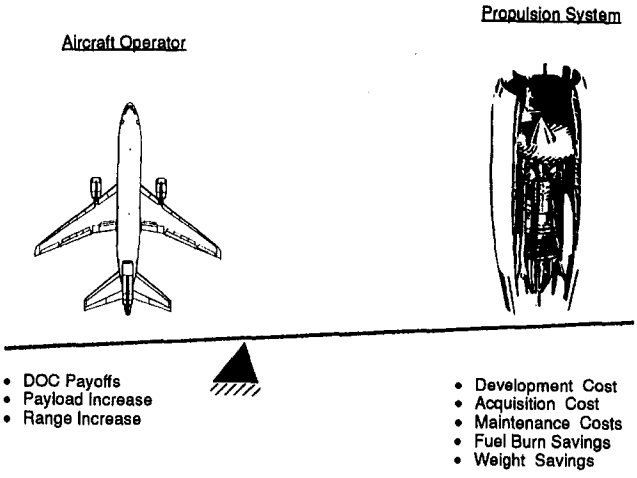

Fig. 2 Balancing the propulsion economic impacts on the aircraft

Contributed by the International Gas Turbine Institute and presented at the 39th International Gas Turbine and Aeroengine Congress and Exposition, The Hague, The Netherlands, June 13–16, 1994. Manuscript received by the International Gas Turbine Institute March 12, 1994. Paper No. 94-GT-419. Associate Technical Editor: E. M. Greitzer.

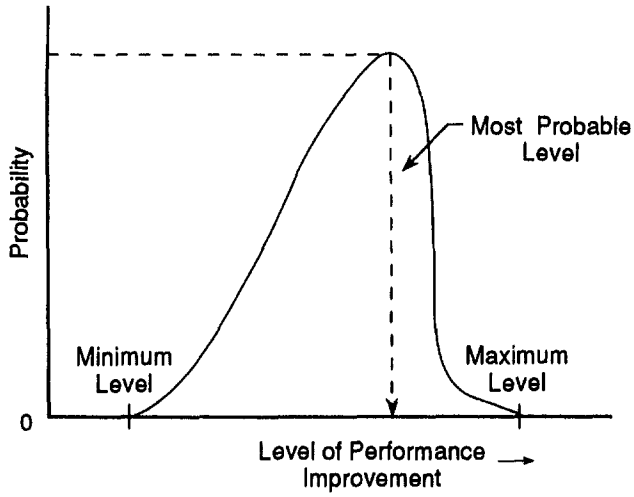

Fig. 3 Quantifying development uncertainty

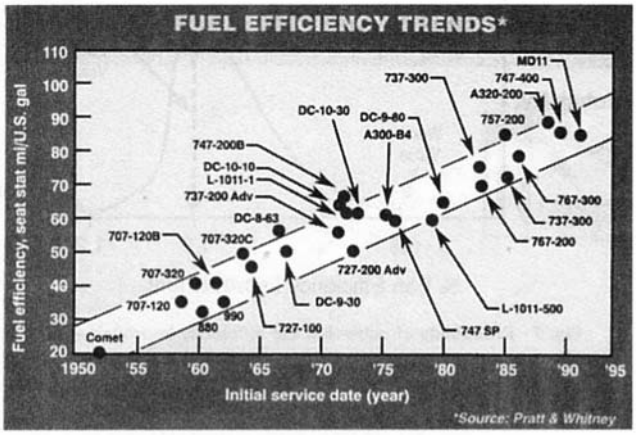

Fig. 4 Fuel efficiency trends

mance, are modeled in this fashion, it can serve as a ranking or prioritization criterion for the development of these technologies, as will be subsequently discussed. This concept can also be applied in an eclectic sense to quote or guarantee levels of propulsion system performance, weight and cost, as will be subsequently presented.

Assessing Technology Opportunities for Advanced Propulsion Systems. The need for advanced propulsion technology is driven primarily by the desire to produce viable advanced aircraft such as the High-Speed Civil Transport (HSCT), to add capability to current aircraft (i.e., increased range and/or payload) or to reduce propulsion ownership costs for current and advanced aircraft. Significant progress has been made in the last 40 years in achieving fuel-efficient aircraft (Fig. 4) [2]. This progress is a result of improved propulsion system sfc characteristics as well as improved aircraft lift-to-drag ratios.

Table 1 Advanced engine technology impact on engine configuration and aircraft economics

Advanced Propulsion Development Goals	Propulsion Changes To Achieve Goals	Aircraft Impact of Achieving Propulsion Goals
Reduced SFC	• Increased propulsive efficiency – higher bypass ratio • Increased thermal efficiency – improved component efficiency – higher cycle pressure ratio • Reduced cycle parasitic cooling air – higher temperature materials – improved blade cooling technology	• Increased range • Increased payload • Reduced fuel costs
Reduced Ownership Cost	• Smaller engines – increased thrust per pound of airflow • Reduced parts count – higher stage loading • Reduced manufacturing costs • Reduced maintenance costs • More affordable advanced materials • Improved installation integration	• Reduced DOC • Reduced LCC
Increased Thrust to Weight Ratios	• Reduced weight – higher stage loadings – improved strength to density materials • Increased thrust – higher fan pressure ratio – higher turbine temperatures – improved component efficiencies • Unconventional architecture – variable cycle technology	• Reduced A/C size • Reduced A/C weight • Reduced A/C Cost
Higher Thrust Per Pound of Airflow	• Increased cycle energy – higher turbine temperatures • Increased fan pressure ratio • Reduced cycle parasitic cooling air • Unconventional architecture – variable cycle technology	• Reduced A/C size • Reduced A/C weight • Reduced A/C cost • Reduced engine cost per pound of thrust
Reduced Emissions – Combustion By-products – Acoustic Noise	• More efficient combustors • Lower cycle pressure ratios • Lower turbine temperatures • Alternative fuels • Source noise reduction • Increased acoustic treatment effectiveness • Efficient jet mixing	• Comply with environmental regulations

Lists of propulsion development opportunities, the propulsion system mechanisms to realize these opportunities, and the aircraft system benefits of achieving them are contained in Table 1. Although Table 1 contains a thorough listing of potential technology enhancements for propulsion systems, it lacks any prioritization based on economic value and the cost to develop and implement the technology. The dilemma facing the designer is how efficiently and simultaneously to satisfy performance and customer cost goals and be environmentally compliant while addressing risk and uncertainty.

Turbomachinery component designers understand how their particular component affects aspects of system performance, but they may not address whether or not it is cost effective to improve its performance. For example, is there more system payoff (Cost savings − Development cost) for one technology relative to another? The relative sfc improvements of technologies presented in Fig. 5 do not provide the necessary input to select which technologies are most cost effective. Similarly, input from the aircraft end users is usually qualitative because they desire the engine manufacturer to improve some or all of the Table 1 items such as sfc, cost, thrust-to-weight, thrust per pound of airflow, and emissions. Table 1 contains the relevant propulsion changes to achieve these goals, but has no quantitative information on identifying which technologies are the most

Nomenclature

A/C = aircraft
DOC = Direct Operating Cost
Fn/Wgt = engine sea level static thrust/engine weight
FOM = Figure of Merit
FV_i = DOC-related fan dependent variable i
HSCT = High-Speed Civil Transport
LCC = Life Cycle Cost
sfc = specific fuel consumption
TIC = Technology Investment Cost
Δ = difference
∂ = partial derivative
% = percent

Subscript

i = ith variable

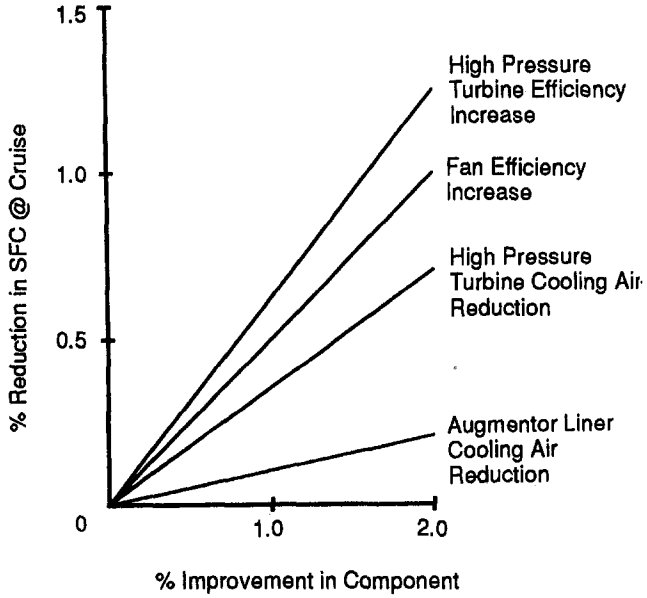

Fig. 5 Sensitivity of augmented turbofan sfc to component technology improvements

cost effective. The propulsion manufacturer is still left with the quandary of what is the most cost-effective usage of limited advanced technology resources. The dilemma is depicted in Fig. 6 and a methodology for resolving it will subsequently be discussed.

Component Technology Ranking Considering Economic Value and Uncertainty. Uncertainty in component technology can be modeled in a probabilistic fashion and should consider at least the uncertainties associated with performance, cost, and weight. The data on variability can be collected by asking the component design experts three simple questions:

1 What is the predicted value?

- Assume that the predicted value is also the most likely value

2 What are the one-chance-in-a-thousand best and worst possible values?

- Most people can relate to this as a very unlikely chance, but a chance nonetheless

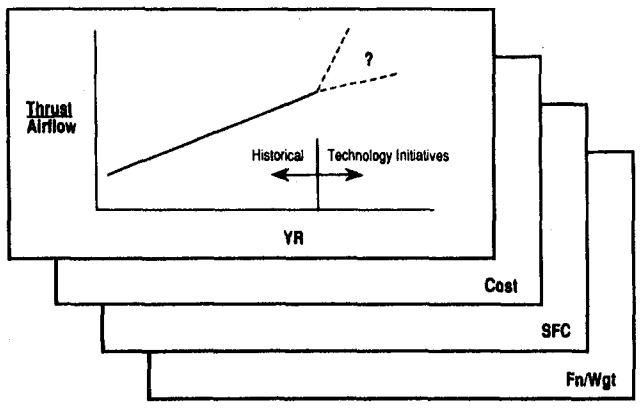

Fig. 6 Advanced propulsion plan for augmented turbofans

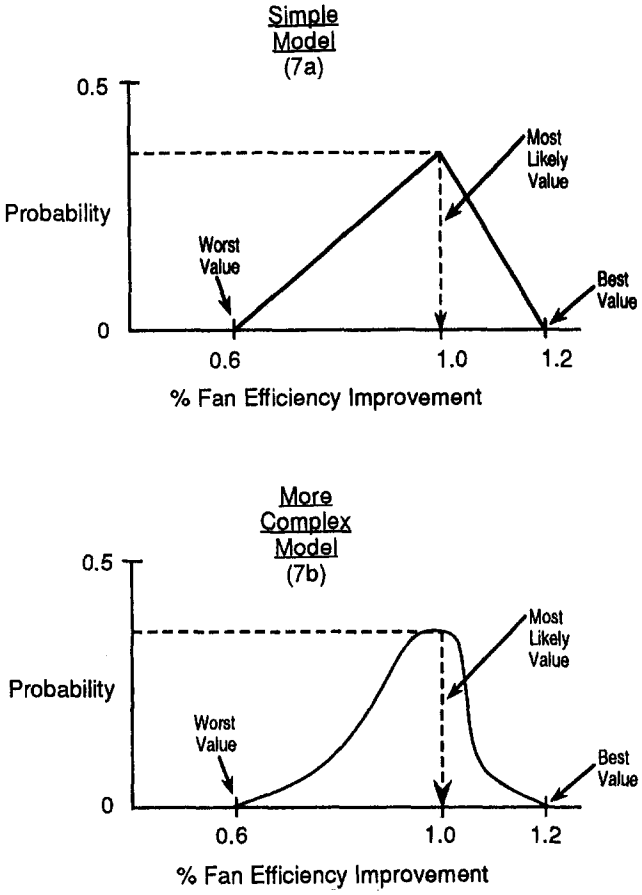

Fig. 7 Probability of achieving fan efficiency improvements

- For modeling purposes, these values can be used as the 0 percent probability values

3 If you did ten such designs, how many of them would fall within "X" of your prediction?

- Units and size of interval "X" can be tailored to specific discipline and component
- Provides additional confidence information

Questions one and two provide sufficient information for simple distributions (triangles); question three can be used to generate more complex types of probability distributions.

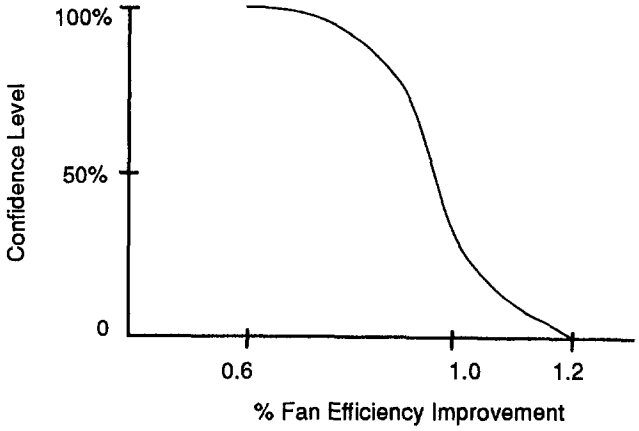

Fig. 8 Confidence level representation of fan efficiency improvements

Statistics:	Value
Trials	800
Mean	6.933
Median (approx.)	6.790
Mode (approx.)	6.517
Standard Deviation	1.435
Skewness	0.43
Kurtosis	3.13
Range Minimum	2.778
Range Maximum	12.010
Range Width	9.232
Mean Std. Error	0.051

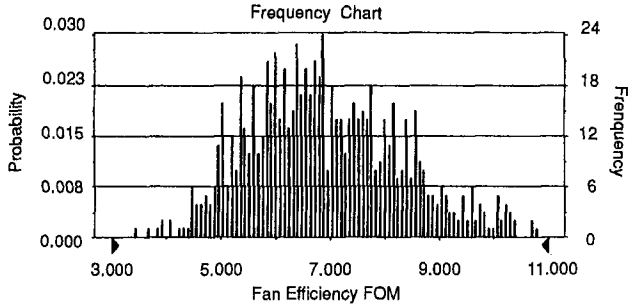

Fig. 9 Fan efficiency FOM probability distribution

Table 2 Fan efficiency impacts on overall aircraft DOC

Component Variable	DOC-Dependent Propulsion Variables	DOC Sensitivity to Propulsion Variables
Improvement in fan efficiency	• Reduction in fuel burn due to improved thermal efficiency resulting from fan configuration change (FV_1)	Change in DOC with fuel burn ($\partial DOC/\partial FV_1$)
	• Change in manufacturing cost due to fan configuration change (FV_2)	Change in DOC with manufacturing cost ($\partial DOC/\partial FV_2$)
	• Change in maintenance cost due to a configuration change (FV_3)	Change in DOC with maintenance cost ($\partial DOC/\partial FV_3$)
	• Change in engine weight due to fan configuration (FV_4)	Change in DOC with engine weight ($\partial DOC/\partial FV_4$)

The data from these three simple questions are then utilized to construct a probability distribution for a component like the fan of a high bypass turbofan. Figure 7(a) represents the type of distribution that could be constructed if the designer answered only questions 1 and 2, while Fig. 7(b) represents the additional probability details available if the designer can answer all three questions.

Appropriate ranges of the normalized probability distribution from Fig. 7(a) or 7(b) can be integrated to produce a confidence level plot as depicted in Fig. 8. Confidence level is a desirable parameter to obtain, because it ultimately allows decisions based on equal risk, which is difficult to quantify based on visual inspection of Fig. 7.

It should be noted that the probability distributions of Fig. 7 produce less than a 50 percent confidence level that the most probable level of 1 percent fan efficiency improvement will be achieved. Similarly any other major uncertainties, like development cost and weight, that impact any technology affordability metric should be modeled.

A representative economic Figure of Merit (FOM) for an airliner gas turbine engine might evaluate all the direct operating cost (DOC) propulsion variables associated with a component technology improvement, as well as the technology investment cost (TIC) to obtain the component technology improvement. Equation (1) reflects this hypothesis:

$$\text{FOM} = \frac{\sum_{i=1}^{n} \%\Delta\text{DOC}}{\text{TIC}} \tag{1}$$

where the numerator is the total DOC impact associated with the n dependent variables impacted by a technology improvement.

In the case of a fan efficiency improvement, the appropriate interactions have to be quantified (see Table 2). The change in DOC due to the DOC-dependent propulsion variables is dependent on aircraft type and usage, so a representative set of values should be utilized and the resulting FOM is unique to that application and usage.

Utilizing the information from Table 2 (if there were no uncertainty associated with the FV_i and TIC values), the FOM could be evaluated as follows:

$$\text{FOM} = \frac{\sum_{i=1}^{4} \left(\text{FV}_i \times \frac{\partial \text{DOC}}{\partial \text{FV}_i} \right)}{\text{TIC}} \tag{2}$$

Since uncertainty does potentially exist for FV1–FV4 as well as TIC, a statistical assessment of this uncertainty can be made using commercially available software such as Crystal Ball® [3]. Utilizing Monte Carlo simulations of the FOM variables, a FOM distribution can be calculated using Crystal Ball®. Having done this, a fan efficiency FOM result is contained in Fig. 9, with its statistical uncertainty displayed graphically and quantified numerically in the table. High values for FOM represent goodness and appropriate selections of advanced technology development opportunities can be made based on the magnitude of the advanced technology FOM. Since there is a range of FOM values for Fig. 9, the question arises as to what "the FOM" is we should use to

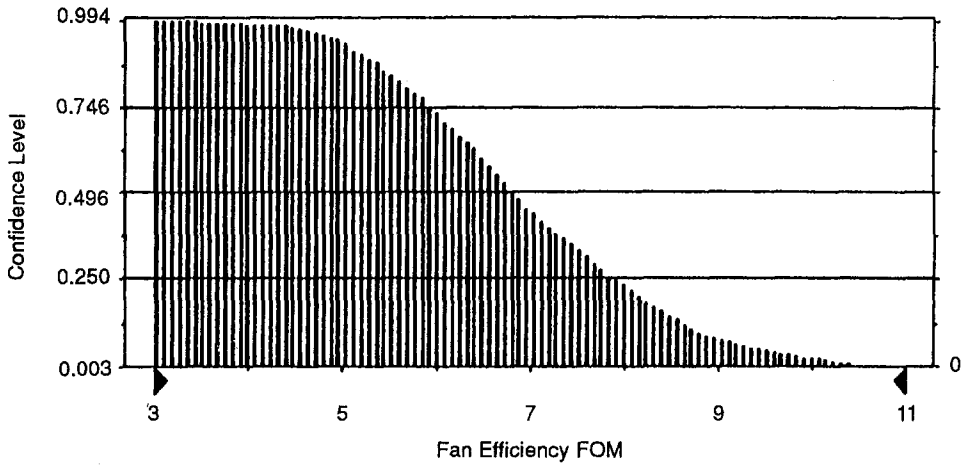

Fig. 10 Fan efficiency FOM confidence level distribution

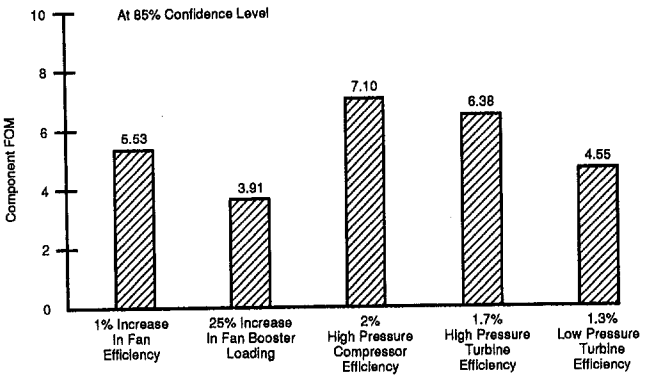

Fig. 11 FOM ranking of component technology opportunities

quantify the technology opportunity and make appropriate selections. For this reason, it is useful to construct confidence level distributions from the FOM probability distributions, and compare FOM values at the same confidence level. Figure 10 is the confidence level distribution generated from the fan efficiency FOM probability data contained in Fig. 9. Utilizing this probabilistic econometric methodology for other turbomachinery components yields results for several technology opportunities, as depicted in Fig. 11. Since high FOM values represent goodness, the identified technologies that result in a 2 percent increase in high pressure compressor efficiency (FOM = 7.10) should be developed first. The technologies that provide a 25 percent increase in fan booster pressure rise (FOM = 3.91) result in the lowest FOM and would be selected for development only after all the other technologies on the chart had been developed. Since the FOMs consider reduction in DOC as well as the impact of the relative technology development costs, they now offer an economically prioritized development list, which can be used to aid in constructing the advanced technology roadmaps depicted in Fig. 6. The process steps and information utilized are graphically depicted in Fig. 12. It should be noted that not all of the FOM's will be positive. For example, if the manufacturing cost and maintenance cost for implementing a technology would increase the DOC more than any reduction in DOC due to decreased fuel burn, the overall FOM will be negative and should be excluded from further consideration, since there is no net economic benefit to the propulsion system user.

Quoting New Engine Performance and Incorporating Component Design Uncertainty. Gas turbine engine manufacturers typically quote engine performance with margins to account for engine-to-engine variation, which is based on historical trending of production performance experience, and performance deterioration with engine usage. The production margins deal with parts and control tolerances and do not address performance uncertainty in the design of the components. Utilizing all the component performance uncertainty models, similar to those depicted in Fig. 7, a performance parameter probability distribution can be obtained utilizing the methodology contained in Fig. 13. Figure 14 contains the sfc probability distribution relative to design intent and indicates a skewing to the positive region relative to design intent (worse sfc). The confidence level distribution associated with Fig. 14 is presented in Fig. 15 and indicates a 50 percent confidence level that the sfc will be no worse than 1 percent over design value and a 85 percent confidence level that it will be no worse than 4.5 percent over design value. Overall engine performance uncertainty can also take the form of:

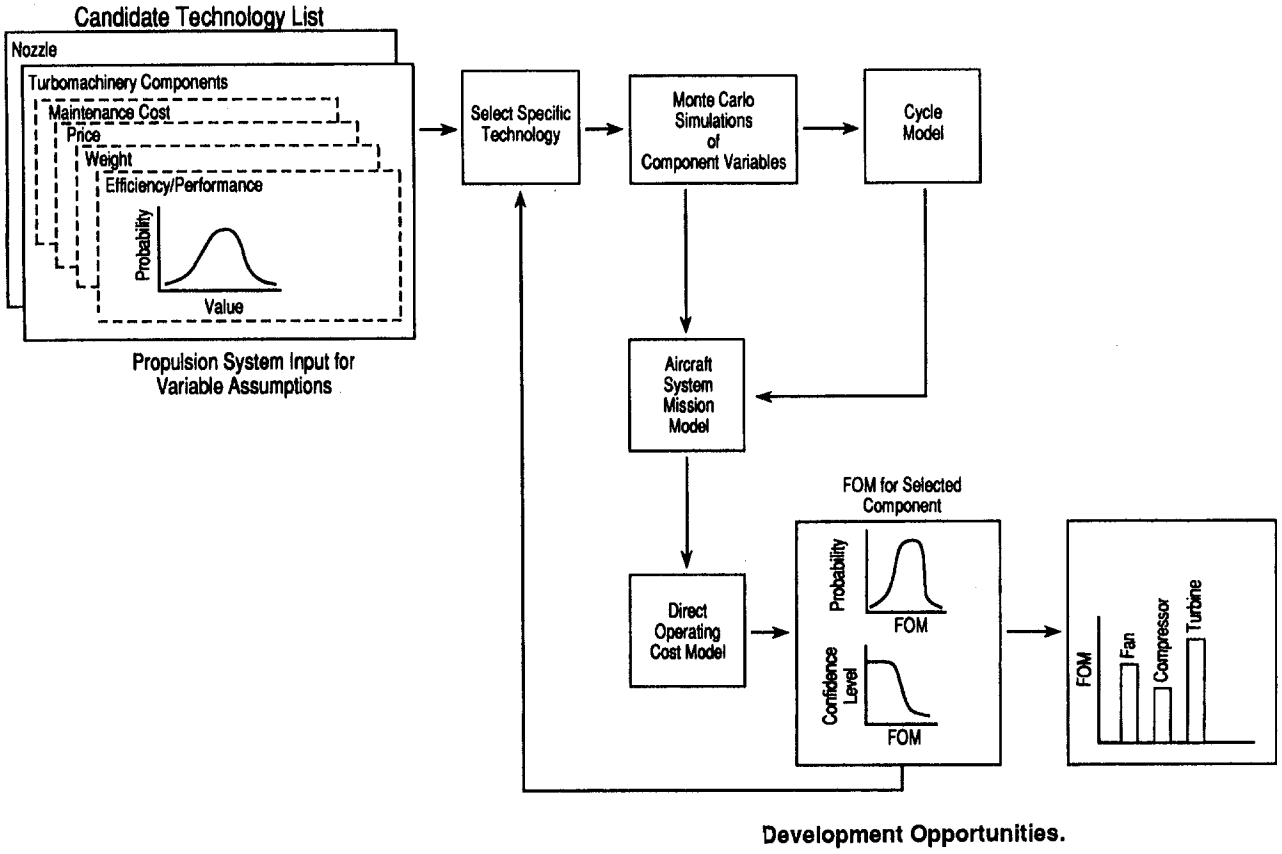

Fig. 12 Methodology for prioritizing technology development opportunities

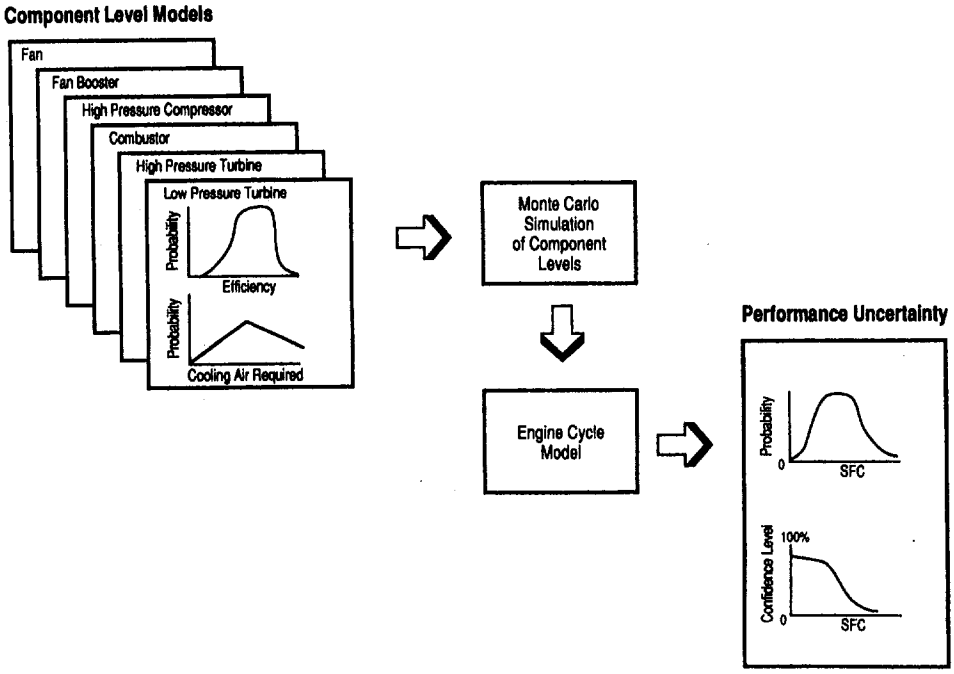

Fig. 13 Methodology to address engine performance uncertainty

- Thrust probability distributions
- Cycle airflow probability distributions
- Turbine temperature probability distributions
- Acoustic noise probability distributions

as well as the sfc uncertainty modeled. Any performance metric can then be quoted at a user-specified confidence level.

The engine developer does have other options if the predicted results of Fig. 14 are unacceptable. He can allocate more money for component development and strive for additional component performance enhancements. The results of such an exercise are depicted in Fig. 16(*a*), where the most likely levels of sfc are improved with additional development expenditure. The worst sfc expected is improved with increased development expenditures. Probable cruise sfc improvements with component technology investment increases are portrayed in Fig. 16(*b*).

Summary

Declining development budgets and customer desires to purchase gas turbine engines with the most economic utility dictate that only cost-effective technology be developed. A probabilistic analysis methodology and a sample economic Figure of Merit were presented that dealt with design uncertainty and measurement of economic value in evaluating alternative component technology developments. Utilization of this methodology for technology ranking requires the designer to provide and acquire additional data. The new data consist of a probabilistic distribution of design performance,

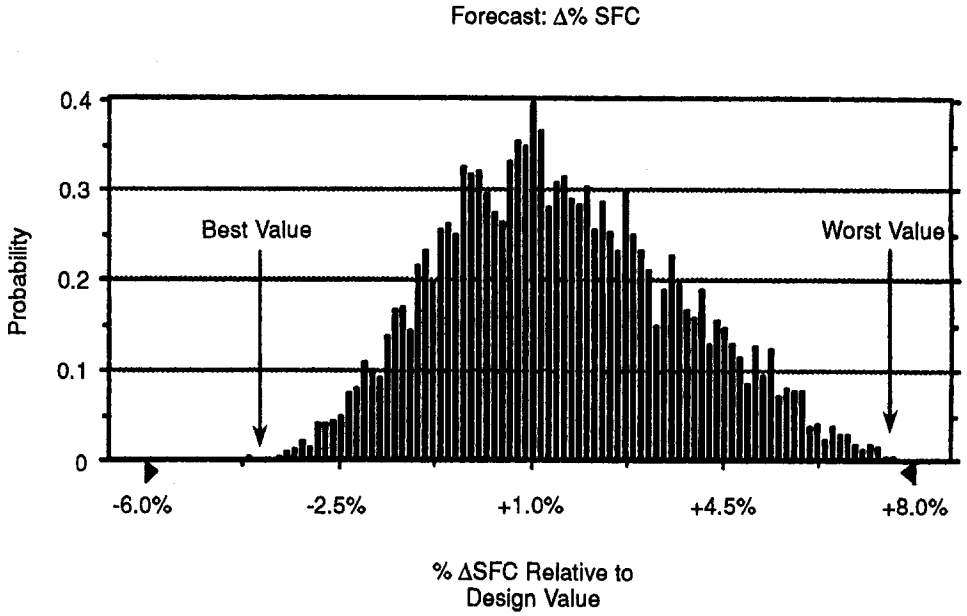

Fig. 14 The sfc probability distribution for the engine

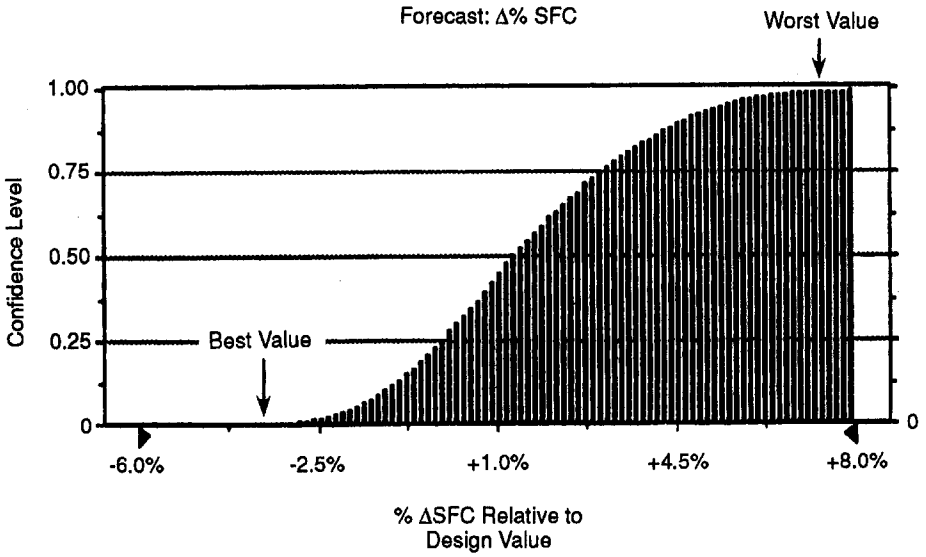

Fig. 15 The sfc confidence levels for the engine

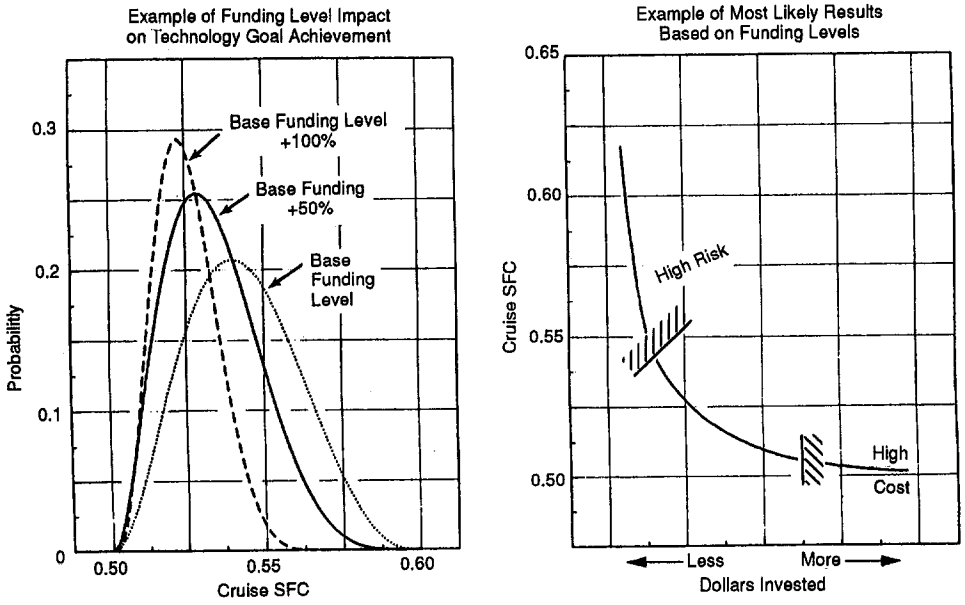

Fig. 16 Balancing performance risk with development expenditures

rather than a discrete value; it also includes an assessment of cost differences to manufacture and maintain the proposed technology over the product life. Once this design and cost information is provided, commercially available software and a PC (Personal Computer) can quantify the impacts of design uncertainty for a user-specified FOM. A methodology was also discussed that allows the propulsion system designer to account for all the design uncertainties in component performance while quoting overall levels of engine performance such as thrust and specific fuel consumption.

References

1 Timson, F. S., "Measurement of Technical Performance in Weapon System Development Programs: A Subjective Probability Approach," RAND Memorandum RM-5207-ARPA, Dec. 1968.

2 *Aviation Week and Space Technology,* Nov. 22, 1993.

3 Crystal Ball®; Decisioneering Inc., 1380 Lawrence Street, Denver, CO 80204-9849.

System Evaluation and LBTU Fuel Combustion Studies for IGCC Power Generation

C. S. Cook

J. C. Corman

D. M. Todd

GE Power Generation,
Schenectady, NY 12345

The integration of gas turbines and combined cycle systems with advances in coal gasification and gas stream cleanup systems will result in economically viable IGCC systems. Optimization of IGCC systems for both emission levels and cost of electricity is critical to achieving this goal. A technical issue is the ability to use a wide range of coal and petroleum-based fuel gases in conventional gas turbine combustor hardware. In order to characterize the acceptability of these syngases for gas turbines, combustion studies were conducted with simulated coal gases using full-scale advanced gas turbine (7F) combustor components. It was found that NO_x emissions could be correlated as a simple function of stoichiometric flame temperature for a wide range of heating values while CO emissions were shown to depend primarily on the H_2 content of the fuel below heating values of 130 Btu/scf (5125 kJ/NM^3) and for H_2/CO ratios less than unity. The test program further demonstrated the capability of advanced can-annular combustion systems to burn fuels from air-blown gasifiers with fuel lower heating values as low as 90 Btu/scf (3548 kJ/NM^3) at 2300°F (1260°C) firing temperature. In support of ongoing economic studies, numerous IGCC system evaluations have been conducted incorporating a majority of the commercial or near-commercial coal gasification systems coupled with "F" series gas turbine combined cycles. Both oxygen and air-blown configurations have been studied, in some cases with high and low-temperature gas cleaning systems. It has been shown that system studies must start with the characteristics and limitations of the gas turbine if output and operating economics are to be optimized throughout the range of ambient operating temperature and load variation.

Introduction

Gasification systems, including air-blown, integrated oxygen-blown and oxygen-blown followed by heavy moisturization processes can produce fuels that have heating values as low as 100 Btu/scf (3942 kJ/NM^3). A joint EPRI/DOE/GE sponsored combustion program was created to provide a set of screening tests for the advanced GE MS7001F combustion system and determine its combustion characteristics with low-Btu fuels. The program was structured to uncouple the gasification process from the turbine combustion process in order to provide fundamental data regarding the combustion of syngas, making the results applicable to oil and biomass gasification as well as industrial processes (e.g., coke oven gas). During 1990, a joint EPRI/Shell/GE program began the combustion screening test process with simulated Shell, oxygen-blown coal gas. Steam, blended with the syngas, was used as a diluent and fuel gas compositions with heating values as low as 110 (4337 kJ/NM^3) to 120 (4721 kJ/NM^3) Btu/scf were tested. The current program links those 1990 results with recent tests, which consider other diluents for a variety of H_2/CO/CO_2 ratios.

Definition of the combustion characteristics of the various LBtu fuels has allowed full utilization of an IGCC system optimization methodology to provide least cost, highest performance IGCC power generation systems within gas turbine operating constraints.

Combustion Study Program Description

The present program consisted of six combustion tests. The major screening tests were conducted at approximately $\frac{1}{2}$ normal combustor mass flow and pressure but duplicated actual operating combustor inlet and exit temperatures simulating the "F" operating conditions. A full flow demonstration of injection of nitrogen at the head end of the combustor for NO_x control was included.

The major objectives of the program were:

1 Parametric determination of the effects of moisture, nitrogen and carbon dioxide as preblended diluents, so that the combustion characteristics of gasification product gases could be reasonably predicted without testing each specific gas composition.

2 Determination of NO_x, CO, and UHC (where applicable) emission characteristics, combustor turndown, and flame stability associated with each diluent.

3 Operation with at least two significantly different syngas compositions to confirm that combustion characteristics were in line with predictions.

4 Demonstration of the feasibility of nitrogen injection at the head end of the combustor for thermal NO_x control and comparison of combustion characteristics, including NO_x reduction, with preblended nitrogen combustion data.

5 Investigation of the effect of fuel temperature on emissions, flame stability, and turndown.

6 Further investigation of the effect of H_2/CO/CO_2 ratio on CO emissions, flame stability, and turndown.

The combustion tests were performed in the GE Engineering Development Laboratory in Schenectady, New York. The laboratory contains six full-pressure test stands, each capable of accommodating a single industrial gas turbine combustor and duplicating actual combustion conditions at rated temperature, pressure and air flow. The principal fuel gas combustibles (H_2 and CO) (2832 NM^3) were premixed by a gas supplier and delivered to the site in nominal 100,000 scf tube trailers at 2000

Contributed by the International Gas Turbine Institute and presented at the 39th International Gas Turbine and Aeroengine Congress and Exposition, The Hague, The Netherlands, June 13–16, 1994. Manuscript received by the International Gas Turbine Institute February 15, 1994. Paper No. 94-GT-366. Associate Technical Editor: E. M. Greitzer.

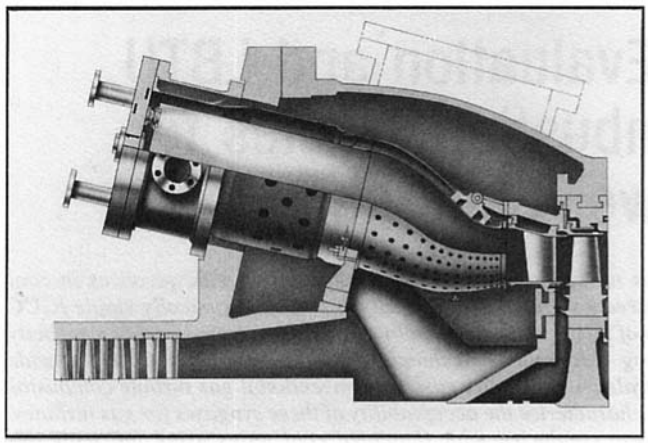

Fig. 1 GE reverse flow "F" technology combustion system

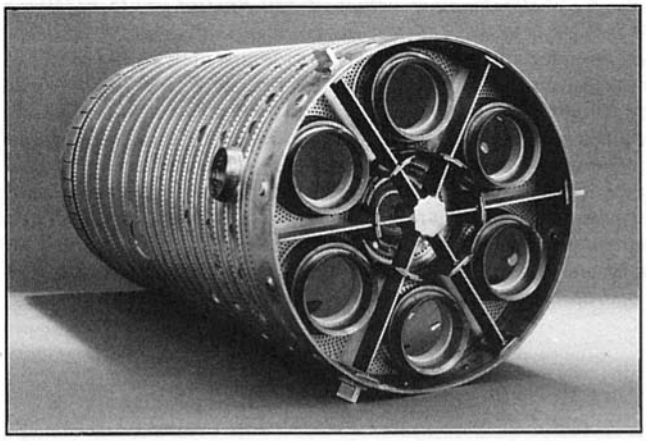

Fig. 2 Standard "7F" combustion liner

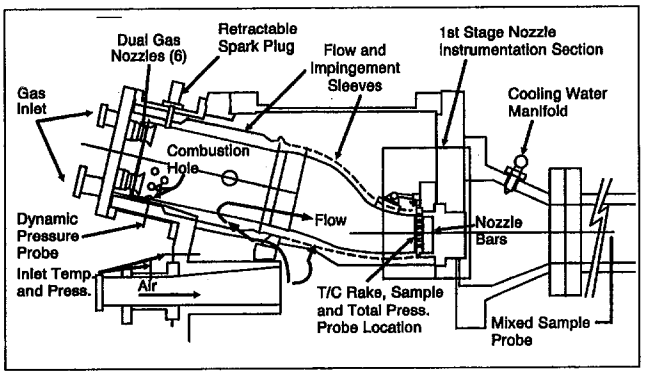

Fig. 3 Model "F" Test stand arrangement

psig (138 bar). The balance of the gas constituents (N_2, CO_2, H_2O, and CH_4) were blended on line.

A conventional GE model 7F combustor (Fig. 1) with a diffusion combustion liner (Fig. 2) was used for all tests. Figure 3 shows the combustion system as mounted in the test stand.

Table 1 compares the fuel gases tested during this program with the Shell gas tested in 1990 under the EPRI/Shell/GE program. A major part of the testing was done with fuel gas mixtures related to an air-blown gasifier with an H_2/CO ratio of 3.3:1. The basic fuel dilution tests were done with this H_2–CO mixture. The combustion test sequence for the most recent test program is outlined in Table 2. All tests were conducted

Table 1 Fuel gas compositions

Constituent	Shell O_2 Blown	Air Blown Dry	Air Blown Wet	Texaco O_2 Blown	Test No. 6
H_2	31.3	23	16.7	34.0	57
CO	62.7	7	4.8	49.0	43
CO_2	1.5	20	14.3	9.7	
N_2	4.5	47	34.2	6.1	
H_2O	(Dry)	0	26.7	(Dry)	(Dry)
CH_4		3	3.1	0.2	
NH_3			0.1		
Other			0.1	1.0	
LHV (Btu/scf)	287	113	89.0	251	295
H_2/CO Ratio	0.5	3.3	3.5	0.69	1.33

Table 2 Combustion test description

Test No.	Fuel Description	Fuel Nozzles	Diluent	Diluent Location
1	Air Blown, H_2/CO = 3.3	Standard	CO_2, Steam	With Fuel
2	Air Blown, H_2/CO = 3.3	Standard	N_2, Steam	With Fuel
3	Air Blown, Wet	Syngas	Steam	With Fuel
4	Air Blown, H_2/CO = 3.3	Syngas	N_2	Combustor Head End
5	Texaco O_2 Blown, H_2/CO = 0.69	Syngas	N_2	Combustor Head End
6	O_2 Blown, H_2/CO = 1.33	Syngas		-

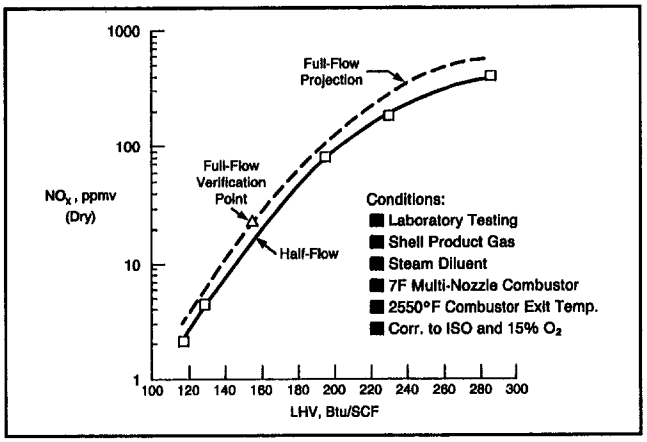

Fig. 4 NO_x Emissions versus heating value from EPRI/Shell tests

at 50 percent combustor mass flow and pressure unless noted otherwise. Tests 1 and 2 used hardware identical to that used during the prior 1990 EPRI/Shell test program. Subsequent tests used modified fuel nozzle gas tips specifically designed for syngas combustion.

Combustion Test Results

Figure 4 shows NO_x levels as a function of moisturized fuel heating value taken from the prior 1990 EPRI/Shell/GE program. As the heating value of the fuel decreases, so does the stoichiometric flame temperature and the amount of NO_x formed. The two lines in the figure show the relationship between the half-flow, half-pressure tests and full-flow, full pressure conditions. In agreement with the well-known relationship between NO_x and pressure in diffusion flames, NO_x formation was found to be proportional to the square root of pressure.

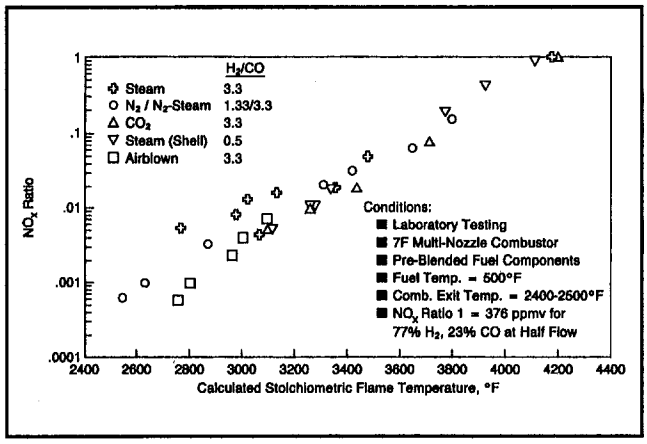

Fig. 5 NO_x reduction ratio versus stochiometric flame temperature

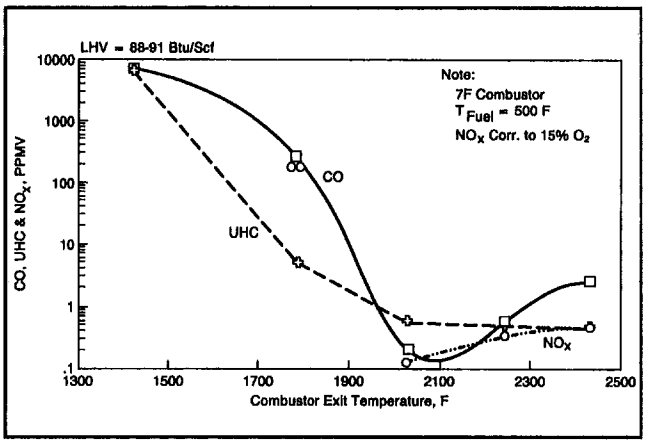

Fig. 7 CO and NO_x emissions versus combustor exit temperature

As illustrated in Fig. 5, the relationship between NO_x reduction ratio and stoichiometric flame temperature holds for all diluents evaluated, whether blended individually or in combination, as was the case for the air-blown gas. All NO_x ratios in the figure are relative to the measured NO_x observed when burning a combustible mixture of 77 percent H_2/23 percent CO and all data have been corrected to 15 percent O_2 and ISO humidity. The experimental data represented in Fig. 5 provide an engineering tool for estimating NO_x for a given fuel composition and have been applied to all fuels, including natural gas and distillate. These results apply over a wide range of heating values and compositions, and show the equivalence of the case of air-blown fuels and high levels of nitrogen dilution for oxygen-blown systems.

The diluent blending tests were designed to determine the effect of diluent type and H_2–CO content on CO emissions at GE 7F base load combustor exit conditions. By determining the minimum heating value for excessive CO emissions for each diluent and H_2–CO mixture, bounds could be established for IGCC application of the standard GE 7F combustion system. CO emissions at low combustor exit temperatures were used as an indication of flame stability and incipient flameout.

CO emissions are shown as a function of volumetric LHV at full load combustor exit temperature in Fig. 6. For the air-blown, 3.3:1 H_2–CO mixture, CO is relatively constant with variation in steam or N_2 dilution but steadily increases with decreasing LHV when CO_2 is used for dilution. The increase with CO_2 is consistent with equilibrium predictions. The prior 1990 EPRI/Shell/GE data showed the existence of a lowest heating value limit of about 128 Btu/scf (5046 kJ/NM^3) based on CO emissions. No such limit could be found for either the fuel with an H_2/CO ratio of 3.3 or the fuel having a H_2/CO ratio of 1.33. CO concentration remained low (<10 ppmv) for heating values approaching 100 Btu/scf (3942 kJ/NM^3) for these mixtures.

The simulated air-blown gas (Table 1) was evaluated using the conventional GE 7F combustion liner but with gas tips redesigned specifically for syngas. The dry syngas was mixed first and steam subsequently added in increments until the saturated fuel composition of Table 1 was obtained. Figure 7 shows emissions as function of combustor exit temperature for the saturated, 89 Btu/scf (3509 kJ/NM^3) fuel. It can be seen that NO_x emissions were extremely low, and fell below the limit of detection. CO and UHC were also very low at exit temperatures above 1880°F (983°C), but below this, increased rapidly although blowout was never reached.

A more practical and efficient method of returning nitrogen to the cycle in oxygen-blown IGCC applications, other than reinjecting it into the syngas fuel stream, is to inject it into the combustion air stream at the head end of the combustor in a manner similar to head-end steam injection for NO_x control. Head-end nitrogen injection was first tested with the air-blown 3.3:1 N_2/CO_2 mixture at reduced flow and then at full flow with simulated Texaco syngas. Figure 8 compares NO_x reduction with head-end nitrogen with that of nitrogen blending. It appears that head-end injection will allow sufficiently low NO_x levels and the IGCC system will be able to realize the full performance benefits of this concept.

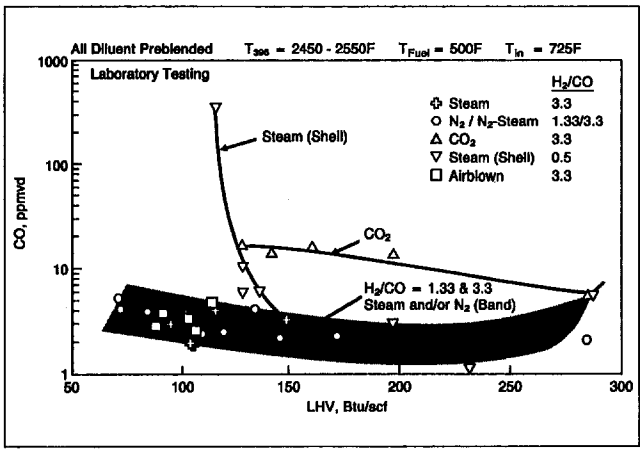

Fig. 6 CO emissions as a function of LHV and H_2/CO ratio

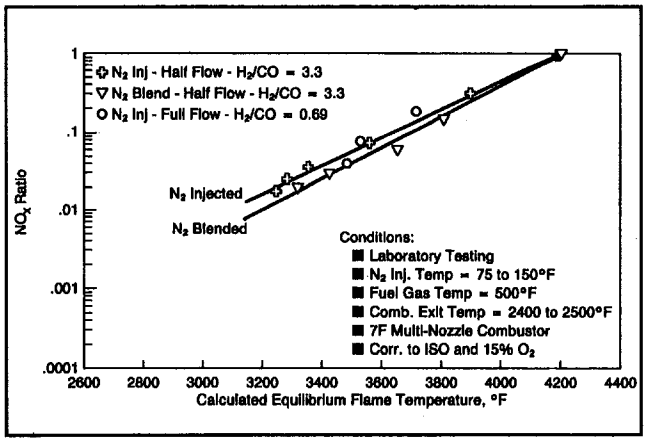

Fig. 8 NO_x emissions for head-end N_2 injection versus N_2 blended with fuel

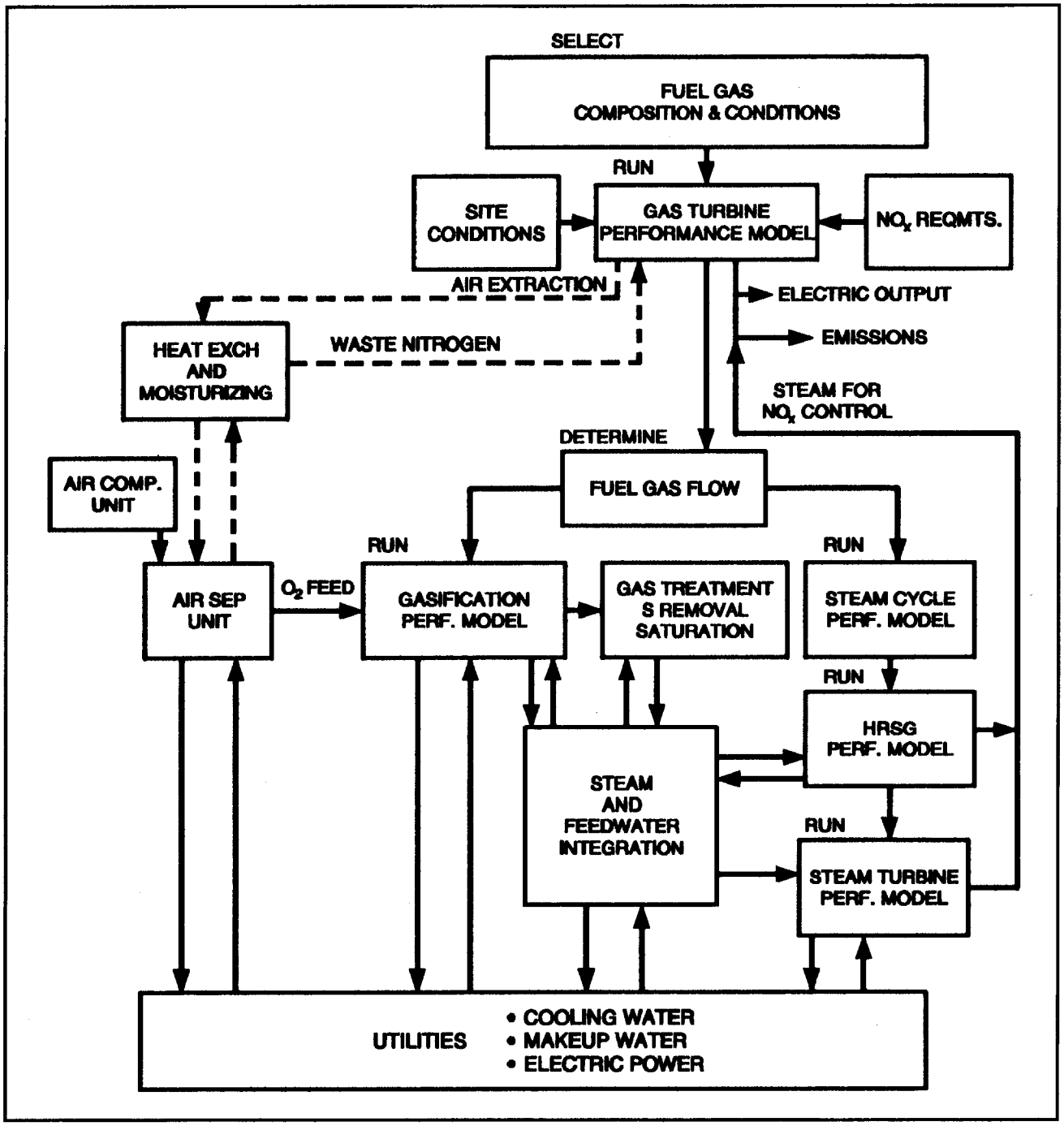

Fig. 9 GE IGCC performance model

A limited number of test points were obtained at different fuel temperatures during the sixth test. For the syngas tested, NO_x varied little at maximum exit temperature for fuel gas temperatures of 500°F (260°C) and 650°F (344°C). CO appeared to increase somewhat with fuel temperature contrary to expectations. When the fuel temperature was dropped from 500°F (260°C) to 350°F (177°C) at part-load exit temperature CO and NO_x levels changed very little.

IGCC System Considerations

It is critical to understand the gas turbine operational limits with respect to fuel composition in order to assess the performance of various IGCC configurations. As more attention has continued to be paid to system integration, and as GE and other gas turbine vendors have continued to elevate firing temperatures for natural gas and distillate fuel operation, it has been necessary to create a standardized IGCC performance model to be used in screening system configurations on a performance basis. The current GE IGCC performance model is shown in Fig. 9.

The combustion testing discussed previously has allowed establishment of lower limits on fuel heating values for standard and modified GE gas turbine combustors as a function of air or oxygen-blown gasification and the required NO_x emission levels. Usually, a utility or an independent power producer will formulate a potential IGCC plant configuration around a limited set of fuel feedstocks and one or two gasification processes and

will then ask a gas turbine manufacturer directly, or in concert with an engineer/constructor, to provide projected IGCC system performance for particular gas turbine, steam turbine-generator configurations the manufacturer offers. It is important to recognize that, although a reasonably wide range of gas turbine sizes is available, this distribution is still quantized while fuel plant size is continuously variable, up to current maximum size limits. Therefore, to start the performance evaluation, the total fuel input to the system is used for preliminary selection of the turbomachinery. This allows a first iteration involving running the manufacturer's gas turbine performance model, as adapted and constrained for other than natural gas or distillate fuel. Site ambient conditions and NO_x limits, as well as fuel heating value and mechanical, thermal, and mass flow limits for the particular turbine, are factored in the analysis, which results in a projected gas turbine output and exhaust energy available as a function of ambient temperature over the range of interest. This then leads to verification of the fuel flow requirements, factoring in air separation unit integration and steam or water injection.

An iterative evaluation can then proceed, involving a match of the gasification system and gas cooling requirements with the gas cleaning subsystem. The significant amount of high-pressure steam generated from the fuel gas heat recovery system in oxygen-blown, entrained flow gasification must be carefully integrated with the Rankine cycle. However, it is the Brayton cycle portion of the IGCC system that has allowed, and will continue to allow, significant improvements in cycle output and efficiency as firing temperatures increase and gas turbine configurations evolve. This will require a continuous evaluation of the combustion of IGCC fuels in standard and modified gas turbine combustors in order to utilize existing, highly developed, lowest cost gas turbine designs while meeting low NO_x and CO emission levels over the operating range required.

Conclusions

The data from the current combustion testing, taken together with those of the prior test program, have resulted in an understanding of trends and relationships regarding syngas combustion. Some of the significant results are:

1 Demonstration of the advanced GE 7F combustion system's ability to accommodate fuel gas from current coal gasifiers and the viability of the can-annular combustor design for low Btu gas operation.

2 Correlations for estimating NO_x applicable to GE 7F class machines over a wide range of fuel heating values and compositions.

3 Determination that a combustion limit based on full-load CO emissions could not be found for $H_2/CO > 1.0$, even for air-blown type fuels with LHV below 90 Btu/scf (3548 kJ/NM^3).

Additionally, it can be concluded that continuing combustion testing of the sort reported here will be required as gas turbine technology evolves with higher firing temperatures and different machine configurations in order to adapt next-generation natural gas and distillate fuel-fired machines to IGCC operation while preserving low cost and low emissions.

It is the gas turbine that has been primarily responsible for the recent dramatic improvements in performance and reductions in projected cost of electricity for IGCC systems. It is unlikely that gas turbines especially designed for IGCC will be either available or cost effective. Therefore, IGCC systems designers must work closely with gas turbine manufacturers to optimize plant size, output requirements, and level of integration in order to ensure the most attractive overall concepts.

Acknowledgments

The authors wish to acknowledge the contributions of Mr. R. Battista and Mr. T. Ekstrom who have been primarily responsible for planning, conducting, and analyzing the results of the low-Btu fuel gas testing reported here. Further, the support of the U.S. Department of Energy and the Electric Power Research Institute is gratefully acknowledged. Mr. E. H. Broadway and Dr. A. K. Anand have been primarily responsible for the organization and performance of the GE IGCC evaluation model.

References

Battista, R. A., Cook, C. S., Corman, J. C., and Ekstrom, T. E., 1993, "Coal Gas Combustion Studies for IGCC Power Plants," presented at the EPRI 12th Conference on Coal Gasification Power Plants, San Francisco, CA, Oct. 27–29.

Detailed Measurements on a Modern Combustor Dump Diffuser System

J. F. Carrotte

D. W. Bailey

Department of Transport Technology,
Loughborough University,
Loughborough, Leics, United Kingdom

C. W. Frodsham

Department of Combustion,
Rolls Royce plc,
Bristol, United Kingdom

An experimental investigation has been carried out to determine the flow characteristics and aerodynamic performance of a modern gas turbine combustor dump diffuser. The system comprised a straight walled prediffuser, of area ratio 1.35, which projected into a dump cavity where the flow divided to pass either into the flame tube or surrounding feed annuli. In addition, a limited amount of air was removed to simulate flow used for turbine cooling. The flame tube was relatively deep, having a radial depth 5.5 times that of the passage height at prediffuser inlet, and incorporated burner feed arms, cowl head porosity, cooling rings, and primary ports. Representative inlet conditions to the diffuser system were generated by a single-stage axial flow compressor. Results are presented for the datum configuration, and for a further three geometries in which the distance between prediffuser exit and the head of the flame tube (i.e., dump gap) was reduced. Relatively high values of stagnation pressure loss were indicated, with further significant increases occurring at smaller dump gaps. These high losses, which suggest a correlation with other published data, are due to the relatively deep flame tube and short diffuser length. Furthermore, the results also focus attention on how the presence of a small degree of diffuser inlet swirl, typical of that which may be found within a gas turbine engine, can result in large swirl angles being generated farther downstream around the flame tube. This is particularly true for flow passing to the inner annulus.

Introduction

The primary function of a gas turbine diffuser system is to decelerate air issuing from the compressor and to distribute this flow in a uniform and stable manner around the flame tube. This also needs to be achieved with a minimal loss of stagnation pressure due to the effect on specific fuel consumption and the penetration of flow entering the flame tube. In current advanced core engines these objectives are usually met with dump diffuser systems, which incorporate a prediffuser followed by a recirculating dump region surrounding the flame tube head. Although such systems have relatively high losses, they are favored because of their inherent flow stability and insensitivity to manufacturing tolerances and thermal expansions.

Fishenden and Stevens [1] initially investigated the overall performance of a dump system by varying several parameters, including the mass flow split to each feed annuli, prediffuser area ratio, and the distance between prediffuser exit and the flame tube head (i.e., dump gap D/h_2). All tests were conducted with a flame tube that had a radial depth, expressed in terms of the passage height at prediffuser inlet (W/h_1) of 3.5. It was concluded that the principal determinants of stagnation pressure loss in such systems are the amount of diffusion being attempted and the radius of curvature undertaken by the flow as it passes around the flame tube. This latter effect is a function of the size and shape of the flame tube and the dump gap. With this in mind it is interesting to note the more recent works of several authors [2–6], which illustrate the trend for flame tubes of increasing depth, with values (W/h_1) in excess of 4.0. In addition, this trend is likely to continue as stricter emission regulations are introduced. For aircraft applications there is also a constant desire to reduce weight, resulting in the demand for shorter length diffusers. These trends imply that, in a modern dump diffuser system, relatively large amounts of flow turning and curvature are required in the vicinity of the flame tube head, which has a significant effect on diffuser performance. It should also be noted that investigations by several authors have shown how the performance of any diffuser is affected by the flow conditions at inlet to the system. For example, Stevens et al. [7], Stevens and Wray [8], and Klein [9] noted the effects on diffuser performance due to wakes from upstream compressor outlet guide vanes. In addition, Lohmann et al. [10] considered tangential momentum within a prediffuser and showed that inlet swirl angles can increase as the flow is diffused due to reductions in axial velocity and flow radius. This latter effect may be of significance when considering the large changes in radius that must be undertaken by flow when passing around the head of the flame tube. It is therefore thought that as performance becomes more critical and designs less conservative, so it is necessary when investigating such systems to simulate accurately the inlet conditions that are typically generated by an upstream compressor.

This paper presents detailed measurements of the mean flow field and pressure distribution within a dump diffuser incorporating a flame tube of radial depth 5.5 times the passage height at pre-diffuser inlet (W/h_1). With the exception of Stevens et al. [2], this represents a significant increase in depth, and hence flow curvature, relative to other published data. In addition to the datum configuration, results are also presented for three other dump gaps. Thus, an assessment can be made of the performance penalty that will be incurred in such a system when the diffuser length is shortened by reducing the dump gap. All measurements were obtained on a fully annular facility with the diffuser located downstream of a single-stage axial flow compressor. This gave a good representation of the secondary flows, blade wakes, turbulence characteristics, rotor tip leakage, and other effects that are present at the inlet of a diffuser system operating within a gas turbine engine.

Experimental Facility

A comprehensive description of the experimental facility is given by Wray et al. [11]. Air is drawn from atmosphere into

Contributed by the International Gas Turbine Institute and presented at the 39th International Gas Turbine and Aeroengine Congress and Exposition, The Hague, The Netherlands, June 13–16, 1994. Manuscript received by the International Gas Turbine Institute February 26, 1994. Paper No. 94-GT-299. Associate Technical Editor: E. M. Greitzer.

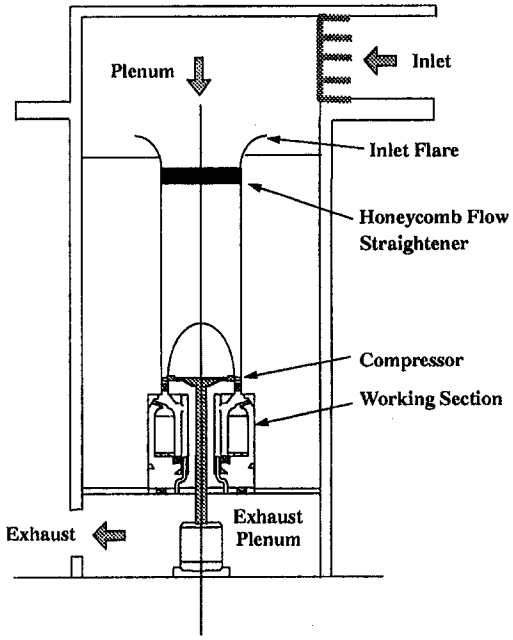

Fig. 1 Experimental facility

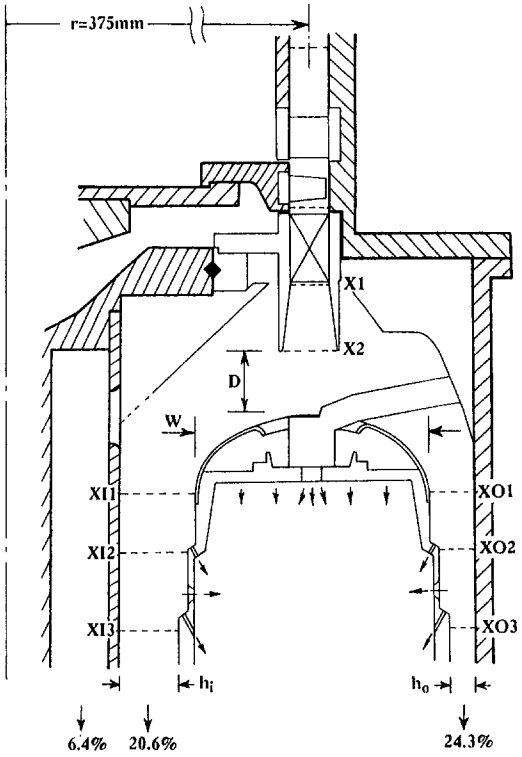

Pre-diffuser inlet height (h_1)	=	36.6mm
Pre-diffuser exit height (h_2/h_1)	=	1.35
Inner annulus height (h_i/h_1)	=	1.41
Outer annulus height (h_o/h_1)	=	0.67
Flame tube radial depth	=	5.5

Fig. 2 Diffuser geometry

a large plenum, above the vertically mounted facility, prior to passing through the entry flare, which also contains a honeycomb flow straightener (Fig. 1). The pressure rise required to draw air through the facility is provided by the single-stage axial flow compressor located immediately upstream of the working section. It consists of stationary inlet and outlet guide vane rows and a rotor, this being driven by a 45 k W DC motor sited in the exhaust plenum below the test rig. The rotor is operated at a constant nondimensional speed ($N/\sqrt{T}$) of 168.7, which, at a typical ambient temperature of 291 K, results in a rotor speed of 2880 rpm. This provides approximately 46 deg of inlet swirl to the compressor outlet guide vanes (OGVs), which are fully shrouded and representative of current engine design practice. Their operational Reynolds number of 2.6×10^5, based on blade true chord, together with the turbulence effects associated with the upstream rotor, means the blades are well above their critical transition value.

The inlet of the combustor diffuser system is located at the trailing edge of the OGVs where the passage height (h_1) is 36.6 mm with a radius of 375 mm at midpassage height (Fig. 2). For a mass flow of 4.6 kg/s, this gives a mean velocity at inlet to the prediffuser of approximately 45 m/s (Mach No. ≈ 0.13). The prediffuser is of area ratio 1.35 and has an axial length 1.5 times the inlet height (h_1). At prediffuser exit the flow enters the dump cavity, where it divides to pass into either the outer and inner feed annuli or flame tube. In addition, the results of Stevens et al. [2] have shown that removal of turbine cooling air from the dump region can significantly affect the flow properties within the feed annuli. Consequently a limited amount of air is removed through a series of plunged holes (ϕ43.5 mm) within the inner dump casing.

In its datum configuration, the distance between the exit of the prediffuser and the flame tube cowl corresponds to the annulus height at prediffuser exit (i.e., dump gap, $D/h_2 = 1.0$). Since the diffuser system is not canted, additional dump gaps of 0.80, 0.65, and 0.50 were obtained merely by raising the

Nomenclature

A = area
C_p = static pressure recovery coefficient
D = dump gas distance (Fig. 2)
h = annulus passage height
L = diffuser axial length (Fig. 14)
m = mass flow
N = compressor rotor speed
OGV = compressor outlet guide vane
p = local static pressure
P = local stagnation pressure
r = radius relative to rig centreline
r_i = inner casing radius relative to rig centerline
r_o = outer casing radius relative to rig centerline
T = ambient temperature, K
U = axial velocity
U_t = tangential velocity
W = flame tube radial depth
W' = radial flow deflection (Fig. 14)
λ = stagnation pressure loss coefficient
ρ = fluid density
θ = flow swirl angle

Superscripts

$\bar{}$ = area-weighted spatial mean value
$\tilde{}$ = mass-weighted spatial mean value
c = circumferentially weighted mean value

Subscripts

1, 2 = stations at prediffuser inlet, exit (Fig. 2)
$O1$, $O2$, $O3$ = stations within outer annulus (Fig. 2)
$I1$, $I2$, $I3$ = stations within inner annulus (Fig. 2)

complete flame tube unit by the required distance. Porosity through the cowl head is provided by holes (ϕ79.5 mm) in each of the 20 burner sectors, this flow then entering the combustor primary zone through the cowl backplate. Also located within the center of each cowl hole is a burner, with representative porosity, and an attached fuel feed arm. Flow can also enter the flame tube through primary cooling rings, primary ports, and secondary cooling rings located in both the outer and inner feed annuli. At the entry plane to each annulus the radial depth of the flame tube is 5.5 times the passage height at prediffuser inlet; however, this ratio increases to 6.3 downstream of the second cooling ring. A series of throttles located below the working section allowed, for a given geometry, the correct mass flow split and overall mass flow to be set. All results presented in this paper were obtained for a mass flow split of:

Outer feed annulus	24.3%
Inner feed annulus	20.6%
Turbine bleed passage	6.4%
(Flame tube)	48.7%

[N.B. Food annulus and flame tube mass flows measured downstream of second cooling rings].

The division of mass flow to the turbine bleed passage and feed annuli were maintained to within ± 0.1 and ± 0.5 percent of their respective nominal values. The flow, having passed through the working section and throttle system, was expelled to atmosphere via the exhaust plenum below the facility.

Instrumentation

Data presented in this paper were mainly derived from measurements with miniature five-hole pressure probes of overall diameter 1.7 mm, hole bore 0.25 mm, which were used in a nonnulled mode as outlined by Wray et al. [11]. Measurements were made 2 mm downstream of the OGV trailing edge, 1 mm downstream of prediffuser exit, and at up to three planes within each feed annulus (Fig. 2). At all these stations area traverses were performed. For measurements within the prediffuser and outer annulus, radial movement of the instrumentation was obtained by attaching the probes to stepper motors located on the outer casing. In addition, to avoid numerous circumferential instrumentation locations, the OGV row and flame tube could be indexed around to provide the required circumferential movement. For measurements within the inner annulus a traversing mechanism was mounted inside the flame tube. As described by Wray et al. [11] this could be rotated circumferentially, independent of the flame tube, while also providing radial movement of the probe. Using these techniques, data were recorded at 20 radial positions, and this was repeated at 21 circumferential locations for each traverse plane. The area traversed either corresponded to one OGV blade space, as at prediffuser inlet, or one burner sector for measurements within the feed annuli. At prediffuser exit measurements were made across an OGV space and a burner sector in order to define accurately the blade wakes and assess the influence of cowl head geometry at this location. Numerous static tappings were also located within the dump cavity, around the flame tube head, and on the casing walls within the feed annuli and turbine bleed passage. Stagnation pressure levels within the turbine bleed passage were derived from fixed pitot rakes. Operation of the test rig, positioning of the instrumentation, and digitizing of all pressure transducer signals was controlled by a Personal Computer (PC).

Data Reduction

At each traverse point, five-hole probes provide information on stagnation and static pressure in addition to velocity magnitude and direction. From this information the overall mean velocity at a traverse plane was calculated using an area-weighted method so that:

$$\bar{U} = \frac{1}{A}\int U dA \tag{1}$$

with the mass flow rate through a traverse plane being defined as

$$m = \int \rho U dA = \rho \bar{U} A \tag{2}$$

Spatially averaged values of stagnation and static pressures at a traverse plane were defined by mass weighting the appropriate individual values, i.e.,

$$\tilde{P} = \frac{1}{m}\int P dm \quad \tilde{p} = \frac{1}{m}\int p dm \tag{3}$$

For radial distributions of circumferentially averaged quantities, this weighting was performed in the circumferential direction only. All flow angles presented were derived from the mass-weighted tangential and area-weighted axial velocity components as outlined by Dring and Spear [12]. It should also be noted that all of these averaged quantities were derived by numerical integration of the data to which had been fitted a spline curve.

Changes in the spatially averaged pressures between various planes within the diffuser system are expressed in terms of the stagnation pressure loss (λ) and static pressure recovery (C_p) coefficients:

$$\lambda_{a-b} = \frac{\tilde{P}_a - \tilde{P}_b}{\tilde{P}_a - \tilde{p}_a} \quad C_p = \frac{\tilde{p}_b - \tilde{p}_a}{\tilde{P}_a - \tilde{p}_a} \tag{4}$$

where "a" and "b" are the upstream and downstream planes, respectively.

Estimate of Experimental Errors

At a given data point the experimental accuracy is influenced by:

(i) the spatial error associated with the finite distance between the five holes on the probe tip; this was eliminated by radial and circumferential interpolation of the side pressures onto the central measurement hole [11].
(ii) the proximity of casing surfaces to a measurement location.
(iii) recording of the pressure signals via transducers and an analogue to digital convertor.
(iv) maintaining the compressor on its correct operating point.

Discrepancies in mass flow of less than 2 percent were recorded between the pre-diffuser inlet and exit planes due to these sources of error. Based on these values and the repeatability of test data it was estimated that the stagnation pressure loss (λ) and static pressure recovery (C_p) coefficients were accurate to within 0.01 of their true values. Flow angles were thought to be in error by up to 1 deg.

Results and Discussion

Results are presented for the diffuser in its datum configuration, with a dump gap of 1.0, and at three additional dump gaps of 0.80, 0.65, and 0.50.

Inlet Conditions. Axial velocity contours indicate the circumferential and radial distribution of fluid at inlet to the diffuser system (Fig. 3). As well as boundary layers on each casing, well-defined blade wakes are present from the upstream compressor outlet guide vanes. Within experimental error, these inlet conditions were the same for all the geometries tested.

Several authors have noted how the performance of a diffuser system varies with inlet conditions. For example, Stevens et al. [8] have shown that blade wakes can have a favorable effect by re-energizing boundary layer flow due to enhanced mixing.

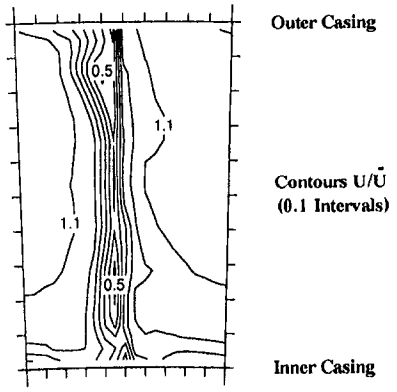

Fig. 3 Axial velocity distribution at prediffuser inlet

However, the presence and mixing out of such flow nonuniformities will lead to an increase in the diffuser system's mass-weighted pressure loss. To try and reduce this loss variation with inlet conditions Klein [9] defines diffuser performance in terms of momentum mix weighted values. In this case, overall stagnation and static pressures at the inlet and exit planes are those which would occur if the respective velocity profiles were to mix out in a frictionless duct of constant area. However, within a diffuser system the flow area increases and, as outlined by Denton [13], the resulting positive pressure gradient increases the mixing losses, which are not accounted for in the momentum mix approach.

It should be noted that all performance data presented in this paper are in terms of mass-weighted pressures and therefore include not only the favorable effects of wake mixing, on boundary layer flow, but also any mixing loss associated with the nonuniform inlet flow.

Datum Configuration. The stagnation pressure losses (λ) between prediffuser inlet ($X1$) and the outer ($XO3$) and inner ($XI3$) feed annuli are 0.483 and 0.430, respectively. Since the loss within the prediffuser is 0.068, this implies that a large proportion of the loss occurs downstream of the prediffuser as the flow passes around the flame tube head and enters the feed annuli. It is also interesting to note the relatively high stagnation pressure loss (λ), of 0.664, that is associated with the flow entering the turbine bleed passage. This represents low-energy high-loss flow that is drawn through the bleed ports from the inner dump cavity. The remaining flow passes to the inner annulus and so, by removing low-energy air, this may account for the relatively low loss within this annulus relative to the outer feed annulus. With this in mind it is interesting to note the combined mass weighted inner annulus and turbine bleed loss of 0.485 is virtually the same as the outer feed annulus loss of 0.483.

The prediffuser static pressure recovery coefficient (C_p) of 0.373 is a significant proportion of the total static pressure recovery values of 0.448 and 0.510 recorded between prediffuser inlet and the outer ($XO3$) and inner ($XI3$) feed annuli. Although there is a relatively large velocity reduction between prediffuser exit ($\approx$33 m/s) and the feed annuli ($\approx$11 m/s), the static pressure rise is significantly reduced by the relatively high stagnation pressure loss around the flame tube head. It can therefore be seen that in terms of overall diffuser performance, the majority of the static pressure rise occurs within the prediffuser.

It should be noted that diffuser performance is based on the overall mean flow properties at each traverse plane. However, there will be slight variations between these values and the actual loss and diffusion incurred along each flow path. This is because the actual values depend on which portion of the prediffuser flow passes into the feed annuli or turbine bleed passage. For example, assuming it is the 24.3 percent of the flow closest to the prediffuser outer casing that passes to the outer feed annuli, then a dividing streamline can be obtained and mass-weighted pressures for that streamtube calculated. This yields, for the flow passing to the outer annulus, a loss of 0.082 within the prediffuser (λout_{1-2}) and a total loss of 0.459 (λout_{1-03}). Applying a similar technique to the inner annulus flow gives, for the prediffuser and total loss, values of 0.048 (λin_{1-2}) and 0.408 (λin_{1-I3}), respectively. Comparison with the data based on overall mean flow properties indicates some differences, but variations are relatively small and show the same trend of high losses around the flame tube head. Similarity of the results is thought to reflect the lack of large radial flow distortions at inlet to, and within, the prediffuser as well as a comparable stagnation pressure loss at different radii. In addition, this streamtube method was first used by Fishenden and Stevens [1] whose flame tube incorporated no porosity. However, the head porosity in this investigation means that, as well as radial location, the flow path at prediffuser exit is also determined by whether it is in line with, or between, cowl holes. Thus, flow entering each feed annuli is more uniformly distributed at prediffuser exit and is not confined to streamtubes adjacent to each casing.

Flow Field Characteristics. Comparison of the axial velocity contours at prediffuser inlet (Fig. 3) and exit (Fig. 4) indicates decay of the compressor OGV blade wakes within the prediffuser. As discussed by Hill et al. [14], in large positive gradients the pressure forces can increase the velocity gradients since the momentum of the slower moving fluid undergoes a greater reduction compared with the faster moving fluid. However, decay of the blade wakes means that in this geometry it is the flow shear forces, rather than the pressure forces, which are predominant. The radial distribution of flow at inlet ($X1$) and exit ($X2$) from the prediffuser is more clearly indicated by the circumferentially averaged axial velocity profiles (Fig. 5). These are nondimensionalized by the calculated mean velocity at each plane and comparison of the profiles indicates the boundary layer growth that occurs along each prediffuser casing. This leads to a radial redistribution of fluid so that, at prediffuser exit, there is a relative increase in the amount of flow in the center of the prediffuser (between 10 and 90 percent of annulus height). The boundary layer growth is promoted by the positive pressure gradient within the prediffuser due to the increasing flow area. This pressure rise is shown by the static pressure profiles at each plane, which are nondimensionalized by the conditions at prediffuser inlet (Fig. 5). It should also be noted

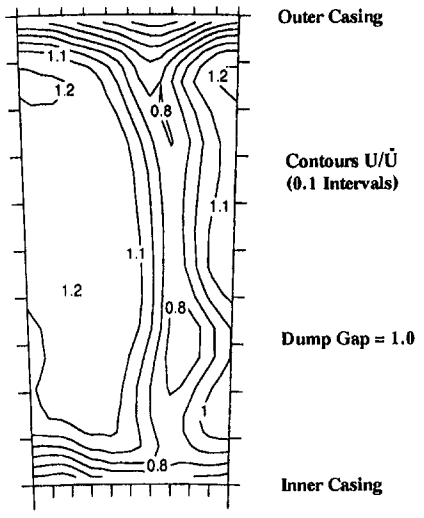

Fig. 4 Axial velocity distribution at prediffuser exit

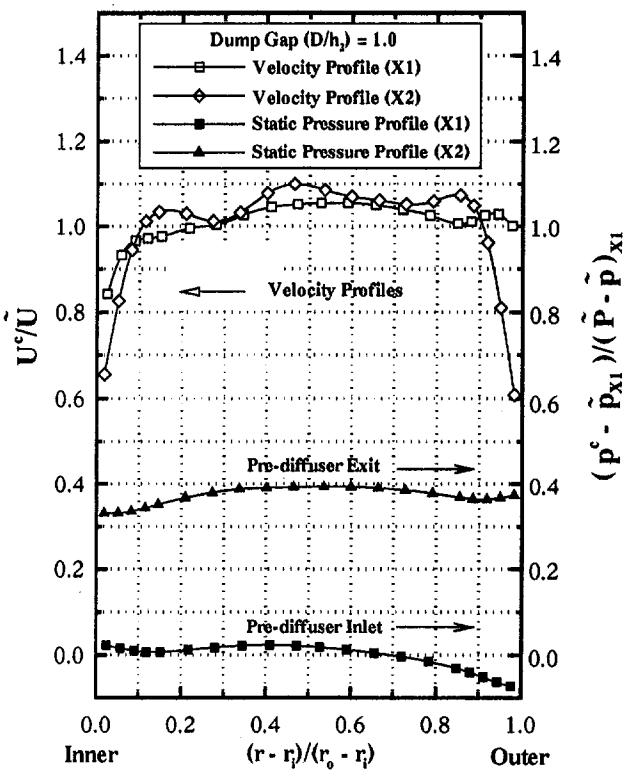

Fig. 5 Axial velocity and static pressure profiles

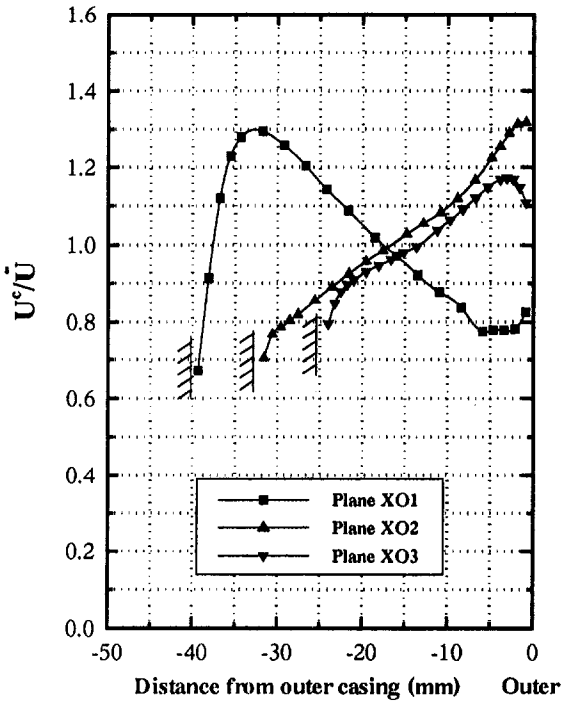

Fig. 7 Outer annulus axial velocity profiles (dump gap = 1.0)

that due to gradients of pressure in the radial direction, the pressure increase along each casing is different. This is thought to contribute to the more pronounced growth of the boundary layer along the outer casing.

At prediffuser exit the flow separates to form a recirculation zone in the dump cavity. This region bounds the mainstream flow, which is discharged into the dump region and impinges on the flame tube head. The flow accelerates around the head, away from the stagnation point, giving rise to high velocities adjacent to the cowl surface (Fig. 6). This is reflected by the measured static pressure distribution on this surface that is presented later (Fig. 12). The maximum velocity acquired is determined mainly by the curvature undertaken by the flow as it passes around the head and into the feed annuli. Measurements by Carrotte et al. [6] and Stevens et al. [2] have also shown how the velocity away from the cowl, toward the recirculation region, decreases rapidly. It is the high-velocity gradients in this region where a significant amount of turbulence, and hence stagnation pressure loss, is generated [6]. At entry to each feed annulus the flow distribution is still biased toward the flame tube, as shown for the outer feed annuli by the circumferentially averaged axial velocity profile at plane $XO1$ (Fig. 7). However, due to the unstable nature of the flow passing around the head, this bias rapidly changes toward the outer casing, as measured at plane $XO2$ downstream of the first cooling ring (Fig. 7). The turbulence in this region is relatively high and, in several other investigations, has led to rapid mixing out of the velocity profile. Comparison of the profiles at stations $XO2$ and $XO3$ shows this is not apparent in the present investigation. However, it is thought the passage of air into the flame tube through primary ports and the secondary cooling ring helps maintain the distorted profile down the feed annulus, features that are often not simulated in other investigations. Although not presented, similar bias characteristics and axial velocity profiles have been measured for the flow passing down the inner annulus.

As well as the radial distribution of flow, significant variations in the swirl angle were found as the flow passed through the diffuser system (Fig. 8). At prediffuser inlet the increased swirl angles close to each casing (within 10 percent of the passage height) reflect the presence of flow overturning due to classical secondary flow within the upstream OGV passage. This is a usual occurrence within the stationary blade rows of axial compressors. Flow overturning by the OGVs, of approximately 3 deg, is also indicated within the central region of the passage. The presence of this tangential momentum at inlet to the system leads to significant changes in the swirl angles (θ) farther downstream, particularly for the flow passing to the inner annulus (Fig. 8). This is due to the change in radius, relative to the engine centerline, that is undertaken by the flow within the diffuser system and the reduction in axial velocity. For example, if tangential momentum is conserved, then the product of a particle's tangential velocity and radius ($U_t r$) is constant so that, as $\tan\theta = U_t/U$, then $\tan\theta \propto 1/Ur$. Within the prediffuser, the mean radius is constant and so the increase of swirl angle at prediffuser exit is mainly due to the reduction in axial velocity (U). For flow passing to the outer annulus, a further reduction in axial velocity occurs, but this is also accompanied by an increase in radius (r) leading to minimal change in swirl angle. In contrast, flow entering the inner feed annulus undergoes both a reduction in axial velocity and radius so that flow swirl significantly increases. This effect may be enhanced further if the flow close to the inner casing of the prediffuser, which has been overturned within the OGV passage, passes into the inner annulus. The calculated tangential momentum per unit mass flow at prediffuser inlet (0.85 $m^2 s^{-1}$), exit (0.83 $m^2 s^{-1}$), and within the outer (0.36 $m^2 s^{-1}$) and inner (0.49 $m^2 s^{-1}$) feed

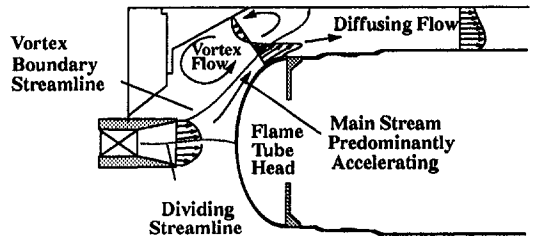

Fig. 6 Flow field downstream of pre-diffuser

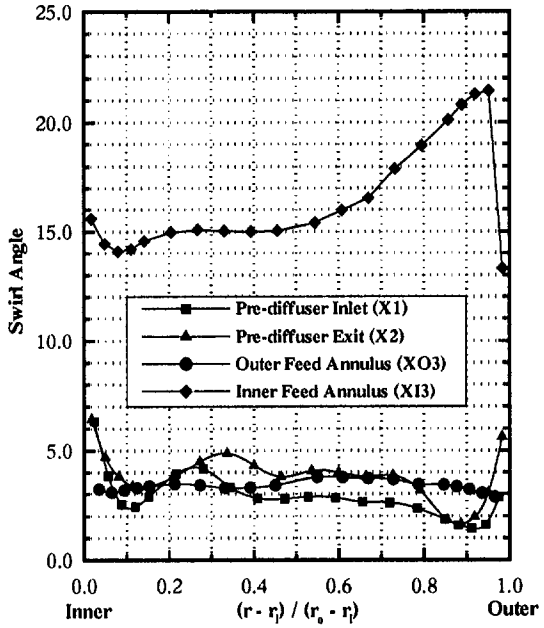

Fig. 8 Swirl angle profiles through the diffuser (dump gap = 1.0)

annuli was calculated using a similar method to that outlined by Dring [15]. Due to friction it can be seen that a relative decrease of tangential momentum occurs through the diffuser system. Although this reduces the magnitude of the swirl, angles in excess of 15 deg are still recorded within the inner annulus. The presence of such swirl is thought to have only a minor effect on the diffuser's static pressure rise and stagnation pressure loss. However, of greater significance is thought to be its effect on the discharge coefficients for the inner annulus cooling rings, primary and dilution ports as well as the behavior and stability of the flow passing through these features. Carrotte and Stevens [16] have already indicated how vortices and other flow instabilities can develop within dilution holes and affect mixing within the combustion chamber. It should also be noted that as radial flame tube depth increases, so this amplification of swirl angle will become greater. Furthermore, for a given geometry the magnitude of the angles within the inner annulus is determined by the swirl at diffuser inlet, and in a gas turbine engine this will vary with engine speed.

Effects of Dump Gap Variation. The variation of stagnation pressure loss to the turbine bleed passage (Xb), outer ($XO3$), and inner ($XI3$) feed annuli increases significantly as the dump gap is reduced (Fig. 9*a*). For example, at a dump gap of 0.50 the loss to the inner and outer feed annuli increases by 48 and 32 percent, respectively, relative to the datum configuration. Since the overall performance of the prediffuser does not vary significantly and the loss within each feed annulus is small, virtually all the increase in stagnation pressure loss occurs within the vicinity of the flame tube head (i.e., between stations $X2$ and $XO1$, $XI1$). In addition to the increased stagnation pressure loss, there is also a corresponding decrease in static pressure recovery (Fig. 9*b*). Although a small proportion of this reduction is associated with more distorted velocity profiles within each feed annulus, the majority of this effect is due to the higher stagnation loss. For all the geometries tested, the static pressure rise within the prediffuser is virtually the same, while at large dump gaps there is an additional pressure rise between prediffuser exit ($X2$) and the feed annuli. As the dump gap reduces, the increased stagnation pressure loss around the head reduces the static pressure rise. Eventually, at dump gaps less than approximately 0.65, the loss is of sufficient magnitude that the static pressure falls downstream of prediffuser exit.

Prediffuser Performance. The overall prediffuser performance does not vary significantly with dump gap, but changes to the flow field do occur in this region. At prediffuser exit the circumferentially averaged radial static pressure profiles, nondimensionalized by the mean flow properties at the inlet plane, indicate that reducing the dump gap causes an increase of static pressure in the central region of the passage and a decrease toward each casing (Fig. 10). This reflects the pressure distribution that is generated by flow curvature around the flame tube head, which, due to the flame tube's upstream influence, becomes apparent at prediffuser exit when the dump gap is small. Fishenden and Stevens [1] also noted this effect and, since inlet conditions are not affected, means that diffusion is increased along the center streamtube of the prediffuser but decreased close to each casing. These effects are also reflected by the axial velocity profiles at prediffuser exit (Fig. 11), the midpassage velocities decreasing with a corresponding rise in velocity close to each casing.

The lower static pressure gradient along the prediffuser casings at small dump gaps reduces boundary layer growth. Hence, as dump gap is reduced, it should be possible to introduce corresponding increases in prediffuser area ratio, within the same axial length, and not adversely affect the condition of the boundary layers on each casing. This should increase the static pressure recovery within the prediffuser and help offset the larger stagnation pressure losses around the flame tube head. With this in mind it is also interesting to note the work of Hestermann et al. [5], who unstalled a prediffuser by operating the system at a reduced dump gap.

Dump Cavity Flow. It is in the region surrounding the flame tube head where most of the loss increase occurs as the dump gap is reduced. Although instrumentation is limited, cowl sur-

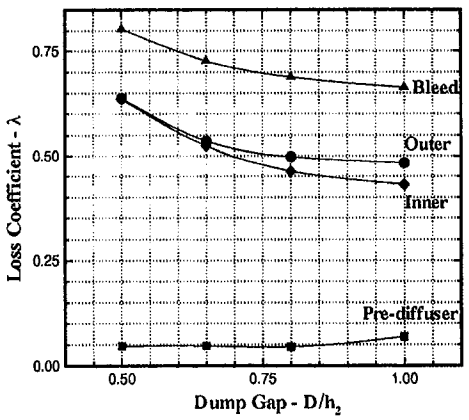

a) Stagnation Pressure Loss (λ)

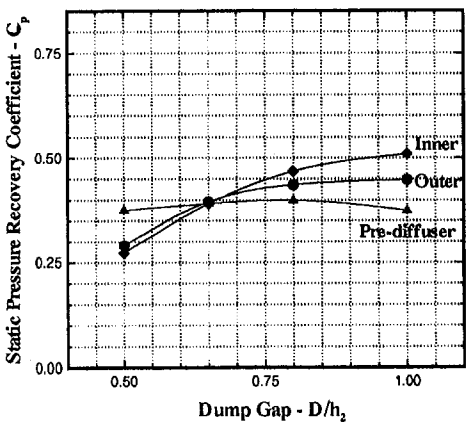

b) Static Pressure Rise (C_p)

Fig. 9 Effect of dump gap on diffuser performance

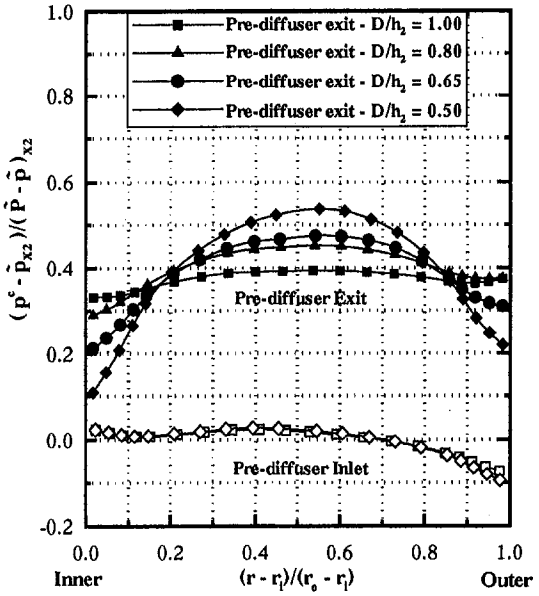

Fig. 10 Prediffuser exit static pressure profiles

face tappings allow the static pressure distribution, averaged over one OGV blade space, to be determined around the head. It can be seen that away from the stagnation point, the pressure decreases rapidly to a minimum before undergoing a rise in pressure prior to entering each feed annulus (Fig. 12). This static pressure distribution reflects the velocities adjacent to the cowl surface, which accelerate from zero at the stagnation point up to a maximum value, at the minimum pressure location, prior to diffusing into the downstream annuli. In addition, as measured by Carrotte et al. [6] away from the flame tube head, toward the recirculation region, the velocity decreases rapidly giving rise to steep velocity gradients. It is these gradients where turbulent energy is produced and the stagnation pressure loss generated. As the dump gap is reduced the minimum pressure on the head decreases, indicating higher velocities adjacent to the surface. A corresponding increase of the velocity gradients around the head must therefore occur, thus explaining the increase in stagnation pressure loss. The higher velocities and

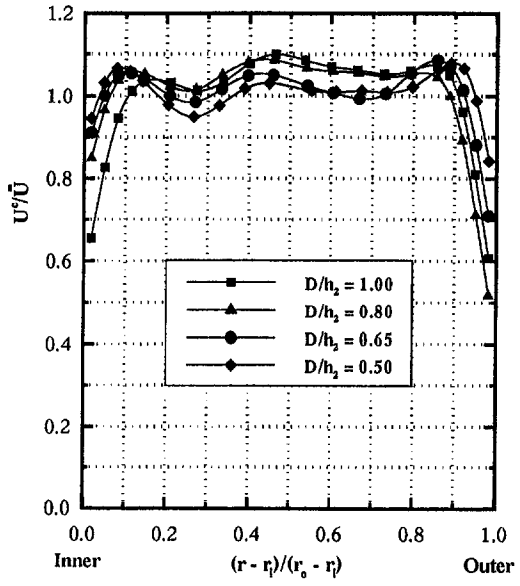

Fig. 11 Prediffuser exit axial velocity profiles

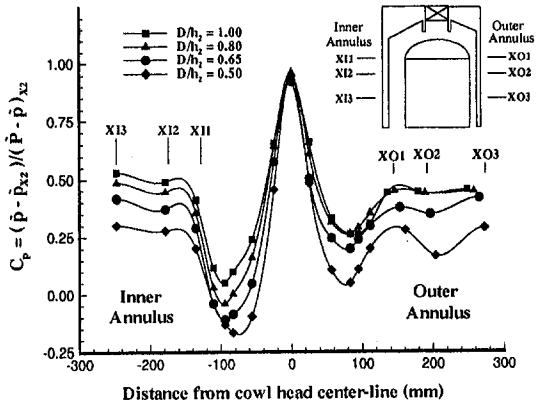

Fig. 12 Flame tube head static pressure distribution

steeper velocity gradients are due to the greater curvature and more rapid rates of deflection that must be undertaken by the flow, at small dump gaps, in order to pass around the flame tube head and into the feed annuli. These more distorted profiles are also indicated by the axial velocity profiles within the downstream annuli (Fig. 13). It should also be noted that as dump gap is reduced, the stagnation pressure loss incurred by fluid passing to the inner annulus increases at a greater rate compared with the outer annulus flow. This is also reflected by the greater reduction in minimum static pressure on the inner annulus side of the cowl surface (Fig. 12). One possible reason for this effect is that flow passing to the outer annulus is subjected to an increasing radius and can therefore diffuse circumferentially around the head. This is in contrast to flow passing to the inner annulus where the decreasing radius may lead to higher cowl velocities, steeper velocity gradients, and increased losses. Furthermore, downstream of the minimum pressure location the rapid rise in pressure, at small dump gaps, means the flow in this region is prone to separate from the cowl surface.

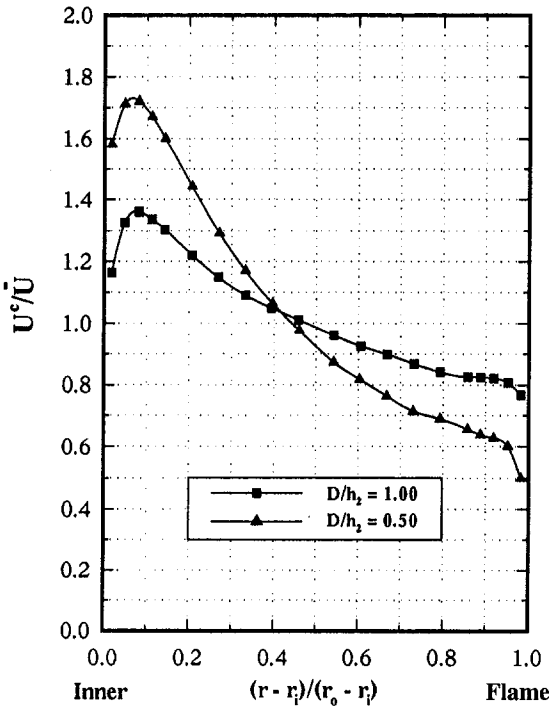

Fig. 13 Inner annulus axial velocity profiles (XI3)

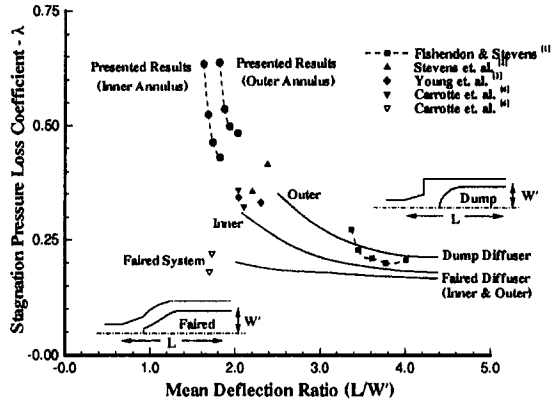

Fig. 14 Comparison of combustor diffuser system losses

Comparison With Other Data. The stagnation pressure losses from a variety of published data are presented (Fig. 14) relative to the ratio of diffuser length (L) to flow deflection (W'). Diffuser length is defined as the axial distance between prediffuser inlet and the combustor primary ports, whereas flow deflection is based on the radial distance between the diffuser centerline and the mean radial location of each feed annulus. This latter parameter is therefore mainly a function of the flame tube radial depth. The diagram contains a wide variety of results from various diffuser systems with differing inlet conditions, various amounts of diffusion, flame tubes with and without porosity, etc. In addition, the definition of diffuser length and deflection can be somewhat subjective, particularly for systems with large cant angles. However, a correlation is suggested between the results, although for a given geometry, minor loss variations will occur due to changes in mass flow split, prediffuser area ratio, cowl shape, etc. The general trend indicates that for diffusers with relatively long lengths and narrow flame tubes, the losses are relatively low and of comparable magnitude to those of a faired system [1]. However, the deeper flame tubes and shorter lengths inherent to more modern systems result in larger flow deflections and a more severe radius of curvature as the flow passes around the head. As already discussed and demonstrated by the results, this leads to increased pressure losses. For diffusers typical of the geometry tested in this paper, any further reductions in length or increases in flame tube depth will lead to relatively large pressure loss penalties. Hence, any potential benefits in terms of weight reduction, for example, may be more than offset by the adverse effect on engine specific fuel consumption.

Included in the comparison are the results of Carrotte et al. [6] obtained for a short faired system. This indicates that for relatively short diffusers with deep flame tubes, there are large differences in loss performance between dump and faired systems. Due to their stability characteristics, it is not thought practical or desirable to operate such faired systems within a gas turbine engine. However, as diffuser systems become shorter and flame tubes deeper, it may be desirable to investigate a possible hybrid or compromise system. This would utilize some of the potential loss reduction offered by a faired system while still achieving acceptable stability performance.

Conclusions

An experimental investigation has been undertaken on a modern dump diffuser system with inlet conditions being generated by an axial flow compressor. Measurements were obtained at a dump gap of 1.0 (datum configuration) and at three other dump gaps (0.80, 0.65, and 0.50). The following conclusions have been drawn:

- For the datum configuration, the stagnation pressure loss coefficients (λ) between prediffuser inlet and the outer and inner feed annuli were 0.483 and 0.430, respectively. The majority of this loss was generated around the flame tube head while most of the static pressure rise occurred within the prediffuser.
- The stagnation pressure losses increased by 32 (outer) and 48 percent (inner) as the dump gap was reduced from 1.0 (datum) to 0.50.
- The high losses were associated with the relatively deep flame tube and short system length. This increases the amount of flow curvature around the flame tube head, which becomes more severe as dump gap is reduced.
- For all the geometries tested, relatively high swirl angles ($\approx$15 deg) were observed within the inner feed annulus compared with those at prediffuser inlet ($\approx$3 deg). This amplification is due to the decrease in axial velocity and radius that is undertaken by the flow passing to the inner annulus.

Acknowledgments

This work has been carried out with the support of Rolls Royce PLC, Bristol, and the Defence Research Agency, Pyestock. The authors would also like to acknowledge Messrs. R. Marson, D. Glover, L. Monk, and W. Nivin for their assistance in the manufacture of the test rig and to Mr. A. P. Wray for his help in the design of this facility.

References

1 Fishenden, C. R., and Stevens, S. J., "Performance of Annular Combustor-Dump Diffusers," *J. Aircraft,* Vol. 14, No. 1, Jan. 1977.

2 Stevens, S. J., Wray, A. P., and Price, P. D., "The Aerodynamic Performance of a Modern Vaporising Combustor Dump Diffuser," Paper No. AIAA-88-3273 1988.

3 Young, K. F., Wray, A. P., and Stevens, S. J., "An Integrated Approach to the Design of Compressor OGVs and Combustor Pre-diffusers," Dept. of Transport Technology, Loughborough University, TT89R03, 1989.

4 Srinivasan, R., Freeman, G., Grahmann, J., and Coleman, E., "Parametric Evaluation of the Aerodynamic Performance of an Annular Combustor-Diffuser System," Paper No. AIAA-90-2163, 1990.

5 Hestermann, R., Kim, S., and Wittig, S., "Geometrical Dependence of the Fluid Dynamic Performance Parameters of Plane Combustor Model Diffusers," AIAA ISABE 91-7105, 1991.

6 Carrotte, J. F., Denman, P. A., Wray, A. P., and Fry, P., "Detailed Performance Comparison of a Dump and Short Faired Combustor Diffuser System," ASME JOURNAL OF ENGINEERING FOR GAS TURBINES AND POWER, Vol. 116, 1994, pp. 517–526.

7 Stevens, S. J., Harasgama, S. P., and Wray, A. P., "The Influence of Blade Wakes on the Performance of Combustor Shortened Prediffusers," *AIAA J. of Aircraft,* Vol. 21, No. 9, 1984.

8 Stevens, S. J., and Wray, A. P., "The Influence of Blade Wakes on the Performance of Outwardly Curved Combustor Pre-diffusers," Paper No. AIAA-85-1291, 1985.

9 Klein, A., "The Relation Between Losses and Entry-Flow Conditions in Short Dump Diffusers for Combustors," *Z. Flugwiss. Weltraumforsch,* Dec. 1988.

10 Lohmann, R. P., Markowski, S. J., and Brookman, E. T., "Swirling Flow Through Annular Diffusers With Conical Walls," ASME *Journal of Fluids Engineering,* Vol. 101, June 1979.

11 Wray, A. P., Carrotte, J. F., and Wilson, C. W., "The Development of a Large Annular Facility for Testing Gas Turbine Combustor Diffuser Systems," Paper No. AIAA-93-2546 1993.

12 Dring, R. P., and Spear, D. A., "The Effects of Wake Mixing on Compressor Aerodynamics," ASME *Journal of Turbomachinery,* Vol. 113, 1991, pp. 600–607.

13 Denton, J. D., "Loss Mechanisms in Turbomachines," ASME *Journal of Turbomachinery,* Vol. 115, 1993, pp. 621–656.

14 Hill, P. G., Scaub, U. W., and Senoo, Y., "Turbulent Wakes in Pressure Gradients," ASME *Journal of Applied Mechanics,* Vol. 85, 1963.

15 Dring, R. P., "Radial Transport and Momentum Exchange in an Axial Compressor," ASME *Journal of Turbomachinery,* Vol. 115, 1993, pp. 477–486.

16 Carrotte, J. F., and Stevens, S. J., "The Influence of Dilution Hole Geometry on Jet Mixing," ASME JOURNAL OF ENGINEERING FOR GAS TURBINES AND POWER, Vol. 112, January 1990.

Flow Field and Performance Characteristics of Combustor Diffusers: A Basic Study

R. Hestermann

S. Kim

A. Ben Khaled

S. Wittig

Lehrstuhl und Institut für
Thermische Strömungsmaschinen,
Universität Karlsruhe
Karlsruhe, Federal Republic of Germany

Results of a detailed study concerning the influence of geometric as well as fluid mechanic parameters on the performance of a plane model combustor diffuser in cold flow are presented. For a qualitative insight into the complex flow field inside the prediffuser, the sudden expansion region, and the flow field around the flame tube dome, results of a flow visualization study with the hydrogen bubble method as well as with the ink jet method are presented for different opening angles of the prediffuser and for different flame tube distances. Also, quantitative data from detailed measurements with LDV and conventional pressure probes in a geometrically similar air-driven setup are presented. These data clearly demonstrate the effect of boundary layer thickness as well as the influence of different turbulence levels at the entry of the prediffuser on the performance characteristics of combustor diffusers. The possibility of getting an unseparated flow field inside the prediffuser even at large opening angles by appropriately matching the diffuser's opening angle and the flame tube distance is demonstrated. Also, for flows with an increased turbulence level at the entrance—all other conditions held constant—an increased opening angle can be realized without experiencing flow separation. The comparison of the experimental data with predictions utilizing a finite-volume-code based on a body-fitted coordinate system for diffusers with an included total opening angle less than 18 deg demonstrates the capability of describing the flow field in combustor diffusers with reasonable accuracy.

Introduction

One of the most challenging tasks in the design of future generations of gas turbine engines is to minimize the pollutant emissions and to maintain at least identical lifetime as well as the reliability of the entire engine at improved efficiency. In order to be successful, the combustion process inside the combustor's flame tube has to be controlled effectively even under the extreme conditions of high temperature and high pressure. With its dominating effect on the flow field inside and outside the flame tube, the combustor diffuser shows considerable potential in optimizing gas turbine engines. For reasons of high efficiency, the combustor diffuser has to decelerate the flow with minimum pressure loss, resulting in a pressure level in the region surrounding the flame tube as high as possible to ensure deep penetration of the air jets into the flame tube. Also, for reasons of reliability, the combustor diffuser has to provide similar flow profiles at the diffuser's exit under a wide range of operating conditions. The factor limiting the performance of diffusers is the onset of flow separation, which is influenced—among other parameters—by the length and the opening angle of the diffuser. The diffuser length is an even more important parameter in the design of jet engines than in the design of stationary gas turbine engines because of its effect on engine weight and rotor stiffness. Modern gas turbine combustor diffusers are of relatively short design comprising a prediffuser to reduce the air velocity followed by a sudden expansion. Whereas for conventional diffusers performance charts exist (see, e.g., Reneau et al., 1967), little information is available for the correlation of the geometric and fluid dynamic parameters and the corresponding performance parameters for combustor diffusers. In comparison with conventional diffusers, additional parameters exist influencing combustor diffuser's performance, especially the shape and the position of the flame tube relative to the prediffuser, the width of the flame tube annuli surrounding the flame tube, as well as the position and size of mixing holes along the flame tube's wall.

Up to now, relatively few studies can be found that consider these parameters systematically. In general, the design is based on the well-known results of Reneau et al. (1967), Kline et al. (1969), Adkins (1983), and Adkins and Wardle (1992). Earlier studies of the characteristics of annular diffusers were presented by Ainley (1945), Johnston (1953), and Howard et al. (1967), but without taking into account flame tube effects. Biaglow (1971) could demonstrate the advantage of dump-type diffuser configurations compared to faired diffusers. He showed that the temperature distribution at the exit of a two-dimensional model of a dump diffuser is insensitive to the inlet velocity profile. In an extensive study, Fishenden and Stevens (1974) examined the influence of the prediffuser geometry, the flow split between the two annuli surrounding the flame tube, and the distance between the flame tube and the prediffuser exit. The largest area ratio of the prediffusers under examination was 1.8. Klein (1988) in his work showed that the radial velocity profile more than the circumferential velocity profile determines the performance characteristics of combustor diffusers. Wagner et al. (1980) investigated the effects of flow splits on the performance of a curved wall dump diffuser with a canted prediffuser. More recently, Srinivasan et al. (1990) published the results of an experimental study concerning the effects of flame tube distance, flow split, prediffuser inlet velocity profile and combustor channel height on diffuser performance in a 60 deg sector element of a combustor diffuser. Despite the increasing efforts to obtain more experimental data to describe the correlation between geometric, fluid dynamic, and diffuser performance parameters, there is still a lack of accurate data. A comparison of the available results is difficult because of the different geom-

Contributed by the International Gas Turbine Institute and presented at the 39th International Gas Turbine and Aeroengine Congress and Exposition, The Hague, The Netherlands, June 13–16, 1994. Manuscript received by the International Gas Turbine Institute February 19, 1994. Paper No. 94-GT-212. Associate Technical Editor: E. M. Greitzer.

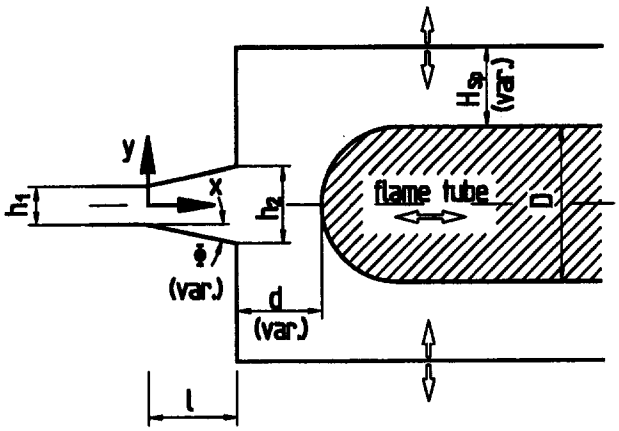

Fig. 1 Sketch of the model diffuser

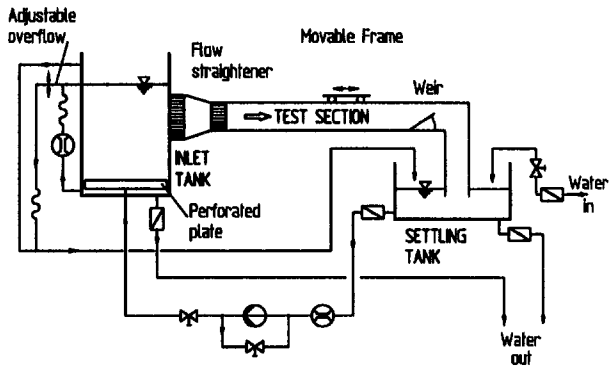

Fig. 2 Water test facility

etries and fluid dynamic boundary conditions. Sovran and Klomp (1967) basically show the correlation between the performance parameters of plane, conical, and annular diffusers. However, the effect of flame tubes is not considered. Therefore, up to now it is not possible to generate a general performance chart for combustor diffusers, comparable to those for plane diffusers (e.g., Reneau et al., 1967).

A solution in the design of diffusers for gas turbine combustor applications is found in the use of numerical codes to predict the flow field. The possibility to calculate the flow field inside complex geometries has been shown by us as well as by various authors (see, e.g., Shyy, 1985; Noll, 1986; Koutmos and McGuirk, 1989; Noll et al., 1989; Noll and Wittig, 1991). To verify and to improve available computer codes, detailed experimental data with well-defined boundary conditions are required. In extending our earlier studies of diffusers (Kim, 1976), two test facilities were developed. Both are equipped with plane model combustor diffusers. The plane arrangement has the advantage of good accessibility and flexibility and in addition is sufficient to demonstrate the flow behavior in annular dump diffusers, as was shown by Little and Manners (1993) in a recently published paper. In the air-driven test rig, detailed measurements with LDV as well as with conventional instrumentation were performed. A description of the setup and the measuring techniques used is presented elsewhere (Hestermann et al., 1991). The second test facility is used mainly for flow visualization studies and uses water as the fluid. In the following, a description of the water test facility and the techniques used for flow visualization is presented along with the results. Also some results of the LDV measurements in the air-driven setup are presented.

Experimental Setup

The diffuser model under investigation in the water test facility is geometrically similar to that used in the air-driven test rig. It comprises a straight-walled prediffuser followed by a dump diffuser and a flame tube, as shown in Fig. 1. All components were made of plexiglass to enable a great variety of flow visualization techniques. Similar to the air-blown test facility, a great number of parameters can be varied independently. In this paper the visualized flow fields for different opening angles of the prediffuser and different flame tube distances are presented. To allow direct comparisons to real engine flow conditions, the experiments were conducted at Reynolds numbers, based on inlet height h_1, of about $\mathrm{Re}_{h_1} \sim 0.4 \times 10^5$. This is a good approximation of real engine conditions.

The water test facility is a closed circuit arrangement as shown in Fig. 2. The main components are the inlet tank, the test section, and the settling tank. It can be operated either with a free surface or as a covered tunnel. The cross section of the test section is 600 × 280 mm with a length of 1800 mm. The walls consist of glass to enable the use of light sheet techniques as well as of other flow visualization methods. The excellent optical access enables observation of the complete flow field all along the length of the test section. To avoid mechanical vibrations, the test section is mounted between two compensators. The flow rate can be controlled by a throttle valve and a bypass. At the exit of the test section, a weir is mounted to adjust the water height inside the test section. To measure the flow rate, a vortex meter is installed in the pipe system. The flow rate through the adjustable overflow can be measured by an additional flow meter, if necessary.

Inside the test section, a contraction module is mounted, followed by a parallel-walled entry section. To ensure turbulent flow conditions, trip wires with a thickness of 5 percent of the channel height are installed on both side walls of the entry section. The diverging diffuser walls are attached to the entry section via two cylinders allowing the adjustment of any opening angle on either side.

Flow Visualization Techniques

For the visualization of the complex flow field, two techniques have been applied: To give an impression of the entire flow field, the hydrogen bubble method is employed. In those regions where it was desirable to get additional information

Nomenclature

AR = area ratio = A_2/A_1
B = blockage factor = $1 - 1/A \times \int \frac{u}{u_{\max}} dA$
$C_{p,R}$ = pressure recovery coefficient
D = flame tube height
d = flame tube distance
d_b = diameter of the turbulence generating bars
h = channel height
H_{Sp} = annulus height
l = prediffuser length
Tu = turbulence intensity
x, y = coordinates
Φ = half-angle of the prediffuser

Subscripts

1 = reference position; $x/h_1 = -2.0$
2 = exit of prediffuser
VD = measured from reference position to prediffuser exit
ges = measured from reference position to the exit of the flame tube annuli

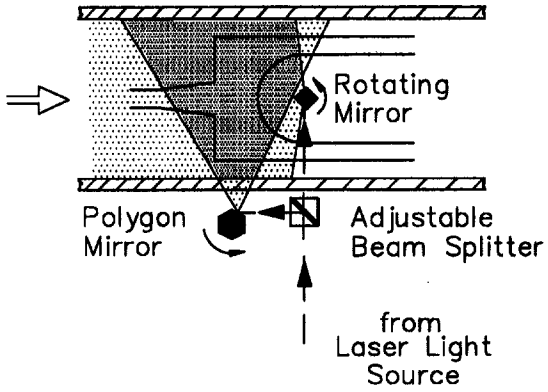

Fig. 3 Laser light sheet setup (top view)

on the flow, the ink jet method was utilized. Two different illumination techniques were used. For the hydrogen bubble method, a laser light sheet was generated by use of two rotating mirrors. The mirror positioned inside the flame tube (see Fig. 3) was encapsulated in a waterproof plexiglass box to illuminate the flow field inside the prediffuser. With the ink jet method, a standard photographic light source and a reflecting white plate were employed (see Fig. 4) resulting in a dark image of the ink in front of a light background.

Photographs of the flow field were taken by a standard camera as well as with a video camera. The application of the hydrogen bubble method made it necessary to use highly sensitive films even with a laser output power of about 2 W. Both cameras can be mounted on a movable frame to allow positioning of the cameras at any position at the top of the test section.

Results

As a result of earlier studies in an air-blown test facility (Hestermann et al., 1991) it was shown that the flow inside the prediffuser has a dominating effect on the flow field of the entire combustor diffuser. On the other hand, the geometry downstream of the prediffuser affects the flow inside the prediffuser. Applying the nonintrusive LDV measuring technique, it could be shown that for moderate diffuser opening angles of $2\Phi = 15$ deg, the velocity distribution at the prediffuser's exit, starting with a nozzlelike profile for large flame tube distances, flattens with decreasing flame tube distances. As a consequence, the flow near the prediffuser walls at its exit exhibits normal components toward the upper and lower walls, respectively, and the velocity near the walls close to the prediffuser exit increases, resulting in a stabilization of the flow with decreasing flame tube distance. For moderate opening angles the flow is attached throughout the prediffuser. The results of the flow

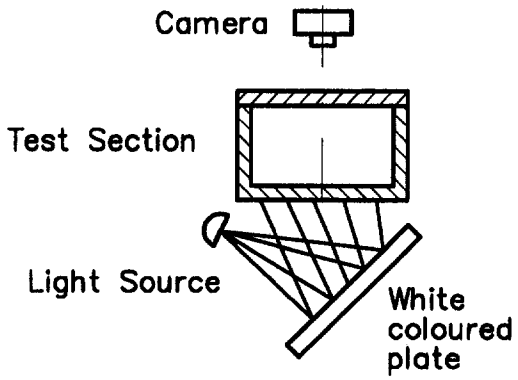

Fig. 4 Ink jet method: illumination

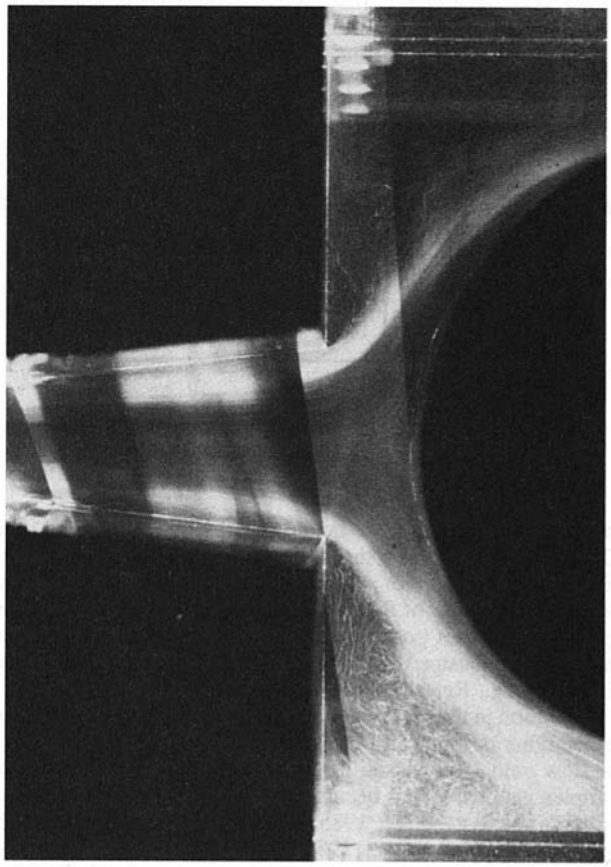

Fig. 5 Hydrogen bubble flow visualization (geometric data: $2\Phi = 15$ deg; $l/h_1 = 3.0$; $H_{Sp}/h_1 = 1.0$; $d/h_1 = 0.74$)

visualization confirm these quantitative results qualitatively, as shown in Figs. 5 to 7. Clearly visible is the attached flow inside the entire prediffuser, the flow separation at the edge of the prediffuser's exit and the reattachment of the flow downstream of the dump diffuser.

At small flame tube distances ($d/h_1 = 0.74$, see Fig. 5), the upstream influence of the flame tube dome inside the prediffuser is indicated by the curvature of the hydrogen bubbles' path lines starting with the curvature already inside the prediffuser. This is in good agreement with the results of the LDV measurements presented earlier. At large flame tube distances ($d/h_1 = 2.51$, see Fig. 7) the flow propagates similarly to a jet for a certain

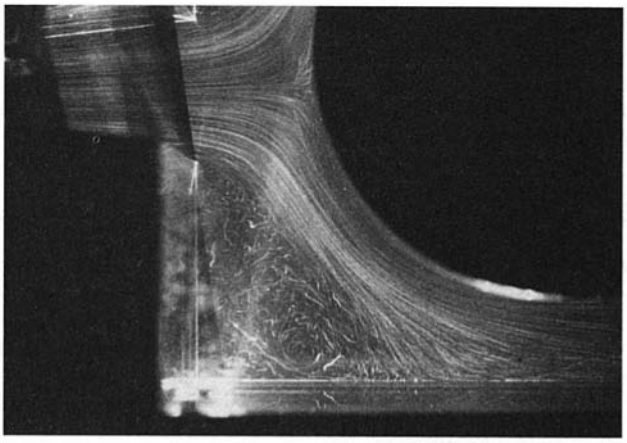

Fig. 6 Hydrogen bubble flow visualization (geometric data: $2\Phi = 15$ deg; $l/h_1 = 3.0$; $H_{Sp}/h_1 = 1.0$)

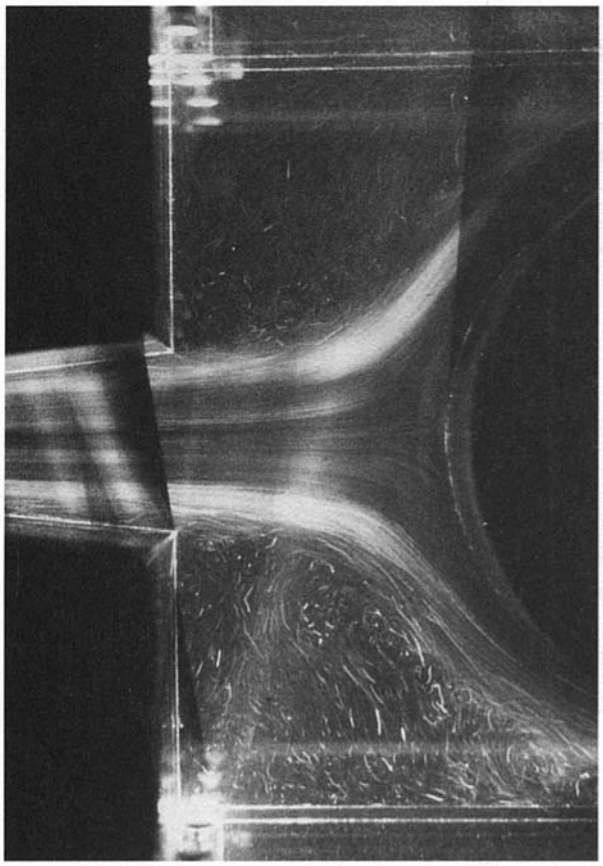

Fig. 7 Hydrogen bubble flow visualization (geometric data: $2\Phi = 15$ deg; $l/h_1 = 3.0$; $H_{Sp}/h_1 = 1.0$; $d/h_1 = 2.51$)

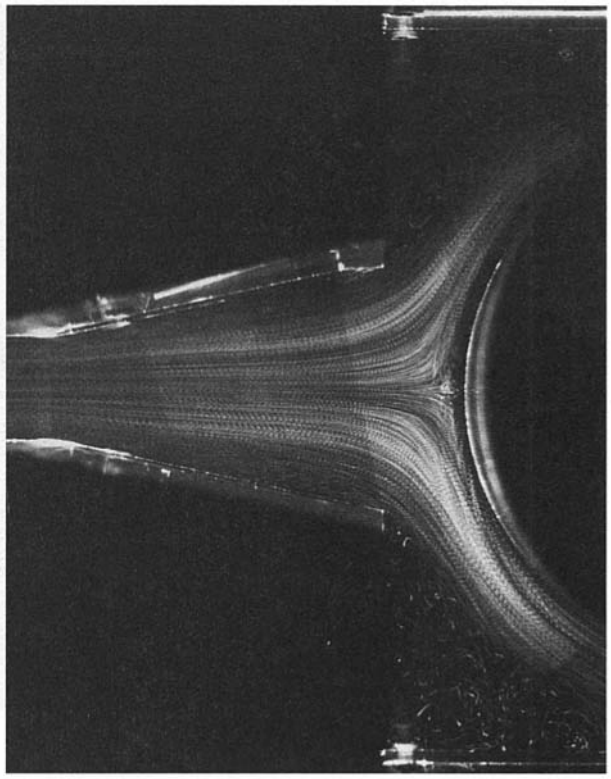

Fig. 9 Hydrogen bubble flow visualization (geometric data: $2\Phi = 25$ deg; $l/h_1 = 3.0$; $H_{Sp}/h_1 = 1.0$; $d/h_1 = 0.74$)

distance downstream of the prediffuser's exit before it is influenced by the flame tube dome. In the corner region of the dump diffuser, a clearly visible vortex exists as expected. A much smaller counterrotating vortex can be recognized at the edge of the prediffuser's exit. At a moderate flame tube distance of $d/h_1 = 1.26$ (see Fig. 6) the deflection of the flow starts directly at the prediffuser's exit without any upstream effect of the flame tube dome visible inside the prediffuser. Obviously, the flow deflection is not affected by the edge at the prediffuser's exit. This is a further demonstration for the existence of an optimum pressure recovery at the moderate flame tube distances mentioned by Fishenden and Stevens (1974). Also visible in the photographs is the location of the reattachment point at the casing walls of the dump diffuser, varying with flame tube distance.

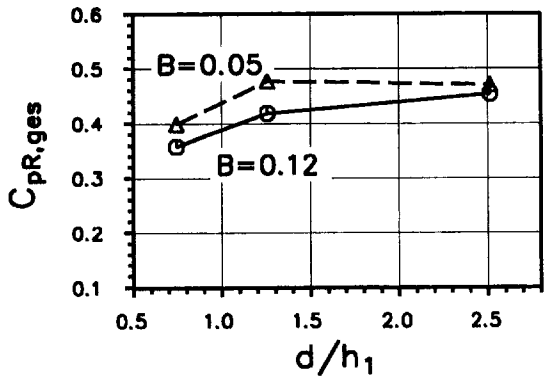

Fig. 8 Effect of boundary layer thickness on overall pressure recovery (B = inlet blockage factor); geometric data: $2\Phi = 15$ deg; $l/h_1 = 3.0$

The photographs shown here have been taken for thin boundary layers at the entrance of the prediffuser. As the results of the LDV measurements inside the prediffuser show (see Hestermann et al., 1991), the strong upstream effect of the flame-tube on the velocity profile at the prediffuser's exit decreases with increasing boundary layer thickness at the prediffuser's entry because of the larger momentum in the core region at thicker boundary layers and at equal mass flow rates. Also, the overall pressure recovery, measured from the entry of the prediffuser to the exit of the flame tube annuli, decreases with increasing boundary layer thickness (see Fig. 8).

In real engines the boundary layer thickness at the diffuser's entry is given by the compressor's discharge flow. So from a designer's point of view, the only way to increase the pressure recovery at a given diffuser length is to increase the opening angle. In doing so, the flow remains attached to both prediffuser walls for moderate opening angles. At an opening angle of $2\Phi = 18$ deg and at large flame tube distances ($d/h_1 = 2.51$), the flow starts separating from the prediffuser's diverging walls for short time intervals. With increasing opening angle, the time intervals showing flow separation grow and the extension of the separated regions increases similarly to the flow phenomena described by Reneau et al. (1967) for conventional two-dimensional diffusers without flame tube. This unsteady separation can be eliminated by decreasing the flame tube distance. The larger the opening angle, the smaller the flame tube distance has to be to suppress flow separation. At a total opening angle of $2\Phi = 22$ deg, the flow separation inside the prediffuser can only be prevented for flame tube distances $d/h_1 < 1$. For larger total opening angles ($2\Phi = 25$ deg) flow separation cannot be prevented even at small flame tube distances. Especially at these large opening angles, the flow stabilizing effect of the flame tube can clearly be demonstrated: At large opening angles and simultaneously at large flame tube distances the flow always separates from one diverging wall inside the prediffuser while the flow on the opposite side remains attached. Thereby two

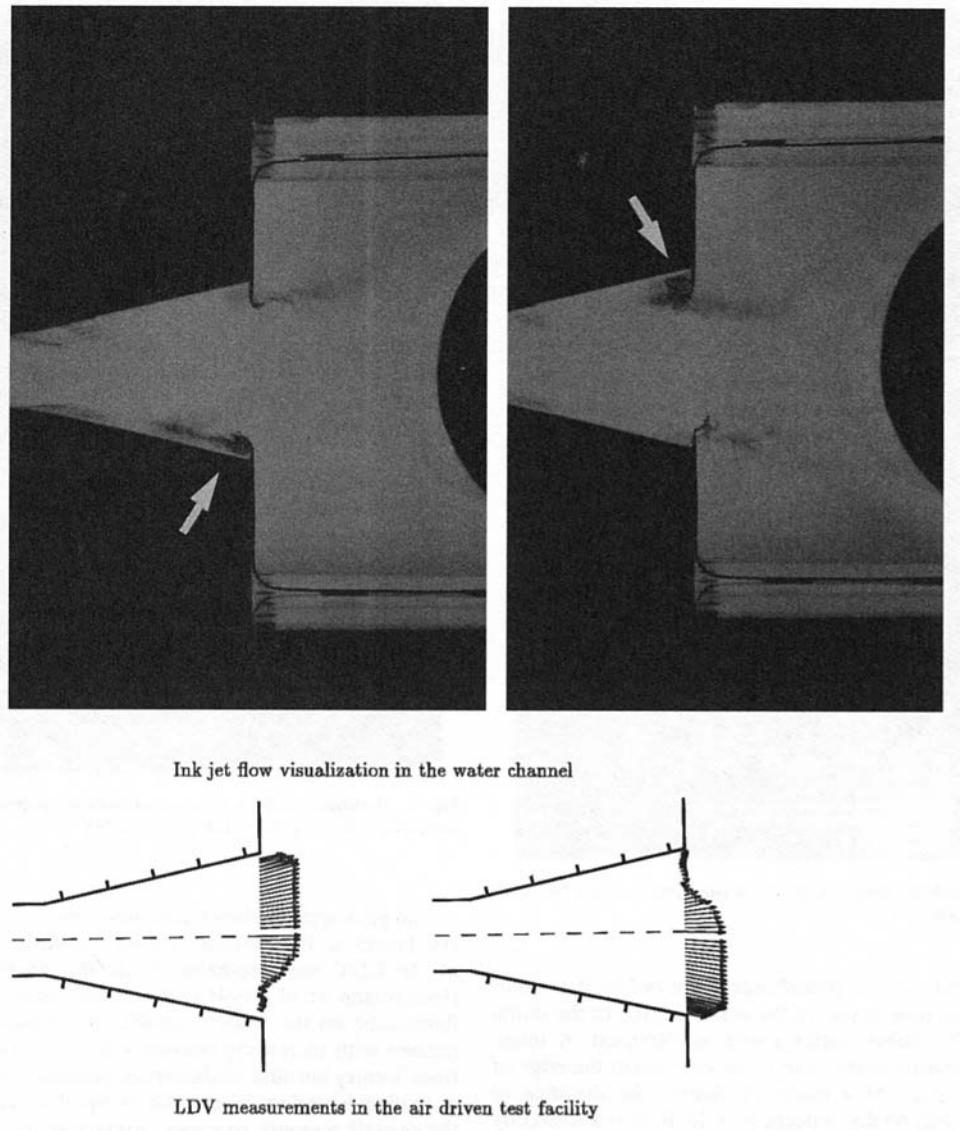

Fig. 10 Occurrence of two similar flow situations in diffusers with large opening angles (geometric data: $2\Phi = 25$ deg; $l/h_1 = 3.0$; $d/h_1 = 2.51$)

possible flow situations may occur with the same probability. Because of the lifetime of these possible flow situations the flow can be regarded as quasi-stationary, but not as a stable flow. The switch from one flow situation to the corresponding mirror-symmetric flow occurs quite stochastically. An impression of this flow is given in Fig. 10 by the visualization of the near-wall flow field applying the ink jet method. In this case, the color was added to the flow at the prediffuser's exit. While in the left-hand photograph the color moves in the upstream direction along the right diverging wall of the prediffuser, viewed in the flow direction, the right-hand photograph shows the opposite effect. Here, backflow occurs along the left diverging wall.

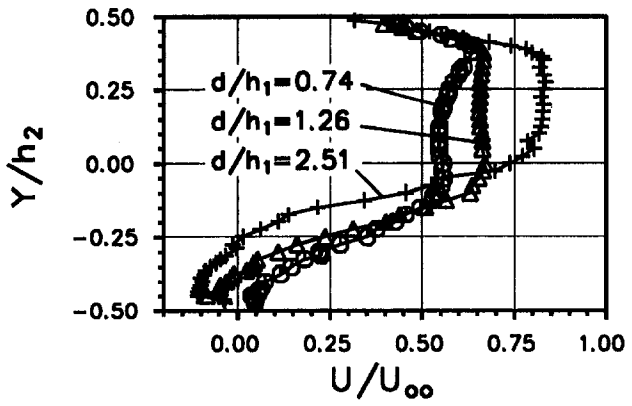

Fig. 11 Measured velocity distribution at the prediffuser's exit at large opening angles (geometric data: $2\Phi = 25$ deg; $l/h_1 = 3.0$)

While the flow visualization only is a qualitative description of this phenomenon, it is confirmed by the results of the LDV measurements taken in the air-blown test facility. The vector diagram in Fig. 10 quantitatively shows the mirror symmetry of the two possible flow situations.

At the smallest flame tube distance under examination, $d/h_1 = 0.74$, the upstream effect of the flame tube causes the flow to reattach near the prediffuser's exit, resulting in a separation bubble inside the prediffuser (see Figs. 9 and 11). Although the flow is attached near the exit of the prediffuser, the velocity profile becomes unsymmetric. Therefore, for prediffuser geometries with a normalized length of $l/h_1 = 3.0$ and large opening angles, an overall pressure recovery similar to that in combustor diffusers with moderate opening angles can be reached only with very small flame tube distances (see Fig. 12).

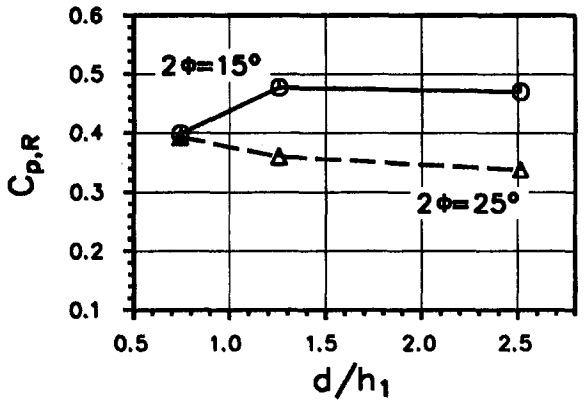

Fig. 12 Experimentally determined overall pressure recovery

Among other parameters influencing the onset of flow separation, the knowledge of the turbulence intensity at the diffuser's entry is of fundamental interest. In the following, some results concerning the influence of turbulence on the pressure recovery attainable in dump diffusers are presented. Elevating the turbulence level increases the momentum exchange between the core flow and the near wall flow. Therefore, the onset of flow separation can be delayed. For example, Stevens and Williams (1980) showed, for an annular diffuser with constant inner diameter, that increasing the turbulence intensity leads to an improvement in flow stability at the diffuser exit. Hoffmann and Gonzalez (1984) showed, for a two-dimensional diffuser with free discharge, that increasing the turbulence level to at least 3.5 percent can improve the pressure recovery drastically. Their data, for example, for a diffuser geometry with a ratio of diffuser length l to inlet height $h_1 = 15$ and an opening angle of $2\Phi = 20$ deg, show an increase in pressure recovery from $C_p = 0.58$ without turbulence generator to $C_p = 0.71$ at increased turbulence level. This improvement in C_p for the condition of increased turbulence intensity is a result of the improved velocity profile with a symmetric velocity distribution because of a delayed flow separation.

The results of our experiments show that this tendency is also valid for combustor dump diffusers. By mounting a turbulence grid consisting of bars with a diameter of $d_b = 8$ mm, the turbulence intensity in the core region was increased from $Tu \approx 1.5$ to $Tu \approx 6$ percent with a nearly identical velocity distribution (see Fig. 13). At small opening angles, where the flow inside the diffuser is attached and remains symmetric even at low turbulence levels, increasing the turbulence intensity results in an increased pressure recovery (see Fig. 14). At larger opening angles, the effect of flame tube distance additionally has to be taken into account; while at small flame tube distances ($d/h_1 = 0.74$) the flow at increased turbulence intensity remains symmetric throughout the prediffuser, the flow becomes unsymmetric at large flame tube distances ($d/h_1 = 2.51$) due to a flow separation despite the increased turbulence intensity (see Fig. 15).

Numerical Calculations

One of the major goals of the research program was to obtain detailed experimental data with well-known boundary conditions to get a better understanding of the complex correlations between diffuser geometry and inlet flow conditions on one hand and flow characteristics in combustor diffusers on the other. Both the air and the water tunnel allow the study of the influencing parameters by isolating the parameters of interest. As a result, a data base is available for the validation of numerical codes. The code used here is a finite volume code solving the time-averaged Navier–Stokes equations on a body-fitted coordinate system first described by Bauer (1989). To take into account the turbulent nature of the flow, the standard $k-\epsilon$ model was used. For all computations the inlet flow conditions as measured two channel heights upstream of the beginning of the

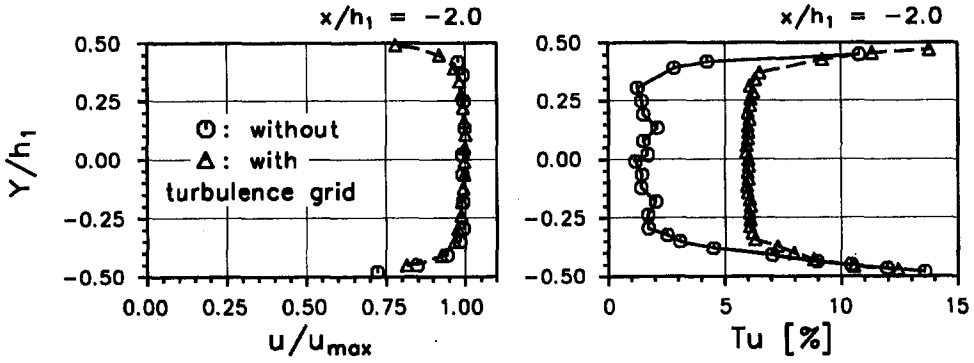

Fig. 13 Velocity and turbulence intensity profiles at the reference position

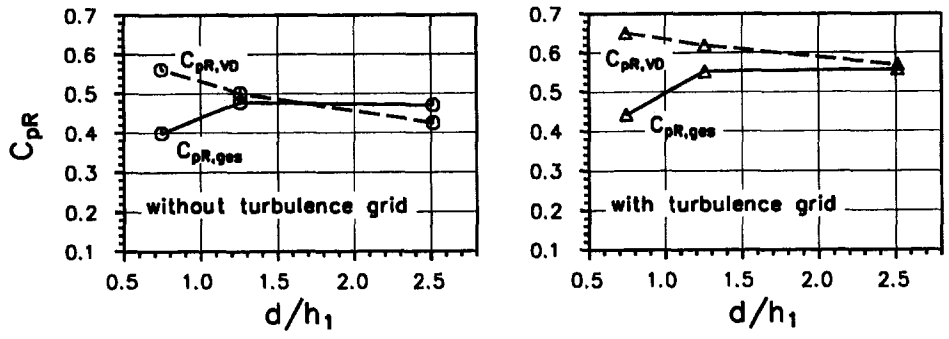

Fig. 14 Influence of turbulence on overall pressure recovery (geometric data: $2\Phi = 15$ deg; $l/h_1 = 3.0$)

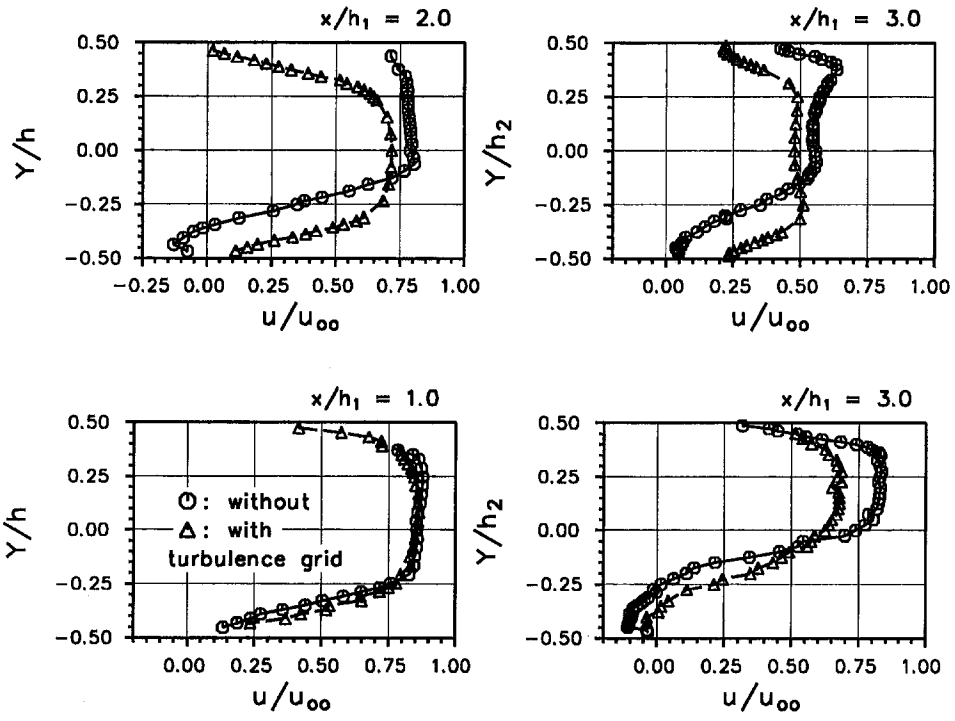

Fig. 15 Influence of turbulence on the velocity distribution inside the prediffuser (geometric data: $2\Phi = 25$ deg; $l/h_1 = 3.0$; upper diagrams: $d/h_1 = 0.74$; lower diagrams: $d/h_1 = 2.51$)

prediffuser have been used as boundary conditions. The length scale was assumed to be 3 percent of the channel height at this reference position. The turbulent kinetic energy was calculated based on the measured fluctuating velocities and based on the assumption of isotropic turbulence. Furthermore, at the exit of the flame tube channels, the gradients were set to zero, and for most of the geometries under examination symmetric conditions were specified along the centerline of the diffuser models for reasons of simplicity.

In the following, the results for a combustor diffuser having a total opening angle of $2\Phi = 15$ deg, a length-to-height ratio of $l/h_1 = 3.0$, resulting in an area ratio of $AR = 1.78$, and a flame tube distance of $d/h_1 = 1.26$ are presented. The grid used for this calculation had 46×30 lines in the x and y directions, respectively. The computed flow field clearly demonstrates excellent agreement between the calculated and the visualized flow field (see Fig. 16). An even better illustration of the capability of the numerical code is the flow field inside the prediffuser. This region is of special importance for the entire flow field in the combustor diffuser. Therefore, a numerical code to predict the flow inside a combustor diffuser should predict the flow in this dominating region with relatively high accuracy. The comparison of the calculated results with the results of the LDV measurements show that the code used here basically is able to fulfill this task. The calculated profiles of the time-averaged velocities shown in Fig. 17 are in excellent agreement with the measured values. The transformation of the velocity profile passing through the prediffuser as well as the upstream effect of the flame tube dome and the relative acceleration of the flow in the near wall region is predicted correctly even though no special attempts were made to discretize the near-wall region. Other effects, for example the correlation between inlet blockage and intensity of the flame tube's upstream effect, were also verified numerically. This is valid for all flame tube distances under examination and for diffuser angles up to $2\Phi = 15$ deg. However, up to now, the phenomenon found in the experiments, that two similar flow situations may occur in diffusers with large opening angles, could not be predicted correctly. Currently, calculations are under way dealing with this problem using an advanced version of the computer code as described in Benz and Wittig (1992). We plan to publish the results of these computations.

Conclusions

Both experimental and numerical results of the flow field in a model combustor diffuser are presented. Emphasis has been

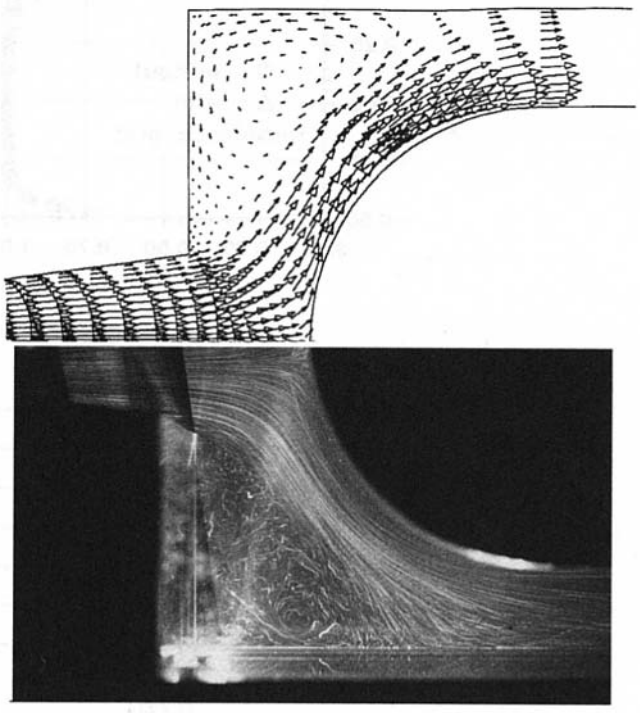

Fig. 16 Comparison of the computed and visualized flow field for a model diffuser with $d/h_1 = 1.26$, $2\Phi = 15$ deg, $l/h_1 = 3.0$

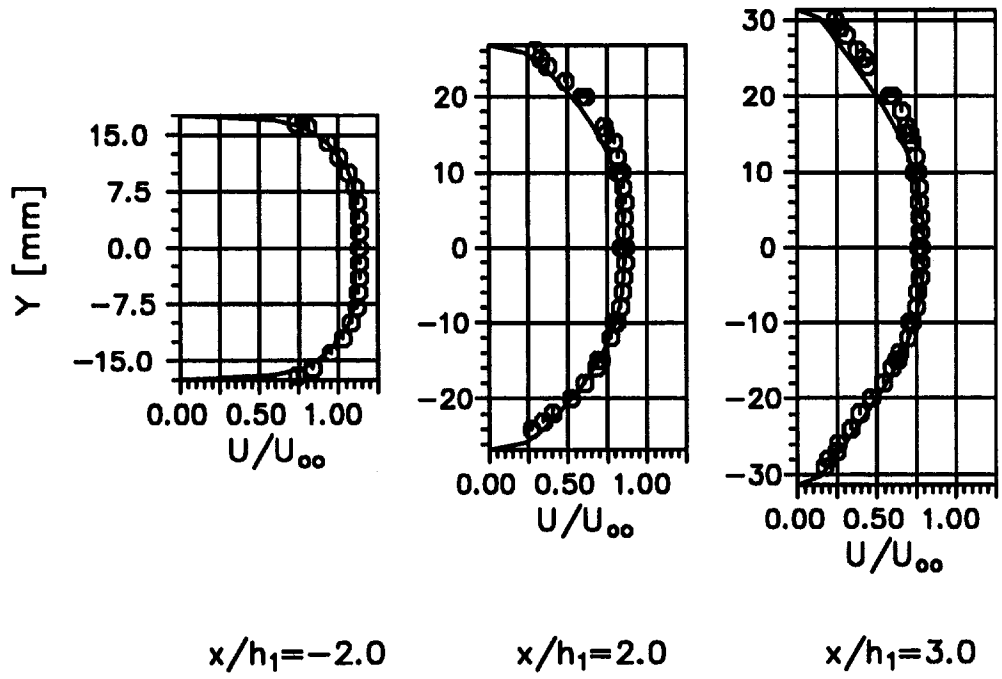

Fig. 17 Measured (= symbols) and calculated (= lines) time averaged axial velocity components inside a prediffuser with $d/h_1 = 1.26$, $2\Phi = 15$ deg, $l/h_1 = 3.0$

directed toward the flow field inside the prediffuser, which is of special importance for the flow field in the entire diffuser–combustor system. Both the experimental and the numerical results show the dominating effect of the flame tube. For a prediffuser length of $l/h_1 \approx 3.0$, flow separation inside the prediffuser can be prevented up to opening angles of about 22 deg by decreasing the flame-tube distance. The largest opening angle under investigation was 25 deg, corresponding to an area ratio of about 2.3. At this opening angle, the flow can be forced to reattach inside the prediffuser only for small flame tube distances, but is strongly distorted at the prediffuser's exit due to a separation bubble inside. At increased turbulence levels at the prediffuser's entry, the flow remains symmetric for small flame tube distances even with large opening angles.

A comparison of the experimental data with the results of a numerical computation demonstrates the capability of predicting the flow field in combustor diffusers with reasonable accuracy, at least for diffusers with an included total opening angle less than 18 deg.

Future work will be directed toward the continuation of our systematic investigations of inlet flow effects and will include the investigation of contoured diffuser walls.

Acknowledgments

The present study was supported by a grant from the Sonderforschungsbereich 167 (high-intensity combustors) of the Deutsche Forschungsgemeinschaft.

References

Ainley, D. G., 1945, "Investigations of Air Flow Through Some Annular Diffusers," Power Jet Report 1151.

Adkins, R. C., 1983, "A Simple Method for Designing Optimum Annular Diffusers," ASME Paper No. 83-GT-42.

Adkins, R. C., and Wardle, M. H., 1990, "A Method for the Design of Optimum Annular Diffusers of Canted Configuration," ASME JOURNAL OF ENGINEERING FOR GAS TURBINES AND POWER, Vol. 114, pp. 8–12.

Bauer, H.-J., 1989, "Überprüfung numerischer Ansätze zur Beschreibung turbulenter elliptischer Strömungen in komplexen Geometrien mit Hilfe konturangepaßter Koordinaten," Dissertation, Universität Karlsruhe, Institut für Thermische Strömungsmaschinen, Germany.

Benz, E., and Wittig, S., 1992, "Prediction of the Interaction of Coolant Ejection With the Mainstream at the Leading Edge of a Turbine Blade: Attached Grid Application," presented at the Int. Symp. Heat Transfer in Turbomachinery, Aug. 24–28, Athens, Greece.

Biaglow, J. A., 1971, "Effect of Various Diffuser Designs on the Performance of an Experimental Turbojet Combustor Insensitive to Radial Distorsion of Inlet Air Flow," NASA TMX-2216.

Fishenden, C. R., and Stevens, S. J., 1974, "The Performance of Annular Combustor-Dump Diffusers," AIAA Paper No. 74-1097.

Hestermann, R., Kim, S., and Wittig, S., 1991, "Geometrical Dependence of the Fluid Dynamic Performance Parameters of Plane Combustor Model Diffusers," ISABE 91-7105, pp. 995–1001.

Hoffmann, J. A., and Gonzalez, G., 1984, "Effects of Small-Scale, High Intensity Inlet Turbulence on Flow in Two-Dimensional Diffusers," ASME *Journal of Fluids Engineering,* Vol. 106, pp. 121–124.

Howard, J. H. G., Thornton-Trump, A. B., and Henseler, H. J., 1967, "Performance and Flow Regimes for Annular Diffusers," ASME Paper No. 67-WA/FE-21.

Johnston, I. H., 1953, "The Effect of Inlet Conditions on the Flow in Annular Diffusers," British Aeronautical Research Council, C. P. No. 178.

Kim, S., 1976, "Experimentelle Untersuchung zur Gas-Flüssigkeitsfilm-Grenzflächenströmung mit mäßigem positivem Druckgradient," Dissertation, Institut für Thermische Strömungsmaschinen, Universität Karlsruhe, Germany.

Kim, S., 1979, "Einfaches Berechnungsverfahren verlustarmer Diffusoren für verschiedene Druckgradienten unter Verwendung der Eigenschaften der Äquilibriumsgrenzschicht," Festschrift zum 70. Geburtstag von R. Friedrich, Universität Karlsruhe, Germany.

Klein, A., 1988, "The Relation Between Losses and Entry-Flow-Conditions in Short Dump Diffusers of Combustors," *ZfW,* Vol. 12, pp. 286–292.

Kline, S. J., Abbott, E. E., and Fox, R. W., 1969, "Optimum Design of Straight-Walled Diffusers," ASME *Journal of Basic Engineering,* Vol. 81, pp. 321–331.

Koutmos, P., and McGuirk, J. J., 1989, "Numerical Calculations of the Flow in Annular Combustor Dump Diffuser Geometries," *Proc. Inst. Mech. Engrs.,* Vol. 203, *Part C: Journal of Mechanical Engineering Science,* pp. 319–331.

Little, A. R., and Manners, A. P., 1993, "Predictions of the Losses in 2D and 3D Model Dump Diffusers," ASME Paper No. 93-GT-184.

Noll, B., 1986, "Numerische Berechnung brennkammertypischer Ein- und Zweiphasenströmungen," Dissertation, Universität Karlsruhe, Institut für Thermische Strömungsmaschinen, Germany.

Noll, B., Bauer, H.-J., Wittig, S., 1989, "Gesichtspunkte der numerischen Simulation turbulenter Brenn-kammerströmungen," *ZFW,* Vol. 13, No. 3, pp. 178–187.

Noll, B., and Wittig, S., 1991, "Evaluation of a Bounded High-Resolution Scheme for Combustor Flow Computations," *AIAA Journal,* Vol. 30, No. 1, pp. 64–69.

Reneau, L. R., Johnston, J. P., and Kline, S. J., 1967, "Performance and Design of Straight, Two-Dimensional Diffusers," ASME *Journal of Basic Engineering,* Mar., pp. 141–150.

Shyy, W., 1985, "A Numerical Study of Annular Dump Diffuser Flows," *Computer Methods in Applied Mechanics and Engineering,* Vol. 53, pp. 47–65.

Sovran, G., Klomp, E. D., 1967, "Experimentally Determined Optimum Geometries for Rectilinear Diffusers With Rectangular, Conical or Annular Cross Section," in: G. Sovran, ed., *Fluid Mechanics of Internal Flow,* Elsevier, New York, pp. 270–319.

Stevens, S. J., and Williams, G. J., 1980, "The Influence of Inlet Conditions on the Performance of Annular Diffusers," ASME *Journal of Fluids Engineering,* Vol. 102, pp. 357–363.

Wagner, W. B., Tanrikut, S., and Sokolowski, D. E., 1980, "Performance of Annular Prediffuser-Combuster Systems," ASME Paper No. 80-GT-15.

Calculation of Two-Phase Flow in Gas Turbine Combustors

A. K. Tolpadi
Fluid Mechanics Program,
General Electric Corporate
Research & Development,
P.O. Box 8, Mail Stop K1/ES-206,
Schenectady, NY 12301

A method is presented for computing steady two-phase turbulent combusting flow in a gas turbine combustor. The gas phase equations are solved in an Eulerian frame of reference. The two-phase calculations are performed by using a liquid droplet spray combustion model and treating the motion of the evaporating fuel droplets in a Lagrangian frame of reference. The numerical algorithm employs nonorthogonal curvilinear coordinates, a multigrid iterative solution procedure, the standard $k-\epsilon$ turbulence model, and a combustion model comprising an assumed shape probability density function and the conserved scalar formulation. The trajectory computation of the fuel provides the source terms for all the gas phase equations. This two-phase model was applied to a real piece of combustion hardware in the form of a modern GE/SNECMA single annular CFM56 turbofan engine combustor. For the purposes of comparison, calculations were also performed by treating the fuel as a single gaseous phase. The effect on the solution of two extreme situations of the fuel as a gas and initially as a liquid was examined. The distribution of the velocity field and the conserved scalar within the combustor, as well as the distribution of the temperature field in the reaction zone and in the exhaust, were all predicted with the combustor operating both at high-power and low-power (ground idle) conditions. The calculated exit gas temperature was compared with test rig measurements. Under both low and high-power conditions, the temperature appeared to show an improved agreement with the measured data when the calculations were performed with the spray model as compared to a single-phase calculation.

Introduction

A gas turbine combustor is a complex combustion device within which there exists a wide range of coupled, interacting physical and chemical phenomena. Some of these phenomena are fuel spray atomization and vaporization, turbulent transport, finite-rate chemistry, NO_x and CO emissions, radiation and particulate behavior. Depending on the issues being addressed, models of varying degrees of sophistication have been employed. The level of sophistication is dictated by the computing capabilities available and physical understanding of the flow. Generally speaking, in order to model three-dimensional flows, a compromise has to be made between the complexity of the model and the speed of the computers available.

The prediction of hydrodynamic and thermal characteristics of the flow in a gas turbine combustor requires consideration of the two phases in the flow field, which are closely coupled through mass, heat, and momentum exchange mechanisms. The main task is associated with the modeling of the discontinuous liquid phase and the coupling between the two phases. Another issue is the assumption that is made about the characteristics of the spray. In a gas turbine engine, it is generally believed that under low power idle conditions, the residence time of the liquid fuel droplets within the combustor is significant enough to warrant a need for a two-phase computation. However, under high-power conditions, the fuel may be assumed to be in a fully vaporized state and therefore a single-phase calculation would suffice.

Two approaches have been used in the literature to predict the flow properties in situations where a spray of droplets is injected in a turbulent gas field. In the first approach, Eulerian conservation equations are applied to the gas phase with the assumption of insignificant influence of local flow discontinuities induced by the presence of droplets in the gas phase. Lagrangian equations of the droplet motion and the thermal balance equations are applied to a finite number of droplet size ranges representing the size distribution within the spray. The trajectory computation of the droplets provides the source terms for all the gas phase equations. The gas phase calculation provides the updated velocity, temperature, and turbulence field required by the Lagrangian analysis. This is the so-called liquid droplet spray model. Crowe et al. (1977) investigated this approach and illustrated its applicability by analyzing a steady two-dimensional spray cooling problem. Banhawy and Whitelaw (1980) calculated the flow properties of a confined two-dimensional axisymmetric kerosene-spray flame. The computed temperature and axial velocity profiles were found to be in good qualitative agreement with measured experimental data. They found the initial spray conditions and the initial velocity of the droplets to be important. Gosman and Ioannides (1983) included a stochastic treatment of turbulent dispersion effects. In this treatment, the gas turbulence is randomly sampled during each droplet's flight, which influences its motion, and the gross spray behavior is obtained by averaging over a statistically significant sample of droplets. This same approach was employed earlier for diesel engine sprays by Dukowicz (1980) and O'Rourke and Bracco (1980). Sabnis and de Jong (1990) compared the calculated flow field of an evaporating spray of liquid freon with corresponding experimental data. The agreement was found to be quite good. Aggarwal and Chitre (1991) computationally studied the structure of turbulent evaporating sprays and examined the sensitivity of their vaporization behavior to transient liquid-phase processes.

In the second approach developed by Williams (1962), the spray was modeled through a conservation equation for a statistical distribution function, defined as the number of droplets per unit droplet diameter and velocity and spatial volume. This equation is integrodifferential in character and its solution together with the gas conservation equations provides the required model of the spray. This approach is costly in terms of computer storage and time unless simplifications are introduced, such as

Contributed by the International Gas Turbine Institute for publication in the JOURNAL OF ENGINEERING FOR GAS TURBINES AND POWER. Manuscript received by the International Gas Turbine Institute October 1992. Associate Technical Editor: G. S. Samuelsen.

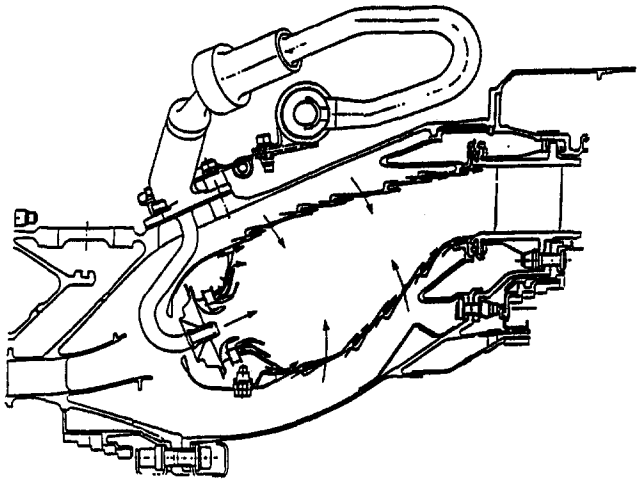

Fig. 1 Geometry of a GE/SNECMA CFM56 single annular turbofan engine combustor

the assumption of no slip between the droplets and the gases or the representation of the spray by a very limited number of droplet sizes. This method was further applied by Westbrook (1977) and Ganesan and Spalding (1979).

This paper describes the development of a spray combustion model that was used in analyzing the flow within an aircraft engine gas turbine combustor. The gas phase equations are solved in an Eulerian frame of reference. A fully elliptic three-dimensional body-fitted computational fluid dynamics (CFD) code based on pressure correction techniques has been developed for the gas phase. The numerical algorithm employs a standard $k-\epsilon$ turbulence model and a combustion model comprising an assumed shape probability density function and the conserved scalar formulation. This CFD code has the capability of analyzing the complex geometric details of a modern gas turbine combustor, including the swirl cup, splash plate, primary and secondary dilution holes, film cooling slots, and multihole cooling zones.

The liquid phase calculation is performed by using a droplet spray model. The motion of the fuel droplets is treated in a Lagrangian frame of reference. This provides the source terms for all the gas phase equations. The gas phase calculation provides the updated velocity, temperature, and turbulence field required by the trajectory analysis. Thus, the overall calculation procedure iterates alternately between the CFD analysis of the gas phase and the fuel spray computation until a converged solution is obtained.

In a broader context, this segment of work is part of an ongoing effort to validate computational tools being used by aircraft engine combustor designers. As computing costs have dropped over the years, CFD is being increasingly used by combustion specialists to study phenomena such as droplet vaporization, fuel–air mixing, particulate emissions, pattern factor studies, etc. While CFD will never replace "hard core" testing, it is a very powerful tool that can provide a good initial guidance to design. It is therefore always essential to verify computations against experimental data. The phenomenon of two-phase flow in a complex piece of combustion hardware such as an aircraft engine combustor is very complex; to this end this work was undertaken to calculate the flow in such a configuration and to examine the effect on the flow field of the two extreme scenarios of (1) the fuel in the gas phase and (2) the fuel initially in the liquid phase. The combustor analyzed was a modern GE/SNECMA single annular CFM56 combustor (schematically shown in Fig. 1) operating under both high-power and low-power conditions. The flow field, fuel distribution, and the temperature field within the combustor were all calculated using both the single-phase and the two-phase model. Comparisons were made with test rig measurements of the exhaust gas temperature field. The calculated exhaust gas temperature field appeared to show better agreement with test data when the spray combustion model was used.

Methodology

Mathematical Description of the Gas Phase. The governing equations are those representing the conservation of mass and momentum in the three coordinate directions. Turbulence is modeled using the standard $k-\epsilon$ model along with the wall function treatment for near-wall regions. The combustion model utilizes a conserved scalar variable for the fuel mixture fraction with assumed probability density function (PDF) and a fast chemistry approach for the turbulence/chemistry interaction (Shyy et al., 1986, 1988). A conservation equation is also written for the fluctuation in the mixture fraction (Jones and Whitelaw, 1982). This fluctuation is modeled as the variance of the mixture fraction. The equilibrium temperature and density for the fuel are initially obtained as a function of the mixture fraction. Assuming a beta PDF, and convoluting this equilibrium distribution with the PDF, a look-up table is generated that contains the density and the temperature as a function of the mixture fraction and variance (Shyy et al., 1986). The fully elliptic form of the three-dimensional conservation equations may be written in general for a conserved variable ϕ in Cartesian coordinates as

$$\frac{\partial}{\partial x}(\rho u\phi) + \frac{\partial}{\partial y}(\rho v\phi) + \frac{\partial}{\partial z}(\rho w\phi) = \frac{\partial}{\partial x}\left(\Gamma\frac{\partial\phi}{\partial x}\right) + \frac{\partial}{\partial y}\left(\Gamma\frac{\partial\phi}{\partial y}\right) + \frac{\partial}{\partial z}\left(\Gamma\frac{\partial\phi}{\partial z}\right) + R(x, y, z) \quad (1)$$

where ρ is the fluid density, Γ is the effective diffusion coefficient, u, v, and w are the three Cartesian velocity components, and R is the source term, which depends on the equation being considered. Eight equations were solved, with the dependent variable ϕ representing each of the variables u, v, w, pressure correction (corresponding to the continuity equation), turbulent kinetic energy k, turbulent dissipation ϵ, mixture fraction, and the variance of the mixture fraction. The temperature field is obtained from the thermochemical look-up table by linear interpolation based on the calculated values of the mixture fraction and its variance.

Using a coordinate transformation, these equations are transformed from, in general, an arbitrarily shaped physical domain to a rectangular parallelepiped. The equations are solved in this boundary-fitted coordinate system. A staggered grid system as described by Patankar (1980) is used for the calculation. The scalar variables are located at the center of the control volumes, while the velocity components are located at the control volume faces. After making finite difference approximations to the equations, they are solved by a SIMPLE-like algorithm (Patankar, 1980) extended to the curvilinear coordinate system. The governing equations together with their discretization and the numerical algorithm have been described in detail by Tolpadi and Braaten (1992) and Shyy and Braaten (1986). The finite differencing scheme used here is a hybrid differencing scheme (Patankar, 1980).

Mathematical Description of the Liquid Phase. This model assumes the fuel is injected into the combustor as a fully atomized spray, which consists of spherical droplets. The droplet size distribution function used is one developed by Rosin and Rammler (1933) and is given by the relation

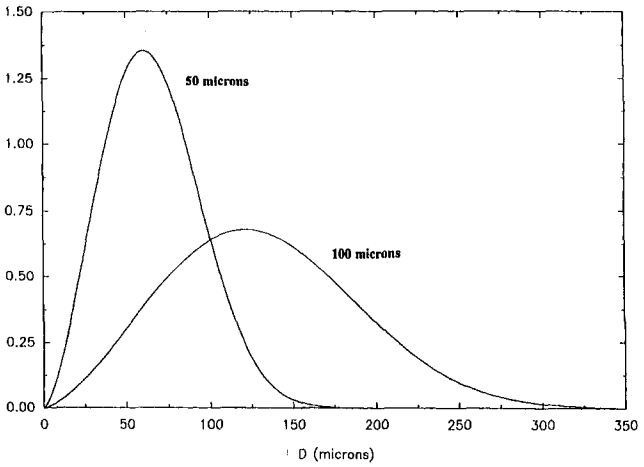

Fig. 2 Rosin-Rammler droplet size distribution function, $q = 2.5$

$$Q = 1 - \exp\left[-\Gamma\left(1 - \frac{1}{q}\right)^{-q}\left(\frac{D}{\text{SMD}}\right)^{q}\right] \tag{2}$$

where Q = fraction of the total volume contained in drops of diameter less than D; SMD = Sauter mean diameter of the spray; q = drop size spread parameter. Figure 2 shows the droplet size distribution function for two different values of the SMD. The maximum droplet diameter is approximately 2.5 times the SMD of the spray. The magnitude of q for most sprays is 2.5 (Lefebvre, 1989). A finite number of size ranges is selected and for each size range, the droplet trajectories, velocities, size, and temperature history are obtained by solving the momentum and thermal balance equations.

The equation of motion of a spherical droplet is given by the following equation, where the dynamic mechanism of the motion is based on the concept of relaxation time:

$$\frac{d\vec{V}_p}{dt} = \frac{\vec{V}_c - \vec{V}_p}{\tau_d} \tag{3}$$

where $\vec{V}_p$ = velocity vector of droplet; $\vec{V}_c$ = velocity vector of continuous gas phase; τ_d = dynamic relaxation time of the droplet. The dynamic relaxation time of the droplet, τ_d, is defined as

$$\tau_d = \frac{4}{3}\left(\frac{\rho_p D^2}{\mu_c}\right)\left(\frac{1}{C_D\ \text{Re}}\right) \tag{4}$$

where D = droplet diameter; ρ_p = droplet density; ρ_c = density of continuous phase; C_D = viscous drag coefficient; μ_c = viscosity of the continuous phase; Re = relative droplet Reynolds number. An important quantity here is the drag coefficient C_D. There are several expressions available in the literature, each of which has an experimental basis. In this study, C_D is taken from Wallis (1969):

$$C_D = \frac{24}{\text{Re}}(1 + 0.15\ \text{Re}^{0.687}), \quad \text{Re} \le 10^3$$

$$C_D = 0.44 \quad \text{Re} > 10^3 \tag{5}$$

The mass transfer rate from the liquid to the gas for a stationary droplet is given by (Spalding, 1953):

$$\dot{m}_p = 2\pi D\,\frac{K_c}{C_{pc}}\ln(1 + B) \tag{6}$$

where $\dot{m}_p$ = droplet mass transfer rate; K_c = thermal conductivity of gas phase; C_{pc} = specific heat of gas phase; B = mass transfer number = $C_{pv}(T_\infty - T_s)/L$; $C_{p,v}$ = specific heat of vapor; T_∞ = temperature of gas phase; T_s = droplet surface temperature; L = latent heat of vaporization at temperature T_s. By combining Eq. (6) and the lumped parameter expression for the droplet mass transfer, the rate of change of droplet diameter is obtained. A correction factor has to be included for a moving droplet (Williams, 1973) and the final equation for the droplet evaporation rate becomes

$$\frac{dD}{dt} = -\frac{C_b}{D}K_s \tag{7}$$

where

$$C_b = \frac{4K_c}{\rho_p C_{pc}}\ln(1 + B)$$

$$K_s = 1 + 0.28\ \text{Re}^{0.5}$$

The droplet temperature during the preheating period is determined by a lumped parameter analysis. A thermal balance equation is written for a droplet moving in a gas stream assuming no evaporation takes place during preheating. This equation is given by

$$\frac{dT_p}{dt} = \frac{6h(T_\infty - T_p)}{\rho_p C_{pp} D} \tag{8}$$

where C_{pp} = specific heat of the liquid; T_p = liquid temperature; h = heat transfer coefficient. The heat transfer coefficient is given by the following correlation for the Nusselt number Nu (Ranz and Marshall, 1952):

$$\text{Nu} = 2 + 0.6\ \text{Re}^{1/2}\ \text{Pr}^{1/3} \tag{9}$$

Equation (8) is solved only during the preheating period until the droplet temperature reaches the boiling point. Subsequently the droplet temperature remains constant.

Equations (3), (7), and (8) form a closed set of equations that are solved with appropriate initial conditions. These equations are solved by a Runge–Kutta method and provide the variation of the droplet position, velocity, size, and temperature as it moves in the gas stream. These equations written above in the time domain are transformed to the space domain in which incremental length steps (Δs) are taken sequentially as a droplet traverses the calculation region. This step size is dynamically adjusted based on the droplet velocity, grid cell size, and evaporation rate.

As stated in the Introduction, the effect of turbulence on the droplet motion is simulated using a stochastic approach. This essentially requires the knowledge of the instantaneous gas velocity in Eq. (2). This is obtained from the computed mean velocity and the turbulence kinetic energy. The turbulence is assumed to be isotropic and to possess a Gaussian probability distribution in the fluctuating velocity, whose standard deviation is $(2k/3)^{1/2}$ (Gosman and Iaonnides, 1983). The distribution is randomly sampled to get the instantaneous gas phase velocity.

Results

A modern General Electric/SNECMA CFM56 turbofan engine combustor is analyzed in this study. The combustor is annular with 20 swirl cups equally spaced along the circumferential direction. Within a single-cup sector of 18-deg span, there are five dilution holes (two primary and three secondary) on both the top and bottom surfaces. There are also seven and six film cooling slots on the top and bottom surfaces, respectively. The calculations are conducted for the flow in a single-cup sector with periodic boundary conditions being imposed on the two side planes. All of the numerical results presented in this paper were obtained on a grid of 58 × 26 × 34 nodes along the ξ (inlet/outlet; I-direction), η (top/bottom; J-direction),

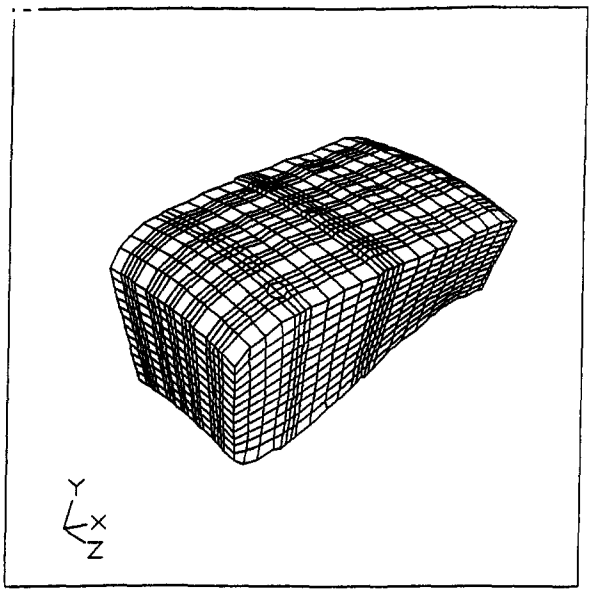

Fig. 3 Three-dimensional view and grid of a single cup sector of an annular combustor

and γ (left/right; K-direction) coordinates. Figure 3 shows the grid with several grid lines removed and this was done to avoid cluttering up the figure. The dilution holes and film cooling slots on the top wall can be clearly seen in this figure. This grid containing 51,272 nodes was the maximum size that could be used within the available computing resources. In previous work (Shyy et al., 1988; Tolpadi and Braaten, 1992), grids with 50,000–60,000 nodes have been used successfully. Numerical diffusion is always present with very coarse grids but is minimized as the grid is made finer.

Calculations were performed at full (high) power and low-power conditions of operation. The fuel used is Jet A. The operating conditions at high power correspond to that at sea level take off. The distributions of the mass flows through the swirl cup, splash plate, film cooling slots, and dilution holes are 18, 13, 39, and 30 percent, respectively. This distribution was obtained with a semi-empirical one-dimensional flow analysis code used at GE-Aircraft Engines. The low power situation corresponds to the one at ground idle. The distribution of the mass flows in this case were 23, 12, 35, and 30 percent, respectively. All solutions were obtained on a Cray Y-MP. A single-phase solution typically required about 45–50 minutes of CPU time with the stated grid while a two-phase calculation took 60–70 minutes for a converged solution. The solutions obtained were declared converged when the maximum residue in the Eulerian transport equations solved was driven below 0.001.

High-Power Conditions. All calculations were performed with a turbulent Schmidt number of 0.5. Figure 4 shows the velocity vectors on a sideview plane obtained using the spray combustion model. The complicated and strong interactions between the flow out of the main dome inlet, holes, and slots is quite evident. The opposing dilution jets impinge on each other, resulting in a multiple core structure of the hot gas in the central part of the combustor. Very strong recirculatory patterns are produced in various cross sections that persist through the exit plane. The film cooling fluid and the dilution jets create large temperature gradients in the flow field and will be seen later.

Comparison will now be made in the predictions of the distribution of temperature and the conserved scalar between the single-phase calculations and the computations with the spray model, which were found to show significant differences. It is important first to understand the differences in the initial and boundary condition specification between the two cases. There are differences in the inlet fuel field. For the single-phase calculation, a finite conserved scalar distribution is specified at a selected number of nodes at the inlet whose profile is based on the inlet swirl cup parameters (the maximum value of the inlet conserved scalar was 0.1258 for the high power case and 0.0566 for the low power case). Thus the fuel is assumed to come into the chamber in a fully vaporized state. With the spray model, the fuel is assumed to enter from the inlet (left boundary) as liquid droplets. The physical locations at the inlet plane where the liquid fuel enters are the same as those where the gaseous fuel entered in the single-phase model. It is very difficult to specify the spray initial conditions as it leaves the atomizer. In this work, the first calculation plane chosen was the swirl cup exit plane, thus eliminating the need to know the exact spray conditions at the atomizer exit. Both experimental (Wang et al., 1992) and computational (Tolpadi et al., 1995) studies are presently being performed to understand the complex two-phase flow in the swirl cup of an engine. These studies are expected to give a better representation of the spray at the inlet plane of this calculation. However, in this work, the initial droplet size distribution was assumed to be the Rosin–Rammler function. In the absence of any experimental evidence, the initial droplet velocity is assumed to be the same as the corresponding gas phase. This is justified considering that the very high droplet velocities at the pressure atomizer would be quickly reduced due to drag by the time the droplets reach the inlet plane of this calculation. A zero conserved scalar field was specified at the inlet, but as the fuel vaporizes within the combustion chamber, the conserved scalar gets set as internal sources of fuel. The fuel mixture fraction variance is set at its maximum possible value. Care was taken to ensure that the flow rate of air at the inlet as well as the dilution holes/slots were identical for both calculations. Also, the inlet mass flow rate of gaseous fuel in the single-phase analysis was the same as the total flow rate of liquid fuel in the two-phase analysis. With these specifications, the calculated exit average fuel to air ratio was found to be identical in both cases, as expected.

The spray parameters were SMD = 50 μm and five size ranges. This value of 50 μm was arrived at by referring to the work of Simmons and Harding (1990) in which among others, SMD measurements have been reported as a function of the injector nozzle pressure difference. From a knowledge of the atomizer pressure drop at high power, and using the appropriate

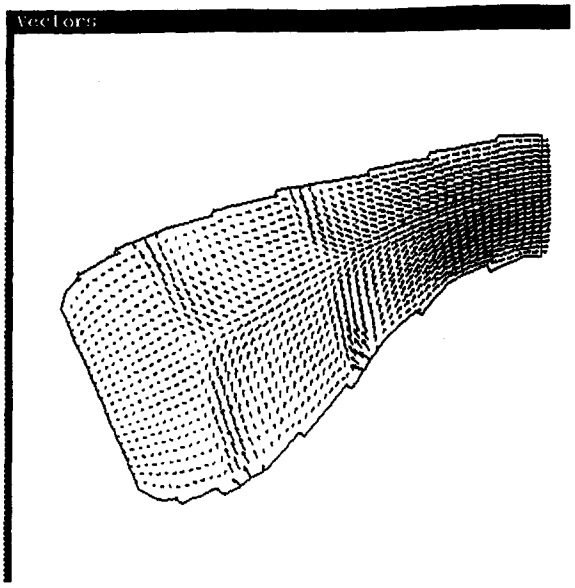

Fig. 4 Velocity vectors in the side view plane K = 28, high power conditions, spray model

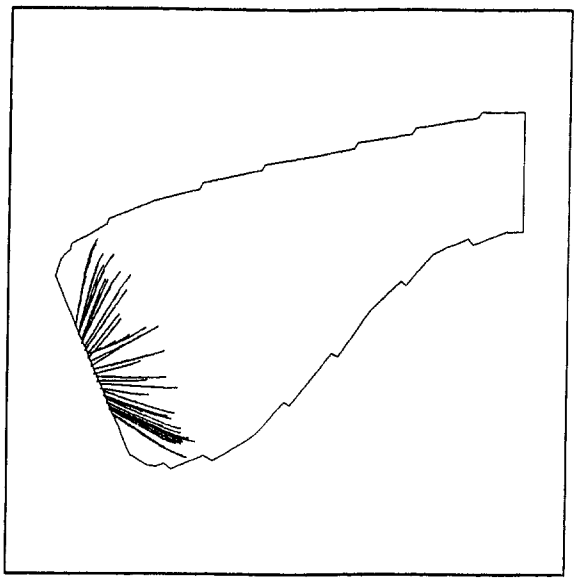

Fig. 5 Fuel droplet trajectories projected on the midplane, high power conditions

SMD versus nozzle pressure curve, the SMD for this work was estimated to be 50 μm. Both deterministic (where the gas phase turbulence is assumed to have no effect on the droplet motion) and stochastic calculations were performed. The flow solutions obtained were practically similar under the inlet conditions used. In the stochastic calculation, ten computational droplets were used per size range and per fuel inlet cell. Out of the 768 computational cells in the inlet plane, the fuel enters from 248 of these locations. Figure 5 shows the deterministic trajectories of the fuel droplets. These trajectories are in three-dimensional space but this figure shows a projection of the paths in a vertical midplane. To avoid cluttering up this figure, only a few trajectories are shown here. The trajectories stop once a fuel droplet vaporizes. It may be observed that most of the fuel vaporizes in the combustion zone over the beginning 15–20 percent length of the combustor. It is not evident from Fig. 5 but it must be remembered that along a trajectory, the droplet diameter is continuously decreasing before full vaporization. The spray model thus gives one an idea of the distance traversed by the fuel before vaporization. Any unburned fuel leaving the back end of the combustor would be predicted. This calculation was also repeated by using ten size ranges; the results obtained did not change significantly.

An interesting effect observed with the spray model was the redistribution of fuel within the combustion chamber. Figures 6(a) and 6(b) show contours of the mean conserved scalar in a vertical plane without and with the spray model. The peak value of the conserved scalar is 0.142 with the spray model and is 0.126 without the spray model. This fuel re-distribution results in differences in the temperature field. Figures 7(a) and 7(b) show contours of the nondimensional temperature in a different vertical plane. In the fast chemistry model used here, the temperature at any location is a function of the mean conserved scalar and the variance of the mean scalar. With the spray model, the redistribution of the field of mixture fraction values together with its variance results in a higher peak temperature within the reaction zone. It also results in a lowering of the temperature field near the upper and lower walls. The cooling fluid entering from the primary and secondary dilution holes and the film slots causes a lowering of the overall temperature near the walls in both cases.

Of most interest to designers is the temperature distribution in the exit plane. Figures 8(a) and 8(b) show contours of nondimensional temperature in the exit plane without and with the spray model. The overall exit temperature field may be seen to have slightly decreased with the spray model. The explanation of this observation lies in the nature of the fast chemistry combustion model used in this study. As stated earlier, there is a significant difference in the specification of the mixture fraction and its variance between the single-phase analysis and the spray calculation. This results in differences in the mixing patterns as seen, for instance, in Figs. 6(a) and 6(b). The fuel gets redistributed when the spray calculation is performed. Although the total quantities of both fuel and air exiting the combustor are identical in the two cases, differences in the mixing result in differences in the field of the local conserved scalar (mixture fraction) and its variance at the exit. Therefore,

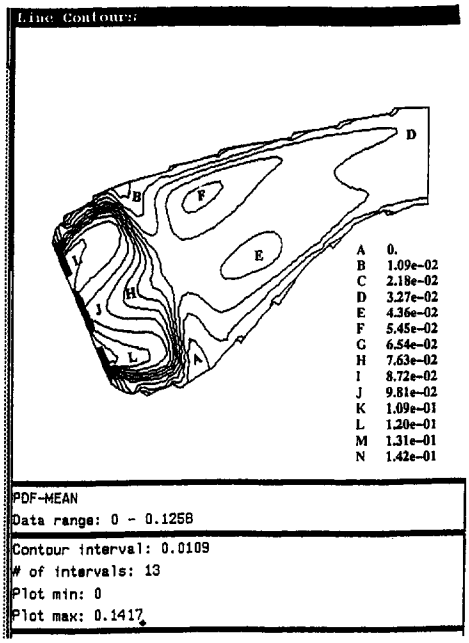

Fig. 6(a) Contours of the mean conserved scalar in the side view plane K = 11, high power conditions, single phase model

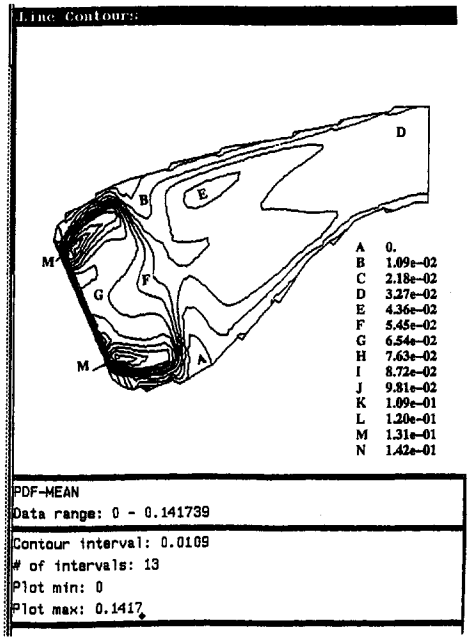

Fig. 6(b) Contours of the mean conserved scalar in the side view plane K = 11, high power conditions, spray model

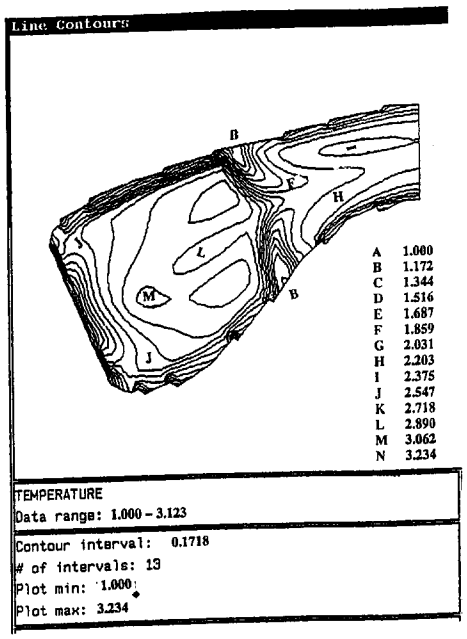

Fig. 7(*a*) Contours of non-dimensional temperature (T/T_{inlet}) in the side view plane $K = 17$, high power conditions, single phase model

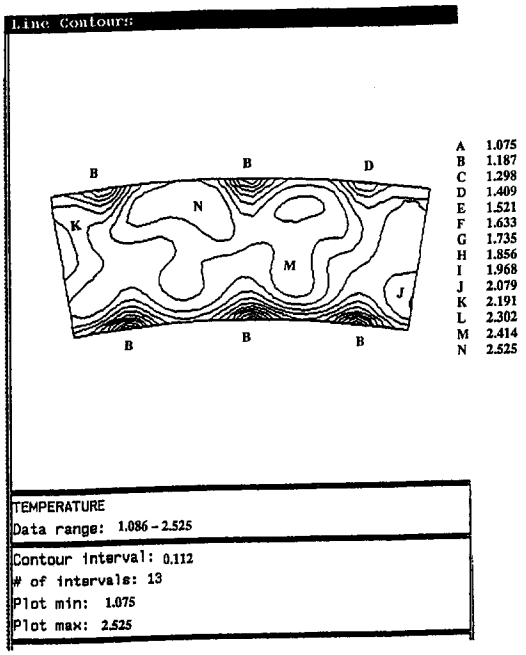

Fig. 8(*a*) Calculated contours of non-dimensional temperature (T/T_{inlet}) in the exit plane, high power conditions, single phase model

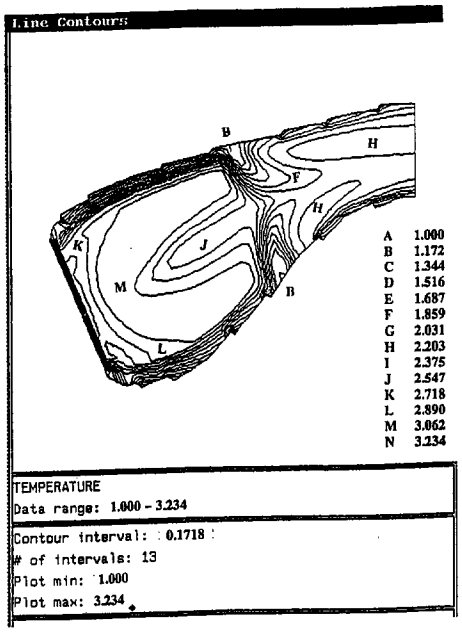

Fig. 7(*b*) Contours of non-dimensional temperature (T/T_{inlet}) in the side view plane $K = 17$, high power conditions, spray model

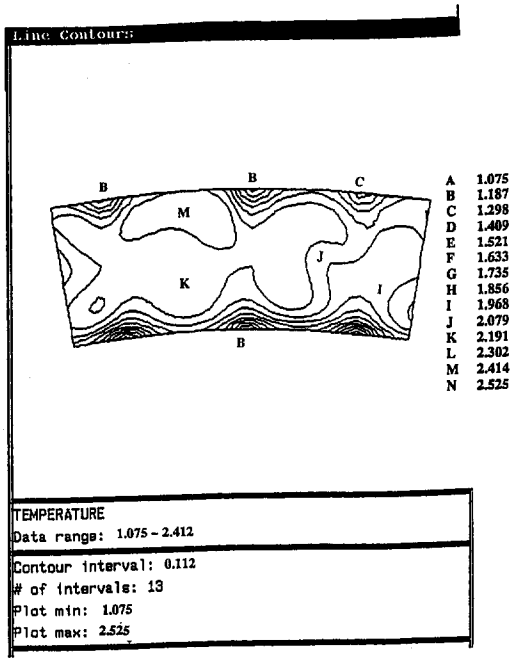

Fig. 8(*b*) Calculated contours of non-dimensional temperature (T/T_{inlet}) in the exit plane, high power conditions, spray model

the temperature field, which in this fast chemistry approach is obtained from a look-up table (based on local values of the mixture fraction and its variance), also changes. Physically, the difference in the calculated mixture fraction field results in differences in the reaction heat release rate (which has a nonlinear dependence on the mixture fraction). This means that there is a difference in the energy of the gas stream leaving the combustion zone. This results in the lower temperature of the exhaust gas.

The measured isotherms for this case are shown in Fig. 9. These measurements were obtained in a full annular test rig using thermocouple rakes at a testing facility at GE-Aircraft Engines. Reasonable agreement may be observed between Figs. 8(*b*) and 9 in terms of the salient features of the flow field such as the wavy pattern and the hot/cold gas distribution. In making a comparison, it should be remembered that there are uncertainties associated with both the experimental and numerical results. The errors in the numerical results are due to the uncertainty of the velocity and mass flow specified at various inlets, the assumption of fast chemistry, the assumption of a standard k–ϵ turbulence model, and neglect of radiation effects. The numerical error may also be associated with the uncertainty in the conditions of the incoming spray, and the fluid flow amounts specified at all inlets. The experimental errors are due to cup-to-cup nonuniformity, radiation losses from the thermocouples, and those caused by the intrusion of the probes into the flow. It should also be noted that the thermocouples can only be placed up to a finite distance from the walls; thus the lower

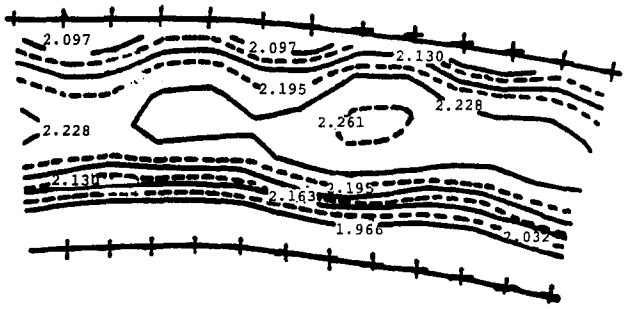

Fig. 9 Experimentally measured isotherms (T/T_{inlet}) in the exit plane

temperature near wall isotherms cannot be captured by the measurements. A fairer method of comparing results is to average the temperature distribution in the circumferential direction and obtain an average profile of the temperature field between the inner and outer end of the annulus. Figure 10 shows the temperature profile in the exit plane. While the calculation with the single-phase model consistently overpredicts the temperature over the entire cross section, the calculation with the spray model overpredicts the temperature in certain regions and underpredicts it in other regions but overall appears to show better agreement with the test data. Considering that several numerical and experimental uncertainties (listed earlier) exist, the agreement obtained here between test data and the calculations is quite encouraging.

Low-Power Conditions. Similar calculations were performed at low-power conditions. The spray parameters were SMD = 100 μm (Simmons and Harding, 1990) and five size ranges. Out of the 768 computational cells in the inlet plane, the fuel enters from 152 locations. Figure 11 shows a few of the trajectories. Comparison with Fig. 5 shows that the fuel traverses a much greater distance before vaporizing when the combustor operates under idle conditions. In fact, some of the fuel remains unburned and escapes through the back end of the combustor, although this is only 0.355 percent of the incoming fuel. Some of the fuel reaches the combustor walls, where it is assumed to evaporate fully upon contact. (It must be noted that even though there are quite a few trajectories in Fig. 11 getting through the back end or reaching the combustor walls, the final diameter of the fuel droplets is significantly less than the initial size.)

The effect of the spray model on the temperature field in the combustor under idle conditions was found similar to the effects

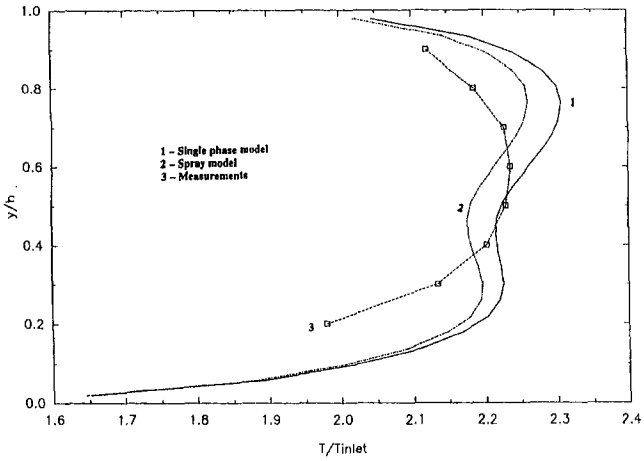

Fig. 10 Profile of circumferentially averaged temperatures in the exit plane-calculated and measured, high power

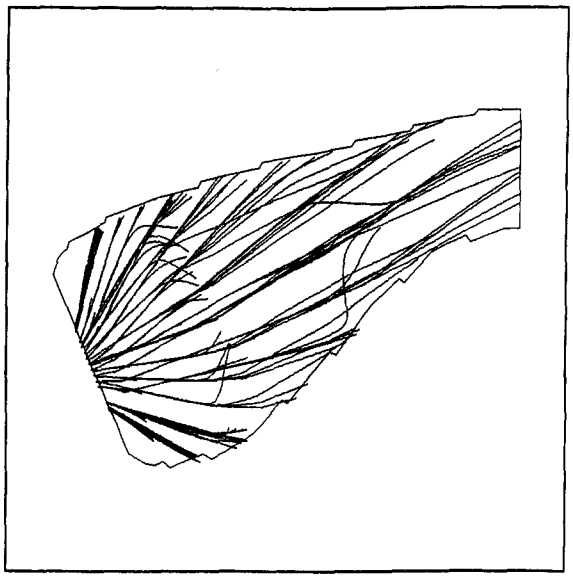

Fig. 11 Fuel droplet trajectories projected on the midplane, low power conditions

observed at high power. Figures 12(a) and 12(b) show contours of nondimensional temperature in a particular vertical plane obtained without and with the spray model. Again, the peak temperature in the reaction zone is found to be higher and the fluid temperature near the upper and lower walls decreases when the spray model is used.

Exit plane temperature data were also obtained at simulated low-power conditions in a full annular test rig. These data were circumferentially averaged and Fig. 13 compares the calculated temperature profile with the measurements. Again, it may be seen that the exit temperature field decreases when the spray model is used. The calculations show a better agreement with the test data with the spray model. Thus, both at high and low-power conditions, the calculations appear to compare better with the measurements when the spray model is employed. The differences observed in the exit temperature profile in going from a single-phase to a two-phase model are no doubt small under both power conditions, but the shifts in both Figs. 10 and 13 are clearly in the direction of better agreement with the data. In a number of two-phase flow situations with droplets, researchers have observed a greater impact on the flow field by using a spray model; a gas turbine engine, however, operates at very high temperatures, which is the reason why smaller differences have been observed in this work.

Conclusions

A liquid droplet spray combustion model has been developed for studying the flow within gas turbine combustors. This model uses an Eulerian–Lagrangian approach whereby the gas phase equations are solved in an Eulerian frame of reference and the liquid phase equations are solved in a Lagrangian frame of reference. The motion of individual fuel droplets is tracked as they vaporize within the combustor; this provides the source terms for the gas phase equations. A typical single annular (CFM56) combustor was analyzed. Calculations were performed at both high and low-power conditions. The flow field, fuel distribution, and the temperatures within the combustor were computed. The fuel distribution showed a change between a single-phase and a two-phase calculation. The calculations indicate that the temperature in the reaction zone increases and the temperature of the fluid near the walls decreases when the spray model was used. The exhaust gas temperature field was found to be lower with the two-phase analysis. This reduction

may be attributed to differences in the calculated mixing patterns, as explained earlier. The spray model also gives a measure of the vaporization distance for the fuel within the combustor. The experimental information available was limited but a comparison revealed that the exit temperature field showed slightly better agreement with the test data when the calculations were performed with the spray model. This was observed for both high and low-power regimes of combustor operation.

Past experience (Shyy et al., 1988, 1986) has indicated that the physical models used have the greatest impact in the modeling of gas turbine combustor phenomena. Although factors such as grid size, entering air, fuel boundary conditions, etc., are important, these do not have as much of an influence on the results as the physical models themselves. The primary contribution of this paper is the application of a two-phase liquid spray physical model to a real piece of combustion hardware,

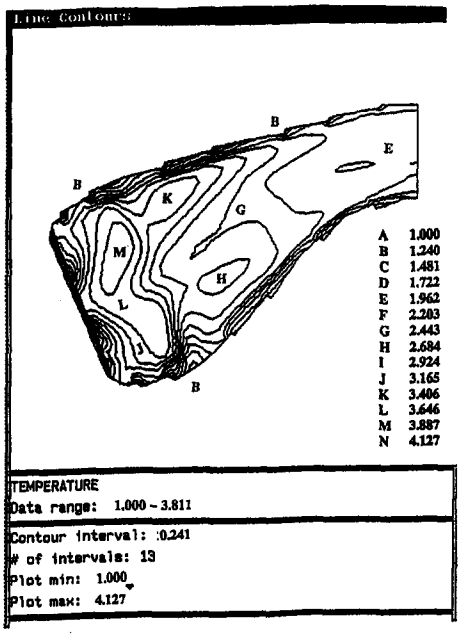

Fig. 12(*a*) Contours of non-dimensional temperature (T/T_{inlet}) in the side view plane K = 10, low power conditions, single phase model

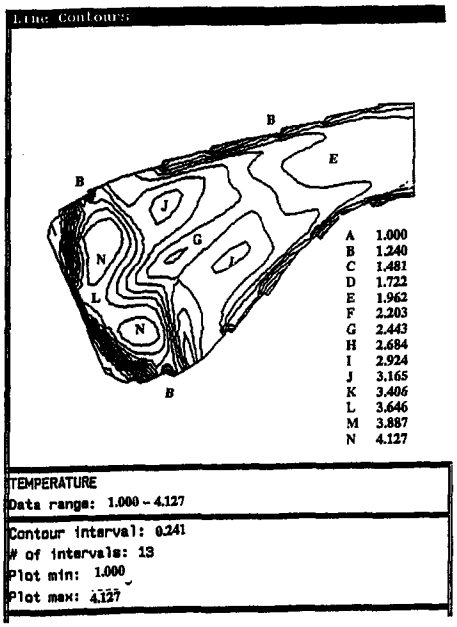

Fig. 12(*b*) Contours of non-dimensional temperature (T/T_{inlet}) in the side view plane K = 10, low power conditions, spray model

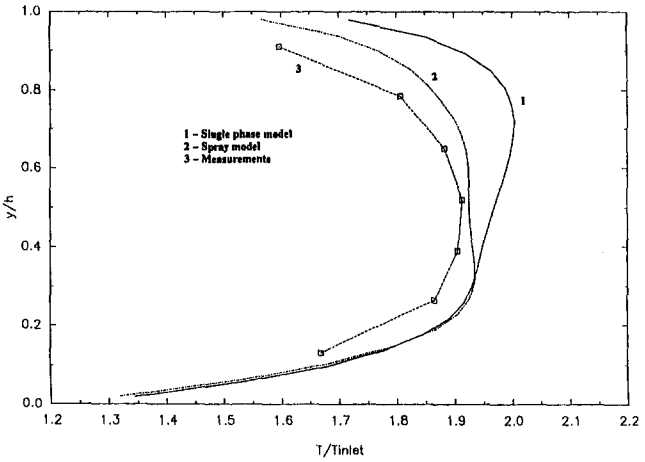

Fig. 13 Profile of circumferentially averaged temperatures in the exit plane-calculated and measured, low power

and its evaluation in the calculation of the corresponding flow and temperature field. With the spray model, the circumferentially averaged exhaust gas temperature field showed a small change relative to the single-phase model but certainly indicated closer agreement. Under most modes of operation of aircraft engine combustors, the assumption of fully vaporized fuel is not a bad one, but under conditions of very low power, a two-phase flow model may have to be used to get more accurate results.

Acknowledgments

The author wishes to thank GE-Aircraft Engines for granting permission to publish this work. Also, the author thanks Dr. Mark Braaten of GE-Corporate Research & Development and Dave Burrus and Tim Valachovic of GE-Aircraft Engines for several useful discussions during the course of this work.

References

Aggarwal, S. K., and Chitre, S., 1991, "Computations of Turbulent Evaporating Sprays," *J. Propulsion,* Vol. 7, pp. 213–220.

Banhawy, Y. E., and Whitelaw, J. H., 1980, "Calculation of the Flow Properties of a Confined Kerosene-Spray Flame," *AIAA J.,* Vol. 18, pp. 1503–1510.

Crowe, C. T., Sharma, M. P., and Stock, D. E., 1977, "The Particle-Source-In Cell (PSI-CELL) Model for Gas Droplet Flows," ASME *Journal of Fluids Engineering,* Vol. 99, pp. 325–332.

Dukowicz, J. K., 1980, "A Particle-Fluid Model for Liquid Sprays," *J. Comp. Physics,* Vol. 35, No. 2, pp. 229–253.

Ganesan, V., and Spalding, D. B., 1979, "Numerical Modeling of the Combustion of Fuel Sprays in Three-Dimensional Can Combustors," *Proc. 4th Int'l Symp. on Air-Breathing Engines,* pp. 177–186.

Gosman, A. D., and Ioannides, E., 1983, "Aspects of Computer Simulation of Liquid-Fueled Combustors," *J. Energy,* Vol. 7, pp. 482–490.

Jones, W. P., and Whitelaw, J. H., 1982, "Calculation Methods for Reacting Turbulent Flows: A Review," *Combust. Flame,* Vol. 48, pp. 1–26.

Lefebvre, A. H., 1989, *Atomization and Sprays,* Hemisphere Publishing Corporation, New York.

O'Rourke, P. J., and Bracco, F. V., 1980, "Modeling of Drop Interaction in Thick Sprays and a Comparison With Experiments," presented at IME Stratified Charge Automotive Engines Conference, London.

Patankar, S. V., 1980, *Numerical Heat Transfer and Fluid Flow,* McGraw-Hill, New York.

Ranz, W. E., and Marshall, W. R., Jr., 1952, "Evaporation From Drops," *Chemical Engineering Progress,* Vol. 48, p. 173.

Rosin, P., and Rammler, E., 1933, "The Laws Governing the Fineness of Powdered Coal," *Inst. of Fuel,* pp. 29–36.

Sabnis, J. S., and de Jong, F. J., 1990, "Calculation of the Two-Phase Flow in an Evaporating Spray Using Eulerian-Lagrangian Analysis," AIAA Paper No. 90-0447.

Shyy, W., and Braaten, M. E., 1986, "Three-Dimensional Analysis of the Flow in a Curved Hydraulic Turbine Draft Tube," *Int. J. Num. Meths. Fluids,* Vol. 6, pp. 861–882.

Shyy, W., Correa, S. M., and Braaten, M. E., 1986, "Computational Models for Gas Turbine Combustors," *Calculations of Turbulent Reactive Flows,* ASME AMD-Vol. 81, New York, pp. 141–183.

Shyy, W., Correa, S. M., and Braaten, M. E., 1988, "Computation of Flow in a Gas Turbine Combustor," *Combust. Sci. and Tech.,* Vol. 58, pp. 97–117.

Simmons, H. C., and Harding, C. F., 1990, "Some Effects of Using Water as a Test Fluid in Fuel Nozzle Spray Analysis," ASME Paper No. 90-GT-90.

Spalding, D. B., 1953, "The Combustion of Liquid Fuels," *Proc. 4th Symposium (Intl.) on Combustion,* Williams and Wilkins Co., Baltimore, MD, pp. 847–864.

Tolpadi, A. K., and Braaten, M. E., 1992, "Study of Branched Turboprop Inlet Ducts Using a Multiple Block Grid Calculation Procedure," ASME *Journal of Fluids Engineering,* Vol. 114, No. 3, pp. 379–385.

Tolpadi, A. K., Burrus, D. L., and Lawson, R. J., 1995, "Numerical Computation and Validation of Two-Phase Flow Downstream of a Gas Turbine Combustor Dome Swirl Cup," ASME JOURNAL OF ENGINEERING FOR GAS TURBINES AND POWER, Vol. 117, this issue, pp. 704–712.

Wallis, G. B., 1969, *One-Dimensional Two-Phase Flow,* McGraw-Hill, New York.

Wang, H. Y., McDonell, V. G., and Samuelsen, G. S., 1992, "The Two-Phase Flow Downstream of a Production Engine Combustor Swirl Cup," in: *Proc. 24th International Symposium on Combustion,* The Combustion Institute, Pittsburgh, PA, pp. 1457–1463.

Westbrook, C. K., 1977, "Three Dimensional Numerical Modeling of Liquid Fuel Sprays," *Proc. 16th Symposium (International) on Combustion,* The Combustion Institute, Pittsburgh, PA, pp. 1517–1526.

Williams, A., 1973, "Combustion of Droplets of Liquid Fuels: A Review," *Combustion Flame,* Vol. 21, pp. 1–31.

Williams, F. A., 1962, "Progress in Spray-Combustion Analysis," *Proc. 8th Symposium (Intl.) on Combustion,* Williams and Wilkens Co., Baltimore, MD, pp. 50–59.

Numerical Computation and Validation of Two-Phase Flow Downstream of a Gas Turbine Combustor Dome Swirl Cup

A. K. Tolpadi
General Electric Corporate Research and Development,
P.O. Box 8, Mail Stop K1-ES 206,
Schenectady, NY 12301

D. L. Burrus

R. J. Lawson

General Electric Aircraft Engines,
1 Neumann Way,
Mail Drop A309,
Cincinnati, OH 45215

The two-phase axisymmetric flow field downstream of the swirl cup of an advanced gas turbine combustor is studied numerically and validated against experimental Phase-Doppler Particle Analyzer (PDPA) data. The swirl cup analyzed is that of a single annular GE/SNECMA CFM56 turbofan engine that is comprised of a pair of coaxial counterswirling air streams together with a fuel atomizer. The atomized fuel mixes with the swirling air stream, resulting in the establishment of a complex two-phase flow field within the swirl chamber. The analysis procedure involves the solution of the gas phase equations in an Eulerian frame of reference using the code CONCERT. CONCERT has been developed and used extensively in the past and represents a fully elliptic body-fitted computational fluid dynamics code to predict flow fields in practical full-scale combustors. The flow in this study is assumed to be nonreacting and isothermal. The liquid phase is simulated by using a droplet spray model and by treating the motion of the fuel droplets in a Lagrangian frame of reference. Extensive PDPA data for the CFM56 engine swirl cup have been obtained at atmospheric pressure by using water as the fuel (Wang et al., 1992a). The PDPA system makes pointwise measurements that are fundamentally Eulerian. Measurements have been made of the continuous gas phase velocity together with discrete phase attributes such as droplet size, droplet number count, and droplet velocity distribution at various axial stations downstream of the injector. Numerical calculations were performed under the exact inlet and boundary conditions as the experimental measurements. The computed gas phase velocity field showed good agreement with the test data. The agreement was found to be best at the stations close to the primary venturi of the swirler and to be reasonable at later stations. The unique contribution of this work is the formulation of a numerical PDPA scheme for comparing droplet data. The numerical PDPA scheme essentially converts the Lagrangian droplet phase data to the format of the experimental PDPA. Several sampling volumes (bins) were selected within the computational domain. The trajectories of various droplets passing through these volumes were monitored and appropriately integrated to obtain the distribution of the droplet characteristics in space. The calculated droplet count and mean droplet velocity distributions were compared with the measurements and showed very good agreement in the case of larger size droplets and fair agreement for smaller size droplets.

Introduction

Imparting of swirl to the incoming air stream is an essential feature of modern gas turbine combustors. By introducing swirl, mixing is enhanced and a recirculation zone is established that improves flame stabilization. This mixing can be further enhanced by having a pair of coaxial swirling streams that are counterrotating. The injected fuel, the oncoming air stream, and the hot reaction products would all get well mixed.

Much work has been done to understand the nature of both reacting and nonreacting single-phase swirling flows (Mehta et al., 1989; Habib and Whitelaw, 1980; Ramos and Somer, 1985; Gouldin et al., 1983). All of these studies have been of experimental nature wherein the mean velocities, turbulence intensities, and Reynolds stresses within the swirl region have been measured using hot wires, five-hole probes, and Laser-Doppler Aneometry (LDA). These measurements have revealed that under both coswirl and counterswirl conditions, a closed recirculation zone is created at the centerline. The recirculation zone was found to contain low-velocity fluid with large turbulence intensities and high dissipation rates.

More recently, experiments have been conducted to characterize the droplet and continuous phase flow fields within a swirling air stream introduced co-annularly around a liquid atomizer (Wang et al., 1992a, 1992b, 1991; Bachalo et al., 1990). Droplet sizes and droplet velocities were measured at several axial stations using a Phase-Doppler Particle Analyzer (PDPA), which provided information regarding the degree and efficiency of atomization. The droplets were found to recirculate together with the continuous phase. Also, significant slip velocities were observed that were greater for larger size droplets.

Motivation

While on one hand, there is a fair amount of droplet spray data available in the literature, unfortunately not much of it has been used to validate computational fluid dynamics (CFD) codes directly. The goal of this present study is to perform a numerical analysis of the two-phase swirling flow in a real

Contributed by the International Gas Turbine Institute for publication in the ASME JOURNAL OF ENGINEERING FOR GAS TURBINES AND POWER. Manuscript received by the International Gas Turbine Institute May 1993. Associate Technical Editor: S. Samuelsen.

combustor swirl cup and to compare the calculated results against corresponding experimental PDPA data. What makes this work unique is the effort to perform a numerical/experimental verification of both the gaseous and liquid phases in a *real* piece of combustion hardware.

In a broader context, this segment of work is part of an ongoing effort to validate computational tools being used by aircraft engine combustor designers. As computing costs have dropped over the years, CFD is being increasingly used by combustion specialists to study phenomena such as droplet vaporization, fuel–air mixing, particulate emissions, pattern factor studies, etc. While CFD will never replace "hard core" testing, it is a very powerful tool that can provide a good initial guidance to design. It is therefore essential to verify computations continuously against experimental data. The phenomenon of two-phase flow in an aircraft engine combustor is very complex; to this end, this work was undertaken to calculate both the continuous and discrete phases present in a combustor dome swirl cup with the objective of comparing them against test data.

The combustor chosen for this purpose is a GE/SNECMA single annular CFM56 engine combustor and is shown schematically in Fig. 1. The encircled portion is the swirl cup region that is shown separately further below in the figure. The swirler is a dual-stage counterrotating swirler assembly shown in greater detail in Fig. 2. The swirler assembly is comprised of four principal components. Air flow from the primary swirler is injected through eight equally spaced holes drilled into the part at a compound angle, 24 deg relative to vertical and 20 deg tangential. The primary swirler component also contains the retainer for the fuel injector. The flow coming out of the primary swirler is strictly three dimensional, but is approximated to be two dimensional axisymmetric to simplify the analysis. This approximation is done by matching the mass flow and by forcing the axial, radial, and swirl velocity components to scale in proportion to the flow angles of the swirler hardware. The inlet velocity distribution is thus determined based on continuity. The secondary swirler is of the radial inflow type. It contains ten equally spaced vanes at an angle of 70 deg relative to the radial. The flow coming out of the secondary swirler is actually two dimensional. A venturi section is used to separate the two counterrotating air streams initially. Fuel from the injector nozzle is initially sprayed onto the surface of the venturi where it forms a thin film. As the fuel film travels to the end of the venturi, it encounters the shear generated between the two counterrotating air streams. The high-intensity turbulence in this shear layer serves to re-atomize the fuel film at the trailing edge of the venturi into fine droplets that then exit the swirler assembly through a 90 deg conical exit flare. The flare controls the radial dispersion of the mixture as it leaves the swirler and enters the combustion chamber. PDPA data for this swirl cup have been obtained by Wang et al. (1992a). The air was at atmospheric pressure and *water was used in lieu of liquid fuel.* The flow conditions and other details of the experiments have been described by Wang et al. (1992a) and will not be repeated here. Droplet size and velocity information have been obtained at three axial stations downstream of the injector.

The flow field was calculated under the same experimental conditions by assuming that it is two-dimensional and axisymmetric. An Eulerian–Lagrangian approach was used. The gas phase equations are solved in an Eulerian frame of reference by using the two-dimensional version of the CONCERT code. CONCERT is a fully elliptic body-fitted CFD code based on

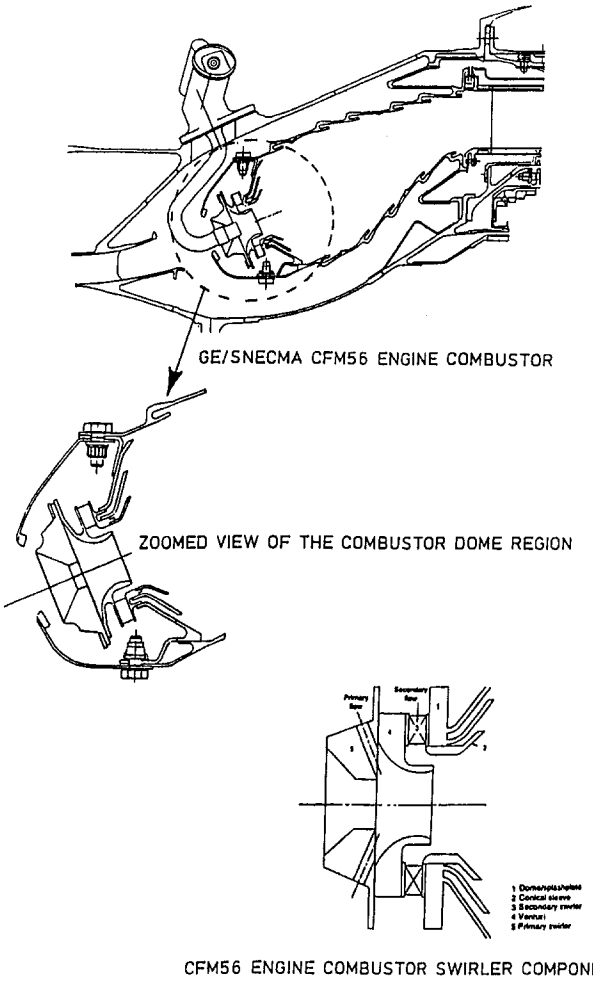

Fig. 1 Schematic diagram of a GE/SNECMA CFM56 engine combustor that shows the swirler

pressure correction techniques (Patankar, 1980) and has been developed extensively (Shyy et al., 1988; Tolpadi, 1992) at General Electric. It represents a comprehensive algorithm that combines reasonable combustion models with good numerical procedures to yield a modeling capability for flows in practical gas turbine combustor geometries. In this work, since the experiments did not involve combustion, the flow was assumed to be isothermal and nonreacting. The liquid phase is modeled by treating the motion of the fuel droplets in a Lagrangian frame of reference. The gas phase calculation provides the updated velocity and turbulence field required by the trajectory analysis. To make a one-on-one comparison with the measurements, a numerical PDPA scheme was set up wherein several sampling volumes were selected, and the trajectories of the different droplets passing through them were monitored and appropriately integrated. The development of this numerical PDPA scheme is the major contribution of this paper.

Methodology

Mathematical Description of the Gas and Liquid Phases. The governing equations for the gas phase are those representing

Nomenclature

dn/n = normalized droplet number count
R = radial distance from the centerline
U = axial velocity
V = radial velocity
W = swirl velocity
x = distance from venturi tip

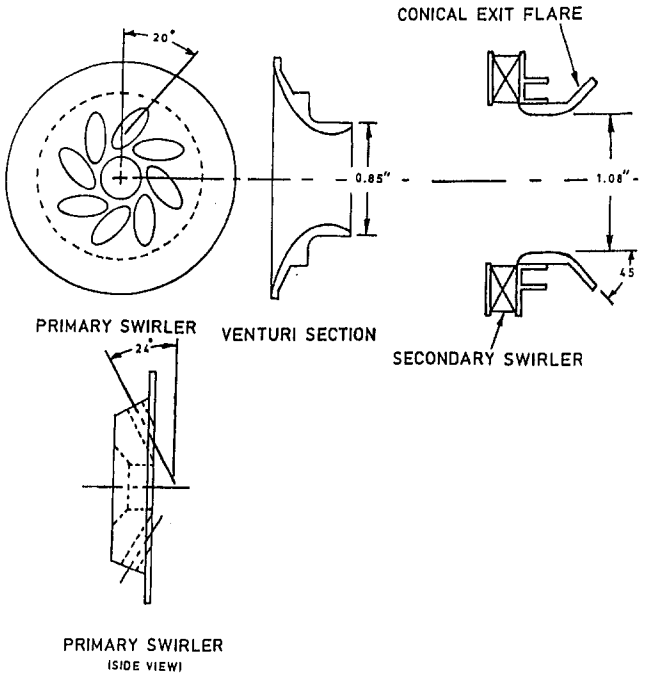

Fig. 2 Details of the CFM56 swirl cup

the conservation of mass and momentum in the two coordinate directions. All three velocity components, including the swirl velocity, are considered, but they are each functions of only two coordinates. Turbulence is modeled using the standard k–ϵ model along with the wall function treatment for near-wall regions. Using a coordinate transformation, these equations are transformed from an arbitrary physical domain to a rectangular parallelepiped. After making finite difference approximations to the equations, they are solved using the SIMPLE algorithm (Patankar, 1980). The numerical algorithm details are available from Tolpadi and Braaten (1992) and Tolpadi (1995).

The treatment of the liquid phase has been described in detail by Tolpadi (1995) and only the important details will be given here. A droplet spray model is used. The trajectories of the fuel droplets that are assumed to be spherical are obtained within the calculation region based on the gas phase velocity and turbulence field obtained from CONCERT. Ordinary differential equations are written for the droplet motion that are integrated to give the drop velocity and position during its travel. The integration is performed using a Runge–Kutta method. It is assumed that there is no evaporation, thus implying that the drop diameter does not change with position. The drag coefficient on the droplet is obtained from experimental correlations taken from Wallis (1969).

Numerical PDPA Scheme. The Phase-Doppler Particle Analyzer makes pointwise measurements that are essentially Eulerian, that is, the PDPA focuses on a point in the flow field and makes measurements of the droplets as they pass through the point. Various droplet characteristics are measured. The PDPA makes measurements over several size ranges. For each size range, the following are measured (among others): (1) the droplet number count, i.e., the number of droplets detected per unit time, (2) the mean droplet velocity, and the (3) rms velocity. The PDPA system used by Wang et al. (1992a) measured two perpendicular velocity components simultaneously. The third velocity component was obtained by rotating the PDPA by 90 deg. This procedure was used to obtain the droplet information at various selected locations in the flow.

Comparison of the droplet phase data with the results from a CFD code is very challenging. This is because of the fact that while on one hand the PDPA makes pointwise Eulerian measurements, on the other hand the numerical calculation of the droplets in any CFD code is usually performed in a Lagrangian frame of reference. Thus, in order to make a one on one comparison of the discrete liquid phase that is meaningful, it is necessary to either transform the PDPA information to the Lagrangian frame of reference or convert the droplet information from the CFD code to the format of the experimental PDPA. In this paper, the latter approach is chosen. Wang et al. (1992a) obtained experimental data at three axial locations at distances of 17 mm, 26 mm, and 36 mm from the end of the venturi (Fig. 2). At each of these axial positions, PDPA measurements were made at several radii. To compare the calculated droplet parameters against this data, the initial condition of the droplets as they leave the swirler assembly is required. Obviously this was not measured and is generally the biggest unknown in such droplet studies. Therefore, the best that can be done is to use the experimental data at the first station (17 mm) as the initial condition for the trajectory analysis. Measurements were made over six droplet size ranges: 1–10.56 μm, 10.57–20.26 μm, 20.27–29.95 μm, 29.97–39.65 μm, 49.37–59.04 μm, and 73.61–88.14 μm. It may be noted that in the work of Wang et al. (1992a), the data in the two size ranges 39.66–49.36 μm and 59.05–73.60 μm were not reported even though they were measured. This was done because from a physics standpoint, these two size ranges did not reveal anything that was different from the other adjacent size ranges. Each size range was considered separately, and a mean droplet size was assigned for the trajectory analysis. The droplet number count information at the first station (which can be thought of as the droplet source station) was normalized, which provided the initial droplet distribution along the radius. A statistically large number of trajectories were initialized at the source station in the same proportion as the normalized distribution. Their initial velocities also corresponded to the measurements.

The second station (26 mm) can be thought of as the detection station. At this station, the radial extent from the centerline to the outer boundary was divided into a number of equally spaced cells (bins) adjacent to each other. Some parametric studies were conducted to determine the best bin size, which was ultimately chosen to be about 100 μm. By following each droplet trajectory from the first station, the bin through which it passes at the detection station was obtained. Every single droplet initiated from the source station would pass through some bin or the other at the detection station. Thus, a similar number count distribution was obtained at the second station, which also normalized and directly compared to the measured number count distribution at this station. In addition, the velocity components of the droplets as obtained from the trajectory calculation at the second station were averaged and compared to the measurements. The experimental PDPA bin size corresponding to the probe volume (Wang et al., 1992a) was about 350 μm. It should be pointed out that the experimental and numerical PDPA bin sizes do not have to be the same because it is the profiles of information that are compared at the detection station. The droplets originating from the source station were followed all the way to the third station (36 mm) as well where the same detection procedure was repeated.

There are certain sources of error that need to be kept in mind when performing such a comparison. For each droplet size, the trajectories are assumed to start at the first station (x = 17 mm) at precisely those radial locations corresponding to the PDPA measurements. In reality, the droplets originate at all other intermediate locations as well but information about these locations is unknown since measurements were made at only a finite number of points. In the absence of the "complete" initial droplet description, the assumption has to be made that these drops start at discrete locations. Also, the PDPA makes point measurements of the flow field in sequence as opposed to measuring the flow field simultaneously. The CONCERT code per-

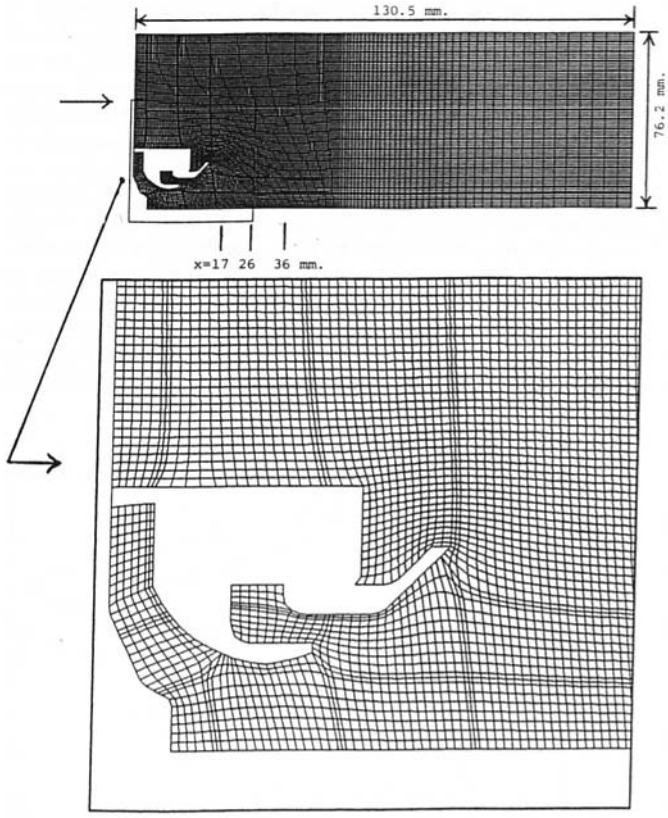

Fig. 3 Grid model of the swirl cup (144 × 93 nodes) together with a close-up view near the cup

forms the calculation to determine the entire steady state flow field. There is an obvious discrepancy in comparing the results from a steady-state calculation with data from a measurement technique that is sequential.

In an earlier piece of work (Tolpadi, 1994), the two-phase flow field present in a simple methanol fuel spray was computed under both nonreacting and reacting conditions. PDPA data for this configuration were also available (McDonell et al, 1992a, 1992b). The calculated droplet attributes showed excellent agreement with the data for the case of the nonreacting spray over all size ranges; with the reacting spray only the larger size droplets showed good agreement. The work described for the simple geometry by Tolpadi (1994) serves as an excellent validation of the overall comparison procedure used in this paper in which the hardware and the flow field are far more complex.

The effect of turbulence on the droplet motion was accounted for by using a stochastic approach, which essentially requires the knowledge of the instantaneous gas phase velocity at every position along the droplet trajectory. This is obtained from the computed mean velocity and the turbulence kinetic energy. The turbulence is assumed to be isotropic and to possess a Gaussian probability distribution in the fluctuating velocity, whose standard deviation is $(2k/3)^{1/2}$ (Gosman and Ioannides, 1983). The distribution is randomly sampled during the flight of a droplet to get the instantaneous gas phase velocity.

Results

Comparison of the Gas Phase Results. As mentioned earlier, calculations were performed under the same conditions as the measurements. Figure 3 shows the grid for the swirl cup corresponding to the hardware shown in Fig. 2. This grid has 144 points in the axial and 93 points in the radial direction. This very dense grid was found to be sufficiently fine for the purpose of these types of swirl cup calculations. The grid was generated by using an elliptic grid generation procedure by treating the swirl cup as an internal obstacle and by suitably meshing around it. The finite differencing scheme used was QUICK (Leonard, 1979). The air flow rate through the primary swirler is 0.0070 kg/s and through the secondary swirler it is 0.0100 kg/s. The inlet turbulence intensity was assumed to be 8 percent. The experiments of Wang et al. (1992a) were performed by placing this swirl cup in a large chamber in which the outer flow was axial and uniform. This outer flow was modeled by specifying a velocity of 0.495 m/s at the boundary as shown. The radial outer boundary is modeled as a wall, which represents the side wall of the plenum tank within which the experimental data was taken. The air was at atmospheric pressure and isothermal (temperature = 289 K). Figure 4 shows the calculated streamlines and indicates the presence of a strong recirculation zone just beyond the swirler close to the centerline. This recirculation zone is produced as a consequence of the counterswirling air streams coming out of the primary and secondary swirler. There is another relatively weak recirculation zone on the outside, which is to be expected since the outer boundary is a wall. However, this outer recirculation zone did not affect the calculated spray characteristics since the location of this zone is axially well beyond and radially well outside the region of the measurements. Zero normal gradient were used used at the exit boundary, which was far removed to ensure that its position did not influence the solution close to the swirler where the measurements were made.

PDPA measurements of the gas phase flow field were made by switching off the fuel injector and by seeding the flow with an agent of size one micron. Figure 3 indicates the locations of the three stations where the axial, radial, and swirl velocity components were measured. The radial profiles of these three velocity components at $x = 17$ mm have been compared against the corresponding calculated profiles in Fig. 5 The calculated axial and radial velocity profiles show excellent agreement with the measurements. Both the calculations and the measurements show negative values of the axial velocity near the centerline, indicating the presence of a recirculation zone there. The profiles of the swirl velocity, although similar in shape, show some disagreement; an explanation of this observation will be given later.

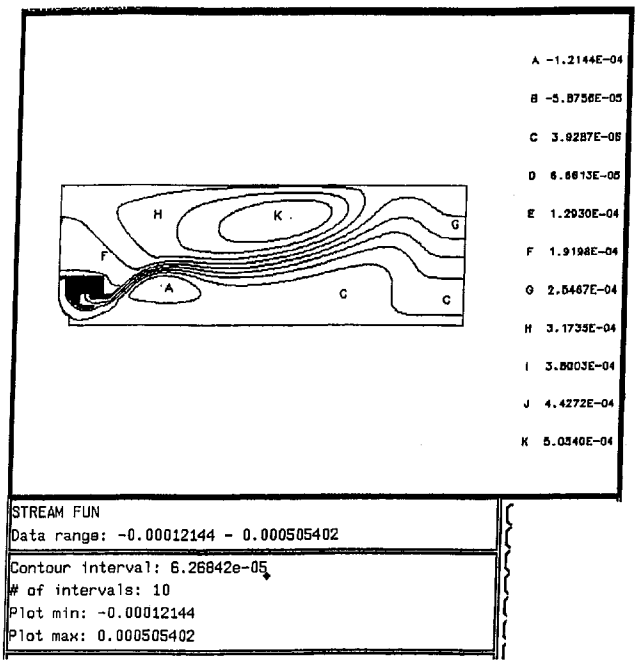

Fig. 4 Computed streamlines of the flow in the swirler

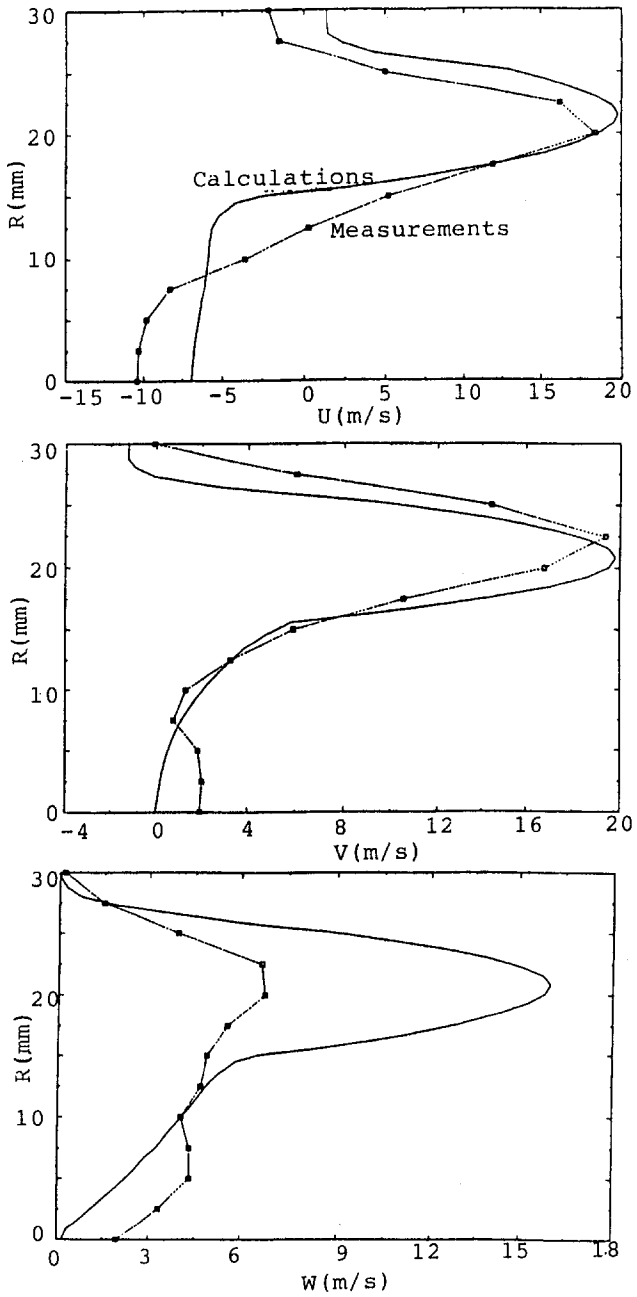

Fig. 5 Calculated and measured radial profiles of the gas phase axial, radial and swirl velocity components at x = 17 mm

Figure 6 compares the profiles of the three velocity components at x = 26 mm. Clearly, the agreement is still good but perhaps not as good as the agreement at x = 17 mm. To understand this fact, it is important first to understand that the computations were performed by assuming that the swirler geometry is axisymmetric, as evidenced from Figs. 5 and 6, in which the calculated radial and swirl velocity components decrease to zero at the centerline. However, the data indicate a nonzero value of the radial and swirl velocity showing that the measurements are nonaxisymmetric. This means that the geometric and aerodynamic centerlines are not coincident. This lack of axisymmetry in the measurements could be due to several reasons. Imperfections in the hardware could be a definite reason. Also, the flow from the swirler enters an open space, creating secondary flows that could certainly displace the aerodynamic center from the geometric center. Since the flow is at atmospheric pressure, gravity could be a factor causing this displacement. This displacement of the two centerlines has also been observed in the LDA measurements of Mehta et al. (1989) and the PDPA measurements of Wang et al. (1991, 1992b). Ideally, at the centerline of an axisymmetric flow, a PDPA system should measure a nonzero axial velocity component and zero radial velocity (the swirl velocity, of course, has no meaning). In reality, because of displacement of the two centerlines, the PDPA would be able to make a meaningful axial velocity measurement close to the centerline, but the perpendicular velocity component measured would be some combination of the radial and swirl velocity components. Away from the centerline, all three velocity components are clearly distinguishable and therefore the PDPA measurement of the radial and swirl velocities would be more reliable. The measured radial and swirl velocity at the centerline may be seen to increase with distance from the

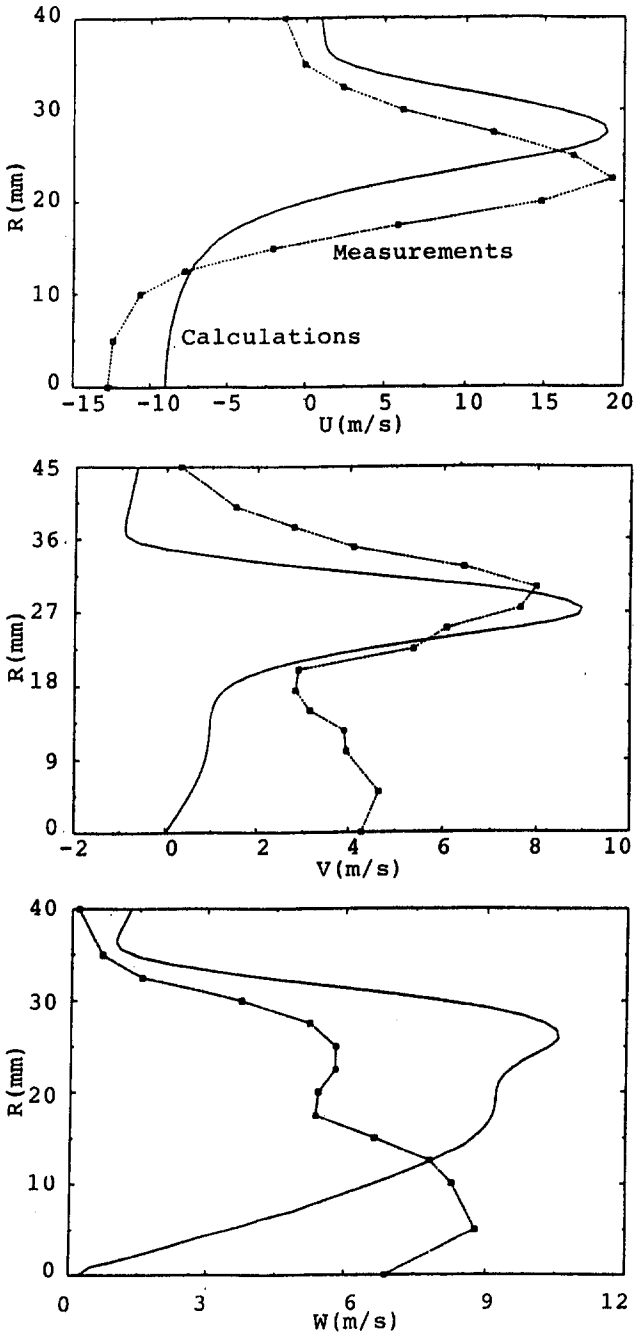

Fig. 6 Calculated and measured radial profiles of the gas phase axial, radial, and swirl velocity components at x = 26 mm

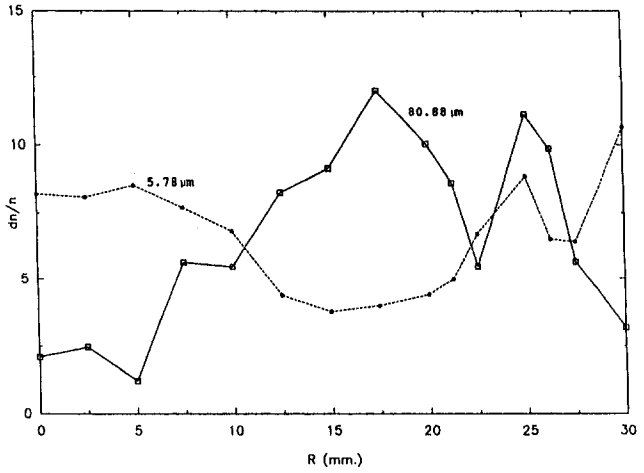

Fig. 7 Normalized initial number count distribution at x = 17 mm for droplets of mean size 5.78 μm obtained from PDPA data (Wang et al., 1992a)

venturi indicating that there is greater deviation between the geometric and aerodynamic centerlines as one moves further away from the swirler. At x = 26 mm, the calculated radial and swirl velocities show better agreement with corresponding data at larger radii consistent with the explanations just given. Although not shown here, similar observations were made when the data were compared at x = 36 mm.

Comparison of the Liquid Phase Results. As explained earlier, the liquid phase results were compared by establishing a numerical PDPA scheme. The experimental PDPA data at x = 17 mm were used to obtain the initial conditions for the trajectory calculations. Six mean droplet sizes were chosen corresponding to each of the six droplet size ranges. These droplet sizes were 5.78 μm, 15.42 μm, 25.11 μm, 34.81 μm, 54.20 μm, and 80.88 μm, respectively. For each drop size, a total of 1000 trajectories were initialized. The distribution of the initial positions along the radius corresponded to the normalized number count (dn/n) data obtained by Wang et al. (1992a). Figure 7 shows, for example, the percentage distribution of the initial trajectory locations (dn/n) for the 80.88 μm and 5.78 μm size droplets. Their initial velocities are taken from Wang et al. (1992a) and will not be repeated here. In what follows, the normalized number count and mean droplet velocities calculated at the next two stations, x = 26 mm and x = 36 mm, will be compared with the PDPA measurements. A calculation was also performed by initializing a total of 10,000 droplets, but the results obtained were essentially identical to those obtained with 1000 droplets. Thus, a total of 1000 droplets in each size range was considered to be statistically sufficient. As can be seen from the two profiles given in Fig. 7, fewer larger size droplets are injected near the centerline and more are injected on the outside, which is vice-versa for the small droplets.

Figure 8 compares the calculated number count, mean axial velocity, mean radial velocity, and mean swirl velocity with the measurements at x = 26 mm and for the droplets of mean size 80.88 μm. To avoid any confusion between the plots, it may be noted that the ordinate of each plot is different and is appropriately indicated. The agreement between the number counts and the axial and radial velocity profiles may be seen to be excellent. The normalized number count shows two peaks in the measurements that can be seen in the computations as well. Generally speaking, the larger size droplets are less affected by the fluid flow field and tend to follow a more independent path, whereas smaller size droplets tend to follow the fluid flow field. It may be seen from Fig. 7 that the initial normalized distribution of the droplet count for the 80.88 μm droplet at x = 17 mm has two peaks, which are still present at x = 26 mm, showing that the fluid velocity field has a lesser influence on the trajectory of this particular size droplet. The mean axial and radial velocity distribution almost precisely follows the PDPA measurements. The mean swirl velocity distributions do not agree as well, which may again be attributed to the deviation between the aerodynamic and geometric centerlines of the flow. In Fig. 8, the swirl velocity shows better agreement away from the centerline. The data again show nonzero velocities near the centerline, indicating once again the shift between the geometric and the aerodynamic centerlines. Figure 9 shows the same comparisons at x = 26 mm for the intermediate size droplet of 34.81

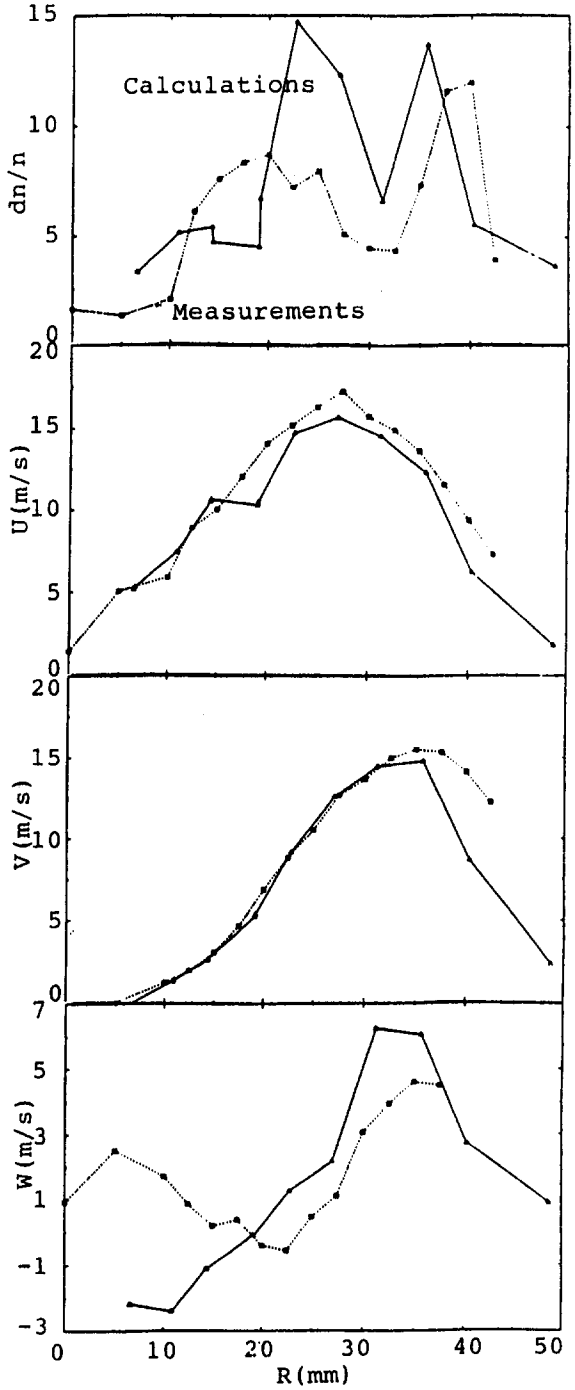

Fig. 8 Calculated and measured radial profiles of the normalized droplet number count and mean droplet velocity components for droplets of mean size 80.88 μm at x = 26 mm

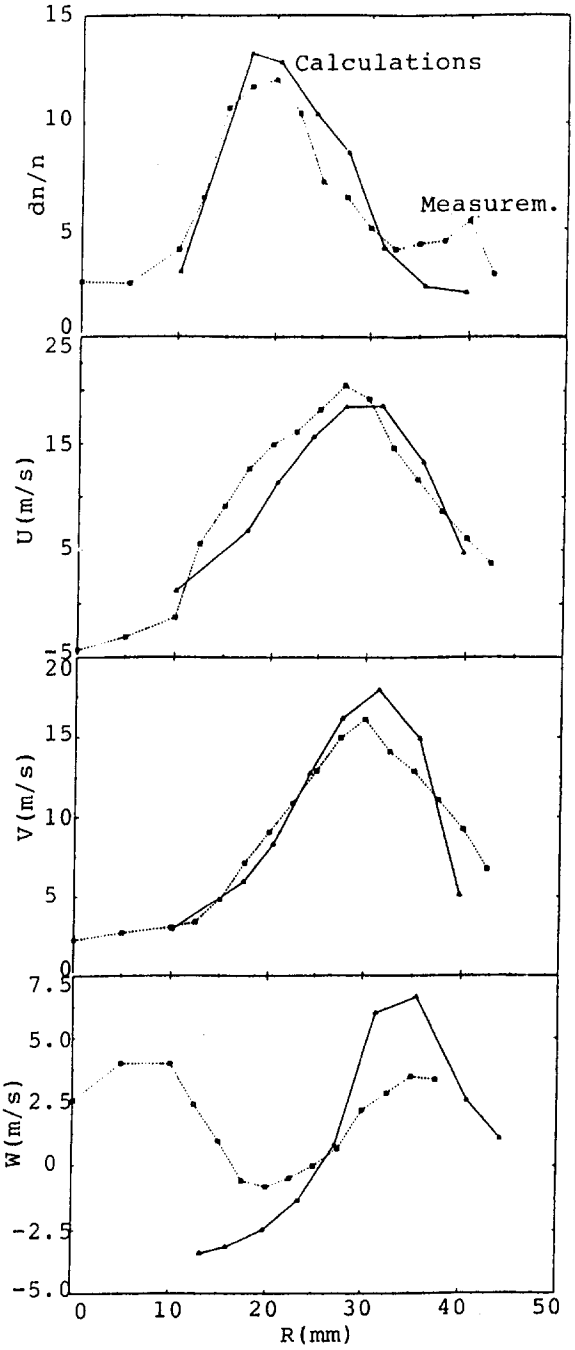

Fig. 9 Calculated and measured radial profiles of the normalized droplet number count and mean droplet velocity components for droplets of mean size 34.81 μm at x = 26 mm

μm. Again, other than the swirl velocity distribution, which shows poor agreement, the other three droplet attributes show excellent agreement.

Figure 10 makes the corresponding comparisons for the case of the smallest droplet of size 5.78 μm at the axial station of x = 26 mm. What is immediately noticeable is that the droplets in the calculations are detected only over the radius interval of approximately 25 to 35 mm, whereas the measurements have detected droplets over the entire range of 0 to 45 mm. Several possible reasons could be hypothesized to explain this discrepancy. An important assumption being made in the spray computations is that the droplets do not evaporate. Strictly speaking, vaporization does occur. Vaporization is caused by gradients in concentration but it has not been accounted for in the computations at the present time. Since the vaporization rate is much greater for droplets of smaller size, this assumption of no evaporation would be less applicable for small droplets and hence the discrepancy in Fig. 10. Another possible reason was alluded to earlier, which is that all droplets are assumed to start at the station x = 17 mm at exactly those radial locations corresponding to the PDPA data. These radial locations can actually be seen in Fig. 7. In reality, the droplets originate at all other intermediate locations as well. This assumption could be a probable reason for the detection over a much shorter range in Fig. 10. Thus, a plausible scenario is that droplets of size slightly greater than 5.78 μm originate from several intermediate locations at x = 17 mm, partially vaporize (due to concentration

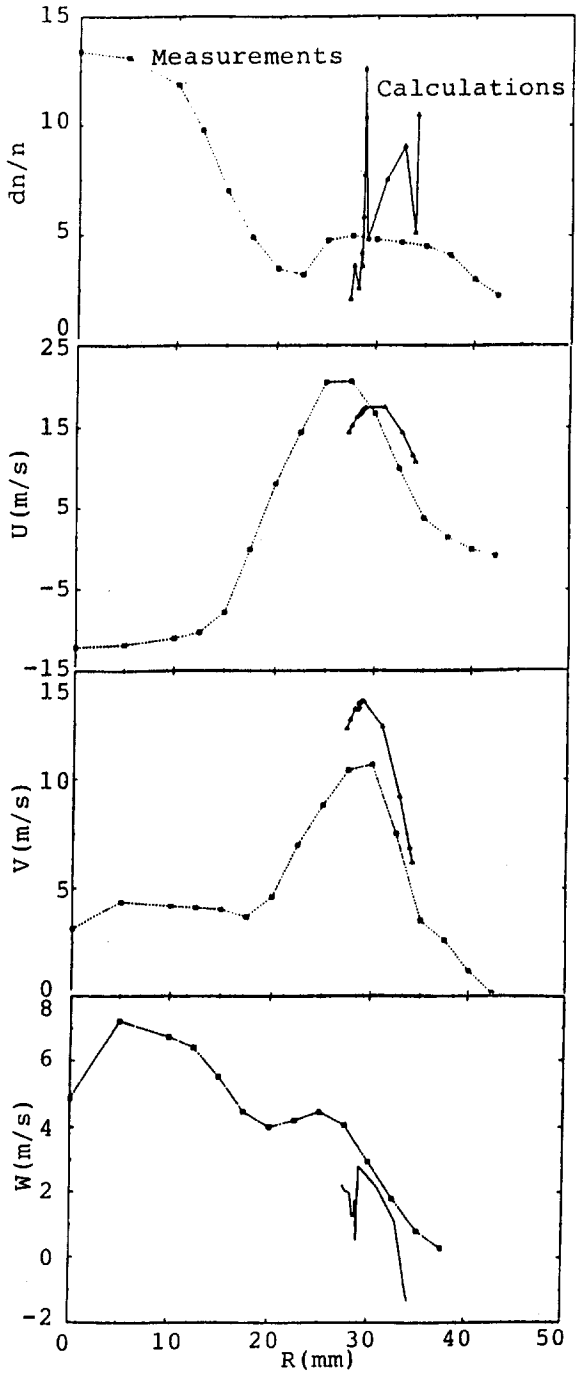

Fig. 10 Calculated and measured radial profiles of the normalized droplet number count and mean droplet velocity components for droplets of mean size 5.78 μm at x = 26 mm

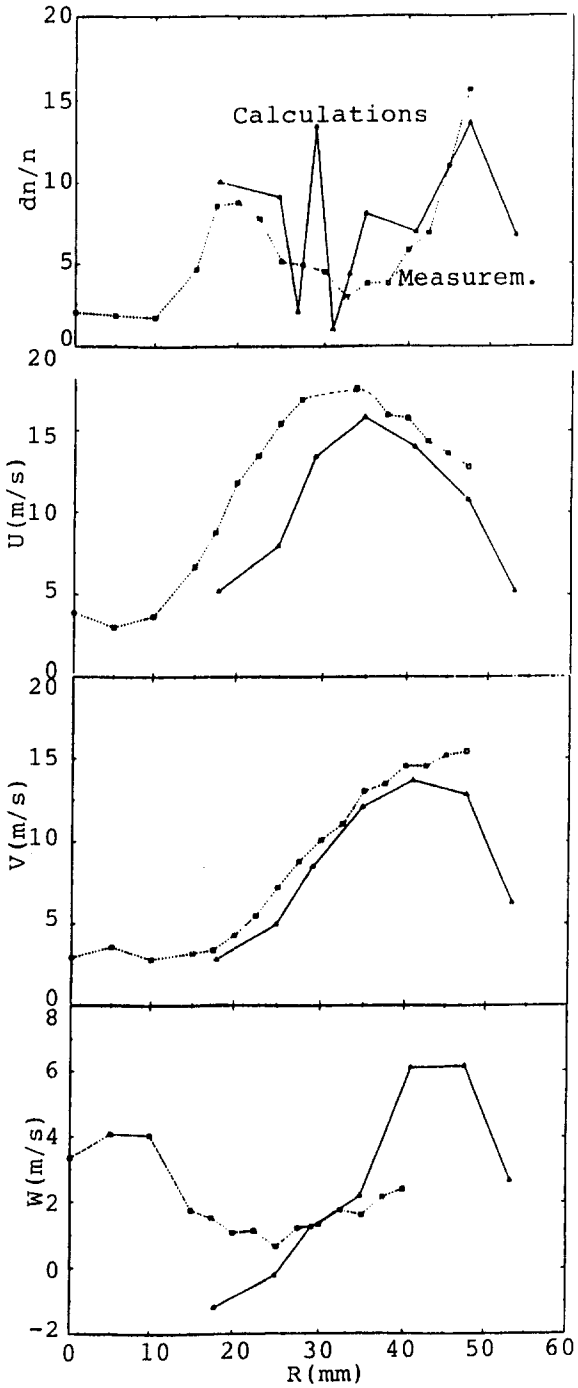

Fig. 11 Calculated and measured radial profiles of the normalized droplet number count and mean droplet velocity components for droplets of mean size 80.88 μm at x = 36 mm

gradients) along their path and become smaller droplets, get trapped in the recirculation zone, and get detected at x = 26 mm. It was seen from Fig. 8 that the calculated normalized number count distribution for the 80.88 μm droplet more closely followed the corresponding initial condition of Fig. 7. The fact that for the 5.78 μm droplet, the distribution is clustered more around a finite radius interval, shows that these droplets follow their way around the outside of the recirculation zone.

The number of comparison plots that can be presented is endless; however, one more figure will be shown that is representative of the comparisons obtained at x = 36 mm. Figure 11 shows the droplet attributes for the 80.88 μm droplet. The comparison between the calculations and the data may be seen to be quite good but not as good as the matching obtained for this droplet size at x = 26 mm. This is again because of greater and greater deviation between the aerodynamic and geometric centerlines further and further downstream from the venturi. The comparisons obtained were found to be relatively poorer for smaller size droplets at x = 36 mm, as expected.

Conclusions

In this work, the gas phase flow field and the spray characteristics have been calculated for a CFM56 engine swirl cup, which represents a real piece of combustion hardware. The calculated gas phase flow field showed the presence of a large recirculation zone near the centerline, which was confirmed by the PDPA measurements. Barring the swirl velocity, the gas phase velocity profiles obtained from the computations compared quite well with the PDPA data. As for the comparison of the liquid phase, the computations of droplet number count and mean droplet velocities showed very good agreement with the PDPA data for large and intermediate size droplets. However, the comparison was poor for small droplets; the corresponding reasons were given earlier. All comparisons of both the gas and liquid phases were found to be best at the initial stations close to the venturi but got worse further downstream because of the deviation observed between the geometric and aerodynamic centerlines in the measurements. Smaller droplets were found to have a tendency to recirculate and follow the gas phase flow field. Larger droplets were observed to be less affected by the flow field.

The primary contribution of this paper is in the development of the numerical PDPA scheme for the purpose of comparing calculations of the liquid phase with corresponding measurements. This technique has been used in the study of the flow field present in a real combustor swirl cup. The problems associated in validating a two-phase flow CFD code against experimental PDPA data have been brought out in this work. Fundamentally, the experimental data are taken from point to point that is essentially Eulerian whereas droplet calculations from a CFD code are made in a Lagrangian frame of reference. Ideally, it would be most beneficial (from the standpoint of CFD) if the droplet characteristics are also measured using a Lagrangian technique, i.e., a single drop is tracked in the flow field and its position, velocity, and other attributes are measured as a function of time. It would also be very useful if the initial conditions of the droplets as they leave the injector are somehow obtained either through direct measurements or by extrapolation from first station PDPA data. These suggestions would make the comparisons a lot easier. It is hoped that this work will provide useful guidance to those that are attempting to model flows using PDPA data and also those that are taking PDPA data for the purpose of establishing CFD model inputs.

Acknowledgments

The authors wish to acknowledge several useful discussions they had at various stages of this work with Dr. Vince G. McDonell and Dr. G. Scott Samuelsen of the University of California, Irvine (UCI). The help offered by Dr. McDonell in interpreting the PDPA data taken at UCI is appreciated.

References

Bachalo, W. D., Rudoff, R. C., and Sankar, S. V., 1990, "Time-Resolved Measurements of Spray Drop Size and Velocity," *Liquid Particle Size Measurement Techniques*, second volume, ASTM, Philadelphia, pp. 209–224.

Gosman, A. D., and Ioannides, E., 1983, "Aspects of Computer Simulation of Liquid-Fueled Combustors," *J. Energy*, Vol. 7, pp. 482–490.

Gouldin, F. C., Depsky, J. S., and Lee, S. L., 1983, "Velocity Field Characteristics of a Swirling Flow Combustor," AIAA Paper No. 83-0314.

Habib, M. A., and Whitelaw, J. H., 1980, "Velocity Characteristics of Confined Coaxial Jets With and Without Swirl," ASME *Journal of Fluids Engineering*, Vol. 102, pp. 47–53.

Leonard, B. P., 1979, "A Stable and Accurate Convective Modeling Procedure Based on Quadratic Upstream Interpolation," *Comp. Meths. Appl. Mech. Eng.*, Vol. 19, pp. 59–98.

McDonell, V. G., Adachi, M., and Samuelsen, G. S., 1993a, "Structure of Reacting and Non-reacting Non-swirling Air-Assisted Methanol Sprays, Part I: Gas Phase Properties," *Atomization and Sprays*, Vol. 3, pp. 389–410.

McDonell, V. G., Adachi, M., and Samuelsen, G. S., 1993b, "Structure of Reacting and Non-reacting Non-swirling Air-Assisted Methanol Sprays, Part II: Droplet Behavior," *Atomization and Sprays*, Vol. 3, pp. 411–436.

Mehta, J. M., Shin, H. W., and Wisler, D. C., 1989, "Mean Velocity and Turbulent Flow Field Characteristics Inside an Advanced Combustor Swirl Cup," AIAA Paper No. 89-0215.

Patankar, S. V., 1980, *Numerical Heat Transfer and Fluid Flow*, McGraw-Hill, New York.

Ramos, J. J., and Somer, H. T., 1985, "Swirling Flow in a Research Combustor," *AIAA Journal*, Vol. 23, No. 2, pp. 241–248.

Shyy, W., Correa, S. M., and Braaten, M. E., 1988, "Computation of Flow in a Gas Turbine Combustor," *Combust. Sci. and Tech.*, Vol. 58, pp. 97–117.

Tolpadi, A. K., and Braaten, M. E., 1992, "Study of Branched Turboprop Inlet Ducts Using a Multiple Block Grid Calculation Procedure," ASME *Journal of Fluids Engineering*, Vol. 114, pp. 379–385.

Tolpadi, A. K., 1994, "Two-Phase Flow Calculation of Reacting and Non-reacting Non-swirling Air-Assisted Methanol Sprays," *Atomization and Sprays*, Vol. 4, pp. 303–323.

Tolpadi, A. K., 1995, "Calculation of Two-Phase Flow in Gas Turbine Combustors," ASME JOURNAL OF ENGINEERING FOR GAS TURBINES AND POWER, Vol. 117, this issue, pp. 695–703; also AIAA Paper No. 92-3468.

Wallis, G. B., 1969, *One-Dimensional Two-Phase Flow*, McGraw-Hill, New York.

Wang, H. Y., Sowa, W. A., McDonell, V. G., and Samuelsen, G. S., 1991, "Dynamics of Discrete Phase in a Gas Turbine Co-axial, Counter-swirling, Combustor Dome Swirl Cup," AIAA Paper No. 91-2353.

Wang, H. Y., McDonell, V. G., and Samuelsen, G. S., 1992a, "The Two-Phase Flow Downstream of a Production Engine Combustor Swirl Cup," in *Proceedings of the 24th International Symposium on Combustion*, The Combustion Institute, Pittsburgh, PA, pp. 1457–1463.

Wang, H. Y., McDonell, V. G., Sowa, W. A., and Samuelsen, G. S., 1992b, "Characterization of a Two-Phase Flow Field Downstream of a 3x-Scale Gas Turbine Co-axial Counter-swirling Combustor Dome Swirl Cup," AIAA Paper No. 92-0229.

D. M. Leis
Black & Veatch,
Kansas City, MO 64114

M. J. Boss

M. P. Melsert

GE Industrial and Power Systems,
Schenectady, NY 12345

Medway: A High-Efficiency Combined Cycle Power Plant Design

The Medway Project is a 660 MW combined cycle power plant, which employs two of the world's largest advanced technology MS9001FA combustion turbine generators and an advanced design reheat steam turbine generator in a power plant system designed for high reliability and efficiency. This paper discusses the power plant system optimization and design, including thermodynamic cycle selection, equipment arrangement, and system operation. The design of the MS9001FA combustion turbine generator and the steam turbine generator, including tailoring for the specific application conditions, is discussed.

Medway's Objective: High Efficiency

The Medway Power Station, a 660 MW combined cycle power plant about 44 miles/70 km east of London, is a first of its kind in the United Kingdom. The plant is the first to install two General Electric (GE) 9FA advanced technology combustion turbines coupled to two triple pressure reheat natural circulation heat recovery steam generators (HRSGs), which feed steam to a reheat steam turbine.

The combustion turbines, rated at 228 MW each, will produce the highest output of any operating combustion turbines in the world, a combination that will result in one of the highest efficiency combined cycle plants in the world.

Medway Power Limited, a joint venture company formed by Applied Energy Services Electric Ltd. (AES) and subsidiaries of Seeboard and Southern Electric, is jointly developing the Medway Power Station on the Isle of Grain, Kent, on the River Medway, east of London. AES Medway Operations (AESMO) will operate and maintain the station. The Medway Station is under construction and commercial operation is planned for 1 August 1995.

In April 1992, Medway Power Limited (MPL) awarded an engineering, procurement, and construction contract for the plant to a consortium of Europower Development Ltd. and TBV Power Ltd. The consortium is providing a turnkey nominal 660 MW gas fired combined cycle plant. Europower, Marubeni Corporation's European branch, is providing the turbines. TBV Power is providing the balance of the plant using its joint venture partners, Tarmac Construction Ltd. for civil construction and Black & Veatch International for engineering and procurement. The mechanical and electrical erection packages are being executed by European Community contractors. MPL has separate contracts for the switchyard with the National Grid Company and for fuel gas with British Gas.

Factors Influencing Selection of the Combined Cycle

MPL chose a gas-fueled combustion turbine combined cycle plant because of the economic advantage of the highly efficient advanced technology over the alternative solid fuel plant options. This selection was reinforced when MPL secured one of the limited long-term fuel gas supply contracts with British Gas. The fuel gas delivery date dictated the overall project completion schedule of 40 months.

The "two-on-one" combined cycle turbine generator arrangement gives MPL greater operating flexibility. Three generators will feed the grid, allowing turndown or prompt surge capability. MPL economic studies included the regional grid limitation of 660 MW connected load at the National Grid Company intertie.

The pro forma economic evaluation excluded bypass stacks and simple cycle operation from the baseload plant operating model.

A reserve fuel oil facility offers revenue stream security and high plant availability to MPL in case the fuel gas supply is cut off for any reason.

Medway Power Block

The Medway Plant is the site of a previous World War II vintage oil storage depot. The 11 acre site, shown on Fig. 1, has provisions for additional capacity beyond the initial 660 MW power block and is elevated above the 200 year flood plain.

The three turbines in the power block are contained in a common expandable generation building. The plant cooling water makeup is taken from the River Medway intake structure, and heat is rejected to the wet mechanical draft cooling tower. Demineralized water for steam cycle makeup and combustion turbine NO_x control is produced in an on-site water treatment plant. An on-site tank battery stores process water and reserve fuel oil. The fuel gas used to supply the combustion turbines is conditioned in an in situ gas compound.

Site effluents are collected, monitored, and treated to meet permitted standards before release. The plant stack emissions are designed to be lower than current United Kingdom standards. The permitted values are 45 ppm NO_x on gas fuel.

The plant is designed for a boundary noise level of 65 dBA. To stay within this level, the turbines are acoustically enclosed, and the HRSGs are also treated and partly enclosed. Plant exterior walls are treated to achieve safe operator noise levels.

Performance and Efficiency. The new and clean net plant overall efficiency, based on lower heating value (LHV), exceeds 53 percent while burning natural gas. The Medway combined cycle baseload efficiency parameters are as follows:

- CTG output = 228 MW at 11°C.
- CTG heat rate = 10,180 kJ/kWh, LHV.
- CTG efficiency = 35 percent.
- STG output = 247 MW.
- STG heat rate = 7934 kJ/kWh.
- STG efficiency = 88.7 percent HP isentropic/91.8 percent IP/LP isentropic.

Contributed by the International Gas Turbine Institute and presented at the 39th International Gas Turbine and Aeroengine Congress and Exposition, The Hague, The Netherlands, June 13–16, 1994. Manuscript received by the International Gas Turbine Institute February 19, 1994. Paper No. 94-GT-434. Associate Technical Editor: E. M. Greitzer.

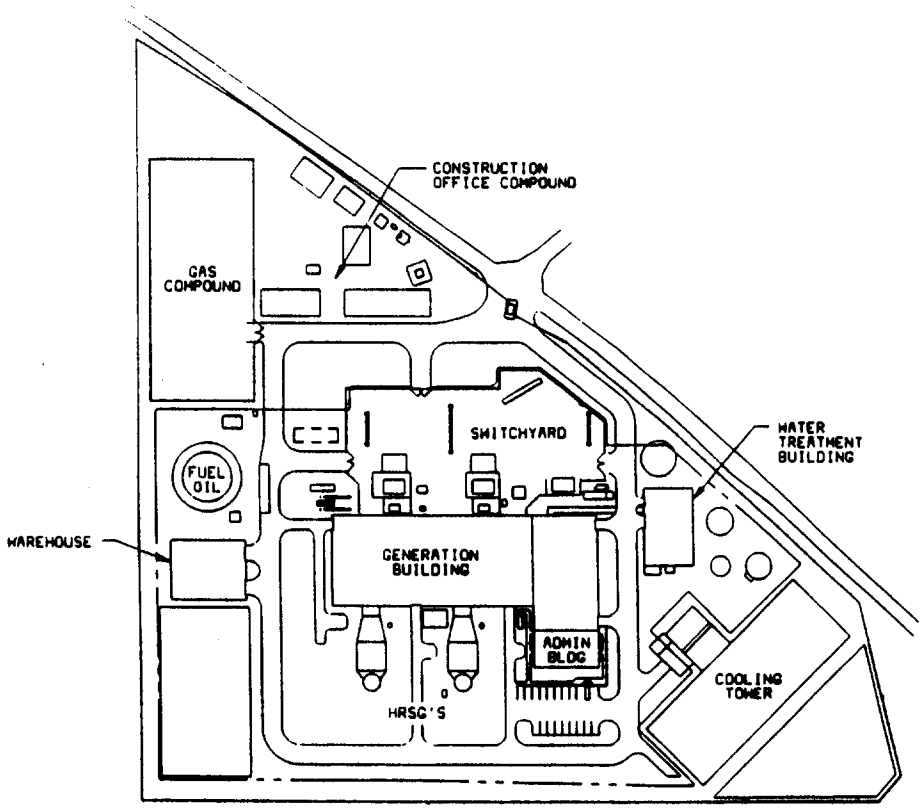

Fig. 1 Medway plant site arrangement

- Auxiliary power and transformer losses ≤ 2.5 percent.
- Net output available = 682 MW.
- Net heat rate = 6800 kJ/kWh.
- Net plant efficiency = 53 percent.

These are conservative values, which are subject to normal wear as the plant matures. These parameters illustrate that the Medway Plant is highly efficient relative to the traditional combined cycle plants preceding it.

The plant also includes an on-line performance monitoring system, which will further improve overall efficiency as operating procedures are optimized.

The combined cycle block contains the turbines and the following major balance-of-plant equipment, all designed to increase the plant efficiency:

- Two Nooter/Eriksen natural circulation, triple pressure, reheat-type HRSG modular packages. Each HRSG vents into a separate 65 m steel stack at an operating temperature of 113°C. The HRSGs are unfired. The selection of the reheat design is key to the high plant efficiency. The HRSGs are fitted with inlet duct acoustic lining instead of the traditional stack silencer. The reduced pressure drop improves cycle efficiency by reducing combustion turbine back-pressure.
- Three GEC-Alsthom generator step-up transformers rated for 290 MVA at 15 kV/420 kV, for transmission to the National Grid via the on-site switchyard. Two 20 MVA main auxiliary transformers power the unit auxiliary loads.
- One Hamon twelve-cell mechanical draft, low drift, low-noise, concrete structure evaporative cooling tower. These features will minimize the environmental impact to the plant neighbors. The cooling tower provides 1.614×10^9 kJ/h of heat rejection capability at a flow rate of 612,000 l/min, ambient temperature of 11°C, and 80 percent relative humidity. The tower is designed for 1.4 cycles of seawater concentration and is chlorinated from an adjacent electrochlorinator.
- One two-train, two-bed Glegg demineralizer plant. The water plant has 4670 lpm capacity for maximum NO_x control water injection to the combustion turbine combustors while burning reserve fuel oil.
- One Senior Thermal surface condenser designed for full steam turbine bypass, fitted with titanium tubes and tubesheet. The water box is coated for brackish cooling water. The condenser is sized to supply 41 mm HgA back pressure to the steam turbine at steam conditions of 538°C and at 97 bar abs for main steam, 355°C at 28 bar abs for hot reheat, and 260°C at 6.7 bar abs low-pressure steam, while condensing 655,000 kg/h using 21°C cooling water.
- One Graham/Crane vacuum-type feedwater deaerator and storage tank common to both HRSG feedwater pumping systems. The vacuum deaerator selection contributes to the improved cycle efficiency. The deaerator will operate at 150 mm Hga and will exhaust to the condenser.
- Two Graham water-to-gas heat exchangers sized to elevate the fuel gas temperature from 27°C to 150°C. These units were selected to add sensible heat to the fuel gas at the combustor inlet. The heat is taken from the HRSG economizer recovering the available flue gas energy during operation.
- Three Alfa-Laval plate-type heat exchangers sized to cool the plant auxiliary cooling loop, including all of the combustion and steam turbine lube oil and generator coolers heat rejection. The titanium metallurgy is selected for the brackish cooling water.

Combustion Turbine Technology

At the heart of the power plant are two GE MS9001FA combustion turbines. These machines, site rated at 228 MW

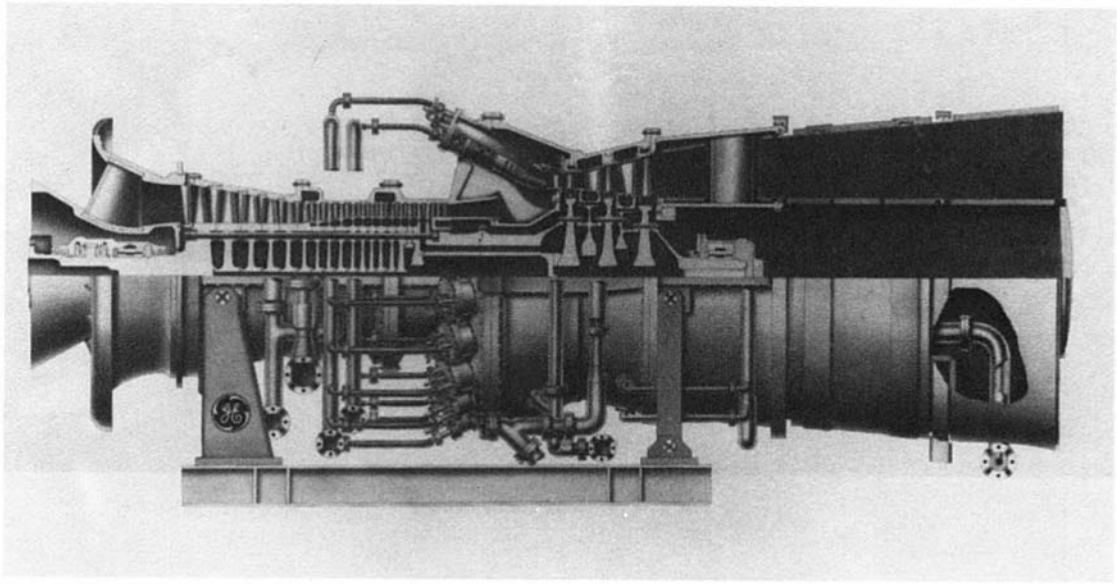

Fig. 2 MS9001FA combustion turbine

on gas fuel, are the latest in high-efficiency, low-emission 50 Hz power generation equipment, which have been scaled up from the 160 MW class MS7001FA 60 Hz combustion turbine.

The packaged arrangement developed for the MS7001FA and MS9001FA combustion turbines and accessories maximizes the efficient use of space within the building and reduces installation cost while maintaining high reliability and redundancy for key components.

Similar to the MS7001FA, the MS9001FA uses advanced aircraft engine technology throughout its design for a rated baseload firing temperature of 1288°C (2350°F). The two-bearing, cold-end drive machines are well suited for combined cycle applications because the axial exhaust to the heat recovery equipment optimizes the plant arrangement. The turbines themselves, shown in cross section on Fig. 2, feature an 18-stage axial flow compressor with modulated inlet guide vanes and a three-stage turbine.

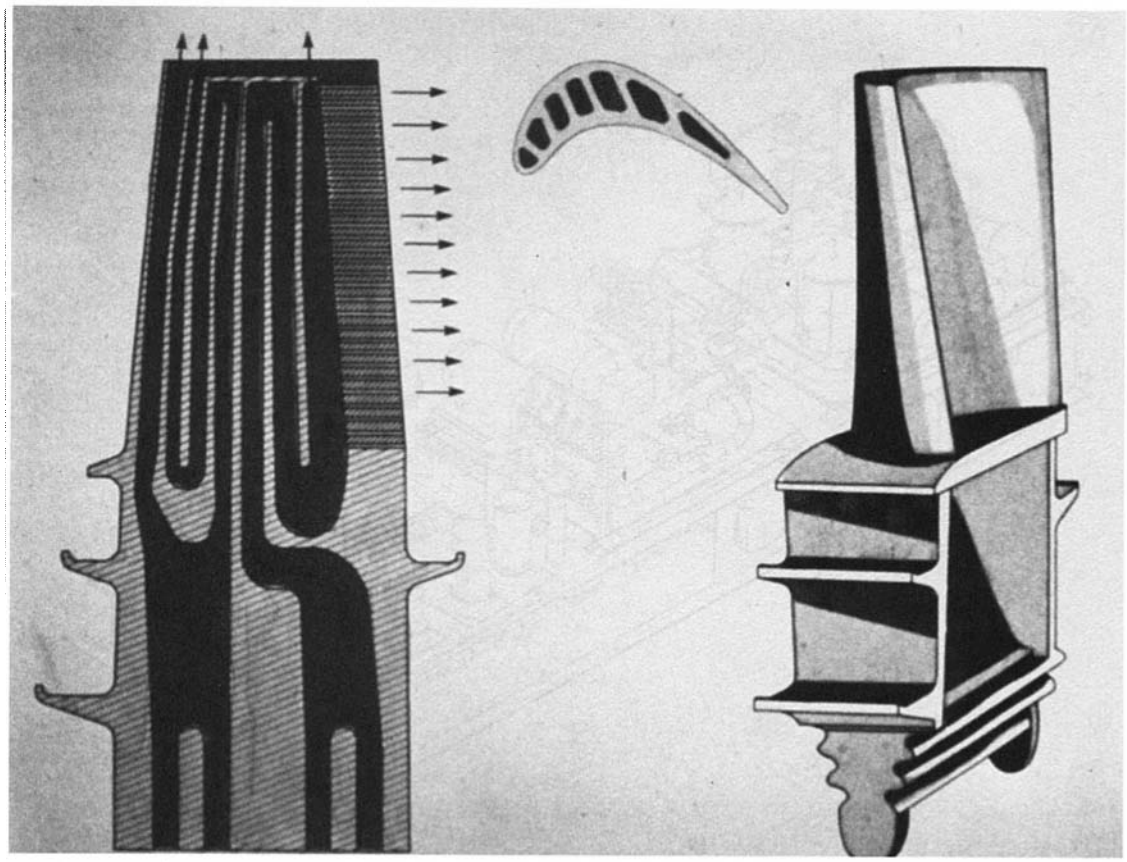

Fig. 3 First-stage bucket cooling passages

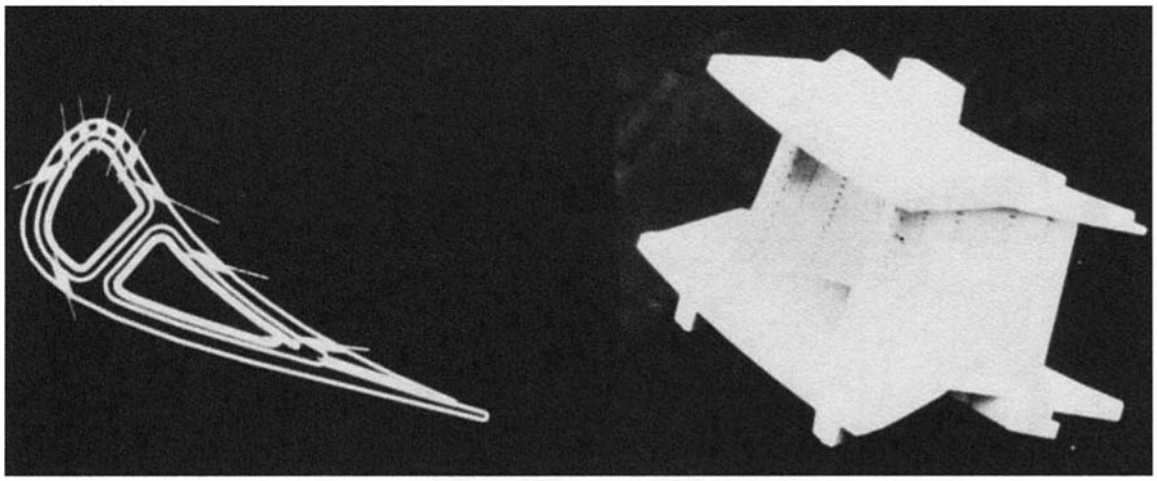

Fig. 4 First-stage nozzle cooling

Fuel, either natural gas or distillate, is provided to 18 combustion chambers. A dry low-NO_x system controls NO_x emissions to 45 ppm while operating on natural gas. NO_x control for operation on distillate fuel is accommodated by water injection to a level of 65 ppm.

A reverse flow, multiple-combustion system similar to "E" class machines is utilized. The combustion liners for the MS9001FA are slightly thicker and shorter than those for the MS9001E, providing increased high-temperature strength. A slot cooling method, which is the standard cooling method for aircraft engines, provides reduced liner metal temperatures compared to that of an equivalent louver system.

The first stage bucket is convectionally cooled by serpentine passages with turbulence promoters formed during casting. Cooling air exits at the bucket tip as well as at the trailing edge, as shown on Fig. 3. The second stage bucket is also convectionally cooled. All of the cooling air exits these buckets radially through drilled holes at the bucket tip.

The first-stage nozzle, as shown on Fig. 4, is cooled by a combination of film, impingement, and convection in both the vane and sidewall regions. The second-stage nozzle is convectionally cooled.

The advanced cooling techniques used on the MS9001FA are the result of extensive aircraft engine developments.

Generator. The generator is connected to the compressor (cold) end of the combustion turbine by a solid load coupling. The GE Model 324S generators for the gas and steam turbines

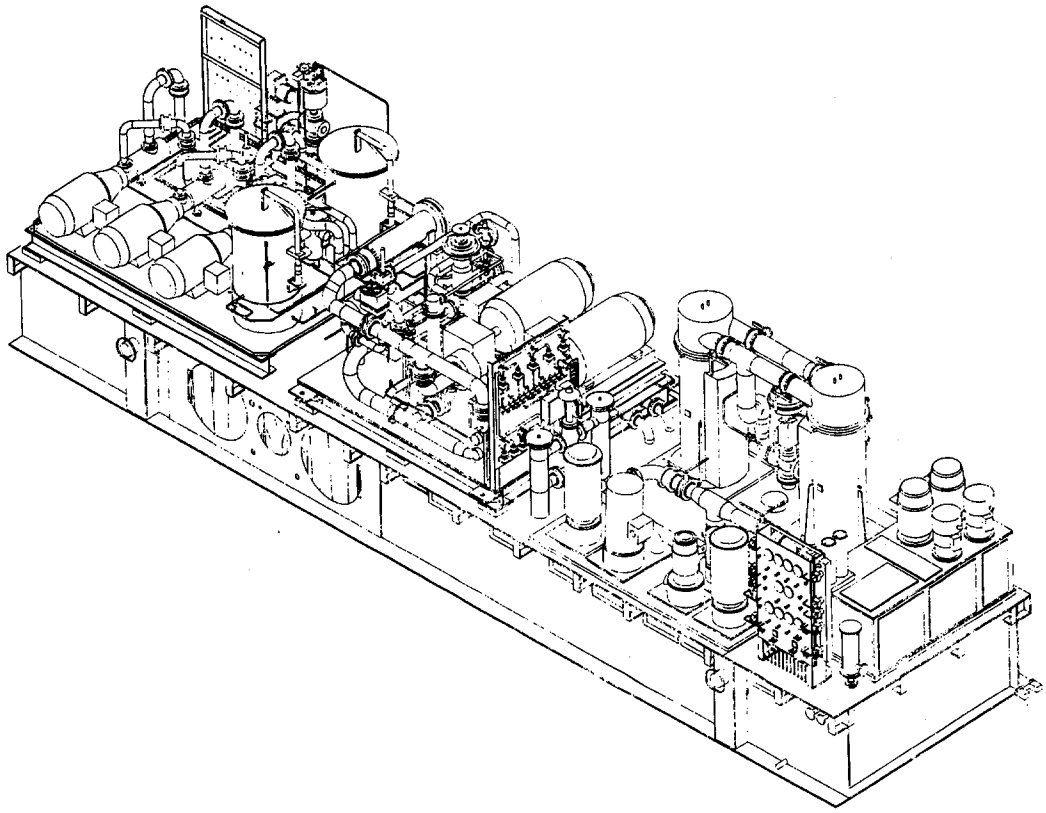

Fig. 5 Accessory module (GT23196)

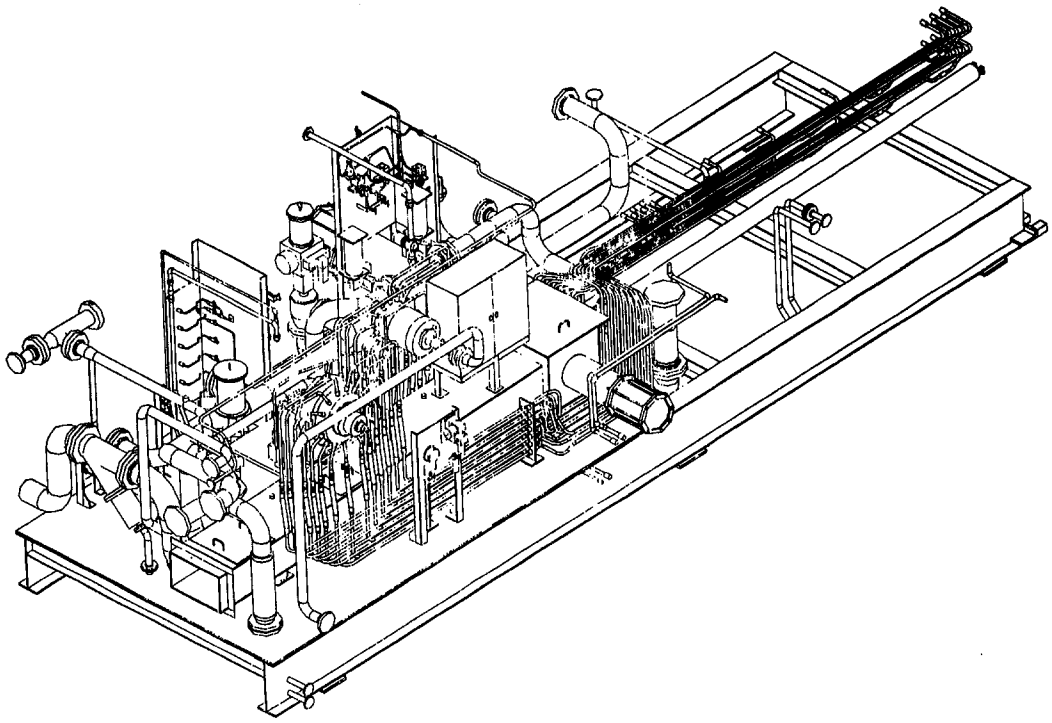

Fig. 6 Interconnecting module

are hydrogen cooled and rated at 291 MVA/15,000 V at 0.85 power factor.

A low-speed turning gear is on the collector end of the generator for breakaway, low-speed operation and cooldown. A static starting system, shared by the two combustion turbines, uses the generator as a synchronous motor to accelerate the units to self-sustaining speed.

Inlet Air. A "down flow" style self-cleaning inlet filter was selected for this project. In this design, the filter cartridges are mounted horizontally. The filtration effectiveness is thereby enhanced by the incoming air flowing down over the cartridges, using gravity to carry pulsed dirt away from the cartridges.

This design provides a more compact filter house arrangement, which enables the entire inlet duct to be shortened, which in turn reduces the system inlet pressure drop and its effect on turbine performance. The inlet system rated pressure drop is 89 mm of H_2O. A compressor water wash skid, capable of off-line and on-line washing, cleans deposits and reduces fouling to retain combustion turbine compressor efficiency close to new conditions.

Packaging/Enclosures. Adjacent to the combustion turbine is the accessory module, which contains the lube oil reservoir as well as the components for the lube oil, liquid fuel, and atomizing air systems as shown on Fig. 5. The majority of the accessory system components are factory assembled, tested, and shipped as integral parts of the accessory and interconnecting modules.

The base of the accessory module houses the lube oil reservoir, which has an operating capacity of 30,280 kL (8000 gal). Dual lube oil filters and heat exchangers with transfer valves, two full size AC motor driven lube oil pumps, AC/DC motor driven seal oil pump, and redundant AC motor driven hydraulic and rotor lift oil pumps are supplied.

This module contains dual low-pressure fuel oil filters, three 50 percent capacity AC motor driven fuel oil pumps, and two 100 percent capacity AC motor driven atomizing air compressors.

The interconnecting module (Fig. 6) is a recently introduced packaging concept for the "FA" product line to house, in a factory-assembled compartment, the majority of components and interconnecting piping, which historically have been shipped loose and field assembled.

This module houses the gas stop ratio control, splitter, and purge valves for the natural gas and purge systems, the water injection staging isolation valve for the NO_x control system, the flow divider for the liquid fuel system, and the associated piping necessary to connect the accessory module to the combustion turbine. This module and the accessory module and combustion turbine have the full complement of enclosure features including lighting, receptacles, CO_2 fire protection, access doors, ventilation, and acoustic insulation. Acoustic insulation and silencing is employed as required to meet a near-field noise level of 85 dBA at 1 m.

The electrical equipment associated with the combustion turbine is packaged in a factory assembled compartment and labeled as PEECC™ (Packaged Electrical Equipment Control Compartment). This enclosure houses the Mark V Speedtronic turbine control, generator control panel, AC motor control centers, unit battery with dual chargers, and the excitation system.

Steam Turbine Technology

The development of the GE Model F combustion turbines, with their higher exhaust temperatures, has made the steam reheat cycle an attractive option. The reheat cycle benefits thermodynamic performance by adding heat to the cycle at higher average temperature than for the nonreheat cycle and by reducing the moisture loss in the low-pressure turbine expansion.

The drier low-pressure steam expansion reduces the potential for last-stage bucket moisture erosion down to that experienced in solid fossil fueled boiler steam plants. This permits the use of longer last stage buckets, and thus the exhaust annulus area can be optimized for maximum efficiency.

The Medway steam turbine is a GE single reheat turbine with a double flow exhaust. There is an admission to the 18-stage from the HRSG. The steam turbine operates in boiler-following mode, which is without control of the main and admission steam flow during normal operation. All valve gear is mounted away from the turbine shell.

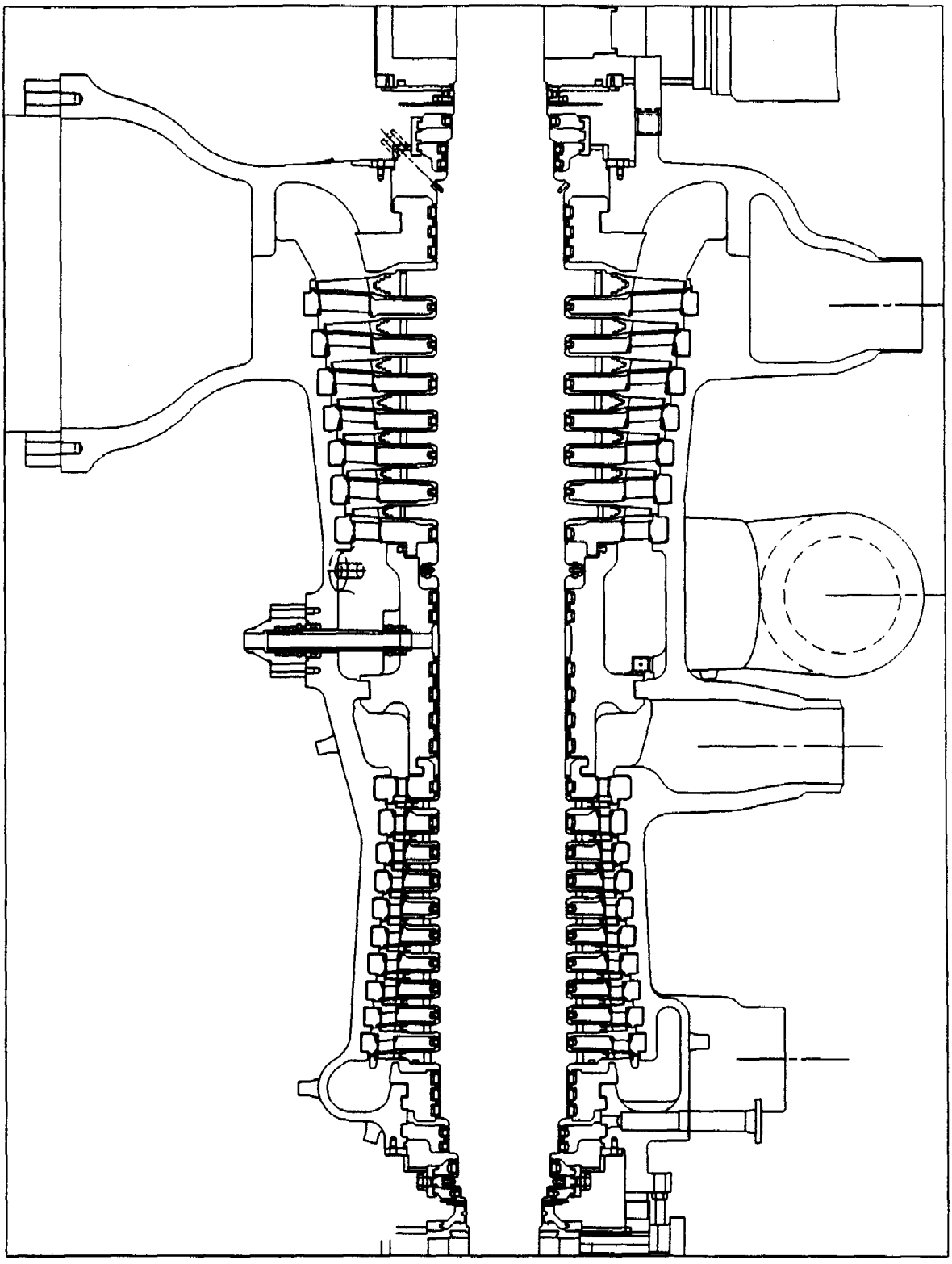

Fig. 7 Cross section of combined HP/IP section of steam turbine

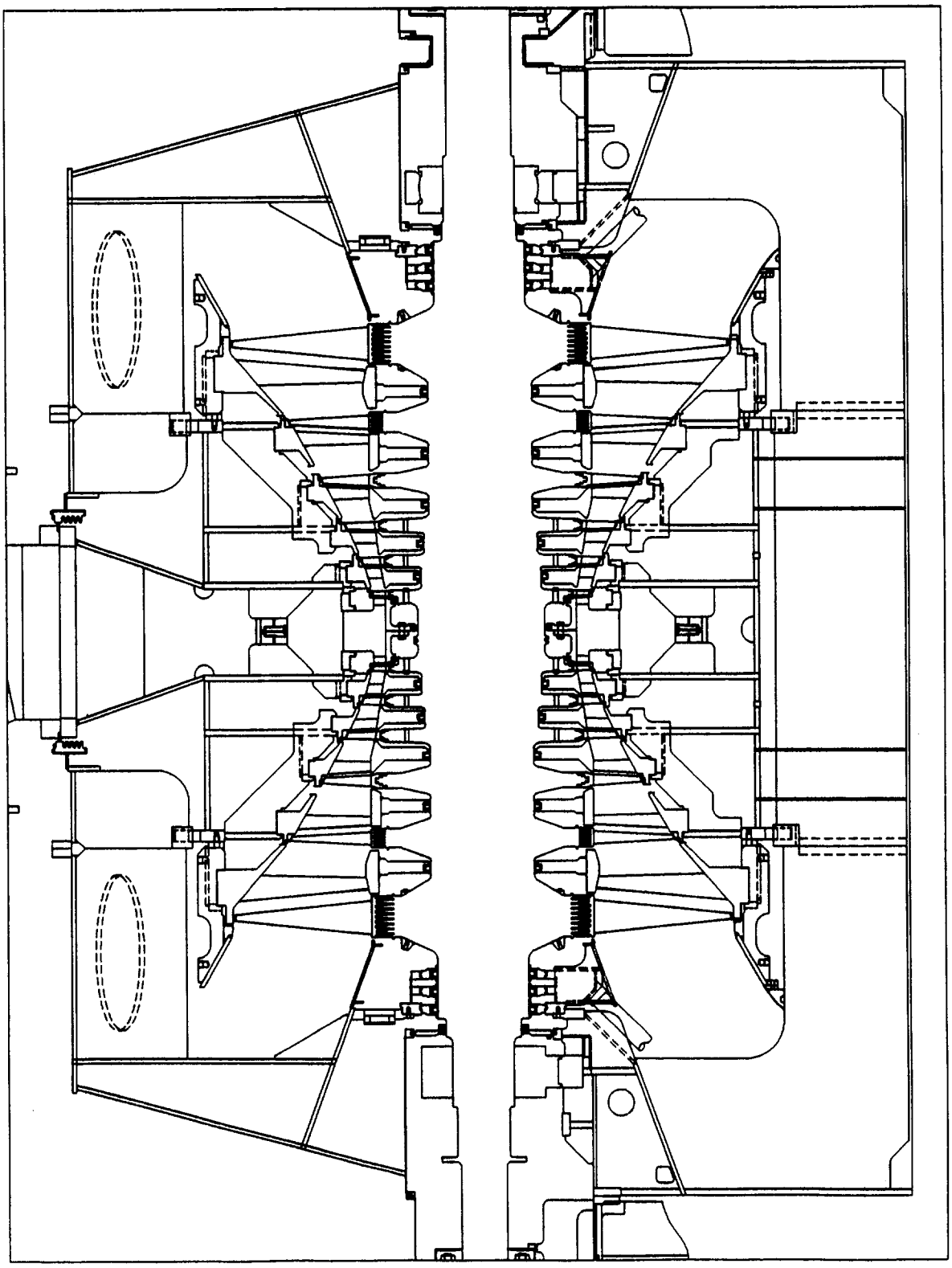

Fig. 8 Double flow low-pressure section and exhaust hood

Normal operation is with the valves fully opened, and the inlet steam pressure varying with load. Heating and cooling of the admission parts is uniform, minimizing thermal stresses and facilitating rapid startup and load following.

Steam Turbine Design Features. The Medway steam turbine is designed with an opposed flow high-pressure and intermediate-pressure turbine casing. This design results in a significantly more compact turbine and station arrangement than that of a separate high-pressure and reheat pressure casing (Fig. 7).

The cross-sectional view shows the high-pressure (HP)/intermediate-pressure (IP) section of the Medway steam turbine in detail. Both the HP section to the left and the IP section to the right are of single shell construction. The use of the off-shell valves and full-arc admission results in simple shell geometry. A smooth continuous transition is made in the shell between the HP steam path and the larger diameters needed by the IP stages. The inlet bowls of the HP and IP inlets are formed by the inner surface of the shell, the packing head in the center, and the first diaphragm of the respective section. This design permits free thermal expansion of these highest temperature regions.

The HP/IP shell employs a horizontal joint with bolted flanges, which are designed with optimum proportions to support the shell and to accommodate the required bolting sizes. The shell horizontal-joint faces are precisely machined to ensure uniform contact between the upper and lower halves and to eliminate opportunities for steam leaks. In addition to the horizontal joint flanges, only flanged pipe connections need to be disassembled to remove the upper half of the outer shell. The entire shell is supported near the centerline, and the internal diaphragms are centerline supported to minimize the distortion and alignment change effects.

Steam Path. For effective resistance to corrosion and erosion, the steam path components are constructed of 12-chrome steels. Rugged impulse-type turbine staging is used, which in turn leads to a construction known as wheel and diaphragm design. With impulse-type staging, the stage pressure drop is nearly all taken across the nozzle or fixed blade. Only a small percentage of the pressure drop occurs across the bucket or moving blade in order to improve the flow characteristics through the bucket. This low-pressure drop on the moving blade results in low leakage loss across the bucket and, therefore, an efficiency advantage, as well as reduced thrust relative to a reaction stage.

Greater pressure drop occurs across the stationary blade; however, the leakage diameter is greatly reduced by machining the rotor shaft diameter down to a small leakage diameter. The diaphragms, which hold the stationary blades, extend down to the rotor and hold a spring-backed packing with generous provision for radial movement and a large number of labyrinth packing teeth.

To attain maximum thermal efficiency, the steam path of the HP/IP section has been designed in a conical fashion. This allows the use of slant root and tip buckets and maximizing the blade lengths in the smaller volume flow stages. Each bucket has root axial seal strips and tip radial seal strips to give additional sealing control and maximum stage efficiency. The radial tip seal strips are set into the diaphragm, and thus they are unaffected by any distortion of the outer shell.

Double Flow Low-Pressure Section. The Medway double flow low-pressure section has been meticulously designed using CFD codes to analyze the exhaust steam flow in the complicated geometry of a down flow hood. The hood design uses diffusing flow plates of the GE "Herzog" hood design concept. This concept involves the use of structural support plates inside the hood to partition the flow areas into passages that have been designed to maximize the diffusion of the exhaust steam. Streamlined steam guides and flow guide vanes are used to improve the aerodynamic performance of the flow passages further and minimize flow separations. Figure 8 shows the details of the double flow low-pressure section.

Last-Stage Bucket. The exhaust annulus area of the Medway steam turbine has been optimized for this steam cycle and it employs a 1067 mm (42 in.) last-stage bucket. This last-stage bucket design is a result of a series of development programs that have resulted in a superior design of a highly efficient continuously coupled last stage bucket. The latest technology, along with proven concepts, have been used to design an efficient aerodynamic blade with a robust mechanical design, superior structural damping, and vibration control.

The aerodynamic profile of all of the stationary blades as well as the rotating buckets of the low-pressure turbine stages have been carefully developed using computational fluid dynamics programs. These programs accurately predict the three-dimensional flow field found in the low-pressure turbine and account for the large radial component of velocity. The low-pressure steam path must be designed to account for the rapidly expanding volume of steam. The cross-sectional view of the Medway LP turbine on Fig. 9 illustrates this expansion.

The last-stage buckets have continuously coupled side entry covers. These covers provide structural coupling and damping, as well as controlling the vane tip flow passage geometry. This vane tip flow passing geometry has been carefully designed to provide a converging–diverging passage to allow for the supersonic expansion and the reduction of secondary flow and shock losses. The side entry cover also employs a rib on its tip, which acts as a radial spill band and ensures a tight radial seal, to minimize steam leakage. Figure 9 shows these design features.

The last-stage bucket diaphragm design employs the "overshot" design, where the outer portion of the diaphragm extends out over the last-stage bucket. This allows a flow path for the moisture droplets in the steam, yet preserves the integrity of the tip seal strip. The moisture droplets will adhere to and run out along the stationary wall of the diaphragm.

The last-stage bucket designed for this Medway turbine utilizes a self-shielding alloy steel for the entire vane section. This self-shielding design provides moisture erosion resistance comparable to Stellite shields. The overshot diaphragm design, used in conjunction with the self-shielding bucket design, results in a highly erosion-resistant designed last stage.

Plant Control

The plant is controlled through a Bailey distributed control and information system (DCIS) designed with redundant architecture. The redundant architecture is intended to minimize the effect of a single point failure on the capability of the DCIS to provide data acquisition and control functions. Operator interface is accommodated through interactive graphic displays and alarm annunciation presented on five 48 cm diagonal CRT (non-touch-screen) operating consoles and keyboards.

The DCIS is a modular microprocessor-based system, which provides modulating control, digital control, monitoring, and indicating functions for the following:

- Operator interface to the steam turbine and combustion turbines Mark V control systems.
- Control signal outputs to the generators in response to unit load demands.
- Operator interface displays and control functions for the balance-of-plant systems.
- Controlled plant equipment and controlled process parameters, with information available to plant operators.
- Historical data storage and retrieval.

The DCIS employs foreign device interfaces for the steam and combustion turbine Mark V control systems, the demineral-

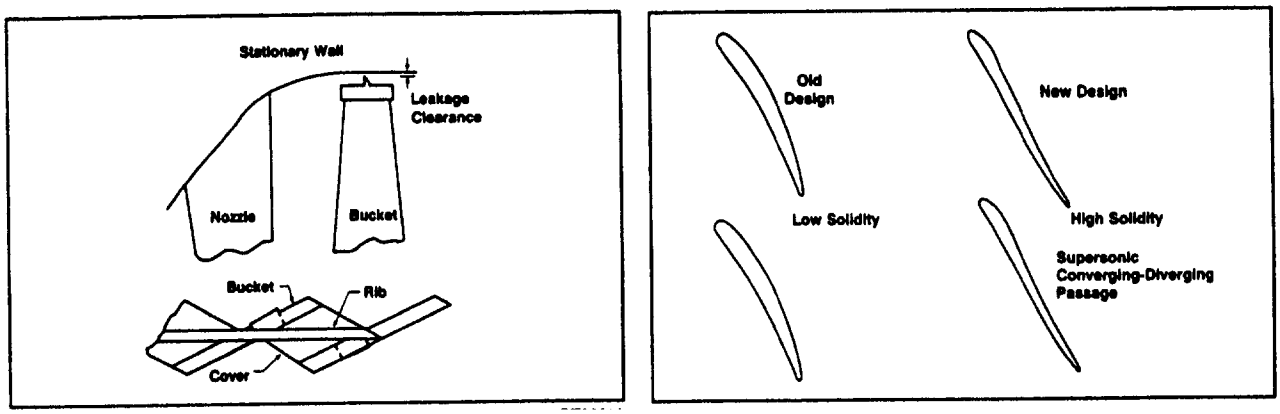

Fig. 9 Last-stage bucket

izer programmable logic controller (PLC) based control system, and the on-line performance monitoring (OPM) computer. All foreign device interfaces are bidirectional data links, capable of originating and receiving points from the system data highway. The data links for the Mark V control systems are designed for full redundancy, including redundant hardware at either end of the link and redundant communications cable. The DCIS software is intended to duplicate the operator interface functions available on the Mark V operator interfaces except that the presentation of information to the operator (status colors, symbol shapes, etc.) is more consistent with the balance-of-plant displays.

Redundancy has also been designed into the Mark V control system for high reliability. During normal operation, three computers share responsibility for control of the combustion turbine. Should one of the triple redundant sensors or one of the computers fail, internal voting logic redirects control of the turbine to the two functioning computers and sensors.

Further redundancy has been provided for this project by placing an additional Mark V operator interface processor in the main control room and providing dual AC power supplies.

Power Block Plant Arrangement

The generation building houses the combustion turbine generators (CTG) and steam turbine generator (STG), turbine accessory modules, isophase bus, switchgear, overhead cranes, feedwater condensate/steam cycle process components, STG lube oil modules, common turbine oil coolers, control room, and auxiliary systems. These are shown on Figs. 10 through 12, which illustrate the plant arrangement.

The HRSGs, transformers, gas heaters, deaerator, and CTG inlet air filters are outdoors. All turbine shafts are oriented in a parallel configuration. The CTG units are each configured in duplicate same hand arrangements. The CTG inlet air duct is routed parallel to and above the generator shafts. The inlet air filter is roof mounted. The CTGs and generators are pedestal-mounted on elevated concrete foundations. The CTG auxiliary modules are elevated on structural frames.

The HRSGs are also duplicate same hand arrangements, arranged to flange directly to the axial exhaust combustion turbines parallel to the rotor shaft. The HRSG inlet duct has an acoustic enclosure surrounding the inlet duct transition.

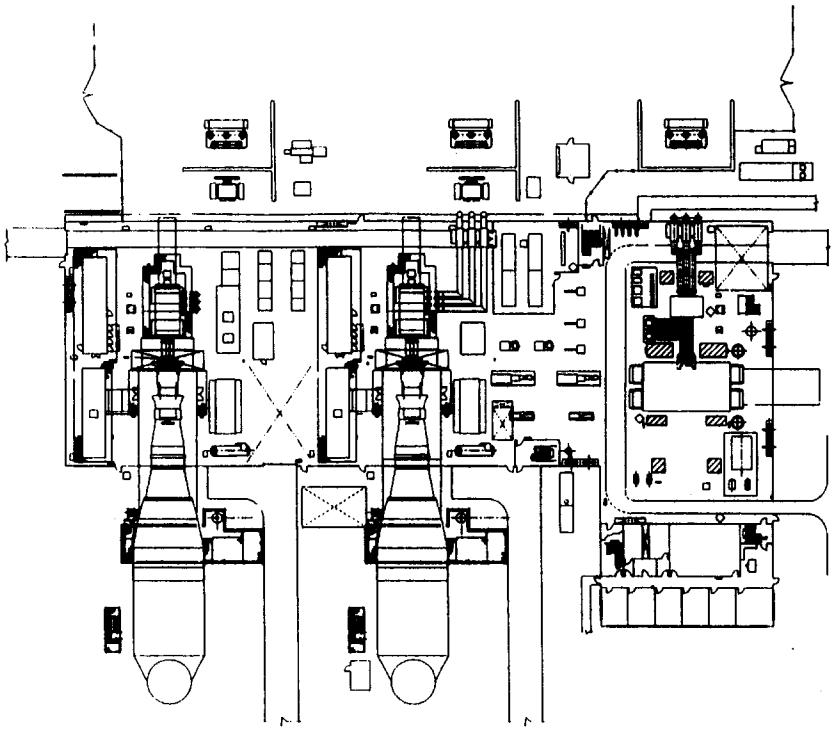

Fig. 10 Ground floor plan

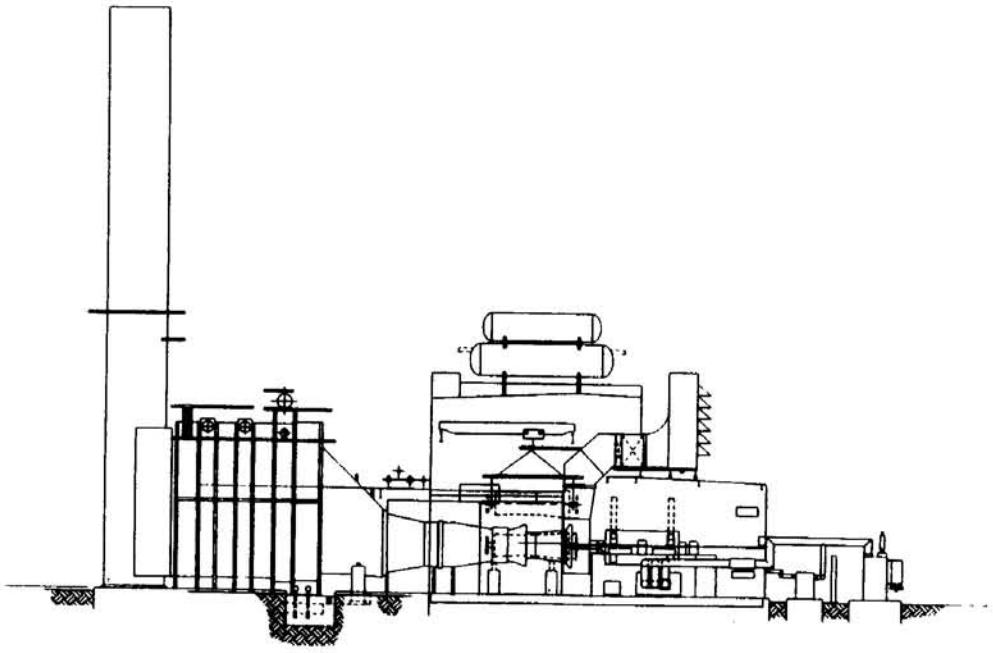

Fig. 11 Combustion turbine elevation

The isophase bus duct is routed under and parallel to the generator centerline directly to the elevated generator breaker. Step-up transformers are located on the isophase bus centerlines.

The deaerator is mounted above the roof, providing maximum boiler feed pump suction head.

The steam turbine and generator are mounted on an elevated concrete pedestal at the operating floor level. Steam turbine auxiliaries are arranged on the mezzanine and ground floors below the steam turbine generator. The DCIS is housed in the plant control room at the operating level and directly below in the electronic room.

The combustion turbines are maintained from a common overhead crane using a common laydown space. The STG is serviced from an overhead crane using a dedicated access portal and the operating floor laydown space (Fig. 13).

The plant arrangement developed from these innovations yields a compact building overall volume, and thus a competitive, cost-effective solution for the owners.

While the plant is operating, the indoor turbines provide sufficient building heating to replace the installed domestic heating.

Combined Cycle Operation

Combined cycle plant startup is initiated with the combustion turbine, which is started using the generator as a motor. The power grid feed is converted to a variable frequency supply to drive the generator. Prior to initiation of the starting sequence, auxiliary systems such as the circulating water system, cooling tower, closed cooling water system, and compressed air system are placed into operation.

When the combustion turbine has reached 10 percent operating speed, fuel gas is admitted and firing begins. The turbine accelerates until it reaches a self-sustaining speed. At that point, the variable frequency supply to the generator is shut down and the turbine continues to accelerate.

Soon after starting the combustion turbine, the turbine exhaust gas begins heating the HRSG. There is no turbine exhaust bypass for the HRSG or auxiliary steam supply, so the entire system must be brought up simultaneously. Initially, steam generated in the HRSG is relieved through vents and drains. When main steam pressure reaches a point where the steam turbine

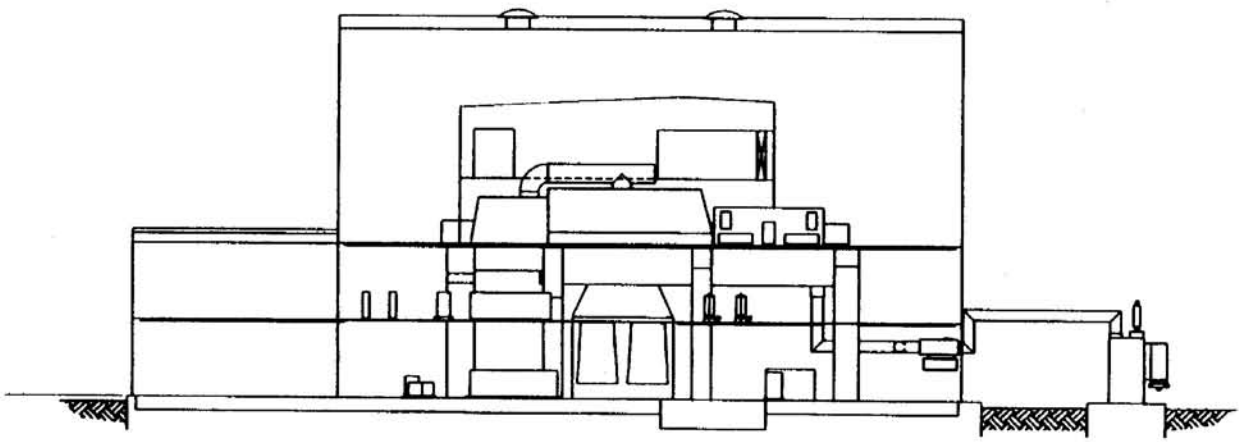

Fig. 12 Steam turbine elevation

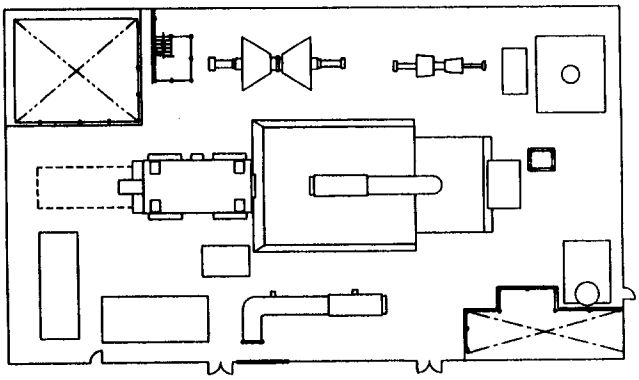

Fig. 13 Steam turbine maintenance laydown

seals can be applied, the condenser exhausters are started and a vacuum is established in the condenser. Once the condenser vacuum is significantly increased, the steam dump valves from the HRSG to the condenser may be opened and the steam turbine can begin warming. Based on the HRSG and steam turbine allowable warmup rates, the combustion turbines can be synchronized and begin ramping to the selected load. The steam turbine follows the output of the HRSGs, throttled to hold a constant boiler pressure to 80 percent load, then a sliding pressure up to 100 percent load.

Electrical power is sent to the grid through three stepup transformers, one for each generator. The generator switchgear is closed through the site switchyard, which is connected to a nearby grid substation. The grid switching occurs at the substation switchgear. During normal operation, plant power output to the grid is adjusted by varying the combustion turbine firing rate. The steam turbine follows the combustion turbine loading.

In the event of a steam turbine trip, the steam generated by the HRSGs will be diverted to the condenser through a series of letdown and desuperheating stations, allowing the continued operation of the combustion turbines. If the eventual circumstances allow a restart of the steam turbine, one of the combustion turbines will be run back in load and a restart of the steam turbine completed.

If the steam turbine cannot be restarted, the combustion turbines may continue generating power as required, dumping the generated steam energy to the circulating water system.

Development Requirements for an Advanced Gas Turbine System

R. L. Bannister

N. S. Cheruvu

D. A. Little

G. McQuiggan

Westinghouse Electric Corporation
Orlando, FL 32826

In cooperation with U.S. Department of Energy's Morgantown Energy Technology Center, a Westinghouse-led team is working on the second part of an 8-year, Advanced Turbine Systems Program to develop the technology required to provide a significant increase in natural gas-fired combined cycle power generation plant efficiency. This paper reports on the Westinghouse program to develop an innovative natural gas-fired advanced turbine cycle, which, in combination with increased firing temperature, use of advanced materials, increased component efficiencies, and reduced cooling air usage, has the potential of achieving a lower heating value plant efficiency in excess of 60 percent.

Introduction

Today's gas turbine systems feature high fuel-to-electricity efficiencies. Efficiencies, on a lower heating value (LHV) basis, for large natural-gas-fired combined-cycle systems for the utility market have been demonstrated at 54 to 55 percent. Even though manufacturers will make improvements in the 1990s, efficiency levels will reach a plateau. Cycle innovations, plus gas turbine design changes, will achieve LHV efficiencies in the 60 percent range for natural-gas-fired utility machines.

Advanced Turbine Systems (ATS) is a highly efficient, environmentally superior, and cost-competitive gas turbine system for baseload application in the utility, independent power producer, and industrial markets. For the post-2005 power-generation market the design must be fuel flexible in that it will operate on natural gas, but also be capable of being adapted to operate on coal, coal-derived, or biomass fuels. Reliability-availability-maintainability (RAM) is to be equivalent to current turbine systems and water consumption is to be minimized to levels consistent with cost and efficiency goals.

Westinghouse, a pioneer of gas turbine development, has developed a product line that mirrors the general gas turbine inlet temperature trend shown in Fig. 1. Combined cycle efficiency improvements have followed the general advance in gas turbine technology reflected in this inlet temperature trend.

For example, in 1970 a Westinghouse supercharged, evaporative cooled, Model 301 (1450°F [788°C] turbine inlet temperature) gas turbine exhausting into a heavy fired, reheat boiler achieved an annual average efficiency (LHV) of 39.6 percent. This West Texas Utilities, San Angelo Power Station reportedly held the distinction of achieving the highest operating efficiency in the U.S. for a number of years (Stephens et al., 1990).

Today, with a gas turbine burner outlet temperature (BOT) of about 2460°F (1350°C) [2300°F (1260°C) rotor inlet temperature (RIT)], a Westinghouse 501F based combined cycle is in the range of 54–55 percent (LHV) plant efficiency, ISO with: (1) dry low NO_x; (2) three-pressure level, reheat, heat recovery steam generator (HRSG); (3) rotor cooling; and (4) fuel gas heating.

The bottoming cycle has been fine tuned to convert as much of the turbine's exhaust heat into electricity as possible. Additionally, the gas turbine incorporates all the material, aerodynamic and cooling technology gains of the last 25 years.

As suggested by the Department of Energy (DOE), the target of 60 percent combined cycle efficiency by the year 2000 is shown to be a challenging target in Fig. 2, where cycle efficiency is plotted against the turbine inlet temperature trend of Fig. 1.

Proposed Reference System

In the first phase of the ATS program, the effect on efficiency of reconfiguring the gas turbine based combined cycle was studied, to see if a step gain in efficiency was possible. As reported in a previous paper (Little et al., 1993), it was found that a significant increase in combined cycle efficiency could indeed be expected by reconfiguration into an intercooled, recuperative combined cycle, with closed-loop steam cooling as shown in Fig. 3. All rotating components will be directly coupled to form a single shaft running at 3600 rpm, and the generator rotor will be double ended so that the steam turbine and gas turbine can drive from opposite ends.

Intercooling could take the form of: (1) surface heat transfer, where heat is extracted from air, leaving a compressor section and transferred to cooling water; (2) evaporative intercooling, where the temperature of air leaving a compressor section is reduced by evaporation of water into the air stream; (3) either one intercooler [low pressure (LP) and high pressure (HP) compressors], or two intercoolers [LP, intermediate pressure (IP), HP compressors]; or, (4) continuous evaporative cooling in all stages of a single compressor.

Recuperation could take the form of: (1) surface heat transfer between turbine exhaust gas and HP compressor delivery air; (2) evaporative recuperation where heat extracted from turbine exhaust would both heat and evaporate water into HP compressor delivery air; and (3) chemical recuperation whereby turbine exhaust energy would be transferred back into the turbine through a reformed natural gas fuel. In most cases, intercooling and recuperation would not entirely displace the bottoming cycle, but would instead reduce its size.

The initial ATS study, although preliminary in nature, showed increases in advanced turbine system efficiencies ranging from 0.5 to 4.0 percentage points depending on the cycle configuration and assumptions made. A change in configuration from the basic single shaft gas turbine to that of the reference system is thus anticipated to provide about 2.0 percentage points increase in system efficiency. Closed-loop steam cooling of hot gas path components is anticipated to improve cycle efficiency approximately 1.5 percentage points.

Contributed by the International Gas Turbine Institute and presented at the 39th International Gas Turbine and Aeroengine Congress and Exposition, The Hague, The Netherlands, June 13–16, 1994. Manuscript received by the International Gas Turbine Institute March 9, 1994. Paper No. 94-GT-388. Associate Technical Editor: E. M. Greitzer.

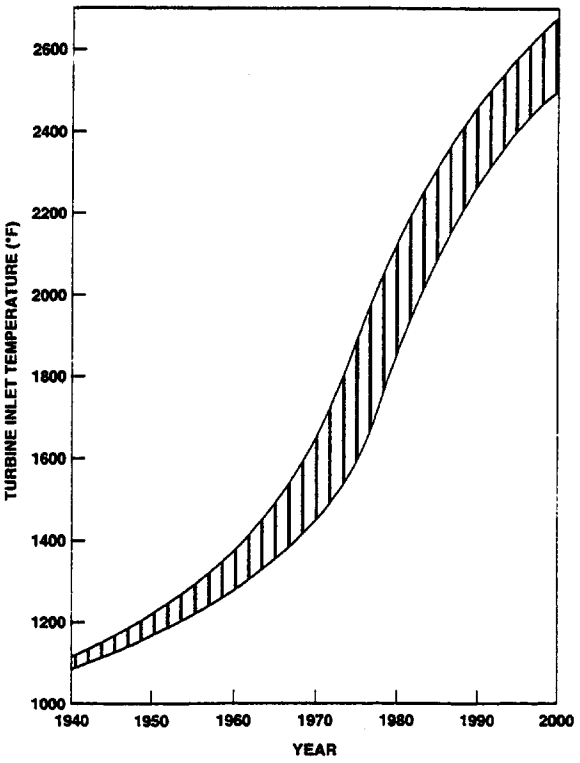

Fig. 1 Gas turbine inlet temperature trend

Within the reference system configuration, additional efficiency gains can be made by: (1) high temperature developments in materials, coating systems, and cooling techniques to allow the attainment of a 2600°F (1427°C) rotor inlet temperature; (2) reduction in cooling air requirements; (3) application of advanced aerodynamic design techniques to further enhance component efficiencies; and (4) reduction in leakages, clearances, and parasitic losses.

It is expected that higher firing temperature in combination with cooling air reduction should yield about 2.5 percentage points in efficiency, while advanced aerodynamics, and reduced leakages, clearances, and losses would give a further 1.0 percentage point. Therefore, within the reference system structure, 60 percent (LHV) target ATS efficiency is obtainable.

Cycle Studies

Intercooling between compressor stages to reduce compression power has long been a feature of centrifugal compressor installations. The radial delivery of compressor air from each impeller lends itself to flow through an external water-to-air cooler before being introduced to the following impeller. Stages in the axial compressor of the industrial gas turbine are extremely close coupled, as shown in the 501F longitudinal (Fig. 4), making intercooling impossible without significant configuration changes.

Intercooling between separate axial compressors has been done successfully in the past, where air is ducted from the LP compressor to a large water-spray evaporative cooler, and returned to the HP compressor inlet. More recently the compact water-to-air surface intercooler configuration, shown in Fig. 5, is being developed by Westinghouse/Rolls-Royce for the U.S. Navy intercooled, recuperative (ICR) engine program (Crisall and Parker, 1993).

In the ATS program, either of these concepts may be adopted, depending upon the results of detailed thermodynamic cycle analysis comparing evaporative to surface intercooling. Additionally, the number of positions through the compressor where air is intercooled will be studied. It may be that double intercooling could prove most effective.

The major problem in the entire intercooling area is the conflicting requirements of the compression and intercooling functions. Velocity through the blading is high, approximately 640 ft/s (195 m/s) between stages, while for cooling (either evaporative or surface) velocity must be very low to reduce pressure loss and maximize residence time. In surface intercooling, a face velocity of approximately 32 ft/s (9.8 m/s) would result in a $\Delta P/P$ for the core elements of about 1 percent, and an effectiveness of over 90 percent. Diffusing, turning, and reaccelerating air through a 20:1 area ratio will require careful engineering to minimize loss, as pressure loss cuts cycle efficiency and defeats the purpose of intercooling. A trade-off between area ratio, loss, and effectiveness will have to be taken.

Evaporative intercooling requires an enormous pressure vessel. It would be a great advantage if evaporation could be done in a shorter length; in fact, the ultimate scheme could be to evaporate in the compressor itself.

There is the possibility of introducing a water mist into the air flowing through the compressor. If the droplet size were of the order of 5 μm, collisions with the compressor blades would be minimized; such droplets would follow the flow streamlines. (It should be noted that the LP ends of steam turbine expanders have coped well with water droplet concentrations of up to 14 percent of the total flow.) A continuous cooling of the compression process by droplet evaporation might then be achieved. A preliminary analysis of such a compression process indicates a 25–30 percent reduction in the work of compression; a corresponding reduction in the temperature increase over the compressor; and, perhaps surprisingly, a reduction in the water used over a staged inter- and after-cooler process.

Techniques have recently been developed to produce such fine droplets, to maintain a uniformly distributed spray, and to avoid droplet coalescence. Incorporation of the water distribution system within the thin stationary aerofoils is an obvious means of access into the tightly spaced compressor stages, which will not disrupt the main flow. Spraying of these tiny, 5 μm droplets into the air stream with minimum momentum mixing penalty would be the objective.

Designing the aerofoil shapes to account properly for the evaporation of the water mist in a finite distance downstream of the introduction points will require careful analysis of the time required for evaporation. Vaporization will be a function of water droplet temperature, injection velocity, air temperature,

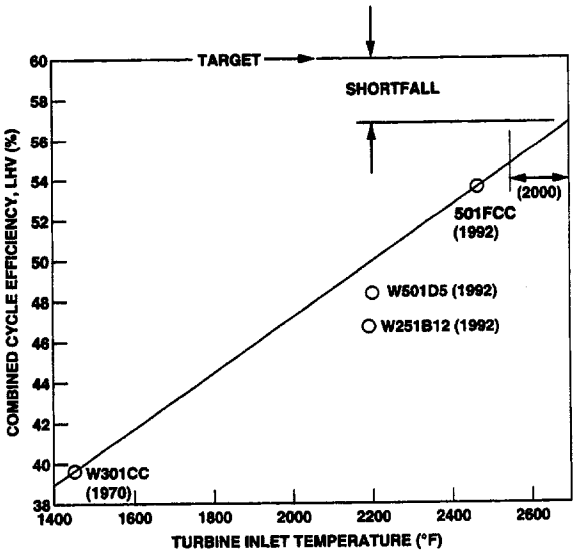

Fig. 2 Combined cycle efficiency trend

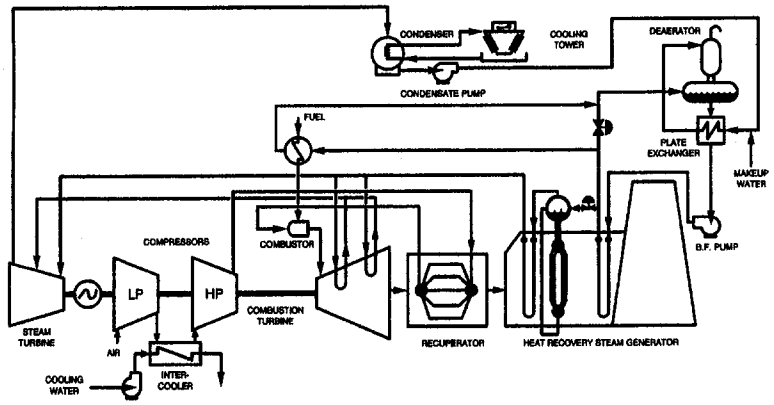

Fig. 3 Proposed reference system (ICRCC)

pressure, velocity, and humidity. The modeling and experimental verification of the processes just described will be key prerequisites to being able to incorporate a design procedure into existing compressor blading design systems. Continuous evaporation within the compressor appears to be an attractive innovation, which could improve the performance and reduce the cost of the ATS.

In the last 30 years, Westinghouse has supplied recuperative gas turbines from 5000 hp (Model 52) to 35,000 hp (Model 352) to the industrial market; thus, although recuperation is an innovation to the 2600°F (1427°C) RIT combined cycle, the surface recuperator itself is tried and proven. AiResearch, a Westinghouse team member, who will size, specify, and supply the recuperator for the ATS, has designed and produced recuperators for large industrial gas turbines ranging in power levels from 6000 to 60,000 hp. Gas turbines with AiResearch recuperators are being used for gas pipeline pumping, electric utility peaking power, and chemical plant power generation.

The standard core shown in Fig. 6, utilized by AiResearch for large industrial recuperators, has a stainless-steel, brazed, plate fin construction. It is designed for 5000 start/stop cycles and 120,000 hours of operation with exhaust gas temperatures up to 1200°F (650°C). The design has proven to be completely compliant by extensive laboratory tests and over 1,000,000 hours of field experience.

Higher temperature capabilities, if needed in the ATS engine, will be facilitated by the substitution of a new material, which has 1300°F (704°C) temperature capability. Material development work is currently being done at 1500° to 1800°F (815 to 980°C).

AiResearch has performed a rough sizing for the ATS recuperator, at possible system operating conditions to achieve an effectiveness of 0.942 with a combined pressure drop of no more than 3.45 percent at an exhaust flow rate of about 1146 lb/s (520 kg/s). The high effectiveness, low pressure drop, and high flow rates dictate the size of the design, as shown in Fig. 7. The requirements can be met by a system of counterflow heat exchangers, each handling part of the total flow of air and of gas.

The temperature drops and pressure losses in the piping leading from the combustor shell to, and from, the recuperator must be added to the estimated core performance to assess the full

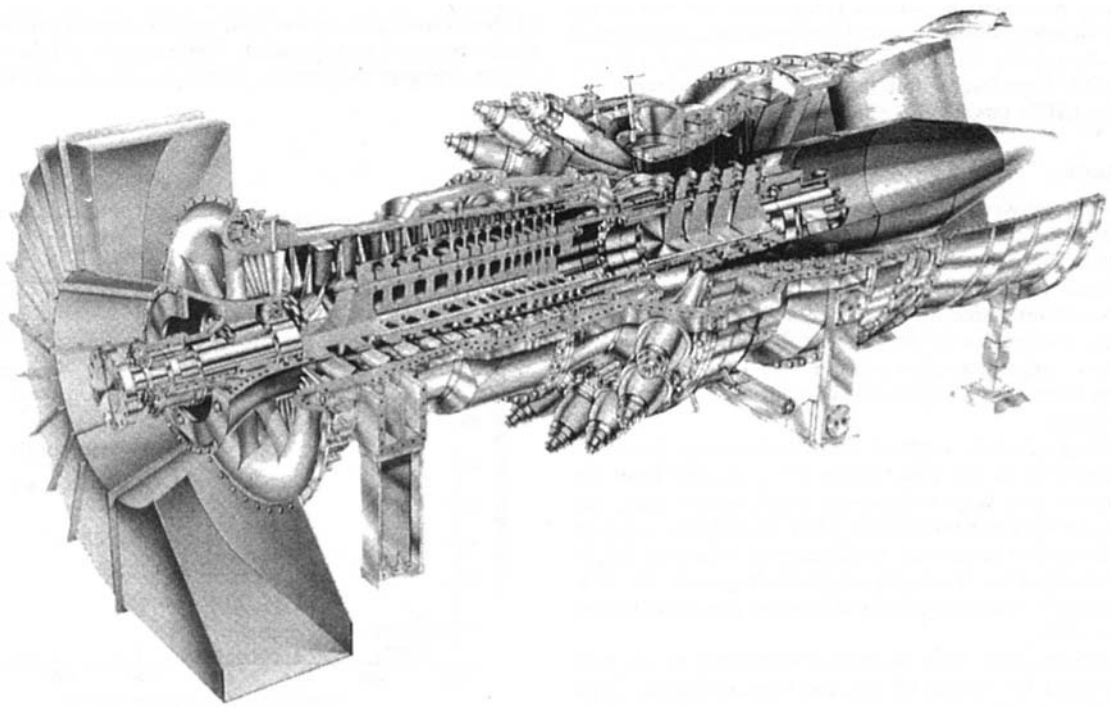

Fig. 4 Westinghouse 501F gas turbine

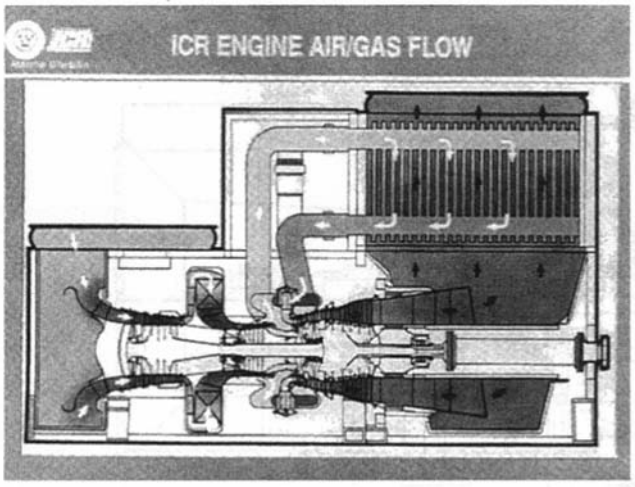

Fig. 5 WR21 engine system with compact surface intercooler

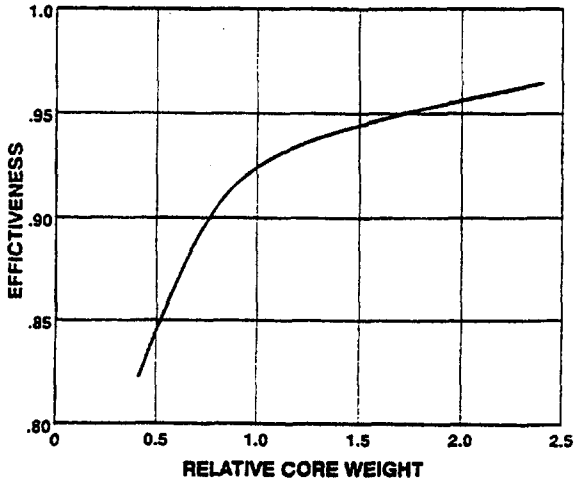

Fig. 7 Recuperation weight versus effectiveness

impact on the cycle efficiency. In the case of the Westinghouse Model 352 unit, air leaves the combustor shell, and returns to the unit through pipes located both above, and below, the horizontal split line on the shell (as shown in Fig. 8 for the lower half). Within the shell itself, hot and cold air are separated by a flexible dividing wall. Turbine casing structural connectivity was obtained by the use of ribs (struts), each bolted at one end to the compressor cylinder, and at the other end to the turbine cylinder. The horizontally split combustor shell could thus be designed to contain the pressurized gases, yet be flexible.

Additionally the lessons learned in the Model 352 unit that will be factored into the ATS design include the absolute necessity of sealing all clearances in the dividing wall and in the transition-basket, and transition-row 1 vane interfaces to ensure that compressor delivery air is actually forced to flow to the recuperator. Often in the past, when recuperated engine efficiency targets were not met, the cause was determined to be the bypass of air around the recuperator (in the combustor shell region). Also, the minimization of (using closed-loop steam cooling in combination with thermal barrier coatings) and accounting for, heat pickup by compressor delivery air as it flows around the hot transitions while heading to the recuperator, needs to be considered. Every Btu picked up by compressor air reduces the heat that can be transferred from the exhaust, and thus, reduces cycle efficiency.

Initial studies suggested the possibility that evaporative recuperation may improve ATS efficiency, since more exhaust heat could be transferred into the topping Brayton cycle through moisture evaporation. In the current study, if the detailed thermodynamic cycle evaluation confirms this idea, then the possibility of water injection in the recuperator cores (either within the air side fin sections, or in the outlet headers) will be investigated.

Thermochemical recuperation of gas turbine exhaust energy, as shown in Fig. 9, was also considered. Here only the gas turbine would produce power (no longer a combined cycle) by burning reformed, recuperated fuel. Methane and sufficient steam in the presence of a catalyst, and at appropriate temperature, will reform into a fuel consisting of H_2 and CO. None of the latent heat of vaporization of steam generated in the HRSG is lost to the cycle, and so the potential exists for efficient exhaust energy recuperation.

In current reforming technology, methane conversion efficiency is a function of pressure, temperature, and excess steam/methane ratio. Therefore, the reformed fuel could consist of CO, H_2, and CH_4 in various ratios depending on process variables.

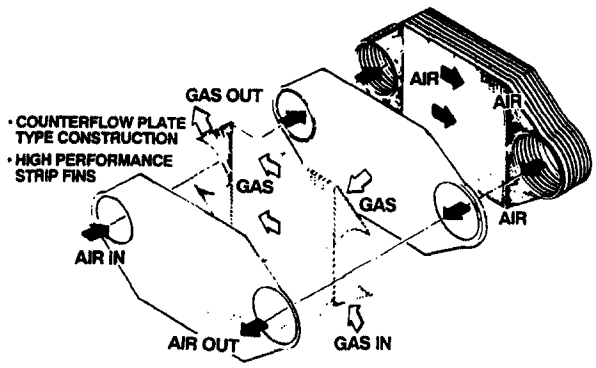

Fig. 6 Recuperation core design features

Cooling Requirements and Possible Alternatives

Currently the first three (of four) stages in the 501F turbine are cooled. First-stage vane cooling is accomplished by a combination of impingement, film, and convective cooling. First-stage blade cooling incorporates serpentine, ribbed, and pin passages with external film. Both of these highly complex cooling schemes may be further refined, but potential cooling air reductions may be small. Alternatively, several approaches that have been investigated in the past may be reconsidered.

One of the most promising of these is shell/spar construction. Shell/spar vanes and blades may be formed by bonding a thin nonporous aerofoil-shaped metal sheet (the shell) to an inner hollow cast support member (the spar), or by casting. Cooling air for the assembly is supplied from alternate cavities within the spar (the supply cavities). It flows along chordwise convection cooling channels between the spar and the shell and returns to the remaining spar cavities (the discharge cavities). The heated or spent cooling air is then routed from the discharge cavities to the main gas stream through exit holes in the shrouds or aerofoil.

Westinghouse, together with Allison/General Motors (GM), made an extensive study of air cooling approaches suitable for industrial size gas turbines at the elevated firing temperature of 2650°F (1454°C) and 3000°F (1650°C) under a U.S. Energy Research and Development Administration High Temperature Turbine Technology program. This work identified the feasibility of reaching these temperature levels using an advanced transpiration-type air cooled technology.

One candidate for the row 1 vane is shown in Fig. 10. This transpiration design consists of two layers of sheet material diffusion bonded to a hollow, cast spar. In the leading edge

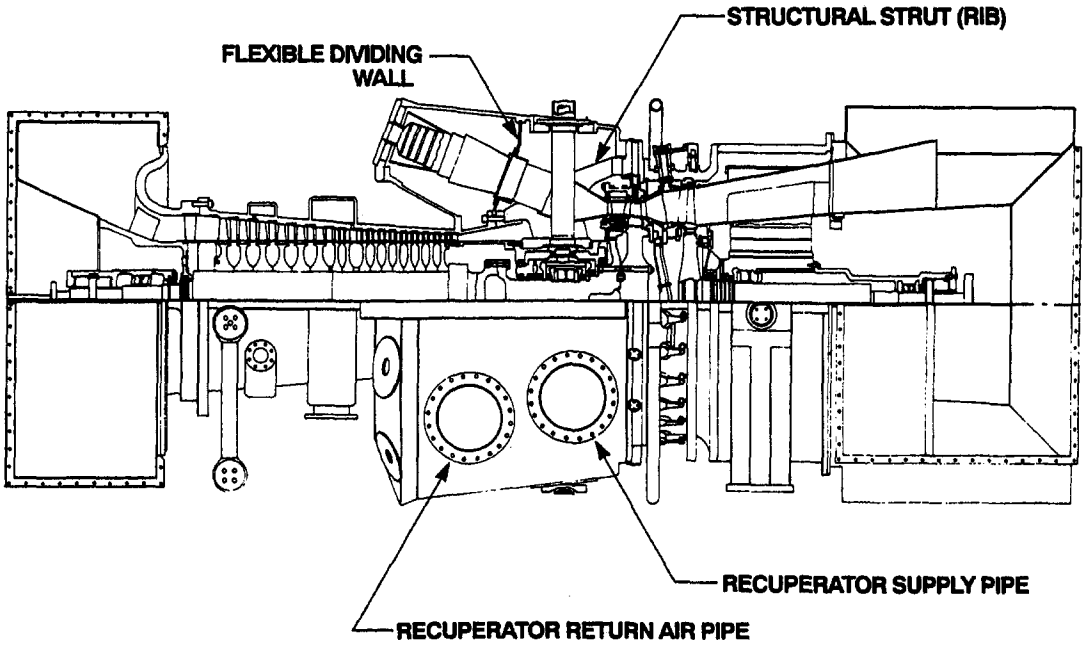

Fig. 8 Model 352 recuperated gas turbine

region, the sheet material is solid to minimize susceptibility to erosion and deposition. It is cooled by a multiple diffusion bonded scheme. In the trailing edge region, the outer layer of the sheet material is solid for aerodynamic and fabrication reasons and is cooled via chordwise channels located in the inner layer of the skin. Over the rest of the airfoil, the skin is tangential injection Lamilloy®, which is a porous material that produces quasi-transpiration cooling. A cutaway drawing of a typical Lamilloy geometry is shown in Fig. 11 (Lamilloy is a registered trademark of Allison Division/GM). Preliminary studies have demonstrated the improved heat transfer effectiveness of Lamilloy over conventional multipass cooling.

Spanwise holes that taper from hub to midheight represent an improvement over constant-diameter holes used in rotor blade cooling. With this technique, increased cooling in the critical midheight region is obtained by reducing over cooling in the hub region resulting from the lower coolant temperature as the cooling air enters the hub region. Increased hub region flow area obtained by tapering reduces heat transfer in that region, thus reducing temperature rise in the coolant as it flows radially outward.

Another variation in cooling hole geometry is integrally to cast circumferential ribs periodically spaced along the length of each cooling hole. These act as flow turbulators to produce turbulent rather than laminar heat transfer for the cooling air. Field tests have been run on a Model 501 engine comparing smooth and turbulated holes. These tests verified that the heat transfer coefficient doubled by the use of the turbulators. A combination of turbulators and tapered holes could provide a very significant improvement in the cooling effectiveness required for the first-stage rotating blade and possibly the second-stage rotating blade.

Westinghouse policy has been to use high-strength ferritic steel for rotating parts such as disks and torque tubes. The advantages of the low-alloy, time-proven NiCrMoV turbine disk material over Ni-based alternatives are better fracture toughness, lower cost, availability in industrial size forgings, and higher strength at the 750°F (400°C) design temperature. This material can only be used up to approximately 800°F (427°C) for temper embrittlement concerns.

For the ICR cycle, the HP compressor discharge temperature will always be sufficiently low so that it can be used, uncooled, for rotor cooling. The use of compressor discharge or interstage bleed air to cool engine parts reduces engine efficiency by up to 0.5 percent for each percent of cooling air utilized, depending on the coolant source and flow path entrance conditions. In the 501F engine, some 60 percent of the cooling air is used for aerofoil cooling. Most of the remainder leaks into the turbine hot gas flow through clearances in the parts that bound the coolant flow path as it proceeds to its destinations throughout the engine. These clearances are required to permit differential expansion of parts during temperature transients in order to avoid low cycle fatigue damage.

Another area that has a large potential for cooling air reduction is the reduction of the combustor outlet hot spot that the turbine blading must account for during design. In the case of the stage 1 vane, some vanes in the row will be directly impacted

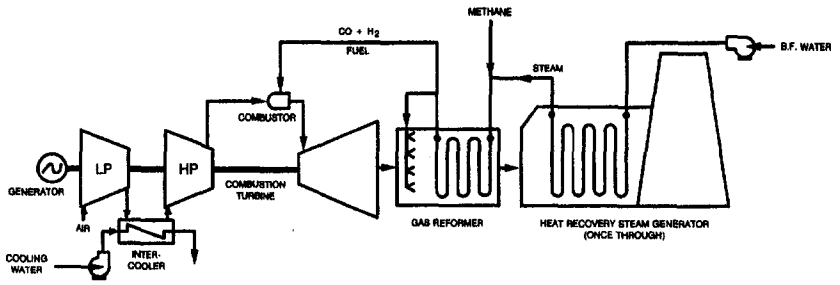

Fig. 9 Intercooled, thermochemical recuperative cycle

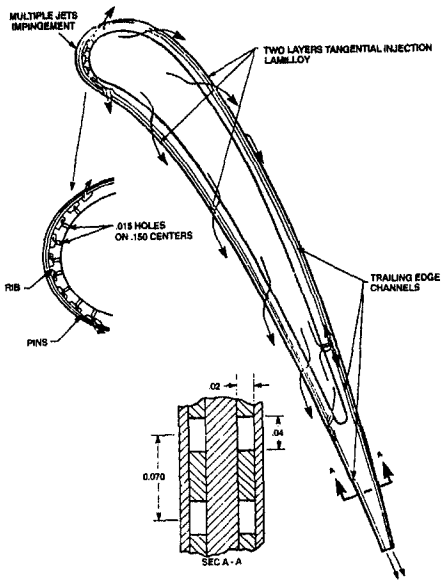

Fig. 10 Cooling geometry, air-cooled first-stage vane

by the hot spot. This hot spot will be carried downstream, but will be attenuated somewhat by the averaging process due to blade rotation. Even so, the hot spot temperature may also have a special effect on the first rotating blade due to time-averaged migration to the pressure side. Once the amount of hot spot reduction is known, the amount of cooling flow reduction can be estimated and the improvement in cycle efficiency predicted. Hot spot reduction will be estimated from ongoing tests of premix lean-burn combustors employing reduced cooling.

Closed-Loop Steam Cooling

Another innovation that will provide increased ATS cycle efficiency at constant RIT is closed-loop steam cooling. Closed-loop steam cooling involves directing a portion of the dry steam raised in the HRSG through the walls of hot end components, such as combustor baskets, transitions, and vanes, prior to expanding it through the steam turbine. The steam is superheated as it removes heat radiated and convected from the hot gas path. The idea of using steam to cool a gas turbine was suggested in the 1960s (Arsen'er et al., 1990).

When a comparison is made of the implications of replacing cooling air with bottoming cycle steam, while maintaining constant RIT, it is found that temperatures in the combustion reaction drop significantly because the same quantity of fuel is burned with much more air (original quantity, plus all the air that was used for basket wall, transition wall, and row 1 vane wall cooling). Thus, emissions may drop because the premix lean-burn, dry low NO_x combustion will be even more lean provided flame stability is maintained.

The total pressure available at the first rotor inlet for expansion through the turbine will be higher, because no momentum mixing loss between cooling air and mainstream gas flow will have occurred. Therefore, extra power will be produced by the gas turbine. Also, the hot spot temperature from each basket will be reduced since much less $\Delta T/T$ was required. This will reduce both row 1 vane and blade cooling requirements. Additional kilowatts will be generated in the steam turbine from the higher temperature (but lower pressure) steam expanding through the steam turbine.

Use of steam cooling in the row 1 vane would raise ATS efficiency 0.8 percentage points. Inclusion of the heat extracted from the baskets and transitions would further raise efficiency. Steam cooling for row 2, 3, and 4 vanes would also produce more power, and would additionally boost ATS efficiency, since exhaust temperature would rise, thus reducing fuel consumption (more heat transferred across recuperator to compressor delivery air), and recuperator exhaust temperature would also rise, resulting in the raising of more steam in the HRSG. The net effect could be to raise ATS efficiency another 0.5 percentage point or more.

Closed-loop steam cooling is a very attractive means of boosting ATS combined cycle efficiency. The technical challenges are significant, but are all understood and lend themselves to design and analysis. Factors that must be considered include: (1) control requirements to ensure an uninterrupted supply of steam; (2) steam pressure loss minimization and leakage elimination; (3) heat transfer requirement and steam capacities; (4) steam cooling paths through components and casting limitations; and (5) maintaining constant thermal stress to assure required low cycle fatigue life.

The possibility of applying closed-loop steam cooling to the rotating blades should also be investigated. A conceptual design of steam transfer into, and retrieval from, the shaft, as well as routing through the disks and blades, will be investigated. The complexity and development effort will be weighed against the potential gain in cycle efficiency to determine the advisability of pursuing this option.

Advanced Aerodynamic Design

The 501F compressor was designed between 1986 and 1988 by Westinghouse using 20 years of successful design experience on the 501 frame (501AA to 501D5). The experimental knowledge gained in the 501 compressor was incorporated into a design system using appropriately prescribed aerofoil shapes with their loss and deviation characteristics incorporated into a compressible flow. The key element in the design process was to achieve a compressor design, which could be built and applied confidently in the engine without developmental testing. This target was achieved using the base of experience that grew as the 501 evolved from the 501AA to the 501D5. The total experience was developed into compatible parts of a system for design and performance analysis, which provided the necessary confidence to develop the new 501F compressor.

The design was successful, and resulted in the high-efficiency, low-loading, high surge margin, 16-stage compressor. For the compressor(s) of the ATS it is anticipated that this traditional Westinghouse approach will be strengthened.

The 501F turbine aerodynamic design benefited from turbine design experience and the application of advanced three-dimensional design techniques. The resulting high-efficiency four-stage turbine configuration contributed greatly to the success of the 501F. Within this basic four-stage turbine philosophy, it is anticipated that further aerodynamic refinement can be incorporated.

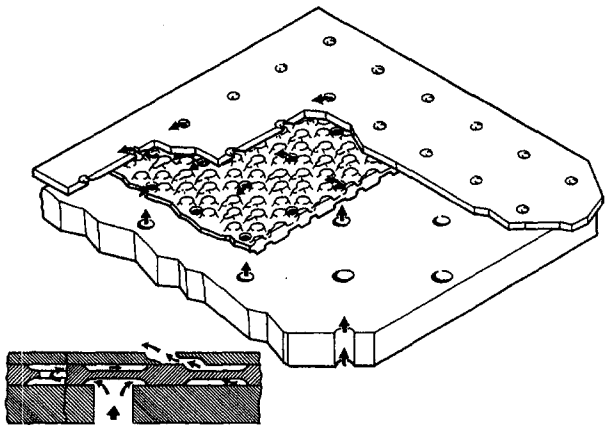

Fig. 11 Schematic of typical lamilloy geometry

Reduction in Leakages, Clearances, and Mechanical Losses

Additional gains in ATS efficiency can be realized through more efficient utilization of cooling and sealing air, and reduction in mechanical losses. It is intended to incorporate ideas that have in many cases been formulated, but not implemented in the past.

Improvement of component performance is possible by reducing clearances in both the compressor and turbine. The use of knife edge seals on disk seal arms that wear into abradable material such as felt metal or filled, honeycomb surfaces that are mounted on the stationary compressor and turbine seal housings, is a method of minimizing running clearance. The process of rubbing the knife edge into the abradable surface during both steady-state and transient operation will produce a groove in the abradable material and establish both a minimum radial and axial running clearance. The final steady-state clearance will be smaller than when seals are designed not to rub. With the knife edge seal rubbing into the abradable material, the frictional heat generated by rubbing is not large enough to cause structural distortion.

Innovative brush seals, which are gradually finding acceptance in gas turbines, will be considered for the ATS engine. These seals restrict the flow of air through a gap between stationary and rotating components by filling the gap with a brush of very fine (0.0025 in. [0.0064 cm]) alloy wires. The wires are oriented at 45 deg to the radial direction so they can bend and accommodate transient reduction of radial clearance. Cost versus benefit from reduced leakage flow is the major tradeoff to be considered.

Further clearance reduction beyond wear-in type seals would be to utilize an active clearance control design that would reduce the running clearance caused by transients. It is well documented that the largest clearance required between rotating and stationary parts occurs during startup of a cold engine. If a method can be developed to minimize or eliminate this added clearance, then operation with a running clearance set only by steady-state operation can be achieved. Reduction of the transient clearance is important because, in most cases, especially for the blade tips, the transient clearance requirement is more than double that required for steady state. The effect of elimination of the transient allowance is to reduce the steady-state leakage area and resulting flow by one half.

Some improvement in overall cycle efficiency is possible with a reduction in mechanical and/or windage losses. The use of a directionally lubricated thrust bearing to replace the more conventional flooded design will reduce the mechanical loss. These bearings are being used commercially and could be used for this application. If a concern exists that a sudden loss in oil supply would cause damage to the bearing and rotor, an oil reservoir could be designed to protect the bearing during an emergency shutdown.

Another area for even greater improvement would be the application of active magnetic thrust and radial bearings in place of the conventional oil lubricated bearings. These types of bearings are currently being used in small gas turbines ($\approx$2 MW), and special applications, and are under development for large-size applications such as gas turbines. This system would eliminate the need for an oil lubrication system. It would benefit the cycle by reducing mechanical losses for the turbine bearings, oil system pumps, oil cooler fans, etc., and would also eliminate the oil cooler, piping, fire protection, controls, etc.

Another area that translates into a mechanical loss is windage created by any rough or protruding surface, such as uncovered coupling bolts, blade root projections, etc. In any design, attention to minimizing areas that create windage must always be considered.

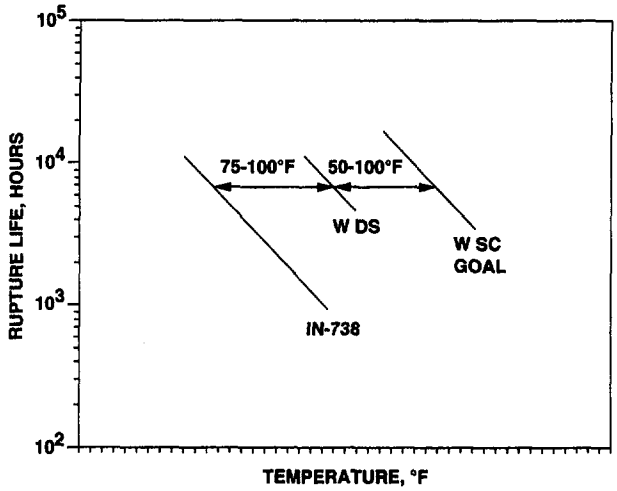

Fig. 12 Temperature advantage of Westinghouse DS and Westinghouse SC alloys

High-Temperature Material Requirements and Needed Development

Materials play a critical role in the design of engines with higher firing temperatures, since the temperature capability of materials establishes the cooling requirements, which in turn affects the engine efficiency. Hot section components for land-based engines typically require materials with superior mechanical properties and good corrosion/oxidation resistance at elevated temperatures. Ni and Co-base superalloys with high Cr content are extensively used for this application, the chemistry of these alloys having been adjusted to yield an optimum combination of strength and corrosion/oxidation resistance. At higher firing temperatures, additional protection of hot section superalloy components by coatings has become an absolute necessity. It may not be possible to adjust the composition of superalloys further to obtain higher strength and better hot corrosion and oxidation resistance at elevated temperatures without adversely affecting their stability. The high-temperature strength of superalloys arises from a combination of various hardening mechanisms, the most potent being precipitation hardening. The commercial superalloys are solution treated (around 2050° to 2300°F [1121° to 1260°C]) and aged to obtain optimum elevated temperature properties. Thus, the ultimate temperature capability of these materials is limited by the solution treatment temperature. The advent of single crystal casting, which eliminates the need for grain boundary strengthening elements, makes it possible to increase the solution treatment temperature.

The third and fourth-generation Ni-base single crystal alloys offer a temperature advantage of about 200°F (111°C) compared to conventionally cast IN-738, which is used as a blading material in land-based engines. The French have developed a single crystal alloy with 16 percent Cr, which offers a 90° to 100°F (50° to 56°C) temperature advantage at about 22 kpsi (1547 kg/cm^2) stress level when compared to conventionally cast IN-738.

Westinghouse has been developing corrosion resistant directionally solidified (DS) and SC Ni-base superalloys for land-based engine applications (Cr levels around 16 percent). At typical row 1 blade operating stress levels, these new alloys in the DS condition offer a temperature advantage of around 75° to 100°F (42° to 56°C) when compared to equiaxed IN-738, as shown in Fig. 12. Westinghouse SC alloys are expected to exhibit 50° to 100°F (28° to 56°C) higher temperature capability than that of the corresponding DS alloys.

Coatings used for land-based hot section components fall into the categories of corrosion resistant and thermal barrier. As

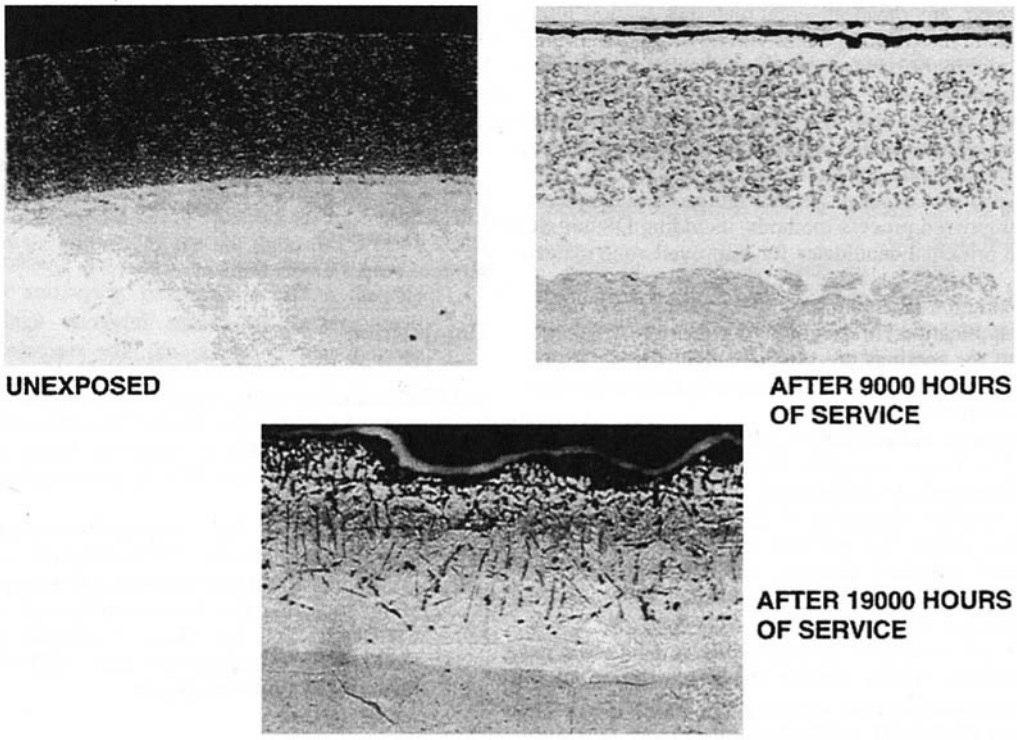

Fig. 13 MCrAlY coating degradation

the name implies, the former is applied for corrosion and/or oxidation protection, while the latter is used to reduce the heat transfer between the gas stream and the substrate of the coated component. It is known that when corrosion-resistant MCrAlY coatings are exposed to elevated temperature, they degrade due to inward and outward diffusion of elements present in the coating. The extent of degradation depends both on service temperature and time. Figure 13 shows MCrAlY coating degradation as a function of service exposure at a temperature of around 1700°F (927°C). After 9000 hours of operation, the coating structure reveals denuded zones at the outer surface as well as at the coating–substrate interface. The coating was also locally corroded/oxidized at its outer surface. After 19,000 hours of operation, the coating was almost completely corroded/oxidized, and the substrate was oxidized significantly. These results show that current MCrAlY type coatings do not offer reliable protection at ATS target metal temperatures.

Advanced coatings are needed to realize the full potential of new DS and SC alloys. At present, thermal barrier coatings (TBCs) are being used in service on static components and are being evaluated for application to rotating parts. The TBC is needed to lower the substrate temperature and to improve the reliability of MCrAlY coatings. Although these coatings are being used industry wide, development work is needed to increase their temperature capability for reliable service in ATS engines.

For both corrosion-resistant and TBCs, programs to evaluate all available coatings, select candidate coatings, perform screening tests, and outline long term development plans will be established.

The target RIT for an ATS engine requires implementation of SC and DS components coupled, with advanced coatings (including TBC) to minimize cooling air/steam usage in the ATS engine. The key is to take advantage of increasing creep strength by letting the blade temperature increase. Corrosion-resistant SC materials are expected to exhibit about a 150°F (83°C) temperature advantage compared to current conventionally cast blading materials, while TBCs typically lower service metal temperature of the coated component by an additional 150°F (83°C).

Ceramics and ceramic composites offer excellent temperature capability and are less significantly affected by the environment (corrosion and oxidation) than superalloys. For continuous advancement in high temperature capability, it will be necessary to consider implementing ceramics, composites, and intermetallics. In these cases, available structural ceramics, and composites will be assessed for their potential application. Ceramics and ceramic composites will be considered for stationary components of the ATS engine.

Component Specific Materials

Combustors. Improved metallic materials with TBC or fiber-reinforced ceramics will reduce cooling air requirements. Minimization of cooling air flows will reduce NO_x emissions.

The use of combustors fabricated from advanced ceramics and fiber-reinforced ceramic composites, which provides mechanical integrity, greatly advance the technology. Ceramic composites will allow the use of uncooled or minimally cooled combustors systems. Ceramics will be evaluated as alternatives to conventional metal-based combustors for the long-term.

Transitions. Advanced Ni-based materials and high-temperature coatings coupled with TBC will be considered for the ATS engine. Recently developed oxide dispersion (Y_2O_3) strengthened superalloys offer excellent creep strength, as well as superior oxidation and hot corrosion resistance. These alloys, along with ceramics and ceramic composites, may be evaluated to replace conventional Ni-base transitions.

Vanes and Blades. Given the time frame of the ATS program, intermetallics and composite materials may not be available for the subject application. These materials will be evaluated for future engine applications. Availability of these materials for this application depends on how rapidly the technology advances and how many design data would be generated and

available. However, any developmental materials such as intermetallics and metal matrix composites will be evaluated as they become viable within the development time frame for both vane and blade applications.

Stationary vanes do not have to withstand the rotating stresses that are imposed upon blades, but are subjected to environmental attack and the thermomechanical stresses imposed by thermal cycling. Advanced superalloys that are processed by conventional and improved process methods, including DS and SC casting, are the principal candidates for improved vane materials.

Improved oxidation-resistant MCrAlY coatings are candidates for this application. In addition to corrosion resistance, the properties of the coatings need to be evaluated with respect to mechanical stability for candidate vane materials under thermal cycling conditions.

TBCs are expected to help improve the cooling efficiency of vane systems. Key issues regarding the application of TBCs to vanes are the mechanical compatibility of the TBCs with the vane substrate and the interaction of the porous coating with molten corrosive oxides and sulfides. TBCs, primarily those based upon yttria-stabilized zirconia, will be evaluated with respect to mechanical and chemical effectiveness for application as improved coatings for vanes.

Intermetallic and composite systems will also be considered for vane applications. These systems are currently limited by the very few intermetallics that display good high-temperature ductility and are chemically stable in oxidizing/hot corrosion atmospheres. The most promising systems are those based on NiAl intermetallic. The properties of these systems will be reviewed for prospective vane applications.

Ceramic materials will be assessed for vane applications in the natural gas-fired advanced turbine systems. While ceramics, particularly those based on oxide systems, offer increased temperature capability, the structural integrity of the large-sized components that are required in the power generation ATS must be demonstrated. Currently, fiber-reinforced ceramic composites for advanced gas filter systems are under development at Westinghouse as part of a DOE sponsored program (Newby and Bannister, 1993).

The most viable candidate materials for improved capability turbine blades are advanced nickel-base superalloys that are processed by DS and SC casting methods, in combination with improved oxidation/hot corrosion resistant coatings and thermal barrier coatings.

The study of improved alloy compositions and processes will be based upon current Westinghouse approaches to develop DS and SC alloys for land-based turbine blades. Ongoing Westinghouse programs have demonstrated that improved high temperature creep and fatigue performance can be delivered by directional solidification of modifications of current turbine alloys. Production of SC alloys has also been demonstrated. The key to utilization of these alloys is to develop coatings that can operate at the high temperature capability of DS and SC materials.

Hot corrosion/oxidation protection of the turbine blades is expected to be provided by advanced coatings based upon existing MCrAlY coatings and oxidation-resistant alloy modifications. Candidate coating materials will be assessed based upon their ability to protect against environmental attack and their compatibility with candidate blade alloys. Improved coatings will be evaluated based upon their ability to withstand hot corrosion attack at intermediate temperatures on the cooler portions of the blade, high temperature oxidation attack at the maximum temperatures of the blade, and their impact upon the mechanical performance of the underlaying blade alloy.

The current risks of TBCs are mechanical and corrosion related. The mechanical properties of TBCs must be demonstrated to ensure integrity against spalling under thermal cycling conditions. The corrosion issue is not due to corrosion of the coating itself but derives from the ability of the coating to absorb and retain corrosive molten oxides and sulfides that attack the underlaying metallic blade and coating. Processing of the TBC to avoid this accelerated form of attack will be required to improve the capabilities of TBCs.

Turbine Disks. High strength, low alloy steel disks are used in the turbine section of the 501F with 2300°F (1260°C) RIT. The service temperature of these disks is maintained below 750°F (400°C) through the use of cooling air to minimize in-service temper embrittlement.

Combustion

The extremely low NO_x (8 ppmvd @ 15 percent O_2), CO, and UHC emission levels, which must be achieved at the higher temperature of the fully developed ATS, are a serious challenge. Significant internal R&D is currently being devoted to the achievement of single-digit NO_x by pursuing the premix, lean-burn strategy.

Alternatively, it has been proposed to investigate catalytic combustion, which in the past did demonstrate single-digit NO_x emissions. In the current investigation, a test program is outlined to begin investigating the thermomechanical stability of the catalyst substrate, and the effect on catalyst performance of prolonged exposure to high temperatures. ATS emission control will be discussed in a future paper.

Selection of Coal-Fired Plant Reference System

Within the natural-gas-fired ATS program, a brief effort will be expanded to select a reference coal-fired ATS (Webb et al., 1993). Westinghouse will apply its background with advanced coal-fueled power generation (Bannister et al., 1993) to provide the information needed. The selected coal-fired ATS will be described in sufficient detail to provide information that can be used to identify any conversion issues from natural gas to coal. The natural gas-fired ATS is to be applied to a coal-fueled ATS combined cycle. Modifications to the gas turbine components are to be minimized. Modifications should account for the differences in fuel.

Estimates will result for the reference coal-fired system with respect to thermodynamic cycle efficiency, turbine tolerance factors (e.g., expansion gas particle loading, particle size distributions, and alkali vapor content), turbine maintenance (i.e., blade replacement and cleaning frequency), and environmental emission levels (e.g., particulate, NO_x, CO, SO_2, and CO_2).

Materials for Coal-Derived Fuels

Conversion of a coal-fired advanced turbine systems operation imposes more severe environmental constraints on the materials selection for the turbine components. Specifically, sulfur, halides, and low levels of metallic elements, such as vanadium, will be carried by the coal-derived fuel and will present significant corrosion attack to the hot section components of the engine.

Under conditions of increased corrosion in the coal-fired ATS, advanced superalloys will be required to form corrosion-resistant chromia scales rather than alumina scales; this capability may significantly impact the availability of higher strength alloys under these conditions.

Ceramic materials are expected to be less significantly affected than metallic materials. In specifically severe cases, it will be necessary to consider ceramics for some selected applications. For these cases available structural ceramics will be assessed for potential applications.

The suitability of coatings will also be significantly affected by the atmosphere. Chemically protective coatings will, in a similar manner to the effect on metals, be required to display corrosion resistance. Coating selection for coal-fired ATS com-

ponents will be more significantly weighted by the ability of the coating to form corrosion resistant chromia coatings. Coatings will be assessed by evaluating the available coating corrosion data for oxygen/sulfur atmospheres that are similar to the coal-fired ATS atmosphere.

The conversion to coal as a fuel is also expected to impact the use of TBCs. Although TBCs themselves are expected to be only minimally corroded by the more aggressive nature of this atmosphere, significant effects may be expected on the substrate and bond coat. The acceptability of TBCs will be determined by evaluating the data that define the role of the TBC in accelerating the corrosion of the bond coat and the underlaying substrate. These data will be evaluated with respect to the more corrosion-resistant atmosphere.

Conclusions

The feasibility of achieving a 60 percent (LHV) efficiency in a natural-gas-fired ATS cycle within an 8-year period has been established. Cycle innovations, a 2600°F (1427°C) RIT, reduced cooling air usage, improved component efficiencies, and improved material/coating systems will all be needed to accomplish this goal. The ATS needs to be cost competitive, as well as be fuel flexible to use coal-derived and biomass fuels.

This paper has outlined some of the development work that Westinghouse is pursuing to identify the equipment requirements and technological barrier issues that need to be solved during the component development phase of the ATS program. Critical components will be tested. Subscale assemblies will be evaluated. The laboratory experimental data will lead to the testing of full-scale components and integrated subsystems in the next stage of the ATS program.

Acknowledgments

The work described in this paper is being conducted under a DOE sponsored program, Advanced Turbine Systems Program-Conceptual Design and Product Development, Contract No. DE-AC21-93MC30247. The program is administered through the Morgantown Energy Technology Center under the guidance of METC's Program Manager, Mr. Donald W. Geiling.

References

Arsen'er, L. V., Korsov, Yu. G., Khodak, E. A., and Romakhova, G. A., 1990, "A Highly-Efficient Combined Cycle Plant With Steam Cooled Gas Turbine," *Teploenergetika,* Vol. 37, No. 3, pp. 19–22.

Bannister, R. L., Bevc, F. P., and Newby, R. A., 1993, "Advanced Clean Coal Power Plants—A Status Update," *Proceedings International Energy Conference, Energex '93,* Oct. 18–22, Seoul, Korea.

Crisall, A. J., and Parker, M. L., 1993, "Overview of the WR-21 Intercooled Recuperated Gas Turbine Engine System, a Modern Engine for a Modern Fleet," ASME Paper No. 93-GT-231.

Little, D. A., Bannister, R. L., and Wiant, B. C., 1993, "Development of Advanced Turbine Systems," *ASME Cogen Turbo Power '93 Proceedings, IGTI—Vol. B,* pp. 271–280.

Newby, R. A., and Bannister, R. L., 1993, "Hot Gas Cleaning Makes Promising Progress," *Modern Power Systems,* Vol. 13, Issue 9, pp. 51–57.

Stephens, J. O., Little, D. A., Hunt, P. J., and Stanaland, R., 1990, "Efficient Part-Load Combined Cycle Operations," *Proceedings 19th Turbomachinery Symposium,* Texas A&M, pp. 31–36.

Webb, H. A., Parsons, E. L., and Bajura, R. A., 1993, "Advanced Turbine Systems Program and Coal Applications," ASME Paper No. 93-GT-356.

A Combined Cycle Designed to Achieve Greater Than 60 Percent Efficiency

M. S. Briesch

R. L. Bannister

I. S. Diakunchak

D. J. Huber

Westinghouse Electric Corporation, Orlando, FL 32826

In cooperation with the U.S. Department of Energy's Morgantown Energy Technology Center, Westinghouse is working on Phase 2 of an 8-year Advanced Turbine Systems Program to develop the technologies required to provide a significant increase in natural gas-fired combined cycle power generation plant efficiency. In this paper, the technologies required to yield an energy conversion efficiency greater than the Advanced Turbine Systems Program target value of 60 percent are discussed. The goal of 60 percent efficiency is achievable through an improvement in operating process parameters for both the combustion turbine and steam turbine, raising the rotor inlet temperature to 2600°F (1427°C), incorporation of advanced cooling techniques in the combustion turbine expander, and utilization of other cycle enhancements obtainable through greater integration between the combustion turbine and steam turbine.

Introduction

The purpose of the Department of Energy's Advanced Turbine Systems (ATS) contract is to investigate technologies and innovative concepts applicable to natural gas-fired combined cycle power generation systems, which will allow thermal efficiencies greater than 60 percent,[1] while providing electricity at significantly lower cost than current combined cycle power plants and operating with much reduced environmental impact. Additionally, reliability-availability-maintainability (RAM) will be competitive or superior to current power generation systems. The ATS cycle fired with natural gas is to be commercially available by the year 2000. The final ATS design must also be able to be adapted to operate on coal-derived or biomass fuels for the post-2005 power generation market.

Westinghouse has developed a product line that mirrors the general gas turbine inlet temperature trend shown in Fig. 1. To make gas turbines more competitive than steam turbine plants, it has been necessary to develop efficient cycles. Over the years, Westinghouse has performed many engineering studies to determine optimum cycles to minimize the cost of electricity. Some of the more promising cycles (intercooled, multiple shafts, reheat, steam injected, and water injected at various locations) have been studied in detail (Scalzo et al., 1994). In the final analysis, the simple cycle gas turbine combined with a steam bottoming cycle (a synergistic combination of the Brayton and Rankine cycles) was developed to increase overall cycle efficiency. Stephens (1952) and Baldwin et al. (1965) are two references that summarize earlier Westinghouse work on optimizing plant cycle efficiency.

Current large natural-gas-fired combined cycle power generation systems are capable of net efficiency levels in the range of 54 percent. Within the ATS program, Westinghouse has been given the opportunity to re-evaluate cycle efficiencies using older, established concepts, such as intercooling and recuperation, and newer concepts, such as thermochemical recuperation (Little et al., 1993). In addition, efficiency enhancements within the ATS selected cycle are to be evaluated to determine the best approaches to raising overall thermal plant efficiencies to greater than 60 percent while adhering to the other ATS program goals. The concepts considered in the Westinghouse analyses are required to be capable of demonstration within a three to four year time frame. From a baseline cycle definition, this paper reports on how different concepts will affect the overall plant thermal efficiency. Results given in the paper show that a plant efficiency of greater than 60 percent is achievable.

Baseline Cycle

In order to evaluate different technologies and concepts applicable to combined cycle power generation systems, a baseline combined cycle configuration first had to be developed to provide a basis for comparison of all the cycle concepts and technologies to be considered. For this purpose, a conventionally configured combustion turbine coupled with a three-pressure level reheat steam cycle (Fig. 2) was modeled to provide a baseline cycle. The combustion turbine rotor inlet temperature (RIT) was set at 2600°F (1427°C) to approximate near-term temperature capabilities (Bannister et al., 1995). Compressor pressure ratio was set at 18. High-pressure steam conditions entering the steam turbine were specified at 1450 psi (10.2 MPa) and 1000°F (538°C) and the hot reheat steam temperature was also set at 1000°F (538°C). Note that this configuration utilizes turbine rotor cooling air heat to produce additional low-pressure steam in the steam cycle via a heat exchanger located in the heat recovery steam generator (HRSG). Also, the natural gas fuel is preheated by feed water recirculation flow.

Component Improvements

Incorporation of several component improvements, available through recent technological developments and advanced design techniques, into the power generation system of Fig. 2 results in significant efficiency gains.

The application of advanced compressor analysis and design tools results in increased efficiency compressors. Additionally, the application of brush seals in the compressor, as well as in the combustion turbine expander and the steam turbine, results in further plant efficiency improvements. At the compressor inlet, an advanced inlet design improves efficiency via reduced pressure loss.

Westinghouse is currently engaged in full-scale rig tests of several diffuser/combustor configurations. These tests will

[1] All plant efficiency values in this paper are based on lower heating value (LHV).

Contributed by the International Gas Turbine Institute and presented at ASME Cogen Turbo Power '94, Portland, Oregon, October 25–27, 1994. Manuscript received by the International Gas Turbine Institute July 20, 1994. Associate Technical Editor: E. M. Greitzer.

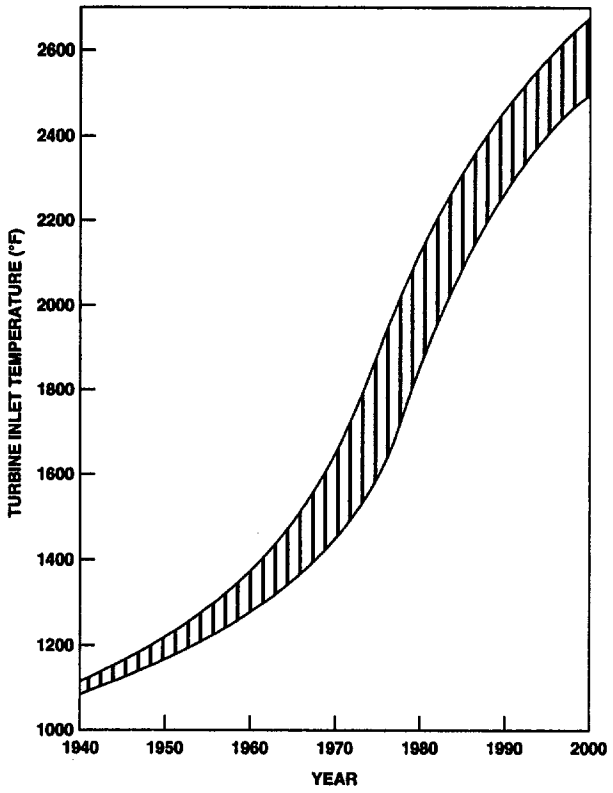

Fig. 1 Gas turbine inlet temperature trend

allow the design of diffusers and combustors with reduced pressure loss, which will improve plant efficiency.

Several advanced turbine technologies may be applied to the combustion turbine expander. These include the application of single crystal and ceramic components to increase material operating temperatures and reduce turbine cooling requirements, active blade tip clearance control to minimize tip leakages and improve turbine efficiency, and the use of a three-dimensional (3-D) airfoil design philosophy. By utilizing 3-D analytical design tools, airfoils can be designed that are more efficient than those designed with 2-D design tools because they can accommodate more effectively the complex flows inside a turbomachine. The use of a 3-D airfoil design philosophy may also be applied to the steam turbine to enhance its efficiency.

There are two generators in the baseline configuration. One of these is the combustion turbine generator, while the other is the steam turbine generator. Current generator designs are capable of higher efficiency than those chosen for the baseline cycle. While the combustion turbine generator of the baseline configuration is of sufficient size to apply this technology cost effectively, the steam turbine generator is not. By utilizing a single shaft arrangement, however, the smaller steam turbine generator is eliminated and the remaining single generator may be designed at the higher efficiency.

When the component improvements listed above are all incorporated into the baseline cycle, the net plant thermal efficiency is increased by approximately 2 percentage points.

Steam Cycle Enhancements

The basic reason for raising the steam pressure and temperature of the Rankine cycle is to improve the potential thermal efficiency (previous Westinghouse studies to optimize steam cycle configurations for subcritical and supercritical applications are summarized by Ernette and Silvestri, 1990, and Silvestri et al., 1992). The first cycle variations investigated within this study were modifications to the baseline cycle in which the steam cycle was enhanced. The results of these studies indicated that increasing either high-pressure steam superheat temperature or reheat steam temperature by 50°F (28°C) results in an improvement in combined cycle thermal efficiency of 0.1 percentage point. Increasing high pressure steam pressure from 1450 psi (10.2 MPa) to 1800 psi (12.6 MPa) results in an increase in net plant thermal efficiency of 0.1 percentage point. A further increase in pressure to 2400 psi (16.8 MPa) yields only an additional 0.05 percentage point in thermal efficiency, while adding to the cost of the high-pressure steam system. Also, since the steam turbine size is set by the exhaust energy of the combustion turbine, increasing steam pressure reduces the blade heights in the high pressure steam turbine. For 2400 psi (16.8 MPa) high-pressure steam, the resulting blade heights are much

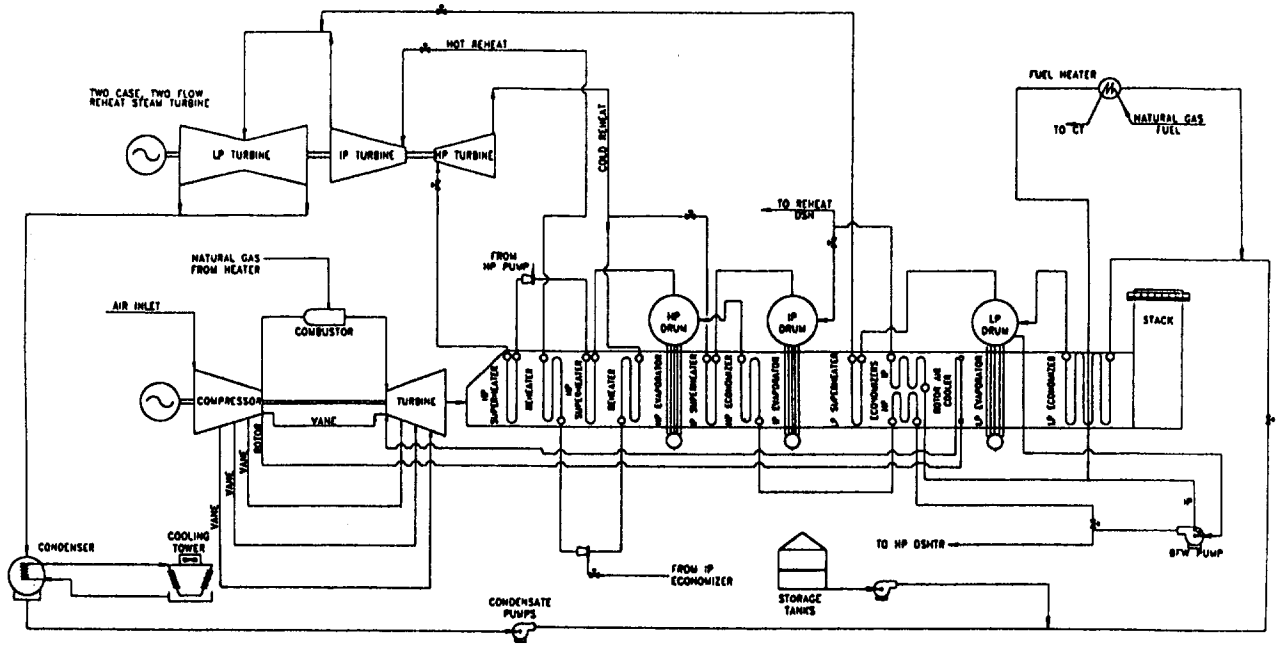

Fig. 2 Baseline combined cycle

smaller and less efficient than for the 1800 psi (12.6 MPa) steam. Therefore, the optimum steam cycle was determined to be at 1800 psi (12.6 MPa) with 1100°F (593°C) high pressure superheat steam and 1100°F (593°C) reheat steam (both 100°F (56°C) over the baseline temperature). This results in a 0.5 percentage point increase in net plant thermal efficiency and also in a slight increase in output due to the increased efficiency of the steam cycle. The steam temperatures were limited to 1100°F (593°C) for this study. The steam temperature of 1100°F (593°C) plus a reasonable steam superheater approach T determined the gas turbine exhaust temperature and this set the baseline cycle pressure ratio.

Rotor Air Cooler Heat Utilization

The Westinghouse 501F combustion turbine combined cycle provides two options for rotor air cooler heat utilization. The first option is an air-to-air cooler to cool the rotor cooling air after it exits the compressor and prior to its introduction into the rotor. The rotor air heat is rejected to the atmosphere via an air-to-air cooler. The other option is to cool the rotor air via an air-to-exhaust gas heat exchanger located in the heat recovery steam generator upstream of the low-pressure evaporator, as was done in the baseline cycle. With this configuration, the rotor air cooler heat is recovered by the steam cycle, which produces low pressure steam with the heat. This results in higher plant efficiency than that of the air-to-air cooler method since the rotor air cooler heat is recovered by the low pressure steam system.

Another concept involves removing the HRSG rotor air cooler used in the baseline configuration and installing a rotor air cooler which exchanges heat with the incoming natural gas fuel (after the fuel has been preheated by feed water recirculation flow). This returns the rotor air heat back to the combustion turbine, which then requires less fuel to achieve the desired rotor inlet temperature. Therefore, the rotor air heat is recovered at the combustion turbine efficiency (typically about 40 percent), which is much higher than the low-pressure steam system efficiency. This is, therefore, a much more effective recovery of the heat than is obtained via low pressure steam production, and results in an increase in net plant thermal efficiency of 0.4 percentage point over the baseline configuration.

Closed-Loop Steam Cooling

Most current technology gas turbine engines utilize air to cool the turbine vanes and rotors. This allows the turbine inlet temperature to be increased beyond the temperature at which the turbine material can be used without cooling, thus increasing the cycle efficiency and power output. However, the cooling air itself is a detriment to cycle efficiency in four ways. First, it is ejected from the turbine airfoils, causing a disruption in the surrounding flow field. This increases the airfoils' irreversible pressure losses and results in a reduction in turbine efficiency. Secondly, since the cooling air is ejected from the airfoil into the gas path, the resulting mixing of the cooling air into the gas path results in irreversible pressure losses due to the nonideal mixing of the streams, which have very different velocity vectors. The third loss mechanism is caused by the reduction in gas path temperature that accompanies the mixing of the cooling air into the gas path. This reduction in temperature reduces the work output of the turbine and, therefore, compromises cycle efficiency. Finally, the turbine cooling air must be pumped to pressures significantly higher than that of the gas path pressure at the location it is injected. This is done to assure that the cooling flow rate will be sufficient during certain operating conditions where the ratio of coolant pressure to gas path pressure drops below its design level. While some of this pressure is recovered by the turbine, there are internal losses as the cooling air passes from the compressor to the turbine gas path.

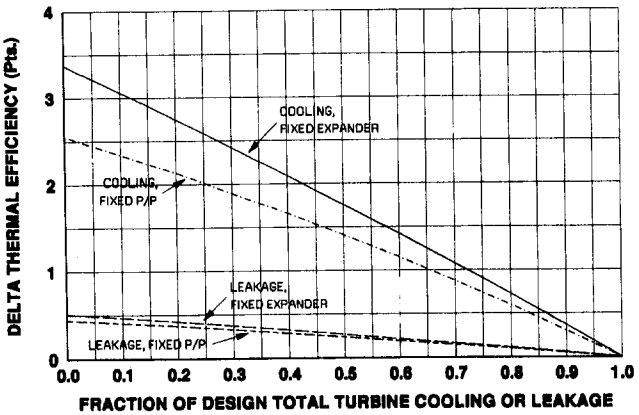

Fig. 3 Turbine cooling and leakage, effect on combined cycle thermal efficiency

The additional pumping work required to raise the cooling air to the required pressure is the associated loss.

The effect of cooling air on cycle efficiency is shown in Fig. 3. This figure shows the potential increase in combined cycle thermal efficiency for fractional reductions in cooling or leakage flows. In this figure, the lines labeled "Fixed P/P" show the effect for fixed compressor pressure ratio (i.e., the turbine expander is increased in size to handle the additional flow resulting from the reduction in cooling or leakage) and the lines labeled "Fixed Expander" show the effect for fixed expander size (the compressor pressure ratio is allowed to rise so that the additional flow caused by the reduction in cooling or leakage can be accommodated by a turbine of the original size). Note that, although turbine leakage generally carries a larger efficiency penalty than turbine cooling per given amount of flow, the fact that the amount of leakage flow is far less than the amount of cooling flow results in far less efficiency benefit from reducing turbine leakage flows by a given fractional amount compared to reducing turbine cooling flows by the same fraction of their baseline value.

By using closed-loop steam cooling, the loss mechanisms described above can be largely eliminated, while still maintaining turbine material temperatures at an acceptable level. In combined cycles, the steam used for cooling the combustion turbine hot parts will be taken from the steam bottoming cycle. This steam is then returned to the bottoming cycle after it has absorbed heat in the closed-loop steam cooling system. For an advanced bottoming steam cycle, closed-loop steam cooling would route cold reheat steam from the exit of the high pressure steam turbine to the combustion turbine vane casing and rotor. The steam is passed through passageways within the vane and rotor assemblies and through the vanes and rotors themselves, then collected and sent back to the steam cycle intermediate pressure steam turbine as hot reheat steam. This approach to turbine cooling relies solely on convective heat transfer. Since no steam or cooling fluid is ejected from the airfoils, aside from a small amount of steam leakage through the rotor seals, there is very little influence of the cooling steam on the airfoil flow fields, and hence minimal mixing losses. Also, the reduction in gas path temperature is minimized, since the convective heat flux across the airfoils is relatively small. Typically, first vane cooling air mixing reduces the gas path temperature approximately 100°F to 150°F (56°C to 83°C). For closed-loop steam cooling however, the reduction in gas path temperature is only about 10°F to 15°F (6°C to 8°C), or one tenth of the reduction of conventional cooling techniques. Application of closed-loop steam cooling to the baseline configuration yields a 2 percentage point increase in combined cycle efficiency.

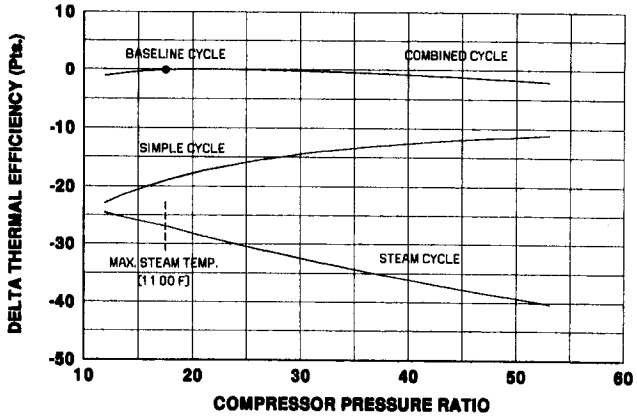

Fig. 4 Compressor pressure ratio, effect on thermal efficiencies

Increased Turbine Inlet Temperature

Since thermal efficiency increases with increasing turbine inlet temperature, the potential benefits of increased turbine inlet temperature was investigated. The turbine inlet temperature for the baseline cycle was increased 300°F (167°C) to 2900°F (1593°C). This resulted in a cycle output increase of 10 percent, and combined cycle thermal efficiency increase of slightly more than 1 percentage point. The reason that the performance increase was relatively small for such a large increase in turbine rotor inlet temperature is that, since the (air) cooling technology remained constant as the temperature was increased, large amounts of additional turbine cooling air were required to maintain turbine material operating temperatures at an acceptable level. This increase in cooling flow decreased cycle efficiency by the three mechanisms described earlier, and this significantly offset the benefit of increasing the turbine rotor inlet temperature. Therefore, since efficiency and output would have been increased much more if turbine cooling was held at the same level as in the baseline cycle, increased turbine operating temperature must be accompanied by corresponding advancements in turbine cooling. However, even if cooling technology advancements were available to allow operation at much higher rotor inlet temperatures, the formation of NO_x at these higher temperatures would result in unacceptable emissions characteristics.

Increased Compressor Pressure Ratio

Commercial aircraft gas turbine engines are designed with high overall pressure ratio. This is done to maximize the simple cycle efficiency. For the ideal Brayton gas turbine cycle, the cycle efficiency is a function solely of the cycle pressure ratio and increases with cycle pressure ratio (the ratio of specific heats of the working fluid also effects the cycle efficiency, but for air-breathing cycles there is little that can be done to change this property). In fact, for this ideal cycle, the maximum efficiency occurs at the point where the compressor exit temperature is very close to the combustor exit temperature. Of course, the cycle output for this case is very close to zero.

In real cycles, the effect of nonideal components causes the peak efficiency pressure ratio to decrease significantly from that of the Brayton cycle. Figure 4 shows the effect of compressor pressure ratio on simple cycle performance for a family of engines based on the combustion turbine of the baseline configuration. Also included in Fig. 4 are the corresponding steam cycle and combined cycle efficiencies. Note that the simple cycle efficiency curve is relatively flat above a pressure ratio of approximately 40. This indicates that it is nearing the peak simple cycle efficiency. The steam cycle efficiency is seen to decrease with increasing combustion turbine pressure ratio. This is due to the reduction in combustion turbine exhaust temperature, which in turn reduces the maximum steam temperature and pressure and the steam's availability, and results in lower steam cycle efficiency. The effect of all of this on combined cycle efficiency is that it peaks around a pressure ratio of about 20, but remains approximately constant for a relatively large increase in compressor pressure ratio.

Reducing the compressor pressure ratio below the baseline value of 18 results in a significant decrease in combined cycle efficiency. This is due to the fact that, since the maximum steam temperature considered for this study was 1100°F (593°C), any decrease in pressure ratio below the baseline value of 18, where the maximum steam temperatures are reached, will increase the turbine exhaust temperature while maintaining the steam temperatures at 1100°F (593°C). This results in a much smaller increase in steam cycle efficiency than that obtainable by allowing the steam temperatures to rise with the turbine exhaust temperature. Figure 4 shows the significant reduction in the slope of the steam cycle efficiency line at this point, which causes the combined cycle efficiency decrease.

The maximum specific work output of the Brayton cycle occurs at a significantly lower value of pressure ratio than that for the peak efficiency. Figure 5, which includes intercooled cycle characteristics to be discussed later, shows the specific output of the cycles in Fig. 4 (solid lines). The simple cycle peak specific output occurs at a pressure ratio of approximately 18. Also, note that the steam cycle specific output is reduced as pressure ratio is increased, since there is less exhaust energy available to the steam cycle. The combined cycle specific output, which is merely the sum of the simple cycle and steam cycle specific outputs, decreases for increasing pressure ratio across the entire range shown.

It, therefore, is optimum to select the lowest pressure ratio at which the peak combined cycle efficiency level is obtained. In this way both efficiency and output are maximized, and the cost of electricity is minimized (the baseline cycle is designed in this fashion).

Compressor Intercooling

The most typical arrangement for compressor intercooling involves removing the compressor air flow halfway through the compressor temperature rise, sending it through an air-to-water heat exchanger, and returning it to the compressor for further compression to combustor inlet pressure. The heat removed from the compressor air flow by the intercooler is rejected to the atmosphere, because, at the pressure ratios considered in this study, the heat quality is too low to be of use to the cycle.

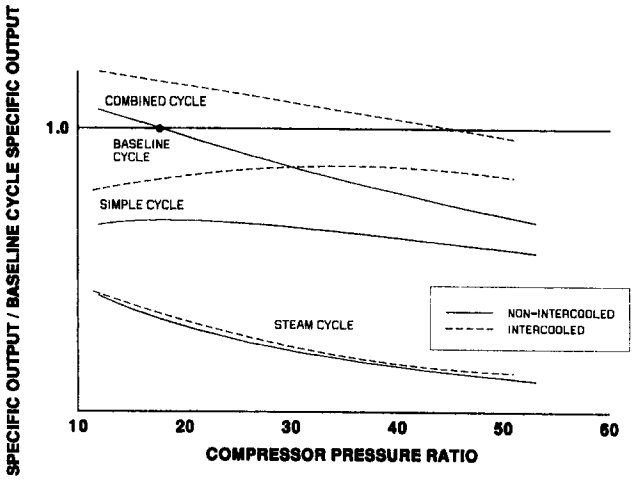

Fig. 5 Compressor intercooling, effect on specific output

Another intercooling concept is to spray water droplets into the compressor. As the air is compressed and increases in temperature, the water evaporates and absorbs heat. This results in a continuous cooling of the compressor. Note that for this concept the heat absorbed by the water is also rejected to the atmosphere, since this water is never condensed by the cycle but instead exhausted with the stack gases as low-pressure steam.

Compressor intercooling reduces the compressor work, because it compresses the gas at a lower average temperature. Since the combustion and steam turbines produce approximately the same output as in the nonintercooled case, the overall cycle output is increased. However, since the compressor exit temperature is lowered, the amount of fuel that must be added to reach a given turbine inlet temperature is greater than that for the nonintercooled case. The ratio of the amount of compressor work saved to the amount of extra fuel energy added is about equal to the simple cycle efficiency. It can therefore be said that intercooling adds output at approximately the simple cycle efficiency. Since combined cycle efficiencies are significantly greater than simple cycle efficiencies, it would be expected that the additional output at simple cycle efficiency would reduce the combined cycle net plant efficiency for the intercooled case. Figure 6 verifies this expectation and shows that this trend is the same for a wide range of cycle pressure ratios. Note that the simple cycle shows almost no change in efficiency for intercooling, which is expected since output is added at approximately the simple cycle efficiency.

Figure 5 shows the effect of intercooling on specific output. Since the compressor work requirement is reduced while the gas and steam turbine work outputs remain approximately the same as in the nonintercooled case, the net power output of both the simple and combined cycles is increased. Also, since the turbine exhaust temperature is increased slightly due to the exhaust gas composition effects, the steam cycle specific output is also increased slightly.

Recuperation

In recuperative cycles, turbine exhaust heat is recovered and returned to the combustion turbine combustor, usually via a heat exchange between the turbine exhaust gases and the compressor exit air flow. The discharge from the compressor exit is piped to an exhaust gas-to-air heat exchanger located aft of the combustion turbine. It is then heated by the turbine exhaust and returned to the combustor. Since the resulting combustor air inlet temperature is increased above that of the nonrecuperated cycle, less fuel is required to heat the air to a given turbine inlet temperature. Because the turbine work and the compressor work are approximately the same as in the nonrecuperated cycle, the decrease in fuel flow results in an increase in thermal efficiency. This is especially true for the simple cycle, since the heat recovered by recuperation is rejected to the atmosphere in the nonrecuperative case. For combined cycles the efficiency is also increased, because the combustion turbine recovers the recuperated heat at the simple cycle efficiency, which is larger than the 30 to 35 percent thermal efficiency of the bottoming steam cycle, which recovers this heat in the nonrecuperated case.

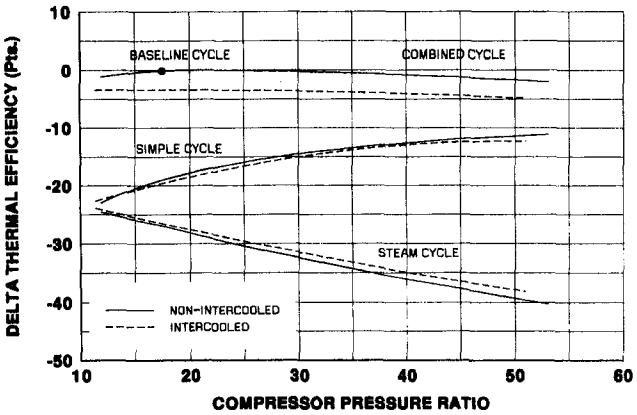

Fig. 6 Compressor intercooling, effect on thermal efficiencies

Installation of a recuperation system on the baseline configuration results in an increase in thermal efficiency of 1 percentage point. The steam cycle in this recuperated cycle has a lower efficiency than the steam cycle in the baseline configuration, because the recuperator exit temperature is significantly lower than the turbine exhaust temperature. However, the effect of reduced steam cycle efficiency is smaller than the effect of recovering the recuperated heat at the combustion turbine efficiency.

The thermal efficiency of the recuperated cycle can be increased further. Since the combustor inlet flow is smaller than the turbine exhaust flow (due to the removal of the turbine cooling air prior to combustion) and has a higher specific heat (due to the combustion products of the fuel), the heat capacity of the turbine exhaust flow is somewhat higher than that for the burner inlet flow. This means that the recuperated cycle described above does not fully utilize the quality of heat available in the turbine exhaust. By placing a steam superheater in parallel with the recuperator, the remainder of the available turbine exhaust heat can be recovered at its maximum quality. The maximum steam temperature can then be raised to that of the baseline cycle (1000°F (538°C)) and the cycle efficiency is increased by an additional 0.1 percentage point.

Since recuperative cycles return exhaust energy to the combustion turbine, less energy is available to the steam cycle, and the resulting steam turbine output is lower than that of the baseline configuration. However, the combustion turbine output is approximately the same as in the baseline cycle (minus losses in the recuperation system). This means that recuperative cycles carry a significant output penalty, with this penalty being proportional to the amount of recuperation performed.

Intercooling With Recuperation

From a simple cycle standpoint, the combination of intercooling with recuperation eliminates the problem of the reduced combustor inlet temperature associated with intercooled cycles. The simple cycle then gets the benefit of the reduced compressor work and, at all but high pressure ratios, actually has a higher burner inlet temperature than the corresponding nonintercooled, nonrecuperated cycle. This results in a dramatic increase in the simple cycle efficiency.

However, the bottoming cycle receives even less energy than in the recuperated cycle, since the recuperator removes much more heat from the turbine exhaust than in the recuperated, nonintercooled cycle. The additional heat removed corresponds to the heat rejected to the atmosphere by the intercooler. This means that we have merely displaced the lost energy of the intercooler by taking energy from the bottoming cycle. this is in addition to the energy already removed from the bottoming cycle in the nonintercooled, recuperative cycle. The result is a very low recuperator exit temperature, which in turn translates into a low generated steam pressure (low availability) and a low efficiency steam bottoming cycle. Thus, while simple cycle efficiency can be increased to over 50 percent, the combined cycle efficiency is reduced for the entire useful range of compressor pressure ratios. For conventional air-to-water heat exchanger intercooling of the compressor, the combined cycle efficiency is reduced approximately 1.9 percentage points at the baseline cycle pressure ratio. For continuously cooled compressors utilizing water droplet spraying into the compressor, the combined cycle efficiency is reduced by 0.4 percentage point.

Since the continuously cooled compressor with recuperation is not far below the baseline level of combined cycle thermal

efficiency, it is worth investigating further optimization of the steam cycle in this case. As mentioned earlier, steam may be superheated in parallel with the recuperator, yielding more efficient recovery of the heat available to the steam cycle. Utilizing this approach, along with a two-pressure level steam cycle, results in an increase in net plant efficiency of 0.8 percentage point over the baseline efficiency level.

Another approach to optimizing the intercooled recuperative cycle is to place a saturator between the compressor exit and the recuperator entrance, as illustrated in the combined cycle shown in Fig. 7. This saturator, also called an aftercooler, evaporates water into the compressor exit flow, resulting in a lower temperature, higher mass flow entering the recuperator. While this may be seen as a way to balance the heat capacities of the hot and cold streams better in the recuperator and thereby increase the amount of heat recuperated by the combustion turbine (in addition to the fact that the air flow is at lower temperature), it is important to realize that all of this additional recuperation is accomplished by the evaporation of water in the saturator. Since this water is never condensed by the cycle but instead is rejected through the stack as low-pressure steam, the additional amount of energy recuperated is not recovered anywhere in the cycle. Furthermore, the recuperator exit temperature is reduced even further than in the intercooled recuperative cycle, resulting in an even lower efficiency steam cycle. Finally, note that, since the heat capacity of the cold side recuperator flow now closely matches that of the hot side flow, parallel steam superheat cannot be utilized to increase the steam cycle efficiency. The application of this concept to the baseline cycle results in a decrease in thermal efficiency of 2 percentage points.

Reheat Combustion Turbine

Reheat combustion turbines utilize a sequential combustion process in which the air is compressed, combusted, expanded in a turbine to some pressure significantly greater than ambient, combusted again in a second combustor, and finally expanded by a second turbine to near ambient pressure. For a fixed turbine rotor inlet temperature limit, the simple cycle efficiency is increased for a reheat combustion turbine compared to a nonreheat cycle operating at a pressure ratio corresponding to the second combustor's operating pressure. This is because the reheat cycle performs some of its combustion and expansion at a higher pressure ratio, which increases simple cycle efficiency (see section on increased compressor pressure ratio). From a purely thermodynamic standpoint, the average temperature at which heat is added is raised, thus raising the Carnot efficiency of the cycle. For combined cycles the turbine exhaust temperature can be controlled by the selection of second turbine inlet temperature and expansion ratio. This in turn allows control over the efficiency of the steam bottoming cycle.

Another beneficial feature of reheat combustion turbine cycles is that they exhibit higher output for a fixed compressor flow rate and turbine inlet temperature than nonreheat cycles. This is due to the fact that they burn sequentially with an expansion between the combustors. This allows for the addition of more fuel (in the second combustor) without violation of the turbine rotor inlet temperature limit. Also, since this results in a higher fuel-to-air ratio than in nonreheat cycles, they burn closer to stoichiometry and exhaust lower concentrations of excess oxygen.

Applying combustion turbine reheat to the baseline cycle, with the second combustor operating at the exit pressure and temperature equal to those of the baseline cycle, results in nearly identical turbine exhaust temperatures, and therefore the steam cycle of the combustion turbine reheat case is not compromised and is identical to the steam cycle of the baseline cycle. However, the compressor pressure ratio has been increased to 36. This necessitates the addition of six compressor stages, and an additional combustor and turbine stage located upstream of the second combustor. The simple cycle efficiency is increased nearly 2 percentage points from the baseline simple cycle level. Since steam cycle efficiency remains at the level of that in the baseline cycle, the combined cycle efficiency is increased 1.3 percentage points.

An investigation was made into the application of intercooling and recuperation to reheat combustion turbine cycles. The results showed the same reduced efficiency as for nonreheat combined cycles.

Thermochemical Recuperation

In a thermochemical recuperative (TCR) power plant, a portion of the stack exhaust (flue) gas is removed from the stack,

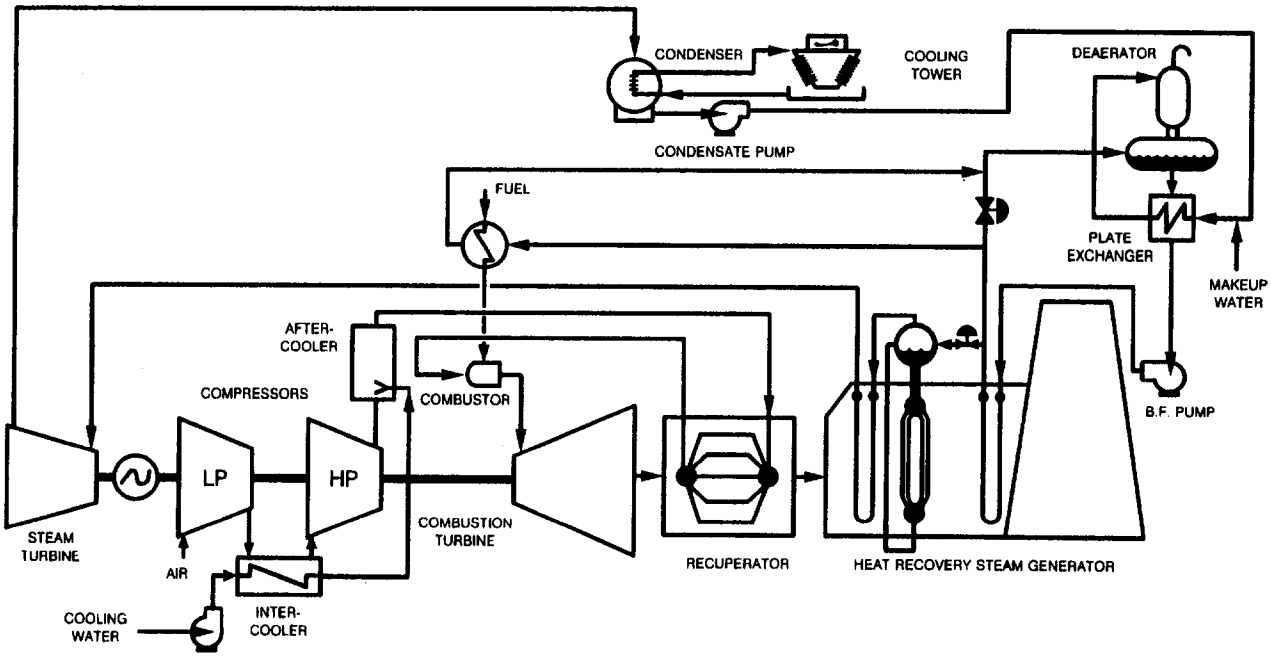

Fig. 7 Intercooled, aftercooled (evaporative), recuperative combined cycle

compressed, mixed with natural gas fuel, heated with exhaust heat from the combustion turbine, and mixed with the air compressor exhaust as it enters the combustor. As the mixture of natural gas and flue gas is heated by the combustion turbine exhaust, an endothermic reaction occurs between the methane and the carbon dioxide and water in the flue gas. This reaction occurs in the presence of a nickel-based catalyst, and results in the production of hydrogen and carbon monoxide. For complete conversion of the methane, the effective fuel heating value is increased approximately 30 percent. Therefore, the natural gas/flue gas mixture absorbs heat thermally (as it is heated) and chemically (via the endothermic reaction), resulting in a larger potential recuperation of exhaust energy than could be obtained by conventional recuperation, which recovers energy by heat alone. In fact, with full conversion of the natural gas fuel to hydrogen and carbon monoxide, up to twice the energy recuperated by the standard recuperative cycle may be recovered.

The endothermic reaction described above is accelerated for low excess oxygen in the reacting mixture, low pressures, and high mass ratios of recirculated flue gases to methane. Therefore, in order to take full advantage of this concept, the engine is controlled by running the combustor at near stoichiometric fuel-to-air ratios (10 percent excess air at the combustor exit) and using flue gas recirculation to quench the combustion products down to the desired turbine inlet temperature. This maximizes flue gas recirculation and minimizes excess oxygen in the flue gas. For typical cycles utilizing this control philosophy, the resulting recirculation rate of flue gas is over 50 percent of turbine flow. This means that both the air compressor flow rate and stack exhaust flow rate are less than half that of conventional cycles with the same turbine size.

Another advantage of the thermochemical recuperation/flue gas recirculation (TCR/FGR) concept is that, because the fuel has a low adiabatic flame temperature and operates with very low levels of excess oxygen in the exhaust, the resulting emissions of NO_x and CO are much lower than those for conventional design power plants.

When applied to the baseline configuration, thermochemical recuperation yields a combined cycle thermal efficiency over 2 percentage points greater than that of the baseline cycle for several different TCR/FGR configurations. Additionally, there are many possible cycle configurations, other than those described above, which can utilize thermochemical recuperation. For example, steam reforming may be used instead of flue gas reforming, as illustrated in Fig. 8.

Steam Injection

To apply steam injection to the baseline configuration, both the high-pressure and low-pressure steam systems are eliminated, leaving only the intermediate pressure steam system. The intermediate pressure superheated steam is then routed into the combustion turbine combustor inlet. Therefore, all steam turbines are eliminated, along with the condenser and the cooling tower. This results in a cycle that is significantly less expensive to build than the baseline cycle and it provides a means to reduce NO_x emissions via the large amount of steam injection. However, the cost associated with demineralization of the large cycle makeup flow must also be considered.

For a given turbine flow area, the compressor flow size must be reduced significantly, due to the addition of a large amount of steam, which now must pass through the turbine in addition to the compressor exit air flow. Since the steam is generated with exhaust heat, which is not used in a simple combustion turbine cycle, this concept provides a significant portion of the combustor inlet gas flow with very little work requirement (a small amount of energy is needed to run the feed water pumps that pump the water to the intermediate steam pressure). Therefore, from a simple cycle standpoint, the work of compression is much reduced due to the fact that some of the combustor inlet gas flow is compressed as a liquid. Also, the turbine output is increased significantly, since the average specific heat of the working fluid is increased considerably by the presence of the steam. The simple cycle efficiency and output are therefore increased by steam injection.

Compared to combined cycles, however, elimination of the high-pressure steam system results in generating more intermediate pressure steam, but this steam is at significantly lower availability due to its lower pressure. Also, since the low-pressure steam system has been eliminated as well, the exhaust stack gas temperature is much higher, as is the associated heat loss. Finally, since the steam injected into the gas turbine is effectively throttled to its partial pressure upon mixing with the compressor exit air without doing any work, and is only expanded to its partial pressure in the exhaust stack (which is significantly higher than typical low-pressure steam turbine exit pressure), the resulting steam expansion ratio is much smaller than that of the conventional steam turbine cycle. These losses result in a reduction in combined cycle efficiency in the range of 5 to 8 percentage points. Net plant output, while much higher than the baseline configuration simple cycle output, is less than the combined cycle output.

Conclusions

Through component improvements and cycle innovations, the goal of achieving a 60 percent efficiency natural gas-fired power plant for industrial application can be met within an 8-year time frame. The selected cycle and efficiency enhancements will be cost competitive, as a result of not only high thermal efficiency, but also low plant construction and maintenance costs and high plant power output. Additionally, the cycle

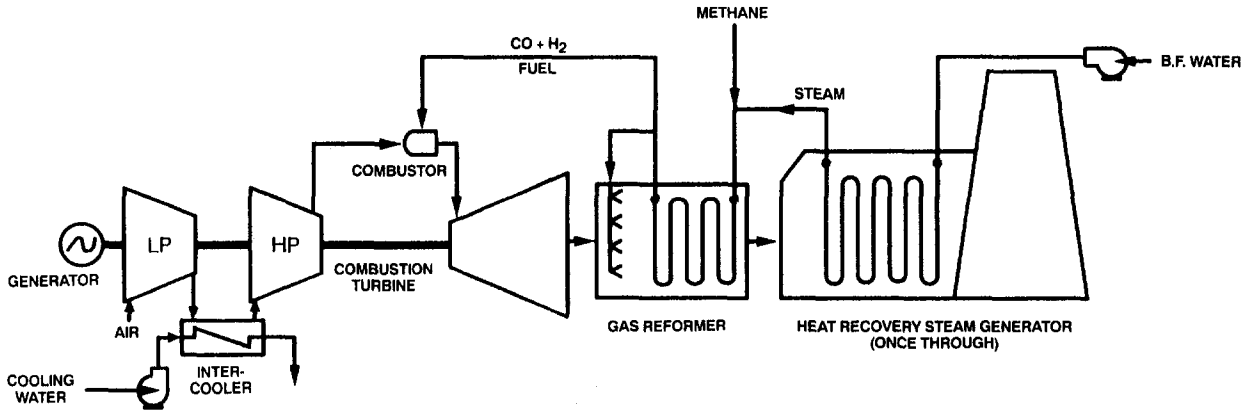

Fig. 8 Thermochemical recuperation cycle

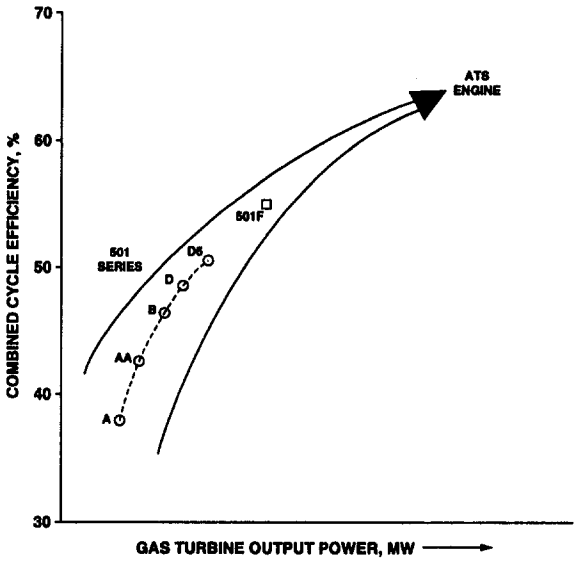

Fig. 9 Evolution of large Westinghouse gas turbines

will demonstrate reduced environmental impact through innovations to reduce emission levels.

This paper has outlined a number of technologies and cycle innovations, which will allow Westinghouse to design and build an ATS plant for power generation which meets or exceeds the goals of the DOE-sponsored program. This advanced power plant will demonstrate the continued evolution of Westinghouse large frame gas turbines as depicted in Fig. 9. Starting with the 501A engine through the ATS engine, gas turbine output versus combined cycle efficiency is plotted. The data shows the step change that will occur with the successful completion of the ATS program.

Acknowledgments

The innovative cycle and gas turbine component concepts applicable to raising the efficiency of natural gas-fired combined cycles to greater than 60 percent were studied under DOE Contract No. DE-AC21-93MC30247. The program is administered through the Morgantown Energy Technology Center under the guidance of METC's Program Manager, Mr. Donald W. Geiling.

The authors also acknowledge the technical assistance provided by the Institute of Gas Technology on the thermochemical recuperation/flue gas recirculation and steam reforming concepts evaluated in this study.

References

Baldwin, C. J., Boho, M. J., Beeley, E. W., and Stephens, J. O., 1965, "Future Role of Gas Turbines in Power Generation," *Proceedings American Power Conference,* Vol. 27, pp. 484–500.

Bannister, R. L., Cheruvu, N. S., Little, D. A., and McQuiggan, G., 1995, "Development Requirements for an Advanced Gas Turbine System," ASME JOURNAL OF ENGINEERING FOR GAS TURBINES AND POWER, Vol. 117, this issue, pp. 723–732.

Ernette, D. J., and Silvestri, G. J., 1990, "Optimized Steam Cycle Configurations for Subcritical Applications," ASME Paper No. 90-JPGC/Pwr-5.

Little, D. A., Bannister, R. L., and Wiant, B. C., 1993, "Development of Advanced Turbine Systems," *ASME Cogen Turbo Power '93 Proceedings,* IGTI-Vol. 8, pp. 271–280.

Scalzo, A. J., Bannister, R. L., DeCorso, M., and Howard, G. S., 1994, "Evolution of Heavy-Duty Power Generation and Industrial Combustion Turbines in the United States," ASME Paper 94-GT-488; ASME JOURNAL OF ENGINEERING FOR GAS TURBINES AND POWER, in press.

Silvestri, G. J., Bannister, R. L., Fujikawa, T., and Hizume, A., 1992, "Optimization of Advanced Steam Condition Power Plants," ASME JOURNAL OF ENGINEERING FOR GAS TURBINES AND POWER, Vol. 114, pp. 612–620.

Stephens, J. O., 1952, "Gas Turbine Power Plant Designs," *Proceedings American Power Conference,* Vol. 14, pp. 267–271.

A Theoretical and Experimental Investigation of a Gas-Operated Bearing Damper for Turbomachinery: Part I—Theoretical Model and Predictions

P. Sundararajan
Graduate Research Assistant.

J. M. Vance
Professor.

Department of Mechanical Engineering,
Texas A&M University,
College Station, TX 77843

This is the first (Part I) of two papers describing recent results of the research program directed at developing a vibration damper suitable for high-temperature turbomachinery applications. It is expected that such dampers will replace squeeze-film dampers, which use oil as the working fluid and have limitations at higher temperatures. A novel gas-operated bearing damper has been evaluated analytically and experimentally for its damping characteristics. A theory based on the isentropic assumptions predicts the damper performance characteristics reasonably well. A maximum damping level of 2311 N-m/s (13.2 lb-s/in.) at a frequency of 100 Hz was measured with a single actuator of the gas damper. Since many such actuators could be placed circumferentially around the squirrel cage, considerable damping levels can be realized. The study also shows that significantly higher damping levels can be achieved by modifying the current design. Part I describes the theoretical model that has been developed based on isentropic assumptions. This model is an improved version of the previous theory (Vance et al., 1991) and includes the supply groove effects, dynamic area changes of the inlet feeding holes, and the effects of flow choking on damper behavior. The governing equations are derived and theoretical predictions using these equations have been made for two hardware designs that were experimentally investigated (see Part II for experimental results).

Introduction

Future military engines and engines for civil aircraft designs such as the National Aerospace Plane are being designed to operate at higher efficiencies and Mach numbers. This requires lightweight rotor designs along with higher operating temperatures that will effectively eliminate oil from the engine. Squeeze-film dampers will therefore no longer be viable devices for controlling engine dynamic response.

In the non-oil, high-temperature environment of future military engines, a suitable replacement for the squeeze film damper must be found. These engines, with their light-weight design, will rely more heavily on vibration control devices rather than on structural mass and stiffness for safe operation under normal operating conditions.

To address this need, Vance et al. (1993) presented a new damper concept that works on a compressible fluid medium such as air. Since an air source (such as bleed-off air from the compressor) is generally available in aircraft, this damper concept is particularly attractive. Figures 1 and 2 show the two damper designs they examined. Both designs have a sliding head, which slides smoothly on a stationary piston and is preloaded against the bearing support by a spring. As the bearing support vibrates, the sliding head follows this motion and this results in the dynamic variation of the inlet or exit flow area of the pocket. The damper in Fig. 1 has the exit area to the pocket varying with the vibrational displacement of the sliding head, while the damper in Fig. 2 has the inlet area to the pocket varying with the displacement. As the flow areas vary, dynamic fluctuations in the gas mass flow rate through the damper cause corresponding dynamic pressures inside the pocket. The fluctuating pressure component produces dynamic forces that has stiffness and damping components. The objective of the damper design is to arrive at a configuration that produces the maximum damping component of this force. Vance et al. (1993) presented a theory for gas dampers based on isentropic flow assumptions. This theory identified the important parameters that affect damping levels and provided qualitative trends when such parameters were changed. However, accurate prediction of the damper performance was not possible since supply groove effects, dynamic variations of the inlet area to the groove, and the effect of choking on damper performance were not considered in their theory. The experimental results reported by Sundararajan (1992) showed that these effects are quite significant and cannot be neglected in many cases. The objective of the current work is to modify the gas damper theory to include these effects and arrive at better theoretical predictions.

A theory is presented, based on isentropic flow assumptions, that agrees surprisingly well with the experimental results (see Part 2 of this paper). Theoretical predictions are given for each of the two different hardwares that were experimentally tested.

Dynamic Analysis of Gas Damper

A dynamic analysis is performed for small-amplitude harmonic motion of the sliding head about an equilibrium position and the linearized governing differential equations are derived.

Contributed by the International Gas Turbine Institute for publication in the JOURNAL OF ENGINEERING FOR GAS TURBINES AND POWER. Manuscript received by the International Gas Turbine Institute July 15, 1994. Associate Technical Editor: R. E. Kielb.

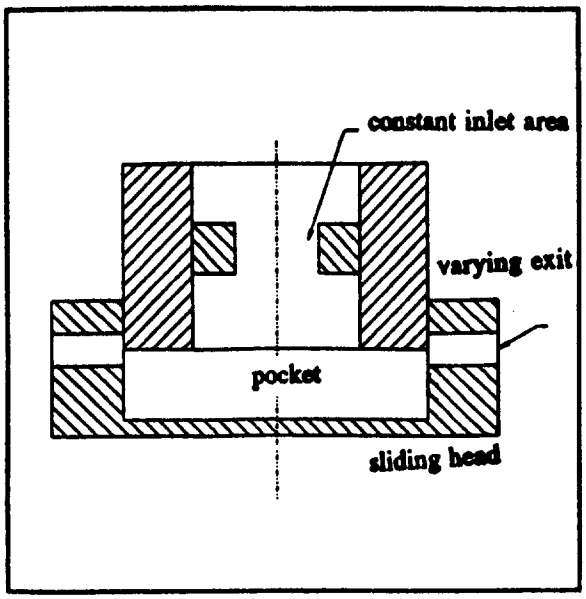

Fig. 1 Exit: varying design of pocket gas dampers

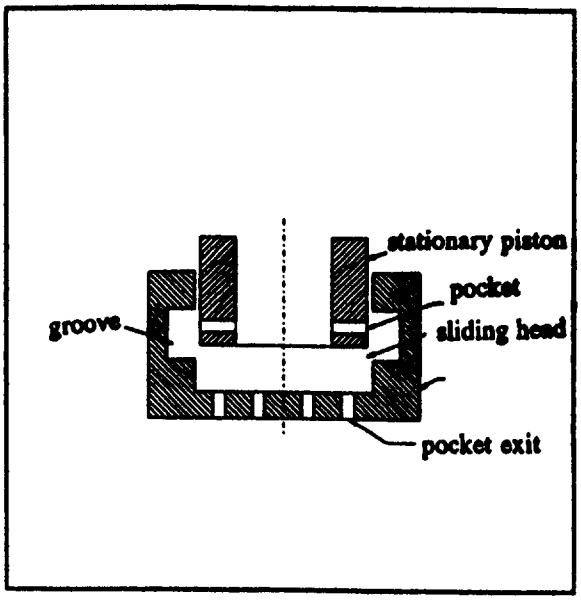

Fig. 2 Inlet: varying design of pocket gas dampers

For harmonic response these equations can be transformed to a set of linear algebraic equations, which can be solved for the dynamic pressures in the groove and pocket. The coefficients of the differential equations depend on the gas damper geometry and mass flow relations. The isentropic mass flow rate relations used in the present work are depicted in Figs. 3 and 4. The isentropic mass flow equation is used for pressure ratios above the critical ratio for flow choking and Fleigner's formula (Shapiro, 1953) is used for cases involving choking.

Referring to the location numbers on Fig. 5, consider the flow of a perfect gas from a supply source at P_s, T_s across restriction A_{sg} to a groove volume at conditions P_g, T_g and then across another restriction A_{gp} to a pocket volume at conditions P_p, T_p before finally exiting through restriction A_{pe} to the exit conditions P_e, T_e. On static equilibrium, the mass flow rate across each of the restrictions is equal and is given by

$$\dot{m} = \dot{m}_{sg} = \dot{m}_{gp} = \dot{m}_{pe} \tag{1}$$

where

$$\dot{m}_{sg} = \frac{P_s A_{sg} \Psi(z_{sg})}{\sqrt{\gamma RT}} \quad \text{where}$$

$$\Psi(z_{sg}) = \sqrt{2 \frac{\gamma^2}{\gamma - 1} [z_{sg}^{2/\gamma} - z_{sg}^{(\gamma+1)/\gamma}]} \tag{2}$$

$$\dot{m}_{gp} = \frac{P_g A_{gp} \Psi(z_{gp})}{\sqrt{\gamma RT}} \quad \text{where}$$

$$\Psi(z_{gp}) = \sqrt{2 \frac{\gamma^2}{\gamma - 1} [z_{gp}^{2/\gamma} - z_{gp}^{(\gamma+1)/\gamma}]} \tag{3}$$

$$\dot{m}_{pe} = \frac{P_p A_{pe} \Psi(z_{pe})}{\sqrt{\gamma RT}} \quad \text{where}$$

$$\Psi(z_{pe}) = \sqrt{2 \frac{\gamma^2}{\gamma - 1} [z_{pe}^{2/\gamma} - z_{pe}^{(\gamma+1)/\gamma}]} \tag{4}$$

and $z_{ij} = P_j/P_i$ is the ratio of the downstream pressure to the upstream pressure.

Let us consider the case in which the inlet areas A_{sg}, A_{gp} and/or the exit area A_{pe} change with time; i.e., $A_{sg} = A_{sg}(t)$, $A_{gp} = A_{gp}(t)$, $A_{pe} = A_{pe}(t)$. Then the conservation of mass states that

$$\dot{m}_{sg}(t) = \dot{m}_{gp}(t) + \frac{\partial}{\partial t}(\rho_g V_g)$$

$$\dot{m}_{gp}(t) = \dot{m}_{pe}(t) + \frac{\partial}{\partial t}(\rho_p V_p) \tag{5}$$

Nomenclature

A, A_{sg}, A_{gp}, A_{pe} = area of pocket chamber, area of inlet to the groove, area of groove to the pocket, area of pocket to the exit, m^2

A_i, A_e = same as A_{gp}, A_{pe}, m^2

c = nominal equilibrium opening to the pocket, in.

K, C = stiffness and damping coefficients, N/m, N-s/m

$\dot{m}$ = mass flow rate, kg/s

P_s, P_g, P_p = absolute pressure at supply, groove, and pocket, N/m^2

$\bar{p}_g(t)$, $\bar{p}_p(t)$ = dynamic groove and pocket pressures, N/m^2

T = absolute temperature, K

V_g, V_p = volume of the groove, m^3

$V_p = A(1 + \delta(t))$ = volume of pocket chamber, m^3

X = amplitude of dynamic displacement, m; $x = X \sin(\omega t)$, $\dot{x} = X\omega \cos(\omega t)$

z_{sg}, z_{gp}, z_{pe} = pressure ratios = P_g/P_s, P_p/P_g, P_e/P_p

ω = frequency of motion, rad/s

$\delta(t) = c + X \sin(\omega t)$, m

$\bar{\delta}(t) = X \sin(\omega t)$ = dynamic displacement, m

Subscripts

g = groove

gp = groove to pocket

p = pocket

pe = pocket to exit

s = supply conditions

sg = supply to groove

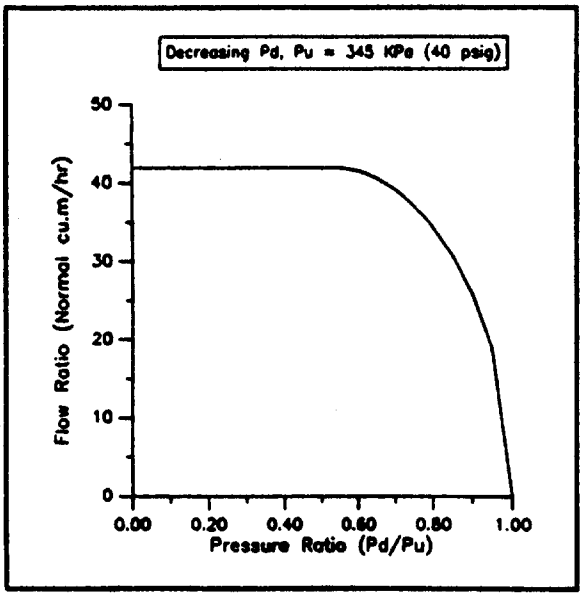

Fig. 3 Flow rate versus pressure ratio: decreasing downstream pressure (isentropic)

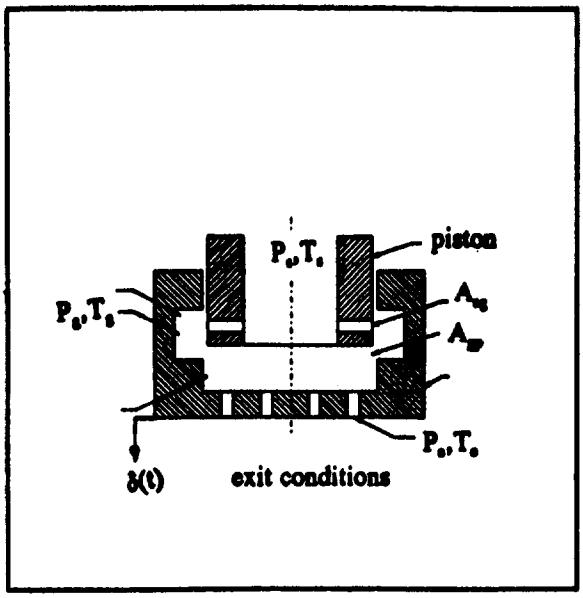

Fig. 5 A model gas damper for isentropic analysis

Using the known relation,

$$\frac{\partial}{\partial t}(\rho V) = \rho \frac{\partial V}{\partial t} + V \frac{\partial \rho}{\partial t}$$

$$= \frac{P}{RT} \frac{\partial V}{\partial t} + \frac{V}{\gamma RT} \frac{\partial P}{\partial t} \tag{6}$$

and for a constant groove volume, we may rewrite the mass conservation equations as,

$$\dot{m}_{sg} - \dot{m}_{gp} - \frac{V_g}{\gamma RT_g} \frac{\partial P_g}{\partial t} = 0$$

$$\dot{m}_{gp} - \dot{m}_{pe} - \frac{P_p}{RT_p} \frac{\partial V_p}{\partial t} + \frac{V_p}{\gamma RT_p} \frac{\partial P_p}{\partial t} = 0 \tag{7}$$

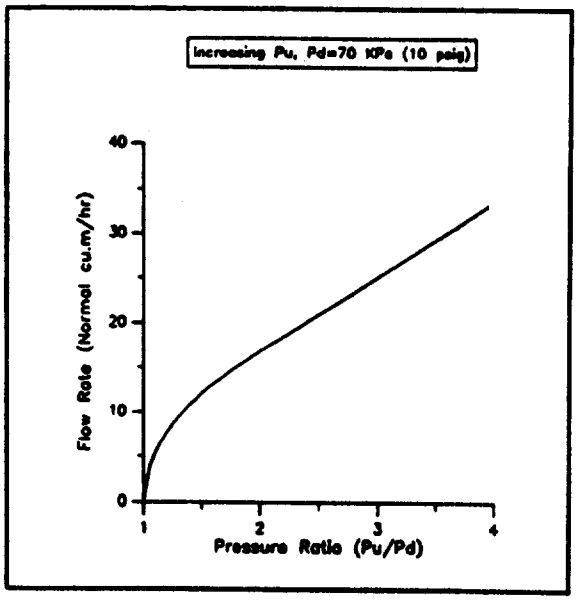

Fig. 4 Flow rate versus pressure ratio: increasing upstream pressure (isentropic)

We assume that the inlet and exit areas, A_{sg}, A_{gp} and A_{pe}, as well as the groove and pocket volumes, V_g and V_p, are all general functions of the dynamic displacement $\delta(t)$,

$$\delta(t) = c + X \sin(\omega t)$$

where c is the equilibrium clearance at the inlet to the pocket. Thus,

$$\dot{m}_{sg}(t) = \dot{m}_{sg}(P_g(t), \delta(t))$$

$$\dot{m}_{gp}(t) = \dot{m}_{gp}(P_g(t), P_p(t), \delta(t))$$

$$\dot{m}_{pe}(t) = \dot{m}_{pe}(P_p(t), \delta(t)) \tag{8}$$

Considering small-amplitude harmonic motion about the equilibrium position, i.e., for $X \ll c$, enables us to assume that the dynamic pressures in the groove and the pocket are given by:

$$P_g(t) = P_g + \overline{p_g}(t)$$

$$P_p(t) = P_p + \overline{p_p}(t)$$

$$\dot{m}_{sg} = \dot{m} + \left.\frac{\partial \dot{m}_{sg}}{\partial p_g}\right|_{p_g} \overline{p_g}(t) + \left.\frac{\partial \dot{m}_{sg}}{\partial \delta}\right|_{c} \overline{\delta}(t)$$

$$\dot{m}_{gp} = \dot{m} + \left.\frac{\partial \dot{m}_{gp}}{\partial p_g}\right|_{p_g} \overline{p_g}(t) + \left.\frac{\partial \dot{m}_{gp}}{\partial p_p}\right|_{p_p} \overline{p_p}(t) + \left.\frac{\partial \dot{m}_{gp}}{\partial \delta}\right|_{c} \overline{\delta}(t)$$

$$\dot{m}_{pe} = \dot{m} + \left.\frac{\partial \dot{m}_{pe}}{\partial p_p}\right|_{p_p} \overline{p_p}(t) + \left.\frac{\partial \dot{m}_{pe}}{\partial \delta}\right|_{c} \overline{\delta}(t) \tag{9}$$

where $\dot{m}$ is the equilibrium mass flow rate.

Substitution of Eq. (9) into Eq. (7) gives:

$$a_1 \frac{\partial \overline{p_g}}{\partial t} + b_1 \overline{p_g}(t) + c_1 \overline{p_p}(t) + d_1 \overline{\delta}(t) = 0$$

$$a_2 \frac{\partial \overline{p_p}}{\partial t} - b_2 \overline{p_g}(t) + c_2 \overline{p_p}(t) + d_2 \overline{\delta}(t) + e_2 \frac{\partial \overline{\delta}}{\partial t} = 0 \tag{10}$$

where

$$a_1 = \frac{V_g}{\gamma R T_g}; \quad a_2 = \frac{V_p}{\gamma R T_p}$$

$$b_1 = \left[\frac{\partial m_{gp}}{\partial p_g} - \frac{\partial m_{sg}}{\partial p_g}\right]; \quad b_2 = \frac{\partial m_{gp}}{\partial p_g}$$

$$c_1 = \frac{\partial m_{gp}}{\partial p_p}; \quad c_2 = \left[\frac{\partial m_{pe}}{\partial p_p} - \frac{\partial m_{gp}}{\partial p_p}\right]$$

$$d_1 = \left[\frac{\partial m_{gp}}{\partial \delta} - \frac{\partial m_{sg}}{\partial \delta}\right]; \quad d_2 = \left[\frac{\partial m_{pe}}{\partial \delta} - \frac{\partial m_{gp}}{\partial \delta}\right]$$

$$e_2 = \frac{p_p A}{R T_p} \tag{11}$$

Since the particular solution for the linearized Eq. (10) will be harmonic for a harmonic input $\bar{\delta}(t) = X \sin(\omega t)$, we can write the solutions as

$$\overline{p_g}(t) = p_{gc} \cos \omega t + p_{gs} \sin \omega t$$
$$\overline{p_p}(t) = p_{pc} \cos \omega t + p_{pg} \sin \omega t \tag{12}$$

Substituting these assumed solutions into Eqs. (10) we get the following four algebraic equations in the four unknowns p_{gc}, p_{gs}, p_{pc}, and p_{ps}:

$$-a_1 p_{gc}\omega + b_1 p_{gs} + c_1 p_{ps} + d_1 X = 0$$
$$a_1 p_{gs}\omega + b_1 p_{gc} + c_1 p_{pc} = 0$$
$$-a_2 p_{pc}\omega - b_2 p_{gs} + c_2 p_{pc} + d_2 X = 0$$
$$a_2 p_{ps}\omega - b_2 p_{gc} + c_2 p_{pc} + e_2 X \omega = 0 \tag{13}$$

In matrix form these equations can be represented as,

$$\begin{bmatrix} -a_1\omega & b_1 & 0 & c_1 \\ b_1 & a_1\omega & c_1 & 0 \\ 0 & -b_2 & -a_2\omega & c_2 \\ -b_2 & 0 & c_2 & a_2\omega \end{bmatrix} \begin{Bmatrix} p_{gc} \\ p_{gs} \\ p_{pc} \\ p_{ps} \end{Bmatrix} = \begin{Bmatrix} -d_1 X \\ 0 \\ -d_2 X \\ -e_2 X \omega \end{Bmatrix} \tag{14}$$

Now using Cramer's rule, the solutions for p_{pc} and p_{ps} can be written as

$$p_{pc} = \frac{X\omega C_p}{\Delta};$$

$$p_{ps} = \frac{X S_p}{\Delta};$$

$$C_p = (a_1^2\omega^2 + b_1^2)(a_2 d_2 - c_2 e_2) + a_2 b_1 b_2 d_1 + a_1 b_2 c_2 d_1 - b_1 b_2 c_1 e_2 - a_1 b_2 c_1 d_2$$

$$S_p = -(a_1^2\omega^2 + b_1^2)(a_2 e_2 \omega^2 + c_2 d_2) + a_1 b_2 c_1 e_2 \omega^2 + b_1 b_2(-c_1 d_2 + c_2 d_1) - a_1 a_2 b_2 d_1 \omega^2 + b_2^2 c_1 d_1$$

$$\Delta = (a_1^2\omega^2 + b_1^2)(a_2^2\omega^2 + c_2^2) - 2a_1 a_2 b_2 c_1 \omega^2 + 2b_1 b_2 c_1 c_2 + c_1^2 b_2^2 \tag{15}$$

The local force exerted by the uniform dynamic pressure $\overline{p_p}(t)$ on the journal surface is equal to:

$$f_x(t) = \overline{p_p}(t) A = Kx(t) + C\dot{x}(t)$$

where K and C are the stiffness and damping coefficients resulting from the action of the gas damper. These coefficients are given by,

$$K = -\frac{S_p A}{\Delta}$$

$$C = -\frac{C_p A}{\Delta} \tag{16}$$

The Isentropic Model

The coefficients a_i, b_i, c_i, d_i, and e_i of the two linearized differential Eq. (10) depend on the gas damper geometry and the flow resistances (i.e., rate of change of mass flow rate across a constriction with up/downstream pressures) across different restrictions. For our isentropic model, Eqs. (2), (3), and (4) were used for deriving the coefficients for unchoked flow conditions. In this case, the partial derivatives (flow resistances) appearing in the coefficients are given by

$$\left[\frac{\partial \dot{m}_{sg}}{\partial p_g}\right] = \frac{\dot{m}}{P_s} Z_{sgg}(z_{sg});$$

$$Z_{sgg}(z_{sg}) = \frac{1}{2\gamma} \frac{[2z_{sg}^{(2-\gamma)/\gamma} - (\gamma+1)_{sg}^{1/\gamma}]}{[z_{sg}^{2/\gamma} - z_{sg}^{(\gamma+1)/\gamma}]}$$

$$\left[\frac{\partial \dot{m}_{gp}}{\partial p_g}\right] = \frac{\dot{m}}{P_s} Z_{gpg}(z_{gp});$$

$$z_{gpg}(z_{gp}) = \frac{1}{z_{sp}} \frac{1}{2\gamma} \frac{[2(\gamma-1)z_{gp}^{(2-\gamma)/\gamma} + (1-\gamma)z_{gp}^{1/\gamma}]}{[z_{gp}^{(2-2\gamma)/\gamma} - z_{gp}^{(1-\gamma)/\gamma}]}$$

$$\left[\frac{\partial \dot{m}_{gp}}{\partial p_p}\right] = \frac{\dot{m}}{P_s} Z_{gpp}(z_{gp});$$

$$Z_{gp}(z_{gp}) = \frac{1}{z_{gp}} \frac{1}{2\gamma} \frac{[2z_{gp}^{(2-\gamma)/\gamma} - (\gamma+1)z_{gp}^{1/\gamma}]}{[z_{gp}^{2/\gamma} - z_{gp}^{(\gamma+1)/\gamma}]}$$

$$\left[\frac{\partial \dot{m}_{pe}}{\partial p_p}\right] = \frac{\dot{m}}{P_s} Z_{pep}(z_{pe}); \tag{17}$$

$$Z_{pep}(z_{pe}) = \frac{1}{z_{sp}} \frac{1}{2\gamma} \frac{[2(\gamma-1)z_{pe}^{(2-\gamma)/\gamma} + (1-\gamma)z_{pe}^{1/\gamma}]}{[z_{pe}^{(2-2\gamma)/\gamma} - z_{pe}^{(1-\gamma)/\gamma}]}$$

These partial derivatives can be calculated from the slopes of the curves shown in Figs. 3 and 4. The isentropic mass flow Eqs. (2), (3), and (4) cannot be directly used for cases involving choking, i.e., for pressure ratios below 0.528 (the critical pressure ratio for choking). In such cases, the flow resistances are calculated using Fleigner's formula (Shapiro, 1953):

$$\frac{\dot{m}}{A} \frac{\sqrt{T_0}}{P_0} = 0.532 \tag{18}$$

where T_0, P_0, A, $\dot{m}$ are the upstream temperature (in Rankine), upstream pressure (in psi), the throat area (where choking occurs, in square inch), and the mass flow rate (lb/s), respectively.

It can be seen from Fig. 3 that, for choked flow conditions, the rate of change of mass flow rate with downstream pressure (flow resistance) is zero for a given upstream pressure. The rate of change of mass flow rate with upstream pressure, under choked flow conditions, is linear as in Fig. 4. The flow resistance calculated using Fleigner's formula depends only on the upstream stagnation temperature and the area of choked throat.

In order to calculate the damping and stiffness coefficients of the gas damper, first the equilibrium mass flow rate is determined. Since the upstream (supply) and the downstream (ambient/atmospheric) pressures are known, the intermediate pressures in the groove and the pocket can be calculated by applying conservation of mass principle and from this the equilibrium mass flow rate can be calculated. Now, the partial derivatives

Table 1 Groove and pocket dimensions for the experimental hardware

	GDIV #0	GDIV #1	GDIV #2
Pocket Diameter	4.57 cm (1.8")	4.57 cm (1.8")	4.57 cm (1.8")
Groove Diameter	5.60 cm (2.2")	5.60 cm (2.2")	5.60 cm (2.2")
Pocket Length	0.5 cm (0.2")	1.14 cm (0.45")	1.14 cm (0.45")
Groove Length	0.5 cm (0.2")	1.0 cm (0.4")	1.0 cm (0.4")
No.inlet hole	4 of 0.25cm (0.1")	4 of 0.25 cm (0.1")	8 of 0.25 cm (0.1")

in Eq. (11) can be evaluated using the relations (17) or (18) depending on whether the flow is unchoked or choked, respectively. For a given damper geometry, and using the calculated partial derivatives, all the coefficients in Eq. (11) can be determined. Equation (12) can now be solved for the dynamic pressures in the groove and the pocket and from this the damping and stiffness coefficients can be calculated from relations (15) and (16).

These equations were computer coded and in what follows, the computer simulations of the damper characteristics for two of the three sets of hardware that were evaluated experimentally are presented. These hardwares have been named GDIV #0, GDIV #1, and GDIV #2. The salient pocket and groove geometry dimensions of these three hardwares are given in Table 1.

Theoretical Predictions—GDIV #0

As can be read from Table 1, this hardware has four inlet feeding holes and eight exit holes each 0.1 in. diameter. The groove and pocket are each of length 0.2 in. This hardware has dynamic variations of the inlet area to the groove in addition to the dynamic variations of the inlet area to the pocket.

Figure 6 shows the predicted variation of the exit pressure ratio (P_e/P_p) with the supply pressure for the two equilibrium pocket inlet openings of 127 and 178 μm (5 and 7 mils). The supply pressures for which the flow chokes at exit can be read from this figure as 517 kPa (75 psig) and 3.79 kPa (55 psig), respectively (the pressures corresponding to $P_e/P_p = 0.528$),

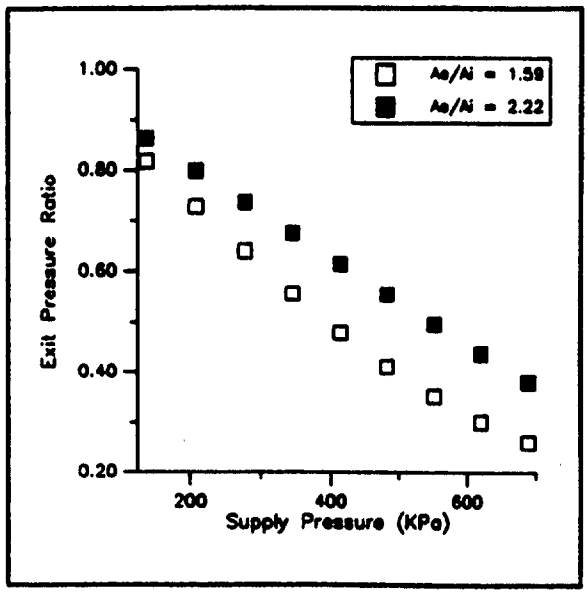

Fig. 6 Exit pressure ratio versus supply pressure: GDIV #0

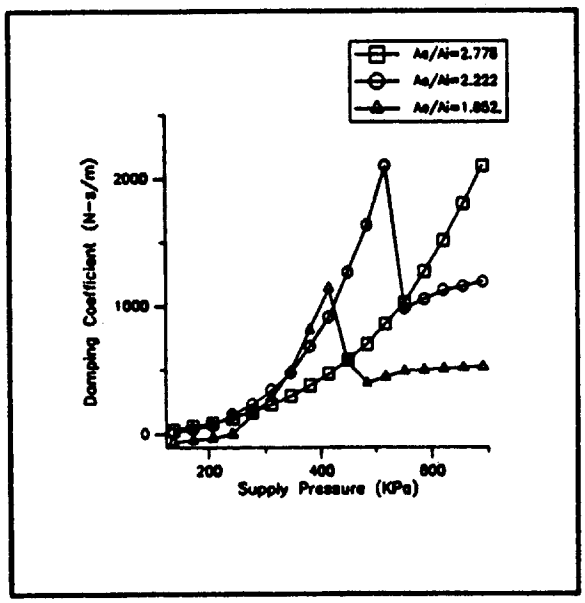

Fig. 7 Damping versus supply pressure: GDIV #0 (theoretical)

for the two positions. Figure 7 shows the predicted variation of damping with the supply pressure for three different equilibrium positions. It is seen that for inlet openings to pocket of 127 and 152 μm (5 and 6 mils), the damping drops when the supply pressure exceeds the value (517 kPa for 127 μm opening and 420 kPa for 152 μm opening) required to choke the flow at exit area. For inlet openings less than 127 μm (5 mils), the flow does not choke at the exit for the supply pressures in the range of 0 to 690 kPa (0 to 100 psig) and hence a drop in the damping levels is not observed. For both the 127 and 152 μm (5 mil and 6 mil) open positions, the inlet area to the pocket is choked for the plotted pressure range. Thus, it is seen that when the flow is choked at the inlet area (to pocket), the damping increases with the supply pressure until the flow is choked at the exit area. When the flow starts to choke, there is a sharp drop in damping, and further increase in the pressure does increase the damping but with a reduced rate. It is also observed that the rate of increase in damping with the supply pressure is higher as we approach the value of supply pressure at which the flow chokes at exit. For a supply pressure of 60 psig, a maximum damping of 1156 N-s/m (6.6 lb-s/in.) is predicted.

Figure 8 shows the predicted variation of damping with the amount of inlet opening to the pocket (for a given inlet area to groove and exit area) for three different supply pressures. It is interesting to see that the damping increases with the inlet opening initially, then decreases with further increase in the inlet opening and then again starts to rise as the opening is further increased in the plotted range of 0 to 254 μm (0 to 10 mils). For a supply pressure of 414 kPa (60 psig), the flow is choked only at the inlet for inlet openings up to 152 μm (6 mils) and the flow is choked at exit also for positions between 152 and 178 μm (6 and 7 mils) and choked only at exit for positions beyond 178 μm (7 mils). Thus, the damping increases with the inlet opening for positions up to 152 μm (at which the exit also starts getting choked) and then decreases with further inlet opening until 178 μm opening is reached and then increases as the inlet area starts getting unchoked for inlet openings beyond 178 μm. However, the increasing trend does not continue much beyond 254 μm (10 mils) and in fact drops steadily after 355 μm (14 mils). Figure 9 shows the variation of damping with frequency for three different supply pressures at a 5 mil open position of the damper. It can be noted that the damping increases with frequency initially and then starts falling steadily with increase in frequency. The shift of the peak from 0 Hz is

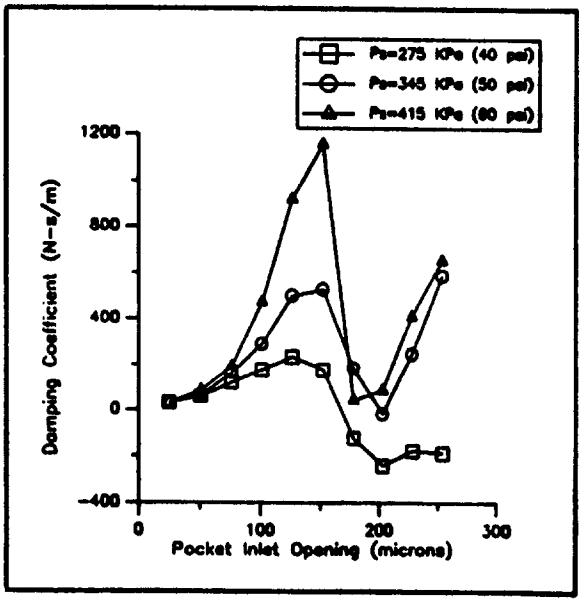

Fig. 8 Damping versus pocket inlet opening: GDIV #0 (theoretical)

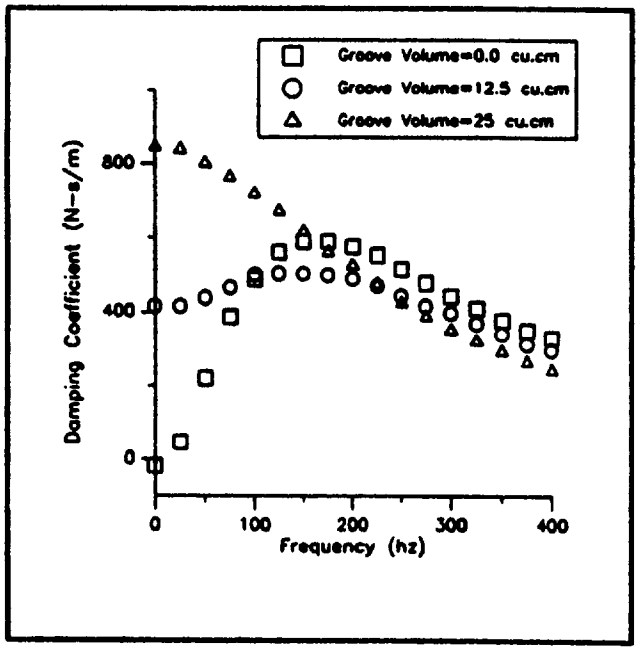

Fig. 10 Damping versus frequency for different groove volumes: GDIV #0 (theoretical)

due to the influence of the groove. It can also be noted that the damping levels are higher for higher supply pressures owing to the fact that these pressures are less than 517 kPa (75 psig), which is required to choke the flow at exit. Theory predicts that the damping is linearly proportional to the pressure action area (higher area means higher damping). The effect of groove volume on damping is illustrated by Fig. 10. It is seen that the effect of the groove is to shift the frequency of maximum damping. At frequencies below 100 Hz, increase in groove volume tends to decrease the damping levels and at higher frequencies an opposite effect is seen. As expected, in the absence of a groove (0 groove volume) the maximum damping occurs at 0 Hz. The effect of pocket volume on damping is shown in Fig. 11 and its effect is opposite to that of the groove volume. For frequencies below 200 Hz, higher pocket volume means higher damping and for frequencies higher than 200 Hz, the pocket volume has less significant effect on the damping.

Theoretical Predictions—GDIV #2

The GDIV #2 hardware is similar to the GDIV #0 hardware discussed in the previous section except that it has twice the number of inlet holes (8 compared to the 4 in GDIV #0) and twice the groove and pocket lengths (see Table 1). Figure 12 shows the predicted variation of the exit pressure ratio with the supply pressure for the two inlet pocket openings of 127 and 178 μm (5 mils and 7 mils). The supply pressures for which the exit pressure ratio is 0.528 (pressure ratio at which choking begins), as seen from this figure, are 310 kPa and 241 kPa (45 psig and 35 psig), respectively. Figure 13 shows the variation of damping with supply pressure for the three equilibrium positions 100, 128, and 152 μm (4, 5, and 6 mils). It is seen from this figure that the damping increases smoothly with increase

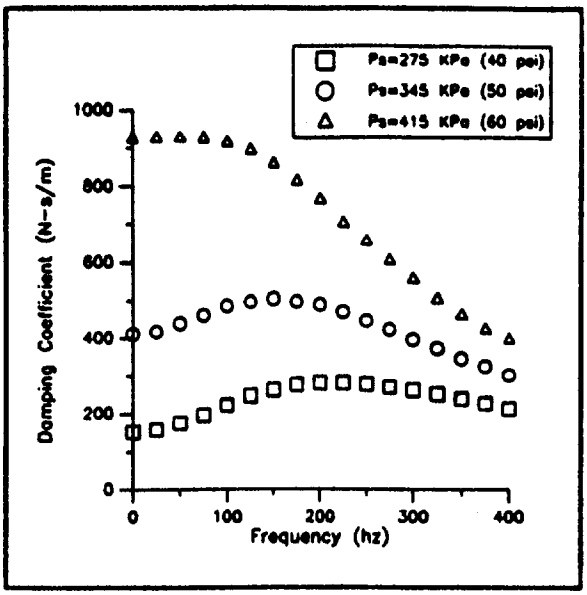

Fig. 9 Damping versus frequency for different supply pressures: GDIV #0 (theoretical)

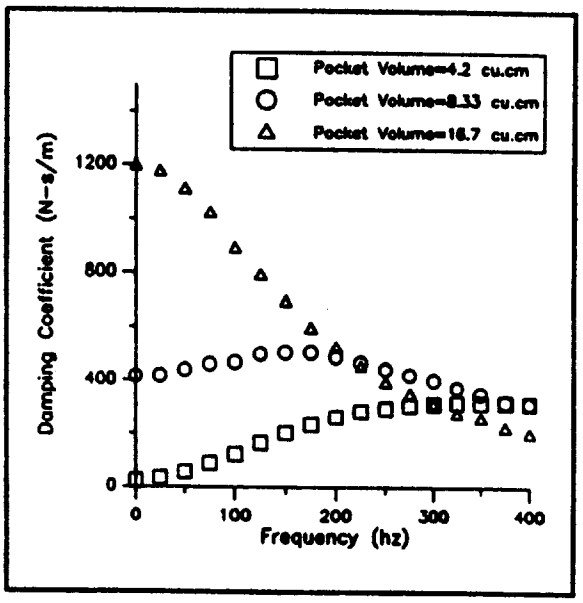

Fig. 11 Damping versus frequency for different pocket volumes: GDIV #0 (theoretical)

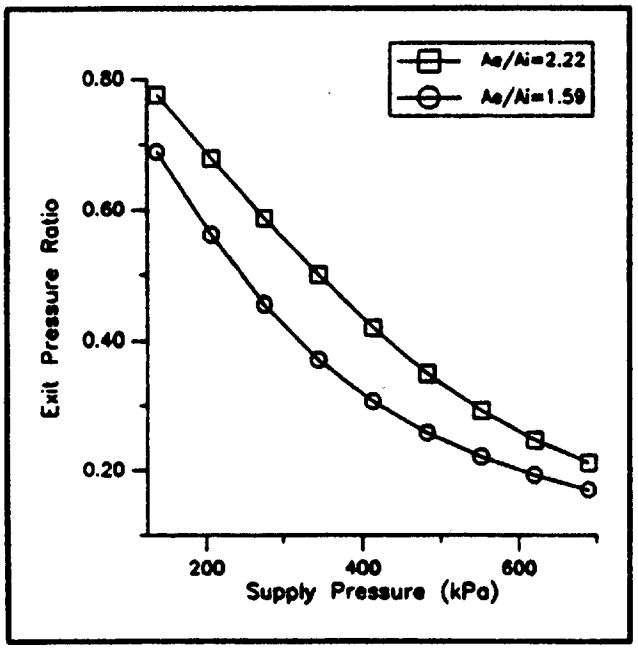

Fig. 12 Exit pressure ratio versus supply pressure: GDIV #2 (theoretical)

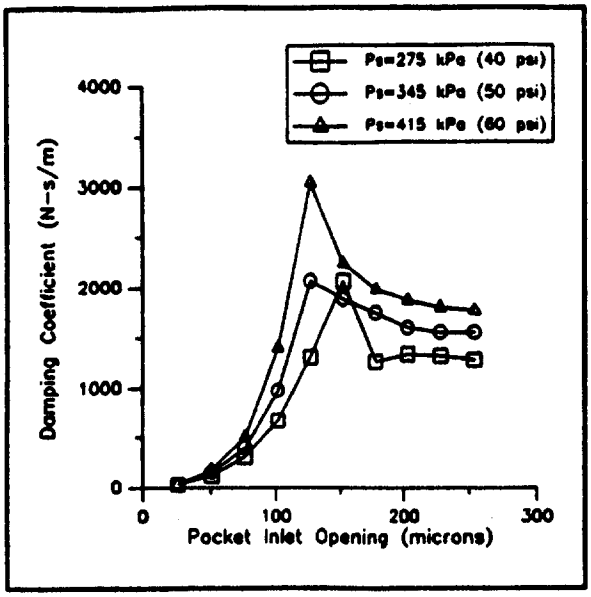

Fig. 14 Damping versus pocket inlet opening: GDIV #2 (theoretical)

in pressure for the 100 μm open position in the plotted supply pressure range 138 to 690 kPa (20 to 100 psig). However, for the 152 and 178 μm (5 mils and 6 mils) positions, the damping increases with supply pressure until the exit area is choked. There is a drop in the damping level when the flow starts getting choked at the exit. Further increase in the supply pressure increases the damping, but the rate of increase of damping with pressure is less compared to the prechoking levels. For the 128 and 152 μm (5 and 6 mils) open position, the supply pressures required to choke the flow at exit are 448 kPa and 310 kPa (65 and 45 psig), respectively. For a supply pressure of 414 kPa (60 psig), the theory predicts a maximum damping of 3065 N-s/m (17.5 lb-s/in.). Figure 14 shows the variation of damping with the inlet opening to the pocket. It is seen that the damping increases with the inlet opening until there is a change in the condition of choking at the inlet area/exit area. There is a drop in the damping level when this condition is reached and the damping remains relatively insensitive to any increase in inlet opening up to 300 μm (12 mils). For inlet openings above 300 μm, the damping sharply falls with increase in the inlet opening. The relative insensitiveness of damping to the inlet opening to the pocket over a wide range of openings is a noticeable prediction in this design. Theory also predicts that the groove volume has insignificant effect on the damping. The influence of the pocket volume on the damping is depicted in Fig. 15. It is seen that for frequencies below 100 Hz, higher pocket volume results in higher damping and for frequencies above 100 Hz, the pocket volume has no significant effect on the damping.

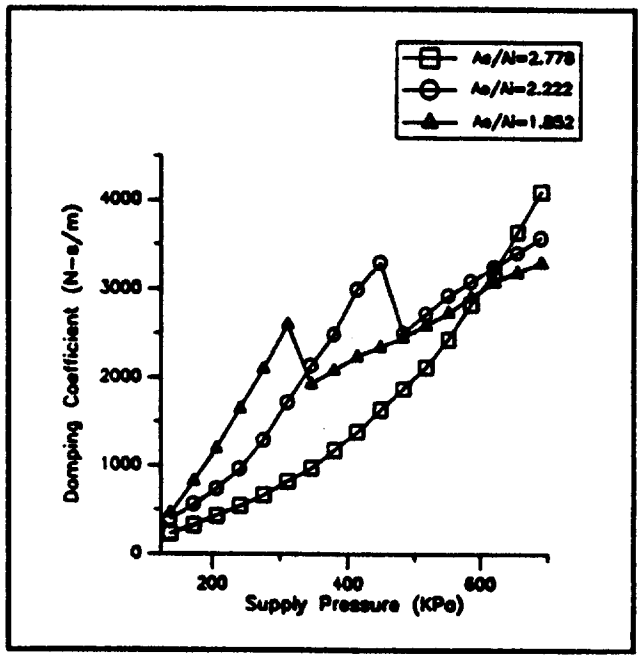

Fig. 13 Damping versus supply pressure: GDIV #2 (theoretical)

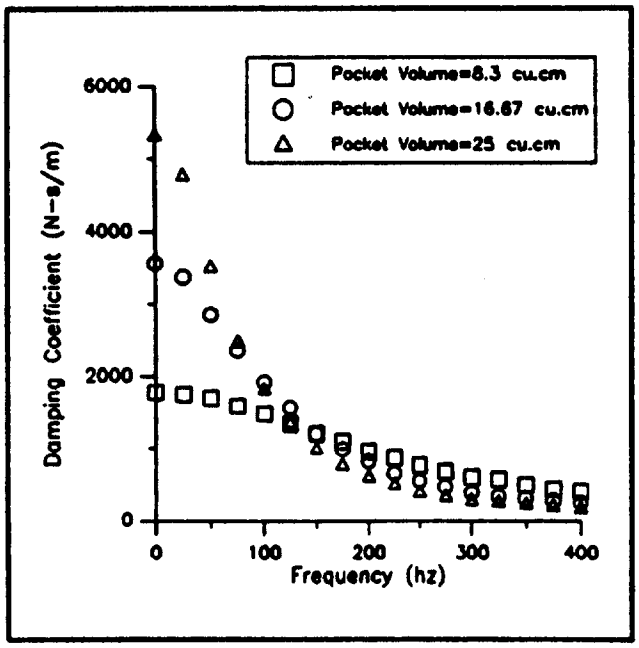

Fig. 15 Damping versus frequency for different pocket volumes: GDIV #2 (theoretical)

Conclusions

From these isentropic theoretical predictions for the three sets of hardware GDIV #0, 1, and 2, certain general conclusions can be drawn. When the inlet area to the pocket is choked, damping increases with the supply pressure until the exit area also begins to choke. When the exit area starts to choke, there is a fall in the damping level and further increase of supply pressure does increase the damping but at a slower rate. The increase or decrease of damping with the inlet opening to pocket occurs whenever there is a change in the condition of choking at the inlet or exit area. The effect of the groove volume is to shift the frequency at which the maximum damping occurs and is insignificant for higher supply pressures and flow rates. The effect of the pocket volume is to increase the damping levels at lower frequencies and has no significant effect at higher frequencies. The damping is linearly proportional to the pressure action area of the pocket. The theory predicts that the GDIV #2 hardware would produce more damping than those produced by the other two hardware. A maximum damping value of 3065 N-s/m (17.5 lb-s/in.) is predicted for this hardware at an excitation frequency of 100 Hz. The theory also predicts that the damping is relatively insensitive to inlet opening of the pocket for a range of inlet openings. The effect of the groove is more prevalent in the first two hardwares GDIV #0 and GDIV #1.

To verify these theoretical predictions, experiments were done to determine the damping characteristics for each of the three hardwares. Part II of this paper describes the experimental results and makes a comparison between the theory and the experiment.

References

Shapiro, A. H., 1953, *The Dynamics and Thermodynamics of Compressible Fluid Flow,* The Ronald Press Company, New York, Vol. 1, pp. 85.

Sundararajan, P., 1992, "A Theoretical and Experimental Investigation of a Gas Operated Bearing Damper for Turbomachinery," Master's Thesis, Texas A&M University, College Station, TX.

Vance, J. M., Cardon, B. P., San Andres, L. A., and Storace, A. F., 1993, "A Gas-Operated Bearing Damper for Turbomachinery," ASME JOURNAL OF ENGINEERING FOR GAS TURBINES AND POWER, Vol. 115, pp. 383–389.

A Gas-Operated Bearing Damper for Turbomachinery—Theoretical Predictions Versus Experimental Measurements: Part II—Experimental Results and Comparison With Theory

P. Sundararajan
Graduate Research Assistant.

J. M. Vance
Professor.

Department of Mechanical Engineering,
Texas A&M University,
College Station, TX 77840

This is the second of two papers describing results of a research project directed at developing a gas-operated vibration damper for high-temperature turbomachinery applications. This part presents the experimental measurements made on a gas damper hardware and compares them with the theoretical predictions given in Part I. It is found that the isentropic theoretical model predicts the damper characteristics quite well. A maximum damping of 2310 N-s/m (13.2 lb-s/in.) was measured at a natural frequency of 118 Hz using the present design and the results suggest that significantly higher damping levels are possible with design modifications.

Introduction

Future turbomachines for aircraft applications are being designed to operate at higher Mach numbers and temperatures to achieve better efficiencies. These engines will require a damper that is effective at high temperatures to replace conventional squeeze-film dampers, which use oil. Research in the rotordynamics laboratory at Texas A&M University has resulted in a novel damper concept that uses air as the operating fluid and hence is suitable for high-temperature applications. A typical gas damper hardware assembly is shown in Fig. 1. In actual rotating machinery, several such actuators can be circumferentially placed around the vibrating bearing housing to enhance damping. The design features of this damper are depicted in Fig. 2. The theory behind the operation of this damper was presented in Part I of this paper (Sundararajan and Vance, 1995). In that paper, theoretical predictions were given for the damping characteristics of three hardware designs that were taken up for experimental study. According to these predictions the supply pressure, area ratio of pocket exit to pocket inlet, and the rate of change of pocket inlet/exit area with respect to the motion of the sliding head are the important parameters that determine the damping. The current paper (Part II) gives the experimental measurements of damper performance made on one of the test hardwares and compares them with the theoretical predictions given in Part I. The hardware was tested for a wide range of supply pressures and exit/inlet area ratios and the dependence of damping on these parameters was experimentally determined. Although three hardwares were tested, results are given here for only one hardware for brevity. The complete set of experimental measurements for all three hardwares is given by Sundararajan and Vance (1993). As a part of the experimental program, a dedicated test rig was built to test a single actuator of the gas damper and experimental techniques were developed to maximize the repeatability and accuracy of damping measurements.

Contributed by the International Gas Turbine Institute for publication in the JOURNAL OF ENGINEERING FOR GAS TURBINES AND POWER. Manuscript received by the International Gas Turbine Institute July 15, 1994. Associate Technical Editor: R. E. Kielb.

Test Hardware

As seen in Figs. 1 and 2, the actuator hardware mainly has two components, a stationary piston and a sliding head, which slides over the piston. The sliding head is attached to the vibrating bearing housing and follows the bearing motion. The sliding head has two chambers inside, namely the groove and the pocket. Air from the supply reservoir is fed into the groove volume through the feeding holes in the stationary piston and from there the pressure is communicated to the pocket through the pocket inlet opening. The air exits the pocket through the holes in the sliding head. It can be seen that inlet area to the pocket varies with the dynamic displacements of the sliding head. This dynamic change in the pocket inlet opening causes pressure fluctuations in the pocket, which in turn produces a damping force component. The inlet-varying design was experimentally found to produce more damping than the exit-varying designs (Vance et al., 1993) and hence was chosen for this study. Three variations of the inlet-varying design were evaluated in a laboratory test rig for their damping performance characteristics. The hardwares are named GDIV #0, GDIV #1, and GDIV #2 (GDIV is an acronym for Gas Damper Inlet Varying). The damper hardwares differ from one another in the pocket and groove geometries and in the number of inlet feeding orifices to the groove. Table 1 summarizes the salient dimensional details for each of the three hardwares. The hardware GDIV #0, which was earlier tested at a lower frequency of excitation in a rotordynamic test rig (Vance et al., 1993) was chosen as the "baseline" hardware for this study. The hardwares GDIV #1 and 2 are variations of this baseline design.

Test Apparatus

A test rig was designed to test a single actuator of the gas damper. The objective of the test rig design was to be able to test several gas damper design concepts accurately in a relatively short time. The design required ease of installation, quick alignment, and repeatable results. Figure 3 shows drawings of the front and top views of the rig. In this test setup, the gas damper actuator reacts against a vibrating stainless steel beam with clamped ends. A helical spring is used to hold the sliding

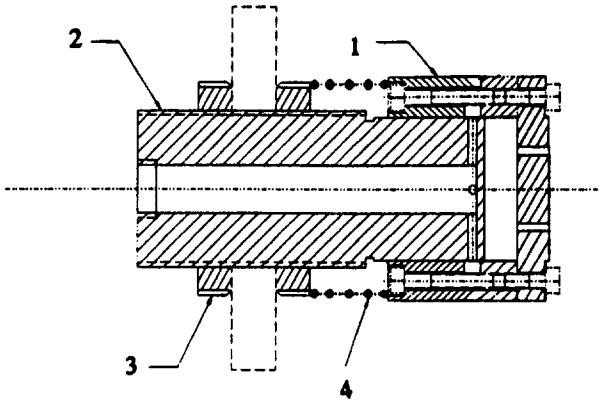

1. Sliding Head
2. Stationary Piston
3. Lock-nut
4. Spring

Fig. 1 Gas damper assembly

head in place against the beam. The beam is excited at its center by an electromagnetic shaker through a specially designed mass attachment. The shaker is suspended vertically from a rigid frame by means of an elastic cord to reduce its effect on the beam vibration characteristics. Air was supplied from a reservoir tank through a pressure regulator. The stationary piston of the gas damper actuator was held in place through two lock nuts that are tightened back to back against a fixed block. The piston has external threads over which the two lock nuts engage and the horizontal portion of the piston inside the sliding head can be adjusted by turning the lock nuts. The specially designed mass attachment was used to increase the critical damping of the beam. This attachment was rigidly held at the center of the beam.

A Wilcoxon Research Model F4 electromagnetic shaker was used in the tests. The shaker is connected to the mass attachment of the test beam through a Wilcoxon model Z820W impedance head through a threaded bolt. The dynamic weight added to the system due to the shaker is relatively low since the rubber-suspended weight does not affect the axial or rotational inertia of the system above the resonant frequency of the suspension system. This resonant frequency was measured to be about 30 Hz. The noise or excitation signals to the shaker was obtained from a HP 3311A function generator and the noise source built

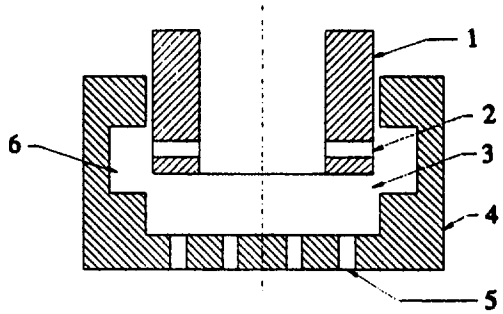

1. Stationary Piston
2. Feed Holes
3. Pocket Inlet Opening
4. Sliding Head
5. Exit Holes
6. Groove

Fig. 2 Inlet: varying design of pocket gas dampers

Table 1 Groove and pocket dimensions for the experimental hardware

	GDIV #0	GDIV #1	GDIV #2
Pocket Diameter	4.57 cm (1.8")	4.57 cm (1.8")	4.57 cm (1.8")
Groove Diameter	5.60 cm (2.2")	5.60 cm (2.2")	5.60 cm (2.2")
Pocket Length	0.5 cm (0.2")	1.14 cm (0.45")	1.14 cm (0.45")
Groove Length	0.5 cm (0.2")	1.0 cm (0.4")	1.0 cm (0.4")
No.inlet hole	4 of 0.25cm (0.1")	4 of 0.25 cm (0.1")	8 of 0.25 cm (0.1")

in the spectrum analyzer (HP 5820A) itself and these signals were amplified by a Wilcoxon Research model PA7 power amplifier before being fed to the shaker. The impedance head

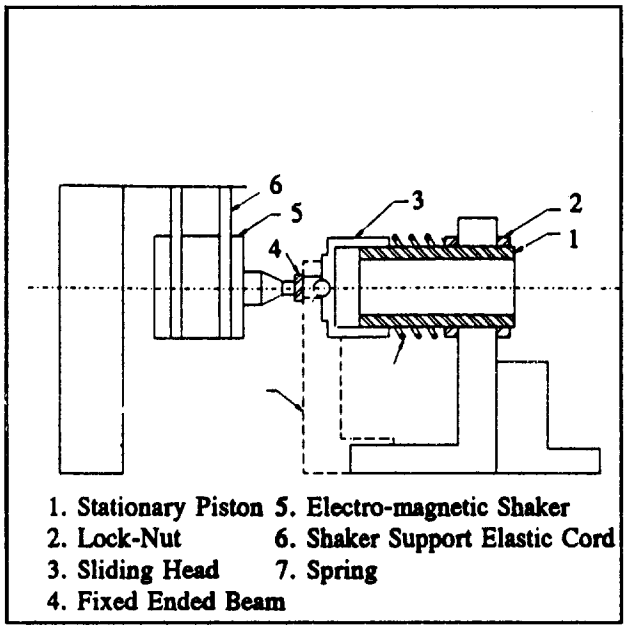

1. Stationary Piston
2. Lock-Nut
3. Sliding Head
4. Fixed Ended Beam
5. Electro-magnetic Shaker
6. Shaker Support Elastic Cord
7. Spring

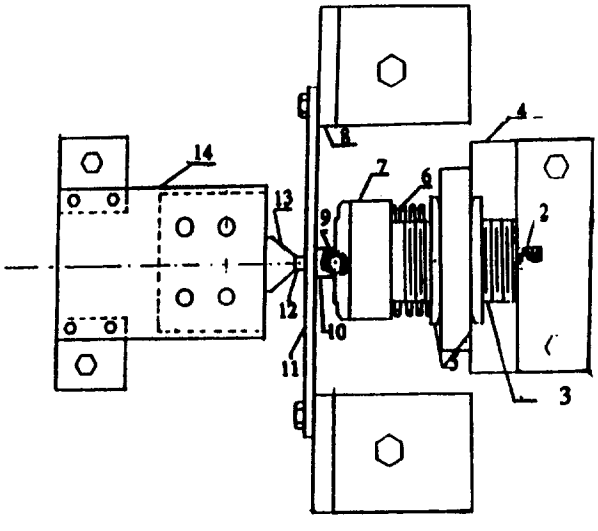

1. DAMPER MOUNTING BRACE
2. GAS INLET
3. PIPE (STATIONARY PISTON)
4. DAMPER MOUNT
5. ADJUSTING NUTS
6. PRELOAD SPRING
7. SLIDING HEAD ASSEMBLY
8. SUPPORT FOR FIXED BEAM
9. BALL
10. BALL HOLDER
11. FIXED ENDED BEAM
12. IMPEDANCE HEAD ADAPTOR
13. SHAKER/IMPEDANCE HEAD
14. SHAKER MOUNT

Fig. 3 Front and top views of gas damper test rig

contains a piezo-electric accelerometer and a piezo-electric force gage with three-pin Bendix connecters providing the output.

Instrumentation

The test rig is instrumented to measure the input force to the beam, the response acceleration of the beam, pressures in various chambers of the damper hardware, and the gas flow rate. The pressures were measured at the supply, groove, and pocket of the gas damper. The input force and the response acceleration were measured using the piezo-electric force gage and accelerometer built in the Wilcoxon F4/Z820W impedance head. Pressures were measured using Kulite and Entran strain-gage type pressure transducers, which produce a voltage proportional to the pressure. Two 2-channel spectrum analyzers, an HP 5820 A and an HP 3582A, were used for measurement of the inertance transfer function (a/F) and the a/P (acceleration/Pressure) transfer functions. A Wilcoxon power amplifier was used to amplify the excitation signals before they were fed to an electromagnetic shaker. A Nicolet two-channel digital oscilloscope was used to monitor the time signals. A HP 9816 computer system with an Infotek multichannel analog-digital board was used for data acquisition and post-data processing. Flow was measured using a standard rotameter.

Test Concepts

The basic principle that was used to determine the damping coefficient was that the damping force equals the applied force when a structure is excited at its undamped natural frequency. This principle is illustrated vectorially in Fig. 4. It can be seen from this figure that the acceleration leads the applied force by 90 deg at resonance. The damping coefficient "C" was determined as follows:

$$C = F/v \text{ at resonance}$$

where C is the damping coefficient in N-s/m (lb-s/in); F is the applied force in N (lb); v is the velocity m/s (in/s). Substituting $v = a/\omega$, where "a" is the acceleration m/s^2 (in/s^2) and ω is the angular velocity in rad/s, in the above relation for damping coefficient, we get

$$C = F\omega/a$$

where all the variables have the same meaning as defined earlier.

The relationship given above was used to determine the damping coefficient of the gas damper. The damping coefficient was evaluated from the experimental measurements of the inertance transfer function a/F (or the dynamic mass F/a) at the first natural frequency of the beam. Since the acceleration and force signals were measured in volts, appropriate calibration constants were used to convert volts to physical units.

Test Procedure

The three hardwares, GDIV #0, GDIV #1, and GDIV #2, were tested experimentally using the test setup discussed in the previous paragraphs. The test objective was to determine the damping coefficients from the measurements of the natural frequency and the magnitude of the inertance transfer function at the natural frequency. The natural frequency will be the frequency at which the acceleration would lead the input force by 90 deg. It was desired to characterize the damper by testing it under different supply pressures and pocket inlet openings and measuring the damping coefficient for each case.

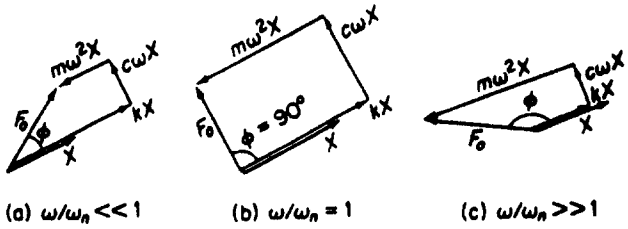

Fig. 4 Calculation of damping coefficient: test concept

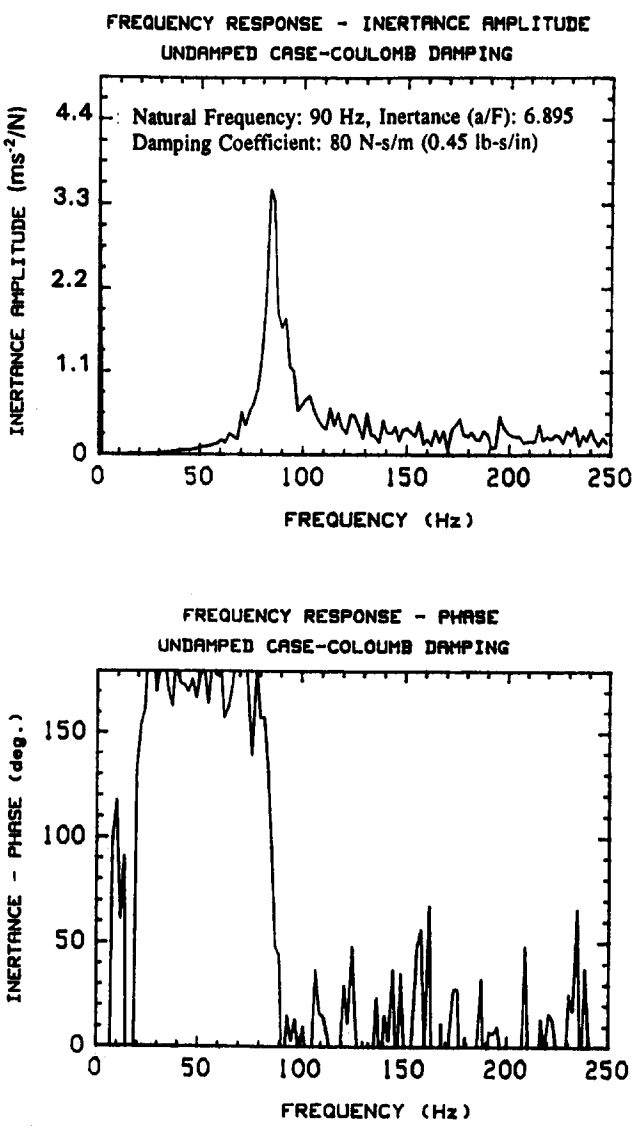

Fig. 5 Inertance measurement for damping due to Coulomb friction

Accurate determination of the pocket inlet opening of the damper was a very important part of the experiment since the damping is sensitive to this parameter. A depth micrometer was used to set the damper accurately at the desired equilibrium pocket opening position. Since the flow rate and the pressures at the supply, groove, and pocket were also measured, the amount of inlet opening of the damper was calculated from these values and was cross checked with the depth micrometer readings. To maintain consistent levels of input vibration to the damper, good alignment was required between the shaker impedance head center and the damper sliding head center.

A consistent test procedure was designed to evaluate experimentally the damping characteristics of the gas damper. First the equivalent viscous damping (due to coulomb friction) of the damper assembly without the air pressure was determined using the mobility measurement techniques. The undamped natural frequency of the beam without the air pressure was deter-

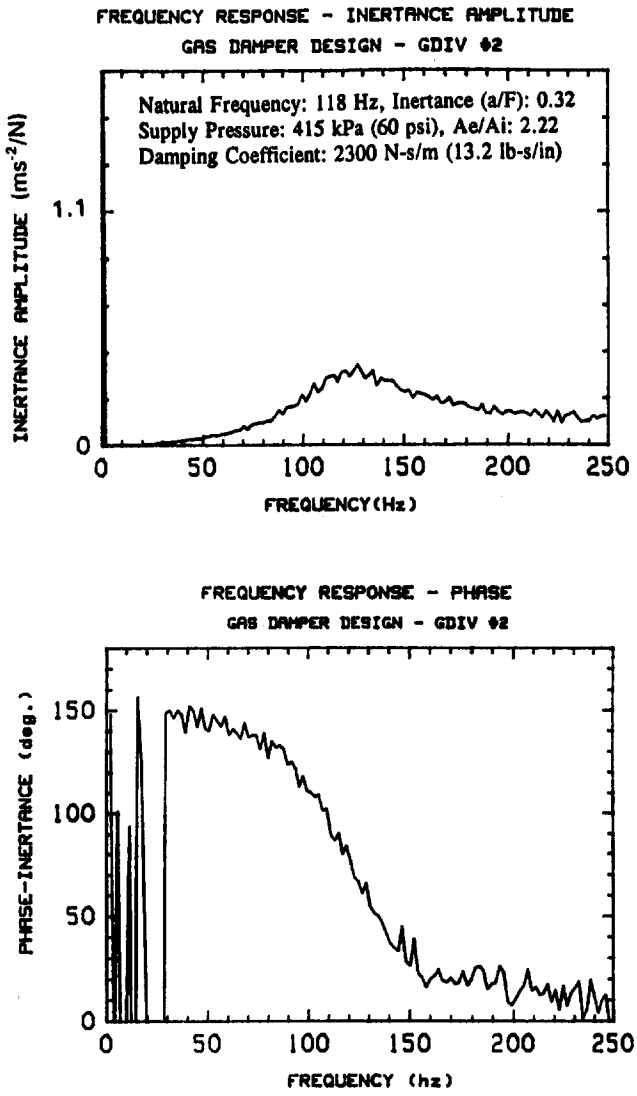

Fig. 6 Inertance measurement at 415 kPa and 125 μm pocket inlet opening

mined at the 90 deg phase angle using the white noise excitation. Then the inertance (a/F) transfer function amplitude at this undamped natural frequency was measured using harmonic excitation at this frequency. With the knowledge of the transfer function magnitude and the natural frequency, the damping was determined using the method discussed previously.

The procedure described above for determining the coulomb damping was also used to measure the damping coefficients arising from the gas damper action. To verify these damping measurements independently, dynamic pocket pressures were measured along with their phase angles and were used to calculate the damping. This value was used to cross check the damping measurements obtained from the mobility measurements. For each pocket inlet opening, the static measurements of pocket pressure, groove pressure, and flow rates were made at a wide range of supply pressures (20 to 60 psi). Then, the beam was dynamically excited using white noise excitation. The frequency response to white noise identifies the approximate natural frequency of the beam. The natural frequency and inertance transfer function were then accurately measured using harmonic excitation. Measurements were made for equilibrium pocket inlet openings of 25 μm to 250 μm (1 to 10 mils). Tests and measurements were repeated to check for consistency. The damper performance characteristics were extracted from the measured data. The procedure was repeated for all the three hardwares tested. The test results and the discussions follow. Although three hardwares were experimentally evaluated, the results are given for only one hardware, namely GDIV #2, for brevity. This hardware produced more damping than the other two and showed considerable promise.

Experimental Results—GDIV #2

The dimensions of the hardware GDIV #2 are given in Table 1. GDIV #2 has eight inlet feeding holes compared to four in GDIV #0 and #1. Figure 5 shows a typical measurement of the inertance amplitude with no air supply. The value of inertance at the natural frequency gives the value of the equivalent viscous damping due to coulomb friction present in the system. Now, with the air supply turned on, inertance measurements were obtained for a range of supply pressures and pocket inlet openings. One such measurement is shown in Fig. 6 for a supply pressure of 415 kPa (60 psi) and 125 μm (5 mils) pocket inlet opening. It is seen that the phase angle is 90 deg at a frequency of 118 Hz. This is the natural frequency of the beam with the air pressure on. The inertance amplitude at the natural frequency of 118 Hz corresponds to a viscous damping coefficient of 2310 N-s/m (13.2 lb-s/in.). The inertance amplitude measurement for a lower supply pressure of 275 kPa (40 psi) is shown in

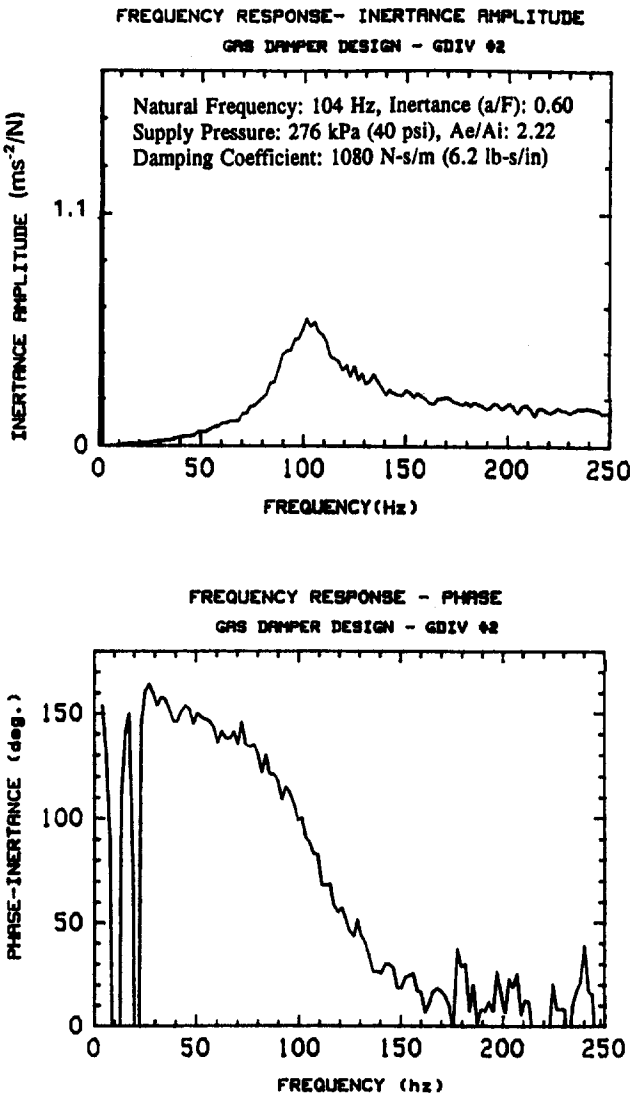

Fig. 7 Inertance measurement at 275 kPa and 125 μm pocket inlet opening

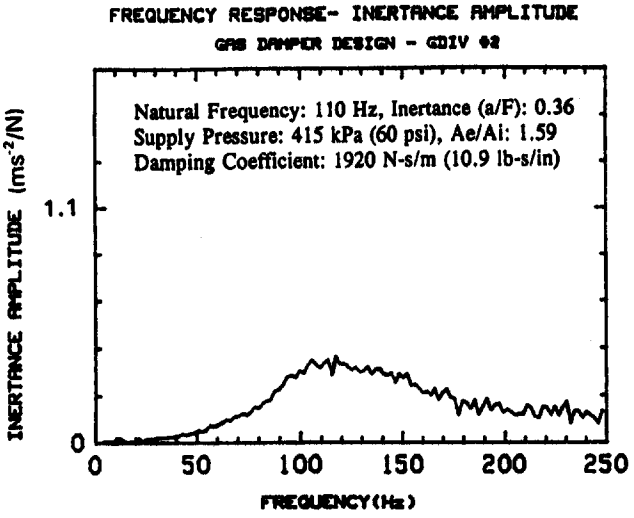

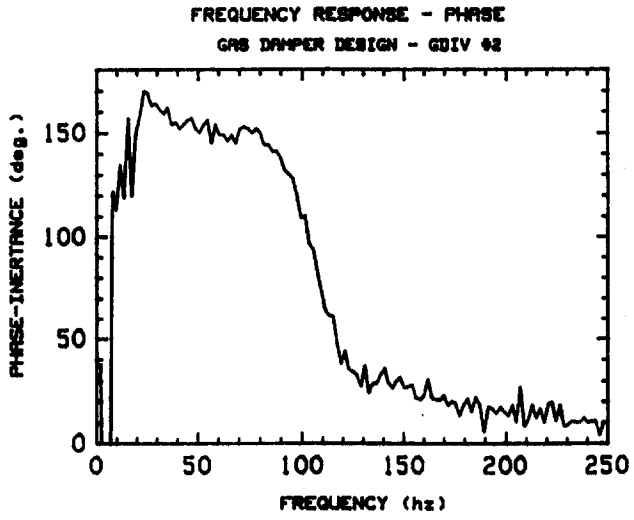

Fig. 8 Inertance measurement at 415 kPa and 175 μm pocket inlet opening

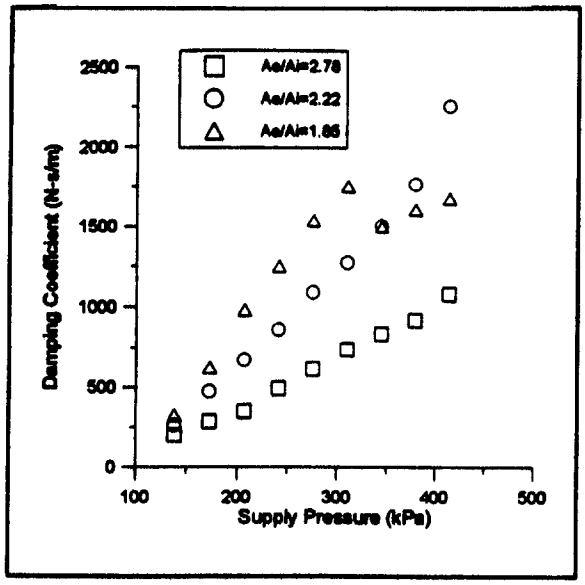

Fig. 9 Experimental measurement of damping versus supply pressure: GDIV #2

Fig. 7. This gives a damping coefficient of 1085 N-s/m (6.2 lb-s/in.). It is seen that the damping falls by about 50 percent when the pressure is reduced from 60 to 40 psi for this equilibrium pocket opening. Figure 8 shows an inertance measurement taken at an inlet opening of 175 μm (7 mils) and 415 kPa (60 psi). A damping of 1880 N-s/m (10.75 lb-s/in) was measured for this position. It is seen that the damping drops when the pocket inlet opening is increased from 125 μm (5 mils) to the 175 μm (7 mils) though the drop is not significant. Figure 9 shows the variation of damping with the supply pressure for the three equilibrium pocket inlet openings of 100 μm, 125 μm, and 150 μm (4, 5, and 6 mils). It is seen that for the 100 μm and 125 μm (4 and 5 mils) inlet openings, the damping increases with pressure throughout the plotted supply pressure range. The pressure measurements in the supply, groove, and pocket indicated that flow is choked at the inlet to the pocket for the supply pressures 275 kPa, 345 kPa, and 415 kPa (40, 50, and 60 psi) at these equilibrium positions. However, for the 150 μm (6 mils) open position of the damper, there is a small drop in the damping level from 1750 N-s/m to 1490 N-s/m (10 lb-s/in. to 8.5 lb-s/in.) when the supply pressure is increased from 310 kPa (45 psi) to 345 kPa (50 psi) and the damping starts, increasing with the supply pressure thereafter but with a reduced slope. The pressure measurements showed that the flow started getting choked at the exit area when the supply pressure was close to 310 kPa (45 psi). It was at this supply pressure a drop in damping was noticed in the measurements. The measured variation of damping with the inlet opening to the pocket is described in Fig. 10 for the three supply pressures 275 kPa, 345 kPa, and 415 kPa (40, 50, and 60 psi). It is seen from this figure that the damping initially increases with pocket opening and reaches a maximum for a pocket inlet opening of 125 μm (5 mils). Further increase of pocket inlet opening shows a drop in damping and for increased pocket inlet openings the damping curve levels off. For a supply pressure of 415 kPa (60 psi), the damping reaches a maximum of 2300 N-s/m (13.2 lb-s/in.) at the 125 μm (5 mil) open position and for further increase in the opening, the damping drops to about 1750 N-s/m (10 lb-s/in.) and stays at that value for openings up to 250 μm (10 mils) in the plotted range. Figure 11 shows the measured variation of the pressure drop with the flow rate when the pocket inlet

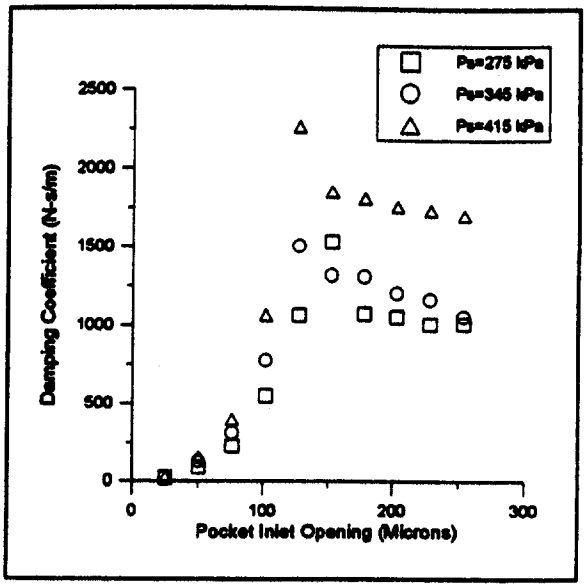

Fig. 10 Experimental measurement of damping versus pocket inlet opening: GDIV #2

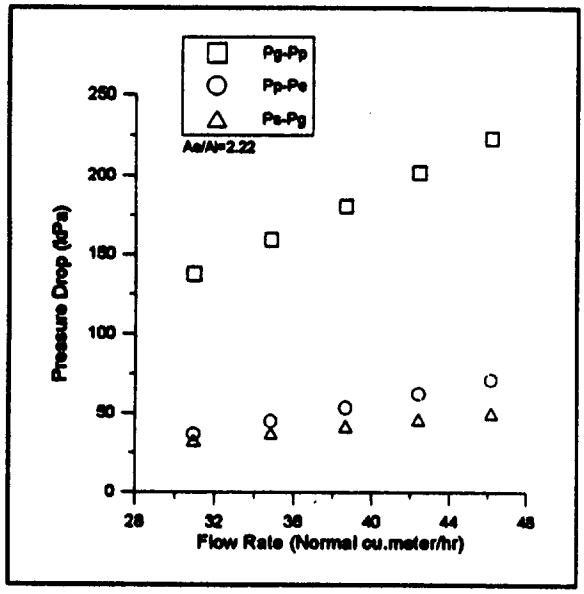

Fig. 11 Experimental measurement of pressure drop versus flow rate at 125 μm pocket inlet opening

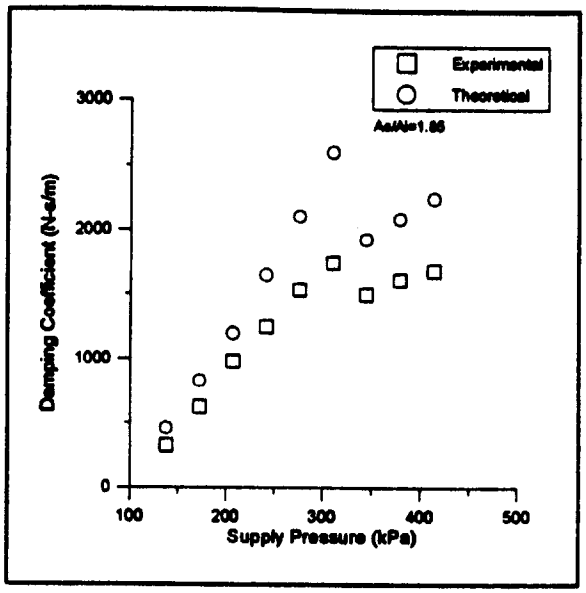

Fig. 13 Comparison of theory with experiment: damping versus supply pressure at 150 μm pocket inlet opening: GDIV #2

opening is 125 μm (5 mils). This measurement was used to calibrate the various flow restrictions in the gas damper.

In summary, a maximum damping of 2300 N-s/m (13.2 lb-s/in.) was measured for the GDIV #2 hardware at a supply pressure of 415 kPa (60 psi) and 125 μm (5 mils) pocket inlet opening. The measurements showed that the damping is maximum for an exit to inlet area ratio of about 2. For the present hardware with given exit area for the damper, it was found that damping is maximum for a supply pressure at which flow is choked at the exit.

Comparison of Theoretical Predictions With Experimental Results

The theoretical predictions of the gas damper performance were presented in Part I of this series. Now, a comparison of the theoretical predictions with the experimental results is made for the experimentally tested hardware GDIV #2. The following paragraphs discuss how well the theoretical predictions match the experimental results.

Figures 12–14 show the comparison between the theory and the experiments for the GDIV #2 hardware. The variation of damping with supply pressure is compared in Figs. 12 and 13 for the two equilibrium pocket inlet openings close to the maximum damping position. Theory and experiments agree that the damping increases with pressure uniformly over the plotted pressure range of 138 to 415 kPa (20 to 60 psi) for the inlet openings of 100 and 125 μm (4 and 5 mils) and abruptly falls at a supply pressure of 310 kPa (45 psi) for the 150 μm (6 mil) open position. This fall and rise in damping at 310 kPa (45 psi) for an inlet opening of 150 μm (6 mils) is due to the fact that the flow starts getting choked at the exit area that was confirmed by the experimental measurements as well. It may, however, be noted that the theory predicts a larger drop in the

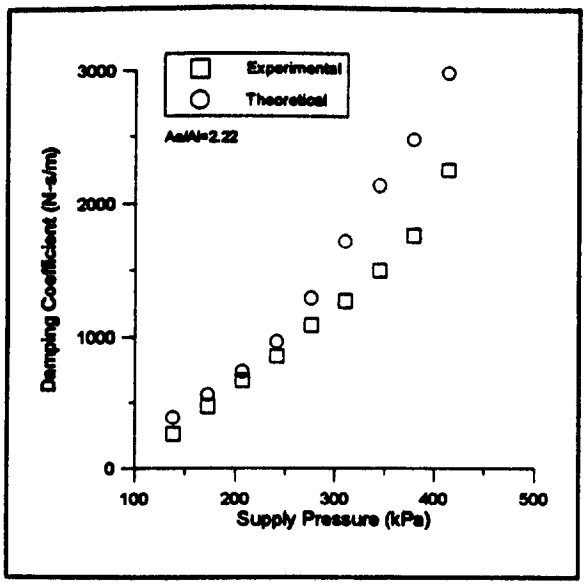

Fig. 12 Comparison of theory with experiment: damping versus supply pressure at 125 μm pocket inlet opening: GDIV #2

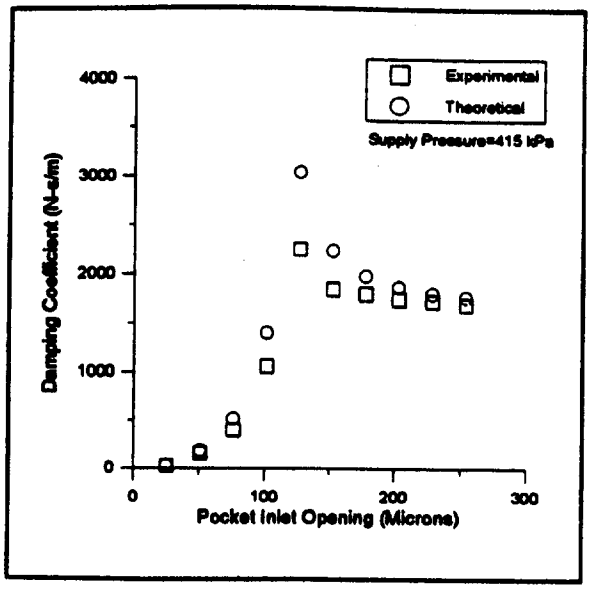

Fig. 14 Comparison of theory with experiment: damping versus pocket inlet opening at 415 kPa supply pressure

damping compared to the measured drop. The rate of increase of the damping with the supply pressure as predicted by the theory matches well with the experimental results for all the three equilibrium positions. The variation of damping with the inlet opening for a supply pressure of 415 kPa (60 psi) is compared in Fig. 14. For a supply pressure of 415 kPa (60 psi), the theory predicts a maximum damping of 3065 N-s/m (17.5 lb-s/in.) at an inlet equilibrium position of 125 μm (5 mils) while the measured damping was 2300 N-s/m (13.2 lb-s/in.). The theory and the experiments agree very well on the rate of change of damping with the equilibrium position. Importantly, both agree that this hardware is relatively insensitive to pocket inlet opening over a 125 μm (5 mils) range beyond the 125 μm (5 mils) inlet opening at which maximum damping occurred. In general, the measured damping levels are less by 20 to 25 percent of the theoretical values for most equilibrium positions and pressures. This is probably due to the fact that real flow is not isentropic as assumed in the theory and hence dynamic pressures that produce the damping are less in reality. An uncertainty analysis of various measured parameters showed the error in estimated values of damping coefficient to be within 4 percent.

Conclusions

The performance characteristics of the inlet-varying gas damper design have been evaluated both theoretically and experimentally. The results show a good correlation between the two. A maximum damping of 2310 N-s/m (13.2 lb-s/in.) at an excitation frequency of 118 Hz was measured compared to a theoretical prediction of 3065 N-s/m (17.5 lb-s/in). Since several such single actuators can be installed circumferentially around the rotor bearing, significant damping levels can be achieved. Based on the theoretical and experimental study, an improved design of the damper that will produce higher levels of damping has been conceived. It is important to note that unlike all other bearing dampers, which rely on viscous effects to produce the damping, this damper design relies on the compressibility of the working fluid to produce the required pressure-phase relationship in the actuator pocket. Simplicity in design and reliability in performance make the gas damper a potential candidate for high-temperature turbine applications.

References

Sundararajan, P., and Vance, J. M., 1993, "A Theoretical and Experimental Investigation of a Gas Operated Bearing Damper for Turbomachinery: Part II—Experimental Results and Comparison With Theory," *Vibration of Rotating Systems*, ASME DE-Vol. 60, pp. 85–119.

Sundararajan, P., and Vance, J. M., 1995, "A Gas-Operated Bearing Damper for Turbomachinery: Theoretical Predictions Versus Experimental Measurements: Part I—Theoretical Model and Predictions," ASME JOURNAL OF ENGINEERING FOR GAS TURBINES AND POWER, Vol. 117, this issue, pp. 741–748.

Vance, J. M., Cardon, B. P., San Andres, L. A., and Storace, A. F., 1993, "A Gas-Operated Bearing Damper for Turbomachinery," ASME JOURNAL OF ENGINEERING FOR GAS TURBINES AND POWER, Vol. 115, pp. 383–389.

Modeling and Control of HSFDs for Active Control of Rotor-Bearing Systems

A. El-Shafei

J. P. Hathout

Department of Mechanical Design and Production, Cairo University, Giza, Egypt

This paper summarizes the development of hybrid squeeze film dampers (HSFDs) for active control of rotor vibrations. Previously, it was shown both theoretically and experimentally that HSFDs can be used for controlling rotor vibrations (El-Shafei, 1993). This is done by controlling the flow in a squeeze film damper through movable end seals, thus achieving the ability to change the damper from a short damper to a long damper and vice versa. However, the control of the HSFD was manual. In this paper, an automatically controlled circuit is developed for the HSFD, incorporating a pressure control servovalve for controlling the pressure in the sealing chambers. A complete mathematical model of this open-loop system is developed and is implemented on a digital computer. The transient behavior of the system, including the sealing ring dynamics, illustrates that the open-loop system exhibits well-behaved, stable, and fast response. In addition it is shown that the HSFD can achieve any amount of damping between the short and long damper modes through the accurate positioning of the sealing rings. The simulation results illustrate that the automatically controlled HSFD can be a very useful device for the active control of rotors. A closed-loop control strategy with feedback on rotor speed is also investigated both from the points of view of steady state and transient behaviors. It is shown that this closed-loop strategy results in a much improved behavior of the rotor system.

Introduction

Active vibration control of rotors of aircraft jet engines, rocket turbopumps, and high-speed compressors has been investigated in the last decade or so. Passive vibration control has been used for over twenty years, using squeeze film dampers. However, active vibration control is sought because of its effectiveness in wide speed ranges and its adaptability to changing operating conditions. Three active vibration control devices have been suggested: (1) magnetic bearings, (2) lateral force actuators, and (3) active squeeze film dampers.

Magnetic bearings have been investigated for actively controlling the vibration of rotating machinery (Schweitzer and Ulbrich, 1980; Bradfield et al., 1989). Yet, as far as aircraft engines are concerned, magnetic bearings are still at a developmental stage and have not been used in aircraft engines for several reasons, including: (1) the inability of magnetic bearings to withstand high temperatures, (2) the control algorithms for magnetic bearings are still under development, and most importantly (3) magnetic bearings have still to prove their reliability. Lateral force actuators have recently been suggested as active vibration controllers (Palazzolo et al., 1989; Nonami et al., 1989) and also are still at a developmental stage. Their shortcomings include: (1) possible coupling of motion in orthogonal directions, (2) they require large size actuators, and (3) they also have still to prove their reliability.

Squeeze film dampers (SFDs), on the other hand, have a proven track record. They have been used successfully for the last twenty years to damp rotating machinery passively, in particular aircraft engines (White, 1972; Gunter et al., 1977; Holmes and Dogan, 1985). They provide the primary source of damping in aircraft engines since the rolling element bearings on which these engines are mounted provide very little damping. Thus, because of their reliability, it seems natural to develop SFDs to control rotor vibrations actively. Burrows et al. (1983) investigated the possibility of controlling rotating machinery vibration by controlling the pressure in a SFD, and they point out that control of rotors using active SFDs is much cheaper than using magnetic bearings, and is more simple and reliable. Adams and Zahloul (1987) studied the control of rotors by controlling the pressure in hydrostatic SFDs. Mu et al. (1991) proposed an active SFD by using a movable conical damper ring. El-Shafei (1991b, 1993) proposed using hybrid squeeze film dampers (HSFDs) for active vibration control of rotors. The basic idea is to control the flow in the SFD through movable end seals, thus achieving the ability to change the damper from a short damper to a long damper and vice versa. The performance of HSFDs was verified experimentally, and it was shown that HSFDs are effective in controlling the amplitude of rotor vibrations and in reducing the force transmitted to the support. Also it was shown that the hybrid damper is much more effective in controlling rotor vibrations than the previous strategies of controlling the pressure in a conventional squeeze film damper.

Because of its demonstrated capability and excellent performance in controlling rotor vibrations and because of the reliability of SFDs, it is desirable to develop the hybrid squeeze film damper. This paper is concerned with the development of the HSFD for actively controlling rotating machinery vibration. The current state of development of the HSFD (El-Shafei, 1993) is that it has been used in the laboratory in a manually controlled configuration as an on-off controller. In this paper, an automatically controlled circuit is developed for the HSFD, incorporating a pressure control servovalve for controlling the pressure in the sealing chambers. A complete mathematical model of this open-loop system is developed and is implemented on a digital computer. This mathematical model of the rotor-HSFD-control system includes a proposed model for the HSFD that emulates the behavior of the HSFD for various positions of the sealing ring. The transient behavior of the system, including the sealing ring dynamics, illustrates that the open-loop system exhibits well-behaved, stable, and fast response. In addition it is shown that the HSFD can achieve any amount of

Contributed by the International Gas Turbine Institute and presented at the 39th International Gas Turbine and Aeroengine Congress and Exposition, The Hague, The Netherlands, June 13–16, 1994. Manuscript received by the International Gas Turbine Institute February 4, 1994. Paper No. 94-GT-52. Associate Technical Editor: E. M. Greitzer.

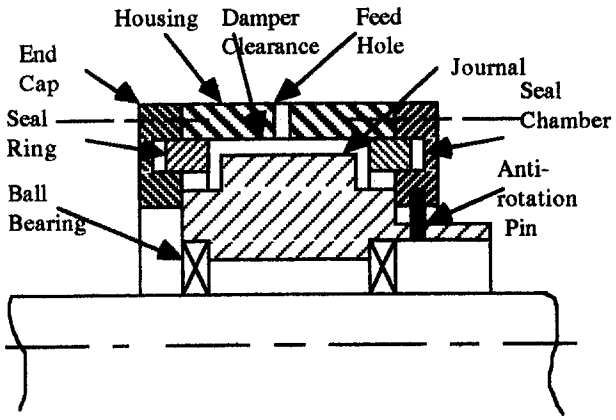

Fig. 1 Schematic of the hybrid damper

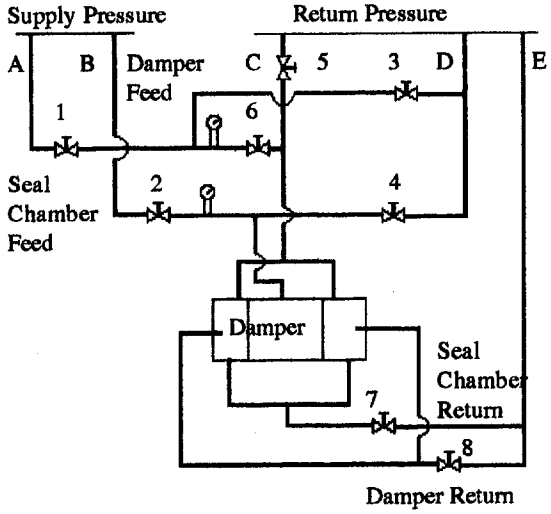

Fig. 2 Original hydraulic circuit

damping between the short and long damper modes through the accurate positioning of the sealing rings. The simulation results illustrate that the automatically controlled HSFD can be a very useful device for the active control of rotors. A closed-loop control strategy with feedback on rotor speed is also investigated both from the points of view of steady-state and transient behaviors. It is shown that this closed-loop strategy results in a much improved behavior of the rotor system. The development of the control system is, in fact, the crucial phase in the development of the HSFD (Akin, 1990).

Automation of the HSFD Control Circuit

The original design of the HSFD (El-Shafei, 1993) used two movable metal sealing rings with sliding fit both to the end caps and to the housing, one on each end of the damper as shown in Fig. 1. The principle of the seals' operation is simple. The damper oil film and the hydraulically actuated seals are supplied from independently variable sources. In order for the damper to operate as a long damper, the pressure to the seal chambers is elevated above the internal pressure of the damper. The seal rings will move in axially and seal the oil film inside the damper clearance. In order to return to the short damper configuration, the seal pressure is lowered until it is less than the internal pressure of the damper. This causes the seal rings to return to their original positions. In addition a spring acts to aid in locating the seal ring at any required position.

In the previous testing of the HSFD, the objective of controlling the pressure in the sealing chambers was achieved through manually controlling the flow in the hydraulic circuit (Fig. 2) through needle valves (El-Shafei, 1993). Redundancy was an objective in the design of this circuit.

In order to achieve the objectives of active control of rotor vibration, the hydraulic circuit needs to be automated, in the sense that electrically controlled valves will be required for the circuit control. Moreover, at this stage of development of the HSFD, redundancy in the hydraulic circuit is not required and needs to be eliminated. The automated hydraulic control circuit of Fig. 3 fulfills these objectives. An electrohydraulic pressure control servovalve 2 is used to control the pressure in the sealing chambers. The servovalve is normally closed; however, when it receives a current signal, it connects the supply line, through an orifice, to the sealing chamber, thus increasing the pressure in the sealing chamber. If, on the other hand, a reduction in pressure is required, the servovalve connects the drain, also through an orifice, to the sealing chamber, thus reducing the pressure in the sealing chamber. When the required pressure is achieved the valve is closed.

The pressure control servovalve was chosen over the more common flow control servovalve, since the associated hydraulic circuit is simpler in this particular application, and in addition continuous flow would be required to maintain a constant pressure with the flow control servovalve, which is an unnecessary energy loss.

Several important features of the automated hydraulic circuit of Fig. 3 need to be discussed. First, the supply to the damper is still the same, only a check valve 3 and a pressure reducing valve 8 were added to the circuit. The damper drain is also through a needle valve as before. Second, the sealing chamber, in this design, has only one port. This port is used both to supply and to drain the sealing chamber. Third, the pressure control servovalve is the only component required to control the pressure in the sealing chambers. The feed and drain of the seal chamber is provided through the pressure control servovalve. This simple design of the automated pressure control circuit provides for an efficient control loop. Moreover, because of the current control of the servovalve, it can be easily interfaced to a computer to provide computer control.

It should be pointed out that there are three supply holes to the damper distributed circumferentially at the center of the damper. It is anticipated that only two ports will be used as supply ports to the damper, while the third port can be used either as a supply to or a drain from the damper. This is useful in the long damper configuration, since in the long damper mode the fluid is trapped in the damper, and the heat generated will cause an increase in the fluid temperature, thus decreasing the viscosity of the fluid. This is highly undesirable, and the fluid drained from the center of the damper through a small feed hole will aid in cooling the fluid. However, this may not be sufficient, and in our test rig we have made arrangements (through temperature feedback) to

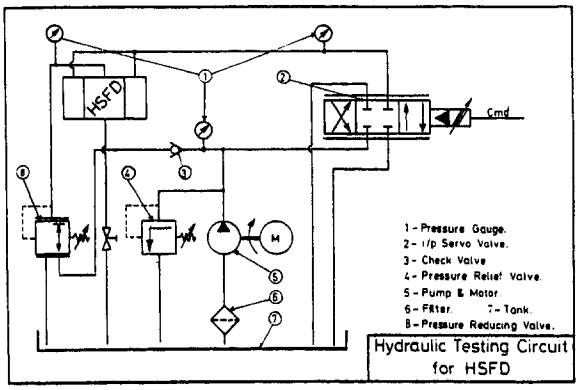

Fig. 3 Automated hydraulic control circuit

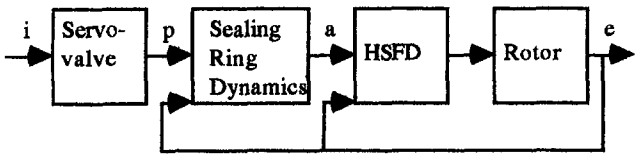

Fig. 4 Block diagram

change momentarily to the short damper mode, thus flooding the damper and cooling it, if needed.

Development of a Model for the HSFD and the Control Circuit

The HSFD-rotor-control system consists of a pressure control servovalve, the HSFD, and the rotor. This system can be considered as an open-loop system, where the current i actuates the servovalve, which in turn controls the pressure p in the sealing chamber, thus controlling the position of the sealing rings, which control the amount of damping applied to the rotor. Figure 4 shows a block diagram of the open-loop system.

It should be emphasized that, as shown in Fig. 4, the sealing ring dynamics depend both on the pressure in the sealing chambers p and the pressure in the damper, which depends on the eccentricity e of the journal in the damper. In addition, the damping provided by the HSFD depends both on the position of the sealing ring a and the eccentricity e. Thus there is an unmistakable coupling between the whole system in the sense that the rotor behavior depends on the HSFD and the sealing ring dynamics, yet the sealing ring dynamics and the HSFD depend on the rotor behavior. Moreover, it should be stressed that the system under investigation is nonlinear in nature because of the nonlinearity of squeeze film dampers.

The Rotor. It was decided to use the Jeffcott rotor as a model for the first mode of a test rig, currently being built at Cairo University, both because of the simplicity of the Jeffcott rotor and its resemblance to the test rig rotor. Figure 5 shows a Jeffcott rotor mounted on two identical ball bearings, each of which is surrounded by an HSFD. The outer race of each ball bearing, which is assumed rigid and massless, is constrained from rotating by a retainer spring of stiffness K_r, which also acts to center the journal in the clearance of the oil film. The rotor is assumed massless with a stiffness of $2K$, the disk is assumed rigid with mass $2m$, and the damping acting at the rotor center has a damping coefficient of $2C$.

The equations of motion of the center of the disk S are

$$m\ddot{x}_S + C\dot{x}_S + K(x_S - x_E) = m\Omega^2 u \cos \Omega t - m\alpha u \sin \Omega t \quad (1)$$

$$m\ddot{y}_S + C\dot{y}_S + K(y_S - y_E) = m\Omega^2 u \sin \Omega t + m\alpha u \cos \Omega t \quad (2)$$

where x_S, y_S, x_E, and y_E are the positions of the center of the disk S and the center of the journal E, respectively, and Ω and α represent the angular speed and angular acceleration of the rotor, respectively.

Assuming that the rotor journal has a mass m_b (which would include the part of the rotor mass lumped at the damper location), the equations of motion of the journal center E are

$$m_b\ddot{x}_E + C_{xx}\dot{x}_E + C_{xy}\dot{y}_E + K(x_E - x_S) + K_r x_E = 0 \quad (3)$$

$$m_b\ddot{y}_E + C_{yx}\dot{x}_E + C_{yy}\dot{y}_E + K(y_E - y_S) + K_r y_E = 0 \quad (4)$$

where C_{xx}, C_{xy}, C_{yx}, and C_{yy} are the damping coefficients of the HSFD. A model of the HSFD that does not include fluid inertia is used. This is a simplifying assumption that will be removed later on; however, it was deemed necessary at the development stage of the control algorithm because of the simplicity afforded. It should be noted that the effect of fluid inertia can be approximately introduced by judiciously increasing m_b (El-Shafei and Crandall, 1991). In addition, it is assumed that the damper is pressurized and operates uncavitated. Usually, aircraft engines have a supply pressure of 4 bar (58.8 psi) to 5.5 bar (80.85). In some applications this may be adequate in suppressing cavitation. However, in a general condition, cavitation will occur and should be addressed. On the other hand, in order to develop a robust controller, a simple model will be needed, and we chose to follow an uncavitated model in the control development. Cavitation can be avoided experimentally by using a supply pressure as high as 14 bar (205.8 psi) in our test rig. The damping coefficients for uncavitated short and long dampers are well known and are used here in a stationary Cartesian frame (El-Shafei and Eranki, 1994). The extension of this model to the cavitated case is straightforward, and has been developed in our most recent simulations. The main effect of cavitation is to reduce the damping, by as much as a factor of 2, and to possibly introduce undesirable nonlinear vibrations such as the jump resonance (El-Shafei, 1990).

It should be noted that in Eqs. (3) and (4) we have neglected the effect of friction of the metallic sealing rings on the journal face in the long damper mode. This may be an important consideration; however, communication with aircraft engine manufacturers (Akin, 1990) indicated that such an effect is minimal in SFD applications in aircraft engines. We intend to investigate this effect experimentally, but all the results that are shown in this paper rely on a model that does not include the effect of the friction of the sealing ring on the journal, and the results show that the HSFD can be very effective in controlling rotor vibrations.

The HSFD. The damping coefficients C_{xx}, C_{xy}, C_{yx}, and C_{yy} for the HSFD should reduce to those of the short damper at one extreme and to those of the long damper at the other extreme. To incorporate the effect of a finite damper in the HSFD model, a simple model due to Holmes and Dogan (1985) is used, which is simply a linear combination of the short damper model and the long damper model. Thus

$$C_{ij} = \lambda C_{ijs} + (1 - \lambda) C_{ijl} \quad (5)$$

where λ is a measure of the finiteness of the damper, and C_{ijs} and C_{ijl} represent the short and long damper coefficients, respectively, and i and j take the values x and y. This model simply says that if λ is equal to zero, then we have the long damper model, and if λ is equal to one, then we have the short damper model. For any intermediate value for λ between 0 and 1 we obtain the corresponding finite damper. Holmes and Dogan (1985) obtained experimentally the appropriate value of λ for the damper they were studying. Moreover, they were experimenting with different sealing conditions and they were able to show that a damper with an end seal at a distance from the end

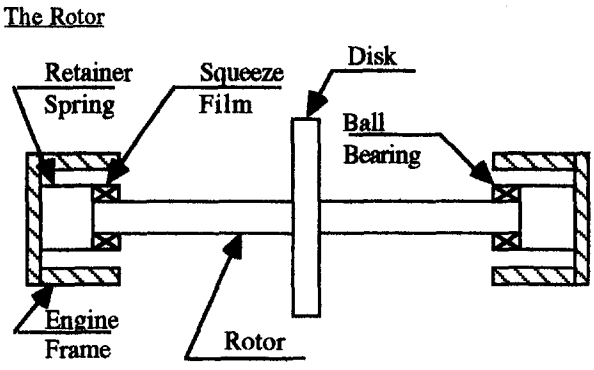

Fig. 5 Jeffcott rotor on HSFDs

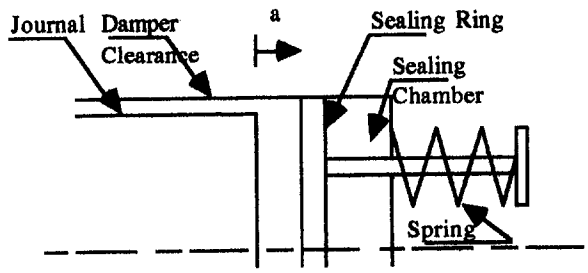

Fig. 6 Schematic of the sealing ring

equal to the radial clearance c approaches the short damper, and a damper with a closed end will approach the long damper. Thus in our model of the HSFD we take the factor λ to be equal to the ratio a/c, where a is the distance of the seal ring from the end of the damper.

The Seal Ring Dynamics. Figure 6 shows a schematic of the sealing ring. The position of the sealing ring from the journal end is the distance a. The forces acting on the ring are those due to the pressure in the sealing chamber, the pressure at the journal end, the spring stiffness, and possibly some damping acting on the sealing ring. Thus the equation of motion of the sealing ring becomes

$$m_r\ddot{a} + C_1\dot{a} + K_s\,(a - a_{\max}) = F_d - pA_r \qquad (6)$$

where m_r is the mass of the sealing ring, F_d is the force at the journal end, p is the pressure in the sealing chamber, A_r is the area of the sealing ring exposed to the pressure p, K_s is the spring stiffness, and C_1 is the damping coefficient on the sealing ring. The maximum travel of the sealing ring $a_{\max}$ can be taken equal to the radial clearance c, since the HSFD achieves the short damper mode by placing the sealing ring at a distance equal to c (Holmes and Dogan, 1985).

To obtain the force F_d acting on the sealing ring due to the pressure in the damper, the pressure at the end of the journal is integrated over the exposed area of the sealing ring. Thus

$$F_d = \int_{\theta_1}^{\theta_2}\int_{R+c-h}^{R+c} p_d r\,dr\,d\theta \qquad (7)$$

where p_d is the damper pressure at the journal end, R is the journal radius, and h is the film thickness given by

$$h = c - e\cos\theta$$

The pressure at the journal end is assumed to have the same behavior as the damping coefficients, Eq. (5), in the sense that it is assumed to be a linear combination of the pressure at the journal end for the short damper case and that for the long damper case. However, for the short damper case the pressure at the journal end is assumed to be zero gage, since it is directly connected to the drain. Thus, the pressure at the journal end for the HSFD is given by

$$p_d = (1 - \lambda)p_{dl}$$

where p_{dl} is the pressure in the long damper, which is given by (Trumpler, 1966; El-Shafei, 1991a)

$$p_{dl} = \left(\frac{6\mu R^2}{c^3}\right)\left(\left[\frac{1}{\epsilon(1-\epsilon\cos\theta)^2} - \frac{1}{\epsilon(1+\epsilon)^2}\right]\dot{e} + \left[\frac{2\sin\theta(2-\epsilon\cos\theta)}{(2+\epsilon^2)(1-\epsilon\cos\theta)^2}\right]e\dot{\psi}\right)$$

where ϵ is the eccentricity ratio e/c, and $\dot{e}$ and $e\dot{\psi}$ are the radial and tangential velocities of the journal, respectively. The radial and tangential velocities of the journal are related to the journal velocities in the (x, y) frame by

$$\begin{bmatrix}\dot{x}_E\\ \dot{y}_E\end{bmatrix} = \begin{bmatrix}\cos\psi & -\sin\psi\\ \sin\psi & \cos\psi\end{bmatrix}\begin{bmatrix}\dot{e}\\ e\dot{\psi}\end{bmatrix}$$

Substituting the equations above into Eq. (7), and performing the integrations neglecting terms $O(c/R)$ and assuming an uncavitated film in the damper as before, the force F_d becomes

$$F_d = \frac{6\mu R^3(1-\lambda)}{c^2}\frac{2\pi}{\epsilon} \times\left[\frac{1}{(1-\epsilon^2)^{0.5}} - \frac{1}{(1+\epsilon)^2}\right]\{\cos\psi\,\dot{x}_E + \sin\psi\dot{y}_E\} \qquad (8)$$

where $\epsilon = e/c$ and

$$e = \sqrt{x_E^2 + y_E^2} \quad \text{and} \quad \psi = \tan^{-1}\frac{y_E}{x_E}$$

Servovalve. The pressure control electrohydraulic servovalve provides a pressure increase or decrease in response to a current input. Thayer (1965) reports that the dynamic characteristics of the pressure control servovalve can be adequately represented by

$$\frac{\ddot{p}}{\omega_{n1}^2} + \frac{2\zeta_1}{\omega_{n1}}\dot{p} + p = K_1 i \qquad (9)$$

where p is the controlled pressure, i is the input current (which usually has a maximum value of 10 mA), K_1 is the valve's static gain (usually of the order of 125 psi/mA), ζ_1 is the valve's apparent damping ratio (usually between 0.3 and 0.5), and ω_{n1} is the valve's apparent natural frequency (usually of the order of 250 Hz).

Equations (1) to (6), (8), and (9) constitute a complete model of the open loop control system for the HSFD shown in Fig. 4. It is desirable to nondimensionalize the governing equations before implementing them on a digital computer. This is because the nondimensional equations are less prone to numerical difficulties since the parameters and variables are sealed, and also the nondimensionalization results in a reduced number of parameters and generalizes the analysis.

To nondimensionalize the system equations, we define the following nondimensional quantities:

$\epsilon = e/c$ = eccentricity ratio
$\bar{x}_S = x_S/c$ = nondimensional x displacement of point S
$\bar{y}_S = y_S/c$ = nondimensional y displacement of point S
$\bar{x}_E = x_E/c$ = nondimensional x displacement of point E
$\bar{y}_E = y_E/c$ = nondimensional y displacement of point E
$U = u/c$ = nondimensional unbalance
$K^* = K/m\,\omega_n^2$ = nondimensional rotor stiffness
$K_r^* = K_r/m\,\omega_n^2$ = nondimensional retainer spring stiffness
$\Omega^* = \Omega/\omega_n$ = nondimensional rotor speed
$\alpha^* = \alpha/\omega_n^2$ = nondimensional rotor angular acceleration
$\eta = C/m\,\omega_n$ = damping loss factor
$R_k = K_r^*/K^*$ = stiffness ratio
$m_0 = m/m_b$ = mass ratio
$\lambda = a/c$ = nondimensional displacement of the sealing rings
$\overline{C_{ij}} = C_{ij}/m\,\omega_n$ = nondimensional damping coefficients
$B_s = \mu R L^3/m\,\omega_n c^3$ = bearing parameter for the short damper
$B_l = \mu R^3 L/m\omega_n c^3 = B_s(R^2/L^2)$ = bearing parameter for the long damper
$\eta_1 = C_1/m_r\omega_n$ = damping loss factor at sealing rings
$K_s^* = K_s/m_r\omega_n^2$ = nondimensional spring stiffness

$F_d^* = F_d/m_r c\omega_n^2$ = nondimensional force at journal end
$B_e = \mu R^3/m_r\,\omega_n\,c^2$ = end force coefficient
$p^* = pA_r/m_r\omega_n^2 c$ = nondimensional pressure in sealing chambers
$\omega_r^* = \omega_{n_1}/\omega_n$ = ratio of natural frequencies
$K_1^* = K_1 i_{\max} A_r/m_r\omega_n^2 c$ = *nondimensional valve gain*
$i_o = i/i_{\max}$ = nondimensional current
$\tau = \omega_n t$ = nondimensional time and
$d/dt = (\,)^{\cdot} = \omega_n d/d\tau = \omega_n(\,)'$

where $i_{\max}$ is the maximum current at the servovalve, $\omega_n^2 = (K_{eq}/m)$ is the natural frequency of the rotor-bearing system and $K_{eq} = K_r K/(K_r + K)$ is the equivalent stiffness of the rotor and the retainer spring. The damper effect on the stiffness of the rotor system is due to its nonlinearity, and is included in our model within the nonlinear damping coefficients. It should be noted that since we chose to nondimensionalize the parameters by using the natural frequency ω_n, then K^* and K_r^* are determined completely by the knowledge of R_k, since $K_{eq}^* = 1$, then

$$K^* = 1 + 1/R_k$$

and

$$K_r^* = 1 + R_k$$

The nondimensional form of Eqs. (1) and (2) is obtained by dividing through by $m\,\omega_n^2\,c$; thus Eqs. (1) and (2) become

$$\bar{x}_S'' + \eta\bar{x}_S' + K^*(\bar{x}_S - \bar{x}_E) = \Omega^{*2}\,U\cos\Omega^*\tau - \alpha^*\,U\sin\Omega^*\tau \quad (10)$$

$$\bar{y}_S'' + \eta\bar{y}_S' + K^*(\bar{y}_S - \bar{y}_E) = \Omega^{*2}U\sin\Omega^*\tau + \alpha^*\,U\cos\Omega^*\tau \quad (11)$$

Similarly, dividing Eqs. (3) and (4) by $m\,\omega_n^2\,c$, we get

$$\bar{x}_E'' + m_0\,\bar{C}_{xx}\bar{x}_E' + m_0\,\bar{C}_{xy}\bar{y}_E' + m_0\,K^*(\bar{x}_E - \bar{x}_S) + m_0\,K_r^*\bar{x}_E = 0 \quad (12)$$

$$\bar{y}_E'' + m_0\,\bar{C}_{yx}\bar{x}_E' + m_0\,\bar{C}_{yy}\bar{y}_E' + m_0\,K^*(\bar{y}_E - \bar{y}_S) + m_0\,K_r^*\,\bar{y}_E = 0 \quad (13)$$

Dividing Eq. (5) by $m\,\omega_n$, we get

$$\bar{C}_{ij} = B_s[\lambda C_{ijs}^* + (1 - \lambda)\frac{R^2}{L^2}\,C_{ijl}^*] \quad (14)$$

where C_{ijs}^* and C_{ijl}^* are the nondimensional short and long damper coefficients. Also, dividing Eq. (6) by $m_r\,\omega_n^2\,c$, we get

$$\lambda'' + \eta_1\,\lambda' + K_3^*\,(\lambda - 1) = F_d^* - p^* \quad (15)$$

To obtain F_d^*, we divide Eq. (8) also by $m_r\,\omega_n^2\,c$, thus

$$F_d^* = \frac{12\pi}{\epsilon}\,B_e(1 - \lambda)\left[\frac{1}{(1 - \epsilon^2)^{0.5}} - \frac{1}{(1 + \epsilon)^2}\right] \times \{\cos\psi\bar{x}_E' + \sin\psi\,\bar{y}_E'\} \quad (16)$$

Finally multiplying Eq. (9) by $A_r/m_r\,\omega_n^2\,c$, we get

$$p^{*\prime\prime} + 2\zeta_1\,\omega_r^* p^{*\prime} + \omega_r^{*2}p^* = \omega_r^{*2}\,K_1^*\,i_o \quad (17)$$

Equations (10)–(17) constitute the complete nondimensional nonlinear mathematical model for the open-loop system of Fig. 4. This model is used in the simulations described in the next section.

Simulation of the Behavior of the Open-Loop Control System

To simulate the behavior of the open-loop system, the equations developed in the previous section describing the dynamics of the complete open-loop system were implemented on a digital computer. An available computer package (SIMNON, 1990) was used for the simulations. The purpose of the simulations is to illustrate the transient behavior of the open-loop system, in particular the response of the system to a current signal at the servovalve and its effect on the dynamics of the rotor and the sealing ring in the HSFD.

The parameter values used in the simulations are as follows: $m_0 = 9.9$, $\eta = 0.01$, $K^* = 3.6$, $K_r^* = 1.384$, $R^2/L^2 = 2.25$, $B_s = 0.01295$, $B_e = 0.09881$, $\zeta_1 = 0.5$, $\omega_r^* = 8.278$, $K_1^* = 10528$, $K_3^* = 31$, $\eta_1 = 0.08$, $U = 0.1$. These nondimensional parameters correspond to the rotor design parameters at the first critical speed, and the design parameters of the HSFD, for the test rig being built. The HSFD parameters were chosen such that the long damper will be effective in suppressing the critical speeds. For the same long damper dimensions, a short damper will provide much less damping and thus allow a flexibility in providing damping to the rotor system. In general, the design of the HSFD should be optimized for suppressing the critical speeds in the long damper mode. This is a good design methodology that will also result in a relatively large clearance damper, which would allow the HSFD to be an effective high load damper.

The servovalve's parameters were selected from Moog's technical bulletin (Thayer, 1965). In addition, the rotor is assumed to be running steadily at its critical speed, thus $\Omega^* = 1.0$ and $\alpha^* = 0$. In all simulations, the initial conditions were taken as: $\bar{x}_E = \bar{y}_E = 0.01$, $\lambda = 1$, and all other variables equal to zero. It should be noted that the time scale in all the time simulations is in nondimensional time τ, and thus a unity on the time axis in the plots will represent 5.3 ms.

Figure 7 illustrates the transient behavior of the open-loop control system during operation. The simulation is started with zero input current in the servovalve, i.e., short damper mode. At $\tau = 75$, the current is suddenly switched to $i_o = 0.31$ (Fig. 7(*a*)), which is enough to change from the short damper mode to the long damper mode, i.e., a step change in the current is applied at $\tau = 75$. Figures 7(*b*, *c*) illustrate the behavior of the pressure in the sealing chambers p^* and λ to the step change in the input current. It can be seen that both p^* and λ respond almost immediately with a step in their magnitudes. There is a little transient spike in p^* that quickly disappears. The long damper mode is thus achieved in very little time. Figures 7(*d*, *e*) illustrate the displacements of the journal and the disk at the change from short to long damper modes for $U = 0.1$. These figures show a graphic display of the power and usefulness of the HSFD. The large-amplitude oscillations in the short damper mode are replaced by the small oscillations in the long damper mode, after a short transient time of about $\tau = 5$ to 10, which corresponds to about 0.0265 to 0.053 seconds. In addition, Fig. 7 shows that the transient response of the open-loop system is fast, stable, generally well behaved and achieves the required behavior.

This simulation for a step change in current resulting in a step change in amplitude response is quite dramatic and is in fact the objective of this investigation, in the sense that it is required to change the rotor behavior by actively controlling it. This has been achieved in the open-loop sense. The next step is to use feedback in order to investigate the various methods of achieving this on-off control automatically.

The simulation is repeated in Fig. 8, but with a smaller step change in current, resulting in a step change in λ equal to 0.5, i.e., a finite damper is achieved rather than either a long or a short damper. In the work of El-Shafei (1993), the HSFD operated only as a short damper or as a long damper and it was suggested that any amount of damping can be achieved from

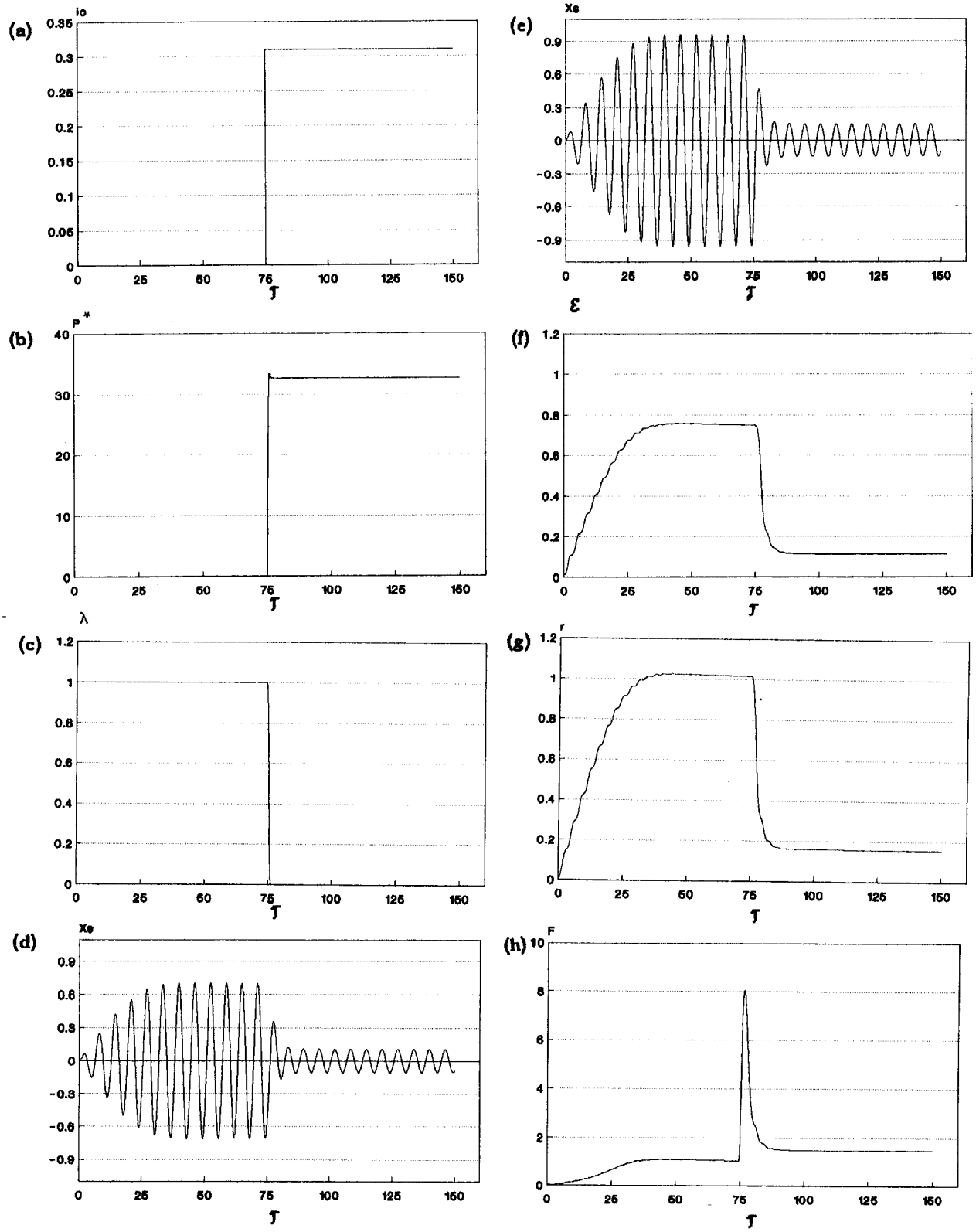

Fig. 7 Simulation of the transient behavior of the open-loop system: short damper mode to long damper mode

the HSFD, provided that the sealing rings can be accurately positioned between the two damper modes. However, when we started the current development stage of the HSFD, we were not able to position the sealing rings accurately with the HSFD design of El-Shafei (1993) shown in Fig. 1. Alternatively, we have added a spring connected to each sealing ring such that the spring acts against the applied pressure in the sealing chamber, as shown in Fig. 6, thus providing a means of controlling the sealing rings' position. Figure 8 illustrates that the finite damper can be achieved actively with this configuration, and as expected provides more damping than the short damper, but less damping than the long damper as compared with the previous simulation. This means that the controller can provide any amount of damping to the rotor that is needed to achieve the

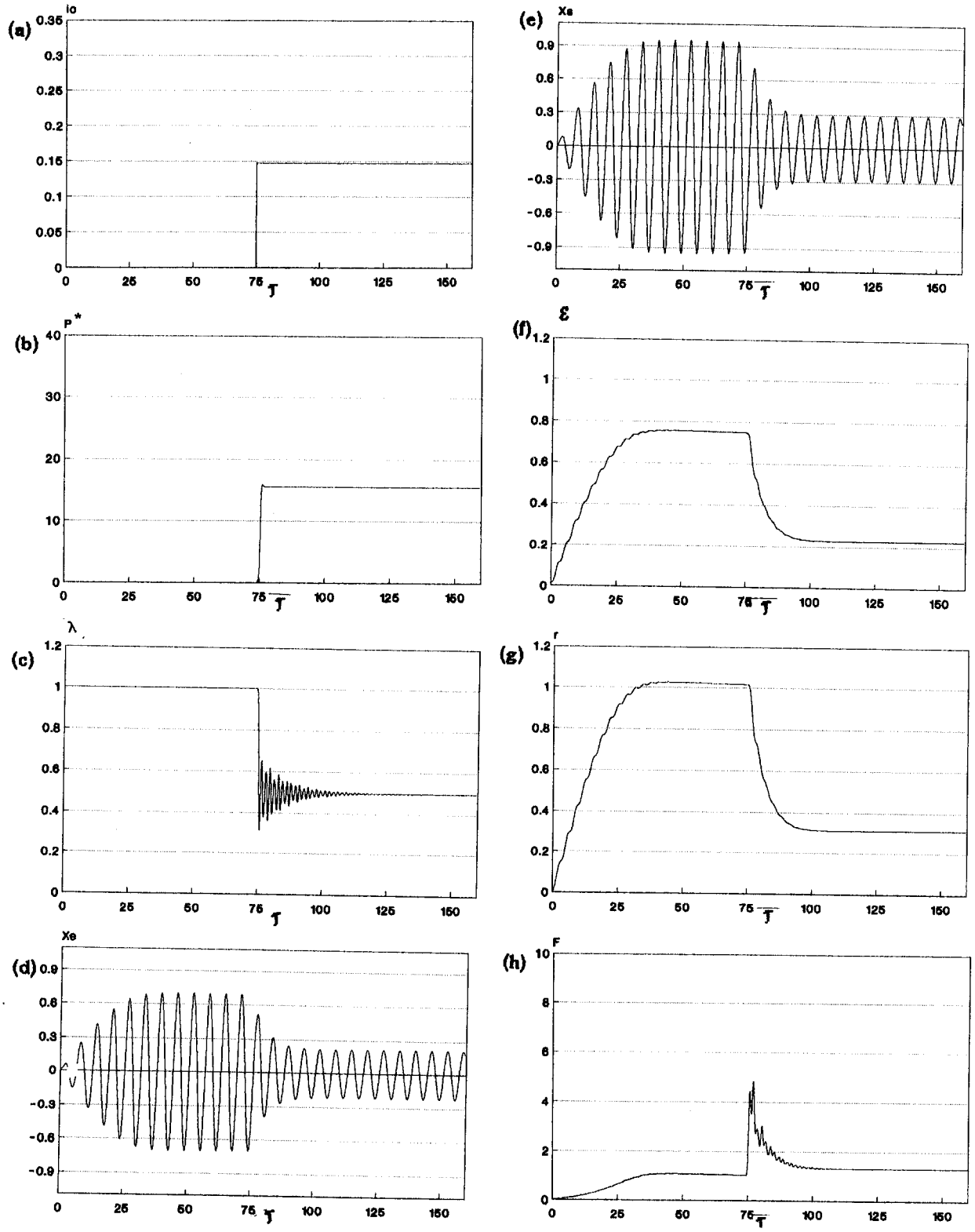

Fig. 8 Simulation of the transient behavior of the open-loop system: short damper mode to finite damper mode

required behavior under any operating conditions, provided that the amount of damping required is between that of the short and the long damper modes.

Figure 8(*c*) shows that λ, i.e., the seal ring, oscillates for time $\tau = 25$, i.e., for 0.1325 seconds about its equilibrium position. This oscillation is caused by the spring attached to the seal ring. This is an undesirable oscillation that can affect the performance of the system; thus additional damping at the seal rings will be required to dampen this oscillation. However, because of the uncertainty of the amount of damping in our test rig, this point will be investigated when the test rig is completely built.

Control Development

It is required to develop an active control algorithm for the HSFD to exploit its capabilities in providing changeable amounts

of damping to the rotor system. It is anticipated that an adaptive control algorithm will be required to achieve the full capabilities of the HSFD. However, at this stage, we limit ourselves to controlling the HSFD to obtain either the long damper mode or the short damper mode only, even though we have shown in the previous section that the HSFD is capable of providing any amount of damping between the short and long damper modes. The basic idea in this limitation, which will be removed in future development of the HSFD, is to start with the simplest algorithm in the control of the rotor system. Simplicity is a major advantage in control system development. In addition, it can be shown (Burrows et al., 1983) that for some rotor systems only two levels of damping will be required to control the behavior of the rotor system. Thus an on-off controller that can actively change between the short and long damper modes can be sufficient for the control of some classes of rotor systems.

To develop an on-off controller that changes between short and long damper modes of operation, the steady-state behavior of the system is studied. The eccentricity ratio ϵ, the vibration amplitude at rotor center r, and the transmitted damper force F (which is defined as the ratio as the damping force to the unbalance force), are studied for short and long damper modes. Figure 9 shows the short and long damper steady behavior for an unbalance of $U = 0.1$. It can be seen from Fig. 9(a) that the short damper system exhibits two critical speeds: the first at approximately $\Omega^* = 1$ and the second at approximately $\Omega^* = 7.2$. The second critical speed is due to the mass of the rotor journal m_b included in our model. On the other hand, the long damper system exhibits only one critical speed at approximately $\Omega^* = 1.2$. At all frequencies the long damper mode journal eccentricity ϵ is lower than that of the short damper mode. Figure 9(b) reveals that the second critical speed for the short damper mode is well damped for this flexible rotor. Figure 9(c) shows that the transmitted damper force in the short damper mode is always less than that of the long damper.

It can be seen from Fig. 9 that the behavior of the rotor system is speed dependent, and the long damper and short damper modes exhibit distinctly different behavior. It is thus proposed that a simple closed-loop system would rely on the feedback of the rotor speed. Other feedback laws for the on-off controller could be based on the feedback of the eccentricity ratio and/or the transmitted force (and will be investigated in the future); however, it is quite clear from Fig. 9 that the feedback on speed is quite effective in controlling the rotor vibration. On the other hand, this feedback law would rely on the knowledge of the rotor behavior at various damping levels and at various speeds. This active on-off controller can thus be actuated at specific speeds to achieve the desired damping level for that particular speed range. It is realized that such a controller will rely on the preknowledge of the system behavior; however, this is not considered to be a serious drawback since usually an elaborate analysis of the system critical speeds is done beforehand, and the results can be easily programmed into the controller. The simplicity afforded by the proposed active control strategy based on speed feedback renders it quite attractive.

As an example consider the system behavior of Fig. 9. The simple active control algorithm based on feedback of speed is applied such that the system operates in the long damper mode from rest until $\Omega^* = 1.8$, thus benefiting from the large damping provided by the long damper while the rotor traverses the critical speed. At $\Omega^* = 1.8$ the system switches to the short damper mode; hence, the first critical speed in the short damper is avoided. Noting that the damping force of the short mode is quite small with respect to the long mode in nonresonant regions, we benefit from the short mode until a speed of $\Omega^* = 3.6$; in this region the short damping force is dramatically less. At $\Omega^* = 3.6$, the system is switched to the long damper mode. The large amplitudes, associated with the second critical in the short mode, are bypassed and replaced with the smaller values of the long damper mode with a penalty of increase in the damping force. The steady-state behavior of the closed-loop

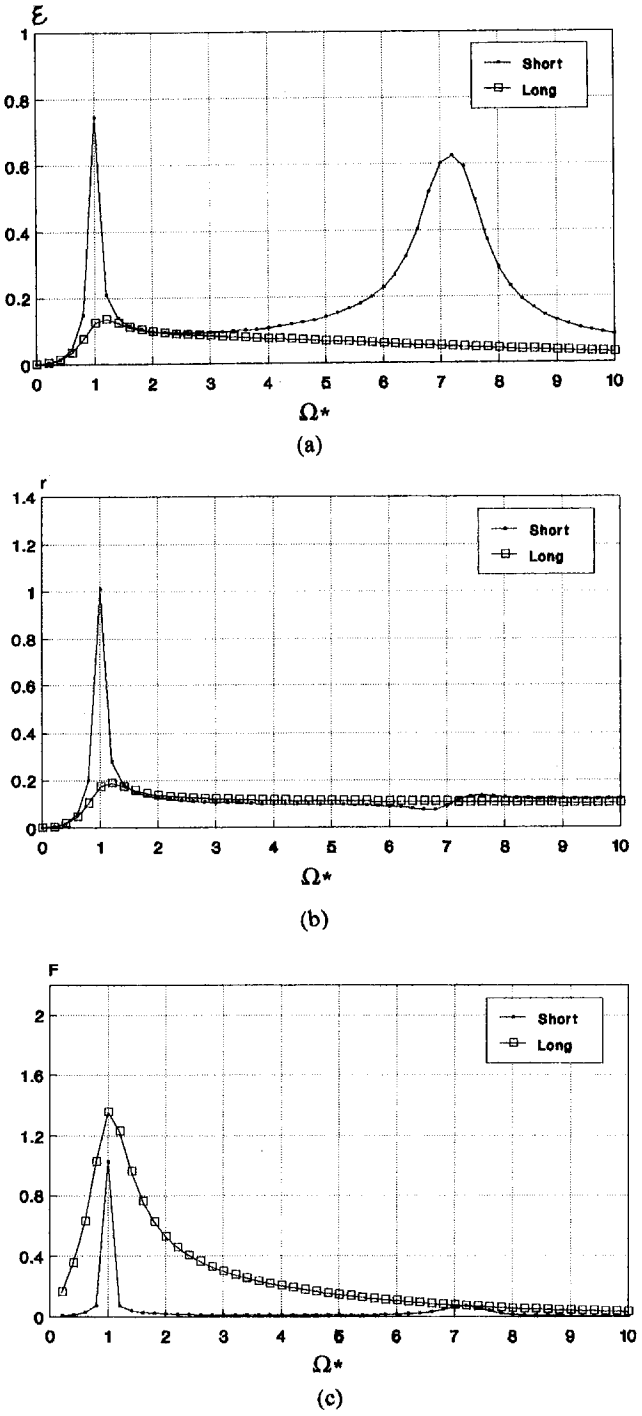

Fig. 9 Steady-state behavior of the open-loop system

system is illustrated in Fig. 10, which shows quite an improved behavior for the closed-loop system. This illustrates the power of the proposed control strategy based on speed feedback.

To assess fully the capabilities of the proposed control strategy the transient behavior of the closed-loop system during the control action is studied and is shown in Fig. 11 and 12. The transient response of the rotor system when switching to the short damper mode at $\Omega^* = 1.8$ exhibits some oscillations, which persist for about 1 second, and are due to the low damping in the short damper mode as shown in Fig. 11. However, the transient response of the rotor system is generally well behaved when switching to the high damping value at the long damper mode for the case $\Omega^* = 3.6$, as shown in Fig. 12. It can be

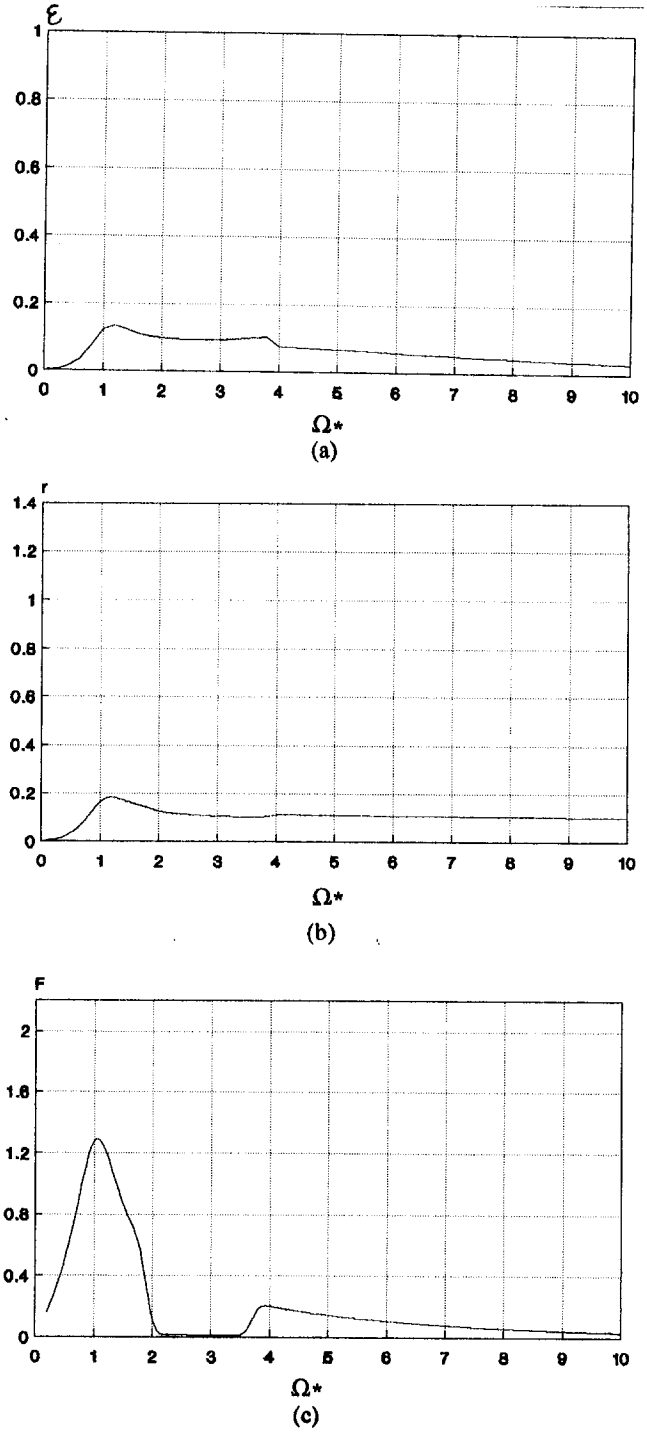

Fig. 10 Steady-state behavior of the closed-loop system

seen that the transient response of the closed-loop system is fast, stable, and achieves the required behavior. Thus the active on-off control algorithm based on speed feedback exhibits satisfactory behavior in both its transient and steady-state responses.

Conclusion

This paper summarizes the development of hybrid squeeze film dampers (HSFDs) for active control of rotor vibrations. An automatically controlled circuit was developed for the HSFD, incorporating a pressure control servovalve for controlling the pressure in the sealing chambers. A complete mathematical model of this open-loop system was developed and was implemented on a digital computer. The simulation results illustrate that the automatically controlled HSFD can be a very useful device for the active control of rotors, which can improve the performance of rotating machinery. A closed-loop control strat-

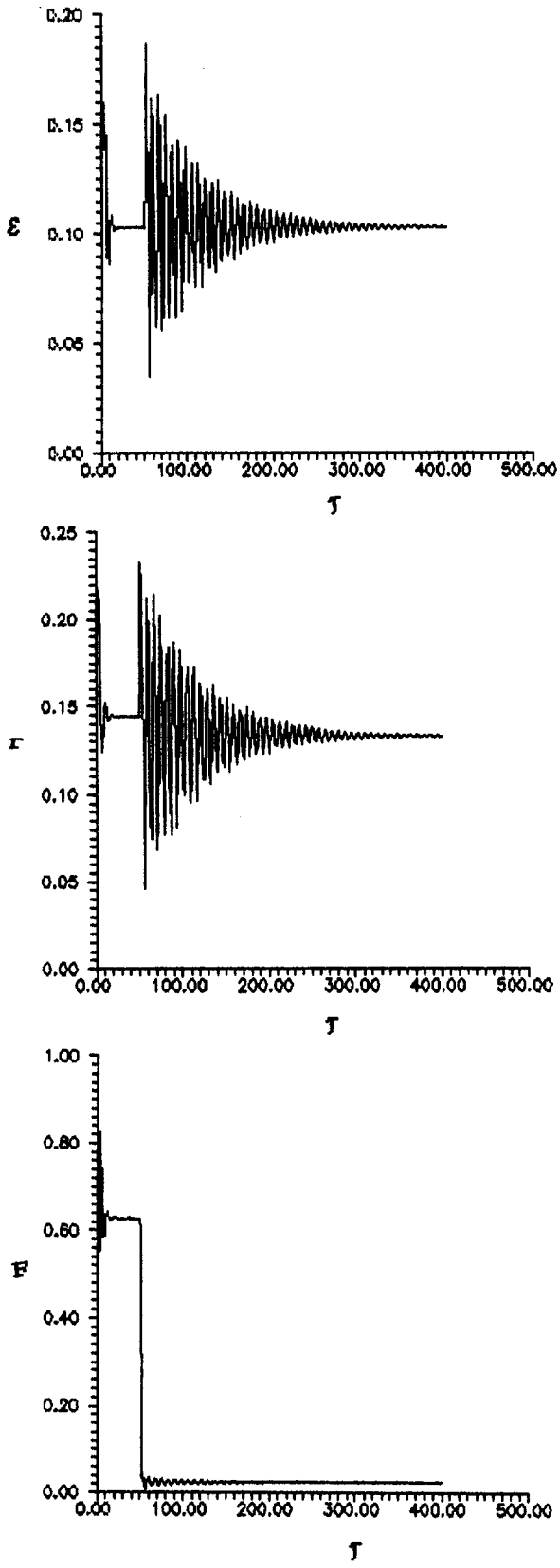

Fig. 11 Transient behavior of closed-loop system while switching from long damper mode to short damper mode at $\Omega^* = 1.8$

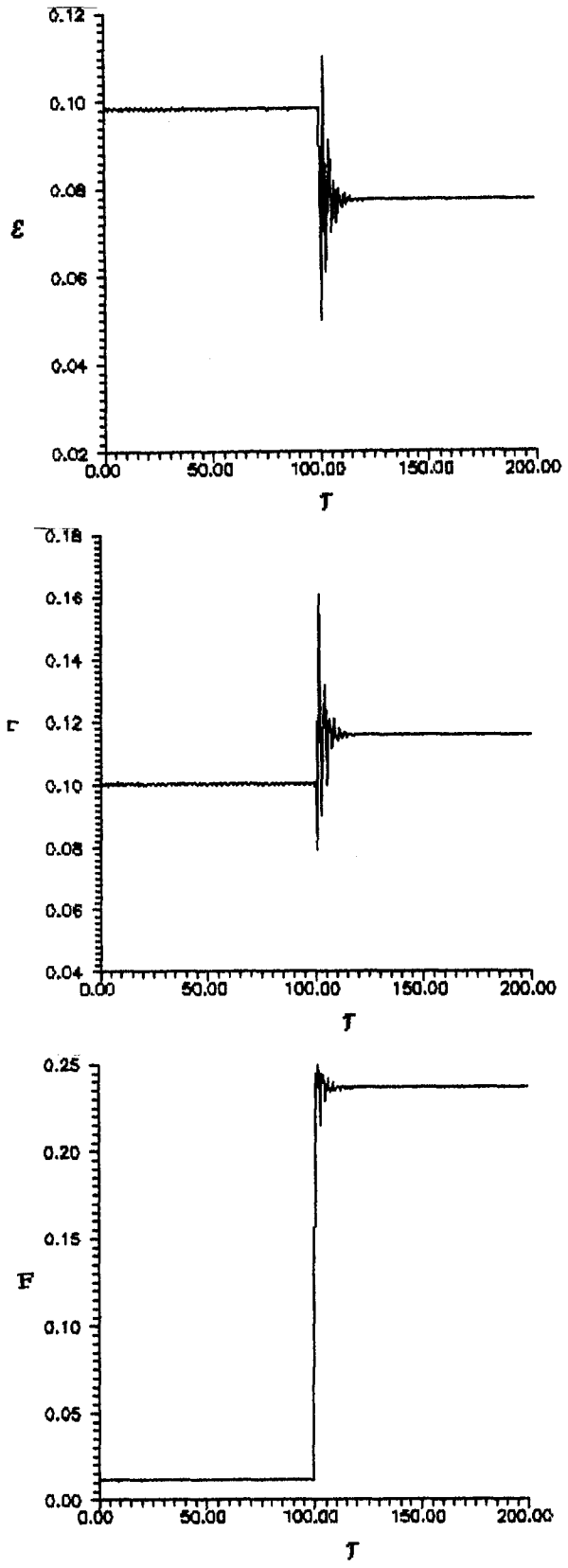

Fig. 12 Transient behavior of closed-loop system while switching from short damper mode to long damper mode at $\Omega^* = 3.6$

egy with feedback on rotor speed is also investigated. Although this active control strategy requires the knowledge of the system behavior and the value of the actual damping required at each speed beforehand, it is envisioned that this control strategy would be quite appropriate because of its simplicity. The steady-state behavior of the closed-loop system showed an overall improved behavior for the system.

Because of the variable damping properties achieved by the hybrid squeeze film damper, it is anticipated that the actively controlled HSFD can:

1 improve the vibration isolation capability of the support,
2 reduce the amplitude of vibration of the rotor,
3 enhance the stability of the rotating machine,
4 allow the rotor and damper to operate at high loads, and
5 result in a rotating machine that is capable of operating under varying and adverse conditions,

which should lead to overall improved performance and safety of rotating machinery, particularly for variable speed machinery.

Acknowledgments

The authors would like to acknowledge the fruitful discussions with Professor M. Elaraby and Mr. M. El-Hakim. The work presented in this paper was supported by EOARD, U.S. Air Force Office of Scientific Research, Grant No. F49620-92-J-0512, Dr. Wladimiro Calarese and Dr. Mark Maurice, program managers. This support is gratefully acknowledged. The U.S. Government has certain rights to this material.

References

Adams, M. L., and Zahloul, H., 1987, "Attenuation of Rotor Vibration Using Controlled-Pressure Hydrostatic Squeeze-Film Dampers," presented at the Eleventh Biennial ASME Vibrations Conference, Boston, MA, Sept.

Akin, J. T., 1990, Pratt & Whitney, private communication.

Bradfield, C. D., Roberts, J. B., and Karunendiran, S., 1989, "A Programmable Electromagnetic Bearing for Vibration Control of a Flexible Shaft," in: *Rotating Machinery Dynamics,* T. S. Sankar et al., eds., ASME DE-Vol. 18-1, pp. 335–343.

Burrows, C. R., Sahinkaya, M. N., and Turkay, O. S., 1983, "An Adaptive Squeeze-Film Bearing," ASME Paper No. 83-Lub-23.

El-Shafei, A., 1990, "Unbalance Response of a Jeffcott Rotor Incorporating Short Squeeze Film Dampers," ASME JOURNAL OF ENGINEERING FOR GAS TURBINES AND POWER, Vol. 112, pp. 445–453.

El-Shafei, A., 1991a, "Unbalance Response of a Jeffcott Rotor Incorporating Long Squeeze Film Dampers," ASME *Journal of Vibration and Acoustics,* Vol. 113, pp. 85–94.

El-Shafei, A., 1991b, "Hybrid Squeeze Film Damper for Active Control of Rotors," U.S. Patent number 5,058,452, Oct.

El-Shafei, A., and Crandall, S. H., 1991, "Fluid Inertia Forces in Squeeze Film Dampers," *Rotating Machinery and Vehicle Dynamics,* T. C. Huang et al., eds., ASME DE-Vol. 35, pp. 219–228.

El-Shafei, A., 1993, "Experimental and Analytical Investigation of Hybrid Squeeze Film Dampers," ASME JOURNAL OF ENGINEERING FOR GAS TURBINES AND POWER. Vol. 115, pp. 353–359.

El-Shafei, A., El-Hakim, M., and Hathout, J. P., 1993, "Control of Rotor Vibrations Using Hybrid Squeeze Film Dampers," Report MDP-EOARD-1/93, Cairo University, Egypt.

El-Shafei, A., and Eranki, R. V., 1994, "Dynamic Analysis of Squeeze Film Damper Supported Rotors Using Equivalent Linearization," ASME JOURNAL OF ENGINEERING FOR GAS TURBINES AND POWER. Vol. 116, pp. 682–691.

Gunter, E. J., Barrett, L. E., and Allaire, P. E., 1977, "Design of Nonlinear Squeeze Film Dampers for Aircraft Engines," ASME *Journal of Lubrication Technology,* Vol. 99, pp. 57–64.

Holmes, R., and Dogan, M., 1985, "The Performance of a Sealed Squeeze-Film Bearing in a Flexible Support Structure," *Proc. IMechE,* Vol. 199, No. C1.

Mu, C., Darling, J., and Burrows, C. R., 1991, "An Appraisal of a Proposed Active Squeeze Film Damper," ASME *Journal of Tribology,* Vol. 113, pp. 750–754.

Nonami, K., DiRusso, E., and Fleming, D. P., 1989, "Active Vibration Control for Flexible Rotor by Optimal Direct-Output Feedback Control," in: *Rotating Machinery Dynamics,* T. S. Sankar et al., eds., ASME DE-Vol. 18-1, pp. 327–334.

Palazzolo, A. B., Lin, R. R., Kascak, A. F., Montague, J., and Alexander, R. M., 1989, "Test and Theory for Piezoelectric Actuator—Active Vibration Control of Rotating Machinery," in: *Rotating Machinery Dynamics,* T. S. Sankar et al., eds., ASME DE-Vol. 18-1, pp. 367–374.

Schweitzer, G., and Ulbrich, H., 1980, "Magnetic Bearings—A Novel Type of Suspension," *Proceedings of the Second International Conference on Vibrations in Rotating Machinery,* I. Mech. E., pp. 151–156.

SIMNON, 1990, User's Guide for MS-DOS Computers, Version 3.0, SSPA systems.

Thayer, W. J., 1965, "Transfer Functions for Moog Servovalves," Moog Technical Bulletin 103.

Trumpler, P. R., 1966, *Design of Film Bearings,* MacMillan, New York.

White, D. C., 1972, "The Dynamics of a Rigid Rotor Supported on Squeeze Film Bearings," *Conference on Vibrations in Rotating Machinery, Proc. IMechE,* pp. 213–229.

Active Vibration Control of Rotating Machinery With a Hybrid Piezohydraulic Actuator System

P. Tang

A. B. Palazzolo

Texas A&M University,
College Station, TX 77843

A. F. Kascak

G. T. Montague

NASA Lewis Research Center,
Cleveland, OH 44135

An integrated, compact piezohydraulic actuator system for active vibration control was designed and developed with a primary application for gas turbine aircraft engines. Copper tube was chosen as the transmission line material for ease of assembly. Liquid plastic, which meets incompressibility and low-viscosity requirements, was adjusted to provide optimal actuator performance. Variants of the liquid plastic have been prepared with desired properties between −40°F and 400°F. The effectiveness of this hybrid actuator for active vibration control (AVC) was demonstrated for suppressing critical speed vibration through two critical speeds for various levels of intentionally placed imbalance. A high-accuracy closed-loop simulation, which combines both finite element and state space methods, was applied for the closed-loop unbalance response simulation with/without AVC. Good correlation between the simulation and test results was achieved.

Introduction

AVC has been applied to various rotor-bearing systems for suppressing vibration by adding active damping or shifting critical speeds. An AVC system consists of sensors, controller (analog or digital), power amplifiers, and actuators. Although considerable research has been done on developing effective active control algorithms, optimal control strategies, robust control, and QFT, much less has been done on actuator development. Piezoelectric actuators, magnetic bearing, and electromagnetic shakers are used as actuators due to their high bandwidth, large stroke, and force. Desirable features for actuators with AVC application on rotating machinery such as jet and rocket engine include: small size for compactness, high force and stroke, and high/low temperature operation. A closed-loop electromechanical simulation model is also essential for designing rotorbearing system AVC. Accurate predictions of forced response, critical speeds, and stability are required to assure machinery health and reliability.

The previous test results of the current authors showed unbalance, subsynchronous and transient suppression by incorporating a PD controller and piezoelectric actuator (Palazzolo et al., 1991). Subsequent papers by the authors examined electromechanical stability simulation for the piezo-actuator AVC system (Lin et al., 1991) and automated feedback gain selection (Palazzolo et al., 1993) for the piezo-actuator AVC system. Piezo stacks may be too large or environmentally susceptible to locate in the volume envelope adjacent to an aircraft engine bearing. Hence, the concept of a hydraulic actuator, remotely driven by a piezoelectric stack, was conceived. The output piston and transmission tube would be sufficiently small to position in the bearing compactment. Rashidi and DiRusso (1991) and also Ulbrich and Althaus (1992) conducted research on a hydraulic actuator system for AVC. These research efforts employed a membrane construction for the piston, which would provide a permanent seal. This configuration may be prone to accumulate bubbles reducing the effectiveness of the actuator, may fail from high cycle fatigue, or may reduce output stroke due to secondary deformation in the membrane. In addition, wear limitations, large space requirements, and low frequency response of mechanical valves limit the engineering application. Montague et al. (1991) detected leakage and fatigue problems in their membrane-type hydraulic actuator experiments. Tang (1993a, b) developed a new piezohydraulic actuator system for rotorbearing AVC. The configuration consists of a piezoelectric actuator and hydraulic transmission line with a liquid plastic fluid. AVC tests on an air turbine driven dual overhung rotating test rig verified the effectiveness of this new actuator system for different stainless tube lengths and diameters.

A closed-loop simulation of the AVC dynamic system is required to predict the system's stability, critical speeds, and unbalance response. Lin et al. (1991) used a second-order low pass electric filter to model the component's frequency characteristics. Maslen and Bielk (1991) presented an approach for coupling the frequency-dependent components of the feedback loop to a structural finite element model with generic defined transfer functions. However, no details were provided for curve fitting, state space variable transformation, and electromechanical system coupling procedure. Ku and Chen (1992) presented a F.E. based method for stability analysis of electromechanical system (ES) model for an industry pump. Ramesh and Kirk (1992) made a comparison of closed loop simulation between the F.E. approach and transfer matrix method. Tang et al. (1993a) presented a general methodology, which couples a finite element based model of the rotor with state space models of feedback control electromechanical components. This method was first applied to a cryogenic magnetic bearing test rig at NASA Lewis to predict the stability boundary and critical speeds with various feedback controllers. Good agreement was achieved between test and simulation.

This paper presents the active vibration control results of an air turbine driven test rig at NASA Lewis with a piezohydraulic actuator system. The closed-loop electromechanical simulation method, which accounts for nonideal behavior of the feedback components, is employed in predicting the unbalance response with and without active vibration control. Figure 1(*a*) shows the air turbine test rig assembly, and Fig. 1(*b*) shows the piezo-

Contributed by the International Gas Turbine Institute and presented at the 39th International Gas Turbine and Aeroengine Congress and Exposition, The Hague, The Netherlands, June 13–16, 1994. Manuscript received by the International Gas Turbine Institute February 4, 1994. Paper No. 94-GT-53. Associate Technical Editor: E. M. Greitzer.

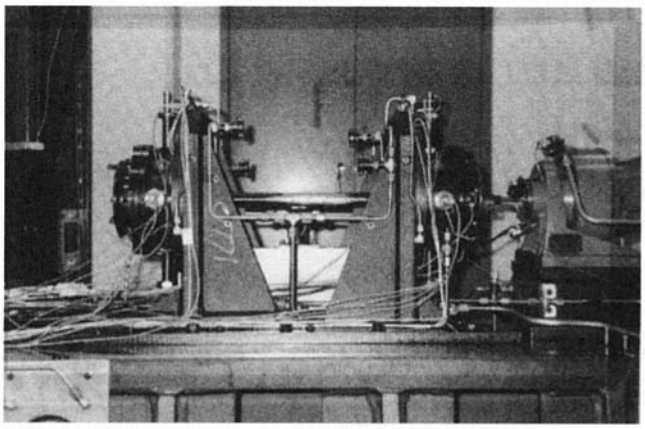

Fig. 1(*a*) AVC setup on the gas turbine test rig at NASA Lewis with piezohydraulic actuator system

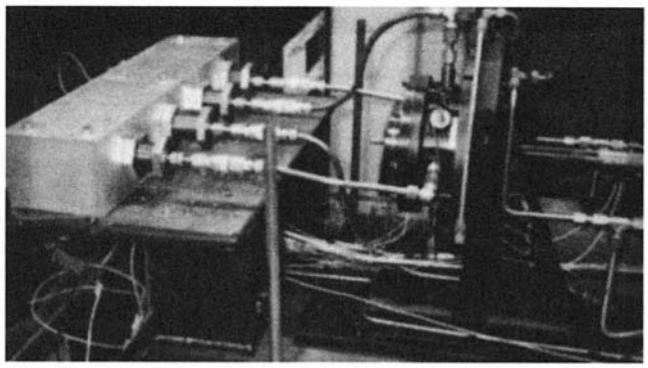

Fig. 1(*b*) Piezohydraulic actuator setup on the air turbine test rig at NASA Lewis

hydraulic actuator system. The hybrid piezohydraulic actuator consists of a piezoelectric tube and output piston/cylinder, as shown in Fig. 2. The piezo stack is rated for a 90 μm stroke, 3000. N maximum force and 3. kHz resonance. The transmission fluid is a specially developed liquid plastic (Tang, 1993) and is sealed at the pistons with double "O" rings. The tubes are vacuum filled to prevent bubble formation in the fluid.

Test Rig and System Model

A sketch of a doubly overhung, air turbine driven test rig, and a diagram of the AVC feedback electromechanical components, is shown in Fig. 3. This test rig includes a 2.5-cm-dia shaft, which is 61.0 cm in length, a 14.0 N overhung disk, which is 13.0 cm in diameter, and two squirrel cage mounted ball bearings. The closed-loop AVC system consists of a hybrid piezohydraulic actuator system, which is integrated in a block with x and y path copper tube transmission lines of OD 9.53 mm ($\frac{3}{8}$ in.), a hybrid PID controller composed of PID analog electric circuits, summer and buckout circuits, a digitally programmable low pass filter, signal amplifier, ATE power supply, and BOP power amplifier. The outboard squirrel cage bearing, which has stiffness $1.4E + 6$ N/m, is externally forced by the x and y piezohydraulic actuators. The inboard squirrel cage bearing is in passive contact with an orthogonal pair of piezoelectric actuators, which are turned off electrically and have a stiffness of $6.6E + 6$ N/m in each direction. Figure 4 shows the rotorbearing finite element model and control flow diagram for the system shown in Fig. 3. The rotor was modeled by beam elements with gyroscopics. The feedback electromechanical components are represented with independent state space equation matrices.

Transfer Function Representations of the Closed-Loop Electromechanical Model

The general equation of an n degree of freedom model for the rotorbearing system may be expressed as:

$$\begin{pmatrix} I & 0 \\ 0 & I \end{pmatrix}_{2n\times 2n} \begin{pmatrix} \ddot{X}(t) \\ \dot{X}(t) \end{pmatrix}_{2n\times 1} + \begin{pmatrix} M^{-1}C & M^{-1}K \\ -I & 0 \end{pmatrix}_{2n\times 2n} \begin{pmatrix} \dot{X}(t) \\ X(t) \end{pmatrix}_{2n\times 1} = \begin{pmatrix} M^{-1}F_u(t) \\ 0 \end{pmatrix}_{2n\times 1} + \begin{pmatrix} M^{-1}F_c(t) \\ 0 \end{pmatrix}_{2n\times 1} \quad (1)$$

where

$F_u(t)$ = unbalance force vector or external force vector ($n \times 1$)
$F_c(t)$ = control force vector ($n \times 1$)
M = mass matrix ($n \times n$)
C = damping coefficient matrix ($n \times n$)
K = stiffness coefficient matrix ($n \times n$)
$X(t)$ = displacement vector ($n \times 1$)
$\dot{\mathbf{X}}(\mathbf{t})$ = velocity vector ($n \times 1$)
$\ddot{\mathbf{X}}(\mathbf{t})$ = acceleration vector ($n \times 1$)
n = number of degrees of freedom for a rotorbearing system dynamic model

where I represents the identify matrix. Equation (1) may be time scaled to reduce the possibility of numerical problems that may occur in the closed-loop dynamic analysis.

Nomenclature

C_{active} = active damping of feedback control system
$F_{\text{out}}(s)$ = piezohydraulic actuator control force to rotorbearing system
f_c = adjustable cutoff frequency of digital programmable low pass filter
f_{co} = cutoff frequency of basic transfer function of digital programmable low pass filter
G_C = adjustable derivative path gain of hybrid controller
G_K = adjustable proportional path gain of hybrid controller
$G_d(s)$ = unit derivative path transfer function of hybrid controller
$G_p(s)$ = unit proportional path transfer function of hybrid controller
$G_i(s)$ = feedback electromechanical component transfer function representations ($i = 1, \ldots, 7$)
$G_{\text{basic}}(s)$ = basic transfer function of digital programmable low pass filter
G = control force distribution matrix
$G_{HC}(s)$ = hybrid controller transfer function
K_{active} = active stiffness of feedback control system
P = probe distribution matrix
$x^*(s)$ = rotor motion at probe location
$x^*_{in}(s)$ = hydraulic actuator input displacement, or piezoelectric actuator tip displacement
$W_i(t')$ = state space variables of feedback electromechanical component ($i = 1, \ldots, 7$)
ξ = sensitivity of the probes (7874 V/m)

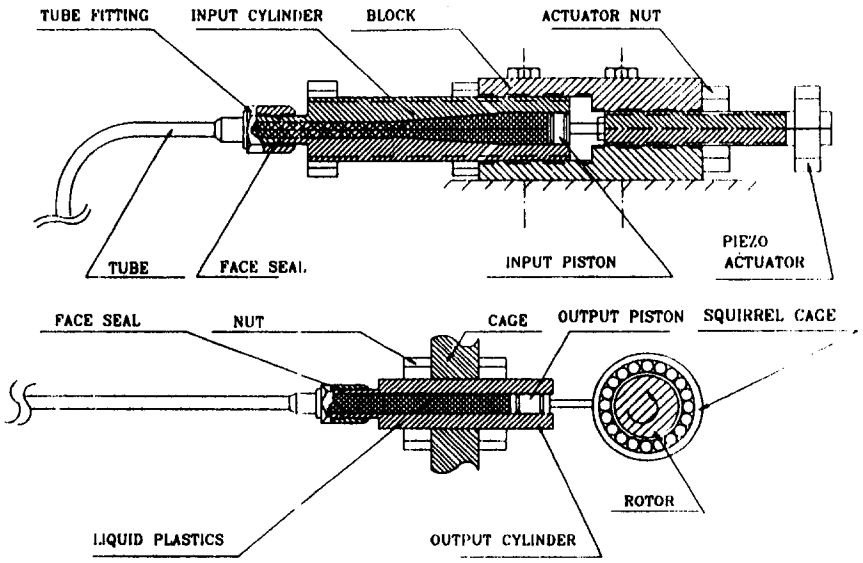

Fig. 2 Combined piezoelectric-hydraulic actuator system

We set:

$$t' = \Delta t \quad \text{and} \quad dt = \frac{1}{\Delta} dt' \tag{2}$$

where Δ represents a time scale factor (usually between $10E + 3$ and $10E + 6$). We substitute Eq. (2) into Eq. (1) to obtain the final form:

$$\begin{pmatrix} I & 0 \\ 0 & I \end{pmatrix} \begin{pmatrix} \ddot{X}(t') \\ \dot{X}(t') \end{pmatrix} + \begin{pmatrix} \frac{M^{-1}C}{\Delta} & \frac{M^{-1}K}{\Delta^2} \\ -I & 0 \end{pmatrix} \begin{pmatrix} \dot{X}(t') \\ X(t') \end{pmatrix}$$

$$= \begin{pmatrix} \frac{M^{-1}}{\Delta^2} F_u(t') \\ 0 \end{pmatrix} + \begin{pmatrix} \frac{M^{-1}}{\Delta^2} F_c(t') \\ 0 \end{pmatrix} \tag{3}$$

The dynamic characteristics of the feedback electromechanical components can be represented in transfer function forms. These forms are obtained by curve fitting experimental data to complex rational functions. This approach may yield open-loop unstable representation of the individual components, indicated by both positive and negative coefficients in the transfer function's denominator. This results from the imperfect representation of the component and may be eliminated by deleting all negative coefficient higher order terms in the denominator. These deleted terms are very small and are thus neglected. This was performed in all cases discussed below, and resulted in no detectable change in the goodness of the curve fit. It should also be recognized that open-loop instability of an individual component in the feedback loop does not necessarily produce total system instability since other sources of phase lead (damping) may exist in the system.

The PID hybrid controller consists of three main parts: PID analog circuits, summer and buckout circuit, and digital programmable low pass filter. In Fig. 4, $G_1(s)$ represents the transfer function of the hybrid controller derivative path from the rotor displacement $x^*(s)$ to the derivative output V_2. Hence,

$$G_1(s, G_C) = \frac{V_2(s)}{x^*(s)} = 1.414\xi G_C G_d^*(s)$$

$$= (1.414\xi G_C 3.97E - 5s)/(1 + 3.21E - 5s + 3.78E - 10s^2 + 2.24E - 15s^3 - 1.48E$$

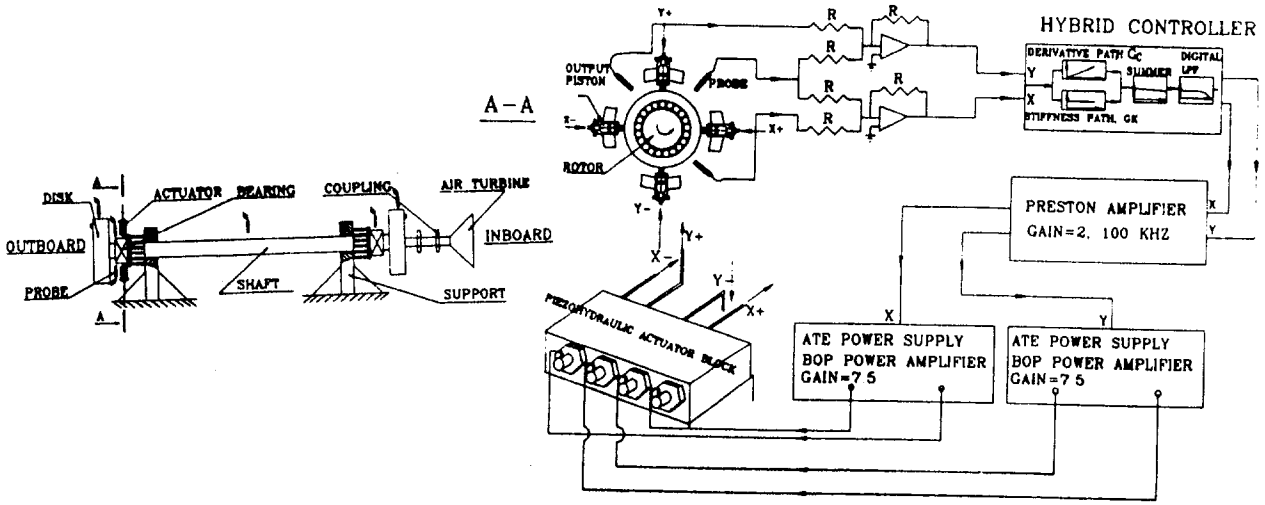

Fig. 3 AVC control system for hybrid actuator testing

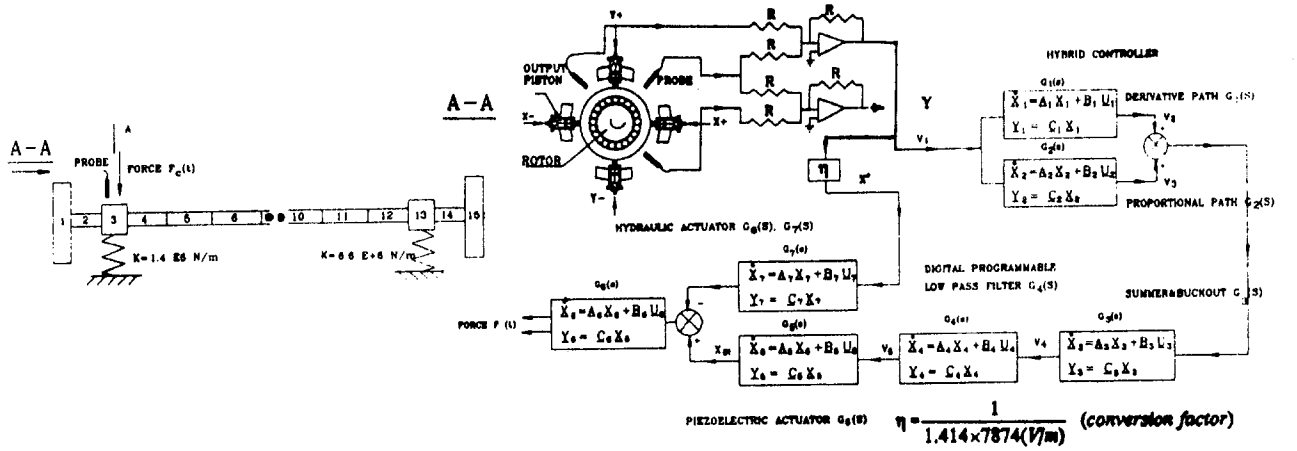

Fig. 4 Closed-loop control system for the AVC testing

$$- 21s^4 + 7.47E - 27s^5)$$
$$= (1.414\xi G_C 3.97E - 5s)/(1 + 3.21E - 5s + 3.78E - 10s^2 + 2.24E - 15s^3) \quad (4)$$

ξ is the sensitivity of the displacement probes (7874 V/m). The term 1.414ξ is the equivalent sensitivity of the probes due to their 45 deg mounting.

$x^*(s)$ is rotor displacement of the node that the probe senses

G_C is the adjustable derivative path gain of the hybrid controller

$G_d^*(s)$ is a unit transfer function of the input signal V_1 to output V_2 in Fig. 4, when $G_K = 0$, and $G_C = 1.0$.

The term $G_d^*(s)$ was measured by spectrum analysis, and has the curve fit shown in Fig. 5. The term $G_2(s)$ is the transfer function of the hybrid controller proportional path from displacement $x^*(s)$ to hybrid controller output V_3.

$$G_2(s, G_K) = \frac{V_3(s)}{x^*(s)} = 1.414\xi G_K G_p^*(s) = (1.414\xi G_K 0.92)/(1 + 1.69E - 5s + 6.39E - 11s^2 + 2.04E - 16s^3 - 8.25E - 23s^4 - 2.05E - 27s^5)$$
$$= (1.414\xi G_K 0.92)/(1 + 1.69E - 5s + 6.39E - 11s^2 + 2.04E - 16s^3 s^5) \quad (5)$$

and G_K is the adjustable proportional gain.

The term $G_p^*(s)$ is the unit transfer function of the input V_1 to output V_3 in Fig. 4, when $G_K = 1.0$ and $G_C = 0$. Figure 6 shows the curve fit for $G_p^*(s)$. The summer and buckout circuits in the controller have frequency-dependent characteristics at the higher frequency ranges. Their transfer function $G_3(s)$ is given by a curve fit to the measured transfer function as shown in Fig. 7. The term $G_4(s, f_c)$ represents the transfer function of the digitally programmable low pass filter, which has a cutoff frequency f_c.

$$G_3(s) = 0 \cdot \frac{92}{1 + 1.42E - 5s + 4.77E - 11s^2} \quad (6)$$

$$G_4(s, f_c) = \frac{K_0}{1 + b_1 s + b_2 s^2 + \ldots + b_n s^n} \quad (7)$$

The complete transfer function of the hybrid controller is a combination of Eqs. (4), (5), (6), and (7), which gives

$$G_{HC}(s) = [G_1(s, G_C) + G_2(s, G_K)]G_3(s)G_4(s, f_c) \quad (8)$$

where $G_{HC}(s)$ = hybrid controller transfer function.

The correlation of results obtained using Eq. (8) and test results at a combination of gains $G_C = 10.0$ db, and $G_K = 3$ db is shown in Fig. 9. The transfer function $G_5(s)$, which represents the dynamic model of the piezoelectric actuator in Fig. 4 is given by (Tang, 1993)

$$G_5(s) = (5.2E - 7 + 2.8E - 17s^2)/(1 + 8.843E - 16s + 1.784E - 9s^2 + 4.35E - 16s^3 + 8.26E - 20s^4) \quad (9)$$

The last component in the feedback path is the hydraulic

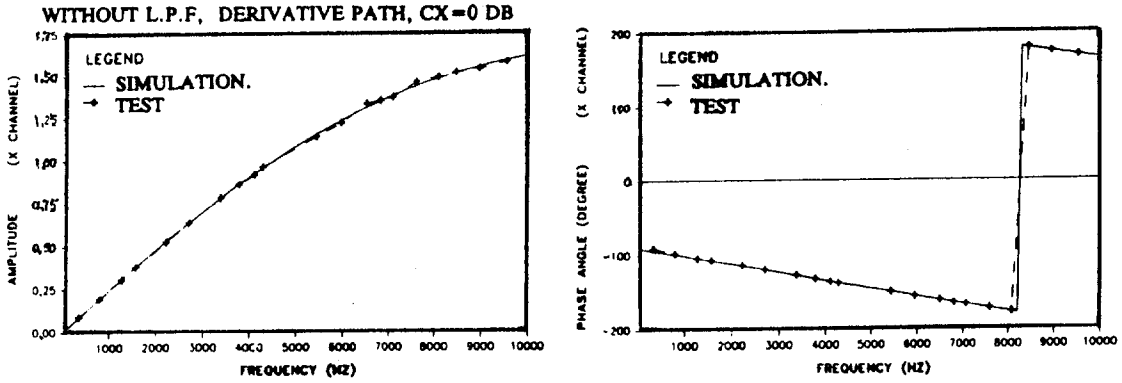

Fig. 5 Curve fit for normalized transfer function $G_d^*(s)$ of the controller derivative path

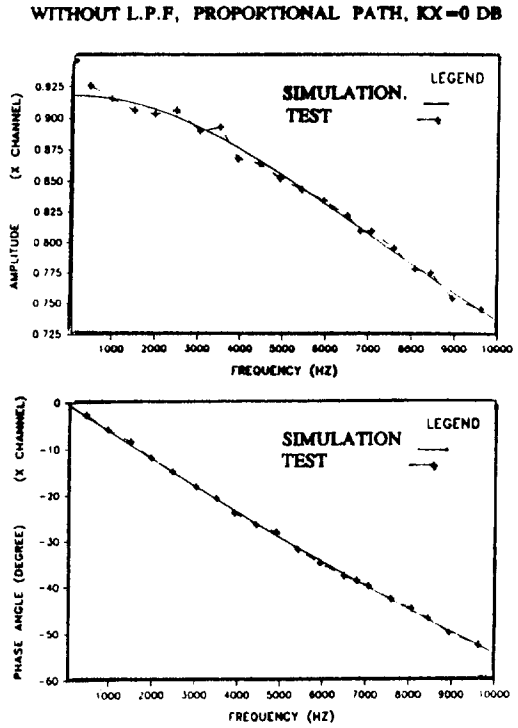

Fig. 6 Curve fit for normalized transfer function $G_5^*(s)$

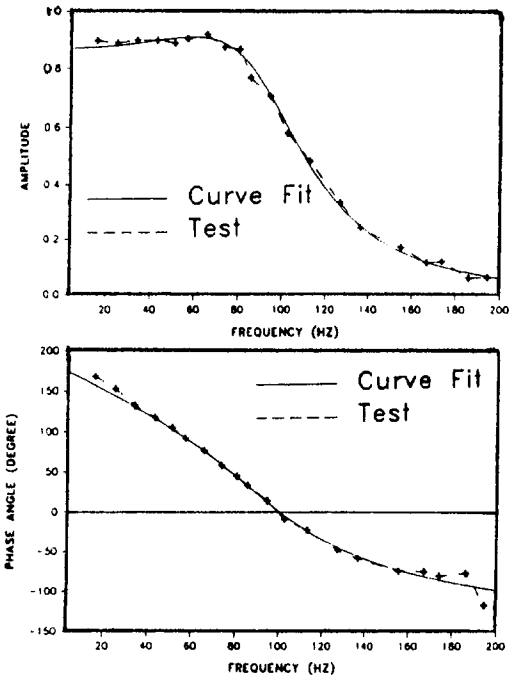

Fig. 8 Curve fit for low pass filter transfer function

actuator. Its output force characteristic was described in Tang (1993) as

$$F_{\text{out}}(s) = G_6(s)(x_{\text{in}}^*(s) - G_7(s)x^*(s)) \tag{10}$$

where

$$G_6(s) = \frac{1.36\ 10^6 + 8.726s}{1 + 1.285\ 10^{-4}s - 1.2638\ 10^{-8}s^2} \cong \frac{1.36\ 10^6 + 8.726s}{1 + 1.285\ 10^{-4}s} \tag{11}$$

$$G_7(s) = -\frac{0.42 + 1.189\ 10^{-3}s}{1 + 1.0411\ 10^{-3}s - 4.861\ 10^{-7}s^2} \cong -\frac{0.42 + 1.189\ 10^{-3}s}{1 + 1.0411\ 10^{-3}s} \tag{12}$$

$x_{in}^*(s)$ hydraulic actuator input piston displacement, or piezoelectric actuator tip displacement.

$F_{\text{out}}(s)$ the control force acting on the outboard bearing case through the hydraulic actuator output piston.

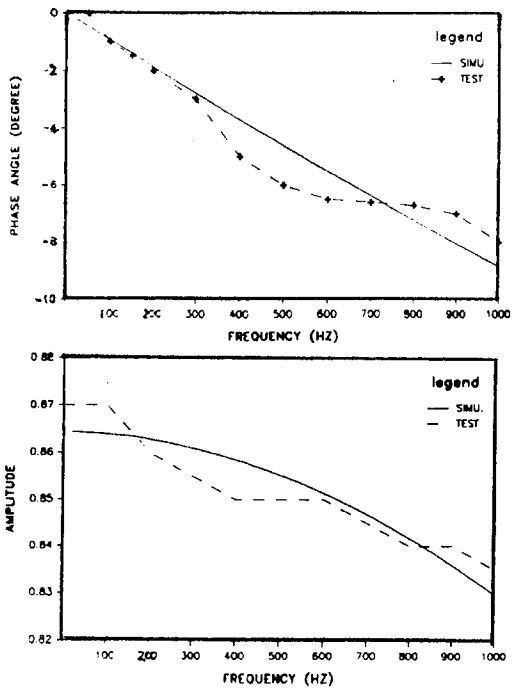

Fig. 7 Curve fit for summer and buckout electric circuit $G_3(s)$

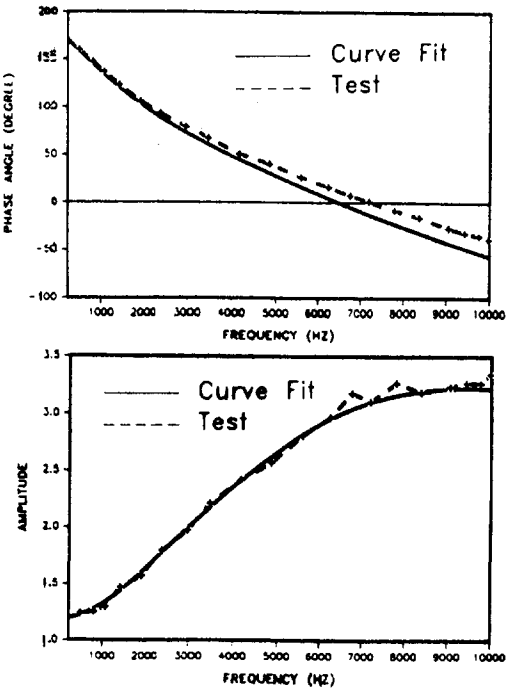

Fig. 9 Correlation of simulation and test result for complete controller transfer function $G_{HC}(s)$ at G_C = 10.0 db, G_K = 3.0 db

The terms $G_6(s)$ and $G_7(s)$ were measured in bench tests of the actuator.

State Space Representation of the Feedback Electromechanical Model

The standard state space representation of transfer functions of any feedback component can be obtained by the transform method (Tang, 1993a, b). Hence, the transfer function $G_1(s, G_C)$ of the hybrid controller derivative path in Eq. (4) can be written in state space equation form as

$$\dot{W}_1(t') = A_1 W_1(t') + B_1 x^*(t')$$
$$V_2(t') = C_1 W_1(t') \tag{13}$$

where $W_1(t')$ is a 5×1 state variable vector, and

$$A_1 = \begin{pmatrix} 0 & 1 & 0 & 0 & 0 \\ 0 & 0 & 1 & 0 & 0 \\ & & & & \ddots \\ 0 & 0 & 0 & 0 & 1 \\ -\frac{1}{\Delta^5 b_5} & -\frac{b_1}{\Delta^4 b_5} & -\frac{b_2}{\Delta^3 b_5} & -\frac{b_3}{\Delta^2 b_5} & -\frac{b_4}{\Delta b_5} \end{pmatrix},$$

$$B_1 = \begin{pmatrix} 0 \\ 0 \\ \vdots \\ 0 \\ \frac{1}{\Delta^5 b_5} \end{pmatrix} \tag{14}$$

$$C_1 = (0 \quad 1.414\xi G_c a_1 \Delta \quad 0 \quad 0 \quad 0)$$
$$a_0 = 0, \quad a_1 = -3.9E-5, \quad b_1 = 3.21E-5,$$
$$b_2 = 3.78E-10 \tag{15}$$
$$b_3 = 2.24E-15,$$
$$b_4 = -1.48E-21, \quad b_5 = -7.47E-27 \tag{16}$$

State space representations of the remaining components are listed below:

Hybrid Controller Proportional Path

$$\dot{W}_2(t') = A_2 W_2(t') + B_2 x^*(t')$$
$$V_3(t') = C_1 W_2(t') \tag{17}$$

$$A_2 = \begin{pmatrix} 0 & 1 & 0 & 0 & 0 \\ 0 & 0 & 1 & 0 & 0 \\ & & & & \ddots \\ 0 & 0 & 0 & 0 & 1 \\ -\frac{1}{\Delta^5 b_5} & -\frac{b_1}{\Delta^4 b_5} & -\frac{b_2}{\Delta^3 b_5} & -\frac{b_3}{\Delta^2 b_5} & -\frac{b_4}{\Delta b_5} \end{pmatrix},$$

$$B_2 = \begin{pmatrix} 0 \\ 0 \\ \vdots \\ 0 \\ \frac{1}{\Delta^5 b_5} \end{pmatrix} \tag{18}$$

$$C_2 = (1.414\xi G_K a_0 \quad 0 \quad 0 \quad 0 \quad 0 \quad 0) \tag{19}$$

$$a_0 = 0.92, \quad a_1 = 0, \quad b_1 = 1.69E-5, \quad b_2 = 6.39E-11$$
$$b_3 = 2.04E-16, \quad b_4 = -8.25E-23,$$
$$b_5 = -2.05E-27 \tag{20}$$

Summer and DC Bias Buckout

$$\dot{W}_3(t') = A_3 W_3(t') + B_3(V_2(t') + V_3(t'))$$
$$= A_3 W_3(t') + B_{31} W_1(t') + B_{32} W_2(t')$$
$$V_4(t') = C_3 W_3(t') \tag{21}$$

$$A_3 = \begin{pmatrix} 0 & 1 \\ -\frac{1}{\Delta^2 b_2} & -\frac{b_1}{\Delta b_2} \end{pmatrix}$$

$$B_{31} = B_3 C_2 = 1.414\xi G_C a_1 \begin{pmatrix} 0 & 0 & 0 & 0 & 0 & 0 \\ 0 & \frac{1}{\Delta b_2} & 0 & 0 & 0 & 0 \end{pmatrix} \tag{22}$$

$$B_{32} = B_3 C_3 = 1.414\xi G_K a_0 \begin{pmatrix} 0 & 0 & 0 & 0 & 0 & 0 \\ \frac{1}{\Delta^2 b_2} & 0 & 0 & 0 & 0 & 0 \end{pmatrix} \tag{23}$$

$$C_3 = (a_0 \quad 0) \tag{24}$$

$$a_0 = 0.92, \quad a_1 = 0, \quad b_1 = 1.421E-5,$$
$$b_2 = 4.775E-11 \tag{25}$$

Low Pass Filter

$$\dot{W}_4(t') = A_4 W_4(t') + B_4 V_4(t')$$
$$= A_4 W_4(t') + B_4 C_3 W_3(t')$$
$$V_5(t') = C_4 W_4(t') \tag{26}$$

$$A_4 = \begin{pmatrix} 0 & 1 & 0 & 0 \\ 0 & 0 & 1 & 0 \\ 0 & 0 & 0 & 1 \\ -\frac{1}{\Delta^4 b_4} & -\frac{b_1}{\Delta^3 b_4} & -\frac{b_2}{\Delta^2 b_4} & -\frac{b_3}{\Delta^1 b_4} \end{pmatrix}, \tag{27}$$

$$B_4 = \begin{pmatrix} 0 \\ 0 \\ \vdots \\ \frac{1}{\Delta^4 b_4} \end{pmatrix}$$

$$C_4 = (a_0 \quad 0 \quad 0 \quad 0) \tag{28}$$

$$a_0 = 0.87, \quad b_1 = \frac{3.95E-1}{f_c}, \quad b_2 = \frac{8.262E-2}{f_c^2},$$
$$b_3 = \frac{9.97E-3}{f_c^3}, \quad b_4 = \frac{5.74E-4}{f_c^4} \tag{29}$$

Piezoelectric Actuator

$$\dot{W}_5(t') = A_5 W_5(t') + B_5 V_5(t')$$
$$= A_5 W_5(t') + B_5 C_4 W_4(t')$$
$$V_6(t') = C_5 W_5(t') \tag{30}$$

$$A_5 = \begin{pmatrix} 0 & 1 & 0 & 0 \\ 0 & 0 & 1 & 0 \\ 0 & 0 & 0 & 1 \\ -\frac{1}{\Delta^4 b_4} & -\frac{b_1}{\Delta^3 b_4} & -\frac{b_2}{\Delta^2 b_4} & -\frac{b_3}{\Delta^1 b_4} \end{pmatrix},$$

$$B_5 = \begin{pmatrix} 0 \\ 0 \\ \vdots \\ \frac{1}{\Delta^4 b_4} \end{pmatrix} \tag{31}$$

$C_5 = GPA(A_0a_1a_2\Delta^2)$ where

$$(G_{PA} = G_{\text{preston}} + G_{BOP+ATE} = 15.0) \quad (32)$$

$$a_0 = 5.20E-8, \quad a_1 = 0, \quad a_2 = 2.8E-18$$

$$b_1 = 1.0E-5,$$

$$b_2 = 2.0E-5, \quad b_3 = 8.0E-15, \quad b_4 = 7.5E-19 \quad (33)$$

and

G_{preston} = Preston Amplifier Gain = 2.0, cut-off frequency 100 K Hz

$G_{BOP+ATE}$ = BOP Power Amplifier and ATE Power Supply Gain = 7.5

Hydraulic Actuator

(I)

$$\dot{W}_7(t') = A_7W_7(t') + B_7x^*(t')$$

$$V_8(t') = C_7W_7(t') \quad (34)$$

$$A_7 = \begin{pmatrix} 0 & 1 \\ -\dfrac{1}{\Delta^2 b_2} & -\dfrac{b_1}{\Delta b_2} \end{pmatrix}, \quad B_7 = \begin{pmatrix} 0 \\ \dfrac{1}{\Delta^2 b_2} \end{pmatrix} \quad (35)$$

$$C_7 = (a_0 \quad a_1\Delta) \quad (36)$$

$$a_0 = 0.42, \quad a_1 = 1.189E-3,$$

$$b_1 = 1.041E-3, \quad b_2 = -4.86E-7 \quad (37)$$

(II)

$$\dot{W}_6(t') = A_6W_6(t') + B_6C_5W_5(t') + B_6C_7W_7(t')$$

$$f_c^*(t') = 2*C_6W_6(t') \quad (38)$$

$$A_6 = \begin{pmatrix} 0 & 1 \\ -\dfrac{1}{\Delta^2 b_2} & -\dfrac{b_1}{\Delta b_2} \end{pmatrix}, \quad B_6 = \begin{pmatrix} 0 \\ \dfrac{1}{\Delta^2 b_2} \end{pmatrix} \quad (39)$$

$$C_6 = (a_0 \quad a_1\Delta) \quad (40)$$

$$a_0 = 1.36E+6, \quad a_1 = 8.726,$$

$$b_1 = 1.286E-4, \quad b_2 = -1.264E-8 \quad (41)$$

The term $f_c^*(t')$ is the control force provided by the hydraulic actuator and is the state variable output of the state space Eq. (38).

Assembly of the Closed-Loop Equations

A complete closed-loop dynamic simulation can be implemented by the following three steps. Step 1 is to identify the transfer function representations of all feedback components that were curve fitted in the previous section. Step 2 is to transform the transfer function to state space representations. Step 3 is to rearrange the state space equations and define the control force distribution matrix and sensor distribution matrix that couple the feedback electromechanical representations with the rotor-bearing dynamic model into a total system matrix.

The closed-loop dynamic equation of the air turbine test rig with the AVC is obtained by combining state space Eqs. (13), (17), (21), (26), (30), (34), and (38). Equation (3), which represents the rotor-bearing dynamic model, can be rearranged by shifting the control force vector from the right side of the equation to the left side

$$\begin{pmatrix} I & 0 \\ 0 & I \end{pmatrix}\begin{pmatrix} \ddot{X}(t') \\ \dot{X}(t') \end{pmatrix} + \begin{pmatrix} \dfrac{M^{-1}C}{\Delta} & \dfrac{M^{-1}K}{\Delta^2} \\ -I & 0 \end{pmatrix}\begin{pmatrix} \dot{X}(t') \\ X(t') \end{pmatrix}$$

$$- \begin{pmatrix} \dfrac{M^{-1}}{\Delta^2} F_C(t') \\ 0 \end{pmatrix} = \begin{pmatrix} \dfrac{M^{-1}}{\Delta^2} F_U(t') \\ 0 \end{pmatrix} \quad (42)$$

Equation (13) represents the derivative path of the hybrid controller and can be rewritten as

$$\dot{W}_1(t') - A_1W_1(t') - B_1x^*(t') = 0 \quad (43)$$

where $x^*(t')$ is the rotor displacement, which the probe senses, and can be represented by

$$x^*(t') = PX(t') \quad (44)$$

By substituting Eq. (44), Eq. (43) can also be written as

$$\dot{W}_1(t') - A_1W_1(t') - B_1PX(t') = 0 \quad (45)$$

where P is defined as the probe distribution matrix. For a probe at the ith global dof number, the P matrix has the following form:

$$P = \begin{array}{c} \\ \\ \\ \\ \\ \end{array} \begin{array}{c} \overset{i}{\text{column}} \\ \begin{pmatrix} 0 & 0 & \cdots & 0 & \cdots & 0 \\ \vdots & \vdots & \vdots & \vdots & \cdots & \vdots \\ 0 & \cdots & 1 & 0 & \cdots & 0 \\ \vdots & \vdots & \vdots & \vdots & \cdots & \vdots \\ 0 & 0 & \cdots & 0 & \cdots & 0 \end{pmatrix} \end{array} \begin{array}{l} \\ \\ \\ \\ i \text{ row} \end{array} \quad (46)$$

By substituting Eq. (46), Eq. (17), which is the state space representation of the proportional path, becomes

$$\dot{W}_2(t') - A_2W_2(t') - B_2PX(t') = 0 \quad (47)$$

Similarly, Eqs. (21), (26), (30), (34), and (38) can be rewritten as

$$\dot{W}_3(t') - A_3W_3(t') - B_{31}W_1(t') - B_{32}W_2(t') = 0 \quad (48)$$

$$\dot{W}_5(t') - A_5W_5(t') - B_5C_4W_4(t') = 0 \quad (49)$$

$$\dot{W}_6(t') - A_6W_6(t') - B_6C_5W_5(t') - B_6C_7W_7(t') = 0 \quad (50)$$

and

$$\dot{W}_7(t') - A_7W_7(t') - B_7x^*(t') = 0 \quad (51)$$

$$\dot{W}_7(t') - A_7W_7(t') - B_7PX(t') = 0 \quad (52)$$

For Eq. (38), the control force can be written as

$$f_c^*(t') - 2*C_6W_6(t') = 0 \quad (53)$$

We define

$$F_C(t') = \begin{pmatrix} 0 \\ \vdots \\ 1 \\ 0 \\ \vdots \end{pmatrix} f_c^*(t') = Gf_c^*(t') = 2.0GC_6W_6 \quad (54)$$

where G is called the control force distribution matrix. If the actuator is located at global degree of freedom number j, G has the following form:

$$G = \begin{pmatrix} 0 \\ \vdots \\ 1 \\ 0 \\ \vdots \end{pmatrix} j\text{th row} \tag{55}$$

By combining Eqs. (42), (45), (47), (48), (50), (51), (52), and (53), the closed-loop system dynamic equations can be written into a state space representation as

$$\dot{Z} + QZ = F \tag{56}$$

where

Q dynamic matrix of closed loop AVC system
Z state space variable vector of closed loop AVC system
F state space force vector of closed loop AVC system

$$Q = \begin{pmatrix} \frac{M^{-1}C}{\Delta} & \frac{M^{-1}K}{\Delta^2} & \underline{0} & \underline{0} & \underline{0} & \underline{0} & -\frac{2M^{-1}GC_6}{\Delta^2} & \underline{0} & \underline{0} \\ -I & \underline{0} & \underline{0} & \underline{0} & \underline{0} & \underline{0} & \underline{0} & \underline{0} & \underline{0} \\ \underline{0} & -B_1P & -A_1 & \underline{0} & \underline{0} & \underline{0} & \underline{0} & \underline{0} & \underline{0} \\ \underline{0} & -B_2P & \underline{0} & -A_2 & \underline{0} & \underline{0} & \underline{0} & \underline{0} & \underline{0} \\ \underline{0} & \underline{0} & -B_{31} & -B_{32} & -A_3 & \underline{0} & \underline{0} & \underline{0} & \underline{0} \\ \underline{0} & \underline{0} & \underline{0} & \underline{0} & -B_4C_3 & -A_4 & \underline{0} & \underline{0} & \underline{0} \\ \underline{0} & \underline{0} & \underline{0} & \underline{0} & \underline{0} & -B_5C_4 & -A_5 & \underline{0} & \underline{0} \\ \underline{0} & \underline{0} & \underline{0} & \underline{0} & \underline{0} & \underline{0} & -B_6C_5 & -A_6 & -B_6C_5 \\ \underline{0} & -B_7P & \underline{0} & \underline{0} & \underline{0} & \underline{0} & \underline{0} & \underline{0} & -A_7 \end{pmatrix},$$

$$F = \begin{pmatrix} \frac{M^{-1}}{\Delta^2} F_U(t') \\ \underline{0} \\ \underline{0} \\ \underline{0} \\ \underline{0} \\ \underline{0} \\ \underline{0} \\ \underline{0} \\ \underline{0} \\ \underline{0} \end{pmatrix} \tag{57}$$

The unbalance force in Eq. (56) can be written as

$$F_U(t') = m_e\omega^2 C_e \begin{pmatrix} \sin \omega t' & (X \text{ direction}) \\ \cos \omega t' & (y \text{ direction}) \end{pmatrix} \tag{58}$$

The steady response of the state variable vector is

$$Z = \underline{Z} \sin \omega t' \tag{59}$$

where

m_e unbalance mass
C_e eccentricity distance
ω frequency (rad/s)
$\underline{Z}$ the complex amplitude of the state space vector

The unbalance response of a system with AVC can be obtained by solving Eq. (56). The stability analysis of a closed-loop AVC system can be performed by letting

$$F = 0, \quad \text{and} \quad Z = \underline{Z}e^{\lambda t'} \tag{60}$$

and solving the following eigenvalue and eigenvector problem:

$$(\lambda I + Q)\underline{Z} = 0 \tag{61}$$

where λ is the eigenvalue and $\underline{Z}$ is the eigenvector.

Correlation of Simulation and Test Results

Active vibration control was used on the air turbine test rig with the piezohydraulic actuator system at NASA Lewis, shown in Figs. 1(*a*), 1(*b*), and 2. The tests were performed to compare unbalance response with and without control. Unbalance response test results were obtained by adding an imbalance to the outboard disk at a radius of 50.8 mm (2.0 in.) and measuring the unbalance response at the outboard disk, outboard bearing, middle shaft, inboard bearing, and inboard disk. Figures 10 and 11 show the first and second mode shapes with the piezohydraulic actuator and feedback PD control at gains $G_K = 5.6$, and $G_C = -40.0$. The first natural frequency in Fig. 11 is less than without control due to an active stiffness (controller proportional gain is 5.6), which shifted the first natural frequency down to about 90 Hz.

Closed-loop unbalance response simulation was obtained by solving Eq. (56) with various test parameters (unbalance mass, controller gains, and probe locations). Figures 12 and 13 show the correlation of simulation and test results for unbalance responses (an unbalance mass $m_e = 0.6$ g on the outboard disk) in the X direction at the outboard bearing location, and outboard disk location, respectively. The passive tare dampings employed to match the uncontrolled response were 150 and 50 N.S./m, and were applied at the outboard bearing location and inboard bearing location, respectively. The derivative gain and proportional gain of the hybrid controller are -40 and 5.6, respectively. The feedback active damping and active stiffness can be calculated by multiplying the derivative path transfer functions

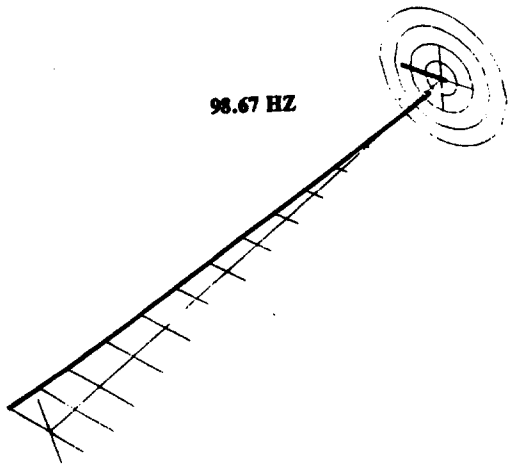

Fig. 10 First mode shape of the air turbine with piezohydraulic actuator system AVC (gains $G_K = 5.6$, $G_C = 40.0$) (98.67 Hz)

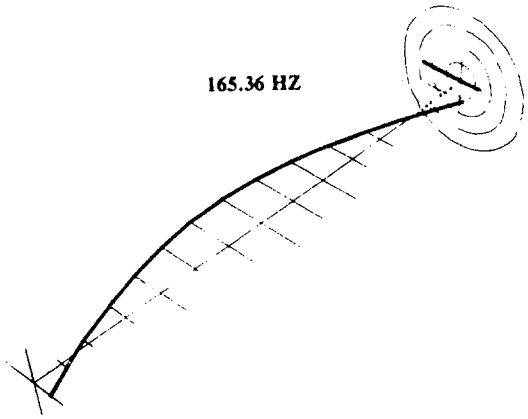

Fig. 11 Second mode shape of the air turbine with piezohydraulic actuator system AVC (gains $G_K = 5.6$, $G_C = 40.0$) (165.36 Hz)

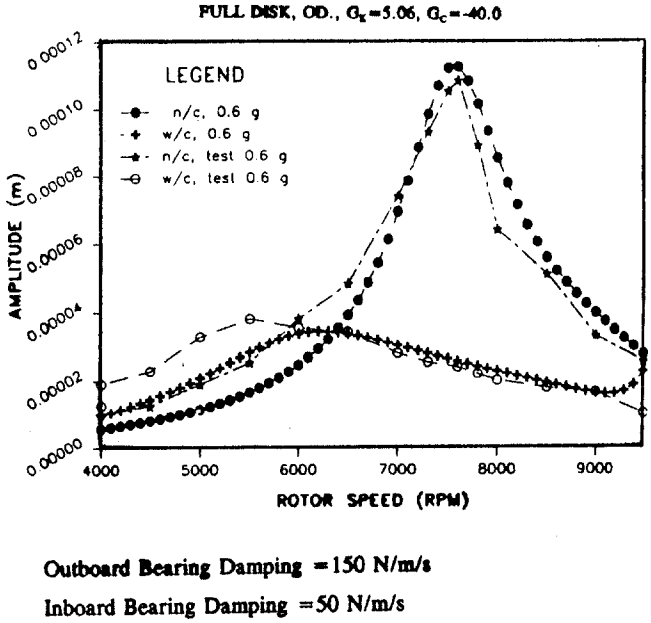

Fig. 12 The simulation and test unbalance responses at outboard disk location with/without AVC

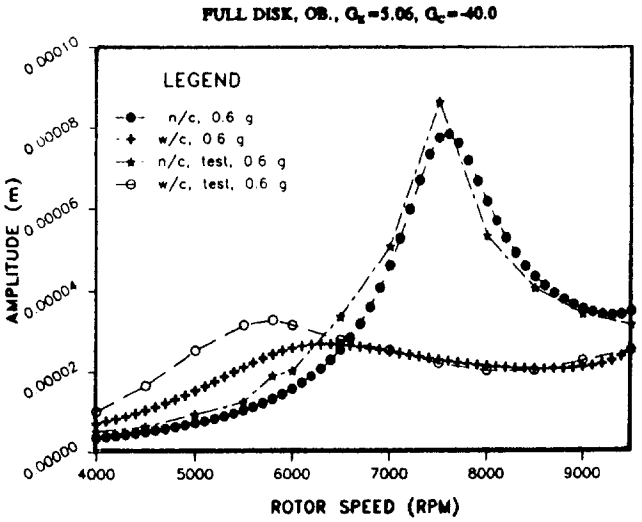

Fig. 13 The simulation and test unbalance responses at outboard bearing location with/without AVC

at frequency = 0 or $s = 0$. Hence, from Fig. 4, the active damping can be written as

$$C_{\text{active}} = 1.414\xi\left(\left(\frac{G_1(s)}{s}\right)G_3(s)G_4(s)G_5(s)G_6(s)\right)_{s=0} \quad (62)$$

and from Eqs. (4), (6), (7), (9), and (11), Eq. (62) can be written as

$$C_{\text{active}} = 1.414 \times 7874 \times 3.97E-5 \times |G_C| \times 0.92 \times 0.87 \times 15 \times 5.2E-7 \times 2 \times 1.36E+6 \text{ Ns/m} \quad (63)$$

When $G_C = -40.0$, the active damping is

$$C_{\text{active}} = 1.414 \times 7874 \times 3.97E-5 \times 40.0 \times 0.92 \times 0.87 \times 15 \times 5.2E-7 \times 2 \times 1.36E+6 = 300 \text{ N s/m} \quad (64)$$

Similarly, by multiplying the proportional path transfer functions, the active stiffness can be written as

$$K_{\text{active}} = 1.414\xi(G_2(s)G_3(s)G_4(s)G_5(s)G_6(s))_{s=0} \quad (65)$$

By applying Eqs. (5), (6), (7), (9), (11), and $G_K = 5.6$, the active stiffness is:

$$K_{\text{active}} = 1.414 \times 7874 \times 0.92 \times 5.6 \times 0.92 \times 0.87 \times 15 \times 5.2E-7 \times 2 \times 1.36E+6 = 0.974E+6 \text{ N/m} \quad (66)$$

Figure 14 shows the effectiveness of the AVC with increasing

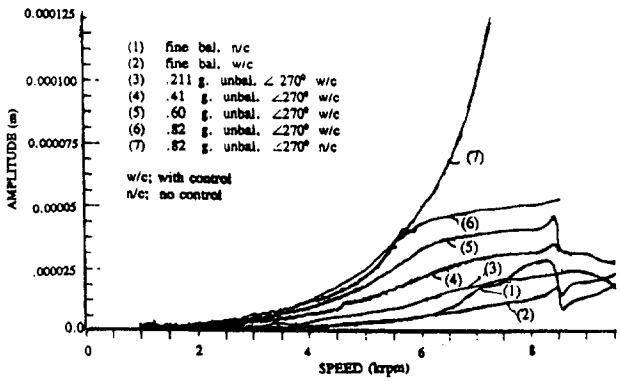

Fig. 14 Test imbalance responses with various imbalance masses at outboard disk location in y direction with/without AVC

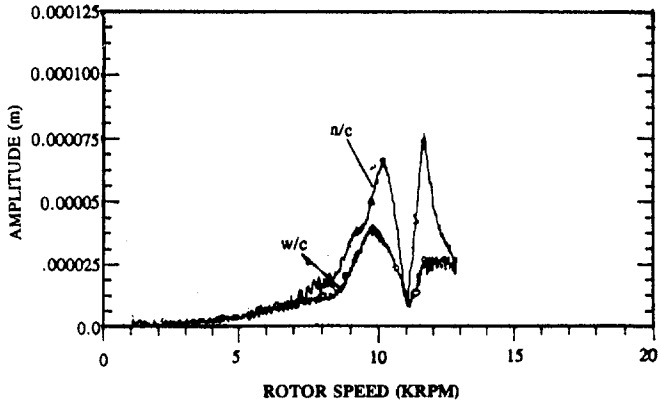

Fig. 15 Test unbalance responses of outboard bearing location with/without AVC with outboard ring removed

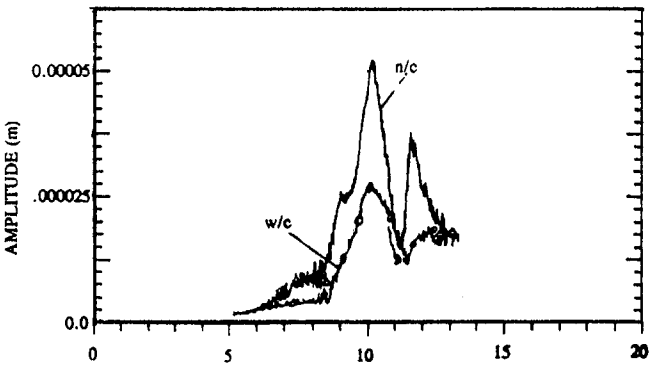

Fig. 16 Test unbalance responses of outboard disk location with/without AVC with the outboard ring removed

levels of imbalance. Figures 15 and 16 show the unbalance responses at the outboard bearing and outboard disk locations after removing a ring that weighs 8.04 N (1.8 lb) from the outboard disk to raise the critical speeds. Significant reductions in vibration were again achieved by the hybrid actuator system.

Summary and Conclusions

A compact piezohydraulic actuator system using liquid plastic as a transmission fluid, and a copper tube as a transmission line, was employed in AVC of an air turbine test rig. Significant reductions of vibration were achieved at the first critical speed. A closed-loop unbalance response simulation with AVC was also developed in this research. The new dynamic models of the piezoelectric actuator, hydraulic actuator, and digital programmable low pass filter were included in the closed-loop system modeling. Transfer functions were identified from measured data and state space representations were employed to account for the nonideal behavior of the feedback electromechanical components. This simulation approach was verified by good agreement with test results.

Acknowledgments

The authors thank NASA Lewis and the U.S. Army at NASA Lewis for funding this research. Sincere appreciation is also extended to Mr. Daniel Manchala for his assistance in testing and data acquisition, and Dr. Wenduan Li (Texas A&M University, Chemical Engineering) and Renee Udell for their assistance in the hydraulic actuator bench test.

References

DiRusso, E., and Brown, G. V., 1992, "Tests of a Cryogenic Magnetic Bearing With Permanent Magnet Bias," *Proceedings of the Third International Symposium on Magnetic Bearings,* Alexandria, VA.

Ku, C.-P. R., and Chen, H. M., 1992, "An Efficient Method for Stability Analysis for Active Magnetic Bearing System," *Proceedings of the Third International Symposium on Magnetic Bearings,* Alexandria, VA, July, pp. 133–142.

Lin, R. R., 1990, "Active Vibration Control of Rotorbearing Systems Utilizing Piezoelectric Pushers," Dissertation, Texas A&M University, Dept. Mechanical Engineering, pp. 49–50.

Lin, R. R., Palazzolo, A. B., Kascak, A. F., and Montague, G. T., 1991, "Electromechanical Simulation and Testing of Actively Controlled Rotordynamic Systems With Piezoelectric Actuators," ASME Paper No. 91-GT-245; ASME JOURNAL OF ENGINEERING FOR GAS TURBINES AND POWER, Vol. 115, 1993, pp. 324–335.

Maslen, E. H., and Bielk, J. R., 1991, "Implementing Magnetic Bearing in Discrete Flexible Structure Models," submitted to ASME *Journal of Dynamic Systems, Measurement, and Control.*

Montague, G., et al., 1991, "Hydraulic Actuator for Active Vibration Control," Senior Project, Cleveland State Univ., Dept. of Mechanical Engineering, June.

Palazzolo, A. B., Lin, R. R., Alexander, R. M., Kascak, A. F., and Montague, G., 1991, "Test and Theory for Piezoelectric Actuator-Active Vibration Control of Rotating Machinery," ASME *Journal of Vibration and Acoustics,* Vol. 113, pp. 167–175.

Palazzolo, A. B., Jagannathan, S., Kascak, A. F., Montague, G. T., and Kiraly, L. J., 1993, "Hybrid Active Vibration Control of Rotorbearing Systems Using Piezoelectric Actuators," ASME *Journal of Vibration and Acoustics,* Vol. 115, pp. XX–00.

Ramesh, K., and Kirk, R. G., 1992, "Subharmonic Resonance Stability Prediction for Turbomachinery With Active Magnetic Bearings," *Proceedings of the Third International Symposium on Magnetic Bearings,* Alexandria, VA, July, pp. 113–122.

Rashidi, M., and DiRusso, E., 1991, "Design of a Hydraulic Actuator for Active Control of Rotating Machinery," ASME Paper No. 91-GT-246; ASME JOURNAL OF ENGINEERING FOR GAS TURBINES AND POWER, Vol. 115, 1993, pp. 336–340.

Tang, P., Palazzolo, A. B., et al., 1993a, "An Electromechanical Simulation Method for Active Vibration Control of a Magnetic Bearing Supported Rotor," ASME Paper No. 93-GT-386.

Tang, P., Palazzolo, A. B., et al., 1993b, "Combined Piezoelectric-Hydraulic Actuator Based Active Vibration Control for Rotordynamic System," ASME DE-Vol. 62.

Tang, P., 1993, "A Combined Piezoelectric-Hydraulic Actuator System and an Electromechanical Simulation Method for Active Vibration Control of Rotordynamic Systems," Dissertation, Texas A&M University, Mechanical Engineering, Sept. pp. 90–109.

Ulbrich, H., and Althaus, J., 1992, "Active Bearing for Rotating Machinery," presented at Fourth International Symposium on Transport Phenomena and Dynamics of Rotating Machinery (ISROMAC-4), Hawaii, Apr. 5–8.

Development of 300 kW Class Ceramic Gas Turbine (CGT303)

I. Ohhashi

S. Arakawa

CGT Project Team,
Technical Research Division,
Yanmar Diesel Engine Company, Limited,
Kyoto, Japan

CGT303 is a two-shaft regenerative ceramic gas turbine with rotary heat exchangers for the purpose of mobile power generator. It is also widely adaptable for industrial machinery and construction machinery as well. The development program of CGT303 is funded by the New Energy and Industrial Technology Development Organization (NEDO). The maximum output power of 300 kW and thermal efficiency of 42 percent at TiT *1350°C are the objectives of this development. The high* TiT *requires all gas passage components to be made of ceramics that are designed appropriately to keep sufficient strength by using sophisticated computer analysis. Hot spin tests on ceramic turbine rotors and thermal shock tests on stationary ceramic components have been carried out to prove their strength. The paper covers the design concept of CGT303 and results of analysis.*

Introduction

A ceramic gas turbine is expected to have many excellent characteristics such as low fuel consumption, low exhaust emissions, multifuel adaptability, etc. In Japan, the three types of ceramic gas turbine (CGT) for cogeneration and for mobile power generator have been researched and developed since 1988, as a part of the "Moonlight Project" conducted by the Agency of Industrial Science and Technology in Ministry of International Trade and Industry (MITI).

A two-shaft regenerative ceramic gas turbine CGT303 has been developed as a power unit for a mobile power generator, by Yanmar Diesel Co., Ltd., Niigata Engineering Co., Ltd., Kyocera Corporation, NGK Spark Plug Co., Ltd., and NKK Corporation.

Considering the usage, the power unit should be small in size and light in weight. Generally the rotary regenerative heat exchanger is lighter and more compact than other heat exchangers, such as recuperators adopted to CGT301 and CGT302, and it is also excellent in terms of heat exchange. CGT303 is equipped with two of these heat exchangers on both sides of the engine. The thermal effectiveness of the rotary regenerative heat exchanger at its design point, i.e., at 300 kW and turbine inlet temperature (TiT) of 1350°C, is expected to be more than 92 percent. With the premise of this thermal effectiveness, the optimum pressure ratio of the compressor in order to attain the target thermal efficiency is selected to be 4.5.

Another requirement for the power unit for a mobile power generator is to maintain high thermal efficiency when partially loaded. For this reason, the nozzle upstream of the power turbine has a variable geometry system controlled corresponding to the load.

In developing CGT303, there are three stages to be followed in order to attain the objectives of thermal efficiency of 42 percent at TiT 1350°C:

First stage: TiT 900°C. Engine components are made of metal. Performance characteristics of main components to be verified and function of bearing, gear, and control units, etc., to be established;

Second stage: TiT 1200°C. Ceramic components built in to endure high temperature to be examined;

Third stage: TiT 1350°C. Adjustment of power unit matching with heat exchanger as well as substituting premixed lean burn combustor for conventional diffusional combustor, and securing of ceramics reliability to be studied in order to attain the objective (thermal efficiency of 42 percent)

Today, the second-stage program is proceeding. Engine heat flow and specifications are shown in Fig. 1 and Table 1.

Design Concept

The cross section of the ceramic gas turbine is illustrated in Fig. 2. For CGT303, ceramics are used mainly in combustor, gas generator turbine and power turbine, their nozzles, scroll, shroud, intermediate ducts, and heat exchangers, which form a hot gas passage.

For ceramic components whose fracture toughness is low, flexibility of support to reduce stress from interference between mutually adjecent components is a great concern. In order to improve concentric alignment of ceramic components and to facilitate their assembly or disassembly, ceramic components are divided into five units in functional terms; they are, from upstream, combustor, gas generator turbine, intermediate duct, power turbine, and heat exchanger, which are supported independently.

The gas generator unit comprises a single-stage centrifugal compressor, combustor, and a radial-inflow turbine. For the single-stage centrifugal compressor, 26 impeller blades (including 13 short blades) and outer diameter of 183 mm are selected. The tip speed of the impeller at the design point (55,000 rpm) is 527 m/s. At this time, this compressor attained a pressure ratio of 4.3 and compressor efficiency of 82.4 percent. In order to get the aimed pressure ratio of 4.5 and the specified surge margin, further modifications will be made.

The combustor is a single can type, mounted tangentially to the scroll swirling direction. In the first and second stages of the CGT development program, the conventional diffusional combustor has been set prior to the premixed lean burn combustor for the final stage.

With respect to the gas generator turbine, the purpose of adopting the radial-inflow concept against the axial flow one is explained as follows;

1 The material temperature decreases with decreasing radius ratio for given expansion ratio and so the temperature at the blade root, where the highest stress occurs, will be kept

Contributed by the International Gas Turbine Institute and presented at the 39th International Gas Turbine and Aeroengine Congress and Exposition, The Hague, The Netherlands, June 13–16, 1994. Manuscript received by the International Gas Turbine Institute February 14, 1994. Paper No. 94-GT-82. Associate Technical Editor: E. M. Greitzer.

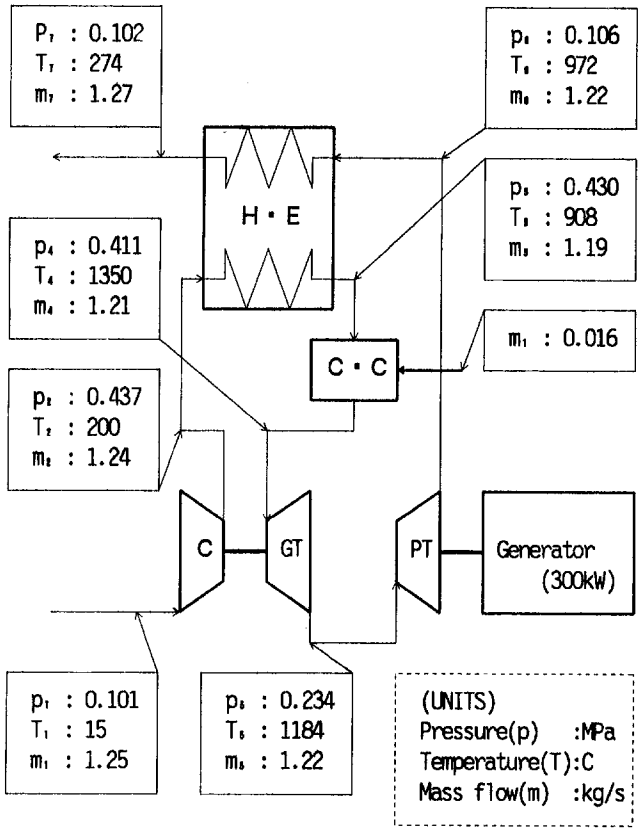

Fig. 1 Engine heat flow

low. This will be advantageous to ensure the sufficient strength of components;

2 The rotor has a simple shape with smaller number of blades, which are allowed to be thicker;

3 The ceramic radial–inflow turbine has been successfully producted for turbochargers. Therefore, this technology and experience are applicable to manufacturing process for this radial inflow turbine rotor.

For the power turbine, an axial turbine allows a compact and simple gas passage from the gas generator turbine through to the power turbine. "Hybrid concept" with ceramic blades set in the metal disk is selected to minimize the size of the ceramic components. For the nozzle of power turbine, a variable geometry system is adopted so that the engine can keep high thermal efficiency over a wide range load. The nozzle blades are driven by a pinion-ring gear system.

The ceramic structural components comprising the gas passage are placed on the central axis of the engine and are supported pressing in the direction of the engine front, with ceramic springs (40 coil springs) mounted on the central main support.

The design target of each component is shown in Table 2 and materials of the main ceramic components in Table 3.

Combustor

The combustor liner is divided into three parts aiming at simplification of their shapes and reduction of thermal stress. With alignment accuracy of the parts kept in the tolerance by taper butt joint, the liner device is supported compressibly in the downstream direction by the spring at the top of the liner, so that thermal expansion is not restricted and vibration is absorbed. The liner at the bottom, in the shape of cone, is supported by a ring having four hooks. The buffer made of silica-alumina fiber woven is inserted between the liner and the hooks. This supporting is also applicable to the premixed lean burn combustor, which has been developed by using a test rig and will be substitute for the conventional diffusional combustor.

Gas Generator Turbine

In the design of gas generator turbine rotor and its nozzle, the stress estimation is regarded as a significant work since these components will be exposed to the most severe condition. The turbine is designed to have an expansion ratio of 1.67, nondimensional specific speed of 0.8, 13 blades, and outer diameter of 162.6 mm. The tip speed at the maximum speed (55,000 rpm) is 470 m/s. The gas generator turbine nozzle has 19 blades. Each of the blades comprises a segment and these segments are put together to be assembled. When mounted on an actual engine, the space between the nozzle and the back shroud shall be filled with buffer so that the oscillation will not injure the nozzle.

With regard to the turbine and nozzle, the performance of the turbine and reliability of the bearings were examined by using the trial turbine rotor made of metal, and the some modifications were carried out to improve. Thermal stress distribution in the nozzle during various operations (startup, maximum power, shutdown) was analyzed by NKK Corporation. It is predicted that the peak stress of 182.5 MPa at the trailing edge would appear at about 40 seconds after the startup, while the stress at the maximum power was as slight as 42 MPa. Figure 3 illustrates the stress contour of the nozzle estimated at the startup.

Stress and temperature distributions for the turbine rotor were estimated by using FE analysis under the condition of maximum power and startup duration. Peak stress (maximum principal stress) was recognized at the root of the scallop, and the value was 163 MPa (1128°C). The worst transient stress appears in the center portion of the hub at about 30 seconds after startup, and the value was 355 MPa (170°C). Reliability estimation based on these stress and temperature was done by using the ceramics reliability estimation program CARES which was developed by NASA (USA). It implied that the survival probability of the turbine rotor as a whole, at maximum power of 1350°C (TiT) engine, is 98.6 percent, while it will be 99.7 percent for 1200°C (TiT) engine.

The estimated result shows unsatisfactory level due to the high-temperature strength of the current ceramic material used.

Table 1 CGT303 specifications

Items		Units	Specifications
Engine configuration		—	Regenerative (1/LP/R)
Output power		kW	300
Output speed		rpm	3600
Outer dimensions		mm	1420L × 865W × 1155H
Dry weight		kg	300
Fuel		—	Gas oil, gaseous fuel
Compressor	Type	—	Single, centrifugal
	Speed	rpm	55,000
Gas generator turbine	Type	—	Single, radial
	Speed	rpm	55,000
Power turbine	Type	—	Single, axial
	Speed	rpm	39,000
Combustor		—	Single, can
Heat exchanger		—	Rotary regenerative
Control system		—	Electric

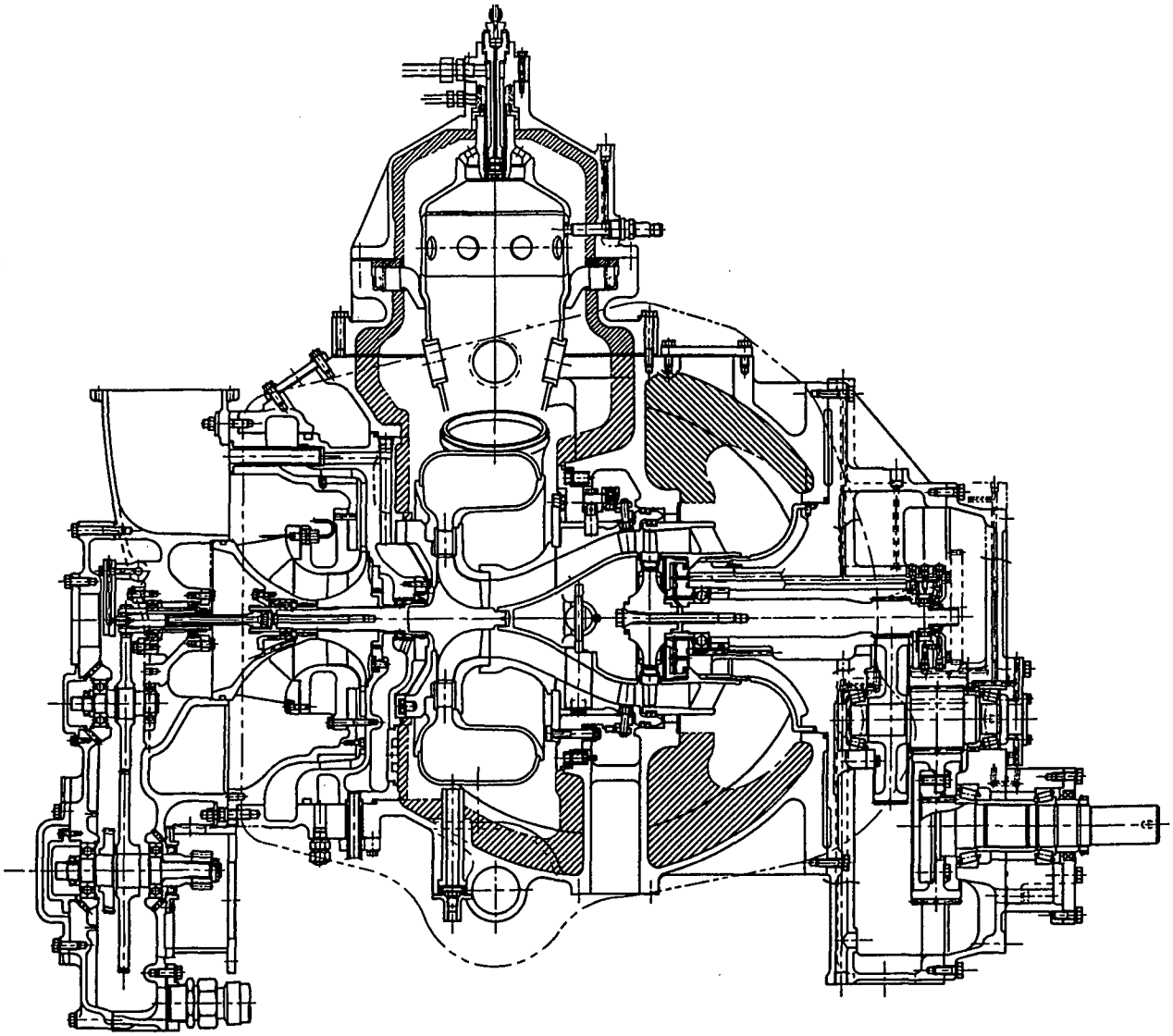

Fig. 2 Cross section of CGT303

Further development of the new ceramic material used. Further development of the new ceramic material having higher strength over 1200°C is intended to be made.

The natural frequencies of the gas generator turbine were then calculated, and are shown in Fig. 4. In the range of 60 to 70 percent of rated speed, the first, second, and third real eigenvalues are found. Although this speed is within the operating range of gas generator turbine, there seem to be no problem since the passing gas speed at that time is low, and the excitation level is low enough for the turbine rotor to endure.

The fitting process of the ceramic rotor to the metal shaft was investigated by Kyocera Corporation. Shrink fit is applied to this fixation together with brazing. The fitting position and shape were initially chosen as shown in Fig. 5(*a*), considering the restraint of the temperature allowed for the metal shaft. However, since the stress analysis predicted that tensile stress

Table 2 Design target

Items	Units	Target performance
Output power	kW	300
Engine thermal efficiency	Percent	42
Pressure ratio	—	4.5
Air mass flow rate	kg/s	1.25
Turbine inlet temperature	°C	1350
Compressor efficiency	Percent	82.4
Gas generator turbine efficiency	Percent	88.3
Power turbine efficiency	Percent	86.8
Combustor efficiency	Percent	99
Regenerator thermal effect	Percent	92

Table 3 Material of ceramic components

Parts	Materials	Manufacturer
Combustor flame tube	Si_3N_4	Kyocera
Gas generator turbine scroll	Si_3N_4	Kyocera
Gas generator turbine nozzle	β-Sialon	NKK
Gas generator turbine rotor	Si_3N_4	Kyocera
Gas generator turbine shroud	β-Sialon	NKK
Gas generator turbine back plate	β-Sialon	NKK
Intermediate ducts	Si_3N_4	Kyocera
Power turbine nozzle	Si_3N_4	NGK Spark Plug
Power turbine rotor blade	Si_3N_4	NGK Spark Plug
Exhaust diffuser	Si_3N_4	Kyocera
Regenerator core	Cordierite	NGK
Support spring	Si_3N_4	NHK

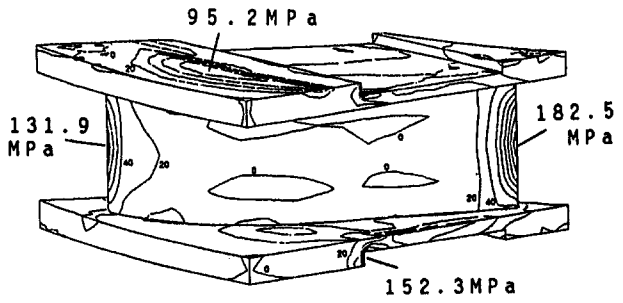

Fig. 3 Stress contour of gas generator turbine nozzle at 38 seconds after the startup

as much as 320 MPa beyond the allowable level for fitting may be generated at the stem of the ceramic rotor, the material of the metal shaft, the fitting position and shape were redesigned as shown in Fig. 5(*b*). As a result, the stress at the ceramics rotor stem was reduced to a safety level of 155 MPa. Sufficient reliability of the modified fitting is proved by heat and quench tests.

A cold spin burst test was conducted on a gas generator turbine at Kyocera Corporation, and it was proved that actual components had a strength expected for the present material. Results of the test and the estimation by CARES are shown in Fig. 6.

Subsequently, a hot spin test was conducted at Niigata Engineering Co., Ltd., which verified the reliability up to 100 percent speed at TiT 1100°C.

Power Turbine

A hybrid concept was applied to the power turbine, with ceramic blades set to the metal disk as follows:

1 The ϕ: 230-mm outer diameter is too large to be realized in a monolythic rotor.
2 The inlet gas temperature (1184°C) for a power turbine is low enough to apply a metal disk. The power turbine has 35 blades while the power turbine nozzle has 29 blades. In the case of hybrid concept, the maximum stress occurs at the dovetail shown in Fig. 7.

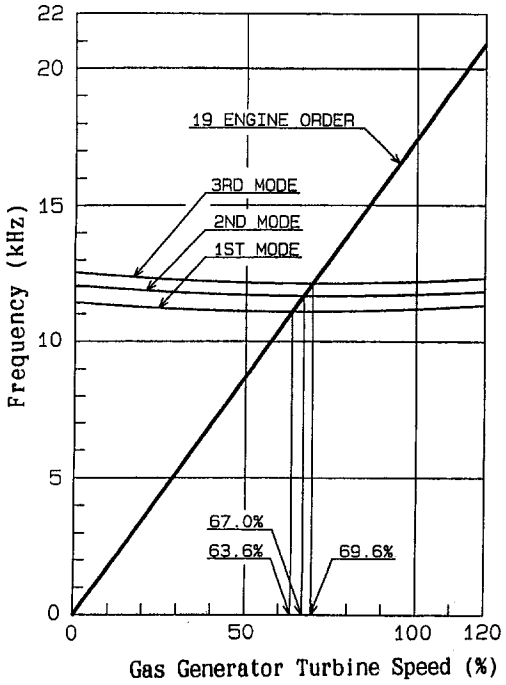

Fig. 4 Gas generator turbine Campbell diagram

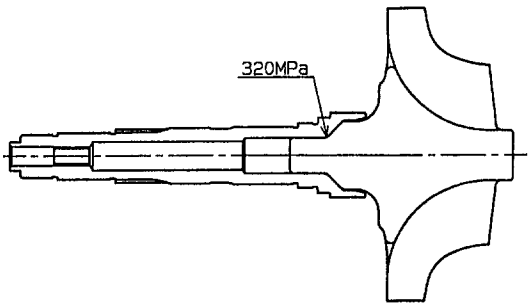

Fig. 5(*a*) Preliminary design of gas generator turbine

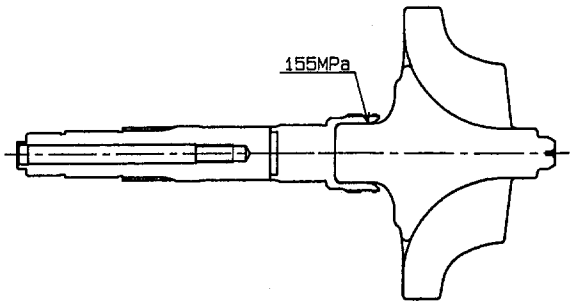

Fig. 5(*b*) Final design of gas generator turbine

Since the stress differs depending on the taper angle of the dovetail and the fillet radius of the top end of the taper portion, the design was optimized by FE analysis.

The stress at the maximum power is 349 MPa (862°C), and the worst transient stress at the startup is 425 MPa (830°C), which occurs in 300 seconds after the startup. The survival probability of the blades under this condition is more than 99.98 percent.

Thin nickel plates as a pliable layer are inserted between the ceramic blades and the metal disk. This may reduce any stress concentration due to irregular contact from the surface roughness and thermal distortion.

Ceramic Structural Components

In the stress estimation of ceramic structural components such as scroll, shroud, intermediate duct, etc., the thermal load is more important than the mechanical load. Since the thermal

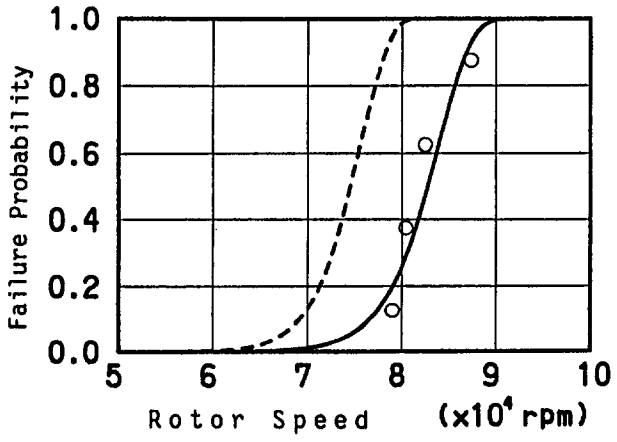

Fig. 6 Cold spin burst test results

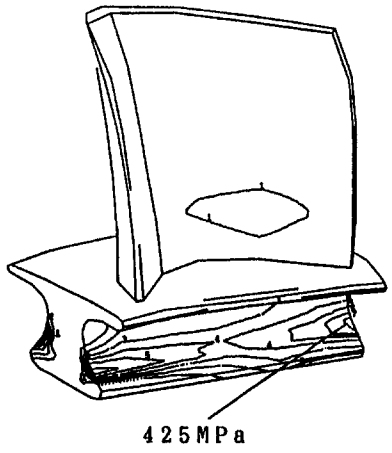

Fig. 7 Stress contour of power turbine blade at 300 seconds after startup

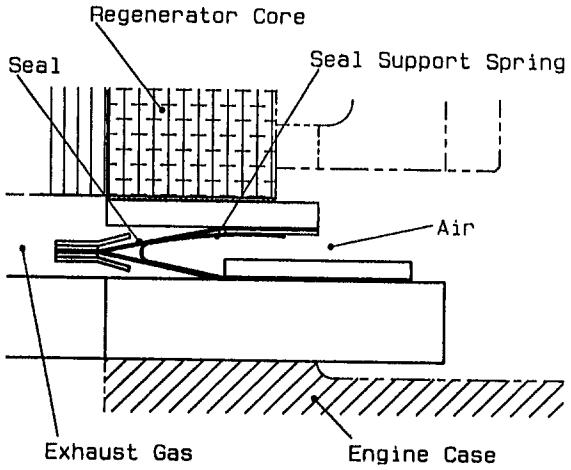

Fig. 9 Diaphragm design for regenerator seal

stress appears in a broad area, even though it is relatively low, the scale effect must be accounted for in brittle materials such as ceramics. With regard to manufacturing easiness and scale effect of the ceramics, ceramic components comprising a hot gas passage were designed to be divided into nine parts.

Flexible support is a key technology in designing ceramic structural components. They are essentially designed to be assembled on the engine axis and then be supported compressively by the springs forcing toward the engine front, so that any thermal expansion can be free from mechanical restraint and vibration will be absorbed. On the other hand, for the supporting in the radius direction, which is required to keep centricity to the engine axis, the taper butt joint or oldham device were adopted in the initial design. The taper butt joint, which is applied in "ceramic-to-ceramic" contact, conforms cone-shaped face. The oldham device, which is applied in "ceramic-to-metal" contact, uses four sliders mounted on ceramics, which are allowed to slide within the grooves on the metalic component. However, the thermal shock test showed that the scroll supported by taper butt joint tended to be out of centricity. Irregular stiffness in scroll B (its shape is not completely axisymmetric because of a gas inlet) and thermal distortion in scroll C (it has a place where hot gas from the combustor hits, so there is a local temperature rise) result in irregular contact force on the taper face, which may cause misalignment. Thus, the fitting method was changed to faucet fitup as shown in Fig. 8.

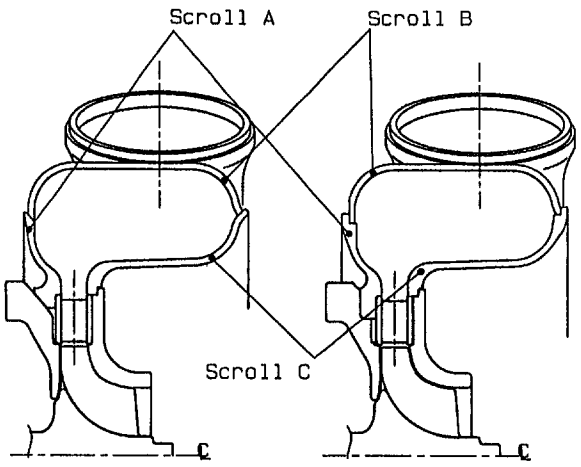

Fig. 8(*a*) Initial design for scroll (taper butt joint); (*b*) final design for scroll (faucet fitup)

At present, the modified structural ceramic components were proved to be reliable under the thermal shock test up to 1200°C.

Regenerator

A rotary regenerative heat exchanger is comprised of the core (made of cordierite) and the seals. Since the heat exchanger must operate under conditions where high temperature and low temperature or high pressure and low pressure coexist, thermal or pressured distortion of the seals and seal housing may cause leakage of the compressed inlet air into the expanded exhaust gas. This will reduce the engine thermal efficiency.

The first applied seal was a curtain seal device, but the leakage caused by thermal distortion on the cross bar (seal plate located between inlet air and exhaust gas) was too much to keep the specified engine performance, and therefore, a new diaphragm design is being developed that will control and absorb thermal distortion (see Fig. 9). This seal attained 5 percent of air leakage to total air flow rate in the steady-state cold rig test. This seal is programmed to go through the high-temperature leakage test and the wear test with heat exchanger core, before it is finally mounted on the engine.

Conclusion

1 In the development program for ceramic gas turbine, the primary function of the engine was established by using a metal gas turbine (TiT 900°C), and then all-ceramic components have been developed to be feasible for practical use. These ceramic components are going to be mounted on the engine at the coming second stage.

2 The combustor is a single can type mounted tangentially to the scroll swirling direction. The liner device, mounted compressibly by the spring at the top of the liner, is supported by hooks with the buffer, which is made of silica-alumina fiber, so that thermal expansion is not restricted and vibration is absorbed.

3 For the turbine components, a radial-inflow turbine is adopted as the gas generator turbine, and hybrid axial turbine as the power turbine. Both in the FE and CARES analysis, survival probabilities at TiT 1200°C are estimated to be 99.7 percent for the gas generator turbine, and 99.98 percent for the power turbine.

4 Ceramic components are grouped into five units according to their function, and each of them is supported independently. Ceramic structural components forming a hot gas passage are supported compressively loaded by the springs. The scroll supported by the taper butt joint is apt to cause misalign-

ment in the assembled components as a result of irregular contact force, so the fitting method was changed to faucet fitup.

5 Since the seals of the regenerative heat exchanger are exposed to severe conditions such as high temperature and high pressure, it is necessary to reduce and absorb their thermal distortion. For this purpose, the diaphragm design for the seal is being developed and it has attained 5 percent of the leakage in the steady-state cold rig test.

Acknowledgments

The authors wish to acknowledge the Agency of Industrial Science and Technology of the Ministry of International Trade and Industry, New Energy and Industrial Technology Development organization and three national laboratories participating in the project.

The authers also appreciate the aid of Niigata Engineering Co., Ltd., Kyocera Corporation, NGK Spark Plug Co., Ltd., and NKK Corporation.

References

1 Hamada, Yoshitsugu, "Regenerative Two Shaft Ceramic Gas Turbine for Mobile Power Generation," *Journal of the Gas Turbine Society of Japan*, 1989.

2 Arnold, D. J., and Balje, O. E., "High-Temperature Potential of Uncooled Radial Turbine," ASME Paper No. 77-GT-XXX, 1977.

3 New Energy and Industrial Technology Development Organization (NEDO), "Research and Development on Ceramic Gas Turbine (300 kW Class)," FY 1991 Annual Report, Oct. 1992.

4 Gejima, H., and Yoshida, M., "Reliability Evaluation of Ceramic Radial Turbine Rotor," JSME Organized Session 930-75, Nov. 1993, Japan.

5 Nemeth, N. N., Manderscheid, J. M., and Gyekenyesi, J. P., "Ceramics Analysis and Reliability Evaluation of Structures (CARES)," NASA Technical Paper 2916, Aug. 1990.

Ceramic Gas Turbine Technology Development

M. L. Easley

J. R. Smyth

AlliedSignal Engines,
AlliedSignal Aerospace Company,
Phoenix, AZ

AlliedSignal Engines is addressing critical concerns slowing the commercialization of structural ceramics in gas turbine engines. These issues include ceramic component reliability, commitment of ceramic suppliers to support production needs, and refinement of ceramic design technologies. The stated goals of the current program are to develop and demonstrate structural ceramic technology that has the potential for extended operation in a gas turbine environment by incorporation in an auxiliary power unit (APU) to support automotive gas turbine development. AlliedSignal Engines changed the ATTAP ceramic engine test bed from the AGT101 automotive engine to the 331-200[CT] APU. The 331-200[CT] first-stage turbine nozzle segments and blades were redesigned using ceramic materials, employing design methods developed during the earlier DOE/NASA-funded Advanced Gas Turbine (AGT) and the ATTAP programs. The ceramic design technologies under development in the present program include design methods for improved resistance to impact and contact damage, assessment of the effects of oxidation and corrosion on ceramic component life, and assessment of the effectiveness of nondestructive evaluation (NDE) and proof testing methods to reliably identify ceramic parts having critical flaws. AlliedSignal made progress in these activities during 1993 ATTAP efforts. Ceramic parts for the 331-200[CT] engine have been fabricated and evaluated in component tests, to verify the design characteristics and assure structural integrity prior to full-up engine testing. Engine testing is currently under way. The work summarized in this paper was funded by the U.S. Dept. of Energy (DOE) Office of Transportation Technologies and administered by NASA-Lewis Research Center, under Contract No. DEN3-335.

Introduction

The Advanced Turbine Technology Applications Project (ATTAP) is a continuation of activities sponsored by the U.S. Department of Energy (DOE) to develop the technology for an improved automobile propulsion system under Title III of U.S. Public Law 95-238, "Automotive Propulsion Research and Development Act of 1978." ATTAP is authorized under DOE/NASA Contract No. DEN 3-335, with the National Aeronautics and Space Administration (NASA) providing management and administration. This paper summarizes the progress of the ATTAP/331-200 Ceramic Demonstration Program conducted during 1993 by AlliedSignal Engines (formerly Garrett Auxiliary Power Division), a unit of AlliedSignal Aerospace Company, in developing the needed technologies for a ceramic gas turbine engine.

The thrust of the ATTAP/331-200 program is to "bridge the gap" between ceramics in the laboratory and near-term commercial heat engine applications. The intent is to use this application as a stepping stone to transition the technology into the automotive marketplace where its benefits can have the greatest impact on reducing fuel consumption and gaseous emissions. The project goal is to develop and demonstrate structural ceramic component technology in an auxiliary power unit (APU), so that the technology can be evaluated in an existing commercial gas turbine application. Simultaneously, this work will ready ceramic technology for the aircraft APU application, while gathering extensive laboratory and field experience, and develop ceramic component design methods and fabrication techniques. In this way, ATTAP/331-200 will effectively support the expansion of ceramics technology into automotive designs.

This strategy will augment the maturation of ceramics technology by developing the infrastructure and engineering disciplines within the technology to overcome those barriers which prevent its commercialization. Currently, the principal barriers to the commercialization of ceramics are seen as:

- Immature supporting technologies
- Underdeveloped production capability
- Inadequate demonstration

The ATTAP/331-200 overall program plan provides an approach to resolve each of these issues. The following discussions describe the progress to date in the various ATTAP activities and outlines the go-forward plans to meet the program objectives.

Background

The present ATTAP/331-200 program is following a natural progression based on its predecessors. The focus is on near-term production capability, drawing heavily on "lessons learned" from the problems and successes on the previously completed ceramics development and demonstration programs.

The DARPA/Navy Ceramic Gas Turbine Engine Demonstration Program (1976 to 1981)[1] and the USAF Ceramic Components for Turbine Engines Program (1979 to 1982)[2] provided the foundation for the modern ATTAP/331-200 program. These programs utilized a test bed of similar design to the AlliedSignal/Garrett production Model GTCP331-200 gas turbine APU. Significant progress was achieved in demonstration of ceramic axial inserted turbine blades, as well as initial exploration of

Contributed by the International Gas Turbine Institute and presented at the 39th International Gas Turbine and Aeroengine Congress and Exposition, The Hague, The Netherlands, June 13–16, 1994. Manuscript received by the International Gas Turbine Institute Paper No. 94-GT-485. Associate Technical Editor: E. M. Greitzer.

[1] DARPA/Navy Contract No. N00024-76-C-5352.
[2] USAF Contract No. 33615-77-C-5171.

ceramic design technologies, including contact failure and particle impact damage resistance, and component life prediction.

The DOE/NASA Advanced Gas Turbine AGT101 Engine Program (1980 to 1987)[3] pursued several high-risk technologies, including ceramics for future automobile engine applications. The AGT101 program succeeded in simultaneously demonstrating many related advanced engine technologies, and identified the most critical areas in ceramic engine technology needing further development.

The DOE/NASA Advanced Turbine Technology Applications Project ATTAP/AGT101 Program (1987 to 1992),[4] emphasized the development of critical ceramics technologies, using the AGT101 automotive test bed. Significant progress was made in the ATTAP/AGT101 program toward successful impact-resistant ceramic turbine designs and ceramic component processing. However, the AGT101 engine proved to be inadequate as a test bed for the advanced ceramic technologies. This was because the AGT101 was designed as a demonstrator for several high-risk technologies, including the high-temperature ceramic regenerator, low-emission ceramic combustor, low-friction gas bearings, all-ceramic hot section structures, and impact-resistant ceramic turbine. As such, AGT101 reliability as a turbine test bed was not adequate for long-term endurance testing and evaluation.

The present DOE/NASA ATTAP/331-200 Ceramic Engine Demonstration Program[4] continues refinement of ceramics technologies and design methods, and focuses fabrication development on a scaleup of demonstrated technologies to pilot-production levels. To demonstrate ceramic technology adequately, over 6000 hours of endurance testing is planned, utilizing a reliable test bed based on the AlliedSignal/Garrett Model 331-200 APU (Fig. 1). The 331-200 APU is a fully developed gas turbine with current production applications in the Boeing 757 and 767 aircraft, which has higher capability for successfully accomplishing long-term endurance testing.

The progress of the current DOE ATTAP initiative toward commercialization of ceramic engine technology may be visualized using the chart in Fig. 2. This curve, based on cumulative experience in engine demonstration test hours and quantity of ceramic engine components achieved from 1980 to present and projected through 1997, shows the geometric trend in ceramics technology improvement. Figure 2 shows that ceramic engine technology is on the threshold of exploitation. The ATTAP/331-200 program will enable near-term commercialization in low volume, premium gas turbine applications such as airborne APUs, paving the way toward eventual production of ceramics for automotive gas turbines.

[3] DOE/NASA Contract No. DEN3-167.
[4] DOE/NASA Contract No. DEN3-335.

Technology Development

Ceramic technologies supported under the ATTAP/331-200 program in 1993 included:

- Impact design methods refinement
- Contact design methods refinement
- Ceramic blade attachment technology
- Oxidation/corrosion characteristics of ceramic materials
- Reliability of nondestructive evaluation (NDE) methods

All these technologies were identified as critical to the success of ceramics in commercial gas turbine applications. A description and discussion of the progress in each of these technologies follows.

Impact Design Methods Development. Development of a method capable of accurately predicting structural impact damage for any ceramic component from carbon particles (combustor carbon) is the end goal of this activity, which will result in design guidelines for impact-resistant, axial ceramic turbine blades. In 1993, reduction of the subelement impact test results from the ATTAP/AGT101 program was completed. Trial impact simulations for comparison were conducted using the DYNA3D code. This model will be transferred to workers at the Livermore Research and Engineering Company, Livermore, CA, for addition of a carbon pulverization model to finalize the simulation code.

Contact Design Methods Refinement. The goal of this activity is to develop design tools to predict strength and life for ceramic/ceramic and ceramic/metal interfaces under gas turbine engine operating conditions. A contact test rig (Fig. 3) for evaluation of ceramic contact interfaces of various configurations was designed and fabricated. This test rig was set up and tested to resolve operational issues and to evaluate contact damage in ceramic specimens. Specimen rig tests are currently being conducted and the test data will be compared with the results of contact stress analyses.

Future work will develop preliminary guidelines for ceramic contact interface design, further evaluate subelement contact test specimen designs, and test the subelements to validate the contact failure model.

Nomenclature

AGT = Advanced Gas Turbine
APU = Auxiliary Power Unit
ASR&T = AlliedSignal Research and Technology
atm = atmosphere
ATTAP = Advanced Turbine Technology Applications Project
C = Celsius
Ca = calcium
DARPA = Defense Advanced Research Projects Agency
deg = degrees
DOE = Department of Energy
EBAR = pressure difference ratio
F = Fahrenheit
GN-10 = AlliedSignal ceramic components silicon nitride
Hz = Hertz
DYNA3D = impact simulation computer code from Lawrence Livermore National Laboratory
in. = inch
kg = kilograms
ksi = thousands of pounds per square inch
lbm = pounds mass
kPa = kilo-Pascals
Mg = magnesium
min = minutes
MPa = mega-Pascals
NASA = National Aeronautics and Space Administration
NDE = Nondestructive Evaluation
NT154 = Norton Advanced Ceramics pressure slip cast silicon nitride
ORNL = Oak Ridge National Laboratory
P = pressure
P_{static} = static pressure
P_{tinlet} = turbine inlet pressure
pH = log hydrogen ion concentration (acidity or alkalinity)
POD = Probability of Detection
ppm = parts per million (mass)
psia = pounds per square inch absolute
rpm = revolutions per minute
s = second
TIR = total indicated reading
T_{max} = maximum temperature
UDRI = University of Dayton Research Institute, Dayton, OH
U.S. = United States
s = sigma, stress
s_{max} = maximum stress

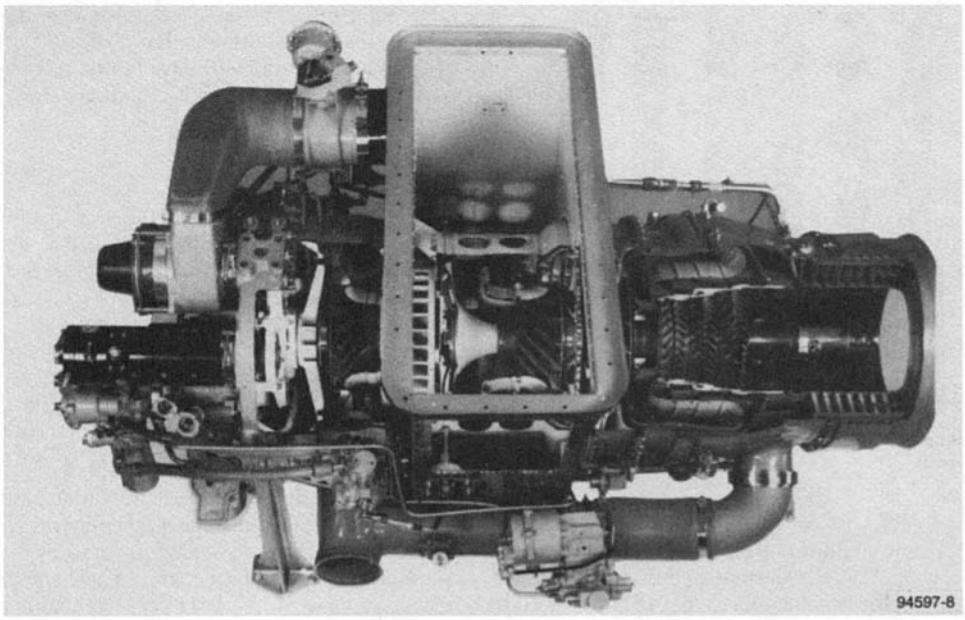

Fig. 1 ATTAP ceramic demonstration test bed is based on AlliedSignal production model 331-200 APU

Blade Attachment Technology. The goal of this activity is to provide the best, most cost-effective design solutions for robust ceramic axial inserted blade attachments for production gas turbines. In 1993, this activity focused on the development of basic design data relevant to the conditions within the ceramic inserted blade attachment. This work included assessment of compliant layers, surface topography and tolerance effects, and surface strength with respect to machining direction.

A test matrix was defined and test specimens were purchased for evaluation of these design elements using the contact test rig.

Ceramic Oxidation/Corrosion. An environmental life model is being developed that will be capable of accurately predicting the influence of engine operating design conditions and mission usage on the strength of silicon nitride turbine blades and vanes in a production gas turbine engine. This activity complements related ceramics research activities conducted by AlliedSignal Engines.[5]

During 1993, burner rig testing was performed on specimens of Norton Advanced Ceramics NT154 silicon nitride, one of the ceramic materials selected for ATTAP/331-200[CT] components. Figure 4 shows the typical glassy surface condition of the NT154 specimens after burner rig exposure. Following exposure, room temperature strength test data was acquired on the specimens. The data were then reduced to establish the oxidation and corrosion regimes for NT154 in air laden with sea salt.

Figure 5 summarizes the test results, showing the time–temperature relationship necessary to reduce the room temperature strength of NT154 by approximately 50 percent in the test environment of hot combustion air laden with 5 parts per million (ppm) sea salt.

These results also indicate that above 1550°F (843°C), NT154 silicon nitride exhibits rapid strength degradation in the hot, salt-laden burner test environment, largely due to pitting and surface roughening from sodium sulfate salts and (pH)-

[5] T. E. Strangman and D. S. Fox, "Strength Retention of NT154 Silicon Nitride Exposed to High-Temperature Oxidation and Hot Corrosion Environments," presented at the 184th Meeting of the Electrochemical Society, New Orleans, LA October 12, 1993; AlliedSignal Engines Report No. 31-11623.

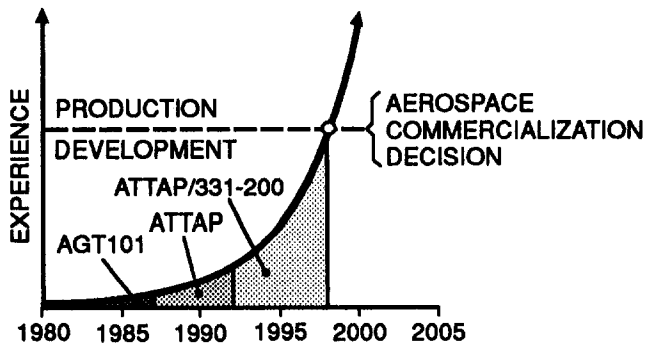

Fig. 2 ATTAP targets solutions for early ceramics commercialization

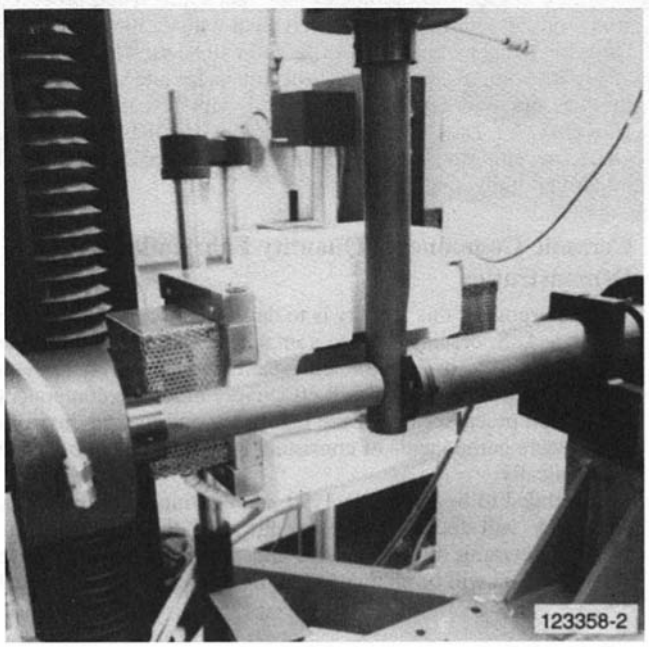

Fig. 3 Contact test rig used to evaluate various ceramic interface configurations

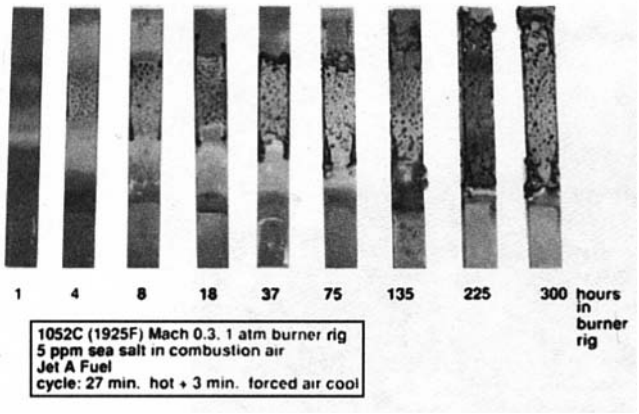

Fig. 4 Condition of ceramic oxidation test specimens after exposure in hot burner environment

basic corrosion, forming sodium-rich silicates. While these tests were performed on NT154, the current understanding of the corrosion mechanism indicates that other types of silicon nitride based ceramics will also suffer similar degradation.

This information will be incorporated into an environmental life model for NT154 and integrated with the life methodology being developed by AlliedSignal Engines under the ongoing DOE/ORNL Ceramic Life Prediction program.[6] Meanwhile, ATTAP work is continuing, to develop and evaluate protective coatings for silicon nitride components exposed to corrosive environments.

Nondestructive Evaluation (NDE) Technology. This ATTAP activity complements a similar activity funded by DOE/ORNL to establish the probability of detection of flaws of various sizes in ceramic components.[6] The ATTAP-funded activity will focus on establishing the probability of detection (POD) for internal flaws. This activity will ultimately establish production requirements for NDE to assure acceptable component quality, demonstrate whether NDE reliability and cost improvements are necessary and provide quantitative data for tradeoff comparisons with proof testing for assurance of component quality.

Silicon nitride turbine blades and vanes have been procured from various sources to establish typical volume flaw characteristics for actual parts. This information will be used in the design and fabrication of seeded defect specimens for later work. Under this activity, work was also initiated with researchers at the University of Dayton Research Institute (UDRI) in Dayton, OH, to develop statistical methods for the internal flaw detection reliability study.

Ceramic Components Quantity Fabrication Demonstration

The purpose of this activity is to develop the capability of the domestic U.S. ceramic engine component suppliers to provide quality components in sufficient quantities to support scaleup to engine production. This will effectively move the component fabrication processes out of the laboratory and into an environment where components of consistent high quality can be made economically.

Scheduled to begin in late 1993 and continue through 1996, this work will focus on the suppliers of the ATTAP/331-200[CT] ceramic turbine blades and nozzle segments. These manufacturers will be challenged to improve their demonstrated fabrication processes and develop methods and procedures to achieve the quantity production goal. By the end of 1996, each of the manufacturers will have built a pilot facility and demonstrated production of over 100 parts per month, on a continuous basis for several months.

Engine Demonstrations

The ATTAP/331-200 engine demonstration activities included redesign and modification of the Model 331-200 APU into the ATTAP ceramic test bed. Within the 331-200[CT] test bed, the first axial turbine stage was redesigned to incorporate ceramic turbine nozzle segments and inserted ceramic blades. This activity included detailed design of the ceramic components and modified metallic support structures, test hardware fabrication, component testing to verify the component performance characteristics, and engine demonstration testing. These tasks are summarized in the sections following.

Turbine Design. The existing production, all-metallic 331-200 APU first-stage turbine assembly was redesigned to incorporate ceramic nozzle segments and inserted ceramic blades. The design guidelines recognized that the redesigned components will be used in a later field evaluation program, in which ceramic-equipped engines replace production all-metallic engines; thus, the ceramic-equipped engines must be aerodynamically similar to the metallic engines. In addition, to maintain the reliability of the test bed, modifications to the metallic engine supporting structures were minimized. The design cycle conditions for the ceramic turbine stage are listed in Table 1.

The ceramic turbine nozzle segments and blades were designed with principal consideration given to component producibility, while also satisfying structural integrity and aerodynamic performance requirements.

The ceramic nozzle assembly (Fig. 6) has 23 segmented ceramic vanes (Fig. 7). For simplicity, the ceramic vane count was reduced to 23, from 29 vanes on the all-metallic engine. Nozzle surface geometry was kept as simple as possible to favor manufacturing, a result of concurrent engineering with the close collaboration of the ceramic nozzle manufacturer.

Nozzle stresses predicted for transient operation during normal engine startup (summarized in Fig. 8) peaked at 33 ksi (228 MPa) at the nozzle trailing edge, nine seconds into the startup cycle, which was within the capability of the selected AlliedSignal Ceramic Components GN-10 silicon nitride material.

An attempt was made to maintain the aerodynamic performance of the ceramic nozzles at the level of the original all-metallic design. The nozzle aerodynamic loadings were high, due to the low number of vanes and the envelope limitations, giving rise to concerns regarding increased losses due to flow separation on the suction side of the vanes. However, both inviscid and viscous analyses of the nozzle loadings (shown in

Table 1 331-200[CT] ceramic turbine design cycle conditions

Parameter	Units	Value
Corrected Flow	lbm/sec	1.556
	(kg/sec)	(0.7058)
Corrected Speed	rpm	19,993
Physical Speed	rpm	41,731
Pressure Ratio	--	8.741
Efficiency	percent	85.7
Inlet Total Temperature	F	1800
	(C)	(982)
Inlet Total Pressure	psia	129.8
	(kPa)	(895)

[6] DOE/ORNL Contract No. 86X-SC674C, "Life Prediction Methodology for Ceramic Components of Advanced Heat Engines"; J. Cuccio, AlliedSignal Engines, Principal Investigator.

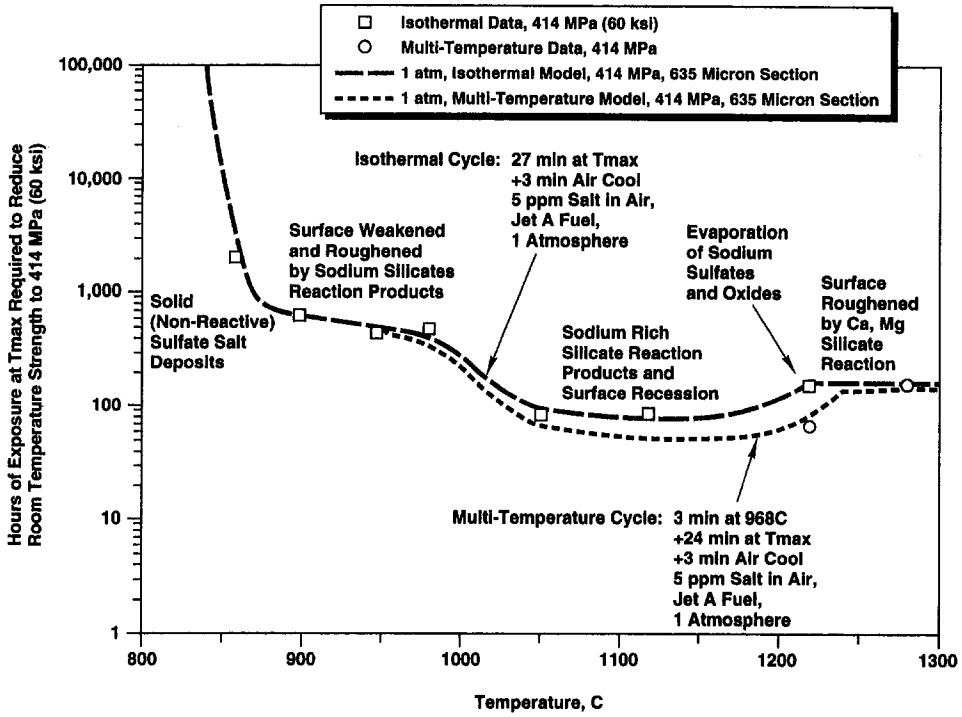

Fig. 5 Reaction with sulfate salt deposits from ingested sea salt and fuel contaminants reduces the strength of NT154 silicon nitride

Fig. 9 for the midspan section) indicated acceptable suction side diffusion.

The number of ceramic blades in the redesigned first-stage turbine wheel (Fig. 10) was reduced to 28 blades from 36 in the original all-metallic engine. This permitted an increase in the size of the ceramic blades (Fig. 11), thickening the blade sections for better fabricability, and increasing the room available for a low-stress blade attachment scheme.

The blade attachment scheme is further illustrated in an exploded view in Fig. 12. This design utilizes a single-tang dovetail with a thin foil of compliant metal to distribute the compressive loads between the ceramic blade dovetails and the metallic turbine disk. Each blade assembly is held in place axially with a conventional metallic bent tab.

Figure 13 shows the predicted principal stress isopleths within the ceramic blade at maximum speed, compared with the corresponding thermal contour lines. Peak stress of 43 ksi (296 MPa) occurs on the surface in the dovetail region near the edge of the contact zone. A life prediction analysis was also performed on the ceramic blade, and the results indicated the probability of survival was better than 99 percent, with 95 percent confidence for 20,000 hours life with 20,000 cycles.

While it is felt that the ceramic-equipped 331-200[CT] engine will meet its performance goals, aerodynamic performance of the ceramic blade may have been lessened, in favor of improved fabricability and mechanical integrity. Aerodynamic loading increased as a result of the reduced blade count and simultaneous restriction of the blade envelope. Figure 14 shows the predicted distribution of kinetic energy loss coefficient

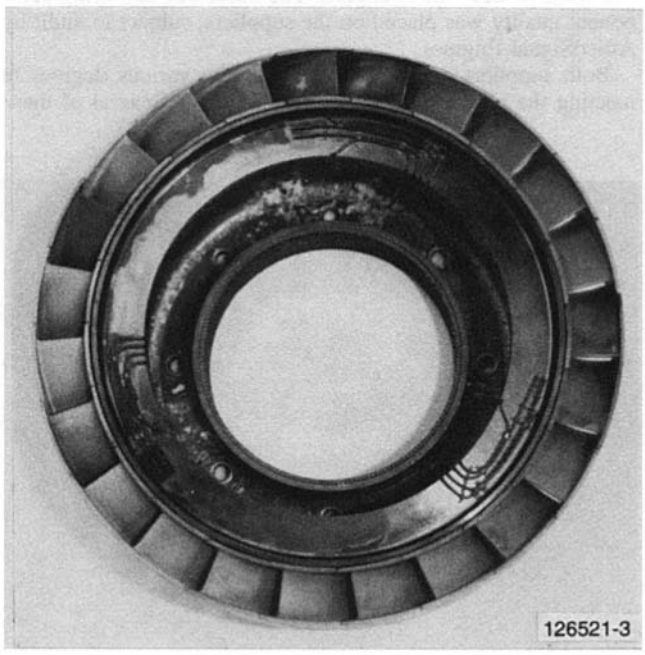

Fig. 6 ATTAP 331-200[CT] ceramic nozzle assembly with 23 segments

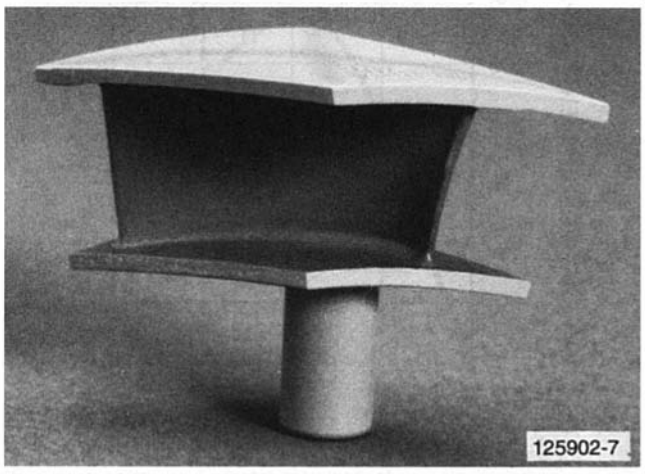

Fig. 7 ATTAP 331-200[CT] ceramic nozzle segment

(EBAR) along the length of the ceramic blade from hub (zero percent span) to shroud (blade tip = 100 percent span). Note that the largest loss distribution occurs over the last 20 percent of the blade, near the blade tip. Engine performance will be monitored closely during testing, and a further turbine redesign for increased performance will be considered if necessary.

Ceramic Hardware Fabrication. Ceramic components for the 331-200[CT] engine were procured from two domestic U.S. sources: Norton Advanced Ceramics in Northboro, MA, and AlliedSignal Ceramic Components in Torrance, CA. Unlike previous ATTAP ceramic parts purchases, which were conducted on a "Best Efforts" basis, these procurements were fixed-price/quantity parts-buy type purchases with quality requirements similar to those that would be required in production. Also differing from previous ATTAP practices, the component designs were "concurrently engineered" in collaboration with the ceramics suppliers. Through this activity, the suppliers and AlliedSignal Engines were able to develop ceramic parts geometries that not only meet functional requirements, but are also fully producible. All of the drawing dimensional tolerances and specifications were mutually understood and agreed upon before any ceramic parts were fabricated.

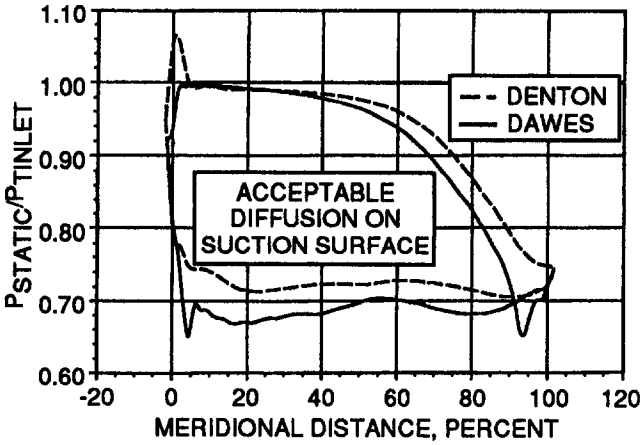

Fig. 9 331-200[CT] ceramic nozzle midspan inviscid and viscous loading analyses showing acceptable aerodynamic performance will be maintained

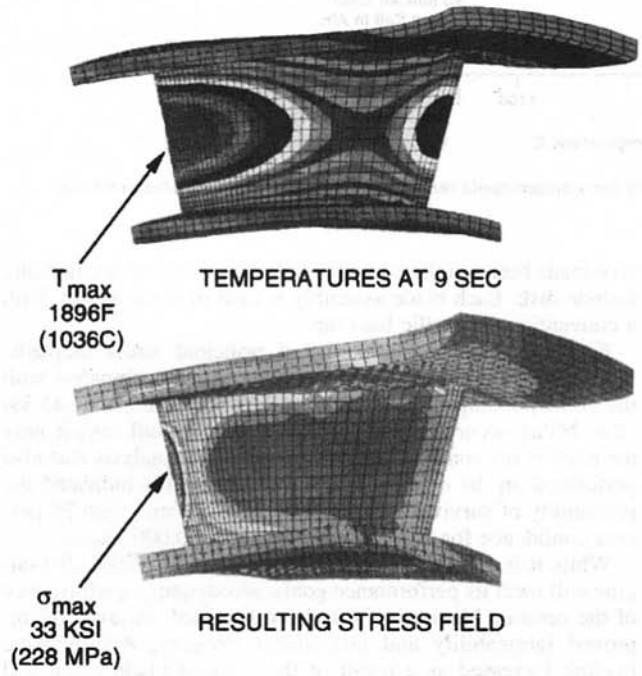

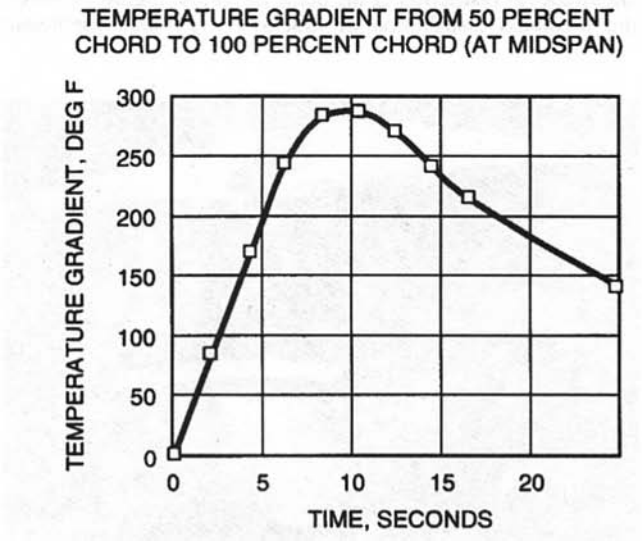

Fig. 8 Predicted stresses for transient (startup) operation peak at 33 ksi (228 mPa) on trailing edge of ceramic nozzle

Norton Advanced Ceramics fabricated the ceramic turbine blades from NT154 silicon nitride. These parts were made using a pressure slip cast process, in which the blades were cast to near-net shape, with final grinding required only on the blade attachment dovetails and the blade tips.

AlliedSignal Ceramic Components fabricated the ceramic turbine nozzle segments from GN-10 silicon nitride. These parts were made by either cold isostatic pressing or pressure slip casting cylindrical blanks, then green machining to near-net shape, densifying the nozzles, and then final grinding the critical surfaces of the parts.

Fabrication of these parts offered significant challenges to both suppliers, and several design, specification, and fabrication issues were identified, which will be addressed in future work.

Component quality was a major issue in both procurements. The blueprint specifications required not only dimensional compliance, but also compliance with material defect specifications, and fixed process specifications. The burden of certifying component quality was placed on the suppliers, subject to audit by AlliedSignal Engines.

Both suppliers experienced problems in various degrees in meeting the production quality requirements. Several of these

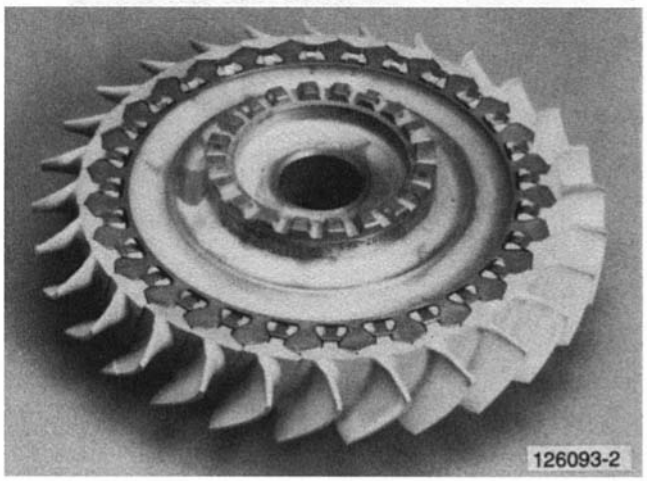

Fig. 10 331-200[CT] turbine wheel with 28 ceramic blades

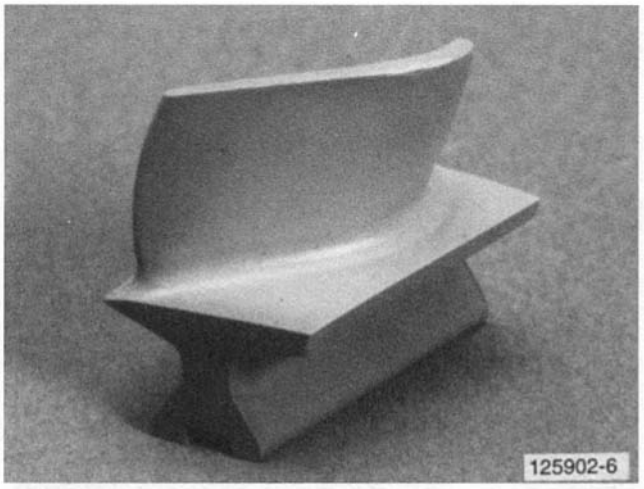

Fig. 11 331-200[CT] ceramic turbine blade employing dovetail attachment scheme

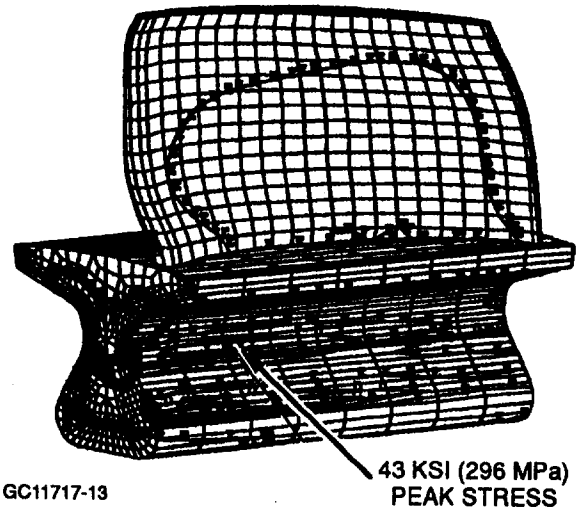

Fig. 13 Predicted peak stress of 43 ksi (296 mPa) on dovetail surface of 331-200[CT] ceramic blade

problems, such as dimensional deviation of machined surfaces, incorrect specification interpretation, and misplaced parts markings, were not unexpected, and were correctable with improvements in the production-level quality systems for aerospace parts at these suppliers.

Significant problems in the control of as-processed surface quality and dimensional control of as-processed surfaces were also common, typically resulting in poor production yields. Since these problems seemed to be characteristic of the ceramic fabrication processes, additional refinement will be required in these areas before these processes will be ready for regular production of precision aerospace components.

Component Testing. Tests were performed on the ceramic components after receipt by AlliedSignal Engines, to verify critical design aspects and the mechanical integrity of the manufactured components. The ceramic blades were spin proof tested and characterized for vibration, and the ceramic nozzle segments were thermally proof tested.

During the ceramic blade proof tests, a total of 60 blades were spin tested at up to 50,000 rpm in an evacuated whirl pit. This test imposed stresses in the blade attachment that were 44 percent higher than predicted for engine operation. Only two blades failed during the proof tests, both during the same run; neither blade failed from internal defects. One of the blades failed due to silicon carbide grit, which contaminated the blade attachment contact zone, and the other blade was damaged from impact with debris from the first blade.

The source of the silicon carbide grit was traced to a hand finishing operation prior to assembly of the ceramic blade into the spin test rotor. A grit particle was deposited on the blade dovetail during hand finishing and was not removed completely during the cleaning operation prior to assembly. The cleaning operation has been improved, and the problem has not recurred.

Two ceramic blades were also tested in an airjet spin test, to verify the blade resonant frequencies. This test was also conducted in the whirl pit, equipped with a ring of air nozzles directed into the path of the whirling blades to simulate the nozzle-passing conditions in the engine. The blades were instrumented with strain gages, to measure the vibration response of the blades to the excitation from the impinging air jets. During the tests, the blade strain levels were monitored as the rotor decelerated from various speeds. Peak responses indicated the blade resonant frequencies, and the strain ratios between various locations on the blades identified the resonant mode(s). The Campbell diagram in Fig. 15 compares the airjet test results with analytically predicted values and the critical engine speed harmonics. Note that the measured first resonant mode was

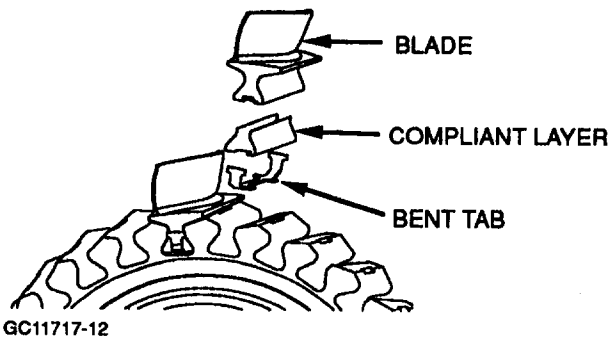

Fig. 12 331-200[CT] ceramic blade attachment scheme employing a compliant layer with a conventional metal bent tab retainer

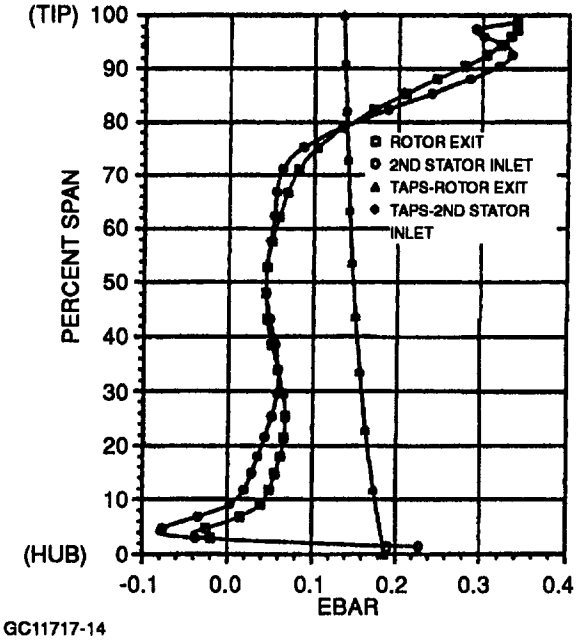

Fig. 14 Kinetic energy loss coefficient (EBAR) distribution near 331-200[CT] ceramic blade tip (100 percent span) attributed to tip leakage flow

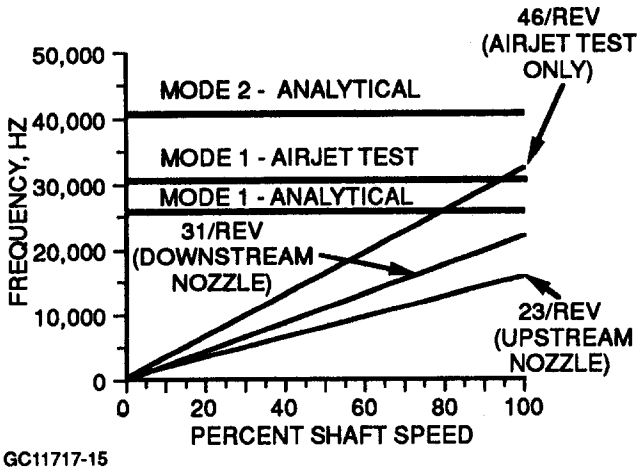

Fig. 15 Campbell diagram of airjet spin test results shows 331-200[CT] ceramic-bladed rotor has acceptable vibratory response

higher than the predicted value, but does not intersect the critical 23/rev and 31/rev engine speed harmonics. This result indicates a reduced risk of troublesome blade vibrations possibly occurring during engine testing.

The ceramic nozzle segments were proof tested in a thermal shock rig, shown schematically in Fig. 16. This test rig was designed to expose a single ceramic nozzle to thermal transients from room temperature up to 2600°F (1427°C) in less than two seconds, and has the capability to impose stress levels 25 percent higher than the predicted peak transient stress value during engine operation. At the time of this writing, 35 nozzles had been tested in the rig proof cycle and all had successfully passed.

Engine Testing. Two production Model 331-200 APU engines were converted to the 331-200[CT] configuration for use as test beds; one engine for evaluating the ceramic nozzles with metallic blades, and the other for evaluating the ceramic blades with metallic nozzles. Using separate test beds reduces the test risks and enhances data collection for each ceramic component set.

The dual-test-bed strategy paid off during the first engine test on the ceramic blades. Approximately 86 seconds into the first engine start, at 33,600 rpm, the engine suffered a failure. Subsequent disassembly, inspection, and analysis identified a number of possible causes; however, contact failure at the blade attachment was the most likely mode. The posttest inspections verified

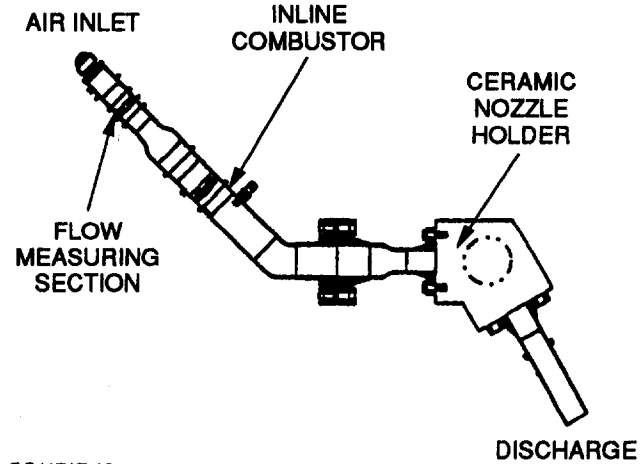

Fig. 16 Ceramic nozzle segments were individually proof tested in a thermal shock rig

Fig. 17 Ceramic nozzle assembly successfully completed first 331-200[CT] engine test

that the contact surfaces of the broached slots in the turbine disk were flat to 0.001 in. TIR, but witness marks on the contact surfaces indicated that the compliant layer did not effectively spread the contact loads over the surfaces.

Corrective actions were identified and implemented, with respect to this and other potential failure causes. This activity includes improved inspections of both the blades and the metallic turbine disks, and revised manufacturing processes to improve flatness in the blade attachment, to ensure proper load transfer.

The first engine test of the ceramic turbine nozzles was successful. This engine operated for 10.1 hours without failure, over the full range of engine operating conditions. Included in this test was a start with immediate loading to maximum power, inducing a 2470°F (1354°C) temperature spike within four seconds after light off, which represents an extreme thermal stress condition in the nozzle segments. Figure 17 shows a photograph of the ceramic nozzle assembly after test completion. All of the nozzle segments were intact and in good condition.

Engine testing will continue to move forward in 1993 with accelerated mission testing of the ceramic nozzles and blades, in separate engines.

Future Work. Engine demonstration testing is planned to continue through 1994, accumulating up to 1000 hours of test time on the ceramic nozzles and blades. This activity will focus on verifying the integrity of the ceramic component designs. Certification test activities will begin in 1995, to qualify the ceramic-equipped 331-200[CT] engine for installation on commercial aircraft for field evaluations, planned to begin in 1996. Extended endurance testing will also begin in 1996, accumulating over 6000 hours of operating experience by program end in 1997.

Summary and Conclusions

During 1993, the ATTAP program was refocused to address more effectively the critical issues surrounding the commercialization of ceramics. The current program addresses ceramic reliability, reliability demonstration, ceramic design technology refinement, and cost-effective component fabrication. Utilizing the AlliedSignal/Garrett Model 331-200[CT] auxiliary power

unit as a test bed/demonstrator, the program will provide the supporting experience, design methodologies, and fabrication capability necessary for limited commercialization of ceramics in aeronautical applications, and provide a solid technological foundation supporting automotive ceramic heat engine applications.

Technical activity through 1993 emphasized the design, fabrication, and integrity demonstration of a ceramic first-stage turbine nozzle and inserted ceramic turbine blade. These components were designed to meet the commercial life goals of 20,000 hours or 20,000 cycles for stress rupture and fast fracture failure modes with 99 percent probability of survival and 95 percent confidence.

Both ceramic components were made of silicon nitride. The ceramic nozzles were fabricated by AlliedSignal Ceramic Components using their GN-10 material. The ceramic blades were fabricated by Norton Advanced Ceramics using their NT154 material. Both suppliers experienced difficulties in meeting the stringent quality requirements of the production procurement specifications; despite this, both suppliers were able to provide acceptable ceramic parts for test rig and engine evaluations.

To ensure adequate component integrity, proof tests were devised for the ceramic turbine nozzles and ceramic turbine blades. A thermal shock test rig was designed and fabricated to expose the nozzles to a peak stress level exceeding 125 percent of the maximum design stress for normal engine operation. The ceramic turbine blades were proof tested in a spin test, which induced stresses exceeding 144 percent of the design maximum at the blade neck. Prior to engine testing, each of the ceramic components passed its respective proof test.

The ceramic nozzles and blades were independently evaluated in two separate engine tests. One test engine was equipped with ceramic nozzles and metallic blades; the other, with ceramic blades and metallic nozzles. The ceramic-nozzle-equipped engine accumulated 10 hours of test operation without distress to the ceramic nozzles. However, the engine equipped with ceramic blades failed during the first start attempt. The problem was traced to insufficient contact in the load bearing surfaces at the ceramic blade/metal disk attachment. Corrective actions were identified and initiated to ensure that contact loads in the attachment bearing surfaces are nominal. Engine test activities on the ceramic turbine nozzles and blades will continue through the remainder of 1993 and into 1994.

The ATTAP/331-200 program has the mission of augmenting the development of ceramic technology in support of automotive gas turbine development. To achieve this goal, the program has a plan to enhance the ceramic technologies required to support the design of gas turbine ceramic components, to refine and scale up the production capability of domestic U.S. ceramic component manufacturers, and to demonstrate the capability of the ceramic components, first in laboratory tests and then in extensive field trials. The engine demonstrations and field evaluations will not only gather the experience required to verify the improvements in ceramic design technology and component fabrication, but will also give feedback of new data to help improve these capabilities on a continuous basis.

References

1 DARPA/Navy, "Ceramic Gas Turbine Engine Demonstration Program," Contract No. N00024-76-C-5352, 1976–1981.

2 USAF, "Ceramic Components for Turbine Engines Program," Contract No. 33615-77-C-5171, 1979–1982.

3 DOE/NASA, "Advanced Gas Turbine AGT101 Engine Program," Contract No. DEN3-167, 1980–1987.

4 DOE/NASA, "Advanced Turbine Technology Applications Project ATTAP/AGT101 Program," Contract No. DEN3-335, 1987–1992.

5 Strangman, T. E., and Fox, D. S., "Strength Retention of NT154 Silicon Nitride Exposed to High-Temperature Oxidation and Hot Corrosion Environments," presented at the 184th Meeting of the Electrochemical Society, New Orleans, LA, Oct. 12, 1993; AlliedSignal Engines Rept. No. 31-11623.

6 Cuccio, J., "Life Prediction Methodology for Ceramic Components of Advanced Heat Engines," DOE/ORNL Contract No. 86X-SC674C, 1986.

Diesel Electro-injector: A Numerical Simulation Code

P. Digesu

D. Laforgia

Istituto di Macchine ed Energetica,
Polytechnic of Bari,
Bari, Italy

A simulation code of an electro-injector for diesel engines is presented with the preliminary parametric analysis carried out with the code. The simulation code is based upon the concentrated volume method as for the chambers of the system. Energy and flow rate conservation equations and dynamic equations are used for the movable parts of the system under stress or friction. The magnetic force acting on the electro-injector actuator has been calculated by means of a finite element simulation. The one-dimensional code simulated the propagation in feeding pipes and the control of the electro-injector. The program, in fact, uses the method of the characteristic equations to solve conservation equations, simulating the propagation in a pipe between two chambers. The sensitivity analysis has pointed out that the parameters that are influenced by the propagation in the pipes are: needle lift, injected flow rate, pressure in each chamber, and volume. The perturbations reduce the effective pressure of injection and are influenced by pipe lengths and diameters.

Introduction

The simulation of injection systems has been investigated by Matsuoka et al. [1] and Laforgia and Ficarella [2–4]. Laforgia started the development of a quite sophisticated numerical code capable of predicting the functioning of both reciprocating [2, 3] and rotating injection pumps [4]. They completed the numerical code with an accurate simulation of cavitation phenomena inside the pipe [5]. Catania et al. [6] have also treated the simulation of reciprocating systems developing a code with an implicit scheme. A recent development of injection systems is directed to electro-injectors at high pressure, which has different problems in the simulation from those treated until now. A previous work of Digesu' [7] developed a calculation code to be applied to a strongly innovative geometry of an electronical injector (Elasis patent) for D.I. diesel engines. The code was an early stage of its development. The present work deals with a completely different geometry characterized by a sole feeding pipe, called one-pipe, and a small control capacity. The code developed unifies the concentrated volume approach of the main capacities of the electroinjector with the simulation of pressure propagation in pipes, which is based on the method of characteristics, and the simulation of the electromagnet of control.

Mathematical Model

In the first version of the code, the pipe volume was included as concentrated volume in the chamber at the ends of the pipe. The code stressed the unneglectable effect of propagation in pipes. The basic equations used for the injection system simulation were the mass and momentum equations [2–4].

The integration of the momentum equation on a solid body allows the modeling of the moving parts, such as valves and needle. Forces due to the pressure on the surfaces, to the spring load and preload and to the friction forces were taken into account as well as the collision forces calculated by means of the elastic collision theory.

An integral approach on a generic volume for the equation of mass is convenient when the main phenomenon is the pressure variation due to the flow rate and volume variation, as in the several chambers of the apparatus. The discharge coefficient was evaluated according to Schmitt's suggestions [8]; furthermore, the leakage between the different chambers was evaluated considering laminar the flow in the gap [9]. Hardenberg's [10], Andoh's [11], and Dereco's [12] theories and data were used to simulate sacless injector discharge coefficient.

Mass and momentum equations were employed to simulate the fluid dynamic phenomena inside the pipes and the connections between the different chambers of the apparatus. Using a further relation between pressure and density, it was possible to solve the equations in one-dimensional form using the method of characteristics. This relation was based on the bulk modulus of the fluid that has been considered variable linearly according to the pressure [13–15], interpolating the data obtained from measurements; air in the fuel was also considered. Nikuradse's theory [16] was used to calculate the friction forces

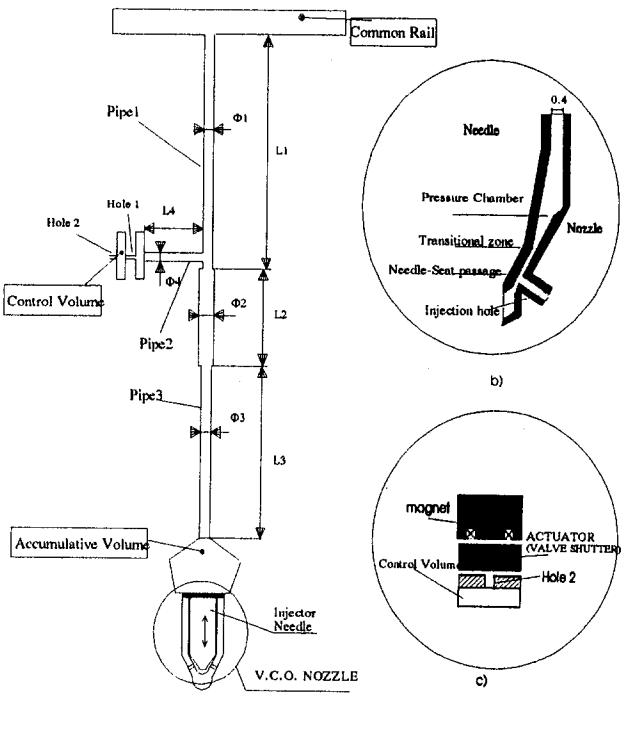

Fig. 1 Electro-injector hydraulic scheme

Contributed by the Internal Combustion Engine Division and presented at the 16th Annual Fall Technical Conference of the ASME Internal Combustion Engine Division, Lafayette, Indiana, October 2–6, 1994. Manuscript received at ASME Headquarters June 1994.

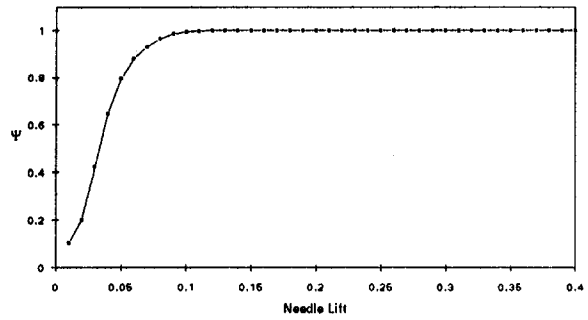

Fig. 2 Vena contracta coefficient versus dimensionless needle lift

while the boundary conditions were calculated according to Matsuoka [1]. All the equations were solved using an explicit first-order Runge–Kutta scheme.

Evaluation of Magnetic Force. By means of a finite element method the schematization of the magnetic actuator was done [7]. The magnet was modeled with bidimensional, axisymmetric elements considering the magnet geometry characterized by an axial symmetry. The analysis was carried out at both steady and transient working conditions. The fixed core, the movable equipment, the coil, and the working gap were also schematized.

The magnetic properties of materials were set using experimental curves. This approach allowed the optimization of designing parameters that have to meet the needs for rapid actuations and low values of exciting current and high values of magnetic force. For this reason, it was possible to optimize the magnetic inductance to reduce current and the weight of the movable equipment to reduce actuation time.

Through the simulation, the magnetic force were mapped as function of exciting current and working gap. This map was introduced in the fluid-dynamic simulation code supplying the controlling parameters of the electro-injector.

Hydraulic Schematization of the Electro-injector. The electro-injector was schematized with three volumes connected by pipes and calibrated holes (common rail, control volume, and reservoir) and with two movable equipments (shutter of valve needle and injector needle) (Fig. 1). The common rail is a high-pressure manifold fed by a pump and connected to the other two volumes by means of a pipe and a calibrated hole (hole No. 1). By means of a calibrated hole (hole No. 1, Fig. 1*a*) the control volume is connected with pipe 3 and with the low-pressure volume of recirculated diesel fuel, respectively. The law of variation of discharge coefficient of the holes was obtained by measurements. The discharge coefficient of hole No. 1 depends on the valve shutter lift as in [7], while the others are quite constant.

In Fig. 1(*c*) a scheme of the shutter of the valve is shown. The shutter closes hole No. 2 and is controlled by the electromagnet. Hole No. 2 controls the fuel flowing from the control volume and then the needle lift.

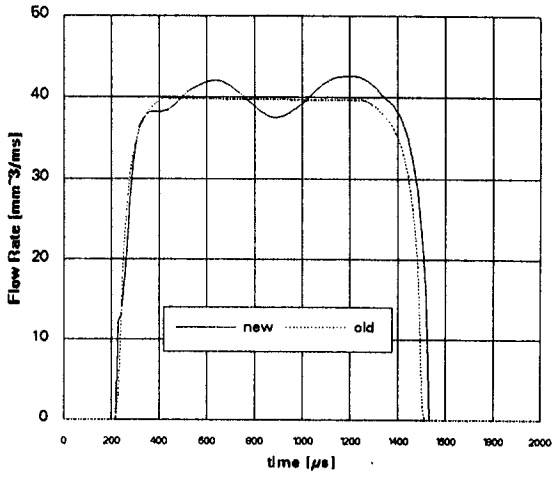

Injected Fuel

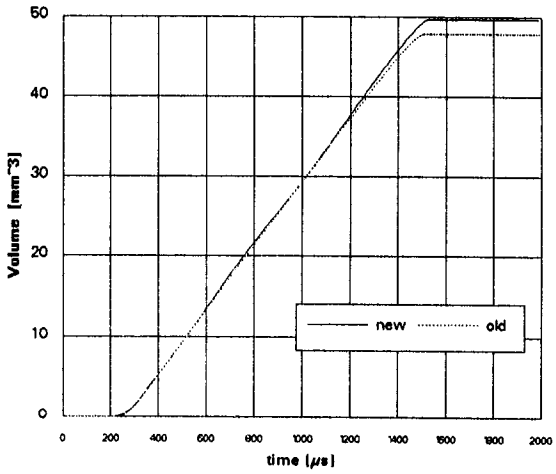

Fig. 3 Comparison between simulations with (new) and without (old) waves effects for injected flow rate and cumulative injected fuel

The V.C.O. nozzle (Fig. 1*b*) needs a reservoir before the nozzle itself, which feeds the injection holes. Such a reservoir is one of the chambers to and from which the pressure pulses move. Taking the suggestion of Schmitt and Andoh, the nozzle discharge coefficient was determined, dividing the energy loss among the three following types:

- leakage between needle and seat

$$\delta p_1 = (B \cdot 1 \cdot \mu \cdot V_2)/Y_0^2$$

Nomenclature

A = area, m^2
B = leakage coefficient
E.T. = exciting time, s
V_2 = velocity at hole inlet, m/s
V_4 = velocity at hole outlet, m/s
Y_0 = thickness, m
c = sound velocity, m/s
f = friction factor, m/s^2
l = needle-seat gap length, m
p = pressure, Pa
s = discharge coefficient of direction change
t = time, s
u = velocity, m/s
x = spatial coordinate, m
α = vapor fraction
δp_i = hydraulic losses, Pa
μ = dynamic viscosity, kg/m/s
ρ = density, kg/m^3
ψ = vena contracta coefficient

Subscripts

l = liquid
v = vapor

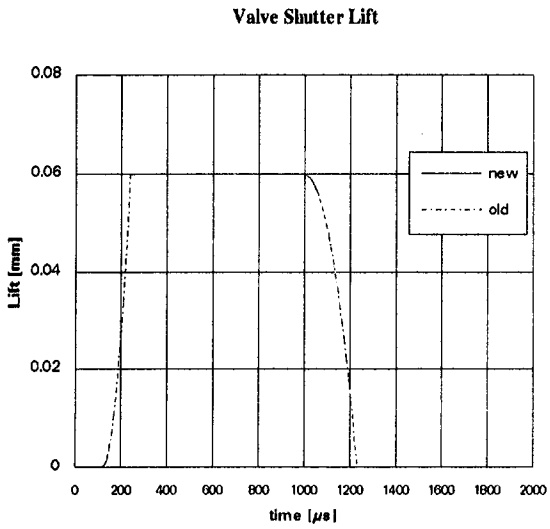

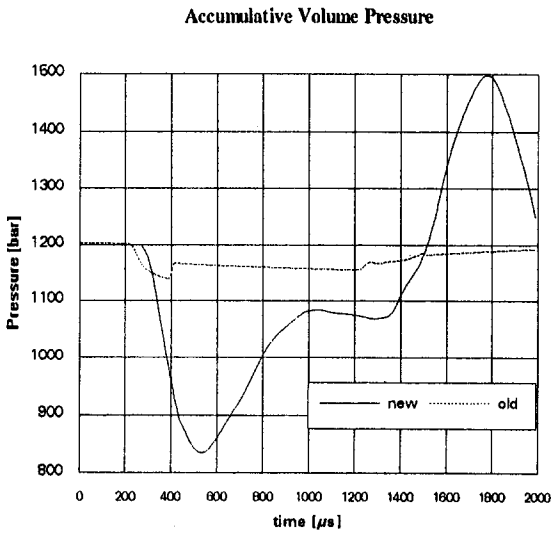

Fig. 5 Comparison between simulation with (new) and without (old) waves effects for the reservoir pressure

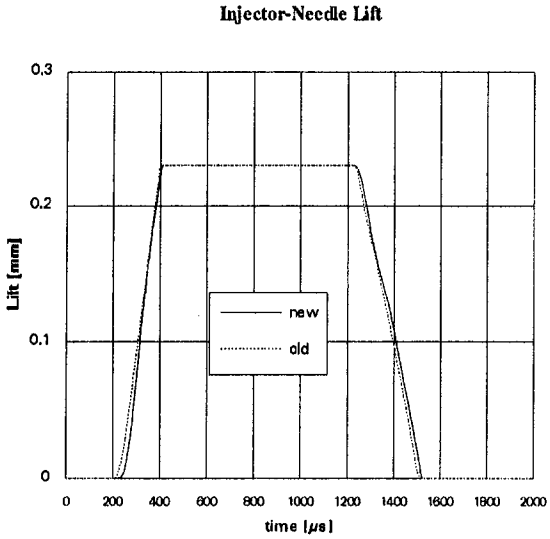

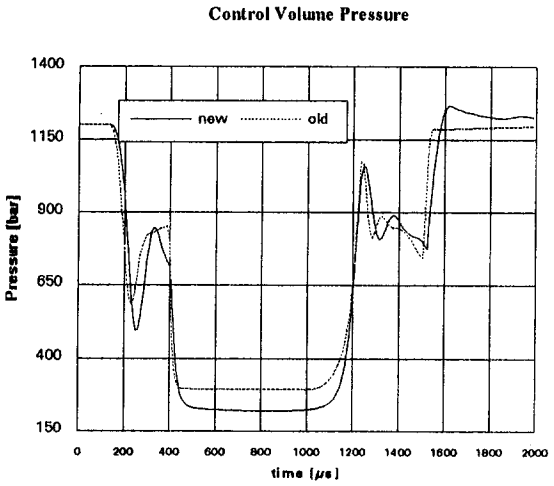

Fig. 4 Comparison between simulations with (new) and without (old) waves effects for actuator and injector needle

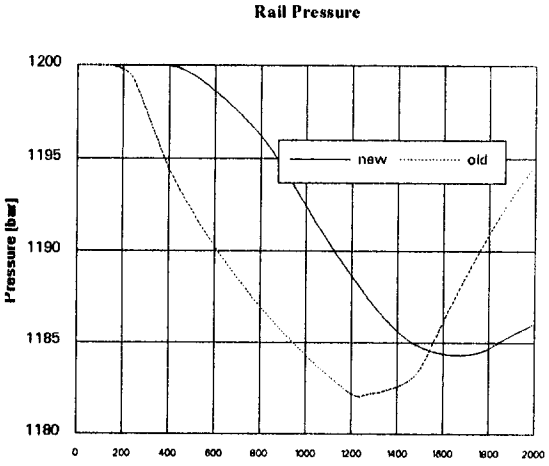

Fig. 6 Comparison between simulations with (new) and without (old) waves effects for control volume and common rail

- loss due to change of direction at hole inlet

$$\delta p_2 = \tfrac{1}{2} \cdot \rho \cdot V_2^2 \cdot s^2$$

- loss in the holes vena contracta

$$\delta p_3 = \tfrac{1}{2} \cdot \rho \cdot V_4^2 \cdot (1/\psi - 1)^2$$

where B, s, Ψ were calculated on experimental basis. In particular, B and s were constant and equal to 10 and 0.8 while Ψ was mapped as function of the needle lift, as in Fig. 2.

The electro-injector is controlled by a magnet-driven electrovalve, excited by a current variable in intensity and duration. The needle motion is controlled by the balance of some forces among which two pressure forces (control volume pressure and reservoir pressure); the first pushes the needle toward the seat and the second one pushes it into the opposite direction. When the closing pressure is reduced by the action of the electrovalve the needle moves starting the injection.

Pipe Simulation. The fluid-dynamic code was modeled on the geometry of the electro-injector and the routine simulating waves effects took into account the feeding pipe of the reservoir, the feeding pipe of the control volume, and the variation of pipe sections and pipes junctions.

Assuming a dependence of density on pressure only, it should be possible to introduce the fuel bulk modulus as defined by

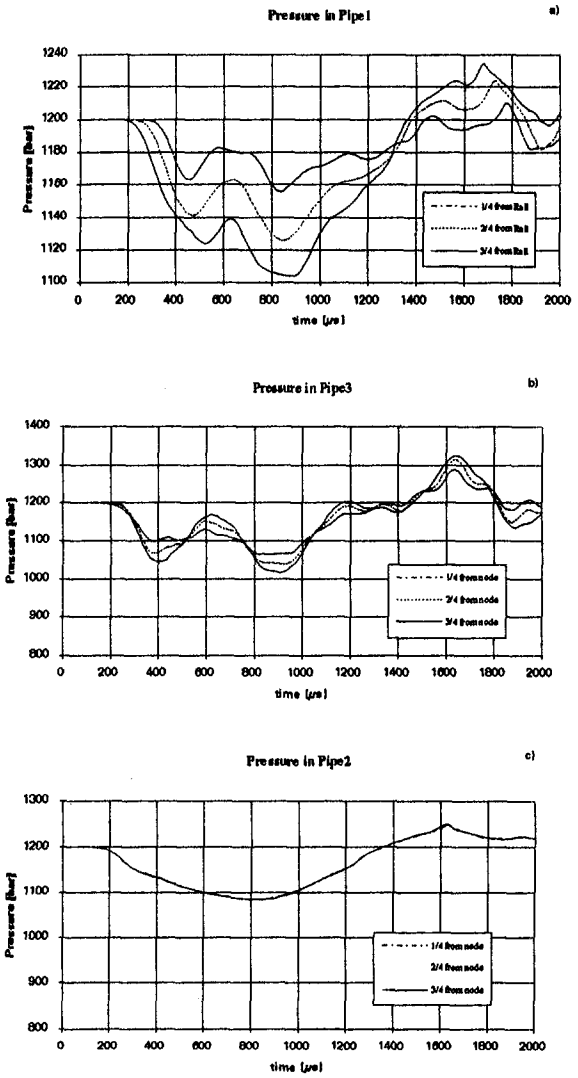

Fig. 7 Pressure in pipes: (*a*) Pipe1; (*b*) Pipe2; (c) Pipe3

Parson [14]; moreover, the elasticity of the pipe walls was calculated by reducing the bulk modulus of the fluid volume contained between them. The equations of flow inside a pipe were solved by writing continuity and momentum equations considering one-dimensional isothermal flow. Taking into account those hypotheses, the equation system is:

$$(\partial p/\partial t) + (u\partial p/\partial x) + (\rho c^2 u\delta)/A + \rho c^2(\partial u/\partial x) = 0$$

$$(\partial u/\partial t) + u(\partial u/\partial x) + (\partial p/\partial x)/\rho + f = 0$$

where $d = dA/dx$.

An explicit first-order accuracy scheme, based upon the method of characteristics, was used to obtain the difference analogue of the one-dimensional governing differential equation. The resultant set of algebraic equations was solved by Gaussian method. As for the boundary conditions, in the case of fuel flow traveling toward the end chambers, the pressure at the end section was assumed to be equal to the chamber pressure; in the opposite case, a pressure loss was assumed due to the contraction of flow as suggested by Matsuoka [1].

Cavitation phenomena were treated as in [2]. The variability of the bulk modulus and the density with the pressure was also taken into account as well as the inevitable quantity of air in the fuel. The values of the bulk modulus and those of the sound velocity as a function of b (ratio of air volume to fluid total volume) and the pressure were calculated according to Pischinger-

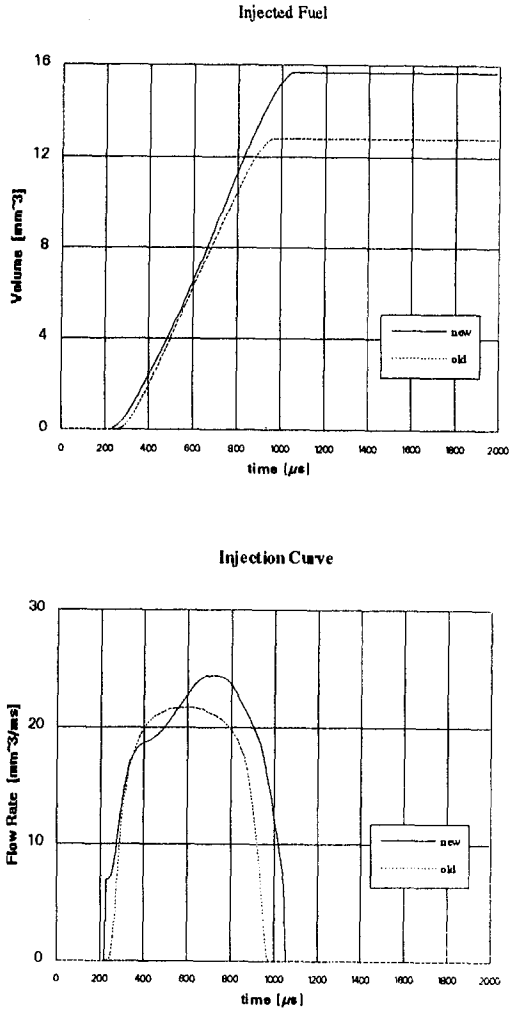

Fig. 8 Comparison between simulations with and without wave effects for injected flow rate (*b*) and cumulative injected fuel (*a*)

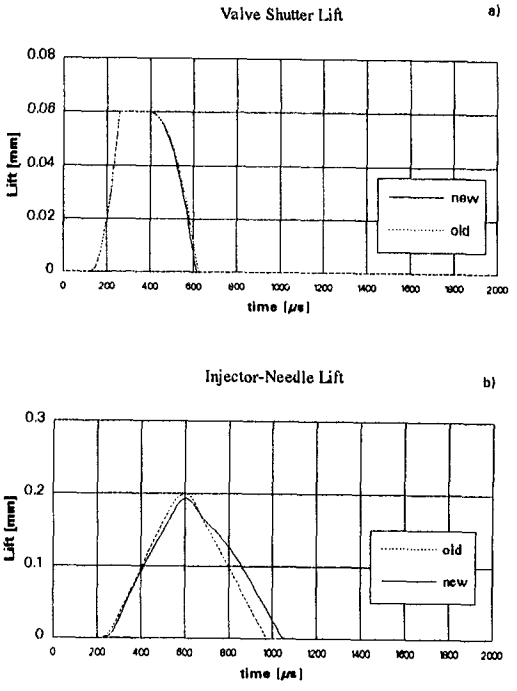

Fig. 9 Lift comparison between simulations with and without waves effects for actuator (*a*) and injector needle (*b*)

Table 1 Summary of parametric analysis cases

FEEDING PIPE		
CASE	DIAMETER [mm]	LENGHT [mm]
A	2.5	85
B	2	85
C	2	155
D	3	85
E	3	155
F	2.5	155

er's models. It can be supposed that the cavitation phenomenon starts when pressure is equal to the vapor pressure at fuel temperature, as suggested by Gibson [9]. In this case, the fluid density can be calculated as:

$$\rho = (1 - \alpha)\rho_l + \alpha\rho_v$$

Supposing again that the density of both phases is only function of the pressure and does not vary, as the section pressure is constant and equal to the vapor pressure until there is vapor, the continuity equation can be written as:

$$(\rho_v - \rho_l)(\partial\alpha/\partial t) + u(\rho_v - \rho_l)(\partial\alpha/\partial x) + \rho(\partial u/\partial x) = 0$$

The pressure drop due to the friction in two-phase flow could not be treated as monophase, since the vapor completely modified the fluid dynamic conditions in the pipe; its evaluation was realized through Lockart's and Martinelli's empirical correlation as shown in [2].

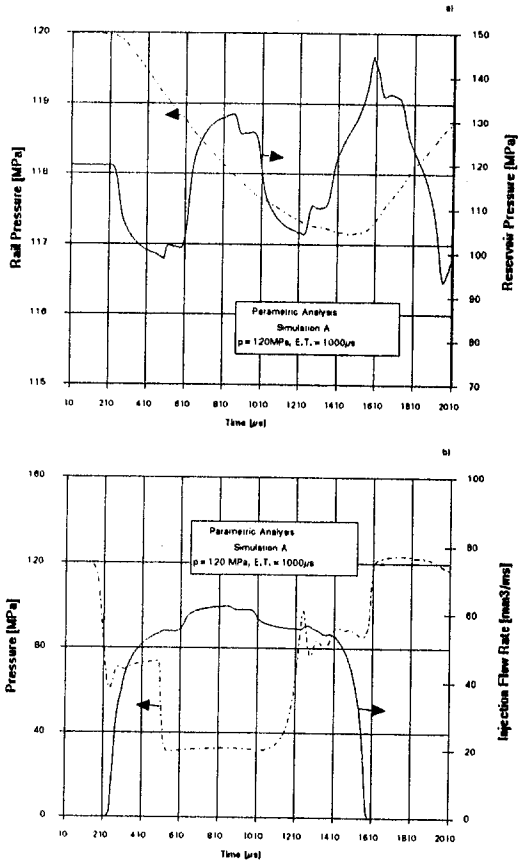

Fig. 10 Predicted trends of rail pressure and reservoir pressure (*a*) and of injected flow rate and control volume pressure (*b*)

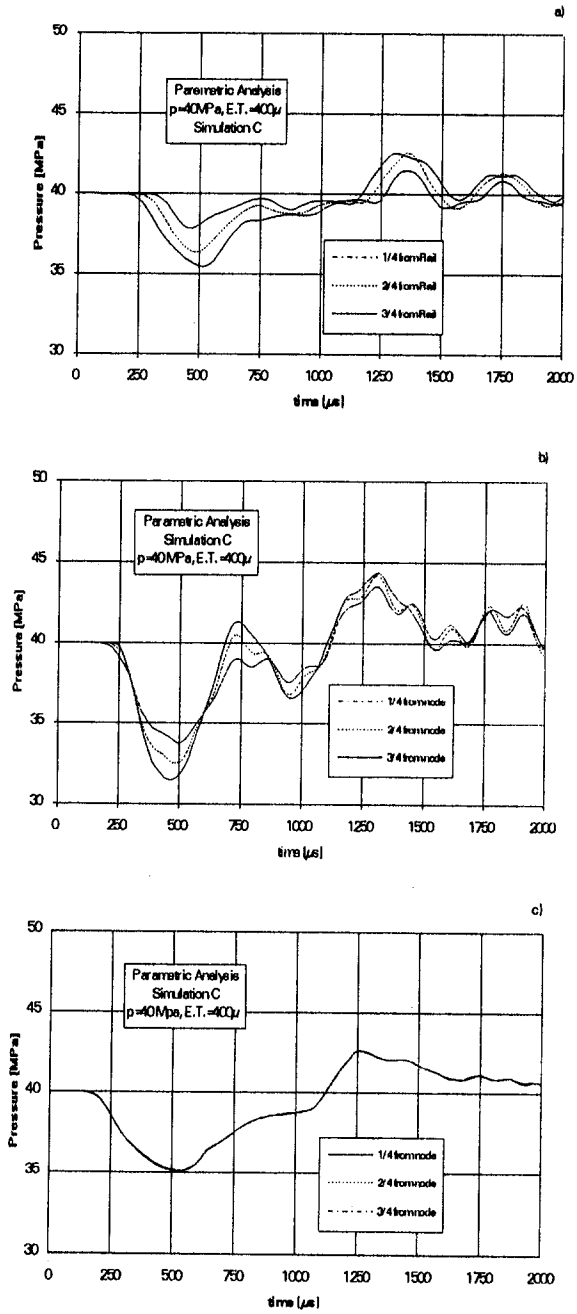

Fig. 11 Predicted trends for different locations of pressure in pipe 1 (*a*) and in pipe 3 (*b*)

Numerical Analysis and Discussion of Results

The positive experimental verification of the code provided in [7] could not be repeated in the present investigation since the injector is being developing and is not yet available. The satisfactory comparison between the theoretical and experimental measures obtained in [7] allows optimistic expectations about the validity of predictions for the new geometry. A sensitivity analysis of the electro-injectors through the code has been carried out, stressing the influence of propagation phenomena, and of geometric parameters such as feeding pipe diameter and length.

Influence of Wave Effects. In Figs. 3–6 the comparison between simulation codes with and without propagation is presented; the calculation conditions were feeding pressure equal to 120 MPa and exciting time of 1000 μs.

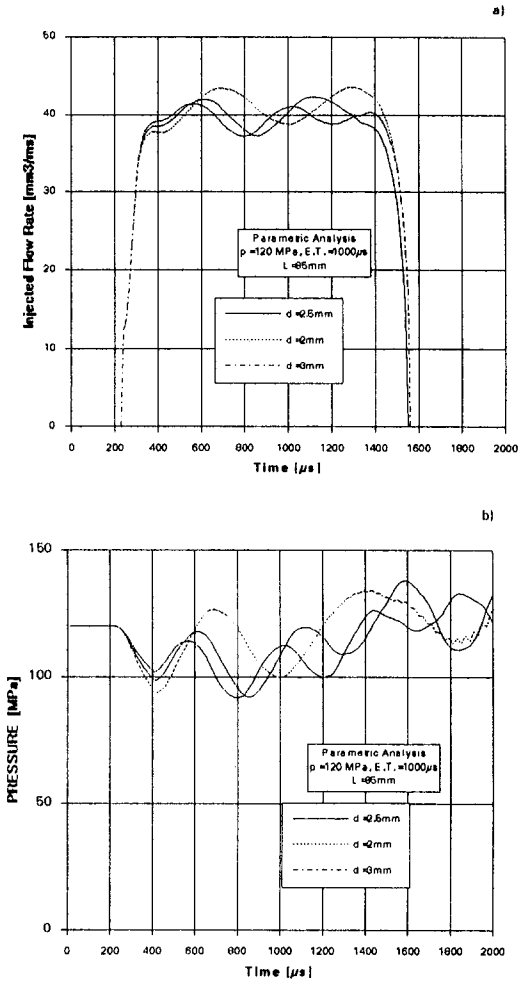

Fig. 12 Predicted trends for different pipe 1 diameters of injected flow rate (*a*) and of reservoir pressure (*b*)

The following parameters have been carefully investigated: injected flow rate (Fig. 3*a*), fuel quantity per cycle (Fig. 3*b*), pilot needle lift (Fig. 4*a*), injector needle lift (Fig. 4*b*), reservoir pressure (Fig. 5), control volume pressure (Fig. 6*a*), common rail pressure (Fig. 6*b*), pressure in pipes 1, 2, and 3 (Fig. 7*a, b, c*). The following considerations could be formulated comparing the two simulations:

- the injected flow rate trends and the injection law are remarkably different in both cases (Fig. 3) and this fact is usually neglected for high pressure electro-injectors;
- the pressure propagation does not influence the pilot needle lift;
- a limited variation of injection duration and delay of needle closing can be noted (Fig. 4*b*);

Generally speaking the injection curve follows the trend of the pressure in the reservoir and of the pressure in the control volume (see for example Figs. 3*a*, 5, 6*a*).

A further comparison was made varying the testing conditions: The feeding pressure was reduced to 40 MPa and E.T. to 400 μs in order to eliminate the needle stop and to stress the transient phases. The results of the simulation are presented in Fig. 8 and 9; the following considerations can be made:

- the pressure propagation causes a strong variation of injection curve, which presents a bulkish shape that is a consequence of the reservoir overpressure (Fig. 8*a*);
- the needle lift is delayed and does not reach the stop because of the low feeding pressure (Fig. 9*b*).

Investigation on the Influence of Pipe Parameters. A parametric analysis of the injector characteristics—hole diameter and lengths—has been carried out. The simulation conditions were: feeding pressure of 120 MPa, exciting time of 1000 μs, nozzle holes 6 × 0.21 mm. The simulation cases are summarized in Table 1.

In Figs. 10 and 11 only the results of case A are presented referring to reservoir pressure (Fig. 10*a*), common rail pressure (10*a*), injection law (10*b*), control volume pressure (Fig. 10*b*), pressure in pipe 1 and pipes 2, 3 (Fig. 11).

In Figs. 12, 13, and 14 the comparison among injection law, reservoir pressure, and needle lift, being equal to either the pipe length with variable diameter or pipe diameter with variable length, are shown.

Some important considerations to be made are that:

- the pipe diameter influences the instantaneous injection (Fig. 12);
- the effect of a different length of the feeding line is clearly visible in Fig. 13, in fact the propagation presents longer duration and the effects of pressure waves reflections combined with E.T. duration causes a different injection law;
- also the needle lift is influenced by the length variation and the diameter variation as shown in Fig. 14.

Conclusions

A simulation code of an electro-injector with new geometry has been developed, considering for the first time also the effects

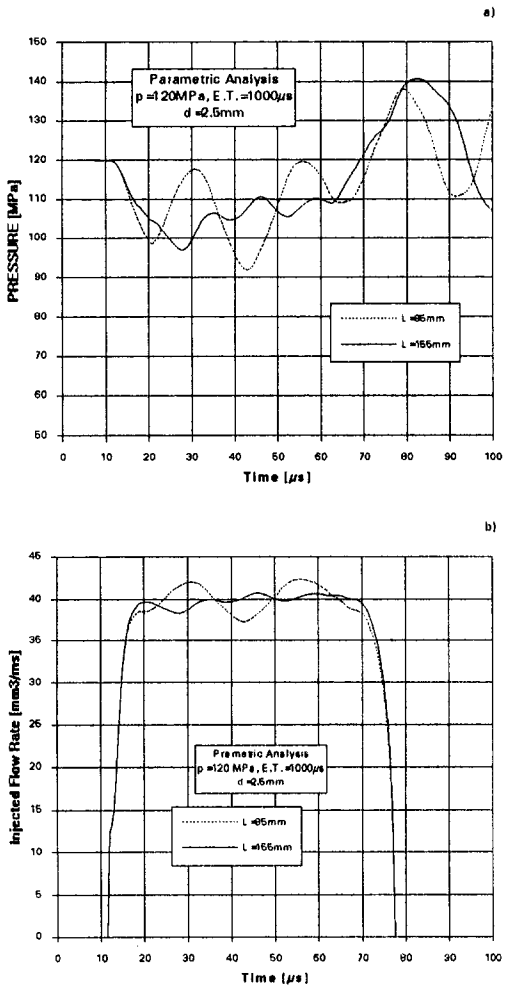

Fig. 13 Predicted trends for different pipe 1 lengths of injected flow rate (*a*) and of reservoir pressure (*b*)

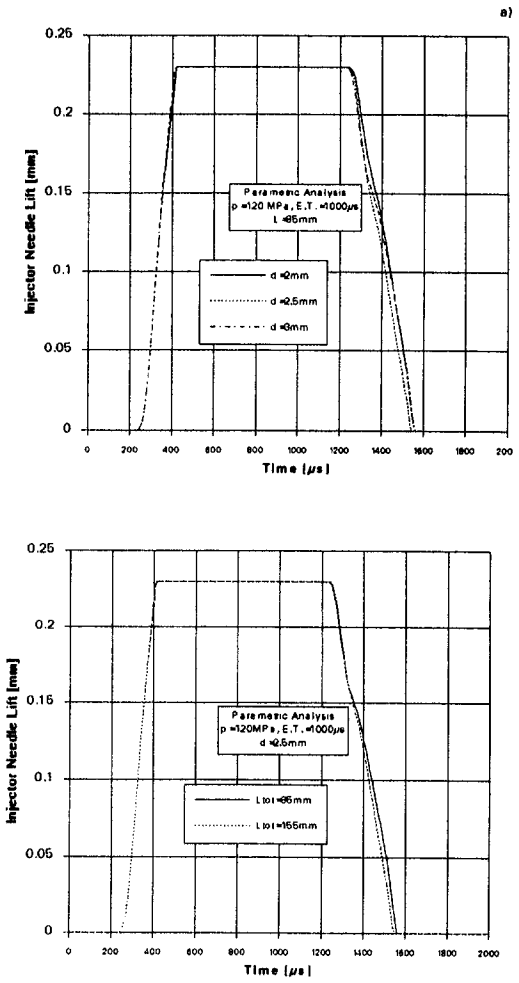

Fig. 14 Predicted trends of needle lift for different pipe 1 diameters (*a*) and lengths (*b*)

of propagation phenomena of pressure waves inside the pipes. The influence of pressure pulses on the injection law and chamber pressure, which assume different values from those predicted, cannot be neglected.

The code is ready to be employed in an extensive parametric analysis of sensitivity aimed at identifying the electro-injector components, which mostly influence the performance parameters.

In the preliminary analysis, the pipe diameter and length showed a certain influence on injection law and pressure time history because they are strictly related to wave propagation.

Such an influence seems limited to diameters lower than those actually employed and it appears to be less important than the length influence on mechanically controlled injection systems.

This research will be continued with a sensitivity analysis using the code to optimize the main parameters to better the electro-injector performances.

References

1 Matsuoka, S., Yokota, K., Kamimoto, T., and Igoshi, M., "A Study of Fuel Injection System in Diesel Engines," SAE Paper No. 851583, 1989.

2 Ficarella, A., and Laforgia, D., "Fluid Dynamic Phenomena in Fuel-Injection Systems," *MTZ,* Vol. 52, No. 1, 1991, pp. 28–35.

3 Ficarella, A., and Laforgia, D., "Contribution to the Simulation of Injection System for Reciprocating I.C. Engine," SAE Paper No. 885016, 1988.

4 Ficarella, A., and Laforgia, D., "Investigation and Computer Simulation of Diesel Injection System With Rotative Pump," ASME JOURNAL OF ENGINEERING FOR GAS TURBINES AND POWER, 1990, Vol. 112, pp. 317–323.

5 Ficarella, A., and Laforgia, D., "Injection Characteristics Simulation and Analysis in Diesel Engines," *Meccanica,* International Journal of AIMETA, Kluwer Academic Publishers, Vol. 28, 1993, pp. 239–248.

6 Catania, A. E., Dongiovanni, C., and Mittica, A., "Implicit Numerical Model of a High Pressure Injection System," ASME JOURNAL OF ENGINEERING FOR GAS TURBINES AND POWER, Vol. 114, 1992, pp. 534–543.

7 Digesu', P., Ficarella, A., Laforgia, D., Bruni, G., and Ricco, M., "Diesel Electro-injector: A Numerical Simulation Code," SAE Paper No. 940193, *Fuel Spray Technology,* SAE SP-1026, pp. 51–64.

8 Schmitt, Th., "Untersuchungen zur Stationaren und Instationaren Stromung durch Drosselquerschnitte in Kraftstoffeinspritzsystemen von Dieselmotoren," Forschungsbericht 2-226/2, 1966.

9 Gibson, D. H., "A Flexible Fuel Injection Simulation," SAE Paper No. 861567, 1986.

10 Hardenberg, H., "Die Nadelhubabhaugigkeit der Dyrchflußbeiverte von Lochdusen für Direkteinspritzdieselmotoren," *MTZ,* Vol. 46, No. 4, 1985.

11 Andoh, H., and Shiraishi, K., "Influence on Injection and Combustion Phenomena by Elimination of Hole Nozzle Sac Volume," SAE Paper No. 860416, 1986.

12 DERECO, "Experimental Evaluation of Flow Coefficient of Fuel Injectors at Different Pressure Drop, Backpressure and Needle Lift," Technical Report No. 185/85, 1985.

13 Pischinger, R., Staska, G., and Gao, Z., "Berechnung des Einspritzeverlaufes von Dieselanlangen bei Kavitation," *MTZ,* Vol. 44, 1983, p. 11.

14 Parson, M. G., and Harkins, R. W., "Investigation of Fuel Injection System Cavitation Problems on the MV J. R. Baker, MV M. Miner, and MV W. R. de Lancey," *Marine Technology,* Vol. 22(3), 1985, pp. 219–237.

15 Marcic, M., and Kovacic, Z., "Computer Simulation of the Diesel Fuel Injection System," SAE Paper No. 851583, 1985.

16 Buchlin, J. M., "Two Phase Flow," Course Note 131/EA, VKI, Bruxelles, Oct. 1988.

Design and Development of a Direct Injected, Glow Plug Ignition-Assisted, Natural Gas Engine

M. L. Willi

B. G. Richards

Engine Research,
Caterpillar Inc.
Peoria, IL 61656

Conventional (Otto cycle) natural gas engines are limited in power and thermal efficiency relative to a diesel engine due to detonation and the need to run a nearly stoichiometric air/fuel ratio. Technology is under development to burn natural gas in a direct-injected diesel cycle that is not prone to detonation or air/fuel ratio control limitations. Direct-injected gas (DIG) technology will allow natural gas engines to match the power and thermal efficiency of the equivalent diesel-fueled engine. Laboratory development now under way is targeted for field experimental evaluation of a DIG 3516 engine in a 1500 kW road switcher locomotive. This paper will describe DIG 3516 engine component design and single and multicylinder performance development.

Background

Natural gas has emerged as a low-cost, clean burning alternative fuel. The majority of natural gas engines operate on the Otto cycle utilizing a premixed fuel/air charge and a spark for combustion initiation. While this type of engine has significant NO_x and particulate emissions advantages relative to a diesel-fueled engine, it has several drawbacks in terms of engine performance. Spark-ignited (SI) engines generally have 30 percent lower power output than the same size diesel engine due to combustion-rate-limited engine speed and detonation-limited brake mean effective pressure (bmep) capabilities. SI engines also suffer from 15 to 25 percent lower thermal efficiency than the diesel-fueled engine due to detonation-limited lower compression ratio and high intake air pumping losses resulting from the need to throttle the intake air pressure at part load conditions. Finally, SI engines have more than 30 percent higher heat rejection than a diesel engine, which leads to a requirement for a larger, more expensive cooling system, which may be prohibitive in terms of space requirements in a mobile application.

A direct-injected natural gas engine operating on the diesel cycle would have the potential to match diesel-fueled engine performance while maintaining the smoke-free operating characteristics of a spark ignited gas engine. Additionally, a DIG engine should be less sensitive to variations in fuel quality than a spark-ignited engine. A DIG engine will require some kind of ignition assist at typical diesel engine compression ratios due to its low cetane number. The ignition/combustion characteristics of methane, the major constituent of natural gas, are compared to diesel and two other alternative fuels in Table 1 (Siebers, 1985, 1994; Katz et al., 1959).

Prior to DIG development, a glow plug ignition assist system had been developed for methanol engines (Kroeger, 1986; Richards, 1990). Glow plug ignition assist had been selected as the best of several diesel cycle ignition assist options, including pilot diesel injection. Although Table 1 indicates that natural gas ignition is more challenging than methanol, the application of glow plug ignition assist technology to the DIG engine was believed to be feasible.

A DIG engine will also require a high-pressure gas supply to allow the gas to be injected at pressure sufficient to overcome cylinder pressure near top dead center. This high gas pressure can either be provided through gas compression, which may require 4–10 percent of the engine's output power depending on inlet supply pressure, or by pressurization of liquefied natural gas (LNG) and subsequent vaporization, which will require less than 1 percent of the engine's output power. A comparison of pressurized LNG versus compressed gas delivery systems is shown in Table 2.

In light of the potential advantages of a DIG engine relative to an SI engine, a development program has been initiated with the near-term objective of demonstrating the ability of a DIG engine to match the power output and thermal efficiency of a diesel-fueled engine. The initial test bed was a single cylinder test engine equipped with laboratory-demonstration-type hardware. Successful completion of this demonstration paved the way for further evaluation of the engine technology for a production engine and aided in matching the technology to its most appropriate application and engine family. This identification led to a prototype design and test phase in preparation for a multicylinder engine development program.

Combustion Feasibility

Combustion feasibility tests were performed with the objectives of matching the power output and thermal efficiency of the diesel-fueled baseline engine while operating on direct-injected natural gas. These tests were performed on a modified 3401 engine (137 mm bore × 165 mm stroke) rated at 50 kW at 2100 rpm in turbocharged/jacket water aftercooled trim.

The fuel system for the 3401 engine utilized a gas compressor to compress utility gas to the desired pressure, a pump and line (diesel fuel) working-fluid system to actuate the injector, and a pressurized engine oil reservoir to provide an oil seal between the gas and diesel fuel areas on the injector check. The combustion system hardware was for laboratory demonstration purposes only and, as such, was configured for easy modification of existing components. A schematic of the fuel system is shown in Fig. 1. The high ignition temperature of methane, the major constituent of natural gas, required the use of an ignition assist device to initiate combustion. The system used was a hot surface of a glow plug that has been previously described by Kroeger (1986) and Richards (1990) as used on methanol-fueled en-

Contributed by the Internal Combustion Engine Division and presented at the 16th Annual Fall Technical Conference of the ASME Internal Combustion Engine Division, Lafayette, Indiana, October 2–6, 1994. Manuscript received at ASME Headquarters June 1995.

Table 1 Fuel properties

	Diesel	Methanol	Methane	Hydrogen
Flammability Range (% vol. in air)	0.6 - 7	7 - 36	5 - 15	4 - 74
Flammability Range Ratio	11	5	3	19
Ignition Temperature (degrees C for 2ms delay)	527	802	857	~757

gines. While this ignition assist system is a key element in DIG technology, it was not the subject of development during the laboratory demonstration and so was not manipulated during the test work.

A hardware configuration was identified to give controllable and repeatable combustion performance, which allowed the demonstration objectives to be met or exceeded. The performance of the DIG 3401 is compared to that of the diesel-fueled engine in Table 3. Steady-state emissions measured on both the diesel and DIG engines at the rated power point are included in Table 3. As expected, there was less visible smoke from the DIG engine, which should lead to reduced particulate emissions relative to the diesel. The NO_x emissions of the DIG engine were lower than those of the diesel-fueled engine, primarily due to the lower adiabatic flame temperature of methane relative to diesel fuel. The CO and total hydrocarbon emissions of the DIG engine, while higher than those of the diesel, are still within acceptable limits. The tabulated data were taken at the diesel rated point of 50 kW at 2100 rpm (1171 kPa bmep) and shows that the DIG engine is capable of achieving power output and thermal efficiency equal to the diesel. In fact, the demonstrated efficiency of the DIG engine is 5 percent better than the diesel due to the shorter combustion duration of the DIG, as shown in Fig. 2.

It is evident from the figure that the DIG combustion is faster during the first 80 percent of the cycle and slower during the last 20 percent relative to the diesel. This leads one to believe that there is room for further improvement in the DIG combustion if the heat release rate can be increased during the last 20 percent of the cycle. The DIG engine combustion exhibits a longer ignition delay than that of the diesel, which leads to less overlap between the injection and combustion events. This lower overlap is believed to reduce the in-cylinder heat transfer and contribute to the DIG engine's higher efficiency relative to the diesel.

Table 2 LNG versus CNG systems

	CNG	LNG
Power Requirement (% of engine)	4 - 10	<1
Gas Storage	Low Press Gas	Liquefied
Size[1]	Large	Small
Cost[1]	High	Moderate[2]
Technology	Mature	Developing

[1] relative to engine
[2] potential for low cost exists as technology matures

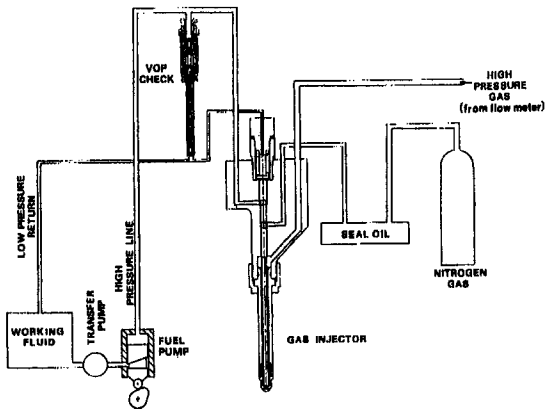

Fig. 1 3401 DIG fuel system

Prototype Design

The successful demonstration of the direct-injected natural gas combustion feasibility on the 3401 engine led to the next step of the development program: prototype design of commercially viable engine components. A market analysis performed with the available engine performance data indicated that the strengths of the DIG engine (power density, efficiency, slightly lower than diesel emissions) were well suited to use in 3500 Series engines (170 mm bore × 190 mm stroke) as a direct replacement for diesel-fueled engines or as an alternative to a lower power SI natural gas engine.

The objective of the prototype design phase was to design engine modifications necessary to operate an engine using direct-injected natural gas where the engine would be suitable for production should the test results and market analysis prove favorable for the use of the technology.

The major components required to modify the production 3500 Series diesel engine to operate on direct-injected natural gas were the cylinder head and the gas injection system. The injection system had specific delivery and opening and closing rate requirements identified from the 3401 tests. Head modifications required for DIG operation included accommodation of the gas injector and its oil and gas supply passages and the need to allow glow plug access to the combustion chamber.

After reviewing several options for power, actuation, and control of the gas injector, a hydraulically actuated, electronically controlled unit injector (HEUI) concept was chosen for

Table 3 3401 DIG versus diesel performance: 50 kW @ 2100 rpm (1171 kPa bmep)

	DI GAS	DIESEL
BSEC (kJ/kW-hr)	8648	9138
Thermal Eff. (%-LHV)	41.6	39.4
Avg. PCP (MPa)	11.5	11.9
A/F Ratio (mass)	31.7	30.9
Airflow (kg/hr)	302	326
Inl Man T (C)	80	90
Inl Man P (kPa)	215	239
Exh T (C)	584	560
Smoke (Cat)	.01	.02
BSNOx (g/hp-hr)	5.08	6.81
BSCO (g/hp-hr)	7.54	.497
BSTHC (g/hp-hr)	.41	.13

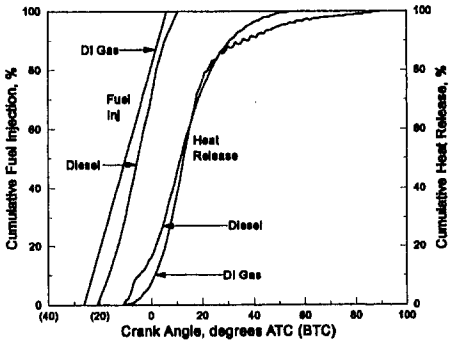

Fig. 2 3401 DIG versus diesel heat release

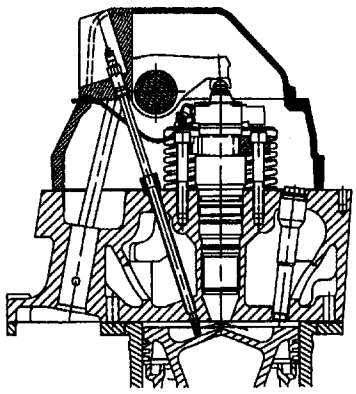

Fig. 4 3500 DIG combustion system

the prototype gas injector. This decision resulted from several considerations, including the desire for flexible control of injection timing and split injection capability and the desire to use proven technology that did not require any "breakthroughs" for successful operation. Additionally, any generic HEUI improvements applicable to diesel fuel injectors would also be transferable to the DIG injector during design updates. A HEUI injector was then designed, with the aid of computer system modeling, to fit within the current diesel injector envelope, while meeting the DIG performance requirements and injector life goals. The injector was designed with a mechanical split injection device, which could be tuned to deliver a small amount of gas prior to and separate from the main gas injection event. This capability was considered to be necessary based on test results of the 3401 DIG engine. A cross section of the 3501 HEUI is shown in Fig. 3.

Minimal modifications to the head design were required to accommodate the DIG injector and its fuel and oil supply passages. Changes to the head that were necessary to accommodate glow plug access to the combustion chamber were included in a finite element model, that was then used to verify that the modified head design would meet production fatigue factor design criteria. A cross-sectional view of the DIG head, injector, glow plug, and combustion chamber is shown in Fig. 4.

Prototype Development

Development work with the 3500 Series DIG hardware was undertaken with three primary objectives:

(*a*) match diesel power and thermal efficiency
(*b*) functionally prove the components and identify areas in need of improvement
(*c*) identify durability issues

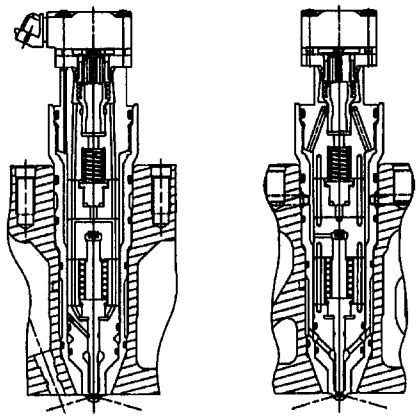

Fig. 3 3500 DIG HEUI gas injector

The 3500 Series initial rating goal of 109 bkW per cylinder at 1800 rpm (1683 kPa bmep) was a significant increase relative to the 1171 kPa bmep demonstrated on the 3401 and required 41 percent thermal efficiency to match the diesel baseline performance.

Prototype development started on a single-cylinder version of the 3500 Series engine (3501), modified with prototype DIG components. Initial testing of the 3501 engine focused on tuning the various split injection device components in order to get the desired fuel injection split and resulting expected smoother start of combustion of the main injection. After testing many modifications it was apparent that the small quantity of fuel available in the initial (pilot) injection was mixing too rapidly to remain as a combustible mixture in the cylinder at the end of the expected ignition delay period. As a result there was no expected split injection effect of a slower/more consistent start to the combustion of the main fuel charge. Additionally, the effect of the split injection device was such that it created a nonlinear fuel delivery versus injector solenoid on-time characteristic that was difficult for the electronic engine control to handle. The split injection device was removed from the injector for the remainder of the engine testing as the performance goals were found to be achievable without it.

Testing of various piston and injector orifice configurations led to a configuration that was used to demonstrate better-than-diesel engine performance as shown in Table 4. The brake specific energy consumption tabulated for both engines is based upon the lower heating value of the fuels and does not account for the energy needed to raise the fuel to injection pressure in the case of the DIG engine. The intended application for the DIG

Table 4 3501 DIG versus diesel performance: 109 kW @ 1800 rpm (1683 kPa bmep)

	DI GAS	DIESEL
BSEC (kJ/kW-hr)	7828	8933
Thermal Eff. (%-LHV)	46.0	40.3
Avg. PCP (MPa)	14.2	14
A/F Ratio (mass)	31.4	25.3
Airflow (kg/hr)	572	574
Inl Man T (C)	42	88
Inl Man P (kPa)	235	263
Exh T (C)	614	655
Smoke (Cat)	nil	.08
BSNOx (g/hp-hr)	9.8	10.1
BSCO (g/hp-hr)	1.46	2.47
BSTHC (g/hp-hr)	.53	.16

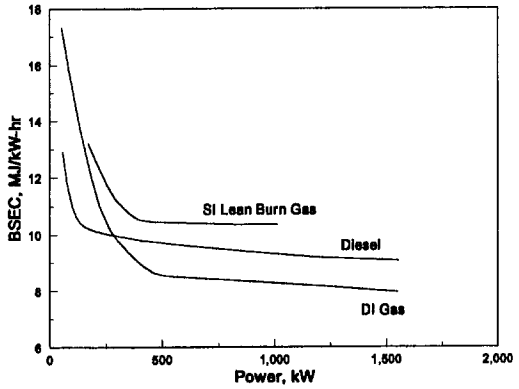

Fig. 5 SI/diesel/DIG performance 3516 engine—locomotive switcher application

engine dictated a lower intake air temperature, which resulted in a lower boost pressure at the same airflow as the diesel. The significantly lower exhaust temperature of the DIG engine results from a higher air/fuel ratio, lower intake air temperature, and more efficient combustion. There was no visible smoke from the DIG engine. NO_x emissions were slightly lower and hydrocarbon emissions slightly higher than the diesel, as in the results of the 3401 tests. CO emissions from the DIG engine were lower than the diesel due to more rapid and complete combustion.

As combustion development continued on the 3501, a road switcher locomotive application was selected for the initial field experimental evaluation. A road switcher locomotive requires the power density and efficiency of a diesel engine and is not currently emissions regulated. This application is not expected to be regulated as tightly as stationary applications for which very low NO_x emissions capability is a requirement. 3501 DIG performance development then shifted toward the road switcher locomotive application with a maximum rating of 97 kW/cyl at 1500 rpm (1798 kPa bmep). Figure 5 summarizes how brake specific energy consumption from these 3501 tests (with power multiplied by 16) compare to that of a production 3516 diesel and of a production lean-burn SI 3516 natural gas engine.

Each increasing increment of power output on the operating (notch) curve is accompanied by an increase in engine speed, which enables the high efficiency at low power output levels. The DIG engine has a significant advantage in efficiency relative to both the diesel and the lean-burn SI engines over most of the notch curve. Operational and hardware modifications have been identified to reduce the DIG energy consumption at light loads to be comparable to the diesel.

3516 Laboratory Development

The next step in the program is the development of a 3516 (V-16) DIG engine and its associated systems for use in a field experimental evaluation to prove the viability of the DIG technology in a real-world application. The primary purpose of this engine development is to apply the 3501 results to the multicylinder engine and demonstrate 3516 DIG engine performance equal to or better than the production diesel engine in terms of power density, efficiency, and steady-state emissions. Additionally, 250 hours of lab durability testing will verify that the engine and its systems are developed to the point where a field experimental evaluation is practical.

In addition to the requirement of operating 16 cylinders with a common turbocharged/aftercooled air system, which was simulated on the 3501, operation of the multicylinder engine requires the use of several systems that were not integral with the engine during 3501 engine testing. The major additional systems required by the multicylinder engine are a hydraulic system that uses engine oil to power the gas injectors, a gas compressor and switching/venting system to provide fuel to the engine at high pressure, and a glow plug power and control system to supply the required power to the glow plugs across the engine operating range.

The hydraulic injector driver system (schematically shown in Fig. 6) uses an engine-driven hydraulic pump to supply the required flow of 21 MPa oil to the injectors. The operation of the injectors is controlled electronically through the use of an Advanced Diesel Engine Management (ADEM II) control system common to Caterpillar's newest electronically controlled diesel engines. This system is designed to operate with 10W-30 oil over a temperature range of −40 to 110°C.

An electric-motor-driven, three-stage, air-cooled gas compressor is the heart of the fuel supply system, providing compressed utility natural gas to the facility-mounted fuel system at 21 MPa. The facility fuel system provides the final filtration, pressure regulation, switching, venting, and fuel flow measurement functions prior to sending the gas to the engine at pressures up to 19 MPa. Engine fuel system functions are limited to heating the fuel with jacket water in a heat exchanger prior to distributing the fuel to the cylinder heads through twin manifolds in the vee of the engine. The fuel heating function is provided to maintain a nearly constant gas supply temperature to the engine to simplify injection timing and quantity control functions.

Power for the continuously energized glow plugs is provided by two alternators that feed power to a glow plug control, which then feeds power to the glow plugs as required to maintain the desired temperature based on engine operating conditions. The glow plug control also has a fault detection system that will alert the ADEM II control of a glow plug failure so that the fuel can be shut off to that cylinder until repairs can be made.

Status

As of this writing the engine has been operated to 900 kW at 1300 rpm at which point glow plug system problems associated with cylinder-to-cylinder hardware variations have delayed further testing. Troubleshooting of the various engine systems is occurring with testing to higher power levels and will enable full power testing in the near future.

Summary/Conclusions

The technology to burn direct-injected natural gas with glow plug ignition assist in a diesel cycle engine has been developed. Although further system development is necessary prior to field

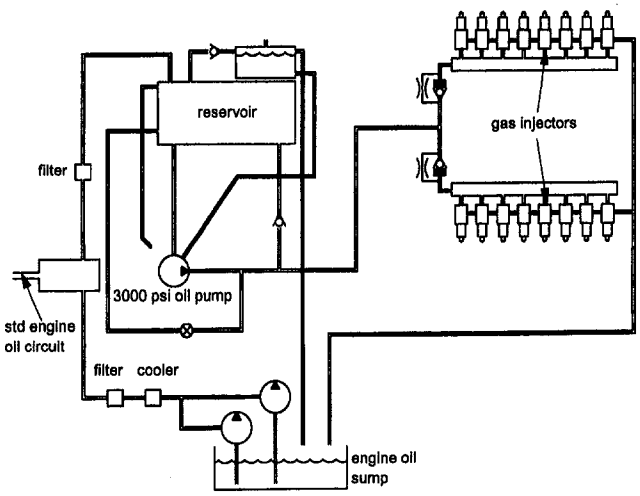

Fig. 6 3516 DIG HEUI driver system

experimental evaluation, enough operational experience has been accumulated to show that this technology will result in a viable engine for burning natural gas fuel while providing performance equal to or better than the same diesel-fueled engine. The additional requirements of high-pressure gas and glow plug ignition assist systems result in higher initial engine costs that can be recovered from lower fuel costs in certain applications.

This single-fuel DI gas technology has commercial potential in a variety of applications and engine sizes. The demonstrated performance characteristics of a DI natural gas engine (power density, thermal efficiency, and heat rejection equal to a diesel, zero smoke, NO_x emissions equal or less than a diesel) fit best in mobile applications that consume large quantities of fuel, where compressed natural gas (CNG) or liquefied natural gas (LNG) fuel cost savings can potentially pay for the higher initial DI gas system cost. Planned laboratory and field experimental development will better define the best commercial potential for this unique and promising natural gas-related technology. This basic technology is also applicable to other gaseous fuels, including propane and, in the longer term, coal-derived gases and hydrogen.

Acknowledgments

The authors would like to express their thanks to Gas Research Institute for co-funding this development and to the many dedicated persons at Caterpillar Inc. who are involved in this project. Earlier portions of this work are documented in Gas Research Institute reports No. GRI-88/0271, GRI-89/0244, and GRI-92/0260.

References

Katz, D. L., et al., 1959, *Handbook of Natural Gas Engineering,* McGraw-Hill, New York, pp. 708–709.

Kroeger, C. A., 1986, "A Neat Methanol Direct Injection Combustion System for Heavy-Duty Applications," SAE Paper No. 861169.

Richards, B. G., 1990, "Methanol-Fueled Caterpillar 3406 Engine Experience in On-Highway Trucks," SAE Paper No. 902160.

Siebers, D. L., 1985, "Ignition Delay Characteristics of Alternative Diesel Fuels: Implications on Cetane Number," SAE Paper No. 852102.

Siebers, D. L., 1994, private communication.

Low-Cost NO_x Reduction Retrofit for Pump Scavenged Compressor Engines

E. N. Balles
Arthur D. Little, Inc.,
Cambridge, MA 02140

R. C. Peoples
Cooper-Bessemer Reciprocating Products,
Grove City, PA 16127

The Clean Air Act Amendments of 1990 and the resulting individual State Implementation Plans will require many natural gas pipeline operators to install NO_x reduction equipment on existing compressor station engines. A program was undertaken to develop lower cost NO_x control options for these engines as compared to traditional techniques. The initial work, described in this paper, focused on the development of a low-cost retrofit package for Cooper-Bessemer GMV and GMV-TF pump scavenged integral compressor engines. The retrofit concept relied on highly dilute combustion to achieve low engine-out NO_x emission rates. A significant portion of the effort concentrated on low-cost methods for delivering the required air charge and ignition enhancements to achieve reliable and robust combustion. The prototype retrofit kit has been installed on a GMV-6 in gas compressor service. Performance results showed a 70 percent reduction in NO_x emission rates without a corresponding increase in HC emission rates.

Background

Compressor Station Overview. It is estimated that 4000 Cooper-Bessemer two-cycle integral engines are in operation in the United States and Canada. These units have the capability to produce five million aggregate horsepower for compression of various process gases. A large portion (approximately 80 percent) of these engines are used in natural gas transmission, storage, and gathering services, and therefore the operation and maintenance of these units is a primary concern of the natural gas industry.

Recent Regulatory Driving Forces. The Clean Air Act Amendments of 1990 and the resulting individual State Implementation Plans (SIP) will require many natural gas pipeline operators to install emission reduction equipment on existing compressor station engines. Most regulators in geographic regions that are in nonattainment of the National Ambient Air Quality Standards (NAAQS) for ozone, NO_x, HC, or CO will require the implementation of Reasonable Available Control Technology (RACT) on existing equipment as part of their strategy for bringing regions into compliance with federal standards. While there is currently a wide range in the target emission rates associated with RACT (primarily state-to-state variation), most NO_x targets fall in the 2.5 to 6 grams per brake horsepower hour (g/bhp-h). This is a significant reduction in NO_x emission rates given that most uncontrolled gas transmission engines produce roughly 10 to 20 g/bhp-h (U.S. EPA, 1988; Martin and Thring, 1989). The development of low-cost, alternative emission control retrofit technologies for use with existing, older model stationary gas engines is an urgent priority for the natural gas industry.

In addition, Title V of the Clean Air Act Amendments of 1990 requires operating permit applications for major sources beginning in 1995. Sources subject to the ozone nonattainment area provisions include those with the potential to emit 100 tons per year (TPY) of NO_x in marginal and moderate nonattainment areas. Lower emission rate limits of 50, 25, and 10 TPY apply to serious, severe, and extreme ozone nonattainment areas, respectively. In practice, this requirement will extend to most compressor stations and will at the same time *spotlight* the need for control technology on existing engines.

Current Status of Retrofit Emissions Controls. The most widely accepted technique for NO_x reduction for natural gas spark-ignited two-cycle engines is lean combustion. The application of lean combustion on large two-cycle integral engines was pioneered by Cooper-Bessemer in the 1970s and has been successfully adapted to all of Cooper-Bessemer's product offerings (under the trademark name CleanBurn™). The cost in hardware could range from three hundred thousand dollars to over a million dollars, depending on the particular unit and the desired emissions and fuel consumption levels. In addition, there are the additional costs for labor and auxiliary equipment that is required for installation of the hardware. These additional costs can amount to 50 to 100 percent of the initial hardware cost.

Prototype Development Program Overview. A research and development program was initiated in 1990 with the primary objective of developing new, less costly, retrofit NO_x reduction technology for two-stroke gas transmission engines. At that time, the Gas Research Institute formed strategic alliances with major reciprocating engine manufacturers, including Cooper-Bessemer, to develop emission control technology that can be applied in the near term to lower the cost of emission regulation compliance at pipeline compressor stations (Gas Research Institute, 1994). The goals of the program included a 50 percent cost reduction relative to the emissions retrofit equipment available from the manufacturer and a NO_x emission target in the range of 3 to 6 g/bhp-h.

Cooper-Bessemer and Arthur D. Little, Inc., together undertook a research and development effort that has culminated in a prototype emission reduction retrofit package. The early work focused on a feasibility analysis to establish the key technical and commercial parameters required of a retrofit package for a target engine population. The subsequent laboratory work included single-cylinder research aimed at developing a better understanding of lean combustion, as well as multicylinder proof-of-concept prototype development of low-cost air charging techniques and ignition enhancements. The effort culminated in a successful field experiment demonstration at an operating gas compression station (Peoples Natural Gas Valley

Contributed by the Internal Combustion Engine Division and presented at the 16th Annual Fall Technical Conference of the ASME Internal Combustion Engine Division, Lafayette, Indiana, October 2–6, 1994. Manuscript received at ASME Headquarters June 1995.

Station), which has logged over 6000 operating hours and demonstrated the cost and emissions targets set at the program start.

Initial Product Definition

Engine Model Focus. The focus of this development program has been the Cooper-Bessemer GMV integral engine compressor. The GMV engine was produced from the 1930s up through the 1950s. There were 1373 of these units built with a potential of 1,200,000 horsepower. According to a recent AGA study (American Gas Association, 1989), there are at least 450 of these units in service (with AGA member companies) and we suspect the number to be closer to 1000.

The GMV is naturally aspirated and was built in 4-, 6-, 8-, and 10-cylinder configurations and was rated at 100 bhp/cylinder and later 110 bhp/cylinder.

The relatively low brake mean effective pressure (bmep) of 67 psi and the high overall industry acceptance of these units made them ideal for a lower cost approach to a lean combustion retrofit.

Targets. The objectives of this program are threefold:

1 Reduce the NO_x emissions to a range of 3 to 6 g/bhp-h.
2 Reduce the overall cost of retrofitting the existing GMV units by 50 percent.
3 Bring the product to the marketplace in time to allow for compliance with the Clean Air Act deadline of May 1995.

Approach and Rationale. At the beginning of the development program, the team was not restricted to any one technical approach for in-cylinder NO_x control. A number of control options were identified and evaluated in terms of the overall objectives, development timetable, and likelihood of technical and commercial success. The highly dilute combustion approach was selected primarily because of its high probability of success, the high technical risk associated with other options, and the short development time required for commercial success. The resulting strategy used in this emissions retrofit development then was to:

- take advantage of Cooper-Bessemer's CleanBurn™ experience;
- add new concepts (perhaps from other industries or outside perspectives) to reduce costs; and
- focus on near-term commercialization to meet the regulatory timetable.

Given that highly dilute combustion was the selected in-cylinder NO_x control approach, several technical requirements were identified and addressed during the prototype development:

- increased trapped diluent mass
- ignition enhancement
- burn rate enhancement
- improved mixture uniformity

Increasing the in-cylinder diluent mass reduces the peak flame temperatures, which reduces the NO_x production rate. Highly dilute mixtures are harder to ignite and burn more slowly than conventional mixture strengths and therefore require special attention for achieving robust ignition and timely burn durations. In addition, highly dilute mixtures need to be well mixed (i.e., entire mixture close to the overall air/fuel ratio) since portions of the mixture that are significantly leaner than the overall in-cylinder air/fuel ratio will likely not support flame propagation and may not oxidize later in the cycle.

Increased Trapped Diluent Mass. One of the paramount requirements was the selection and implementation of a cost-effective method for increasing the trapped diluent mass. Diluents considered were fresh air, recirculated exhaust gas, residual gas, CO_2, and water. For a number of reasons, including cost and site considerations, the effort focused on developing and trapping additional fresh air. (For example, water injection was considered, but many compressor stations are in remote locations where water is not readily available.) Exhaust turbines, engine shaft drives, electric motors, and high-pressure natural gas expanders were evaluated as a means to drive the air charger device. Conventional radial compressors were considered along with scroll compressors, liquid ring pumps, and jet pumps. The most cost-effective option for increasing the trapped diluent mass appeared to be multiple low-cost turbochargers, manifolded together, in series with the original crosshead scavenging pumps.

Ignition Enhancement. Highly dilute mixtures are difficult to ignite using conventional spark plug systems. It is critical to have an ignitable mixture in the gap at the time of spark. This may not always be the case when the spark plug is mounted in the combustion chamber due to spatial variations in mixture strength resulting in less than perfect fuel–air mixing. An alternative ignition approach that has been successfully applied by several engine manufacturers is the use of a prechamber with a separate fuel supply. The prechamber typically is fueled richer than the main chamber to ensure an ignitable mixture. The prechamber design parameters such as volume, orifice geometry (number of holes, diameter, and length), and overall prechamber geometry are carefully developed for each engine model. In addition, special attention is paid to mechanical and thermal stresses to ensure durability of the prechamber itself as well as the fuel valve and spark plug. The most cost-effective and expedient ignition enhancement option appeared to be adaptation of Cooper-Bessemer's successful jet cell technology (a type of modular prechamber) to existing cylinder heads.

Burn Rate Enhancement. Highly dilute mixtures are known to burn more slowly than richer mixtures. If the burn duration becomes too long, the combustion process may be quenched late in the expansion stroke leading to high unburned HC emission rates. Increasing the turbulence level before and/or during combustion likely will shorten the burn duration for a given equivalence ratio. An additional benefit of a well-designed prechamber is that additional mixing and turbulence are generated by the jet of hot combustion products as they enter the main chamber. This burn rate enhancement feature reinforced the decision to adapt jet cell technology to existing cylinder heads.

Mixture Uniformity Enhancement. In-cylinder mixture uniformity is important in highly dilute systems since the portion of the mixture that is beyond the flammability limit becomes a potential source of unburned hydrocarbon emissions. Typically, the natural gas fuel charge is admitted to the main chamber at relatively low pressure (<100 psi) through a mechanically actuated valve during the early part of the compression stroke. In-cylinder fuel–air mixing is primarily governed by the turbulence level and bulk gas motion resulting from the scavenging process, the jet momentum flux during fuel injection, and the piston-induced gas motion during compression. While it was recognized that mixture uniformity is an important issue effecting HC emissions, no specific additional enhancements were incorporated in the first prototype; however, it is likely that the jet exiting the prechamber creates additional mixing and better mixture uniformity, albeit late in the cycle.

Laboratory Development

Development Requirements. The Cooper-Bessemer facility includes a Research and Development Laboratory that has several engine models installed for the purpose of developing new technology. One of these units was retrograded to a GMV complete with scavenging pumps and air chest scavenging. This

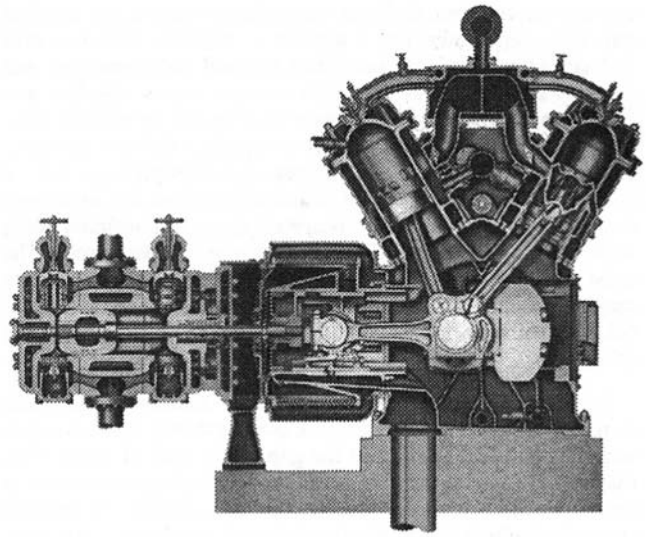

Fig. 1 GMV cross section

metamorphosis was necessary to properly simulate the results of the conversion on existing field units; see Fig. 1.

Turbocharger Selection/Optimization. A turbocharger manifold assembly was developed to mount the multiple turbochargers and testing was done to evaluate the effectiveness of the turbocharging. This testing included multiple turbocharger manufacturers and multiple turbocharger configurations from each manufacturer. The operational goal of the selection process was to achieve NO_x emissions levels that met the 3 to 6 g/bhp-h, a fuel rate of 8500 btu/bhp-h, and good combustion stability. The cost goal was to develop a package to incorporate high-production, cost-effective multiple turbochargers that offered a significant savings over the traditional single custom turbocharger.

Ignition Enhancement. As previously discussed, the accepted means of ignition enhancement is prechamber technology. The question became how to cost effectively incorporate this technology on a retrofit basis. Three techniques were evaluated:

1 Prechamber installation through existing air starting valve opening. This involved machining the opening to accept a standard jet cell. This technique was proven acceptable, but had two major drawbacks. It required the retrofit of ring gear starting and the resulting orientation of the jet cell was directly toward the catwalk (potential safety concern).

2 Prechamber cell installation through an existing spark plug hole was evaluated. Although combustion was acceptable, a problem developed with cracking of the cylinder heads due to difference in expansion rates between the jet cell body material and the cast iron head. This approach was not deemed worthy of pursuit given the development timetable.

3 Prechamber installation using a previously developed power head that incorporated both a prechamber and air starting valve opening was chosen as the most cost-effective means of obtaining the necessary ignition enhancement. This head has the advantage of retaining the existing starting system and therefore eliminating the need for a costly conversion to ring gear start; see Fig. 2.

Intercooling. The need for intercooling was evaluated during the development testing and as expected it was found the turbocharger compression resulted in relatively low blower discharge temperatures. These low temperatures in combination with the large mass of the engine base resulted in only modest effect of the turbocharging on the air chest temperature. This made intercooling and the required auxiliary equipment (pump, radiator, piping, etc.) unnecessary.

Field Experiment

Peoples Natural Gas, a CNG company, was contacted to determine their interest in providing a GMV-6 for the first field experiment. The engine in question was a GMV-6 rated at 600 bhp that was built in the early 1950s and moved to PNG's Valley Station near Kittanning, PA, in 1963. This engine is operated in excess of 8000 hours per year on a gas gathering system at near full load.

This geographic area is considered to be noncompliant by the EPA; in addition, the station is in excess of the 100 tons per year NO_x and therefore the GMV-6 was a prime candidate for conversion.

After discussions between the interested parties, including Gas Research Institute, Arthur D. Little, Inc., Cooper-Bessemer Reciprocating Products, Peoples Natural Gas, and the Pennsylvania Department of Environmental Resources, an agreement was made to convert the subject GMV-6. It needs to be recognized that all of the parties involved in the discussion were very supportive of the project.

Installation of the Retrofit Kit. Installation of the retrofit kit involved four basic phases:

1 *Engine Modifications.* The existing power cylinder heads, pistons and power cylinder liners were removed. The power cylinder liners were modified by grinding the exhaust ports to increase the available exhaust energy to drive the turbochargers. This is a common modification when two-cycle engines are retrofitted with turbochargers; see Fig. 3. The existing pistons were reinstalled with new piston rings. The previously mentioned precombustion chamber heads were installed along with the associated hardware.

2 *Turbocharger Installation.* The exhaust and inlet piping outside the building was sectioned to allow the installation of the turbocharger module; see Fig. 4. Due to the increased intake and exhaust flow (approximately 50 percent) it was necessary to replace both the inlet filter and exhaust silencer with larger units to keep the allowable pressure drops within specification.

3 *Monitoring Panel.* PNG's Valley Station is manned 24 hours a day and operated with no automated monitoring equipment and few monitoring devices. Because this was a field experiment, the decision was made to install a monitoring panel that would provide a complete data set including engine horsepower. The monitoring panel involved a significant portion of the effort and cost for the project.

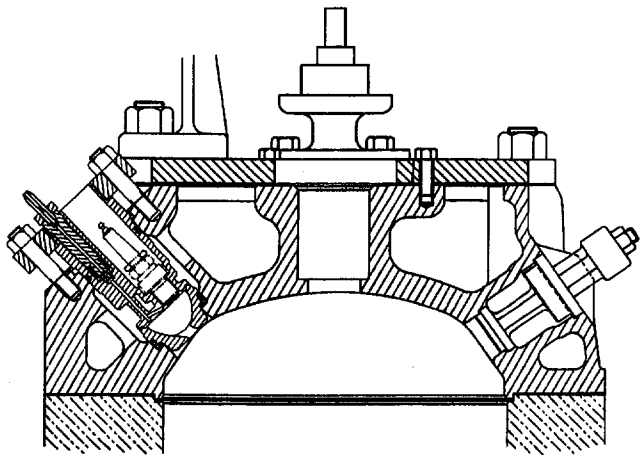

Fig. 2 GMV prechamber head

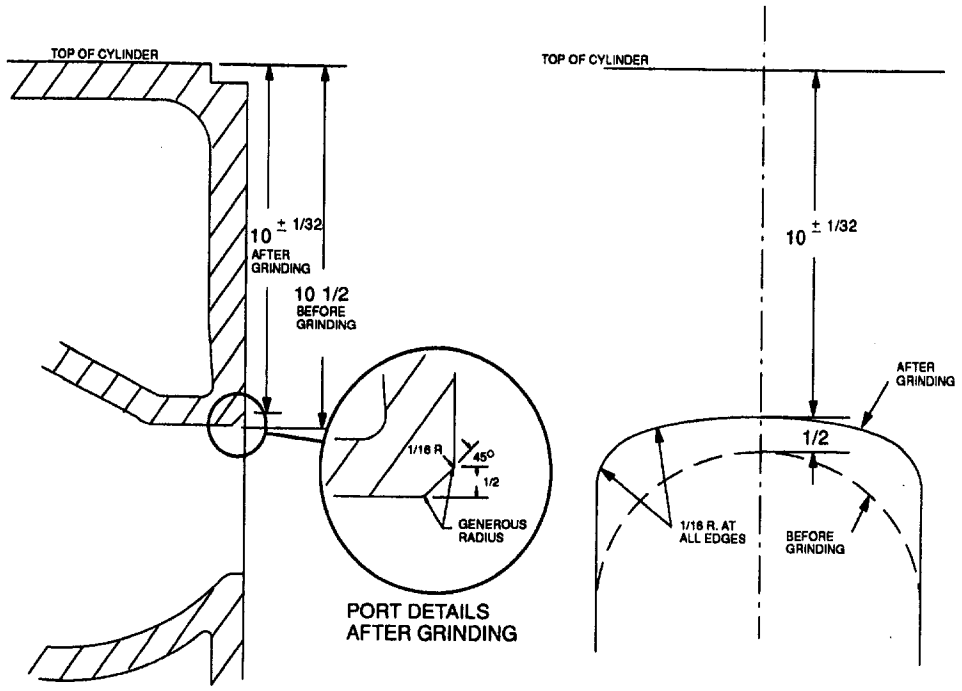

Fig. 3 (*a*) Exhaust port heights; (*b*) exhaust port outline

4 *Air Fuel Ratio Control.* The turbocharger module includes an exhaust bypass that is controlled pneumatically. This control allows air manifold pressure to be adjusted and therefore controls combustion air flow. The programmable logic controller was mounted in the monitoring panel.

Retrofit Performance Data. A series of performance tests were conducted on the field experiment engine to document the retrofit kit performance. The tests were done at three separate times and included emission rate, engine power and fuel consumption measurements.

- Baseline performance: engine performance prior to the installation of the retrofit kit. The engine was determined to be in good operating condition at the time of testing and baseline results were considered typical of normal operation.
- Initial retrofit performance: engine performance was measured immediately after installation of the retrofit kit.
- 4000 hour retrofit performance: engine performance was again measured after six months (approximately 4000 hours) of base loaded operation. As with the baseline tests, the engine was tested in its normal operating condition (i.e., no special maintenance prior to testing).

Testing was performed by a subcontractor following standard EPA protocols and procedures typically employed in emission compliance testing. These tests were conducted while the engine was in gas compression service to document the in-use performance of the retrofit as well as the degradation in performance, if any, over the initial 4000 hours of operation.

Performance data for the field experiment test series are presented in Table 1. The data are presented for the engine rated conditions (300 rev/min; 67 psi bmep; 600 bhp). Baseline emission rates were 11.4 g NO_x/bhp-h and 6.0 g HC/bhp-h. These emission rates are typical of uncontrolled pump scavenged, low bmep engines and the values compare well with Cooper-Bessemer's experience. Emission rates immediately after installation of the retrofit kit were quite low, showing an almost 10-fold reduction in NO_x (1.4 versus 11.4 g/bhp-h). Also important was that HC emission rates did not increase as a result of achieving low NO_x emissions (measured HC emission rates actually decreased slightly). After several days of testing, modifications were made (primarily in the air/fuel ratio controller programming) that further reduced HC emission rates, improved fuel consumption, and increased the turbocharger performance margin while still meeting the NO_x target. This resulted in an NO_x emission rate of 2.4 g/bhp-h and a HC emission rate of 3.9 g/bhp-h. Performance measured at 4000 hours showed no deterioration in the retrofit kit performance, which is demonstrated by the test data at rated conditions (Table 1).

An air/fuel ratio traverse was conducted during initial performance testing and 4000 hour performance testing. Emission

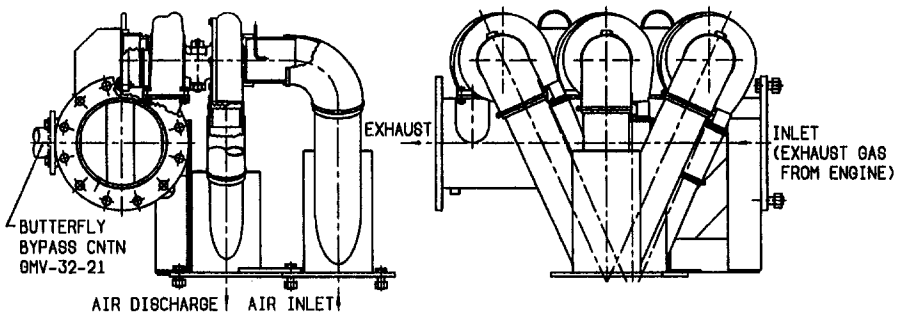

Fig. 4 Turbo module kit

Table 1 Baseline and retrofit kit performance of the field experiment engine (GMV-6, Valley Station, Kittanning, PA) at rated conditions (300 rev/min, 600 bhp)

	Baseline (Unmodified Engine)	Initial Retrofit Performance		4,000 Hour Retrofit Performance
		As Installed	After A/F Controller Adjustment	
NOx (g/bhp-hr)	11.5	1.4	2.4	1.8
THC (g/bhp-hr)	6.0	5.1	3.8	4.0
CO (g/bhp-hr)	0.6	1.4	1.0	1.0
BSFC (btu/bhp-hr)	8,900	---	8,250	8,750

results are shown in Fig. 5, which plots NO_x and HC emission rates as a function of air chest pressure. Air chest pressure was varied by manually controlling the turbocharger bypass, which effectively changed the amount of air delivered to the engine and trapped in the power cylinder. Engine speed and power were maintained at the rated setpoint by controlling the process conditions. As expected, NO_x emission rates were a function of air chest pressure, decreasing with increasing air chest pressure. HC emission rates increased with increasing air chest pressure, which is typical of lean combustion systems. This air/fuel ratio traverse data illustrates the basic trade-off between NO_x and HC emission rates and it shows the turbocharger performance margin for hot ambient or high-altitude operation. The two sets of data (initial and 4000 hour) also reinforce that the turbocharger performance and the overall retrofit kit performance did not deteriorate over the initial six months of operation.

Operating Experience. Operating experience with the retrofit kit in gas compression service has been excellent. Over the first 4000 hours of operation, most of which was at full speed and load, the field experiment host site experienced less than five hours of retrofit kit related down time. Two brief shutdowns were required within the first two months to rework a binding exhaust bypass valve. A minor exhaust leak was detected at the turbocharger manifold inlet flange and has been solved with an alternate gasket material.

Routine maintenance consisted of spark plug and jet cell check valve inspection and/or reconditioning at approximately 2000 hour intervals. Overall, in-use retrofit kit reliability and maintenance experience have met both manufacturer and host site expectations.

Summary

A prototype NO_x emission reduction retrofit kit has been developed for a pump scavenged two-stroke Cooper-Bessemer engine and successfully demonstrated in the field with over 6000 hours of gas compression service. Key performance attributes of the new retrofit kit demonstrated during the field experiment include:

- NO_x reduction: significant reduction in NO_x emission rates (>70 percent reduction at rated conditions). Brake specific NO_x emission rates were less than 3 g/bhp-h over most of the operating range. Original target called for 3 to 6 g/bhp-h at rated conditions.
- HC emission: overall decrease in HC emission rates. Original target called for reducing the high HC emissions typically associated with achieving low NO_x levels (no increase over the baseline HC emission levels).
- Fuel consumption: overall decrease in brake specific fuel consumption of approximately 3 to 9 percent.

Key commercial attributes of the system include:

- Cost: Preliminary cost/pricing estimates indicate a major cost savings relative to traditional emission reduction retrofit approaches. Original target called for 50 percent cost reduction compared to commercial retrofit kits available at the start of the development effort.

The following estimates indicate a cost reduction of approximately 49 percent comparing the traditional retrofit to the low cost retrofit. This reduction is the result of utilizing lower cost turbocharging equipment, providing a turbocharging package that is simpler to install and reducing the required plant modifications; see Table 2.

- Availability: commercial package available. Original target was to meet the timetable of individual state imple-

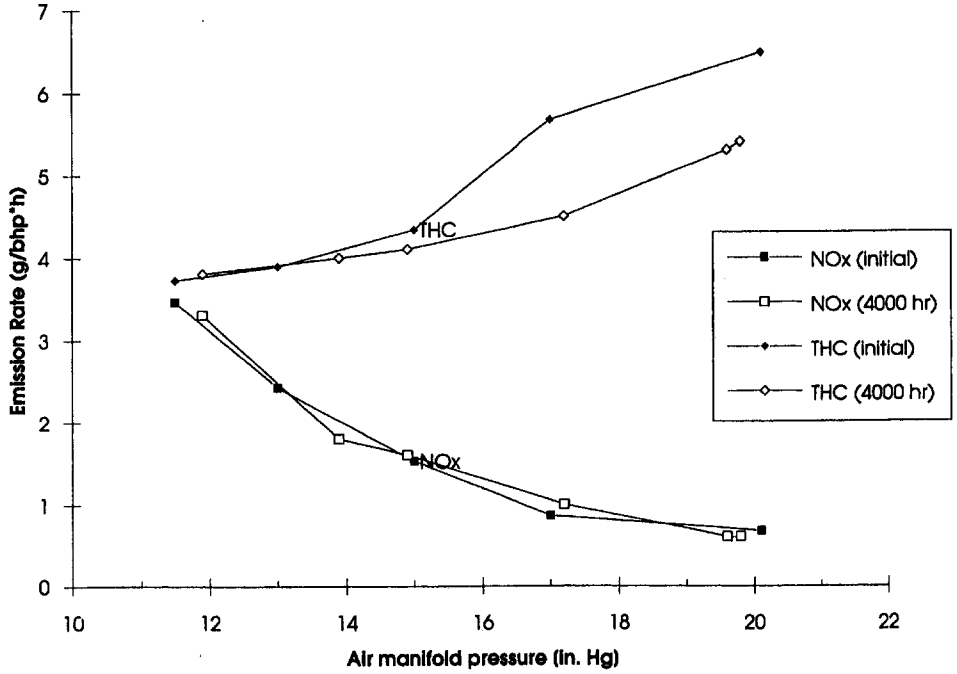

Fig. 5 Emissions results

mentation plan RACT requirements (equipment installed by 31 May '95).

This new emissions reduction retrofit kit provides engine owners faced with NO_x emission reduction requirements a cost-effective alternative to the existing slate of engine retrofit and exhaust treatment options.

Acknowledgments

It is difficult to recognize all of the people and companies who had a major role in making this project. However, the following people were instrumental in its success.

Mike Whelan and Allen Wells of the Gas Research Institute who provided valuable guidance during the development program.

Cooper-Bessemer Reciprocating Products, Mel Helmich, Retired Director of Engineering; V. Alan Squires, Senior Designer; Bob Hubbard, Supervisor of R&D Lab; Steve Harding, Senior Service Rep.

Peoples Natural Gas, Louis Hudecek, Manager, Compressor and Mechanical Systems.

The authors also would like to acknowledge the significant financial cofunding provided by the Gas Research Institute and the support provided by the field experiment host (Peoples Natural Gas).

Table 2 GMV-10-TF conversion estimate

GMV-10-TF Conversion Estimate	Traditional CleanBurn™	Low Cost NOx Retrofit
Conversion Hardware	$300,000	$150,000
Labor	$150,000	$ 85,000
Plant Modifications	$ 50,000	$ 20,000
	$500,000	$255,000

References

American Gas Association, 1989, "Survey of Natural Gas Compressor Prime Movers," AGA-XF0484.

Gas Research Institute, 1994, *Gas Transmission, Gas Flow,* Vol. 2, No. 1, Jan.

Martin, N. L., and Thring, R. H., 1989, "Computer Database of Emissions Data for Stationary Reciprocating Natural Gas Engines and Gas Turbines in Use by the Gas Pipeline Transmission Industry," GRI-89/0041.

U.S. Environmental Protection Agency, 1988, *Emissions Factors,* AP-42.

Development of the 2400G Stationary Gas Engines

B. M. Chrisman

P. D. Freen

Cooper Cameron Corporation,
Cooper-Bessemer Reciprocating,
Springfield, OH 45501

Development of the in-line versions of the 2400G Series of spark ignited, gas-fueled engines has been in process for the last six years. The main objective of this program is to produce a new series of 1200 rpm gas engines having a continuous duty rating of 200 bhp per cylinder. This paper deals with the highlights of the engine development program from the initial concept stage through the operation of prototype engines at customer sites. Development procedures are described that led to substantial advances in performance improvement and exhaust emissions control. A focal point of this work is the combustion analysis, which was conducted through computer simulation and through the operation of a gas-fueled, single-cylinder test facility. This preliminary analysis resulted in the definition of the basic configurations for the prechamber and the main combustion chamber. The applicability of the modeling and the single cylinder test work to the six and eight cylinder engines is evaluated in this paper. Development of appropriate manifolding, turbocharging, and cylinder balance was a critical part of the multicylinder phase of this program. Another key issue was the design and testing of the electronic feedback control system that assures continuous operation at conditions that produce optimized fuel economy and exhaust emissions. The satisfactory operation of the six and eight cylinder 2400G prototype engines in the field is based on the foundation of the developmental work described in this paper.

Introduction

Product Rationale. For many years, nearly all Superior spark-ignited, gas-fueled engines have been based on the 825 Series. Included are all models of the GTL and SGT engines, which comprise both open chamber and prechamber (CleanBurn™) versions. Nearly all of these engines are rated at 900 rpm, with one model having a 1000 rpm rating.

By the mid-1980s, market analysis was indicating that new engine lines would soon be required. The main criteria for these engines clearly defined the direction to take with the development program:

1 Substantial reduction in price per bhp.
2 Increased rpm, preferably to 1200.
3 Compact design with ease of maintenance.
4 All components value engineered and of the latest technology.
5 Fuel consumption and exhaust emissions better than previous models.
6 Rugged and reliable.

The resulting engine development program led to the initial production of the 2400G Series of engines in late 1993. These engines have a bore and stroke of 240 mm × 260 mm and are design rated at 1200 rpm and 150 kW (200 bhp) per cylinder.

They use the standard Superior approach for achieving low exhaust emissions, which is the CleanBurn™ (prechamber) combustion control system. Other key specifications are listed in Table 1.

Selection of Approach. To provide assurance that the lower end of the engine would operate reliably at 1200 rpm, it was decided that the new engines should be based on a field-proven short block. Through a license with Mitsubishi Heavy Industries, the rights to manufacture the SU diesels were obtained. The new engine program then took on two distinct aspects: (1) develop the capability to produce the short block, and (2) develop the components required for the spark-ignition, gas versions.

This paper focuses on the gas engine development process and its results. Of primary interest is the progression of the combustion and control system development from the simulation stage through the single-cylinder research, and then to the multicylinder performance and endurance testing.

Design Analysis

Engine Description. The main mechanical features of the 2400G inline engines are presented in the transverse cross section (Fig. 1). The block is a single piece, ductile iron casting, having integral air, water, and oil manifolds. A forged steel crankshaft is rigidly supported with seven main bearing caps for the six-cylinder engine (2406G and with nine mains for the eight-cylinder engine (2408G). These main caps fit tightly into the block and each is secured by two vertical hydraulically tensioned studs and two horizontal bolts. Table 1 expresses key specifications for the 2406G and 2408G engines.

Designs for some major components are described below:

Cylinder Head. The heads are compacted graphite castings having two intake and two exhaust valves with rotators. Figure 2 is a cutaway view through the area containing the prechamber, the pilot fuel supply, and the spark plug. The prechamber is centrally mounted in the combustion chamber. Also evident in Fig. 2 are the intake port and the substantial water jacket passages around the valves and prechamber.

Piston. Figure 3 illustrates the piston design features. It is a single piece, aluminum casting with three compression rings and one oil control ring. Crown cooling is provided by an oil annulus located between the combustion bowl and the top piston rings. Much development work focused on the main combustion chamber shape. The Performance Development Section of this paper describes the methods used to arrive at the shape shown in Fig. 3, which consists of a deep dish concentrated near the

Contributed by the Internal Combustion Engine Division and presented at the 16th Annual Fall Technical Conference of the ASME Internal Combustion Engine Division, Lafayette, Indiana, October 2–6, 1994. Manuscript received at ASME Headquarters June 1994.

Table 1 Specifications for 2406G and 2408G engines

Speed Range for Rated Torque (RPM)	900 - 1200	
Rated Torque (N·m)	9495	7003 lbf·ft
Rated BMEP (KPa)	1262	183 PSI
Rated Power (KW/Cyl)	150	200 BHP
Bore & Stroke (mm)	240 x 260	9.45" x 10.24"
Displacement (l/Cyl)	11.76	718.2 in3
Compression Ratio	10.9	
BSFC (KJ/KWH)	9615	6800 BTU/BHP·hr.
Crank Main Diameter (mm)	200	7.87"
Crank Pin Diameter (mm)	180	7.09"

center of the piston crown. Combustion analysis that optimized performance and knock limit margin led to the use of a 10.9:1 compression ratio.

Prechamber. The prechamber assembly shown in Fig. 4 incorporates a poppet valve for the pilot fuel and a superalloy nozzle that has eight holes through which the burning charge is projected into the main chamber.

Connecting Rod. The forged steel rod is angle split as the crankpin diameter is large relative to the cylinder bore. For additional clamping integrity, the rod and cap joint is serrated. The rod is rifle-drilled for full pressure wrist pin lubrication and piston crown cooling.

Camshaft. Both the 2406G and 2408G use two-piece, forged-steel camshafts, which are bolted together near the center of the shaft. The intake and exhaust cams are integral with the shaft. Cam timing resulted from extensive tests described later in this report.

Value Engineering. Throughout the 2400G development program, the components being designed were reviewed by design engineers, manufacturing personnel, and external suppliers. A major objective for the new engine program was the achievement of a substantial reduction in cost per bhp.

Application of value engineering principles included:

1 market analyses to determine the benefits of various design alternatives to engine end users;
2 reviews by the probable producers of most components in the early stages of design, which were aimed at facilitating the manufacturing of the components.

The goal of this process is to optimize design feature, manufacturability, and cost relationships. Much design iteration was

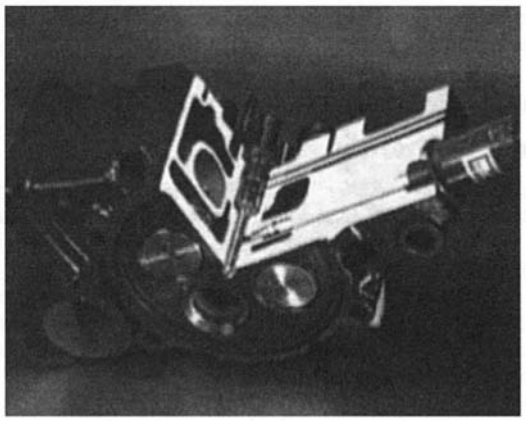

Fig. 2 Cutaway of 2400G cylinder head

Fig. 3 2400G piston

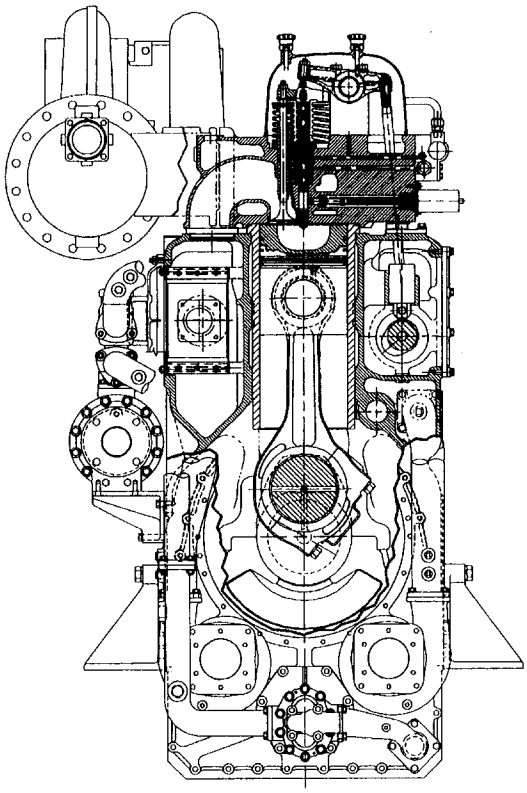

Fig. 1 2408G cross-section

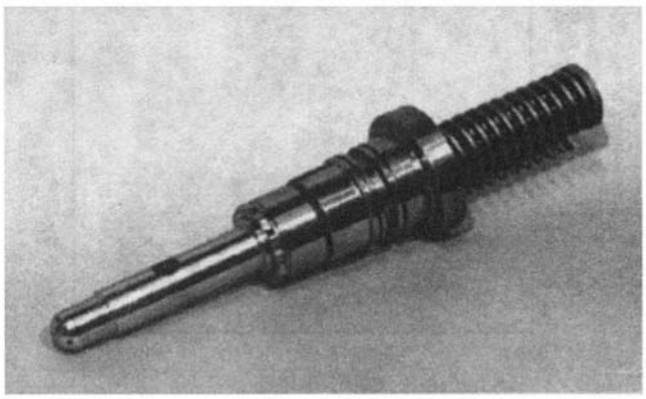

Fig. 4 2400G prechamber assembly

required for some components to achieve the optimum value for the product.

Performance Development

Simulation Program

Modeling of Cylinder Flow and Combustion. Computer simulation provided important input to the design parameters used for the first prototype engine. A computer model was developed for a prechambered, spark-ignition, gas engine. This model was used to conduct parametric analyses of key factors, including cam timing, combustion rate, intake and exhaust port flow coefficients, prechamber volume and nozzle size, compression ratio, and ignition timing.

The model is based on a filling and emptying principle. Mass and energy equations coupled with an orifice flow equation are used to define the gas state within each control volume. The gas states are computed for every degree of crank angle in the following control volumes:

1 Intake manifold
2 Intake port
3 Cylinder
4 Prechamber
5 Exhaust port
6 Exhaust manifold

Assumptions used to analyze each of these control volumes are:

1 Uniform temperature, pressure, and equivalence ratio are used.
2 Heat transfer rates are based on Annand (1962) relations for the cylinder and prechamber, and on Rohsenow relations (Karlekar and Desmond, 1977) for the other control volumes.
3 Mass transfer is through fixed or variable orifices.
4 Thermodynamic properties are determined from equilibrium concentration of 13 constituents using the methods described by Olikara and Borman (1975).
5 Combustion duration is an input to the program with the heat release rate based on a curve fit using the Wiebe function as described by Watson and Janota (1982).
6 Valve flow coefficients are provided from curve fits of actual data, and they can be scaled up or down as required. The time-averaged output of the computer model includes: IMEP, ISFC, pumping MEP, air–fuel ratio, heat loss, energy balance, required turbocharger efficiency, NO_x emissions, and scavenged hydrocarbon emissions.

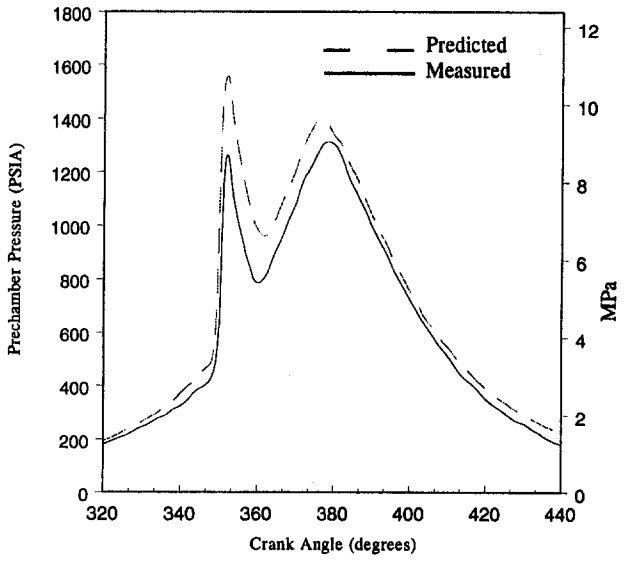

Fig. 5 Prechamber combustion pressure

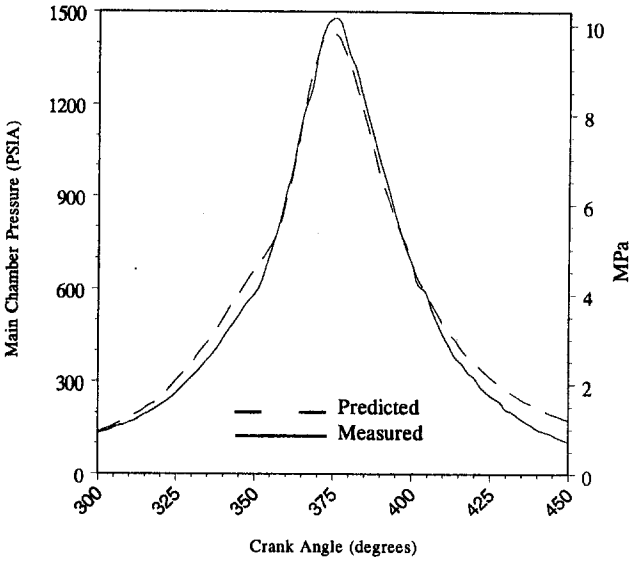

Fig. 6 Main chamber combustion pressure

Figures 5 and 6 indicate the predicted and measured prechamber and main chamber pressures as functions of crank angle. The ability to predict combustion conditions with the degree of accuracy shown greatly facilitated the engine test program. After calibrating the model, a parametric study was conducted to design the 2400G combustion system.

An important discovery from the modeling was that the majority of the NO_x emissions are formed in the prechamber when the total trapped theoretical air–fuel ratio is greater than 180 percent (mass basis). Figures 7 and 8 present curves of NO_x versus the total relative air–fuel ratio for one of the larger and one of the smaller prechambers considered (volumes = $3 \times A$ and A, respectively). The NO_x emissions formed in the prechamber are reduced with richer air–fuel mixtures because the amount of fuel in the prechamber decreases with lower air

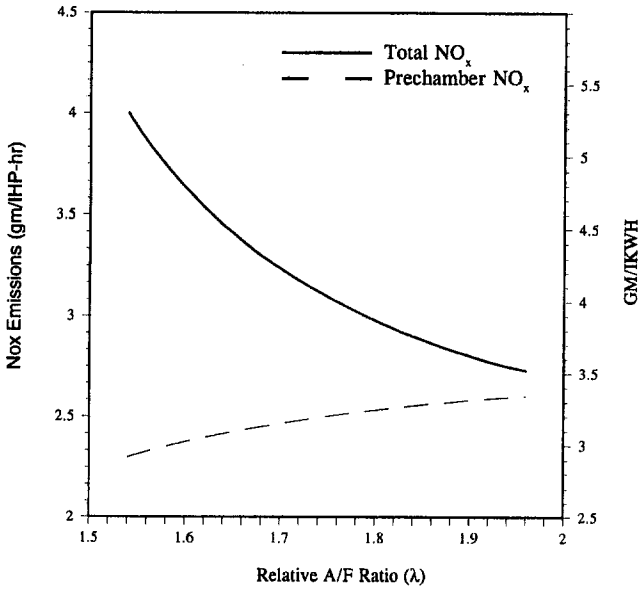

Fig. 7 Predicted NO_x emissions for a large prechamber (volume = 3A); 1200 rpm, IMEP = 215 psi (1.48 MPa)

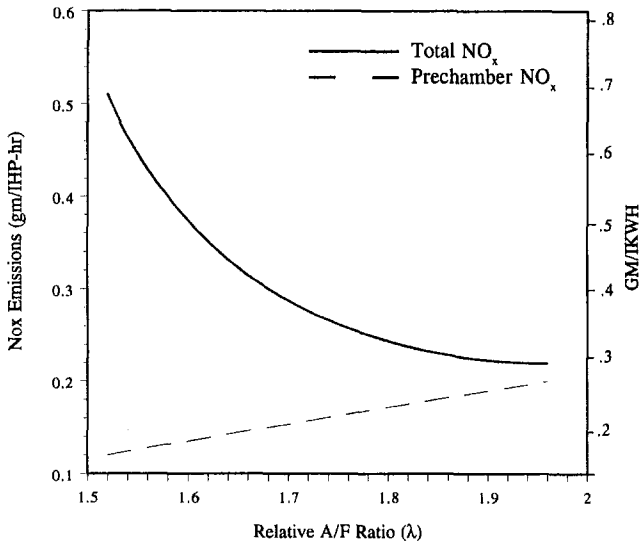

Fig. 8 Predicted NO_x emissions for a small prechamber (volume = A); 1200 rpm, IMEP = 215 psi (1.48 MPa)

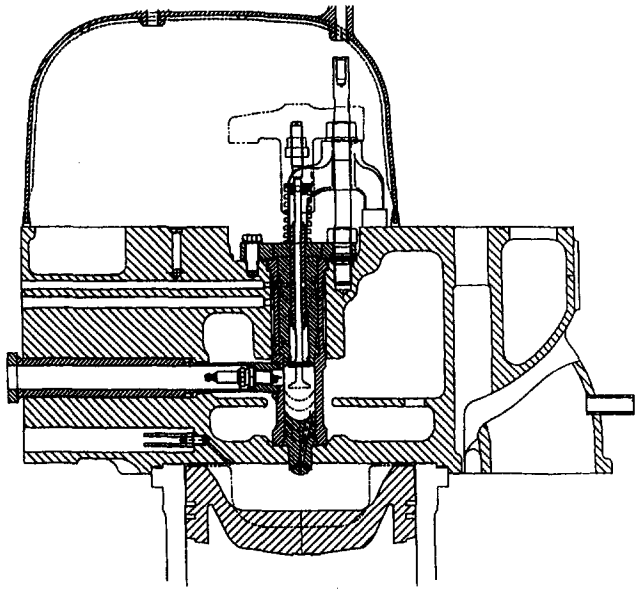

Fig. 10 2401G head and combustion chamber

manifold pressure. This discovery provided direction for the single cylinder combustion testing phase of this program. It became evident that focus should be placed on the smallest prechamber that would produce reliable ignition with total trapped relative air–fuel ratios leaner than $\lambda = 1.8$.

One initial objective of the development program was to eliminate the necessity of timed fuel injection. Timed injection is normally required to accommodate sufficient overlap of intake and exhaust valve timing, primarily for the purpose of reducing combustion temperatures and turbine inlet temperatures. A goal for the simulation program was to define a combustion system that would have minimal valve overlap, but would operate lean enough to produce low NO_x formation rates and satisfactory turbine inlet temperatures.

The model was used extensively to identify intake and exhaust valve timing, which would maximize volumetric efficiency while minimizing scavenged hydrocarbons. Air–fuel ratios were identified that would result in acceptable NO_x and exhaust temperature characteristics. Figure 9 provides an example of predicted turbine inlet temperatures and NO_x emissions as functions of air–fuel ratio.

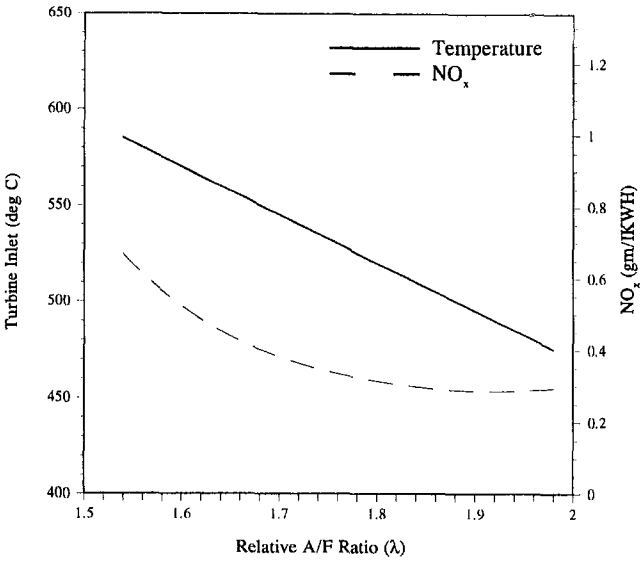

Fig. 9 Predicted NO_x and turbine inlet temperature; 1200 rpm, IMEP = 215 psi (1.48 MPa)

Concept Evaluation With the Single-Cylinder Prototype. The 2400G gas engine development program had as its foundation a 2400D diesel engine. As an expeditious means of conducting the initial spark-ignition, gas-fueled testing, it was decided that one cylinder of a six-cylinder diesel would be converted for gas operation. Working with one cylinder for the gas engine development offered much flexibility in the testing of a variety of design parameters.

Several steps were required to isolate the one cylinder needed for the gas engine development. A special exhaust manifold was designed for the gas cylinder. To produce exhaust pressure pulsation conditions similar to those for a multicylinder engine, a manifold volume of 30 times the swept cylinder volume was used. The five diesel cylinders exhausted into a separate manifold. Separating the intake charges was relatively easy as the same blower discharge supply could be used for all six cylinders. Diesel fuel injection was direct into five cylinders, while gas admission was into the intake port of the sixth cylinder. Test evaluation was focused on the single gas cylinder by using indicated, real-time data acquisition.

The flexibility of the single gas cylinder is indicated in Fig. 10. This drawing presents the arrangement of the prechamber, main chamber, pilot and main gas supply, spark plug, and pressure transducers. The actuation of the pilot fuel poppet valve by the intake valve bridge can be noted. Dotted lines in this figure are used to show some of the variations of prechamber and main chamber shapes tested. Many design and operating parameters were evaluated with the single-cylinder facility.

Cam Timing. To facilitate the single-cylinder evaluation, a camshaft was designed that allowed different lobe profiles with different orientations to be tested with the gas cylinder, while the remainder of the camshaft had the standard diesel timing for the other cylinders. Selection of the optimum timing involved a balance between low ISFC, low NO_x, low scavenged hydrocarbons, and low exhaust temperatures. Figure 11 is presented to indicate typical results of cam configuration comparisons, including the frequently observed result that combinations that provide low NO_x levels also have higher fuel consumptions.

Main Chamber Shape. A few piston crown shapes and compression ratios were evaluated. A rapid burn combustion with excellent fuel economy was achieved with a deep bowl chamber

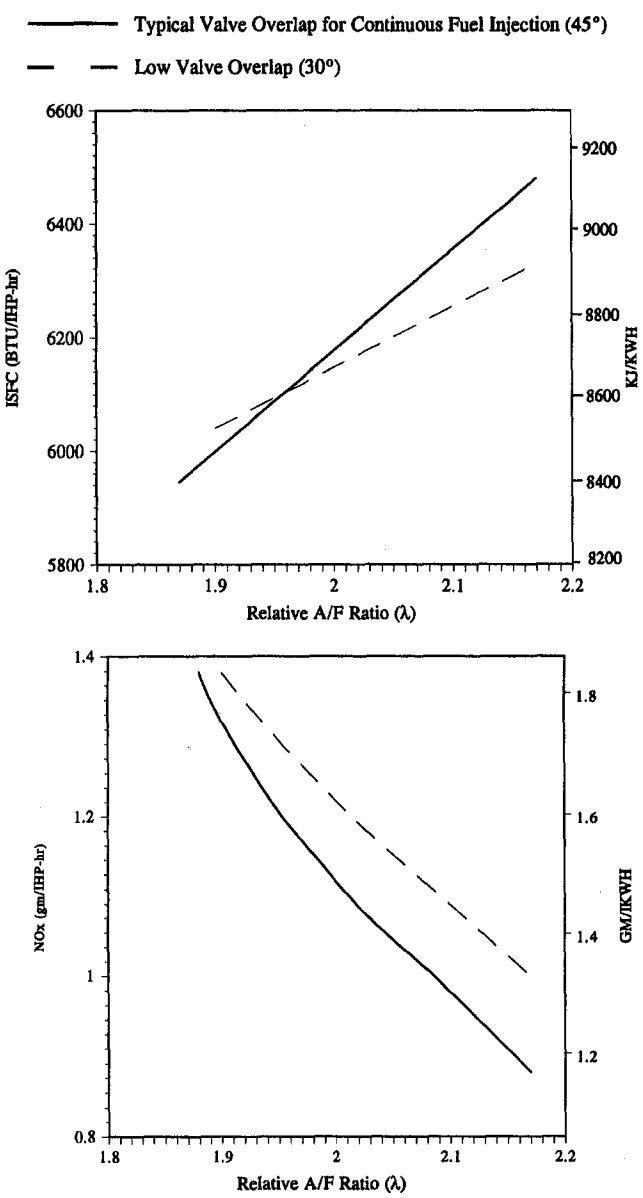

Fig. 11 2401G engine performance: effects of valve timing

concentrated near the center of the piston crown. Optimizing the compression ratio involved a balance between low ISFC, low NO_x, and high knock limit margin. The resulting compression ratio that was used for the first prototype multicylinder engines was 10.9:1. It is an important criterion for engines in gas compressor applications to have a high tolerance for heavy hydrocarbons in the fuel. Therefore, fuel sensitivity tests were conducted using mixtures consisting primarily of methane and butane. A method for evaluating fuel sensitivity in terms of available continuous rating at different normal butane numbers (NBN) was used to assure that knock limit margins would be adequate for expected field applications (Schaub and Hubbard, 1985).

Prechamber Configuration. Principal design criteria used for the prechamber include: swirling flow to maximize the energy available, high L/D for orifices to increase penetration into the main chamber, and low volume to minimize NO_x formation. Prechambers were evaluated based on several factors during the single cylinder testing. As an example of this portion of the work, Fig. 12 compares exhaust emissions results for two prechambers having different volumes. Results for the smallest prechamber that would successfully ignite the air–fuel mixture and project the burning charge into the main chamber are expressed in these curves. The figure compares the performance of this small prechamber with one having twice its volume. Clearly the small prechamber produces substantially reduced NO_x with minimal effect on CO, while increasing hydrocarbons by small amounts.

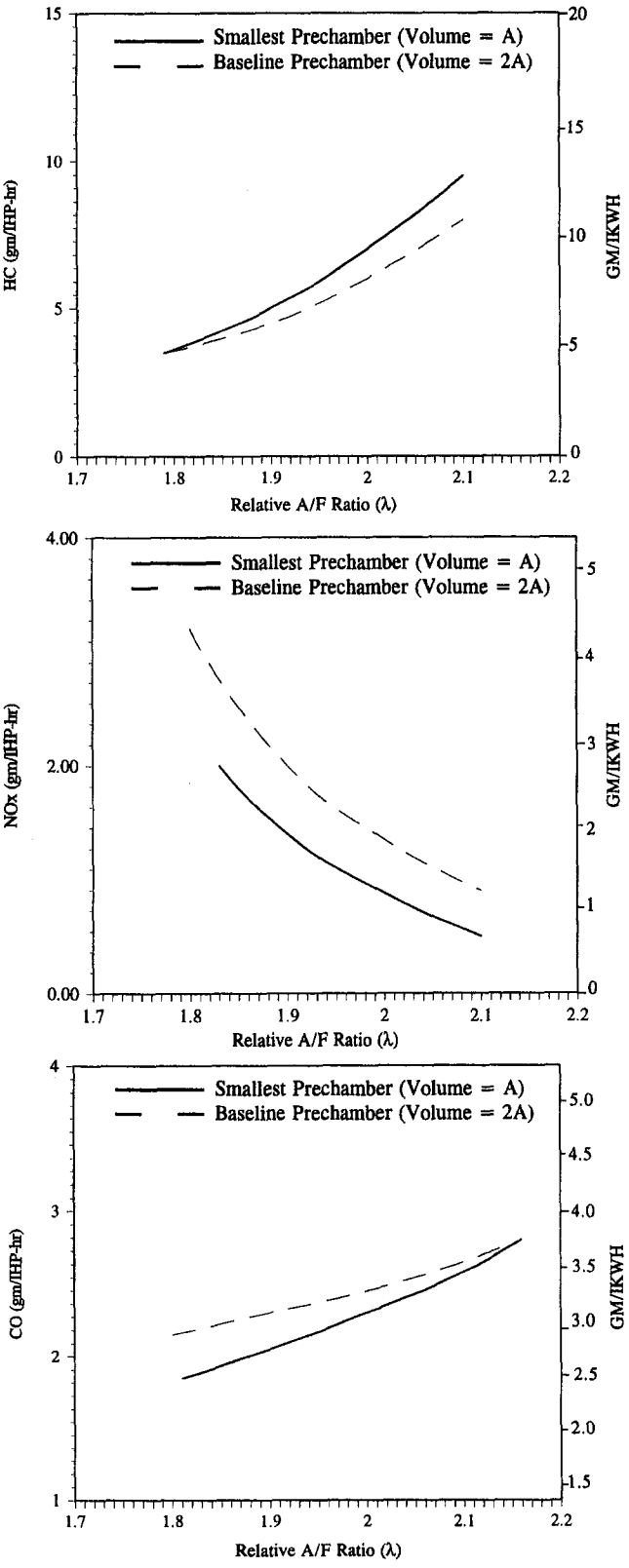

Fig. 12 2401G engine performance: effects of prechamber volume

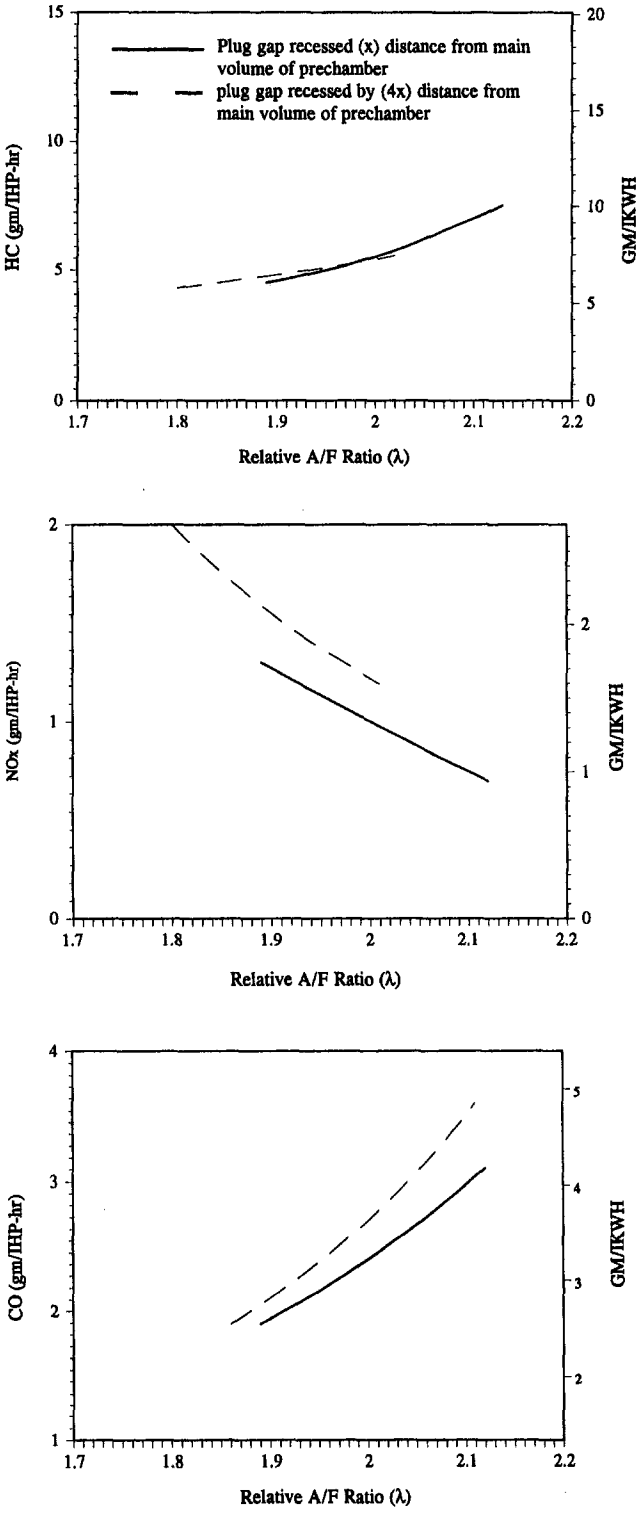

Fig. 13 2401G engine performance: effects of spark plug position

Spark Plug Location. Based on modeling results, it was determined that the spark plug should be in the side of the prechamber, while the inlet fuel injection should be from the top. Testing with the single cylinder was then used to determine the appropriate distance between the plug electrodes and the main portion of the prechamber volume. Figures 13 and 14 contain curves of parameters useful for evaluating the effects of spark plug position. Included are exhaust emissions, peak combustion pressure, and combustion stability as indicated by standard deviation. The configuration with the spark plug electrodes slightly recessed from the main volume of the prechamber produced a large advantage in combustion stability, which naturally translates into lower hydrocarbon and CO levels. This location also produced some of the lower NO_x levels as the peak combustion pressures were reduced.

Application of Results From the Single Cylinder Testing. Information gained from the single-cylinder work about the combustion, porting, cam timing, and fuel and air flow requirements was applied directly to the production of components for the multicylinder engine. This process dramatically reduced the design configuration variables that needed to be evaluated with the multicylinder engine.

Development of the Multicylinder Gas Engines

Initial Tests. The first multicylinder Lab prototype was a 2408G (eight cylinder). Initially these development tests focused on appropriate manifolding, turbocharging, fuel supply, and balancing the inlet conditions to each cylinder. Problems that had to be resolved in the early stages of testing the 2408G were mainly related to leaking pilot valves and to balancing air flows and air inlet temperatures to the eight cylinders. Refinement of the pilot fuel valve resulted in the design shown in Fig. 4. After these valves achieved suitable sealing, the engine

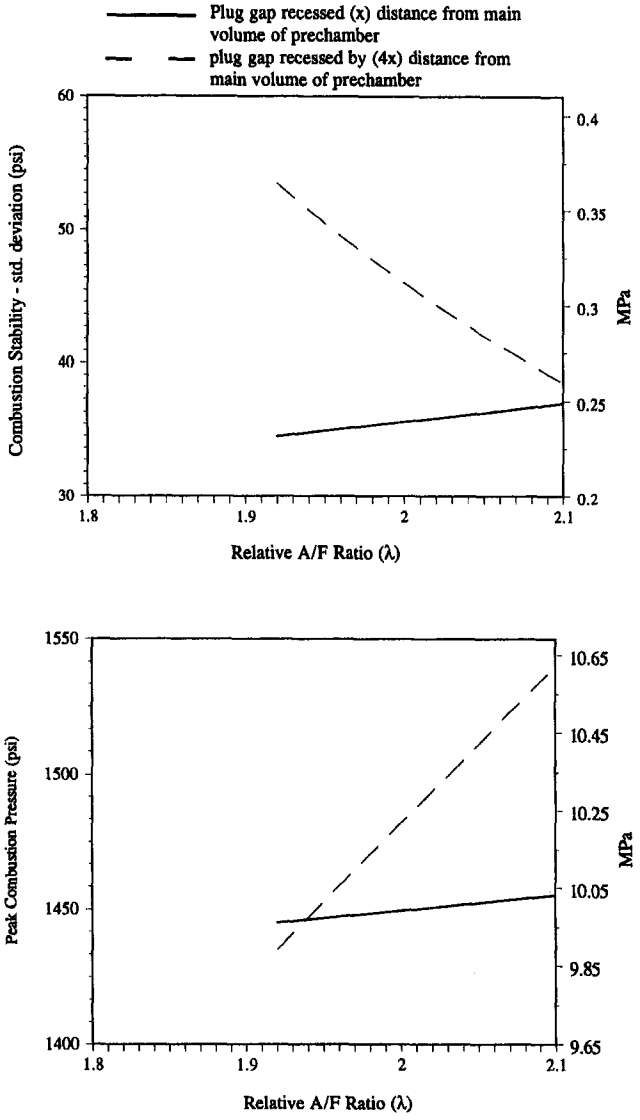

Fig. 14 2401G engine performance: effects of spark plug position

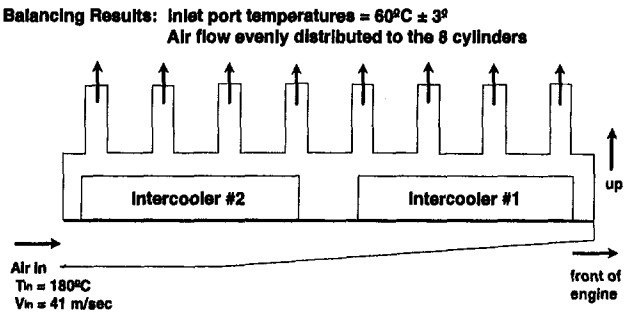

Fig. 15 2408G intake and intercooling system

operation improved substantially. A balance of the cylinder inlet air flows and temperatures was achieved through analysis and experiment. As shown in Fig. 15, air from the turbocharger blower enters the air intake box at the rear of the engine. Two intercoolers are mounted inside the air box, which is integral with the engine block. Results of the balancing process are described in the figure.

Fuel Injection. Defining the design and orientation of the main fuel injector required an extensive effort. This injector admits fuel continuously into each of the intake ports. Several design variations were tested to determine which provided the best mixing of the fuel with the air in the intake port. Several directions for the fuel injection were evaluated with respect to their effects on combustion stability. The best results were obtained by injecting the fuel in the direction counter to the incoming air flow.

Turbocharger Match. A critical input from earlier work with models and with the single-cylinder engine was the design of the water-cooled, constant-pressure exhaust manifold. Based on the preliminary work, the amount of water cooling and the resulting energy input to the turbocharger were estimated. Since the primary applications for 2400G engines involve the driving of gas compressors, these turbocharger matching estimates had to cover a wide range of engine speeds and loads. The initial match was sufficiently close to allow much beneficial testing to occur before the turbocharger was modified. The resulting turbocharger for the 2408G is a radial inflow ABB181, which uses a wastegate for control of boost. This configuration, including the wastegate, is shown in Fig. 16. The final match allows for excellent control of fuel economy and exhaust emissions throughout the engine operating range, and altitudes less than 1300 m have no effect on rating or performance when using the standard turbocharger configuration.

Performance Mapping. After the improvements described above, the 2408G was operating successfully enough to proceed with performance mapping. This mapping was conducted to define the optimum operating parameters throughout the speed and load range. Of primary interest are the air–fuel ratios and the ignition timing. After establishing optimum operating curves, algorithms were then prepared to define these curves for an electronic, closed-loop control system.

Performance Results. Final performance data are presented in Figs. 17 and 18. Figure 17 shows how bsfc and exhaust emissions vary with respect to λ. All the data presented in this figure are at the rated speed and load, and they represent different ways that an engine could be set up depending on customer needs. As expected, the lowest bsfc corresponds to the highest NO_x, and vice versa. To assure adequate safety margins when providing quotations, the following data comprise the standard quotes for the 2406G and 2408G:

bsfc	= 9615 kJ/kWh	(6800 Btu/bhp-h)
NO_x	= 1.2 g/kWh	(0.9 g/bhp-h)
CO	= 3.75 g/kWh	(2.8 g/bhp-h)
nmhc	= 1.34 g/kWh	(1.0 g/bhp-h)

These data are based on pipeline quality gas.

After development of the electronic control system for the 2400G (CleanBurn III), a complete set of performance curves was generated to verify the results of the automatic control system. Fuel economy and exhaust emissions for these tests are plotted in Fig. 18. Satisfactory control is indicated by the minimal variations in emissions throughout the engine operating range. Of particular importance is the fact that specific NO_x remains below the design rated quote throughout the operating range.

After establishing satisfactory performance for the 2408G, several thousand hours of full and overload endurance testing were accumulated with the 2400G inline engines. These tests verified the integrity of the new components.

Application to the Six-Cylinder Version. When the development of the 2408G was completed, this engine was delivered to a customer as the first field prototype. A 2406G was moved into the same lab test facility used for the 2408G. During the latter stages of the 2408G development, all information gained by the program was used to design the components for the 2406G. Therefore, when the initial testing of the 2406G began, the operating and performance characteristics were approaching the production goals. After some tuning of the operating parameters and control system, the 2406G performance exactly matched that of the 2408G on a per-cylinder basis.

Application to the 2400G Vee Engines. Many of the results from the 2400G inline engine development have been applied to the design of the 2400G vee engines. Testing of these engines is currently in process.

Control System Development

Crucial to the success of a modern, low-emissions gas engine is a reliable control system. The CleanBurn III controller is a modular, totally integrated, electronic system that maintains safe operating conditions, low bsfc, and low exhaust emissions

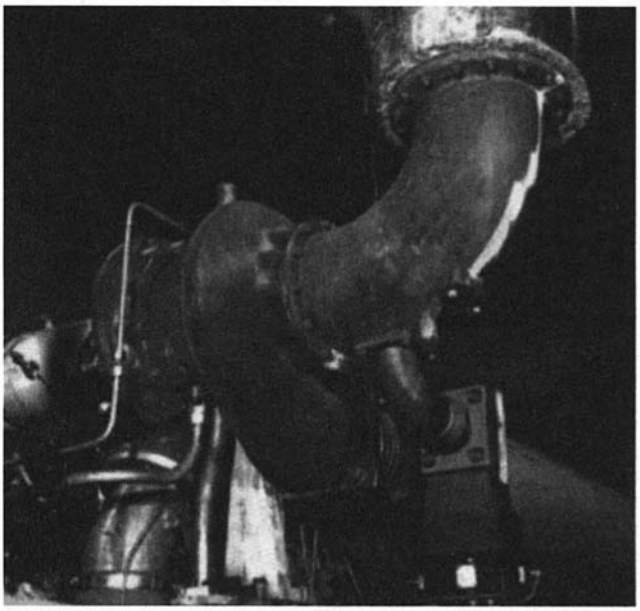

Fig. 16 Turbo and wastegate on 2408G

throughout the engine operating range. Algorithms based on the optimization of the 2400G operating parameters are programmed into the main processor, which is diagrammed in Fig. 19. It controls key operating parameters such as speed governing, main fuel flow, pilot fuel flow, turbocharger wastegate position, and ignition timing. This control unit features:

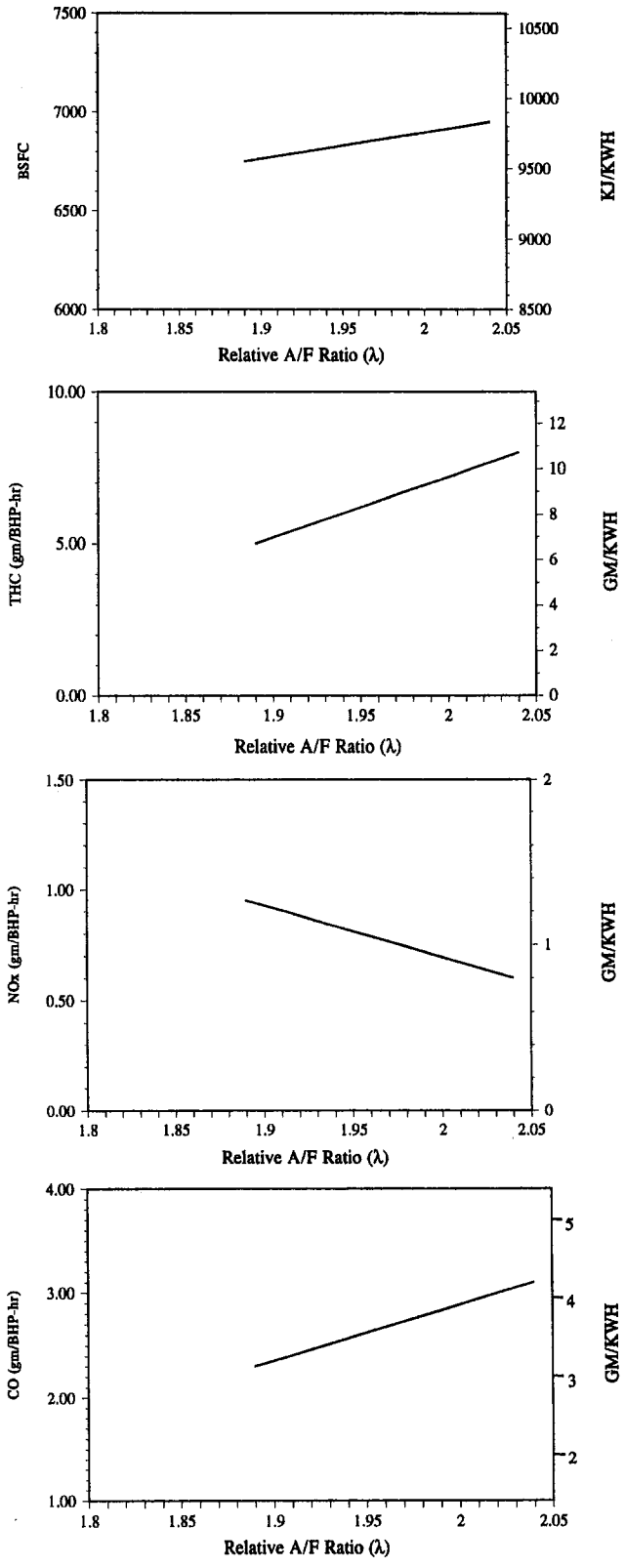

Fig. 17 2408G final performance: effects of air–fuel ratio at 1200 rpm

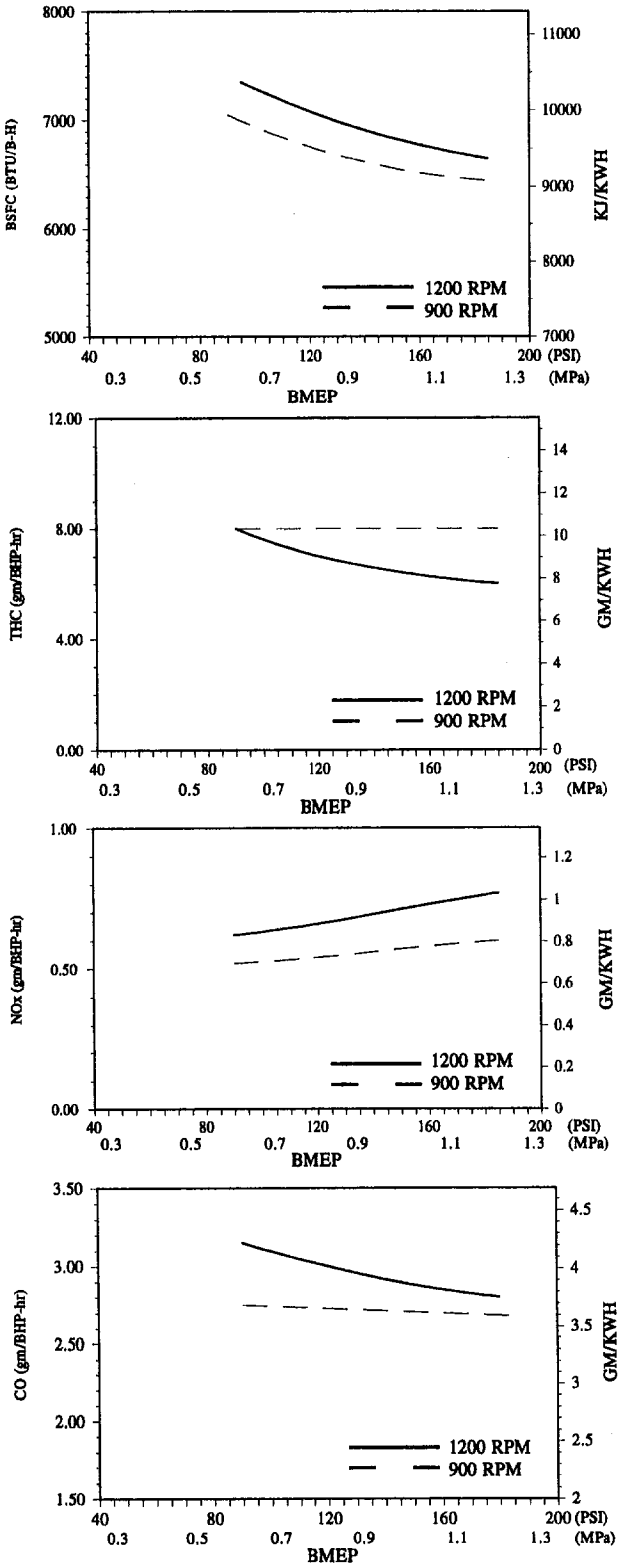

Fig. 18 2408G final performance: air–fuel ratio and pilot fuel controlled automatically throughout engine operating range

1 32 digital inputs
2 16 analog inputs
3 24 thermocouple inputs
4 16 digital outputs
5 6 analog outputs
6 2 RS-232 serial communication ports

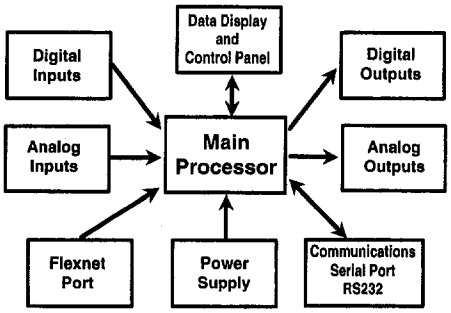

Fig. 19 CleanBurn III control unit

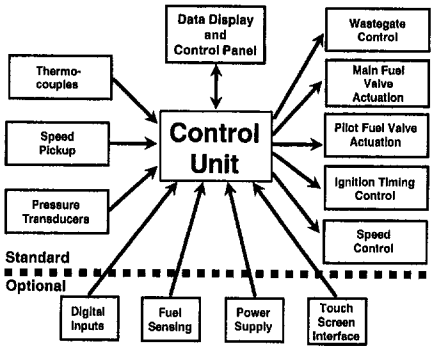

Fig. 20 CleanBurn III control system

7 24 volt power supply
8 flexnet port

The complete CleanBurn III system links several control modules together with connectored cables. Figure 20 presents a block diagram of the complete system. Included is an LCD display of pertinent engine operating data and annunciation features.

The CleanBurn III system provides automatic compensation for changes in ambient conditions and fuel composition. All the components comprising this system are mounted on the engine, and they are shown in Fig. 21. Included in the optional equipment are a fuel gas molecular weight sensor and an exhaust oxygen sensor, which contribute additional capabilities to provide precise control with variable fuel supply composition.

Fig. 21 Components of a CleanBurn III control system

Fig. 22 Right side of 2406G

The molecular weight sensor was developed as part of the 2400G program. It measures the time required for sound waves to traverse a precise distance through the fuel gas supplied to the engine. This time is directly proportional to the molecular weight of the fuel. When there is a significant presence of inert gases in the fuel, then an oxygen sensor is needed in conjunction with the MW sensor to determine the appropriate engine adjustments.

Initial Field Applications

The lab prototypes for the 2406G and 2408G became the first field prototypes. These engines appear in Figs. 22 and 23. The 2406G photograph shows the right side with the exhaust manifold, turbocharger, and oil cooler. The 2408G is pictured from the left side with the control boxes, ignition system, and fuel header.

Most of the 2400G engines will be used in gas compression applications. Design matched to the new 1200 rpm engines are two series of new Superior compressors, the RAM (5 in. stroke) and the WH (6 in. stroke). In Fig. 24, the first 2408G field prototype is shown with a RAM 54 (four-throw) compressor.

Summary and Conclusions

Descriptions of the various stages of the 2400G engine program in this paper are provided as documentation of an expedient approach to the development of a new engine. Mechanical features were presented to provide background for the basic engine construction and as an indication of the design criteria

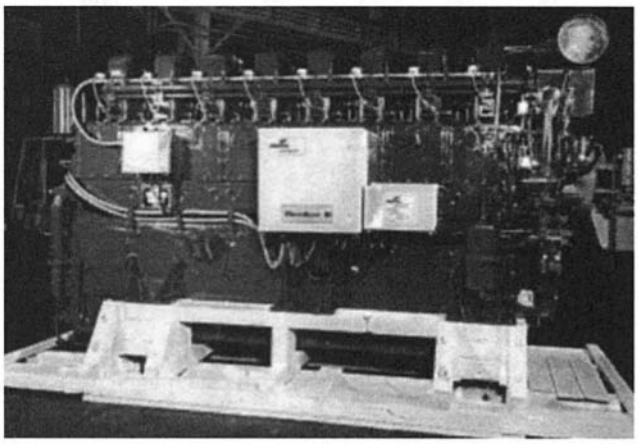

Fig. 23 Left side of 2408G

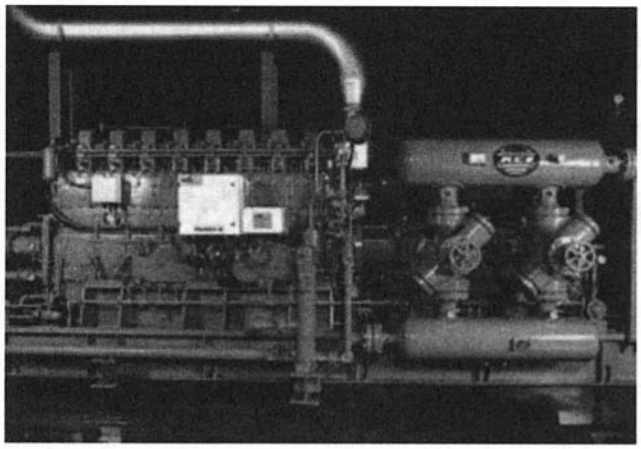

Fig. 24 Gas compression package with 2408G and RAM54 (4 throw compressor)

applied to component development. The main focus of this paper is the logical transition of the development program from simulation to single cylinder testing and then to multicylinder testing.

The success of this program is best indicated by the following accomplishments:

1 Satisfactory agreement between the engine simulation and the engine test results, which was further enhanced with empirical tuning for the model.
2 Design rating goals of 1200 rpm and 150 kW/cylinder were achieved.
3 The initial design concept coupled with value engineering produced a substantial reduction in the cost per kW.
4 Low fuel consumption and NO_x levels represent advances in technology.

Principal stages of the development included:

1 Computer simulation of porting conditions and combustion characteristics.
2 Single-cylinder testing.
3 Design of components for the six and eight cylinder engines.
4 Multicylinder engine testing.
5 Monitoring of field prototype operation and performance.

References

Adams, T. G., 1978, "Theory and Evaluation of Auxiliary Combustion (Torch) Chambers," SAE Paper No. 780631.

Annand, W. J. D., 1962, "Heat Transfer in the Cylinders of Reciprocating Internal Combustion Engines," *Proceedings of the Institution of Mechanical Engineers,* Vol. 177, No. 36, pp. 973–995.

Ballard, H. N., Hay, S. C., and Shade, W. N., 1992, "An Overview of Exhaust Emissions Regulatory Requirements and Control Technology for Stationary Natural Gas Engines," Society of Petroleum Engineers Paper No. 24306.

Caton, J. A., and Heywood, J. B., 1980, "Models for Heat Transfer, Mixing and Hydrocarbon Oxidation in an Exhaust Port of a Spark-Ignited Engine," SAE Paper No. 800290.

Chrisman, B. M., 1983, "Regulations and Control Technology for Stationary Engine Exhaust Emissions," presented at the Casper Oil Show and Conference.

Eckard, D. W., and Servé, J. V., 1987, "Maintaining Low Emissions With Turbocharged Gas Engines Using a Feedback Air–Fuel Ratio Control System," ASME Paper No. 87-ICE-2.

Heywood, J. B., 1988, *Internal Combustion Engine Fundamentals,* McGraw-Hill, New York.

Hires, S. D., et al., 1976, "Performance and NO_x Emissions Modeling of a Jet Ignition Prechamber Stratified Charge Engine," SAE Paper No. 760161.

Karlekar, B. V., and Desmond, R. M., 1977, *Engineering Heat Transfer,* West Publishing Company.

Komizama, K., and Heywood, J. B., 1973, "Predicting NO_x Emissions and Effects of Exhaust Gas Recirculation in Spark Ignition Engines," SAE Paper No. 730475.

Olikara, C., and Borman, G. L., 1975, "A Computer Program for Calculating Properties of Equilibrium Combustion Products With Some Applications to I. C. Engines," SAE Paper No. 750468.

Schaub, F. S., and Hubbard, R. L., 1985, "A Procedure for Calculating Fuel Gas Blend Knock Rating for Large Bore Gas Engines and Predicting Engine Operation," ASME Paper No. 85-DGP-5.

Servé, J. V., 1982, "NO_x Reduction on Large Bore Turbocharged SI Engines," ASME Paper No. 82-DGP-16.

Wall, J. C., and Heywood, J. B., 1978, "The Influence of Operating Variables and Prechamber Size on Combustion in a Prechamber Stratified-Charge Engine," SAE Paper No. 780966.

Watson, N., and Janota, M. S., 1982, *Turbocharging the Internal Combustion Engine,* Wiley, New York, p. 532.

Zeleznik, F. J., and McBride, B. J., 1977, "Modeling the Complete Otto Cycle—Preliminary Version," SAE Paper No. 770223.

Landfill Gas Application Development of the Caterpillar G3600 Spark-Ignited Gas Engine

G. P. Mueller
Engine Development Division,
Caterpillar Inc.,
Mossville, IL 61600

A G3600 engine was developed to operate on landfill gas to demonstrate engine performance and identify any operational problems caused by this application. Fuel system and engine performance development were completed using simulated landfill gas containing carbon dioxide and natural gas at the Caterpillar Technical Center. The engine was packaged as a generator set and has operated for 12,000 hours on landfill gas. Engine performance goals similar to those for G3600 natural gas applications were achieved during development and were attained during the field test. Development work and field test endurance results are presented in this paper.

Introduction

The Caterpillar G3600 spark-ignited gas engine features very low emissions, automatic adjustment to changes in fuel quality, and high thermal efficiency. These features are attained by employing a precombustion chamber, multiple in-cylinder combustion sensors, and sophisticated electronic controls. A detailed description of the G3600 engine and initial development results is given by Nevinger (1991). Initial G3600 engine development focused on electric power generation and industrial power applications for natural gas with a Lower Heating Value (LHV) ranging from 33.5 to 44.7 MJ/m^3 (900–1200 Btu/scf). G3600 engines were field tested and pilot production began in 1991. Field tests and the close field monitoring program were successful and the engine is now available for worldwide distribution to operate on pipeline quality natural gas and selected wellhead gasses.

There is a significant market for generator sets that can operate on Landfill Gas (LFG) fuel. In the U.S. there are more than 600 landfills that will have to collect and dispose of LFG under pending Environmental Protection Agency regulations (Hamilton, 1993). Many of these sites will use the LFG to fuel generator sets to sell electrical power to the local utility and recover some of the costs of gas collection. The Caterpillar G3500 engine family has been successfully developed for landfill gas as described by Macari and Richardson (1987). As of 1993 there were more than 100 MW of G3500 engines installed and operating on LFG. The reliability of LFG-fueled G3500 engines compares favorably to gas turbines, especially when the total availability of generator set and LFG compressor is considered (Markham, 1992). In 1992, work began to increase the G3600 engine fuel quality range to include lower LHV fuels such as landfill gas.

Engine Development for Biogas Fuel

The two most common low-LHV fuels for reciprocating engines are landfill gas and digester gas. Both fuels are commonly referred to as biogasses because they are both byproducts of anaerobic decomposition of organic matter. Landfill gas is produced during the decomposition of organic matter in sanitary landfills. The gas quality varies depending upon the composition of the waste matter and ambient conditions at the landfill site. LFG fuel quality also varies daily at a given site due to changes in ambient conditions and maintenance of the LFG collection system in the landfill. Digester gas is produced at sewage treatment plants during the treatment of municipal and industrial sewage. Biogasses offer approximately one half of the LHV of pipeline natural gas so fuel systems must be sized to handle twice the flow to maintain the same power output. Engine control systems must also correct for the daily variability of the LHV of biogasses, which is not typical for pipeline natural gas. Typical qualities of landfill gas and digester gas are compared to pipeline natural gas in Table 1.

In addition to the constituents listed above, LFG commonly contains contaminants that are detrimental to reciprocating engine life. The contaminants are generally in one of four categories: chlorine-bearing compounds (halides), sulfur compounds, organic acids, and silicon. The source of halides in LFG are primarily volatile organic compounds (VOCs) from industrial and household solvents and chlorofluorocarbons (CFCs) from aerosol propellants and refrigerants. The chlorine and fluorine atoms from VOCs and CFCs form hydrochloric (HCl) and hydrofluoric (HF) acids during combustion. These acids can be introduced into the engine oil from blowby gasses and can cause corrosive damage to engine components if allowed to condense. Sulfur compounds are formed during the decomposition of organic wastes and can also lead to the formations of corrosive compounds in the engine oil. Unprocessed LFG is typically saturated with water vapor, which may combine with organic compounds to form organic acids. To prevent corrosion from water-born acids, the moisture content of the LFG is reduced during gas processing. Silicon found in LFG comes from particulate matter and gaseous compounds known as siloxanes. Particulate matter is often entrained in the LFG during gas collection. These particles are primarily composed of silica smaller than 5 μm. Most solid particulates are filtered out during gas processing. Siloxanes are organic compounds found in many consumer products, which can appear in trace amounts in LFG. Some cases of reduced engine component life have been documented due to silicon deposits in combustion chambers and exhaust systems caused by siloxanes (Bettermann, 1993). Siloxanes can be removed by gas processing, but due to costs this is not typically done in the U.S. An engine design must be able to tolerate some silicon deposits.

A G3600 engine functional specification was compiled for biogas applications, which is summarized in Table 2. The LHV of biogasses tends to vary considerably so fuel specifications based on volumetric levels of contaminants alone are not appropriate. Chadwick (1992) found that it is valuable to quantify the chlorine, fluorine, and sulfur levels in terms of the fuel LHV.

Contributed by the Internal Combustion Engine Division and presented at the 16th Annual Fall Technical Conference of the ASME Internal Combustion Engine Division, Lafayette, Indiana, October 2–6, 1994. Manuscript received at ASME Headquarters June 1995.

Table 1 Comparison of worldwide pipeline quality natural gas to biogasses

	Pipeline Natural Gas[a]	Digester Gas[a]	Landfill Gas[b]
CH_4 (%)	81-97	35-65	40-60
CO_2 (%)	0-1.8	30-40	40-55
N_2 (%)	0-14	1-2	0-13
O_2 (%)	0-1	0-1	0-3
H_2 (%)	0-0.1	0	0
C_2H_6 (%)	3-15	0	0
C_3H_8 (%)	0-3	0	0
C_4H_{10} (%)	0-0.9	0	0
Higher C_xH_x (%)	0-0.2	1-2	<1.0
LHV (MJ/m^3)	31-40	11-22	13-20
LHV (Btu/SCF)	832-1075	320-591	363-545

[a]Pyle and Smrcka (1993)
[b]Gas Chromatograph Records of Test Site

LFG Development Goals

The G3600 engine development goals for low-LHV fuels were derived from G3600 pipeline gas functional specification and G3516 LFG experience. Development goals for G3600 LFG applications are shown in Table 2.

The goal of this initial biogas project was to develop and document engine performance on simulated LFG at the Caterpillar Technical Center and then demonstrate that performance on actual LFG. This would reduce field development and customer down time and ensure the ability to develop the other three configurations of the G3600 series for biogasses with minimum field testing. The second major goal of the project was to accumulate operating hours on LFG to identify any problems caused by contaminants or LHV swings common to biogasses.

A G3606, the six-cylinder G3600 engine, was chosen for initial development and field test due to test engine availability. The selection of the G3606 also minimized development hardware and matched fuel availability at the proposed field test site.

Landfill Gas Simulation

The test engine was installed on a dynamometer in a test cell at the Caterpillar Technical Center, which had been modified to allow blending of two gaseous fuels. A mixture of pipeline natural gas and carbon dioxide was chosen to simulate landfill gas. Methane and carbon dioxide typically represent 95 percent of the volume of LFG and both are commercially available. Gas flow meters were used to monitor the fuel blend to the test engine. Gas chromatograph readings were used to measure the LHV of the fuel during final documentation.

The initial limit to low-LHV fuel engine rating was fuel system flow capacity. Fuel system parts and sensors were originally sized for pipeline natural gas. To meet the functional specification, key components of the fuel system were modified to double the fuel flow capability. As described by Nevinger (1991), the differential pressure between the fuel and inlet air is used by the engine control to calculate fuel flow and engine load. The fuel control valve, fuel manifold orifices, and gas admission valves were modified to allow more fuel flow at similar differential pressures. Figure 1 shows the fuel flow range of the production G3606 fuel system and the LFG configuration developed for the field test. The goal of maintaining full-load operation on fuel with an LHV of 14.9 MJ/m^3 (400 Btu/scf) was not attained with this fuel system due to pressure sensor limits. However, the engine could operate at full load on fuel down to 16.1 MJ/m^3 (432 Btu/scf) and a control strategy was implemented to derate the engine automatically if the fuel pressure limit is reached. Data from the test site showed that the fuel LHV rarely drops below 16.7 MJ/m^3 (450 Btu/scf) so the fuel system was considered acceptable for the field test. Time constraints did not allow for further development; however, production LFG G3600 engines will be developed with camshafts, which increase the dwell of the gas admission valve. The increased gas admission valve dwell will increase fuel flow without increasing fuel system pressure so that operation on 14.9 MJ/m^3 LHV fuel is possible.

Table 2 Functional specifications for G3600 LFG engines versus those used for pipeline natural gas development

	Biogas	Pipeline Natural Gas[a]
Fuel Requirements:		
Fuel LHV (MJ/m^3)	15-20.5[b]	33.5-44.7
Fuel LHV (Btu/SCF)	400-550[b]	900-1200
Maximum contaminants		
Chlorine (μg/kJ)	18.9	-
Sulfur (μg/kJ)	18.9	-
Moisture (g/m^3)	1.85	-
Oil (g/m^3)	0.035	-
Particulates:		
>0.4 μm	0	-
<0.4 μm (mg/m^3)	7.1	-
Maximum bsfc (MJ/bkW-h)	9.83	9.19
Maximum bsfc (Btu/bhp-h)	6950	6500
Exhaust emissions (g/bhp-h)		
NOx	1.0	1.0
CO	2.1	2.0
Non-methane HC	1.0	1.0
Total HC	4.0	4.0
Nominal bsoc (g/bkW-h)	0.31	0.31
Minimum oil drain interval (h)	1200[c]	2000
Minimum service interval (h)	1000	1000
Spark plug life (h)	5000	6000
Engine Overhaul Life (h)		
Minor (top end only)	15,000-20,000	15,000-20,000
Major	40,000	40,000

[a] Nevinger (1991)
[b] Engine should not require adjustments unless fuel LHV fluctuates by more than 10%
[c] Oil drain interval to be determined by oil analysis.

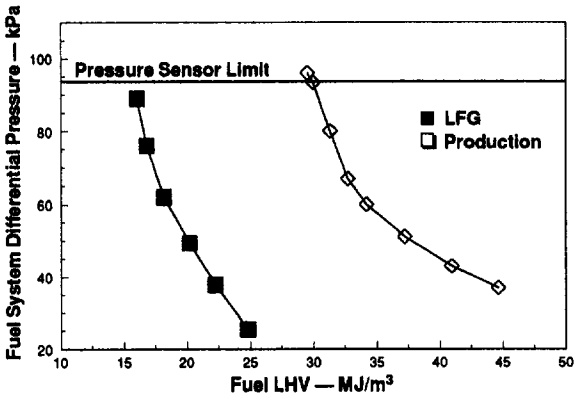

Fig. 1 Comparison of the fuel LHV operating range for production G3606 engines and the LFG fuel system developed for the field test

Table 3 G3606 engine performance results from natural gas and CO_2 blended to simulate landfill gas

	Simulated Landfill Gas	Pipeline Natural Gas
Lower Heating Value (MJ/m^3)	18.26	34.46
Power (bkW)	1185	1185
Speed (rpm)	900	900
bmep (kPa)	1240	1240
bsfc (MJ/bkW-h)	9.79	9.39
bsfc (Btu/bhp-h)	6925	6640
Exhaust Port Temp (°C)	561	510
Air/Fuel (vol./vol.)	8.9	21.0
Excess Air Ratio (λ)	1.73	2.18
Ignition Timing (btdc)	15.5	19.0
Exhaust Emissions (g/bhp-hr)		
NOx	0.78	0.75
CO	1.62	1.45
Total HC	3.2	4.0

Performance Development

After the fuel system was modified to allow sufficient fuel flow, the next step was to optimize the engine settings for LFG. The G3600 control system employs maps to adjust ignition timing, air/fuel ratio, and measured flame speed with operating conditions to maintain optimum engine performance at the desired emission levels. A series of tests was conducted to define the best prechamber fuel valve settings, combustion speed, and ignition timing. A summary of engine performance with 18.26 MJ/m^3 (490 Btu/scf) LHV fuel is shown in Table 3 and compared to pipeline natural gas data. The first engine adjustment was to enlarge the prechamber needle valves to allow more fuel flow to the prechambers. Surprisingly, the ignition timing for best brake specific fuel consumption (bsfc) and combustion stability was retarded from the natural gas timing. Macari and Richardson (1987) found that advanced ignition timing improved bsfc and increased the fuel LHV range for a Caterpillar G3516 engine operating on LFG, which is typical for any open-chamber spark-ignited engine. The high levels of CO_2 were found to increase the ignition delay and reduce the combustion speed when compared to operation on natural gas. The G3600 has an enriched prechamber, which provides a stoichiometric air/fuel mixture at the spark plug. The flame propagates out of the prechamber nozzles to ignite the very lean air/fuel mixture of the main chamber. During this testing it was believed that the retarded timing improved combustion stability because the pressure and turbulence in the prechamber at the time of ignition is higher at later ignition timing. Note that due to the retarded timing and slower combustion, the air/fuel ratio could be reduced to improve bsfc while maintaining the desired NO_x emissions. The natural gas–CO_2 mixture also produced higher exhaust manifold temperatures due to slower combustion and lower air/fuel ratio.

The ability of the control system to adjust to fuel LHV variations was next documented. A plot of bsfc and emission levels on varying LHV fuel is shown in Fig. 2. Emission levels are maintained throughout the desired fuel range and bsfc has an inverse relationship to fuel LHV as expected. As carbon dioxide levels increase, more combustion heat is absorbed by the relatively inert gas and thermal efficiency decreases. The carbon monoxide (CO) emissions did not increase measurably as the CO_2 in the fuel was increased. However, the overall CO emissions were generally 15 percent higher than those taken operating on natural gas. The increase in CO may be due to some disassociation of CO_2 into CO during combustion.

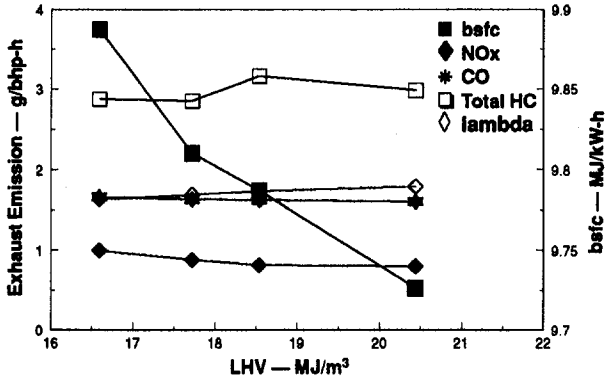

Fig. 2 G3606 engine performance 1185 bkW, 900 rpm on natural gas blended with CO_2 to simulate LFG

Field Test

After performance development was completed, the test engine was remanufactured and packaged as a generator set for the field test. Production parts were used throughout the engine except the fuel system changes described above and some modifications made to reduce potential corrosion problems. Elevated temperature jacket water thermostats, 108°C, were installed in place of the production 85°C thermostats. The higher temperature reduces the amount of blowby condensation in the engine oil and decreases the possibility of corrosion. Valve guides with smaller internal diameters were installed to reduce the valve stem clearance. The reduced clearance will reduce exhaust gas passage through the guides and into the crankcase.

The generator set was installed at an 86 acre landfill with existing LFG recovery equipment. Two gas turbines have been operating at the test site since 1985. Fuel is supplied to the test engine by a compressor package, which draws LFG from the same system of wells, which supplies fuel to the gas turbines. A schematic of the LFG processing is shown on Fig. 3. The compressor package was originally designed for gas turbines, which require 1100 kPag (160 psig) fuel pressure and was modified for the test engine, which requires only 310 kPag (45 psig). Note that moisture is removed at three separate points in the process.

A crankcase ventilation system was installed to remove corrosive blowby fumes from the engine. Three breathers mounted on the crankcase side covers admit filtered air into the crankcase. The blowby gases and air are drawn out of the valve covers by a remote mounted blower. A valve between the engine and blower allows adjustment of crankcase pressure.

The generator set was connected to the local power utility via a switchgear. The switchgear control was designed to paral-

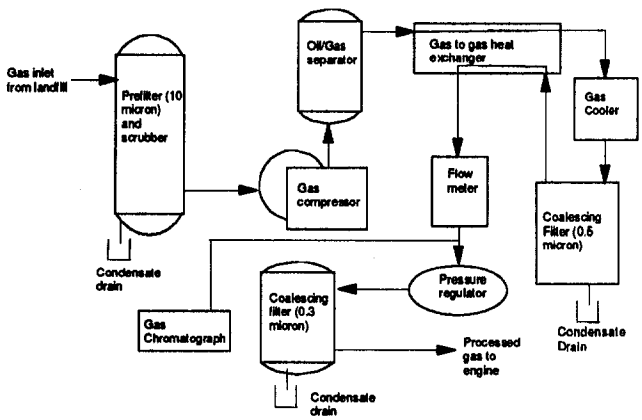

Fig. 3 Schematic of LFG processing at test site

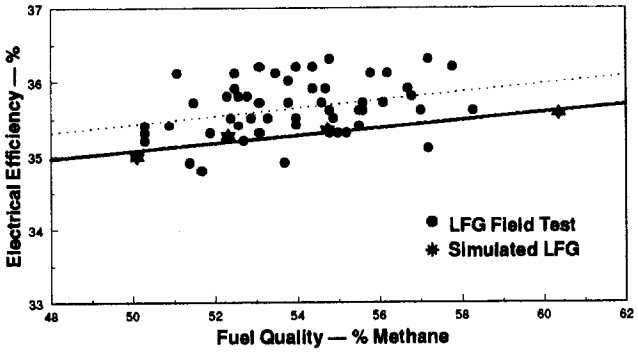

Fig. 4 Generator set electrical efficiency from field test and development test on simulated LFG

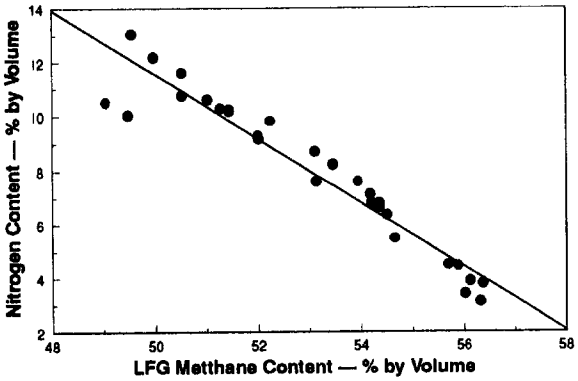

Fig. 5 Landfill gas nitrogen constituent variability versus methane content

lel the generator set manually and then automatically control the engine load with a load share module. After some initial control system adjustments, the engine easily starts and parallels the generator to the utility grid. The load share module ramps the engine load from no load to rated power in two minutes. The generator set began continuous, full-load operation on October 1, 1992, and is shut down only for maintenance or repairs. Engine control parameters, generator output, and LFG compressor data are recorded daily by plant operators.

LFG Performance

The generator set has completed over 12,000 hours of operation on LFG. The fuel methane content has varied from 45 percent (15.24 MJ/m^3) to 58 percent (19.64 MJ/m^3) with a mean value of 53.6 percent. The engine can maintain full load on fuel with 49 percent methane, which is an LHV of 16.59 MJ/m^3. When the fuel quality drops below this point, the engine control maintains the maximum fuel pressure and the load share module reduces the generator load. The LFG methane content only drops below 50 percent during maintenance on the gas collection system. The generator set has run below the rated load of 1135 kW for less than 3 percent of the total test hours.

The performance of the test engine matches the performance documented on simulated landfill gas to within the precision of the field test measurement equipment. A plot of the relationship of electrical efficiency to fuel LHV is shown in Fig. 4. Electrical efficiency is defined as the electrical output of the generator divided by the fuel energy input to the engine. The large scatter of the data is probably due to the lack of averaging of the fuel flow and power output readings; the digital displays for these quantities often fluctuate by approximately 2 percent of the reading at each update. The nitrogen content of the LFG may also contribute to the scatter in engine efficiency. Karim and Wierzba (1992) showed that CO_2 absorbs combustion energy more effectively than N_2. It was also proven that of fuels composed of CH_4 and N_2 or CO_2, the CH_4–N_2 blend will yield a higher engine thermal efficiency at equivalent LHV. Data were not available to correlate N_2 levels in the LFG to test engine efficiency, but N_2 data from the landfill prior to engine installation are shown in Fig. 5. The N_2 generally has an inverse correlation to CH_4 but there is some variability not related to CH_4 content.

Engine Oil Life

The engine oil drain interval for large gas engines fueled with pipeline natural gas is usually limited by oil oxidation and nitration levels. This is typically the case with G3600 engines, which successfully operate to 5000 hour oil change periods. Engines operating on biogasses typically have to change the oil based on the depletion of the oil's ability to absorb acids or the increase in the acidity of the oil. The Total Base Number (TBN) quantifies an oil's ability to absorb acids and the Total Acid Number (TAN) measures the amount of acids in the oil. The TBN and TAN levels of the test engine oil have been monitored closely and are plotted in Fig. 6. The oil reaches the condemning limits at approximately 1000 hours. During the test, unacceptable valve recession was observed; valve recession is discussed in detail below. Part of the valve recession resolution included the installation of heads with production valve guide clearance. There was concern that the larger valve guide clearance would increase combustion gasses in the crankcase and reduce oil life. As shown in Fig. 6, the oil life was not adversely affected by larger valve guide clearance.

Brake specific oil consumption (bsoc) has ranged from 0.24 to 0.37 g/bkW-h with an average of 0.34 g/bkW-h. These

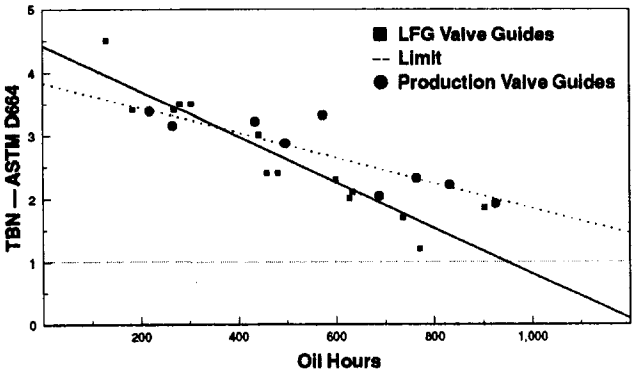

Fig. 6(*a*) Engine oil total base number depletion from five consecutive oil change periods

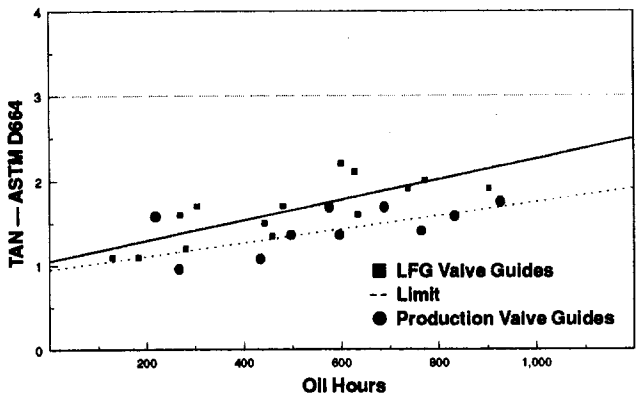

Fig. 6(*b*) Field test engine oil total acid number increase from five consecutive oil change periods

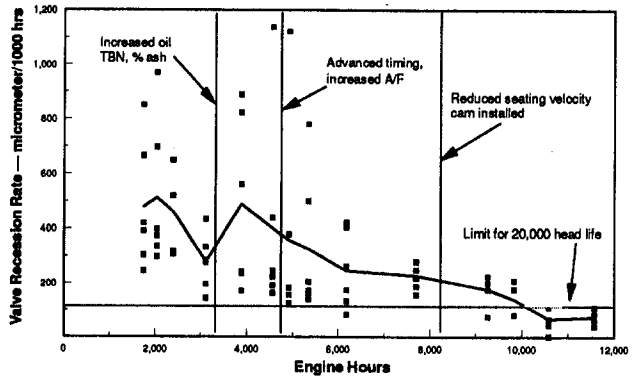

Fig. 7 Exhaust valve recession rate recorded on G3606 LFG field test engine; 1135 ekW, 900 rpm

bsoc values are acceptably close to the target bsoc of 0.31 g/bkW-h.

Operational Problems

A common limiting factor for gas engine top end overhaul life is valve recession. Valve recession is the wear of the valve face and/or seat, which allows the valve to "recede" into the head. Pyle and Smrcka (1993) detail some of the causes of valve recession on gas engines and note that engines operating on LFG often have increased valve recession rates. The initial exhaust valve recession rates measured on the test engine were above the rate required for 20,000 hour cylinder head life. Initial corrective actions focused on LFG related causes of valve recession such as higher exhaust temperature and high levels of silicon in the engine oil. To reduce exhaust temperature, the control maps were modified to advance the ignition timing and increase the air/fuel ratio. The timing and excess air ratio are now similar to those used for natural gas engines. Both of these changes reduced valve temperatures measured on a running engine at the Technical Center at simulated landfill conditions. The turbocharger was also reconfigured to increase the operating margin with the increased air flow necessary at higher air/fuel ratios. The engine control maps were modified so that bsfc and exhaust emission levels were maintained.

Analysis of worn valves and lubricating oil showed increased amounts of silicon compounds, which are not present in natural gas engines. The majority of the silica particles in the oil were less than 5 μm, but it was theorized that the particles might coagulate and cause abrasion of the valve and seats, increasing the wear rate. The engine oil was changed to an oil with higher amounts of sulfated ash. The ash content in stationary gas engine oil is usually kept to a minimum to reduce combustion chamber deposits but in this case, the ash may combine with the silicon and reduce the potential for abrasive wear. Figure 7 shows the exhaust valve wear rates throughout the field test. The wear rate decreased after reducing exhaust valve temperatures and changing the engine oil, but it was still too high to achieve 20,000 hour head life.

A review of the field population of G3600 engines operating on natural gas revealed that the recession rate was lower than observed on the LFG field test engine but unacceptable in some cases. Further testing revealed that high exhaust valve seating velocity may be contributing to the unacceptable wear. A new camshaft was designed to reduce the valve speed during valve and seat contact. These camshaft segments and new cylinder heads with increased valve guide cooling were installed at 8000 hours into the test. The recession rate is now acceptable for all exhaust valves as shown in Fig. 7. Low seating velocity camshafts are now installed on all G3600 production engines.

The only operational problem attributed to LFG contaminants is corrosion pitting at the joint between the precombustion chamber and the ignition body, which secures the prechamber into the cylinder head. The seals in this area were replaced due to corrosion after 3000 hours of operation. The seal material was changed and seal life is now acceptable. A similar material change is being implemented for the ignition bodies.

Combustion chamber, exhaust manifold, and turbine housing deposits have been monitored throughout the test. Deposits in these areas often shorten component or overhaul life on engines operating on LFG. Deposits observed on the test engine are not significantly greater than those seen on natural gas engines. Fuel system components have also been inspected regularly. To date, no premature fuel system failures have been caused by landfill gas.

The availability of generator sets is of prime concern to landfill operators. Availability is defined as total hours of generator set power production divided by the demand hours. Demand hours are defined as any time sufficient LFG is available to the engine and no other problems exist such as electric power utility unavailability. The availability of Caterpillar G3516 engines operating on LFG has been documented at 96 to 98 percent while availability for gas turbines was documented at 93 to 99 percent for the same period of time (Markham, 1992). The availability goal for this field test was 92 percent. At the end of 11451 hours, the availability of the G3606 test engine was 91.1 percent. If down time for valve recession development is not added to the demand hours, the availability is 96.9 percent. Since the projected valve life is now above the minimum of 20,000 hours, G3600 engine availability similar to gas turbines should be attainable.

Conclusion

The test engine has met the functional goals established at the beginning of the project. The engine performance and exhaust emissions, developed on simulated landfill gas in the laboratory, have been successfully demonstrated on landfill gas. Oil change interval is the only maintenance item that has not fully met the original performance goal; however, the oil change periods are currently being extended now that a repeatable baseline has been established. No other component or maintenance schedule changes in addition to those mentioned above have been found to be necessary for operation on landfill gas. Knowledge gained from this test is being applied to develop the rest of the G3600 family of engines for biogas fuels.

Acknowledgments

Special thanks are extended to Paul Orvis, Bill Torzewski, and Tom Dixon of Waste Management North America. Also, thanks to Chuck Anderson and Mike Markham of Rust Environment and Infrastructure for sharing their landfill knowledge and their assistance throughout the project. Gratitude is also extended to employees of Patten Power Systems for engine installation and engine service work during the field test.

References

Bettermann, D., 1993, Lecture presented at German Society of Engineering, Dusseldorf, Germany, McCarthy, T.M. translator.

Chadwick, C. E., 1992, *Caterpillar Gas Engines Application and Installation Guide: Low Btu Engines,* Caterpillar Publication LEKQ2456, pp. 10–15.

Hamilton, S. M., 1993, "Application of Emission Analysis Results Under the Proposed Clean Air Act Rule," *Proceedings, SWANA 16th Annual Landfill Gas Symposium,* Solid Waste Association of North America, Silver Springs, MD, pp. 125–133.

Karim, G. A., and Wierzba, I., 1992, "Methane-Carbon Dioxide Mixtures as a Fuel," SAE Paper No. 921557, *Proceedings, Future Transportation Technology Conference and Exposition,* Society of Automotive Engineers, Warrendale, PA, pp. 81–91.

Macari, N. C., and Richardson, R. D., 1987, "Operation of a Caterpillar 3516 Spark Ignited Engine on Low-Btu Fuel," ASME JOURNAL OF ENGINEERING FOR GAS TURBINES AND POWER, Vol. 109, pp. 443–447.

Markham, M. A., 1992, "Landfill Gas Recovery to Electric Energy Equipment: Waste Management's 1991 Performance Record," *Proceedings, SWANA 15th Annual Landfill Gas Symposium,* Solid Waste Association of North America, Silver Springs, MD, pp. 149.

Nevinger, R. D., 1991, "Design and Development of the Caterpillar 3600 Spark Ignited Engine Family," presented at the ASME Internal Combustion Engine Symposium of the Energy Sources Technology Conference.

Pyle, W. R., and Smrcka, N. R., 1993, "The Effect of Lubrication Oil Additives on Valve Recession in Stationary Gaseous-Fueled Four Cycle Engines," SAE Paper No. 932780, *Proceedings, SAE Fuels and Lubricants Meeting and Exposition,* Society of Automotive Engineers, Warrendale, PA, pp. 89–109.

Advanced Gas Engine Cogeneration Technology for Special Applications

D. C. Plohberger

T. Fessl

F. Gruber

G. R. Herdin

Jenbacher Energiesystem AG, Jenbach, Austria

In recent years gas Otto-cycle engines have become common for various applications in the field of power and heat generation. Gas engines in gen-sets and cogeneration plants can be found in industrial sites, oil and gas field application, hospitals, public communities, etc., mainly in the U.S., Japan, and Europe, and with an increasing potential in the upcoming areas in the far east. Gas engines are chosen sometimes even to replace diesel engines, because of their clean exhaust emission characteristics and the ample availability of natural gas in the world. The Austrian Jenbacher Energie Systeme AG has been producing gas engines in the range of 300 to 1600 kW since 1960. The product program covers state-of-the-art natural gas engines as well as advanced applications for a wide range of alternative gas fuels with emission levels comparable to Low Emission (LEV) and Ultra Low Emission Vehicle (ULEV) standards. In recent times the demand for special cogeneration applications is rising. For example, a turnkey cogeneration power plant for a total 14.4 MW electric power and heat output consisting of four JMS616-GSNLC/B spark-fired gas engines specially tuned for high altitude operation has been delivered to the well-known European ski resort of Sestriere. Sestriere is situated in the Italian Alps at an altitude of more than 2000 m (approx. 6700 ft) above sea level. The engines feature a turbocharging system tuned to an ambient air pressure of only 80 kPa to provide an output and efficiency of each 1.6 MW and up to 40 percent @ 1500 rpm, respectively. The ever-increasing demand for lower pollutant emissions in the U.S. and some European countries initiates developments in new exhaust aftertreatment technologies. Thermal reactor and Selective Catalytic Reduction (SCR) systems are used to reduce tailpipe CO and NO_x emissions of engines. Both SCR and thermal reactor technology will shift the engine tuning to achieve maximum efficiency and power output. Development results are presented, featuring the ultra low emission potential of biogas and natural gas engines with exhaust aftertreatment.

Gas Engine Development for High Altitudes

Table 1 provides main engine data. The engines feature a long stroke design and a prechamber combustion system. Each cylinder bank feeds an ABB RR181 turbo charger. The engines are of the mixture compressing type. The custom-made single gas mixer feeds two turbocompressors the high-pressure mixture being drawn through two charge coolers. A single throttle body is used to control engine load and speed, the latter in case of emergency mode operation. This solution provides mechanical simplicity, reliability, and reduced maintainance expenditure. The change from electromechanical ignition generators to an electronic ignition system provides improved control of combustion and permits the application of a knock control system. The engines are running on pure natural gas. The specifications are shown in Table 2. The unit "Nm^3" relates to volume at standard conditions (0°C, 1.01325 hPa pressure).

Each engine drives a 2 MW maximum electric output synchronous generator connected to the local grid. All the heat from the engine's water, oil, and charge cooling system is fed to the local district heating system. The plant total efficiency comes up to approximately 88 percent (Table 3). However, a further potential of three to four percent can be seen in this respect due to exhaust heat exchanger optimization.

Engine Performance. Figure 1 shows the engine's part-load performance and raw emission characteristics, respectively. As can be seen, the engine/genset shows a potential for a further efficiency increase at even higher BMEP outputs. The engines have been set to 500 mg/Nm^3 NO_x raw emissions according to the local emission control requirements. HC and CO emissions are aftertreated by a simple oxidation catalyst. The suitable ignition timing is dependent on the engine's compression ratio, the gas methane number, and the charge temperature, the latter being stipulated by the heating system return temperature. Figure 2 shows the efficiency and raw emission characteristics when the intake ignition timing is varied between 8 and 22 deg CA BTDC. The engine efficiency increases only slightly

Table 1 Main engine data

Total engine displacement	99.8 l
Number of cylinders	16
Bore/Stroke	190/220 mm
Compression ratio	11.36
Engine rated speed	1500 rpm
V-angle	60 deg
Combustion system	prechamber spark ignition
Gas induction system	JES gas mixer
Turbocharger system	2 x ABB RR181
Ignition system	Altronic DISN 801; knock control system
Load control	single throttle body

Contributed by the Internal Combustion Engine Division and presented at the 16th Annual Fall Technical Conference of the ASME Internal Combustion Engine Division, Lafayette, Indiana, October 2–6, 1994. Manuscript received at ASME Headquarters June 1994.

Table 2 Natural gas specifications

Gas fuel density	0.787 kg/Nm³
Calorific value (lower)	36918 kJ/Nm³
Methane number	81

beyond 14 deg BTDC. As NO_x numbers should be kept below 500 mg/Nm³ and HC, which is lowest at 18 deg BTDC, is partially aftertreated in the catalyst, the final ignition setting has been chosen to be 14 deg CA BTDC. The safety margin against knock amounts to approximately 8 deg CA protecting the engine against hazardous methane number deviations of the gas. The rate of heat release (ROHR) (Fig. 3, recorded with an AVL Indimeter/INES system) indicates the combustion to be very fast and complete even at a retarded ignition setting of 10 deg BTDC, due to the optimized prechamber design.

Varying the excess air ratio there is only a rather small influence on engine efficiency and engine-out emissions as indicated in Fig. 4. There exists a significant trade-off between NO_x and HC emissions. As the latter is partially removed by the catalyst to a sufficiently low level the engine's LEANOX™ controller is set to provide an excess air ratio of approximately 1.86 at rated output to keep NO_x below 500 mg/Nm³. Comparing the influence of ignition timing on the one hand and excess air ratio variation on the other, it is evident that the combustion is mainly influenced by ignition timing, which is also demonstrated by Figs. 3 and 5.

As the combustion evidently is dominated by the prechamber, future development toward further increase of efficiency and reduced NO_x emissions will focus on the prechamber layout design.

Turbocharging System. Because of the relatively low altitude of the factory site in Jenbach, it was quite impossible to match the TC system to the engines there. The system specifications therefore had to be predicted by calculation. In close cooperation with the supplier of the TC system, advanced cycle simulation methods have been applied. Figure 6 presents measured and calculated TC efficiency and speed results, respectively. In Figure 7 the calculated and measured engine charging efficiency is compared. All results show excellent correlation. Figure 8 shows the compressor map of the ABB RR181 type turbocharger with the compressor operating and the engine gulp line. The rather steep characteristic is very suitable for the specific application. With a flatter characteristic the compressor would tend to surge at low loads and low ambient temperatures, as frequently occur in this mountainous area.

Further simulation work is going on revealing an additional BMEP output potential of the engine of approximately 1.6 MPa at 2000 m (6700 ft) and 1.5 MPa at 2500 m (8200 ft) above sea level.

Thermal Exhaust Emission After-Treatment of Landfill Gas Engines

Engines operating on landfill or sewage gas commonly face problems with catalytic exhaust aftertreatment due to the content of catalyst poisons in the gas. The thermal reactor offers a

Table 3 Plant performance and efficiency data

BMEP output	1,3 MPa
Engine power output	1600 kW
Plant electric efficiency	0.383
Plant thermal efficiency	0.496
Plant total efficiency	0.879

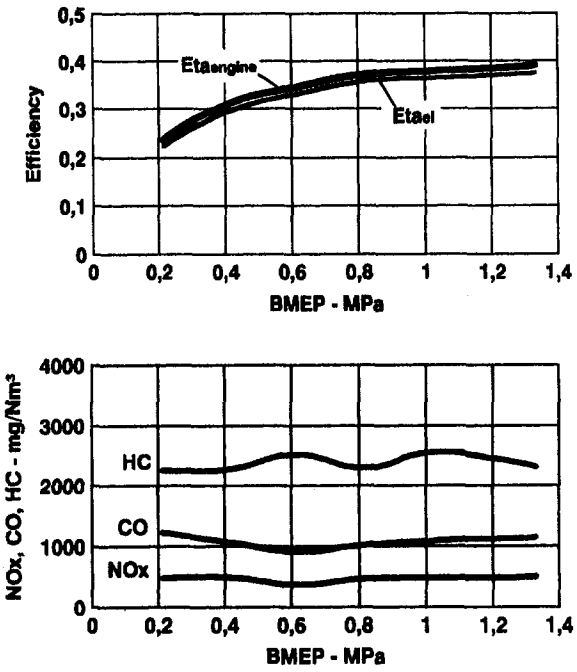

Fig. 1 Engine/electric efficiency and engine-out emissions

possibility for the first time for aftertreating exhaust emissions especially of those engines to achieve outstanding low CO, total HC, and formaldehyde emissions. For lean burn engines running on sufficiently high excess air ratios additional NO_x aftertreatment is required.

Functional Principle. At temperatures beyond 700°C carbon monoxide reacts with oxygen contained in the exhaust gas of lean burn engines. The rate of reaction depends on the temperature of the exhaust gas. The oxidation of the hydrocarbons proceeds at even lower temperatures and is finished within a relatively short time. The exhaust gas is heated in the thermal reactor up to a temperature of about 800°C. The hydrocarbons

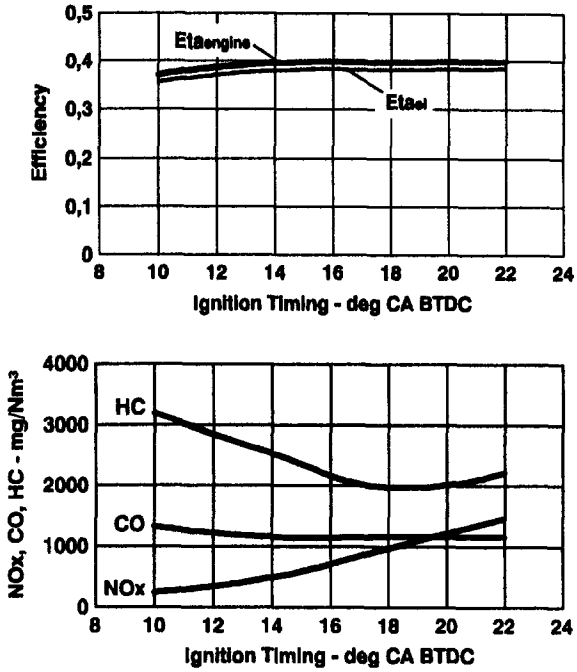

Fig. 2 Efficiency and emission varying ignition timing

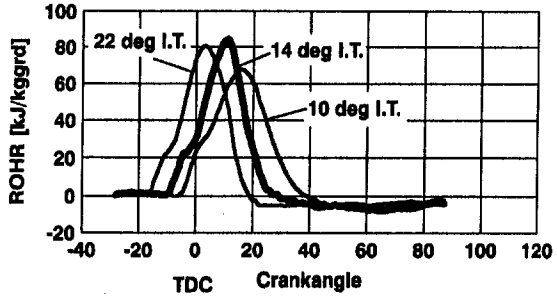

Fig. 3 Rate of heat release (ROHR) varying ignition timing

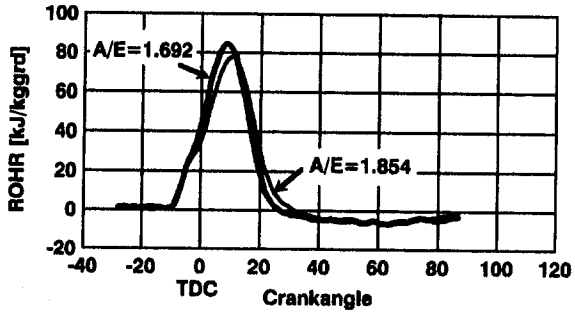

Fig. 5 Rate of heat release (ROHR) varying the excess air ratio

and the carbon monoxide oxidize to water and carbon dioxide there. Figure 9 shows the CO reduction versus time at various gas temperature levels.

In contrast to catalytic exhaust gas treatment, the thermal reactor does not contain any precious materials and therefore disactivation or reduction of catalytic conversion by "poisoning" or physically plugging may not occur.

Design. The thermal reactor is designed as a regenerative heat exchanger (Fig. 10). The exhaust gas from the engine, at a temperature of about 550°C, flows via a switch mechanism into the first heat accumulator where it is heated to approximately 800°C, simultaneously cooling the first heat accumulator.

Subsequently the gas enters the reaction chamber where oxidation of CO and HC takes place and the gas temperature consequently increases. As the gas is passing the second heat accumulator downstream of the reaction chamber, the latter takes over the heat from the gas, which is cooling down consequently. The exhaust gas finally proceeds via the switch mechanism whether directly to the smokestack or previously to a down-line heat recovery boiler. After a time period of 2–3 min, the direction of flow is reversed by means of the switch mechanism. Due to the now reversed flow, the energy required to heat up the exhaust gas prior to the reaction chamber is provided by the second heat accumulator. Heat losses are minimized by suitable thermal insulation; thus the energy initiates the oxidation remaining in the system. Figure 11 shows the temperature–time history of gas entering ("in") and leaving ("out") the thermal reactor, respectively. The thermal reaction inside the reaction chamber has been found not to contribute to NO_x emission.

Emission Limits Achievable With Thermal Exhaust Aftertreatment. Table 4 presents measurement results of a test reactor after continuous operation for 2500 hours connected to a landfill gas engine. Applying a thermal reactor to a lean burn gas engine emission limits as shown in Fig. 12 can be guaranteed. All data presented are based on dry exhaust gas with 5 percent oxygen content.

Besides solving the ever-increasing problem with engine emissions, the thermal reactor provides additional advantages. The plant electric efficiency has been increased by approximately 4 percent by setting a 40 liter displacement engine to maximum efficiency without considering the requirement for low engine-out CO emissions (which have been aftertreated). By the same reason a further increase in engine BMEP output is feasible by higher degrees of supercharging. Up to now the specific engine power output often was limited by the permissible CO emission.

SCR Deno$_x$ Technology

The SCR technology represents a possibility to significantly reduce NO_x emissions by aftertreating lean-burn engine exhaust gas, where "SCR" signifies "Selective Catalytic Reduction". By separating the emission problem from the other engine oper-

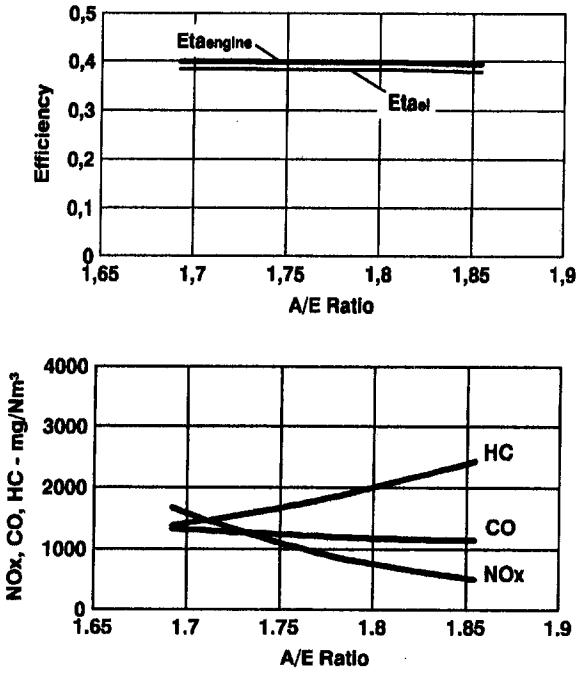

Fig. 4 Efficiency and engine-out emissions at various excess air ratios

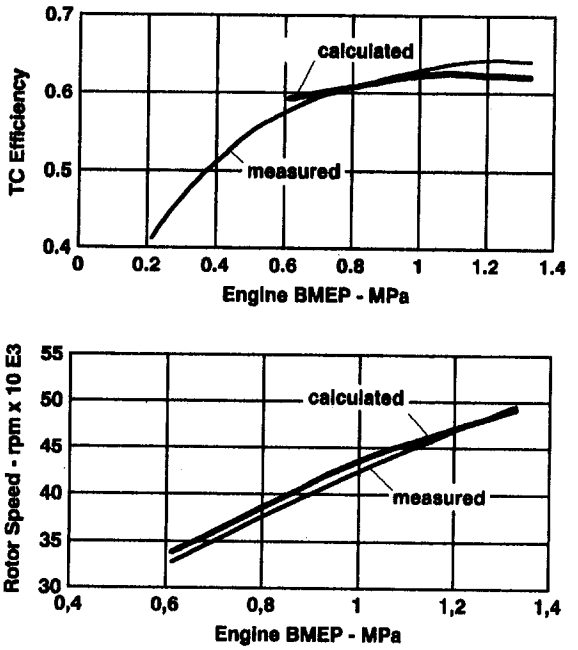

Fig. 6 Calculated and measured TC efficiency and rotor speed

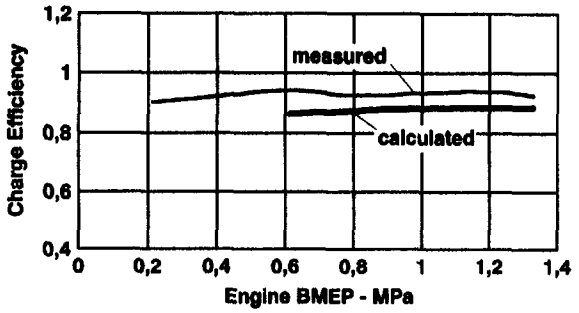

Fig. 7 Calculated and measured engine charging efficiency

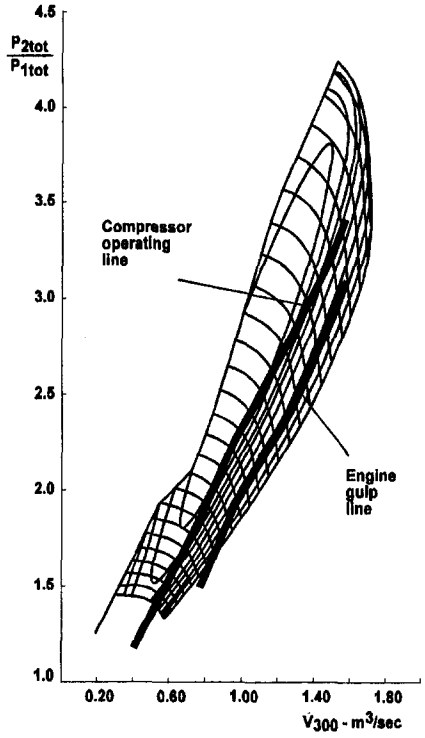

Fig. 8 Map with compressor operating and engine gulp lines

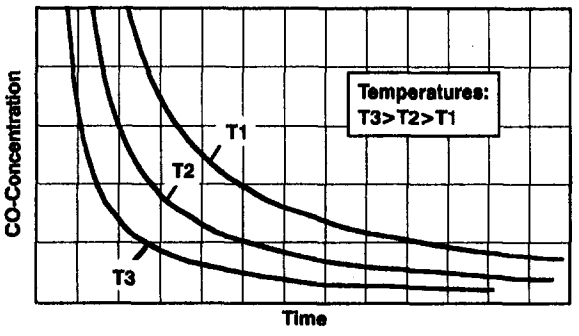

Fig. 9 CO reduction at various gas temperatures

ation parameters, a higher degree of optimization is feasible with regard to both efficiency and nominal power output. Figure 13 shows the correlation between engine BMEP output, NO_x emission, and engine efficiency. It is evident, that the application of the SCR technology can boost the engine efficiency significantly. The then higher engine-out NO_x emissions are abolished by the exhaust gas aftertreatment.

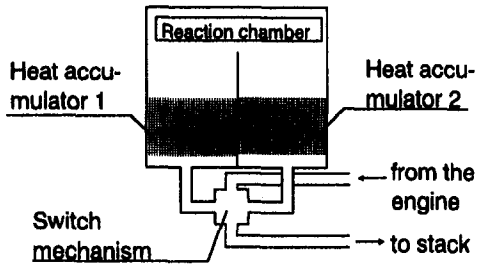

Fig. 10 Thermal reactor design

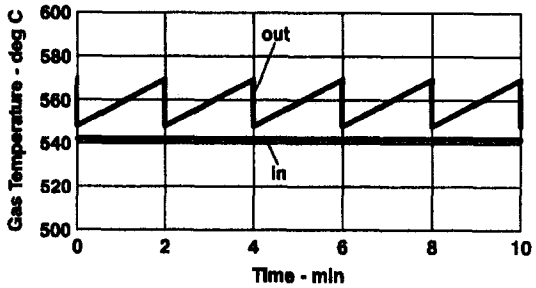

Fig. 11 Temperature-time history of exhaust gas

Functional Principle. An exact proportion of urea solution is spray-injected into the exhaust gas. Due to the temperature level of the exhaust gas, the urea changes into ammonia, reacting inside the catalytic converter with the nitrogen oxides, forming molecular nitrogen, water, and carbon dioxide. However, an eventual surplus of ammonia not reacting in the catalyst will be reconverted into NO_x inside the downstream oxidation catalyst. The precise control of urea dosage is essential therefore. As can be seen in Fig. 14, NO_x is reformulated inside the oxidation catalyst in case the urea dosage becomes too high, represented by an incline of the curve. The combination of SCR and a downstream oxidation catalyst is beneficial as the CO concentration slightly increases in the NO_x converter. As natural gas engines anyhow employ oxidation catalysts for CO reduction in many applications, this will not represent an additional expenditure. The system configuration of a lean burn engine equipped with a SCR-catalyst is shown in Fig. 15.

Reducing Agent. Urea $[(NH_2)_2CO]$ is fully harmless in terms of environment protection. It is delivered as a fluid solution or as a granulate that dissolves very quickly in water. The average urea consumption (40 percent concentration solution) is about 2.5 liters/MWh. Depending on the system layout design, NO_x emission limits of 50 or 100 mg/Nm^3 (dry exhaust gas @ 5 percent oxygen) are achievable in long-term service.

In addition to SCR technology, NO_x reduction is possible by means of stoichiometric engine operation, optionally with exhaust gas recirculation (EGR) where emission values of 100 mg/Nm^3 and even less are feasible. However, the stoichiometric engine requires highly sophisticated control systems based on automotive A/F sensor technology where the problem of sensor aging contradicts the requirement of long-term reliability for power generating applications. Aging of the A/F sensor causes an offset of the output voltage signal. Since the A/F margin the engine has to be operated in is very small, even minor shifts of the signal cause significant increases in emissions as shown in Fig. 16. Frequent check-up on gen-sets in Switzerland applying stoichiometric engine technology revealed nearly no engine to be within the stated emission limits within reasonable maintenance schedules.

Table 4 Pollutant concentration in engine-out and thermal aftertreated exhaust gas

	engine-out emission	after-treated
CO	900	140
total HC	570	25
formaldehyde	35	0

data in mg/Nm³

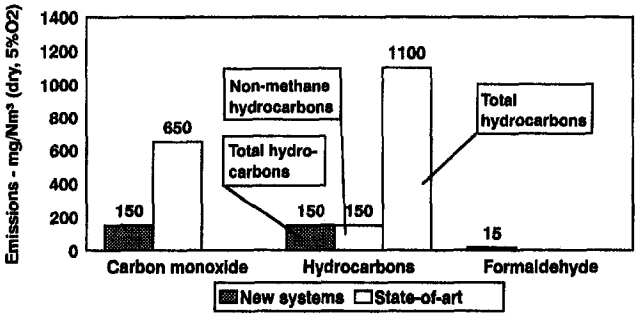

Fig. 12 New engine emission limits to be guaranteed by thermal aftertreatment

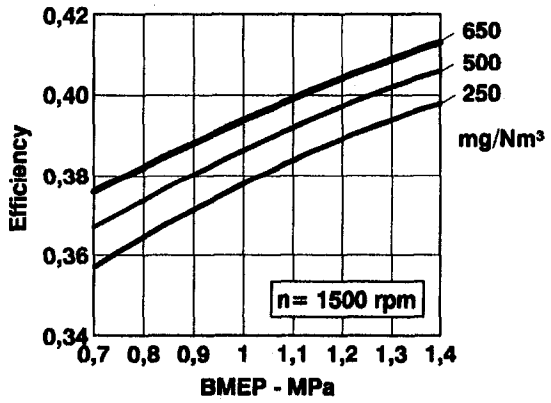

Fig. 13 Correlation of engine efficiency and NO_x emission

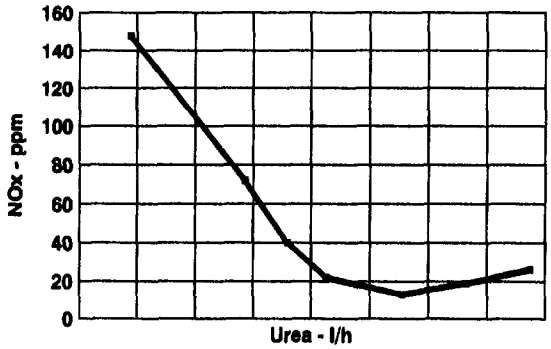

Figure 14: Correlation between NO_X emis-

Fig. 14 Correlation between NO_x emission and urea admixture

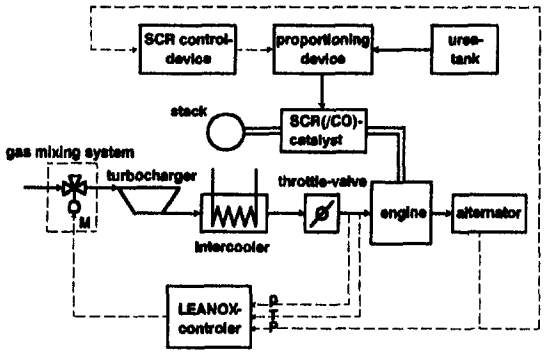

Fig. 15 Schematic of an engine equipped with SCR catalyst

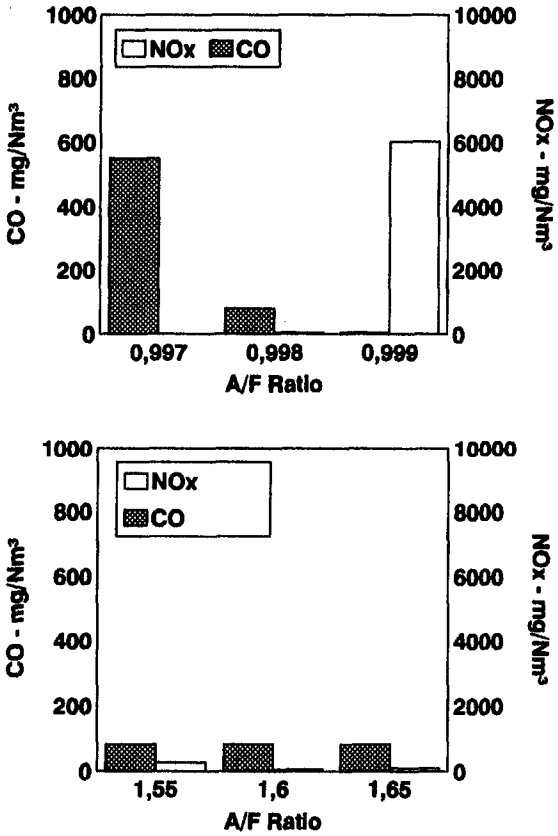

Fig. 16 Exhaust emissions of stoichiometric and lean burn engines

Summary

1 Highly efficient turbocharging and careful engine-TC matching resulted in 16 kW per liter engine displacement specific power output at 1500 rpm at 2000 m above sea level. Thermodynamic cycle simulation proved to be essential to utilize the full potential of the TC system.

2 The prechamber combustion system shows a sufficient safety margin against knock amounting up to 8 deg crank–angle at a methane number of approximately 81.

3 Thermodynamic simulation shows a potential for a further increase of BMEP output up to 1.6 MPa at 2000 m (6700 ft) or 1.5 MPa at 2500 m (8200 ft) above sea level.

4 Thermal reactors represent a future possibility of attaining HC and CO emission limits considerably lower than the state of the art (e.g., German TA-Luft for landfill gas).

5 For the first time it is possible to guarantee extremely low formaldehyde limits of 20 mg/Nm³ in dry exhaust gas at 5 percent oxygen.

6 Lean-burn engines applying SCR technology provide maximum engine efficiency and output at extremely low NO_x emissions; the engine setting need not be compromised by low NO_x/low CO requirements any more.

Acknowledgments

The authors especially thank Mr. Beat Stärkle of ABB Turbo Systems Ltd. for his major contribution to the TC matching and

thermodynamic simulation work. Further thanks are to Mr. G. Nebiolo of the Metan Alpi Teleriscaldamento Sestriere for supporting measurement work, and Mr. B. Bichler, Mr. D. Chvatal, and Mr. M. Götz for contribution to measurement and evaluation work at JES AG.

References

Athenstaedt, G., 1993, "Entwicklung stationärer Gasmotoren seit dem Inkrafttreten der TA-Luft," *MTZ,* Vol. 54, pp. 602–606.

Bulaty, T., and Widenhorn, M., 1993, "Unsteady Flow Calculation of Sophisticated Exhaust Systems Using a Multi-branch Junction Model," ASME Paper No. 93-ICE-14.

Chmela, F., 1994, "The TRI-FLOW Combustion System and Its Effects on Lean Burn Gas Engine Performance (Lean Burn Gas Engines in Utility Vehicles)," presented at the Second Enserv European Stationary and Heavy Duty Utility Vehicle Gas Engine Symposium Workshop, Bad Aibling, Germany.

Gruber, F., et al., 1989, "Arrangement for Regulating the Combustion Air Proportions," U.S. Patent 4.867.127.

Herdin, G. R., et al., 1993, "Das Jenbacher Lambda-1 Konzept mit Aufladung und Abgasrückführung," *Generalversammlung des WKK-Verbandes,* Jenbacher Energie Systeme AG, IWK Zürich, Switzerland.

Kubesh, J., et al., 1992, "Effect of Gas Composition on Octane Number of Natural Gas Fuels," SAE Paper No. 922359.

Pohl, J. M., 1988, "Design and Development of the Waukesha AT25GL Series Gas Engine," ASME Paper No. 88-ICE-24.

1994, "Resultate der Messungen an 11 WKK-Anlagen im Kanton Zürich," *Amt für technische Anlagen und Lufthygiene des Kantons Zürich,* Schlußbericht.

Schiffgens, H. J., et al., 1993, "Einfluß der Methanzahl auf die Verbrennung im Gas-Ottomotor," *MTZ,* Vol. 54, Germany, pp. 350–357.

Staff Report, 1993, "Nearly 4 MWe From Cat G3616 Low NO_x Engine," *Diesel & Gas Turbine Worldwide,* USA, Feb.

Takagi, M., et al., 1977, "The Mechanism of Reaction Between NO_x and NH_3 on V_2O_5 in the Presence of Oxygen," *J. Catalysis* Vol. 50, pp. 441–446.

Tuenter, G., et al., 1986, "Kinetics and Mechanism of the NO_x Reduction With NH_3 on V_2O_5-WO_3-TiO_2 Catalyst," *Ind. Eng. Chem. Prod. Res. Dev.,* Vol. 25, pp. 333–636.

Vogt, E. T. C., et al., 1988, "Selective Catalytic Reduction of NO_x With NH_3 Over a V_2O_5/TiO_2 on Silica Catalyst," *Catalysis Today* Vol. 2, pp. 569–579.

Thermoeconomic Optimization of Sensible Heat Thermal Storage for Cogenerated Waste-to-Energy Recovery

H. A. Abdul-Razzak
Associate Professor,
Department of Mechanical and Industrial Engineering,
Texas A&M University—Kingsville,
Kingsville, TX 78363
Assoc. Mem. ASME

R. W. Porter
Professor,
Department of Mechanical and Aerospace Engineering,
Illinois Institute of Technology,
Chicago, IL 60616
Fellow ASME

This paper investigates the feasibility of employing thermal storage for cogenerated waste-to-energy recovery such as using mass-burning water-wall incinerators and topping steam turbines. Sensible thermal storage is considered in rectangular cross-sectioned channels through which is passed unused process steam at 1307 kPa/250°C (175 psig/482°F) during the storage period and feedwater at 1307 kPa/102°C (175 psig/216°F) during the recovery period. In determining the optimum storage configuration, it is found that the economic feasibility is a function of mass and specific heat of the material and surface area of the channel as well as cost of material and fabrication. Economic considerations included typical cash flows of capital charges, energy revenues, operation and maintenance, and income taxes. Cast concrete is determined to be a potentially attractive storage medium.

Introduction

There is considerable interest in the U.S. in waste-to-energy recovery and cogeneration (sequential production) of useful heat and electricity. Where feasible, local industry agrees to purchase steam at a favorable rate, and the local utility purchases electrical energy under provisions of Public Utility Regulatory Policies Act known as PURPA (Bruderle, 1980).

Unfortunately, many industrial steam users and district heating systems are cyclic in nature. Thus, the benefit of cogeneration is lost when there is no demand for the thermal product. Further, off-peak electrical rates are often too low to provide sufficient revenue for operation in the condensing turbine mode.

While it is possible to operate the facility according to steam demand, it is desirable that the capital-intensive equipment be operated at near capacity in order to generate the revenue necessary to justify the venture. Thus, it might be better logistically if the equipment could be run continuously with excess product energy stored and recovered when in greater demand.

In general, present energy storage devices used in both electric power production and utilization assist in improving overall efficiency through load leveling and benefit from peak-offpeak pricing of electric power. In addition to hydropower and batteries, they are also attractive in the utilization of alternative energy sources such as solar energy and, with energy management systems, they can be used in conjunction with available waste heat.

The task of selecting the type of energy storage device depends on the form of available energy and on the form in which the energy is to be retrieved from storage. For the present study, the interest is in storing and retrieving the thermal energy content of steam. It is necessary to find a sufficiently low-cost storage system to benefit from the value of energy recovered from it.

Direct storage of steam is generally prohibitive due to volume and pressure. However, there are many types of thermal storage device that are potentially attractive for storing the heat content of steam. They include the storage of liquid water, utilization of the heat of fusion of a suitable substance, heat of chemical change of an appropriate material, and utilization of the sensible heat content of a storage liquid or solid. Each of these forms of energy storage has advantages and limitations as described below.

Storage using pressurized liquid water is suitable for providing low-availability energy. During off-peak periods, high-pressure steam is diverted to an accumulator, where it is mixed with stored feedwater from peak operation in order to form pressurized liquid water (Gilli and Beckmann, 1974). During peak periods, the pressurized liquid is flashed to lower pressure steam, which can be expanded through a low-pressure turbogenerator and/or delivered to process. While this technique reduces the volume requirement of storing steam, it requires high-pressure storage. Harman and Lorsch (1985) have considered simple low-pressure hot water storage in order to reduce extraction from the turbogenerators during peak periods for the purpose of feedwater heating, thereby increasing electrical production when it is needed. However, the amount of energy recovered is very small.

Thermal storage systems that utilize the heat of fusion (latent heat) using salts and sensible thermal storage using hydrocarbon liquids or solids can be accomplished through indirect contact with a suitable medium chosen according to thermal-physical properties and cost (Fraas, 1982). These types of system are receiving considerable attention. Current experience in thermal-storage media and devices relates to industrial waste-energy recovery and solar heating and air conditioning applications. Commercial systems are presently already on the market employing hydrocarbons as indirect-contact heat-exchange media, which also possess appreciable sensible-heat capacitance and which are suitable for various temperature processes. A 500 kW(e) solar-thermal generating plant in Almeria, Spain, employs sodium for latent-heat storage with temperature up to 525°C (975°F).

The major advantage of latent heat storage units is smaller size and lower weight per unit of storage capacity. These units have small temperature swings as one cycles from storage to retrieval. The mean storage temperature can be controlled to a large degree by the selection of the storage material. Their disadvantage is that they require a transport fluid as well as a storage material and that in turn requires a heat exchanger. That makes them less attractive than units that use one fluid for both the storage and the transport of energy.

Contributed by the Power Division for publication in the JOURNAL OF ENGINEERING FOR GAS TURBINES AND POWER. Manuscript received at ASME Headquarters February 1995. Associate Technical Editor: David Lou.

The main efforts are associated with the development of low-cost materials that can undergo extended periods of operation with little change in their performance. Lorsch et al. (1976) indicated that paraffin waxes and tetrahydrofuran hydrates appear to be the most promising materials in solar system applications. Salt hydrates in the low-temperature storage range, 30–60°C (86–140°F), sodium hydroxide for storage in the 315°C (600°F) range, and lithium hydroxide, lithium hydride, and lithium fluoride for high-temperature storage systems, 1000–1700°C (1832–3100°F), are considered.

Thermal energy storage utilizing latent heat is not considered here because of the first criterion presented by Lorsch. According to this criterion the material should have a melting point slightly below the heating temperature and slightly above the cooling temperature to permit the desired heat transfer to take place; a single latent heat storage material cannot recover most of the energy content of the steam during the charging period and, at the same time, generate high-quality steam during discharging period, since the energy (to be stored) of the superheated steam is at a pressure of 1307 kPa (175 psig) and temperature of 250°C (482°F), and the energy stored is to be recovered by feedwater (compressed liquid) at the same pressure as the charging steam (1307 kPa, 175 psig) and at a temperature of 102.4°C (217°F). Thus, the system will have high losses from the second-law point of view, in other words, high losses in useful energy. This problem can be avoided by having a series of storage devices that operate at different temperatures and by having a counterflow arrangement. However, this requires the employment of many materials and complicates the analysis and design.

The heat of chemical change can be utilized in constructing thermal storage devices. Gas hydrates, hydrogen zinc reactions, sodium sulfide, and ammonia absorption systems are examples of such applications. However, all involve a considerable safety hazard. Silica gel absorption systems can also be considered but are extremely costly.

In thermal storage devices that operate on the principle of heat of hydration, the discharging process is accomplished by bringing a material such as calcium oxide in contact with water or water vapor. A chemical reaction occurs that produces a considerable amount of heat. In the charging process, electrical or thermal energy can be utilized to drive the moisture from the calcium oxide. There are two major disadvantages of utilization of heat of hydration, and these are the deterioration of the calcium oxide and the removal of noncondensable gases from the system.

The remaining thermal storage system is that using the sensible heat content of the storage material. Solids are particularly attractive because they may serve as both the storage substance and the heat exchange structure.

There are several types of solid that can be used to construct the thermal storage, such as castable metals and firebricks. Firebricks have been long recognized as a low-cost alternative to metals. While firebricks are approximately twice as bulky as castable metals, they are only one-half to one-third the cost. However, firebricks are difficult to fabricate into modern compact heat exchangers. This suggests other low-cost castable material, such as concrete. Concrete's thermal conductivity is low, but its low cost and the fact that the unit can be fabricated on site are responsible for its being given consideration here as a storage material.

The process of storing energy and recovering it is transient in nature, and the temperature and mass flow rates of the working fluids entering the unit are periodic functions of time. Such a unit is usually referred to as regenerator. In order to design these units optimally and evaluate their economic feasibility and thermal efficiency, it will be necessary to predict their transient response or performance.

The analysis to predict the transient response and performance is rather complicated and time consuming in both manpower and computer time as will be shown later. To do so for every material is not feasible. However, a preliminary simplified analysis can show whether such a unit for a certain storage material is potentially feasible or not. The simplified analysis is illustrated in the following section.

Preliminary Analysis

The maximum possible amount of energy, $Q_{\max}$, that can be stored in the thermal storage of a mass, M_m, during one off-peak period and recovered (at 100 percent efficiency) in the following peak period is

$$Q_{\max} = M_m C_m (t_{hi} - t_{ci}) \tag{1}$$

where C_m is the specific heat of the material, t_{hi} and t_{ci} are hot and cold fluids inlet temperatures. Neglecting pressure drop effects, the present worth (maximum), PW, of this maximum thermal storage in terms of initial investment and avoided fuel cost after tax is

$$\text{PW} = 365.25\, Q_{\max}(1 - t)U_p P_a(r, n, e) f_r/\eta_B - C_o M_m P_m \tag{2}$$

where

$$C_o = 1 + t_{ti}(1 - t)P_a(r, n) - td + m \tag{2a}$$

and t is the income tax rate, U_p is the plant utilization factor, f_r is the fuel cost rate, η_B is the thermal efficiency of the conventional boiler on which the value of steam is based, $P_a(r, n, e)$ is the present worth of annual amount at an interest rate r escalating at a compound rate e, n is the life of the system, P_m is the initial cost of storage material and fabrication per unit mass, t_{ti} is the property tax and insurance cost expressed as a percentage of initial investment, d is the present worth of the depreciation of a base one, and m is the charge for operation and maintenance expressed as a fraction of capital cost.

Storage materials exhibiting negative present worth need not be considered further. For potentially feasible storage materials, it is necessary to predict the transient response or performance since the amount of heat that can be stored and retrieved may be less than $Q_{\max}$. Also, the effect of pressure drop may be significant. In the following section, the assumptions and governing equations used to predict the performance of the thermal storage are presented.

Governing Equations and Assumptions

The thermal storage considered here is composed of a number of rectangular cross-sectioned channels for the flowing fluid connected in parallel and separated by the heat storage material as shown in Figs. 1 and 2. The fluid flows in contact with either the inside or the outside surface of the storage material. The surface that is not in contact with the fluid is considered to be adiabatic or perfectly insulated. In order to simplify the analysis, the following assumptions are made:

1. The temperature of the fluid and the storage material is a function of the axial coordinate, z, only.
2. The storage material heat conduction in the z direction is assumed to be zero and the thermal conductivity in the y direction (normal direction) is finite. Neglecting the heat conduction in the z direction generally is valid for a regenerator and can be justified using an order-of-magnitude analysis.
3. The material properties are constant.
4. No heat transfer occurs through the outer surfaces of the channel walls.
5. The regenerator has a counterflow arrangement and constant inlet fluid temperatures and mass flow rates for both charging and discharging streams.

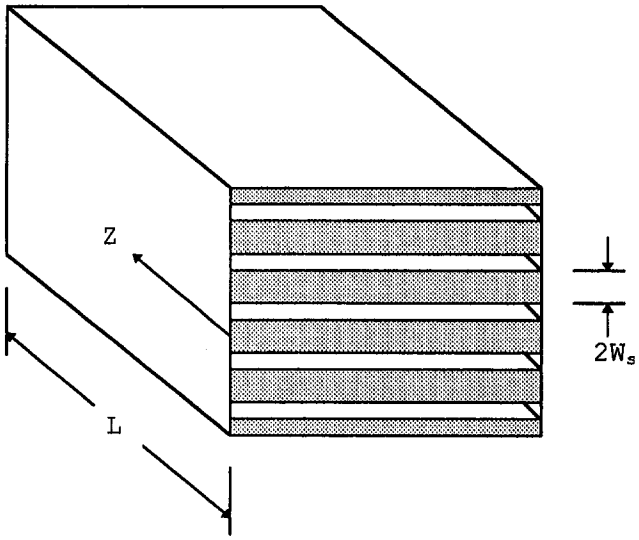

Fig. 1 A parallel-plate regenerator

Based on these assumptions, the energy equation for the fluid is given by

$$UA(t_m - t_f) = \dot{m}_f C_f L \frac{\partial t_f}{\partial z} + m_f C_f \frac{\partial t_f}{\partial \tau} \tag{3}$$

where

t_m = mean temperature of the storage material
t_f = temperature of the working fluid
U = lumped heat transfer coefficient to account for the finite conduction in the y direction by assuming that the mean temperature of the storage material varies linearly with time (Hausen, 1938) = $1/(1/h_c + w_s/3k_m)$
h_c = channel side heat transfer coefficient
w_s = storage material thickness
k_m = thermal conductivity of the storage material
A = surface area
L = length of the regenerator
τ = time
$\dot{m}_f$ = mass flow rate of the working fluid
C_f = specific heat of the working fluid

In most practical applications, the rate of accumulation of energy by the fluid contained within the volume can be neglected. The final form of the energy equation for the fluid is

$$UA(t_m - t_f) = \dot{m}_f C_f L \frac{\partial t_f}{\partial z} \tag{4}$$

The energy equation for the storage material is given by

$$UA(t_f - t_m) = M_m C_m \frac{\partial t_m}{\partial \tau} \tag{5}$$

The lumped heat transfer coefficient and the fluid specific heat depend on the phase, temperature, and the type of flow regime of the working fluid. Thus, the governing equations have nonlinear coefficients.

Equations (4) and (5) are applied separately to the hot and cold periods of operation. The temperature distribution in the storage material, $t_m(z, 0)$, at the start of a period is set equal to that at the end of the previous period of operation. Initially, the temperature distribution is specified arbitrarily. To represent this mathematically, we use a single prime to signify the hot period and double primes for the cold period. At the start of the hot period

$$t'_m(z, 0) = t''_m(L - z, P'') \tag{6}$$

and at the start of the cold period

$$t''_m(z, 0) = t'_m(L - z, P') \tag{7}$$

where P' and P'' are the duration of the hot and cold periods. The boundary conditions are

$$t'_f(0, \tau) = t_{hi} \tag{8}$$

$$t''_f(L, \tau) = t_{ci} \tag{9}$$

where t_{hi} and t_{ci} are the inlet hot and cold fluid temperatures, respectively.

Solution Procedure

The governing differential equations are nondimensionalized and cast in finite difference form using the trapezoidal rule. Nonlinear features are localized into the coefficients of the finite difference equations and evaluated by subroutines. Also, space and time coordinates are stretched as required. Starting with an arbitrary initial temperature distribution in the solid, the periodic steady-state operation is reached after few cyclic iterations.

The space–time dependent working fluid conditions determined by solving the governing equations are used in the calculation of pressure drop and the evaluations of first and second-law efficiencies and the determination of present worth and optimum design. Details of the solution procedure and the empirical formulas used to evaluate the heat transfer coefficients and pressure drop can be obtained from Abdul-Razzak (1988).

Efficiencies, Present Worth, and Optimum Design

The conventional method of evaluating regenerators is through the effectiveness of the regenerator, which is measured in terms of the thermal ratio (η_{REG}). This is defined to be the ratio of the actual heat transfer rate to the thermodynamically limited maximum obtainable heat transfer rate in a counterflow regenerator of infinite heat transfer area.

In the fixed bed regenerator, the exit gas temperatures vary with time. A chronological average exit temperature can be computed. If the average exit temperatures are denoted by t'_{fo} and t''_{fo}, then the thermal ratios may be specified by

$$\eta'_{REG} = \frac{t'_{fi} - t'_{fo}}{t'_{fi} - t''_{fi}} \tag{10}$$

$$\eta''_{REG} = \frac{t''_{fo} - t''_{fi}}{t'_{fi} - t''_{fi}} \tag{11}$$

However, the present problem deals with steam that encounters phase change; thus, there is latent heat involved besides sensible heat. Therefore, the above criteria cannot represent

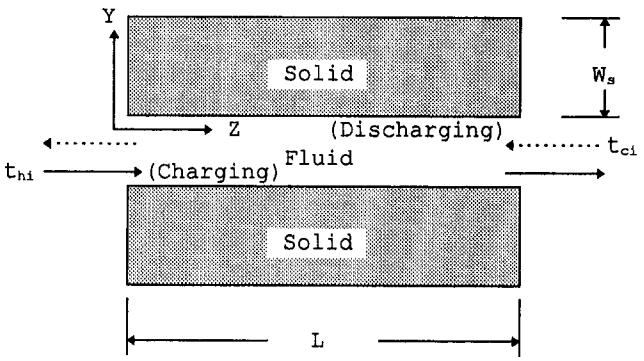

Fig. 2 A single channel

Table 1 Thermal parameters

Parameter	Value	
Charging Period		
Inlet Steam State, kPa/°C (psig/°F)	1307/250	(175/482)
Mass Flow Rate, kg/hr (lbm/hr)	54000	(118800)
Duration, hr	9.6	
Discharging Period		
Inlet Water State, kPa/°C (psig/°F)	1307/102	(175/216)
Mass Flow Rate, kg/hr (lbm/hr)	27000	(59400)
Duration, hr	14.4	
Material - Concrete		
Density, kg/m^3 (lbm/ft^3)	2100	(131)
Specific Heat, kJ/kg-°C (B/lbm-°F)	0.878	(0.210)
Thermal Conductivity, W/m-°C (B/hr-ft-°F)	1.10	(0.636)
Plant Utilization Factor	0.81	
Pump Efficiency	0.71	
Boiler Efficiency	0.85	

adequately the performance of our thermal storage. Instead it is appropriate to consider the overall efficiency of energy recovery and, of course, the net present worth of the system.

Most systems are evaluated based on thermodynamic efficiency based on first law and, more recently, on second law. The first-law efficiency is defined as the ratio of output to input energy. Application of this definition to thermal storage results in the following expression:

$$\eta_{\text{th}} = \frac{\dot{m}_f'' \int_{\tau=0}^{\tau=P'} h''(0,\tau)d\tau}{\dot{m}_f' h_{hi}' P' + \dot{m}_f'' h_{ci}'' P'' + \dot{W}_p P''} \quad (12)$$

where h denotes enthalpy. $\dot{W}_p$ is the pump work to overcome pressure drops. While first-law efficiency is of interest to evaluate energy recovery, it does not consider the quality of energy recovered.

The second-law efficiency is defined as the ratio of output essergy to input essergy and takes into account the quality of energy. The second law efficiency is given here by

$$\eta_{\text{sl}} = \frac{\dot{m}_f'' \int_{\tau=0}^{\tau=P''} \psi''(0,\tau)d\tau}{\dot{m}_f' \psi_{hi}' P' + \dot{m}_f'' \psi_{ci}'' P'' + \dot{W}_p P''} \quad (13)$$

where ψ is the essergy per unit mass. For the present system, the essergy ψ is defined by

$$\psi = (h - h_0) - T_0(s - s_0) \quad (14)$$

where the subscript 0 denotes dead state and s is the entropy.

Once the exit conditions of the cold period are determined, the essergy at the exit $\psi''(0,\tau)$ can be easily calculated. However, neither efficiency definition takes into account both initial and recurring costs and benefits of the system.

The net present worth of the system is given by

Table 2 Economic parameters (1986 $)

Parameter	Value	
Initial Capital Cost (1), $/m^3 ($/ft^3)	182	(5.11)
Initial Unit Energy Prices		
Natural Gas, $/10^{6}kJ ($/10^{6}B)	4.70	(4.96)
Electricity, $/kWh(e)	0.05	
Real Escalation Rates		
Electricity	- 0.0006	
Natural Gas	0.02	
Inflation Rate	0.03	
Effective Income Tax Rate	0.365	
Property Tax and Insurance Cost % of Initial Capital Cost	0.7	
Operating and Maintenance Cost % of Initial Capital Cost	16	
Real Minimum Acceptable Rate of Return	12	
Plant Life, yrs	20	
Tax Life (2), yrs	10	

(1) Includes 15% indirect cost, material and fabrication.
(2) Straight Line (SL) depreciation schedule for simplicity.

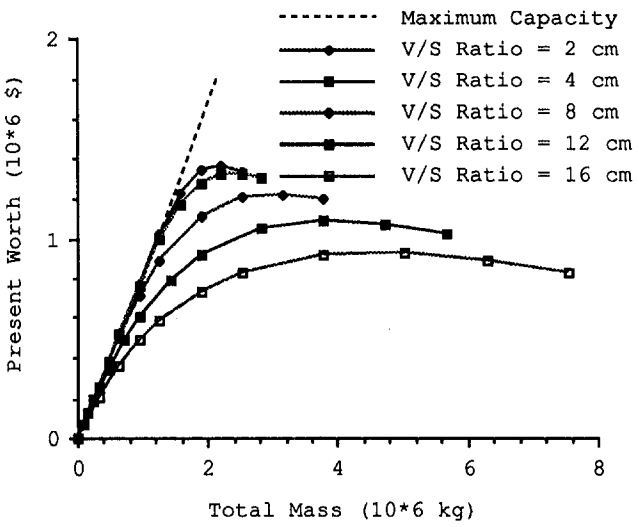

Fig. 3 Present worth versus thermal storage design

$$PW = 365.25(1 - t)U_p\left\{\dot{m}_f''\left(\int_{\tau=0}^{\tau=P''} h''(0,\tau)d\tau - h_{ci}P''\right) P_a(r, n, e)f_r/\eta_B - \dot{W}_p P'' r_e\right\} - C_0 M_m P_m \quad (15)$$

where r_e is the cost rate of electricity.

Results and Conclusion

Based on the parameters of Tables 1 and 2, the preliminary analysis shows that concrete is potentially attractive as a storage material because of its low cost and high specific heat. Besides, it has chemical and geometric stability, high density, and high allowable compressive stress. Also, it is noncombustible, noncorrosive, and nontoxic, and it can operate within the temperature range prescribed earlier. On the other hand, concrete has low thermal conductivity, which results in an undesirable low heat transfer rate from and to the working fluid.

The detailed analysis is simplified further by assuming the heat transfer coefficient on the channel side to be infinity. This assumption can be justified based on the low thermal conductivity of concrete and the high heat transfer coefficients during

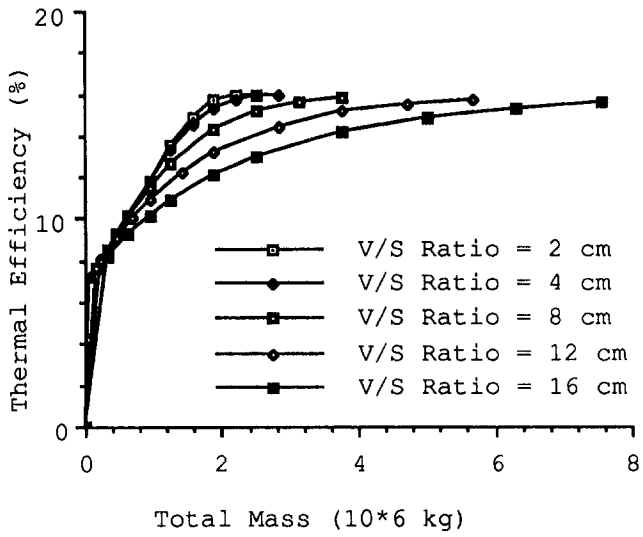

Fig. 4 Thermal efficiency versus thermal storage design

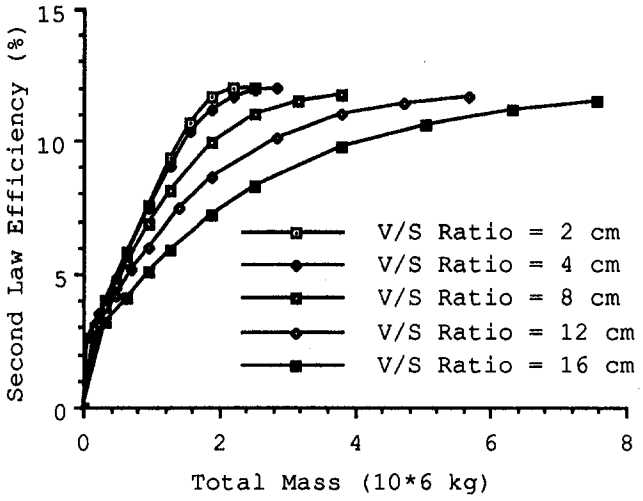

Fig. 5 Second-law efficiency versus thermal storage design

boiling and condensation. Also, it is assumed that the cost of fabrication and material is linear with the total mass of the thermal storage and does not depend on the configuration.

The results of the analysis show that the first-law efficiency, second-law efficiency, and net present worth are functions of two parameters. The first is the volume-to-surface area ratio, v/s. The second parameter is the total mass of the material as illustrated by Figs. 3, 4, and 5. The v/s ratio in effect is the thickness of the slab. Once the v/s ratio is specified, the total mass becomes related to the surface area. The low thermal conductivity of concrete is what makes the v/s ratio a significant parameter, which should be made as small as possible. Scaling effects of the lumped heat transfer coefficient (which is a function of thermal conductivity), the steam flow rate, and the duration of the charging and discharging periods can all be related to these two parameters through the governing Eqs. (4) and (5). For example, nondimensional analysis of the governing equations reveals two nondimensional parameters (Hausen, 1950). The first one is the reduced period, Π ($\Pi = UAP/M_mC_m$) which is directly related to the v/s ratio. The second one is the reduced length, Λ ($\Lambda = UA/m_fC_f$), which is related to the total mass for a given v/s ratio. So long as these dimensionless groups are maintained constant, performance would be unchanged to the present approximation. The accuracy of the results depends on the validity of the lumped heat transfer approach used in the analysis together with the assumption that the steam-side heat transfer coefficient is infinitely large. Considerably more computer time will be required to remove these assumptions, which cannot be justified considering the uncertainties in many thermal and economic parameters.

Results of the analysis also show that it is economically feasible to store the energy content of the excess steam and there is an optimum size of the thermal storage for the minimum possible (constructionwise) v/s ratio. However, the analysis does not consider the fact that the fabrication cost increases with decreasing v/s ratio, which suggests that the optimum design may be at somewhat larger v/s ratio than the minimum possible, and that these results are more reliable for large values of v/s ratio than for small ones. Effect of pressure drop on the results is insignificant. The thermal efficiency levels at about 15 percent and the second law efficiency at about 12 percent. Incidentally, these low levels suggest that it is not beneficial to store the energy content of steam for use in electrical power production to take advantage of the difference between the peak and off-peak electrical rates since the ratio of prices is about 2.

However, it does appear economically feasible to store the energy content of excess steam not needed for process, and recover it later.

References

Abdul-Razzak, H., 1988, "Thermoeconomic Analysis of Cogenerated Refuse Energy Recovery Plant With Thermal Storage," Ph.D. Dissertation, Department of Mechanical Engineering, Illinois Institute of Technology, Chicago, IL.

Bruderle, T. P., 1980, *An Executive Summary of National Energy Act Legislation,* National Society of Professional Engineers, Washington, DC.

Fraas, A. P., 1982, *Engineering Evaluation of Energy Systems,* McGraw-Hill, New York.

Gilli, P. V., and Beckman, G., 1974, "The Nuclear Storage Plant—An Economic Method of Peak Power Generation," Ninth World Energy Conference, Detroit, MI, Paper No. 4.1.10.

Harman, C. M., and Lorsch, S., 1985, "Energy Storage Using Low Pressure Feedwater," ASME JOURNAL OF ENGINEERING FOR GAS TURBINES AND POWER, Vol. 107, pp. 569–573.

Hausen, H., 1938, "Berechnung der Steintemperature in Winderhitzern," *Eisenuttwes.,* Vol. 10, pp. 474–480.

Hausen, H., 1950, *Warmeubertragung im Ggegenstrom, Gleichstrom und Kreuzstrom,* Springer-Verlag, Berlin.

Kandula, M., Chaudhary, Z., and Porter, R., 1983, "Cogenerated Energy Recovery From Modular Refuse Incinerators," *Heat Recovery Systems,* Vol. 3, No. 3, pp. 203–215.

Lorsch, H. G., Kauffman, K. W., and Denton, J. C., 1976, "Thermal Energy Storage for Heating and Air Conditioning," *Further Energy Production Systems,* Vol. 1, p. 69, Academic Press, New York.

Schmidt, F. W., and Willmott, A. J., 1983, *Thermal Energy Storage and Regeneration,* McGraw-Hill, New York.